EUSKAL HERRIKO UNIBERTSITATEA
THE UNIVERSITY OF THE BASQUE COUNTRY

Departamento de Polímeros y Materiales Avanzados: Física, Química y Tecnología

Photon statistics and entanglement from two interacting quantum emitters

Thesis by

Adrián Juan Delgado

Supervised by

Prof. Javier Aizpurua Iriazabal

and

Dr. Rubén Esteban Llorente

Donostia-San Sebastián, June 2025

Financial support statement

This PhD thesis has been developed thanks to the following financial support:

- PhD Grant PRE2020-095013 funded by MICIU/AEI/10.13039/501100011033 and by "ESF Investing in your future".
- Projects PID2022-139579NB-I00 and PID2019-107432GB-I00 funded by MICIU/AEI/10.13039/ 501100011033 and by ERDF/EU.
- Project IT 1526-22 funded by the Department of Education, Research and Universities of the Basque Government.
- Laboratory for Transborder Cooperation LTC TRANS-LIGHT from University of the Basque Country and University of Bordeaux.
- CSIC Research Platform PTI-001 (project 20219PT023).

I also acknowledge the Centro de Física de Materiales (CFM-MPC) for hosting me during my PhD and for providing technical and administrative support.

A mi abuela Catalina
y a mi abuelo Melchor

ACKNOWLEDGMENTS

"Gracias a la vida que me ha dado tanto.
Me dio el corazón que agita su marco
cuando miro el fruto del cerebro humano,
cuando miro el bueno tan lejos del malo"
- Violeta Parra.

En septiembre de 2020 acabé el Máster en Ciencia y Tecnología Cuánticas en Leioa. Sin tener del todo claro qué hacer, me matriculé en el máster de educación en Jaén. Unas semanas después, mientras revisaba el correo de la UPV/EHU no recuerdo muy bien por qué, encontré una oferta de doctorado en Donosti. Como hablaba de un proyecto relacionado con sistemas cuánticos abiertos y otros temas que me llamaban la atención, decidí aplicar. Lo hice sin darle muchas vueltas porque pensaba que no me cogerían y que, si lo hacían, siempre habría tiempo de decidir más tarde. Después de alguna entrevista con Javi y Rubén, me acabaron cogiendo. Acepté. Nunca llegué a asistir a ninguna clase del máster de educación, aunque probablemente hubiera sido también una buena decisión, ya que la vida me hubiera llevado por otro camino, hubiera desarrollado otras habilidades y conocido a otra gente. Pero, sin duda, me hace muy feliz haber decidido venir a Donosti, porque me ha conducido a conocer a personas maravillosas. Aprovecho estas páginas para darles las gracias a ellas y a las que me han acompañado siempre.

En primer lugar, me gustaría dar las gracias a **Javi** y a **Rubén**. Gracias por haberme dado la oportunidad de vivir esta experiencia. Rubén, gracias por estar siempre disponible para charlar. He aprendido mucho con todas las conversaciones que hemos tenido, especialmente aquellas que se alargaban y se alargaban, aunque fuera discutiendo sobre el sexo de los ángeles. Ha sido muy inspirador trabajar contigo; eres una fuente inagotable de ideas. Javi, gracias por involucrarme en proyectos tan fascinantes y por todas las conversaciones a lo largo de estos años. Me has enseñado que ser resolutivo y perfeccionista pueden ir de la mano, o al menos llegar a un buen balance. Gracias a los dos por la confianza y la autonomía que me habéis dado, y por valorar siempre tan positivamente mi trabajo.

Moreover, I am deeply grateful to the Bordeaux Nanophotonics Group, led by **Brahim Lounis**. The core of this thesis lies in the analysis of light emission from interacting quantum emitters and is inspired by the amazing experiments they performed in 2022 [1]. Brahim, thank you so much for the many enriching conversations; I have learned a lot from you. **Jean-Baptiste**, thank you for your

friendliness and all the time you spent discussing physics with me whenever I needed it. It has been a real pleasure working with you. I would also like to thank both of you for the great time I had in Bordeaux during the research stay in 2023.

Furthermore, the results discussed in Chapter 5 of this thesis stem from a collaboration with **Géza Giedke**. I am also very grateful for everything I learned from you, Géza.

Additionally, during the course of this thesis, I had the opportunity to do a research stay in Lausanne, visiting the Laboratory of Quantum and Nano-Optics led by **Christophe Galland**. Thanks for your hospitality and kindness, Christophe. It was truly a great experience to visit your group and have the chance to discuss with you.

I have also had the opportunity to work with many other wonderful people over the years. I spent a lot of time working with **Lukas Jakob** on molecular optomechanics. Lukas, thanks for your kindness, it was a real pleasure, and I wish you all the best. I also teamed up with **Sofia Ribeiro**, working on photon correlations from thermal vapors. That was such a great experience, thank you very much, Sofia. Further, I had the opportunity to collaborate with **Rémi Avriller** in connection with Chapter 4 of this thesis. Thanks for all the insightful discussions, Rémi.

I also had the chance to discuss physics with some other inspiring people, from whom I learned a lot. One of them is **Mikolaj Schmidt**. It was really insightful to meet you and discuss my projects and physics in general, Mikolaj. Thanks also for the careful reading you did of this thesis and your helpful feedback. También tuve la suerte de conocer a **Alejandro González Tudela**. Gracias por tu amabilidad y por el interés en discutir sobre mis proyectos durante tus visitas veraniegas al DIPC.

Además, me gustaría agradecer a todos los miembros del **Theory of Nanophotonics Group** en el que he desarrollado esta tesis. **Jonathan**, contigo empecé esta experiencia en diciembre de 2020. Muchos han sido los viajes que hemos compartido (París, Newry-Boston, Milán, Benasque, ...). Muchas gracias por todo, guacho. **Bruno**, ha sido también un gustazo compartir todos estos años contigo, eres un tío generoso como pocos, ¡te deseo lo mejor! **Rober**, contigo llegué hasta a compartir piso, aunque fuera solo unos pocos meses. Fue suficiente para comprobar que eres de una calidad humana brutal. Gracias por saber siempre animar y por todos los consejos. **Mario**, ¡qué placer haberte conocido! Gracias por tantas conversaciones, parcero. Y gracias por la ayuda con COMSOL al principio del doctorado. **Xabi**, gracias a ti también por todos estos años, espero que te vaya todo fenomenal. Thanks also to **Unai**, **Aurelian**, and **Nikos**, it has been also a pleasure to share these years with you.

Estos años también han sido bastantes más bonitos y agradables gracias a mucha gente del CFM y del DIPC. **Martín**, **Iker**, **Teresa**, **Dani López**, **Marian**, **Josu**, **María**, **Txemikel**, **Sebas**, **Cris Mier**, **Raulillo**, y tantos otros: gracias por todo.

En lo que queda, estos agradecimientos pasan a ser un poco más cursis:

- Para **Carlos Maciel**:
  Hola, Carlitos. Compañero de primera, segunda y hasta tercera jornada. Muchas gracias por ayudarme tantas veces con cualquier duda de COMSOL o Mathematica, con integrales complejas o con lo que hiciera falta. Gracias también por todos los consejos, por las tardes de natación y por todas las conversaciones de la vida en general, cualquier charla contigo es de lo más enriquecedora. ¡Qué buen compañero de viaje has sido!

- Para **Álvaro Nodar**:
  Hola, Álvaro. Mi maestro de las correlaciones y el mejor fisio del CFM (y eso que hay muy buenos fisios según las reseñas de Google). Qué bueno fue poder discutir contigo cualquier cosa que se me pasaba por la cabeza, y cuánto lo eché de menos cuando te marchaste. Gracias también por todos los ratos fuera del CFM, ¡espero que los compartamos muchos años más!

- Para **Antton Babaze**:
  Hola, Antton. Qué buenas plantillas tienes para todo, incluida esta plantilla de tesis. Muchas gracias por estar siempre con ganas de escuchar y charlar de lo que fuera. Qué pena que en todos estos años solo te viera dos o tres veces por la oficina ;). Espero que sigas disfrutando de la vida igual que lo haces de un buen tomate.

- Para **Benjamin Tirado**:
  Hola, Benji. ¡Cuánta falta hacía que vinieras a revolucionar el gallinero! No he podido tener un mejor compañero de despacho en esta última etapa. Hasta en los días en que estaba con peor ánimo me has hecho hartar a reír, y eso es impagable. ¡Te mereces lo mejor del mundo!

- Para **Isabel Pascual**:
  Hola, Isa. No sabes cuánto me alegra que vinieras a Donosti y decidieras quedarte. Qué buena compañía eres, sea en informática, en el indio, en el paparazzi, o en un group meeting. Espero que te vaya todo super bien, te lo mereces. Aquí tienes un amigo para lo que necesites.

- Para **Carmen González**:
  Hola, Carmen, mi ggggggggguapa. Qué alegría me contagias siempre y qué bien nos lo pasamos juntos. Ojalá haber podido disfrutar contigo mucho más tiempo en Donosti. Menos mal que el bueno de **Julen** hace que vuelvas de vez en cuando y podamos seguir disfrutando de vosotros. Por cierto, tenemos que volver a ir a la ópera.

- Para **Miguel Ángel Jiménez**:
  Hola, Miguel Ángel. Hace mucho, mucho, mucho tiempo perdí la cuenta de cuantos indios, coreanos, paparazzis, sustrais, zabaletas, katas, etc., llevamos. No sabes lo afortunado que me siento de poder haber compartido durante

todo este tiempo al menos un ratito cada semana cenando contigo y con quien más se animara (aunque tú y yo sabemos que menos es más). Gracias por todo. Te mereces todos los caballeros del zodiaco del mundo.

- Para **Anne San Román** y **Jon I. Quintana**:
  Hola, Anne. Me acuerdo que te conocí el día de la sidrería aquella en la que casi nos matamos en el autobús que se quedó atascado en la cuesta. Ibas con el gorrito de cumpleaños en la cabeza engañando a todo el mundo. Ahí ya me di cuenta que eras una máquina y que quería hacerme tu amigo. Gracias a ti y JonI por hacer estos años más bonitos y por ser los mejores anfitriones.

- Para **Alina Díez**:
  Hola, Alina. Me alegro mucho de haber encontrado una persona como tú en este camino. Compartir piso contigo ha hecho todo mucho más fácil. Gracias por todos los ratos viendo series chorra, por los domingos de arroz, los bizcochos con hilitos, los panes con plátano, y los mojitos en verano. Te deseo que seas muy feliz y que rías muy alto.

- Para **Erlaitz Pinedo**:
  Hola, Erlaitz. Quiero que sepas que me pareces una persona de lo más auténtica. Me encanta el poco filtro que tienes y tu sentido del humor. Contigo me lo paso bien haciendo cualquier absurda cosa, sea yendo al monte un día lluvioso, al debate del Conquis o recibiendo una visita de María. Gracias también por ser mi estilista personal. ¡Eskerrik asko! (Euskera total).

- Para **David Subires**:
  Hola, David. Hace más de una década que somos amigos. Quién nos iba a decir el primer día de clase en la carrera que acabaríamos viviendo juntos en Granada y en Bilbao, o que nos animaríamos a ir a Donosti a hacer un doctorado. Gracias, por todos estos años, sin duda han sido mucho mejores gracias a ti. Espero que te vaya todo genial, te lo mereces mucho, ¡y espero que yo esté ahí para seguir viéndolo!

- Para **Jorge Olmos**:
  Hola, Jorge. No sé cómo agradecerte todo lo que me has ayudado estos años. Quizás pueda empezar por agradecerte el intento diario de sacarme pronto del CFM para ir a nadar o a tomar algo cuando estabas en Donosti, aunque casi siempre ganara yo y nos fueramos bastante tarde. Gracias también por estar tan presente después de irte de Donosti, llamándome o escribiéndome a menudo, o viajando con la excusa que fuera para poder vernos. Te admiro y aprendo mucho de ti, y espero seguir haciéndolo siempre. Un abrazo enorme, lombriz.

- Para **Cristina Sanz**:
  Hola, Cris. Aún sigo sin entender por qué pensabas que no me caías bien al principio, con lo bien que nos entendemos tú y yo. Que alegría que Jorge te convenciese que no era así, porque no puedo pasarmelo mejor contigo.

Gracias por todas las visitas, fuera en Donosti, en Benasque, o incluso en Lausanne, y por el cariño con el que me tratas. Que sepas que a tí también te admiro y te quiero mucho. Atentamente, uno de tus guardaespaldas.

- Para **Ladilla Rusa**:
  Hola, equipo. Todos estos años han sido mucho más bonitos gracias a vosotras. Los viajes y los ratitos con vosotras han sido siempre un chute de felicidad. **Andrea**, gracias por ser tan genuinamente única, tan genuinamente tú, y por demostrarme tanto aprecio. **Irene**, gracias por ser tan generosa y tan buena, ojalá en el mundo hubiese más personas como tú. **Itzi**, gracias por todo lo que me has ayudado estos años, por todo lo que me has hecho reír y por intentar entender todos mis chistes malos, creo que eres probablemente la persona que más atención les pone. **Alicia**, gracias por todos los viajes que te has dado para que pudieramos echar un ratito juntas, eres genial. Os quiero mucho, amigas. Estoy deseando vivir mil momentos más con vosotras.

- Para mis **amigos de Úbeda**:
  Hola, **Alberto**, **Carlos**, **Dani**, **David**, **Iván**, **Jesús**, **Mari**, **Rafa**. Gracias por ser una constante en mi vida. Si tuviera que describir todo lo que me habéis aportado y ayudado desde que eramos unos críos, necesitaría otras trescientas páginas más. Así que me limito a daros las gracias por ser un apoyo incodicional estos años y una fuente de alegría y felicidad. Gracias también por restarle importancia a que a veces (muchas veces) se me olvide responder al whatsApp o llamaros más, ¡bendita paciencia tenéis! Estoy muy orgulloso de ser vuestro amigo. Os quiero mucho y brindo por todo lo que nos queda por vivir.

- Para mi **familia**:
  Hola, **papá**, **mamá**, **hermano**. Esta es, sin ninguna duda, la parte más complicada de esta tesis. Cualquier ecuación o gráfica que veáis en todas estas páginas es infinitamente más sencilla que poder reflejar con palabras lo afortunado que me siento por tener unos padres y un hermano como vosotros. Gracias por todo lo que me habéis cuidado, por el amor y apoyo que me habéis dado siempre. Todo lo que pueda conseguir en esta vida es y será, en su mayor parte, gracias a vosotros y lo que me habéis enseñado. Gracias por todas las videollamadas estos años, que me han hecho sentirme muy cerca de vosotros. Gracias por haber cuidado tan bien del abuelo. Os quiero mucho.

  Lina, no puedo tener una cuñada mejor. Siempre lo haces todo muy sencillo. Gracias por ser cómo eres. Estoy seguro que vas a ser una mamá estupenda. **Raúl**, gracias por ser un hermano mayor más. **Mariela**, gracias por aparecer en nuestras vidas y por ser la mejor compañera de juegos. Gracias también a mi tía **Ana** por haberme cuidado siempre. Y gracias en general a toda mi familia, a mis tíos, mis primas y mis primos. Soy muy afortunado de teneros.

  Agradezco a la vida por haberme dado a mi abuelo **Melchor** y a mi abuela **Catalina**. Ellos también han sido fundamentales para el desarrollo de mi persona. Si algo pudiera pedir, sería parecerme un poco más a ellos.

Por último, gracias a todos los que intentan hacer de este mundo un lugar más justo o, como decían *La Cabra Mecánica* y María Jiménez, "más amable, más humano y menos raro".

Donostia. Junio de 2025.

Adrián Juan Delgado.

RESUMEN

La interacción entre el campo de vacío electromagnético y un emisor cuántico de dos niveles constituye uno de los ejemplos canónicos de interacción cuántica entre luz y materia. El análisis de esta interacción permite comprender conceptos fundamentales en óptica cuántica como, por ejemplo, la emisión espontánea de fotones por parte del emisor. Asimismo, este análisis revela que un emisor cuántico de dos niveles no puede emitir más de un fotón simultáneamente, lo que puede permitir manipular de forma precisa el estado cuántico de la luz fotón a fotón. Este hecho hace que los emisores cuánticos sean candidatos muy adecuados para el desarrollo de fuentes de luz cuántica, capaces de generar luz en estados cuánticos específicos y con correlaciones cuánticas. En particular, las fuentes de fotones individuales presentan aplicaciones relevantes en campos como la comunicación y la computación cuánticas, razón por la que los emisores cuánticos aislados han sido objeto de una intensa atención durante las últimas décadas. Además, la interacción entre varios de estos emisores posibilita nuevas oportunidades para la manipulación de estados cuánticos de la luz, ya que esta interacción modifica los niveles de energía, tiempos de vida y acoplamientos a campos externos de los emisores. Esta fenomenología hace que la radiación de luz pueda volverse más compleja y sorprendente. Si a esto le sumamos los recientes avances experimentales en el control del acoplamiento entre emisores cuánticos, el desarrollo de un análisis teórico exhaustivo de la radiación de estos sistemas resulta especialmente oportuno. Por todo ello, en esta tesis se desarrolla un estudio teórico de la radiación de luz por parte de dos emisores cuánticos acoplados, con lo que se pretende conseguir dos objetivos principales: profundizar en la comprensión fundamental de esta radiación, y explorar el potencial de estos emisores acoplados como fuente de luz cuántica para aplicaciones tecnológicas.

En el capítulo 1, se realiza una descripción detallada de la cuantización del campo electromagnético, tanto en ausencia como en presencia de fuentes de radiación. Para ello, se adopta un formalismo de segunda cuantización y se deriva el Hamiltoniano estándar que describe la interacción entre el campo de vacío electromagnético y un emisor cuántico de dos niveles. Este formalismo permite introducir los fotones como excitaciones fundamentales del campo electromagnético, así como analizar de forma rigurosa la influencia del vacío cuántico sobre los emisores. Por ejemplo, en este capítulo se presta especial atención a la descripción del fenómeno de la emisión espontánea de fotones por parte de un emisor. Para ello, se adoptan dos

métodos alternativos: la aproximación de Wigner-Weisskopf y la ecuación maestra markoviana. Por un lado, la aproximación de Wigner-Weisskopf permite derivar la dinámica conjunta del emisor y del campo electromagnético, partiendo de un estado inicial específico. Considerando que el emisor se encuentra inicialmente excitado, se demuestra que la probabilidad de que continúe en el estado excitado decae exponencialmente en el tiempo. Este decaimiento va acompañado por la excitación de los modos del campo electromagnético de vacío con diferentes probabilidades, lo que corresponde a la emisión espontánea de un fotón. Por otro lado, la ecuación maestra markoviana se basa en eliminar los grados de libertad de un subsistema que, de esta manera, puede ser tratado como ambiente externo. De esta forma, considerando al campo electromagnético de vacío como el ambiente del emisor, se puede obtener una descripción de la dinámica del emisor directamente en su espacio de Hilbert, la cual también captura el fenómeno de la emisión espontánea. Aunque la ecuación maestra markoviana no proporciona información sobre qué modos específicos del campo electromagnético se excitan (ya que se han eliminado de la descripción), este método simplifica notablemente la resolución de la dinámica del emisor, así como la descripción de su interacción con un láser. Usando esta ecuación maestra, se examina cómo el láser puede modificar los niveles de energía y los autoestados del emisor.

En el capítulo 2, se presenta una introducción a las funciones de correlación del campo eléctrico, que sirven para cuantificar el grado de coherencia óptica y, por tanto, son esenciales para caracterizar las fuentes de luz cuántica. Se comienza describiendo el experimento de interferencia de Young, en el cual la luz emitida por dos fuentes puede producir un patrón de interferencia de franjas sobre una pantalla. La aparición de este patrón depende del grado de coherencia de primer orden de la luz, cuantificado por la función de correlación de primer orden. A continuación, se introduce la función de correlación de segundo orden, también conocida como correlación de intensidad, que juega un papel crucial en esta tesis. Esta función mide la correlación en la intensidad de la luz que llega a dos detectores, lo que proporciona información adicional sobre la estadística de la emisión de la fuente de luz. Más concretamente, la correlación de intensidad nos permite distinguir entre tres tipos cualitativamente diferentes de estadística de emisión: (i) fuente de luz coherente, en la que la emisión de un fotón es completamente independiente de los procesos de emisión previos, como es el caso de la luz emitida por un láser; (ii) fuente de luz agrupada (*bunched light*, en inglés), caracterizada por una mayor probabilidad de emitir dos fotones dentro de un intervalo de tiempo corto en comparación con la luz coherente; y (iii) fuente de luz desagrupada (*antibunched light*, en inglés), en cuyo caso esta probabilidad es menor que la de la luz coherente, reflejando un comportamiento puramente cuántico. Cabe destacar el interés de analizar tanto la correlación de intensidad de todos los fotones emitidos por la fuente como la correlación de intensidad de fotones de frecuencias específicas. Esta última, denominada correlación de intensidad resuelta en frecuencia, puede medirse con la ayuda de filtros ópticos. Para ilustrar las correlaciones de intensidad, se analiza el caso de un emisor cuántico aislado (es decir, que no interactúa con otros emisores cuánticos). Por un lado, la correlación de intensidad que tiene en cuenta

todos los fotones emitidos por el emisor revela que la probabilidad de detectar dos fotones simultáneamente es nula, confirmando que los emisores cuánticos aislados se comportan como fuentes ideales de fotones individuales. Por otro lado, la correlación de intensidad resuelta en frecuencia proporciona información sobre los mecanismos de emisión del sistema, capturando en su descripción tanto las transiciones de un fotón, que suelen ser reveladas también por el espectro de emisión estándar, como otras transiciones menos obvias de dos fotones a través de estados virtuales intermedios.

En el capítulo 3, se aborda el estudio del sistema de principal interés en esta tesis: dos emisores cuánticos acoplados. Para ello, primero se presenta una derivación detallada del Hamiltoniano que describe la interacción entre el campo electromagnético de vacío y dos emisores cuánticos de dos niveles. A continuación, se eliminan los grados de libertad electromagnéticos y se obtiene una ecuación maestra que gobierna la dinámica de los dos emisores. Además de capturar la emisión espontánea de cada emisor, esta ecuación maestra revela que el campo electromagnético de vacío puede mediar una interacción dipolo-dipolo entre emisores cuánticos que están separados por distancias pequeñas en comparación con la longitud de onda característica de la luz. Se desarrolla también una modificación efectiva de esta ecuación maestra para tener en cuenta la influencia de los modos vibracionales internos de los emisores y de los modos fonónicos del medio que rodea a los emisores. Estos modos pueden jugar un papel relevante en el caso de emisores de estado sólido. Bajo esta descripción efectiva, los emisores siguen siendo modelados como sistemas de dos niveles, pero el acoplamiento dipolo-dipolo se renormaliza mediante el factor combinado de Debye-Waller/Franck-Condon. Dicho factor se corresponde con la fracción de fotones emitidos desde el estado electrónico excitado al estado electrónico fundamental (sin asistencia de niveles vibracionales o fonónicos), transición que se conoce como Línea de Cero Fonones. Esta descripción efectiva resulta muy útil para describir la emisión de luz en la Línea de Cero Fonones.

A continuación, se describe cómo el acoplamiento entre los emisores puede modificar los autoestados del sistema. En particular, el acoplamiento puede dar lugar a estados híbridos en los que una excitación está deslocalizada entre ambos emisores. Estos estados híbridos tienen energías y tiempos de vida modificados respecto al caso de los emisores desacoplados, así como diferentes fuerzas de acoplamiento a la iluminación externa. Por ejemplo, cuando los momentos dipolares de transición de los emisores no son ortogonales, uno de los estados deslocalizados decae más rápidamente que el otro. El estado con decaimiento más rápido se conoce como estado superradiante, mientras que el estado con decaimiento más lento se conoce como estado subradiante. Se muestra también que el factor combinado de Debye-Waller/Franck-Condon puede influir de manera significativa en los tiempos de vida de estos estados, lo que pone de manifiesto la necesidad de considerar este factor en la descripción de los emisores de estado sólido acoplados. La aparición de los estados híbridos puede dar lugar a nuevas posibilidades para la manipulación de estados cuánticos de la luz, así como para la generación de fotones con correlaciones cuánticas. Para explorar estas posibilidades, se analizan en primer lugar las

correlaciones de intensidad de los fotones emitidos por el sistema acoplado, lo que permite una mejor caracterización de las propiedades estadísticas de la emisión, y posteriormente se examina la generación de fotones que exhiben correlaciones cuánticas no locales, lo que se conoce como entrelazamiento fotónico, y juega un papel clave en diversas aplicaciones de las tecnologías cuánticas.

En este capítulo, se lleva a cabo un análisis sistemático de las correlaciones de intensidad de los fotones emitidos en la Línea de Cero Fonones. Para ello, se considera el caso en el que los emisores tienen momentos dipolares de transición paralelos y están separados por una distancia muy pequeña, lo que da lugar a la formación de un estados superradiante y un estado subradiante. De esta manera, se encuentra que la correlación de intensidad que no distingue en la frecuencia de emisión puede tomar valores muy distintos, dependiendo de la frecuencia y la intensidad del láser. En concreto, se muestra que cuando la frecuencia del láser es igual a la de la transición del estado superradiante, los emisores acoplados se comportan efectivamente como un único emisor de dos niveles, generando fotones en la Línea de Cero Fonones de forma individual (es decir, el sistema acoplado emite *antibunched light*). En cambio, cuando la frecuencia del láser es igual a la mitad de la frecuencia de transición entre el estado fundamental y el estado doblemente excitado, lo que se conoce como resonancia de dos fotones, la probabilidad de emitir fotones agrupados aumenta considerablemente con respecto a la luz coherente (es decir, el sistema acoplado emite *bunched light*). Curiosamente, el comportamiento de esta correlación de intensidad se vuelve mucho más complejo cuando la frecuencia del láser es la de la frecuencia de transición del estado subradiante, lo que se debe a una influencia significativa de la coherencia cuántica entre los estados superradiante y subradiante en este caso. Finalmente, en este capítulo se analiza la correlación de intensidad resuelta en frecuencia también en función de la frecuencia e intensidad del láser. Este análisis revela un panorama muy rico de mecanismos de emisión del sistema estudiado, incluyendo una amplia variedad de transiciones de dos fotones mediadas por estados virtuales intermedios. Por ejemplo, se encuentra que cuando la frecuencia del láser coincide con la de la transición del estado subradiante, la correlación de intensidad resuelta en frecuencia puede identificar transiciones de un fotón que permanecen ocultas en el espectro de emisión estándar debido a que ocurren con una probabilidad extremadamente baja. Esto demuestra la mayor sensibilidad de la correlación de intensidad resuelta en frecuencia, en comparación con el espectro de emisión a la hora de revelar transiciones que ocurren con una probabilidad muy baja.

Con el objetivo de ampliar la caracterización de la estadística de la luz emitida por dos emisores cuánticos acoplados, en el capítulo 4 se analiza la correlación de los fotones emitidos debido al decaimiento desde el estado electrónico excitado a un nivel vibracional/fonónico en el estado electrónico fundamental. Estos fotones, que son de menor energía que aquellos emitidos en la Línea de Cero Fonones, se conocen como fotones Stokes. El desarrollo de un modelo que describa de forma precisa la correlación de fotones Stokes es particularmente relevante para entender muchos de los típicos experimentos de fluorescencia, en los que los emisores son excitados en resonancia al estado excitado y, además, se utilizan filtros ópticos

para evitar la detección de los fotones del láser (que de otro modo perturbarían la caracterización de la luz radiada por los emisores). Con el objetivo de desarrollar tal modelo, en este capítulo se refina la descripción de la estructura energética de los emisores incluyendo estados adicionales para cada emisor, que corresponden a niveles vibracionales o fonónicos en el estado electrónico fundamental. Este modelo refinado permite abordar tanto la correlación de fotones emitidos en la Línea de Cero Fonones (con resultados que coinciden con los de la descripción basada en sistemas de dos niveles), como la correlación de fotones Stokes. Es importante destacar que este modelo refinado captura el papel de la coherencia cuántica en la emisión de fotones Stokes, cuya influencia ha sido desestimada en modelos previos en la literatura. Usando este nuevo modelo, se analizan las correlaciones de los fotones Stokes radiados por dos emisores acoplados con momentos dipolares paralelos y separados por distancias nanométricas. De esta forma, se demuestra que la coherencia cuántica puede jugar un papel significativo en la emisión de fotones Stokes. Los hallazgos teóricos de este capítulo están respaldados por los resultados de las mediciones experimentales realizadas por el Bordeaux Nanophotonics Group, dirigido por Brahim Lounis, en el Institut d'Optique Graduate School (CNRS). También se analiza el caso de dos emisores lejanos, no acoplados, y se muestra que la coherencia cuántica puede modificar también en este caso la estadística de emisión de fotones Stokes. Este análisis ayuda, además, a clarificar la discrepancia entre las predicciones teóricas y las observaciones experimentales sobre la correlación de fotones radiados simultáneamente por dos emisores independientes. Finalmente, se realiza una comparación de la correlación de los fotones Stokes radiados por dos emisores acoplados con la de los fotones radiados en la Línea de Cero Fonones, demostrando que estas dos correlaciones pueden ser drásticamente diferentes, lo que pone de relieve la importancia de desarrollar una descripción teórica detallada y adaptada a cada configuración experimental.

Finalmente, en el capítulo 5 se investiga el uso de emisores cuánticos acoplados como fuente de fotones entrelazados, destacando el potencial de estos sistemas para manipular los estados cuánticos de la luz y generar correlaciones cuánticas de fotones. Para ello, se proporciona una introducción al concepto de entrelazamiento, así como a diferentes métodos que sirven para cuantificar el grado de entrelazamiento de dos fotones. A continuación, se aplica la aproximación de Wigner-Weisskopf para derivar el estado cuántico completo del campo electromagnético obtenido tras la relajación de dos emisores inicialmente excitados. El estado de dos fotones obtenido mediante la aplicación de esta aproximación permite el cálculo de las probabilidades de emisión de dos fotones en direcciones, frecuencias y modos de polarización arbitrarios. Tras esta introducción se aborda el caso en el que los emisores tienen momentos dipolares de transición perpendiculares y están separados entre sí por distancias cortas, de tal forma que presentan una clara interacción. Se demuestra de esta manera que un estado de dos fotones altamente entrelazados puede ser postseleccionado a partir de la radiación de estos dos emisores usando filtros ópticos. El grado de entrelazamiento fotónico permanece en gran medida inalterado por pequeñas variaciones en la orientación relativa de los momentos dipolares, así como por cambios en el valor del factor combinado de Debye-Waller/Franck-Condon.

Finalmente, se verifica que el estado postseleccionado de dos fotones tampoco se ve significativamente afectado por pequeños cambios en la dirección de detección, lo que sugiere que las lentes ópticas comunes pueden ser utilizadas en la práctica para mejorar la recolección de estos fotones sin reducir notablemente el grado de entrelazamiento fotónico.

En resumen, los resultados presentados en esta tesis profundizan en la comprensión fundamental de la radiación de luz de dos emisores cuánticos acoplados, con especial atención a las correlaciones fotónicas, incluyendo tanto las correlaciones fotónicas de segundo orden (correlaciones de intensidad) como las correlaciones cuánticas no locales (entrelazamiento fotónico). Por ende, estos resultados revelan la gran versatilidad que presentan los emisores cuánticos acoplados como fuentes de luz cuántica. Tal y como se analiza en esta tesis, estos sistemas podrían generar tanto pares de fotones entrelazados como fotones individuales, dependiendo de la configuración específica de los emisores y de las condiciones de iluminación. Por todo ello, este trabajo permite identificar el gran potencial de los emisores cuánticos acoplados para el desarrollo de un amplio abanico de aplicaciones en tecnologías cuánticas.

Contents

Appendices

ABSTRACT

The interaction between the electromagnetic vacuum field and a two-level quantum emitter represents one of the fundamental cases of quantized light-matter interaction. The analysis of this interaction enables the understanding of essential concepts in quantum optics, such as the spontaneous emission of photons from the emitter. Additionally, this analysis reveals that a two-level quantum emitter cannot emit more than one photon at a time, which allows for manipulating light at the single-photon level. This degree of control makes quantum emitters promising candidates for the development of quantum light sources that generate photons in specific quantum states and with non-classical correlations. For example, single-photon sources find applications in quantum communication and quantum computing, which have motivated extensive research on light emission from isolated two-level quantum emitters over the last decades. Moreover, the energy levels, lifetimes, and coupling strengths to external fields of the quantum emitters can be modified when they interact with each other. In this case, light emission from this coupled system becomes even more complex, opening up new possibilities for manipulating and engineering non-classical states of light. Additionally, the analysis of light emission from interacting quantum emitters is particularly timely, as experimental control over emitter interactions has advanced significantly in recent years. Taking all this into account, this thesis focuses on the theoretical analysis of light emission from two interacting quantum emitters, with two main objectives: (i) achieving a deeper fundamental understanding and improved characterization of light emission from these coupled systems, and (ii) exploring their potential as sources of quantum light for applications in quantum technologies.

First, a comprehensive review of the quantization of the electromagnetic field, both in the absence and in the presence of radiation sources, is provided. Specifically, a second quantization formalism is adopted and the standard Hamiltonian describing the interaction between the electromagnetic vacuum field and a single two-level quantum emitter is derived. This formalism allows for introducing photons as the fundamental quantum excitations of the electromagnetic field and analyzing how the electromagnetic vacuum field influences quantum emitters. In particular, a thorough description of the spontaneous emission of photons from the emitter is provided. To this end, two alternative approaches are considered: the Wigner-Weisskopf approximation and the Markovian master equation. On the one hand, the Wigner-Weisskopf approximation enables the derivation of the dynamics of the

entire system, including the quantum emitter and all modes of the electromagnetic vacuum field, starting from a given initial state. When the emitter is initially excited, it is shown that the probability of finding the emitter in the excited state decreases exponentially over time. This decay is accompanied by the excitation of the electromagnetic modes of the vacuum field, each with a different probability amplitude, corresponding to the spontaneous emission of a photon. On the other hand, the Markovian master equation relies on tracing out the degrees of freedom of a subsystem that acts as a reservoir. By treating the electromagnetic vacuum field as the reservoir and reducing the description of the system to the Hilbert space of the emitter, it is shown that this approach also captures the phenomenon of spontaneous emission. In this way, information about which electromagnetic modes become excited is sacrified, but the description of the dynamics of the emitter is greatly simplified, and the excitation of the system by a laser can be straightforwardly included. This methodology serves to examine how the laser modifies the energy levels and eigenstates of the emitter, giving rise to the so-called dressed states.

Next, an in-depth introduction to the correlation functions of the electric field is provided. These correlation functions are key for the characterization of quantum light sources, as they quantify the degree of optical coherence in the quantum realm. Young's interference experiment is described, showing how light emitted from two sources can produce an interference pattern of fringes on a screen. The emergence of this pattern depends on the degree of first-order coherence of the light, which is quantified by the first-order correlation function. The second-order correlation, also known as the intensity correlation, is then introduced. This function measures the correlation in the intensity of light arriving at two detectors, and plays a crucial role in this thesis because it provides key information about the statistics of photon emission. More specifically, the intensity correlation allows for distinguishing between three qualitatively different types of light sources: (i) a source of coherent light, in which the emission of each photon is completely independent of previous emissions, as it is the case for laser light; (ii) a source of bunched light, where the probability of emitting two photons within a short time interval is increased compared to a source of coherent light; and (iii) a source of antibunched light, in which this probability is reduced, reflecting a purely non-classical behaviour. One can measure the intensity correlation of all photons emitted from the source, which is referred to as color-blind intensity correlation, or the intensity correlation of photons at specific frequencies by including optical filters, which is called frequency-resolved intensity correlation. To illustrate these concepts, the intensity correlations of light emitted from a single quantum emitter are analyzed. On the one hand, it is shown that the color-blind intensity correlation exhibits perfect antibunching in this case, meaning that the probability of emitting two photons simultaneously is zero and confirming that single quantum emitters serve as ideal single-photon sources. On the other hand, the frequency-resolved intensity correlation provides information about the emission mechanisms of the system, as it nicely captures the one-photon transitions of the system, typically revealed in the standard emission spectrum, as well as the more involved two-photon transitions through virtual

intermediate states.

Next, the analysis of the interaction between two quantum emitters, the system of primary interest in this thesis, is tackled. To this end, a detailed derivation of the Hamiltonian describing the interaction between the electromagnetic vacuum field and the two-level quantum emitters is introduced first. Using the Markovian master equation formalism again, the electromagnetic degrees of freedom are traced out to obtain a master equation that governs the reduced dynamics of the two emitters. In addition to capturing the spontaneous emission of photons from each emitter, this master equation reveals that the electromagnetic vacuum field can mediate the dipole-dipole interaction between two quantum emitters that are separated by small distances compared to the characteristic wavelength of light. An effective modification of this master equation is then developed to account for the influence of internal vibrational modes of the emitters and phonon modes of the host medium, which are relevant for typical solid-state emitters. Within this approach, the emitters are still modeled as two-level systems, but the emitter-emitter coupling rates are effectively renormalized through the so-called combined Debye-Waller/Franck-Condon factor, defined as the fraction of photons emitted from the excited state directly to the purely electronic ground state, known as Zero-Phonon Line. This approach is appropriate when examining light emitted into the Zero-Phonon Line.

Following the analysis above, the modification of the eigenstates of the emitters resulting from the dipole-dipole interaction is described next. In particular, hybrid states can emerge in which a single excitation is delocalized across both emitters. These hybrid states exhibit modified energies and lifetimes compared to the non-interacting case, as well as different coupling strengths to external illumination. For example, when the transition dipole moments of the emitters are not orthogonal, one of the delocalized states decays more rapidly than the other. The faster-decaying state is referred to as the superradiant state, while the slower-decaying one is known as the subradiant state. Additionally, it is shown that the combined Debye-Waller/Franck-Condon factor can significantly influence the decay rates of these delocalized states, highlighting the importance of accounting for this factor in the description of two interacting solid-state emitters.

As the interaction between two emitters leads to hybrid eigenstates, new possibilities for manipulating quantum states of light and generating non-classical photon correlations can emerge from this system. To explore these possibilities, the intensity correlations of photons emitted from the interacting system are analyzed, which helps to better characterize the statistical properties of the emission, and the generation of photons with non-local quantum correlations, which are referred to as photon entanglement and play a key role in quantum technologies, is also examined. In this context, a systematic analysis of both the color-blind and the frequency-resolved intensity correlations of photons emitted into the Zero-Phonon Line is performed. The case in which the emitters have parallel transition dipole moments and are separated by a very short distance is considered, leading to the formation of superradiant and subradiant states. It is found that the color-blind intensity correlation from this system can be tuned across a wide range of values, from

strong antibunching to strong bunching, depending on the frequency and intensity of the excitation laser. Specifically, it is shown that when the laser is tuned to the two-photon resonance (i.e., to half the frequency difference between the ground state and the doubly excited state), the Zero-Phonon-Line emission can become strongly bunched, as the probability of cascade photon emission is enhanced. In contrast, when the laser is tuned to the transition frequency of the superradiant state, the Zero-Phonon-Line emission is generally strongly antibunched, as the system effectively behaves as a two-level emitter, resulting in highly pure single-photon emission. Interestingly, a more complex behaviour emerges when the laser is tuned to the transition frequency of the subradiant state, due to the significant influence of the quantum coherence between the superradiant and subradiant states in such a case. Next, the frequency-resolved intensity correlation is analyzed as a function of both the laser frequency and the laser intensity. This analysis reveals the rich landscape of emission mechanisms in the coupled system, including a variety of two-photon transitions through virtual intermediate states. When the laser is resonantly tuned to the subradiant state, the frequency-resolved intensity correlation unveils one-photon transitions that remain hidden in the standard emission spectrum because they occur with extremely low probability. This highlights the higher sensitivity of the frequency-resolved intensity correlation to reveal transitions that occur with very low probability as compared to the emission spectrum.

With the objective of extending the characterization of the statistics of light emitted from two interacting quantum emitters, the correlation of the photons emitted due to the decay from the electronic excited state to a vibrational/phononic level in the electronic ground state is tackled next. These photons, which are red-shifted compared to the Zero-Phonon-Line photons, are referred to as Stokes-shifted photons. Developing an accurate model of the Stokes-shifted correlation is particularly relevant for describing usual fluorescence experiments, where the emitters are resonantly driven to the excited state and optical filters are used to avoid detection of laser photons that would disturb the characterization of light scattered from the emitters. To this end, the description of the emitters is refined, going beyond the previously shown two-level-system description. This is implemented by including additional states for each emitter representing vibrational or phononic levels in the electronic ground state. This refined model allows for addressing both the Zero-Phonon-Line correlation (with results matching those of the two-level-system description) and, crucially, the Stokes-shifted correlation. Importantly, the refined model captures the role of quantum coherence in the emission of Stokes-shifted photons, whose influence has been neglected in previous models in the literature. Using this new model, the correlation of Stokes-shifted photons is analyzed for two interacting emitters with parallel dipole moments and separated by a very short distance. It is shown that quantum coherence can play a significant role in the emission process of these photons. These theoretical findings are supported by results from experimental measurements performed by the Bordeaux Nanophotonics Group, led by Brahim Lounis, at the Institut d'Optique Graduate School (CNRS). Additionally, two distant, non-interacting emitters are considered, where it is shown that quantum coherence can also influence the photon

statistics in such a case. This analysis helps to clarify the discrepancy between theoretical predictions and experimental observations concerning the correlation of photons emitted simultaneously by two uncorrelated emitters. Finally, a comparison of the correlation of Stokes-shifted photons emitted from two interacting emitters with that of photons emitted into the Zero-Phonon Line is shown. These correlations can differ drastically, stressing the importance of developing a detailed theoretical description particularly tailored to each experimental configuration.

Finally, the use of interacting quantum emitters as a source of entangled photons is investigated, highlighting the potential of this system for the manipulation of quantum states of light and the generation of non-classical photon correlations. To this end, an introduction to the concept of entanglement, as well as to different approaches to quantifying the degree of photon entanglement, is provided. Next, the Wigner-Weisskopf approximation is applied to derive the full quantum state of the electromagnetic field resulting from the relaxation of two initially excited emitters. The two-photon state obtained using this approximation encodes the probabilities of emitting two photons at arbitrary directions, frequencies, and polarization modes. Particular attention is placed on the case where the emitters have perpendicular transition dipole moments and are separated by short distances, so that they can interact. It is demonstrated that a highly entangled two-photon state can be post-selected from the emission of these two emitters using optical filters. The photon entanglement remains largely unaffected by small variations in the relative orientation of the dipole moments, as well as by changes in the value of the combined Debye-Waller/Franck-Condon factor. Finally, it is verified that the two-photon post-selected state is not significantly affected by small variations in the detection direction, suggesting that typical lenses can be used in practice to enhance photon collection without notably reducing the degree of photon entanglement.

Overall, the results developed in this thesis help to deepen the fundamental understanding of light emission from interacting quantum emitters, with a special focus on photon correlations, including both second-order photon correlations (intensity correlations) and quantum non-local photon correlations (entanglement). These results highlight the remarkable versatility of interacting quantum emitters as sources of quantum light. For instance, it is possible to generate either entangled photon pairs or single photons, depending on the specific configuration of the emitters and on the illumination conditions. Therefore, this thesis can help to uncover potential applications of interacting quantum emitters in quantum technologies.

INTRODUCTION

At the heart of this thesis lies the study of light, which refers to any class of electromagnetic radiation[1]. The primary source of light in our daily lives is natural and beyond our control: the Sun. This star governs the Earth's seasons, as well as the cycle of day and night. Throughout history, humans have devised controllable sources of light. The earliest one was fire, which provided both illumination and warmth in caves. Much later, the invention of the light bulb enabled us to illuminate the night using electricity. More recently (in 1905), Albert Einstein posited that light consists of particles, that we now call photons, to explain the photoelectric effect [2]. A few years later, Niels Bohr postulated the quantum nature of atoms and molecules [3–5]. These discoveries marked the beginning of the development of a full quantum theory of the interaction between light and matter, with pioneering contributions by Paul Dirac, Werner Heisenberg and Enrico Fermi, among many others (e.g., see Refs. [6–18]). The understanding of quantized light-matter interaction has led to the development of light-emitting technologies with a high degree of sophistication. Some examples are the laser [19, 20], which produces highly monochromatic and directional light through the process of stimulated emission, and the light-emitting diode (LED) [21–25], which relies on the recombination of electrons with holes in semiconductor materials.

Moreover, in recent decades, the second quantum revolution and the advent of quantum technologies have motivated the development of new sources of quantum light [26–30], capable of emitting photons in well-defined quantum states and exhibiting non-classical correlations. A particularly important type of quantum light source is one that emits photons individually, known as a single-photon source [31]. This type of source is a promising candidate for applications in quantum communication [32–37] and quantum computing [37–40]. Notably, this source should generate identical single photons on demand in order to be practical for many applications [31, 37, 41]. This means that each time a physical system acting as a single-photon source is excited, it should emit exactly one photon, always in the same electromagnetic mode, and that photon should be collected with perfect efficiency. Finding a physical system that meets all these requirements is a significant challenge. For example, parametric down-conversion (PDC) is frequently

[1] The term *light* is sometimes used to refer specifically to electromagnetic radiation within the frequency range detectable by the human eye. In this thesis, this range is termed the *visible range*, and the corresponding radiation as *visible light*.

used to generate single photons, but this generation is not on-demand, which limits its suitability for many applications. More specifically, in PDC, a pump photon interacts with a nonlinear crystal and is converted into two lower-energy photons [42–44], conserving both energy and momentum. As the two photons are emitted in different directions, the detection of one photon can then signal the presence of a single photon in the other direction [45, 46]. However, the conversion of the pump photon into two photons is a statistical process that occurs with low probability.

Quantum systems with only two relevant energy levels, known as two-level quantum emitters, are promising candidates for achieving on-demand single-photon emission. In such two-level systems, the excitation of the upper electronic state is followed by radiative decay to the ground state, resulting in the emission of a single photon. For instance, highly pure and indistinguishable single-photon emission can be obtained from individual alkali atoms in ultra-high vacuum, coupled to an optical cavity that is resonant with an atomic transition [47–49]. Notably, atoms in vacuum are free from internal vibrations and do not couple to environmental phonons. One of the primary drawbacks of such systems lies in the complexity of the required experimental setup. Furthermore, their excited-state lifetimes are on the order of tens of nanoseconds, which limits the achievable photon generation rate. Single photons can also be generated from individual ions confined in radiofrequency traps [50–52]. These are also gas-phase systems and share similar advantages and limitations with alkali atoms.

Quantum emitters that emit on-demand single photons can also be realized from localized electronic states in condensed matter, commonly referred to as solid-state quantum emitters. Examples include organic molecules embedded in crystals [31, 41, 53–55], vacancies or defects in inorganic crystals (such as nitrogen-vacancy centers in diamond [56, 57]), quantum dots (consisting of nanometer-scale regions where a low-band-gap semiconductor is surrounded by a high-band-gap semiconductor, forming a potential well that confines electrons and holes analogously to an atom) [58–60], and defects in two-dimensional materials such as hexagonal boron nitride [61, 62]. In contrast to alkali atoms, solid-state emitters interact with phonon modes of the surrounding material and can also support internal vibrational modes. As a result, these systems may exhibit more complex behaviour than that of a simple two-level system. Indeed, a common challenge arising from these electron-phonon interactions is the broadening of the electronic emission line, a phenomenon known as dephasing, which significantly reduces photon indistinguishability. To mitigate this effect, solid-state emitters are typically operated at cryogenic temperatures, where dephasing becomes negligible. A key advantage of solid-state quantum emitters is their relative ease of manipulation compared to alkali atoms or trapped ions, even when cryogenic operation is required. Moreover, they generally allow for faster single-photon emission rates.

Furthermore, solid-state quantum emitters can interact electromagnetically with one another when they are separated by sufficiently short distances (in comparison to the wavelength of the light that they emit), through the modes of the electromagnetic vacuum field. The interaction between quantum emitters can also emerge when they couple with a common electromagnetic mode of

a resonator or waveguide. These emitter-emitter interactions open up new possibilities for manipulating non-classical photon states and correlations. For example, these interacting systems could open new directions for the generation of entangled photons [63–65], which exhibit non-local quantum correlations and are key components in quantum communication [34–36, 66–70], with additional applications in quantum sensing and imaging [71–77]. Further, interacting quantum emitters can also be used in quantum computing [78–83], quantum metrology [84], quantum information storage [85–87], and in the design of light-harvesting systems [88–91]. Early experimental demonstration of vacuum-induced interaction between two organic molecules was reported over two decades ago [92], and a few years later experimental evidences of interaction between quantum dots mediated by cavities or waveguides were also provided [93–96]. However, achieving efficient control over such interacting systems is highly challenging, for example, due to dephasing and inhomogeneous broadening caused by interactions with the solid-state environment [97, 98]. Fortunately, substantial progress has been made in recent years in manipulating these interactions. For instance, vacuum-induced coupling between two molecules can now be tailored by tuning the transition frequency of the emitters [1, 99]. Furthermore, the ability to induce long-distance interactions through resonator and waveguide modes has advanced significantly for organic molecules [100, 101], quantum dots [102–106] and color centers in crystals [107–109]. Beyond cavity and waveguide-mediated coupling, alternative approaches are also under investigation, such as molecule-molecule coupling enabled by scanning tunneling microscopy setups [110].

The characterization of light emission from two interacting solid-state quantum emitters is therefore of significant practical interest, especially given the recent experimental progress in achieving precise control over such systems. As a consequence, this thesis presents a detailed theoretical analysis of light emission from such a coupled system under a broad range of configurations, including different emitter arrangements, illumination conditions, and detection schemes. We aim to advance the fundamental understanding and characterization of light emission from such systems, thereby contributing to the identification and realization of potential technological applications, particularly those based on the manipulation of photon states and correlations. The structure of the thesis is as follows:

- In Chapter 1, we quantize the electromagnetic vacuum field in the absence of radiation sources, starting from Maxwell's equations. We then extend this procedure to include the presence of radiation sources, enabling the description of the interaction between the vacuum field and an ideal two-level quantum emitter, such as a single atom in vacuum. Several aspects of this interaction are analyzed, including the electric field radiated by the quantum emitter and the concept of spontaneous emission. The latter is introduced using the Wigner-Weisskopf approximation, as well as the Markovian master equation. Finally, we examine the interaction between the quantum emitter and a continuous-wave laser, and discuss how this excitation affects the dynamics of the emitter.

- In Chapter 2, we introduce the correlation functions of the electric field, originally formulated by Roy J. Glauber in the 1960s [111–114], which have since become essential tools for characterizing the coherence properties of quantum light. Special emphasis is placed on the normalized second-order correlation function, also known as intensity correlation, which plays a key role in this thesis as it provides information about the statistical properties of light emission. Specifically, we examine two distinct types of intensity correlations: one that considers all photons emitted by the source, termed *color-blind intensity correlation*, and another one that focuses on correlations of photons at specific frequencies, referred to as *frequency-resolved intensity correlation*. Both magnitudes are illustrated through the example of a single two-level quantum emitter, showing that such systems emit one photon at a time.

- In Chapter 3, we address the case of two interacting solid-state quantum emitters. To this end, we first describe the interaction between the electromagnetic vacuum field and two two-level quantum emitters. We next derive the Markovian master equation governing the reduced dynamics of the emitters. This demonstrates how the electromagnetic vacuum field mediates an effective interaction between closely spaced emitters. We then introduce a method to model the electronic dynamics of two solid-state emitters, incorporating the combined Debye-Waller/Franck-Condon factor. This factor represents the fraction of photons emitted into the Zero-Phonon Line, corresponding to the transition between the electronic excited and ground states without the assistance of vibrational modes. Afterwards, we investigate both the color-blind and the frequency-resolved intensity correlations of light emitted from two interacting solid-state emitters into the Zero-Phonon Line. Specifically, we provide a thorough analysis of these quantities for different regimes of laser frequency and intensity. In this way, we show that the color-blind intensity correlation can be tailored over a wide range of values, from strong single-photon emission to pronounced photon bunching. Moreover, we demonstrate that the frequency-resolved intensity correlation can reveal both single-photon transitions and two-photon transitions via intermediate virtual states that remain hidden in the emission spectrum.

- In Chapter 4, we extend the description of two interacting solid-state quantum emitters by incorporating vibrational/phononic levels into the electronic ground state. The primary objective of this extension is to address the situation in usual fluorescence experiments, in which the electronic excited states of the solid-state emitters are resonantly driven and optical filters are employed to suppress laser photons during detection. In these experiments, only the photons emitted due to decay to a vibrational/phononic level in the electronic ground state, referred to as Stokes-shifted photons, are measured. Notably, we demonstrate that quantum coherence between the emitters, as well as first-order coherence between the photons emitted, can influence the correlation of Stokes-shifted photons, in contrast to previous

assumptions in the literature. This result is corroborated by comparison with experiments conducted by the Bordeaux Nanophotonics group. Furthermore, we compare the correlations of Zero-Phonon-Line photons and Stokes-shifted photons emitted from two interacting solid-state emitters, revealing significant differences between them.

- In Chapter 5, we introduce the concept of entanglement and show that two interacting quantum emitters can serve as a source of polarization-entangled photons. To demonstrate the generation of polarization-entangled photons from two interacting emitters, we consider again the Hamiltonian describing the interaction between the electromagnetic vacuum field and two two-level quantum emitters, and apply the Wigner-Weisskopf approximation to derive the complete two-photon state resulting from the relaxation of the two emitters. By considering emitters with perpendicularly oriented transition dipole moments and incorporating optical filters, we show that a highly entangled two-photon state can be post-selected. We verify that this entanglement remains robust under small misalignments in the dipole orientations and under deviations in the detection direction. Notably, we also confirm that the photon entanglement is robust against the influence of the combined Debye-Waller/Franck-Condon factor, indicating that the polarization-entangled photons can be generated from the Zero-Phonon-Line emission of any pair of interacting solid-state emitters.

CHAPTER 1

INTERACTION BETWEEN LIGHT AND QUANTUM EMITTERS

In 1905, Albert Einstein extended Max Planck's concept of energy quantization to explain the photoelectric effect, proposing that light consists of discrete packets of energy, now known as photons [2, 115]. In the following decades, significant efforts were made to develop a quantum-mechanical description of the electromagnetic field [3–18], transitioning from the classical wave description formulated by Maxwell to one that accounted for the particle-like nature of the field. This quantum-mechanical framework led to the discovery of several novel phenomena, such as spontaneous emission, quantum coherence, and the development of the laser. In this chapter, we provide a comprehensive review of the quantization of the electromagnetic field. We place special emphasis on the interaction of this field with quantum emitters, which allows us to introduce the spontaneous emission of photons. In this way, this chapter lays the foundation for the analysis of light emission from quantum emitters, which is the main focus of this thesis.

We first present the quantization of the electromagnetic field in the absence of radiation sources, which we then extend to the case in which radiation sources are present. Afterwards, we focus on the case where the radiation sources are modeled as a single two-level quantum emitter (QE), and we provide a detailed description of the dynamics and light emission from this system. Notably, we explore the spontaneous emission of photons from the QE using two different approaches: the Wigner-Weisskopf approximation (WWA) and the Markovian master equation (MME). Finally, we investigate the interaction between the QE and an external laser, showing how this external illumination can strongly influence the dynamics of the emitter as well as its light emission.

1.1 Quantization of the free-space electromagnetic field

In this section, we present the formalism of second quantization for the electromagnetic field in free space, following mainly the procedure described in Refs. [116–120]. The starting point of this procedure is the classical Maxwell's equations, which yield a homogeneous wave equation for the vector potential in the absence of radiation sources. Next, we impose periodic boundary conditions to solve this wave equation and express the energy of the electromagnetic field as that provided by an infinite collection of classical harmonic oscillators. The promotion of the canonical position and momentum of such harmonic oscillators to quantum-mechanical operators yields the Hamiltonian of the quantized free-space electromagnetic field, which is given in this case as an infinite collection of quantum harmonic oscillators. In this formulation, the field amplitudes become operators that create and annihilate quantum excitations, which is the essence of the second quantization formalism. Finally, we introduce photons as the elementary quantum excitations of the electromagnetic field.

1.1.1 General Maxwell's equations

We describe in this section some general aspects of *Maxwell's equations*, before focusing on the case in which no radiation sources are considered. Maxwell's equations constitute a set of coupled differential equations relating the electric $\mathbf{E}(\mathbf{r},t)$ and magnetic $\mathbf{B}(\mathbf{r},t)$ fields, at position $\mathbf{r}$ and time t, through their curl and divergence. In SI units, which are adopted throughout this thesis, Maxwell's equations are given as [121]

$$\boldsymbol{\nabla}\cdot\mathbf{E}(\mathbf{r},t)=\frac{\varrho(\mathbf{r},t)}{\varepsilon_0}, \tag{1.1a}$$

$$\boldsymbol{\nabla}\cdot\mathbf{B}(\mathbf{r},t)=0, \tag{1.1b}$$

$$\boldsymbol{\nabla}\times\mathbf{E}(\mathbf{r},t)=-\frac{\partial}{\partial t}\mathbf{B}(\mathbf{r},t), \tag{1.1c}$$

$$\boldsymbol{\nabla}\times\mathbf{B}(\mathbf{r},t)=\frac{1}{c^2}\frac{\partial}{\partial t}\mathbf{E}(\mathbf{r},t)+\frac{1}{\varepsilon_0 c^2}\boldsymbol{j}(\mathbf{r},t). \tag{1.1d}$$

Here, ε_0 is the vacuum permittivity, c is the speed of light in vacuum, $\cdot$ is the dot product, $\times$ is the cross product and $\boldsymbol{\nabla}=\boldsymbol{e}_x\frac{\partial}{\partial x}+\boldsymbol{e}_y\frac{\partial}{\partial y}+\boldsymbol{e}_z\frac{\partial}{\partial z}$ is the nabla operator, with $\boldsymbol{e}_x$, $\boldsymbol{e}_y$ and $\boldsymbol{e}_z$ the unit vectors along the Cartesian coordinates. The radiation sources are introduced through the charge density $\varrho(\mathbf{r},t)$ and the *current density* $\boldsymbol{j}(\mathbf{r},t)$, which are related through the *continuity equation*

$$\frac{\partial}{\partial t}\varrho(\mathbf{r},t)+\boldsymbol{\nabla}\cdot\boldsymbol{j}(\mathbf{r},t)=0. \tag{1.2}$$

This equation can be derived from Maxwell's equations by taking the divergence on both sides of Eq. (1.1d) and, then, using Eq. (1.1a) and the identity

$$\boldsymbol{\nabla} \cdot (\boldsymbol{\nabla} \times \boldsymbol{F}) = 0, \tag{1.3}$$

which holds for an arbitrary vector field $\boldsymbol{F}$.

Moreover, the *Helmholtz theorem* states that any vector field $\boldsymbol{F}$ can be decomposed into a transverse component $\boldsymbol{F}_\perp$ (which is curl-free) and a longitudinal component $\boldsymbol{F}_\parallel$ (which is divergence-free) [121], which can be summarized as

$$\boldsymbol{F}(\mathbf{r}, t) = \boldsymbol{F}_\perp(\mathbf{r}, t) + \boldsymbol{F}_\parallel(\mathbf{r}, t), \tag{1.4}$$

with

$$\boldsymbol{\nabla} \cdot \boldsymbol{F}_\perp(\mathbf{r}, t) = 0, \tag{1.5a}$$
$$\boldsymbol{\nabla} \times \boldsymbol{F}_\parallel(\mathbf{r}, t) = 0. \tag{1.5b}$$

The physical meaning of this decomposition can be better understood in the reciprocal space (which is discussed in Section 1.2.1), as the longitudinal component of the field $\boldsymbol{F}_\parallel$ is parallel to the direction of the wavevector $\mathbf{k}$, whereas the transverse component $\boldsymbol{F}_\perp$ is perpendicular to such vector. Importantly, according to Eq. (1.1b), the longitudinal component of the magnetic field vanishes $\mathbf{B}_\parallel(\mathbf{r}, t) = 0$. Thus, the magnetic field is always purely transverse:

$$\mathbf{B}(\mathbf{r}, t) = \mathbf{B}_\perp(\mathbf{r}, t). \tag{1.6}$$

The solution of Maxwell's equations is facilitated by introducing the *vector potential* $\mathbf{A}(\mathbf{r}, t)$. This vector is defined through its relation with the magnetic field $\mathbf{B}(\mathbf{r}, t)$, which is given as

$$\mathbf{B}(\mathbf{r}, t) = \boldsymbol{\nabla} \times \mathbf{A}(\mathbf{r}, t). \tag{1.7}$$

This expression guarantees that Eq. (1.1b) is satisfied, as can be checked using the identity in Eq. (1.3). Additionally, substituting Eq. (1.7) into Eq. (1.1c) yields

$$\boldsymbol{\nabla} \times \mathbf{E}(\mathbf{r}, t) = -\boldsymbol{\nabla} \times \frac{\partial}{\partial t}\mathbf{A}(\mathbf{r}, t). \tag{1.8}$$

Taking into account that the curl of a gradient vanishes (i.e., $\boldsymbol{\nabla} \times \boldsymbol{\nabla}\phi = 0$, with ϕ an arbitrary scalar function), then the electric field $\mathbf{E}(\mathbf{r}, t)$ and the vector potential $\mathbf{A}(\mathbf{r}, t)$ are related through the expression

$$\mathbf{E}(\mathbf{r}, t) = -\frac{\partial}{\partial t}\mathbf{A}(\mathbf{r}, t) - \boldsymbol{\nabla}\phi(\mathbf{r}, t), \tag{1.9}$$

where we have introduced the *scalar potential* $\phi(\mathbf{r}, t)$.

Importantly, there is not a unique pair of potentials $\mathbf{A}(\mathbf{r}, t)$ and $\phi(\mathbf{r}, t)$ that determine the electric and magnetic fields in Eqs. (1.7) and (1.9). Indeed, $\mathbf{E}(\mathbf{r}, t)$

and $\mathbf{B}(\mathbf{r},t)$ remain unchanged under the transformation

$$\mathbf{A}'(\mathbf{r},t) = \mathbf{A}(\mathbf{r},t) - \boldsymbol{\nabla}\Xi(\mathbf{r},t), \tag{1.10a}$$

$$\phi'(\mathbf{r},t) = \phi(\mathbf{r},t) + \frac{\partial}{\partial t}\Xi(\mathbf{r},t), \tag{1.10b}$$

with $\Xi(\mathbf{r},t)$ being an arbitrary function of space and time. The transformation in Eqs. (1.10a)–(1.10b) is called *gauge transformation* and $\Xi(\mathbf{r},t)$ *gauge function*. The quantization of the electromagnetic field is facilitated in the *Coulomb gauge* (also called *radiation gauge*), which is defined by choosing that the vector potential is purely transverse $\mathbf{A}(\mathbf{r},t) = \mathbf{A}_\perp(\mathbf{r},t)$. Equivalently, the Coulomb gauge can be defined from

$$\boldsymbol{\nabla}\cdot\mathbf{A}(\mathbf{r},t) = 0. \tag{1.11}$$

We demonstrate in Section 1.2 that an advantage of this choice is that the two terms on the right-hand side of Eq. (1.9) can be directly identified as the transverse $\mathbf{E}_\perp(\mathbf{r},t)$ and the longitudinal $\mathbf{E}_\parallel(\mathbf{r},t)$ components of the electric field [see Eqs. (1.76a)–(1.76b)].

In the rest of this section, we focus on the simpler case in which no radiation sources are considered. The effect of radiation sources is further analyzed in Section 1.2.

1.1.2 Maxwell's equations in free space

We derive in this section a wave equation for the vector potential $\mathbf{A}(\mathbf{r},t)$ in free space, where no radiation sources are present [i.e., $\varrho(\mathbf{r},t) = 0$ and $\boldsymbol{j}(\mathbf{r},t) = 0$]. In this case, Maxwell's equations reduce to

$$\boldsymbol{\nabla}\cdot\mathbf{E}(\mathbf{r},t) = 0, \tag{1.12a}$$

$$\boldsymbol{\nabla}\cdot\mathbf{B}(\mathbf{r},t) = 0, \tag{1.12b}$$

$$\boldsymbol{\nabla}\times\mathbf{E}(\mathbf{r},t) = -\frac{\partial}{\partial t}\mathbf{B}(\mathbf{r},t), \tag{1.12c}$$

$$\boldsymbol{\nabla}\times\mathbf{B}(\mathbf{r},t) = \frac{1}{c^2}\frac{\partial}{\partial t}\mathbf{E}(\mathbf{r},t). \tag{1.12d}$$

Notably, Eq. (1.12a) implies that the electric field is purely transverse in free space, so that

$$\mathbf{E}(\mathbf{r},t) = \mathbf{E}_\perp(\mathbf{r},t). \tag{1.13}$$

Next, we substitute the expression that relates the electric field with the vector and scalar potentials [Eq. (1.9)] into Eq. (1.12a), which yields

$$-\frac{\partial}{\partial t}\boldsymbol{\nabla}\cdot\mathbf{A}(\mathbf{r},t) - \boldsymbol{\nabla}\cdot(\boldsymbol{\nabla}\phi(\mathbf{r},t)) = 0. \tag{1.14}$$

Thus, the free-space scalar potential satisfies the *Laplace equation* $\boldsymbol{\nabla}\cdot(\boldsymbol{\nabla}\phi(\mathbf{r},t)) = 0$ in the Coulomb gauge, where by definition $\boldsymbol{\nabla}\cdot\mathbf{A}(\mathbf{r},t) = 0$. In this gauge and in

the absence of charges, we are then allowed to choose that the scalar potential vanishes,

$$\phi(\mathbf{r},t)=0, \tag{1.15}$$

which further simplifies the derivation and solution of the wave equation for $\mathbf{A}(\mathbf{r},t)$. Last, substituting Eqs. (1.7), (1.9) and (1.15) into Eq. (1.12d), we obtain the homogeneous wave equation

$$\nabla^2\mathbf{A}(\mathbf{r},t)-\frac{1}{c^2}\frac{\partial^2}{\partial t^2}\mathbf{A}(\mathbf{r},t)=0. \tag{1.16}$$

Here, we have used the identity $\boldsymbol{\nabla}\times(\boldsymbol{\nabla}\times\mathbf{A})=\boldsymbol{\nabla}(\boldsymbol{\nabla}\cdot\mathbf{A})-\boldsymbol{\nabla}^2\mathbf{A}$. Therefore, free-space Maxwell's equations in the Coulomb gauge can be solved directly from Eq. (1.16).

1.1.3 Periodic boundary conditions

We impose in this section periodic boundary conditions on the electromagnetic field to solve the wave equation for $\mathbf{A}(\mathbf{r},t)$ [Eq. (1.16)]. With this purpose, a common approach relies on considering that free space is divided into very large cubes of volume $\mathcal{V}=L^3$, with L the side of each of these cubes. This artificial condition has no physical consequences in the *large box limit* ($L\to\infty$) and, crucially, it yields the periodic boundary conditions

$$\mathbf{A}(\mathbf{r},t)=\mathbf{A}(\mathbf{r}+L\boldsymbol{e}_x,t)=\mathbf{A}(\mathbf{r}+L\boldsymbol{e}_y,t)=\mathbf{A}(\mathbf{r}+L\boldsymbol{e}_z,t). \tag{1.17}$$

Under these periodic boundary conditions, the solution of the wave equation for $\mathbf{A}(\mathbf{r},t)$ [Eq. (1.16)] can be given by a Fourier series. Specifically, the vector potential can be expressed as

$$\mathbf{A}(\mathbf{r},t)=\sum_{\mathbf{k},s}\mathbf{e}_{\mathbf{k}s}[A_{\mathbf{k}s}(t)e^{i\mathbf{k}\cdot\mathbf{r}}+A^*_{\mathbf{k}s}(t)e^{-i\mathbf{k}\cdot\mathbf{r}}], \tag{1.18}$$

where $A_{\mathbf{k}s}(t)$ is the complex amplitude of the component with wavevector $\mathbf{k}$ and polarization s. Here, the wavevector $\mathbf{k}$ satisfies the periodic condition

$$\mathbf{k}=(\mathrm{k}_x,\mathrm{k}_y,\mathrm{k}_z)=\frac{2\pi}{L}(m_x,m_y,m_z), \tag{1.19}$$

with (m_x,m_y,m_z) a set of integer numbers. Additionally, $s=1,2$ indexes two independent polarization directions with unit vectors $\mathbf{e}_{\mathbf{k}s}$, which satisfy the *transversality condition*

$$\mathbf{k}\cdot\mathbf{e}_{\mathbf{k}s}=0, \tag{1.20}$$

as can be derived by substituting Eq. (1.18) into Eq. (1.11). Further, the two polarization modes must be orthogonal, so that

$$\mathbf{e}_{\mathbf{k}s}\cdot\mathbf{e}_{\mathbf{k}s'}=\delta_{s,s'}, \tag{1.21}$$

and they form a right-handed system, such that

$$\mathbf{e}_{\mathbf{k}1} \times \mathbf{e}_{\mathbf{k}2} = \mathbf{k}/\mathrm{k}, \tag{1.22}$$

with $\mathrm{k} = |\mathbf{k}|$. Throughout this thesis, we choose $\mathbf{e}_{\mathbf{k}s}$ to be real. Importantly, an *electromagnetic field mode* is thus specified by a particular wavevector $\mathbf{k}$ (determining the propagation direction) and by a particular polarization mode s.

Moreover, substituting the Fourier expansion in Eq. (1.18) into the homogeneous wave equation in Eq. (1.16), we find that the equation of motion of the amplitude $A_{\mathbf{k}s}(t)$ is that of a simple (undriven) harmonic oscillator:

$$\frac{\partial^2}{\partial t^2} A_{\mathbf{k}s}(t) + \omega_{\mathrm{k}}^2 A_{\mathbf{k}s}(t) = 0, \tag{1.23}$$

with $\omega_{\mathrm{k}} = c\mathrm{k}$. Thus, we obtain

$$A_{\mathbf{k}s}(t) = A_{\mathbf{k}s} e^{i\omega_{\mathrm{k}} t}, \tag{1.24}$$

with $A_{\mathbf{k}s} \equiv A_{\mathbf{k}s}(0)$. Importantly, substituting this solution for $A_{\mathbf{k}s}(t)$ into Eq. (1.18), we find that the vector potential becomes a sum of plane waves $\exp[i(\mathbf{k}\cdot\mathbf{r} - \omega_{\mathrm{k}} t)]$.

Last, we substitute Eqs. (1.18) and (1.24) into Eqs. (1.9) and (1.7). In this way, we find that the free-space electric and magnetic fields can also be expressed as plane-wave expansions:

$$\mathbf{E}_{\perp}(\mathbf{r}, t) = i \sum_{\mathbf{k},s} \omega_{\mathrm{k}} \mathbf{e}_{\mathbf{k}s} [A_{\mathbf{k}s} e^{i(\mathbf{k}\cdot\mathbf{r} - \omega_{\mathrm{k}} t)} - A_{\mathbf{k}s}^* e^{-i(\mathbf{k}\cdot\mathbf{r} - \omega_{\mathrm{k}} t)}], \tag{1.25a}$$

$$\mathbf{B}(\mathbf{r}, t) = i \sum_{\mathbf{k},s} (\mathbf{k} \times \mathbf{e}_{\mathbf{k}s}) [A_{\mathbf{k}s} e^{i(\mathbf{k}\cdot\mathbf{r} - \omega_{\mathrm{k}} t)} - A_{\mathbf{k}s}^* e^{-i(\mathbf{k}\cdot\mathbf{r} - \omega_{\mathrm{k}} t)}]. \tag{1.25b}$$

1.1.4 Energy of the electromagnetic field in free space

In order to introduce the canonical quantization of the free-space electromagnetic field, the next key step consists in expressing the energy of this field as that of an infinite collection of harmonic oscillators. To this end, we recall that the energy of the electromagnetic field is in general (even in the presence of radiation sources) given by [121]

$$H_F = \frac{1}{2} \int_{\mathcal{V}} \left[\varepsilon_0 \mathbf{E}^2(\mathbf{r}, t) + \frac{1}{\mu_0} \mathbf{B}^2(\mathbf{r}, t) \right] d\mathbf{r}, \tag{1.26}$$

with μ_0 the vacuum permeability, which is related with the vacuum permittivity ε_0 and the speed of light in vacuum c as

$$c = \frac{1}{\sqrt{\varepsilon_0 \mu_0}}. \tag{1.27}$$

The first term on the right-hand side of Eq. (1.26) corresponds to the electric energy, while the second one corresponds to the magnetic energy. Additionally, H_F can be decomposed into the transverse and longitudinal field contributions

$$H_F = H_{F\perp} + H_{F\parallel}. \tag{1.28}$$

Specifically, these contributions are given by

$$H_{F\perp} = \frac{1}{2}\int_{\mathcal{V}} d\mathbf{r}\left[\varepsilon_0 \mathbf{E}_\perp^2(\mathbf{r},t) + \frac{1}{\mu_0}\mathbf{B}^2(\mathbf{r},t)\right], \tag{1.29a}$$

$$H_{F\parallel} = \frac{1}{2}\int_{\mathcal{V}} d\mathbf{r}\varepsilon_0 \mathbf{E}_\parallel^2(\mathbf{r},t), \tag{1.29b}$$

where we have taken into account that the magnetic field is always purely transverse [Eq. (1.6)], as discussed in Section 1.1.1. Crucially, the electric field is also purely transverse in free space [Eq. (1.13)]. Therefore, $H_F = H_{F,\perp}$.

Substituting Eqs. (1.25a)–(1.25b) into Eq. (1.29a), we find

$$H_{F\perp} = -\frac{1}{2}\sum_{\mathbf{k},s}\sum_{\mathbf{k}',s'}\left[\varepsilon_0\omega_\mathrm{k}\omega_{\mathrm{k}'}\mathbf{e}_{\mathbf{k}s}\cdot\mathbf{e}_{\mathbf{k}'s'} + \frac{1}{\mu_0}(\mathbf{k}\times\mathbf{e}_{\mathbf{k}s})(\mathbf{k}'\times\mathbf{e}_{\mathbf{k}'s'})^*\right]$$
$$\times\int_{\mathcal{V}} d\mathbf{r}\left[A_{\mathbf{k}s}e^{i(\mathbf{k}\cdot\mathbf{r}-\omega_\mathrm{k}t)} - A_{\mathbf{k}s}^* e^{-i(\mathbf{k}\cdot\mathbf{r}-\omega_\mathrm{k}t)}\right]\left[A_{\mathbf{k}'s'}e^{i(\mathbf{k}'\cdot\mathbf{r}-\omega_{\mathrm{k}'}t)} - A_{\mathbf{k}'s'}^* e^{-i(\mathbf{k}'\cdot\mathbf{r}-\omega_{\mathrm{k}'}t)}\right]. \tag{1.30}$$

Additionally, under the boundary condition in Eq. (1.19), the spatial integrals in the above expression satisfy the relation

$$\int_{\mathcal{V}} d\mathbf{r}e^{i(\mathbf{k}\pm\mathbf{k}')\cdot\mathbf{r}} = \mathcal{V}\delta^3_{\mathbf{k},\mp\mathbf{k}'}, \tag{1.31}$$

where $\delta^3_{\mathbf{k},\mp\mathbf{k}'}$ is the Kronecker delta of the vectors $\mathbf{k}$ and $\mp\mathbf{k}'$. As a consequence, we obtain

$$H_{F\perp} = \frac{\mathcal{V}}{2}\sum_{\mathbf{k},s}\sum_{\mathbf{k}',s'}\left[\varepsilon_0\omega_\mathrm{k}\omega_{\mathrm{k}'}\mathbf{e}_{\mathbf{k}s}\cdot\mathbf{e}_{\mathbf{k}'s'} + \frac{1}{\mu_0}(\mathbf{k}\times\mathbf{e}_{\mathbf{k}s})(\mathbf{k}'\times\mathbf{e}_{\mathbf{k}'s'})^*\right]$$
$$\times\left[\delta^3_{\mathbf{k},\mathbf{k}'}[A_{\mathbf{k}s}(t)A^*_{\mathbf{k}'s'}(t) + A^*_{\mathbf{k}s}(t)A_{\mathbf{k}'s'}(t)] - \delta^3_{\mathbf{k},-\mathbf{k}'}[A_{\mathbf{k}s}(t)A_{\mathbf{k}'s'}(t) + A^*_{\mathbf{k}s}(t)A^*_{\mathbf{k}'s'}(t)]\right]$$
$$= \frac{\mathcal{V}}{2}\sum_{\mathbf{k},s}\sum_{s'}\left\{\left[\varepsilon_0\omega_\mathrm{k}^2\mathbf{e}_{\mathbf{k}s}\cdot\mathbf{e}_{\mathbf{k}s'} + \frac{1}{\mu_0}(\mathbf{k}\times\mathbf{e}_{\mathbf{k}s})(\mathbf{k}\times\mathbf{e}_{\mathbf{k}s'})^*\right][A_{\mathbf{k}s}A^*_{\mathbf{k}s'} + A^*_{\mathbf{k}s}A_{\mathbf{k}s'}]\right.$$
$$\left. - \left[\varepsilon_0\omega_\mathrm{k}^2\mathbf{e}_{\mathbf{k}s}\cdot\mathbf{e}_{-\mathbf{k}s'} + \frac{1}{\mu_0}(\mathbf{k}\times\mathbf{e}_{\mathbf{k}s})(-\mathbf{k}\times\mathbf{e}_{-\mathbf{k}s'})^*\right][A_{\mathbf{k}s}(t)A_{\mathbf{k}s'}(t) + A^*_{\mathbf{k}s}(t)A^*_{\mathbf{k}s'}(t)]\right\}. \tag{1.32}$$

Furthermore, the vector identity

$$(\mathbf{A}\times\mathbf{B})\cdot(\mathbf{C}\times\mathbf{D}) = (\mathbf{A}\cdot\mathbf{C})(\mathbf{B}\cdot\mathbf{D}) - (\mathbf{A}\cdot\mathbf{D})(\mathbf{B}\cdot\mathbf{C}) \tag{1.33}$$

provides the relations

$$(\mathbf{k}\times\mathbf{e}_{\mathbf{k}s})\cdot(\mathbf{k}\times\mathbf{e}_{\mathbf{k}s'}) = \mathrm{k}^2\delta_{s,s'}, \tag{1.34a}$$

$$(\mathbf{k}\times\mathbf{e}_{\mathbf{k}s})\cdot(-\mathbf{k}\times\mathbf{e}_{-\mathbf{k}s'}) = -\mathrm{k}^2\mathbf{e}_{\mathbf{k}s}\cdot\mathbf{e}_{-\mathbf{k}s'}. \tag{1.34b}$$

These relations, together with the orthogonality condition in Eq. (1.21), allow for simplifying the expression of the electromagnetic energy in Eq. (1.32). Specifically, this energy becomes a summation over the time-independent contributions from each individual electromagnetic mode $(\mathbf{k}, s)$, such that

$$H_{F\perp} = \varepsilon_0\mathcal{V}\sum_{\mathbf{k},s}\omega_{\mathrm{k}}^2\left(A_{\mathbf{k}s}^*A_{\mathbf{k}s} + A_{\mathbf{k}s}A_{\mathbf{k}s}^*\right). \tag{1.35}$$

At this point, we have decomposed the energy $H_{F\perp}$ of the electromagnetic field into independent contributions from each electromagnetic mode [Eq. (1.35)], each of these contributions being expressed in terms of the complex amplitudes $A_{\mathbf{k}s}$ and $A_{\mathbf{k}s}^*$. These complex amplitudes evolve in time as simple harmonic oscillators [Eq. (1.24)], as discussed in Section 1.1.3. Finally, we show that $H_{F\perp}$ can indeed be expressed as a summation over the energies of simple harmonic oscillators, which facilitates the quantization of the electromagnetic field. To this end, we define the real variables

$$q_{\mathbf{k}s} = \sqrt{\varepsilon_0\mathcal{V}}(A_{\mathbf{k}s} + A_{\mathbf{k}s}^*), \tag{1.36a}$$

$$p_{\mathbf{k}s} = -i\omega_{\mathrm{k}}\sqrt{\varepsilon_0\mathcal{V}}(A_{\mathbf{k}s} - A_{\mathbf{k}s}^*). \tag{1.36b}$$

These new variables allow us to rewrite $H_{F\perp}$ as

$$H_{F\perp} = \frac{1}{2}\sum_{\mathbf{k},s}(p_{\mathbf{k}s}^2 + \omega_{\mathrm{k}}^2 q_{\mathbf{k}s}^2). \tag{1.37}$$

Importantly, from Eqs. (1.36a)–(1.36b) and (1.37), we can verify that $q_{\mathbf{k}s}$ and $p_{\mathbf{k}s}$ satisfy the *Hamilton's equations* in classical mechanics, which are given by

$$\frac{dq_{\mathbf{k}s}}{dt} = \frac{\partial H_{F\perp}}{\partial p_{\mathbf{k}s}}, \tag{1.38a}$$

$$\frac{dp_{\mathbf{k}s}}{dt} = -\frac{\partial H_{F\perp}}{\partial q_{\mathbf{k}s}}. \tag{1.38b}$$

Therefore, $q_{\mathbf{k}s}$ and $p_{\mathbf{k}s}$ correspond to the *canonical position* and *canonical momentum*, respectively. The latter enables to identify that the Hamiltonian in Eq. (1.37) corresponds to an infinite summation over the energies of simple

harmonic oscillators of unit mass.

1.1.5 Quantization of the electromagnetic field in free space

So far, we have shown that the energy of the classical electromagnetic field in free space can be expressed as the energy of a continuum set of harmonic oscillators. We demonstrate in this section that the quantized electromagnetic field in free space becomes a continuum of quantum harmonic oscillators. To this end, the canonical variables $q_{\mathbf{k}s}$ and $p_{\mathbf{k}s}$ are promoted to Hilbert space operators $\hat{q}_{\mathbf{k}s}$ and $\hat{p}_{\mathbf{k}s}$, with commutator $i\hbar$ according to the principles of quantum mechanics [122, 123]. Additionally, the Hilbert space operators of two different electromagnetic modes $(\mathbf{k}, s)$ and $(\mathbf{k}', s')$ commute with each other, as the corresponding classical electromagnetic harmonic oscillators are uncoupled. The commutation relations of the canonical quantum-mechanical operators can be summarized as

$$[\hat{q}_{\mathbf{k}s}, \hat{p}_{\mathbf{k}'s'}] = i\hbar\delta^3_{\mathbf{k},\mathbf{k}'}\delta_{s,s'}, \tag{1.39a}$$

$$[\hat{q}_{\mathbf{k}s}, \hat{q}_{\mathbf{k}'s'}] = [\hat{p}_{\mathbf{k}s}, \hat{p}_{\mathbf{k}'s'}] = 0. \tag{1.39b}$$

The quantum-mechanical Hamiltonian of the electromagnetic field in free space, also called *vacuum field*, is thus given by

$$\hat{H}_V \equiv \hat{H}_{F\perp} = \frac{1}{2}\sum_{\mathbf{k},s}(\hat{p}_{\mathbf{k}s} + \omega_{\mathrm{k}}^2\hat{q}_{\mathbf{k}s}^2). \tag{1.40}$$

This Hamiltonian is often rewritten in terms of the *annihilation operator* $\hat{a}_{\mathbf{k}s}$ and the *creation operator* $\hat{a}^\dagger_{\mathbf{k}s}$ of photons in mode $(\mathbf{k}, s)$, which are non-Hermitian operators that can be expressed in terms of $\hat{q}_{\mathbf{k}s}$ and $\hat{p}_{\mathbf{k}s}$ as

$$\hat{a}_{\mathbf{k}s} = \frac{1}{(2\hbar\omega_{\mathrm{k}})^{1/2}}(\omega_{\mathrm{k}}\hat{q}_{\mathbf{k}s} + i\hat{p}_{\mathbf{k}s}), \tag{1.41a}$$

$$\hat{a}^\dagger_{\mathbf{k}s} = \frac{1}{(2\hbar\omega_{\mathrm{k}})^{1/2}}(\omega_{\mathrm{k}}\hat{q}_{\mathbf{k}s} - i\hat{p}_{\mathbf{k}s}). \tag{1.41b}$$

As a direct consequence of Eqs. (1.39a)–(1.39b) and Eqs. (1.41a)–(1.41b), these operators satisfy the commutation relations

$$[\hat{a}_{\mathbf{k}s}, \hat{a}^\dagger_{\mathbf{k}'s'}] = \delta^3_{\mathbf{k},\mathbf{k}'}\delta_{s,s'}, \tag{1.42a}$$

$$[\hat{a}_{\mathbf{k}s}, \hat{a}_{\mathbf{k}'s'}] = [\hat{a}^\dagger_{\mathbf{k}s}, \hat{a}^\dagger_{\mathbf{k}'s'}] = 0. \tag{1.42b}$$

The Hamiltonian of the vacuum field can then be rewritten as

$$\hat{H}_V = \sum_{\mathbf{k},s}\frac{\hbar\omega_{\mathrm{k}}}{2}\left(\hat{a}^\dagger_{\mathbf{k}s}\hat{a}_{\mathbf{k}s} + \hat{a}_{\mathbf{k}s}\hat{a}^\dagger_{\mathbf{k}s}\right) = \sum_{\mathbf{k},s}\hbar\omega_{\mathrm{k}}\left(\hat{a}^\dagger_{\mathbf{k}s}\hat{a}_{\mathbf{k}s} + \frac{1}{2}\right). \tag{1.43}$$

The comparison of the expressions for the quantized vacuum-field Hamiltonian

$\hat{H}_V$ [Eq. (1.43)] and for the energy of the classical free-space electromagnetic field [Eq. (1.35)] allows for interpreting $\hat{a}_{\mathbf{k}s}$ and $\hat{a}^\dagger_{\mathbf{k}s}$ as the Hilbert-space operators to which the classical amplitudes $A_{\mathbf{k}s}$ and $A^*_{\mathbf{k}s}$ are promoted. More specifically,

$$A_{\mathbf{k}s} \to \sqrt{\frac{\hbar}{2\omega_{\mathrm{k}}\varepsilon_0\mathcal{V}}}\hat{a}_{\mathbf{k}s}, \tag{1.44a}$$

$$A^*_{\mathbf{k}s} \to \sqrt{\frac{\hbar}{2\omega_{\mathrm{k}}\varepsilon_0\mathcal{V}}}\hat{a}^\dagger_{\mathbf{k}s}. \tag{1.44b}$$

Therefore, the vector potential in Eq. (1.18) becomes the quantized *vector potential operator*:

$$\hat{\mathbf{A}}(\mathbf{r}) = \sum_{\mathbf{k},s}\sqrt{\frac{\hbar}{2\omega_{\mathrm{k}}\varepsilon_0\mathcal{V}}}\mathbf{e}_{\mathbf{k}s}[\hat{a}_{\mathbf{k}s}e^{i\mathbf{k}\cdot\mathbf{r}} + \hat{a}^\dagger_{\mathbf{k}s}e^{-i\mathbf{k}\cdot\mathbf{r}}], \tag{1.45}$$

which is written in the Schrödinger picture (see Appendix B for a brief review of the dynamical pictures in quantum mechanics). Similarly, the quantized *electric field operator* and the *magnetic field operator* become

$$\hat{\mathbf{E}}_\perp(\mathbf{r}) = i\sum_{\mathbf{k},s}\sqrt{\frac{\hbar\omega_{\mathrm{k}}}{2\varepsilon_0\mathcal{V}}}\mathbf{e}_{\mathbf{k}s}[\hat{a}_{\mathbf{k}s}e^{i\mathbf{k}\cdot\mathbf{r}} - \hat{a}^\dagger_{\mathbf{k}s}e^{-i\mathbf{k}\cdot\mathbf{r}}], \tag{1.46}$$

$$\hat{\mathbf{B}}(\mathbf{r}) = i\sum_{\mathbf{k},s}\sqrt{\frac{\hbar}{2\varepsilon_0\mathcal{V}\omega_{\mathrm{k}}}}(\mathbf{k}\times\mathbf{e}_{\mathbf{k}s})[\hat{a}_{\mathbf{k}s}e^{i\mathbf{k}\cdot\mathbf{r}} - \hat{a}^\dagger_{\mathbf{k}s}e^{-i\mathbf{k}\cdot\mathbf{r}}], \tag{1.47}$$

with forms analogous to the classical electric and magnetic fields in Eqs. (1.25a)–(1.25b), respectively.

Moreover, the Heisenberg-picture dynamics of an arbitrary operator $\hat{O}$ (with no explicit time dependence) is governed by the *Heisenberg equation* (see Appendix B)

$$\frac{d}{dt}\hat{O}(t) = -\frac{i}{\hbar}[\hat{O}(t), \hat{H}], \tag{1.48}$$

where $\hat{H}$ is the Hamiltonian of the closed system. (For an open quantum system, the Heisenberg-picture dynamics is governed by the adjoint master equation introduced in Section 1.4.4). Applying Eq. (1.48), we find that the time evolution of the operators $\hat{a}_{\mathbf{k}s}$ and $\hat{a}^\dagger_{\mathbf{k}s}$ is analogous to the time evolution of the classical complex amplitudes $A_{\mathbf{k}s}$ and $A^*_{\mathbf{k}s}$ in Eq. (1.24). More specifically, we obtain

$$\hat{a}_{\mathbf{k}s}(t) = \hat{a}_{\mathbf{k}s}(0)e^{-i\omega_{\mathrm{k}}t}, \tag{1.49a}$$

$$\hat{a}^\dagger_{\mathbf{k}s}(t) = \hat{a}^\dagger_{\mathbf{k}s}(0)e^{i\omega_{\mathrm{k}}t}. \tag{1.49b}$$

At the initial time, the Heisenberg-picture operators coincide with their representations in the Schrödinger picture, so that $\hat{a}_{\mathbf{k}s}(0) = \hat{a}_{\mathbf{k}s}$ and $\hat{a}^\dagger_{\mathbf{k}s}(0) = \hat{a}^\dagger_{\mathbf{k}s}$ (see Appendix B).

1.1.6 Spectrum of the vacuum field Hamiltonian

In this section, we describe the spectrum and eigenstates of the vacuum-field Hamiltonian $\hat{H}_V$, which enables the introduction of the concept of photon. To this end, we first derive the set of eigenstates of the Hermitian operator $\hat{n}_{\mathbf{k}s} \equiv \hat{a}^\dagger_{\mathbf{k}s}\hat{a}_{\mathbf{k}s}$. According to Eq. (1.43), the eigenstates of the vacuum-field Hamiltonian coincide with the eigenstates of $\hat{n}_{\mathbf{k}s}$.

We denote the eigenvalues of $\hat{n}_{\mathbf{k}s}$ by $n_{\mathbf{k}s}$ and the eigenstates (normalized to unity) as $|n_{\mathbf{k}s}\rangle$. Thus,

$$\hat{n}_{\mathbf{k}s}\,|n_{\mathbf{k}s}\rangle = n_{\mathbf{k}s}\,|n_{\mathbf{k}s}\rangle\,, \tag{1.50}$$

with $\langle n_{\mathbf{k}s}|n_{\mathbf{k}s}\rangle = 1$. Next, using the commutation relations in Eqs. (1.42a)–(1.42b), we obtain

$$\hat{n}_{\mathbf{k}s}\hat{a}^\dagger_{\mathbf{k}s}\,|n_{\mathbf{k}s}\rangle = \hat{a}^\dagger_{\mathbf{k}s}(\hat{n}_{\mathbf{k}s}+1)\,|n_{\mathbf{k}s}\rangle = (n_{\mathbf{k}s}+1)\hat{a}^\dagger_{\mathbf{k}s}\,|n_{\mathbf{k}s}\rangle\,, \tag{1.51}$$

which implies that $\hat{a}^\dagger_{\mathbf{k}s}\,|n_{\mathbf{k}s}\rangle$ is an eigenstate of $\hat{n}_{\mathbf{k}s}$ with eigenvalue $n_{\mathbf{k}s}+1$. According to Eq. (1.50), $\hat{a}^\dagger_{\mathbf{k}s}\,|n_{\mathbf{k}s}\rangle$ is thus proportional to $|n_{\mathbf{k}s}+1\rangle$. The proportionality constant is obtained by evaluating the norm of $\hat{a}^\dagger_{\mathbf{k}s}\,|n_{\mathbf{k}s}\rangle$, which yields

$$\langle n_{\mathbf{k}s}|\,\hat{a}_{\mathbf{k}s}\hat{a}^\dagger_{\mathbf{k}s}\,|n_{\mathbf{k}s}\rangle = \langle n_{\mathbf{k}s}|\,(\hat{n}_{\mathbf{k}s}+1)\,|n_{\mathbf{k}s}\rangle = n_{\mathbf{k}s}+1, \tag{1.52}$$

where we have used again the commutation relations in Eqs. (1.42a)–(1.42b). Consequently, we have demonstrated that

$$\hat{a}^\dagger_{\mathbf{k}s}\,|n_{\mathbf{k}s}\rangle = \sqrt{n_{\mathbf{k}s}+1}\,|n_{\mathbf{k}s}+1\rangle\,. \tag{1.53}$$

This procedure can be repeated iteratively, yielding that $|n_{\mathbf{k}s}+N\rangle$ is also an eigenstate of this operator with eigenvalue $n_{\mathbf{k}s}+N$, with N any natural number. In other words, the spectrum of eigenvalues $n_{\mathbf{k}s}$ of $\hat{n}_{\mathbf{k}s}$ is unbounded from above.

We can follow a similar argument to demonstrate that $\hat{a}_{\mathbf{k}s}\,|n_{\mathbf{k}s}\rangle$ is also an eigenstate of $|n_{\mathbf{k}s}\rangle$, in this case proportional to $|n_{\mathbf{k}s}-1\rangle$. From the commutation relations in Eqs. (1.42a)–(1.42b), we obtain

$$\hat{n}_{\mathbf{k}s}\hat{a}_{\mathbf{k}s}\,|n_{\mathbf{k}s}\rangle = \hat{a}_{\mathbf{k}s}(\hat{n}_{\mathbf{k}s}-1)\,|n_{\mathbf{k}s}\rangle = (n_{\mathbf{k}s}-1)\hat{a}_{\mathbf{k}s}\,|n_{\mathbf{k}s}\rangle\,, \tag{1.54}$$

and

$$\langle n_{\mathbf{k}s}|\,\hat{a}^\dagger_{\mathbf{k}s}\hat{a}_{\mathbf{k}s}\,|n_{\mathbf{k}s}\rangle = n_{\mathbf{k}s}. \tag{1.55}$$

As a consequence,

$$\hat{a}_{\mathbf{k}s}\,|n_{\mathbf{k}s}\rangle = \sqrt{n_{\mathbf{k}s}}\,|n_{\mathbf{k}s}-1\rangle\,. \tag{1.56}$$

Again, by applying the operator $\hat{a}_{\mathbf{k}s}$ iteratively, we obtain that if $|n_{\mathbf{k}s}\rangle$ is an eigenstate of $\hat{n}_{\mathbf{k}s}$ with eigenvalue $n_{\mathbf{k}s}$, $|n_{\mathbf{k}s}-N\rangle$ is also an eigenstate of this operator with eigenvalue $n_{\mathbf{k}s}-N$. Importantly, according to Eq. (1.55), the norm of the state $\hat{a}_{\mathbf{k}s}\,|n_{\mathbf{k}s}\rangle$ is $n_{\mathbf{k}s}$, which implies that $n_{\mathbf{k}s}-N$ cannot take negative values (otherwise, the corresponding state $|n_{\mathbf{k}s}-N\rangle$ would have a negative norm). As a

consequence, $n_{\mathbf{k}s}$ cannot take non-integers values because the iterative applications of $\hat{a}_{\mathbf{k}s}$ would eventually yield eigenstates with non-integers negatives eigenvalues. In contrast, we do not encounter this problem by considering that $n_{\mathbf{k}s}$ are integer numbers. Specifically, the iterative application of $\hat{a}_{\mathbf{k}s}$ over a non-negative integer number eventually yields

$$\hat{a}_{\mathbf{k}s} \left|0_{\mathbf{k}s}\right\rangle = 0, \tag{1.57}$$

terminating the sequence. Therefore, $|0_{\mathbf{k}s}\rangle$ is the eigenstate of $\hat{n}_{\mathbf{k}s}$ with the lowest eigenvalue and the spectrum of the operator $\hat{n}_{\mathbf{k}s}$ corresponds to the infinite set of non-negative integer eigenvalues. $\hat{n}_{\mathbf{k}s}$ is called *number operator* and its eigenstates $|n_{\mathbf{k}s}\rangle$ are named *Fock states*.

Furthermore, the Hamiltonian of the electromagnetic vacuum field is given by a linear combination of number operators. Consequently, this Hamiltonian is diagonalized as

$$\hat{H}_V \left|\{n_{\mathbf{k}s}\}\right\rangle = \left(\sum_{\mathbf{k},s} \hbar\omega_{\mathrm{k}} (n_{\mathbf{k}s} + \frac{1}{2}) \right) \left|\{n_{\mathbf{k}s}\}\right\rangle . \tag{1.58}$$

Here, we have defined the eigenstate $|\{n_{\mathbf{k}s}\}\rangle$ as the product state

$$\left|\{n_{\mathbf{k}s}\}\right\rangle = \otimes_{\mathbf{k}s} \left|n_{\mathbf{k}s}\right\rangle , \tag{1.59}$$

with $\otimes_{\mathbf{k}s}$ the tensor product over the (infinite) modes $(\mathbf{k}, s)$.

1.1.7 Vacuum state and photons

We have reached at this point the fundamental quantum-mechanical description of the electromagnetic field in free space or vacuum field. We now introduce the concepts of vacuum state and photons. On the one hand, the ground state of the vacuum field Hamiltonian $\hat{H}_V$ is called *vacuum state* and is represented as $|\mathrm{vac}\rangle$. In this state, all the occupation numbers $n_{\mathbf{k}s}$ are equal to zero, namely

$$\left|\mathrm{vac}\right\rangle \equiv \left|\{0_{\mathbf{k}s}\}\right\rangle . \tag{1.60}$$

According to Eq. (1.58), the energy of the vacuum state is

$$E_{ZP} = \frac{1}{2} \sum_{\mathbf{k},s} \hbar\omega_{\mathrm{k}}, \tag{1.61}$$

which is known as *zero-point energy* and has no classical analogue. Notably, although $|\mathrm{vac}\rangle$ is a stationary state of the Hamiltonian of the free-space electromagnetic field (with energy E_{ZP}), this state is neither an eigenstate of the electric field operator $\hat{\mathbf{E}}(\mathbf{r}, t)$ [Eq. (1.46)] nor of the magnetic field operator $\hat{\mathbf{B}}(\mathbf{r}, t)$ [Eq. (1.47)]. As a consequence, the electric and magnetic fields do not have definite values in the vacuum state, which leads to the so-called *vacuum fluctuations* (see Refs. [116–119] for further information).

On the other hand, *photons* are introduced as elementary excitations or quanta of the electromagnetic field. In particular, a quantum state accounting for the presence of a single photon of energy $\hbar\omega_{\mathrm{k}}$, wavevector $\mathbf{k}$ and polarization s is described by the Fock state

$$|1_{\mathbf{k}s}, \{0_{\mathbf{k}'s'\neq\mathbf{k}s}\}\rangle = \hat{a}^{\dagger}_{\mathbf{k}s}\,|\mathrm{vac}\rangle\,. \tag{1.62}$$

The total number of photons in the field is given by the expectation value $\langle\hat{n}\rangle$ of the *total number operator*

$$\hat{n} = \sum_{\mathbf{k},s} \hat{n}_{\mathbf{k}s}. \tag{1.63}$$

We emphasize that the operators $\hat{a}_{\mathbf{k}s}$ and $\hat{a}^{\dagger}_{\mathbf{k}s}$ lower and raise the number of photons in the field, which is the reason why they are called annihilation and creation operators. More specifically, $\hat{a}_{\mathbf{k}s}$ destroys a photon in the electromagnetic mode $(\mathbf{k}, s)$, while $\hat{a}^{\dagger}_{\mathbf{k}s}$ creates a photon in the same mode. Importantly, the eigenvalues of the number operator $\hat{n}_{\mathbf{k}s}$ in mode $(\mathbf{k}, s)$ are unbounded, implying that more than one photon can be found in the same quantum state. Therefore, photons are bosons and follow Bose-Einstein statistics.

Last, we introduce the linear momentum of photons. The quantization of the classical linear momentum $\mathbf{P} = \varepsilon_0 \int_{\mathcal{V}} d\mathbf{r}\mathbf{E}(\mathbf{r}, t) \times \mathbf{B}(\mathbf{r}, t)$ results in the Schrödinger-picture operator [116, 119]

$$\hat{\mathbf{P}} = \sum_{\mathbf{k},s} \hbar\mathbf{k}\left(\hat{a}^{\dagger}_{\mathbf{k}s}\hat{a}_{\mathbf{k}s} + \frac{1}{2}\right) = \sum_{\mathbf{k},s} \hbar\mathbf{k}\hat{n}_{\mathbf{k}s}, \tag{1.64}$$

where the $1/2$ factor cancels in the last equality because for each $\mathbf{k}$ term there is an opposite contribution from the $-\mathbf{k}$ term in the summation. Equation (1.64) indicates that each photon in mode $(\mathbf{k}, s)$ possesses $\hbar\mathbf{k}$ linear momentum. Additionally, the relativistic energy-momentum relation $E^2 - (Pc)^2 = (m_0c^2)^2$, where E represents the energy and m_0 the invariant mass, indicates that photons are massless, as $E = \hbar\omega_{\mathrm{k}}$ and $P = \hbar k$ [119].

1.2 Interaction between the quantized electromagnetic field and a quantum emitter

In this section, we describe the interaction between the quantized electromagnetic field and a quantum emitter with two-level-system behaviour. To this end, we first derive the total energy of the electromagnetic field in the presence of radiation sources. Here, we mainly follow the procedure described in Refs. [116, 119, 120].

1.2.1 Maxwell's equations in the reciprocal space

We have shown in Section 1.1 that the free-space electric field is purely transverse [Eq. (1.13)]. Here, we demonstrate that in the presence of radiation sources $\mathbf{E}_{\parallel}(\mathbf{r},t)$ does not vanish. To this end, we write the general Maxwell's equations [Eqs. (1.1a)–(1.1d)] in the reciprocal-space representation, where any function (such as the charge density or the Cartesian components of the electric and magnetic fields) is obtained from the Fourier transform of its real-space representation. More specifically, the real-space representation $F(\mathbf{r},t)$ and the reciprocal-space representation $\breve{F}(\mathbf{k},t)$ are related as

$$\breve{F}(\mathbf{k},t)=\frac{1}{(2\pi)^{3/2}}\int d\mathbf{r}F(\mathbf{r},t)e^{-i\mathbf{k}\cdot\mathbf{r}}. \tag{1.65}$$

The breve symbol $\breve{}$ is used to emphasize that the function is expressed in the reciprocal space. Additionally, in the reciprocal space, the operator $\boldsymbol{\nabla}$ is transformed into $i\mathbf{k}$. Maxwell's equations in the reciprocal space thus become

$$i\mathbf{k}\cdot\breve{\mathbf{E}}(\mathbf{k},t)=\frac{\breve{\varrho}(\mathbf{k},t)}{\varepsilon_0}, \tag{1.66a}$$

$$i\mathbf{k}\cdot\breve{\mathbf{B}}(\mathbf{k},t)=0, \tag{1.66b}$$

$$i\mathbf{k}\times\breve{\mathbf{E}}(\mathbf{k},t)=-\frac{\partial}{\partial t}\breve{\mathbf{B}}(\mathbf{k},t), \tag{1.66c}$$

$$i\mathbf{k}\times\breve{\mathbf{B}}(\mathbf{k},t)=\frac{1}{c^2}\frac{\partial}{\partial t}\breve{\mathbf{E}}(\mathbf{k},t)+\frac{1}{\varepsilon_0 c^2}\breve{\boldsymbol{j}}(\mathbf{k},t). \tag{1.66d}$$

Furthermore, the conditions $\nabla\times\mathbf{E}_{\parallel}(\mathbf{r},t)=0$ and $\nabla\cdot\mathbf{E}_{\perp}(\mathbf{r},t)=0$ that define the longitudinal and transverse electric fields, respectively, are given in the reciprocal space as

$$i\mathbf{k}\times\breve{\mathbf{E}}_{\parallel}(\mathbf{k},t)=0, \tag{1.67}$$

$$i\mathbf{k}\cdot\breve{\mathbf{E}}_{\perp}(\mathbf{k},t)=0. \tag{1.68}$$

These conditions clarify the geometrical reason behind the labels *longitudinal* (meaning that the field is parallel to $\mathbf{k}$) and *transverse* (meaning that the field is perpendicular to $\mathbf{k}$). Additionally, as the longitudinal component of the electric field is parallel to $\mathbf{k}$, we can write

$$\breve{\mathbf{E}}_{\parallel}(\mathbf{k},t)=\frac{\mathbf{k}\cdot\breve{\mathbf{E}}(\mathbf{k},t)}{|\mathbf{k}|^2}\mathbf{k}. \tag{1.69}$$

Substituting Eq. (1.66a) into Eq. (1.69) we obtain

$$\breve{\mathbf{E}}_{\parallel}(\mathbf{k},t)=-\mathbf{k}\frac{i}{\varepsilon_0|\mathbf{k}|^2}\breve{\varrho}(\mathbf{k},t), \tag{1.70}$$

which reveals that the longitudinal component of the electric field is determined by

the charge density.

We next obtain the real-space representation of the longitudinal electric field in Eq. (1.70). The real-space representation of $\breve{\varrho}(\mathbf{k},t)$ is directly $\varrho(\mathbf{r},t)$, whereas the inverse Fourier transform of the other terms in Eq. (1.70) yields

$$\frac{1}{(2\pi)^{3/2}}\int d\mathbf{k}e^{i\mathbf{k}\cdot\mathbf{r}}\left[-\mathbf{k}\frac{i}{\varepsilon_0|\mathbf{k}|^2}\right]=\frac{(2\pi)^{3/2}}{4\pi\varepsilon_0}\frac{\mathbf{r}}{|\mathbf{r}|^3}. \tag{1.71}$$

The product of two reciprocal-space functions $\breve{F}(\mathbf{k},\boldsymbol{t})$ and $\breve{G}(\mathbf{k},\boldsymbol{t})$ corresponds in the real space to the convolution of their real-space representations $F(\mathbf{r},\boldsymbol{t})$ and $G(\mathbf{r},\boldsymbol{t})$ [120], namely

$$\breve{F}(\mathbf{k},\boldsymbol{t})\breve{G}(\mathbf{k},\boldsymbol{t})=\frac{1}{(2\pi)^{3/2}}\int d\mathbf{r}'F(\mathbf{r}',\boldsymbol{t})G(\mathbf{r}-\mathbf{r}',\boldsymbol{t}). \tag{1.72}$$

Therefore, we obtain

$$\mathbf{E}_{\parallel}(\mathbf{r},t)=\frac{1}{4\pi\varepsilon_0}\int d\mathbf{r}'\varrho(\mathbf{r}',t)\frac{\mathbf{r}-\mathbf{r}'}{|\mathbf{r}-\mathbf{r}'|^3}. \tag{1.73}$$

This expression is independent of the choice of gauge.

Finally, we discuss some further insights into the electric field provided by the reciprocal-space representation. To this end, we transform into reciprocal space the expression that connects the vector potential with the electric field [Eq. (1.9)], which yields

$$\breve{\mathbf{E}}(\mathbf{k},t)=-\frac{\partial}{\partial t}\breve{\mathbf{A}}(\mathbf{k},t)-i\mathbf{k}\breve{\phi}(\mathbf{k},t). \tag{1.74}$$

The decomposition of this expression into transverse and longitudinal components leads to

$$\breve{\mathbf{E}}_{\perp}(\mathbf{k},t)=-\frac{\partial}{\partial t}\breve{\mathbf{A}}_{\perp}(\mathbf{k},t), \tag{1.75a}$$

$$\breve{\mathbf{E}}_{\parallel}(\mathbf{k},t)=-\frac{\partial}{\partial t}\breve{\mathbf{A}}_{\parallel}(\mathbf{k},t)-i\mathbf{k}\breve{\phi}(\mathbf{k},t). \tag{1.75b}$$

Therefore, we obtain $\breve{\mathbf{E}}_{\parallel}(\mathbf{k},t)=-i\mathbf{k}\breve{\phi}(\mathbf{k},t)$ in the Coulomb gauge, where $\breve{\mathbf{A}}_{\parallel}(\mathbf{k},t)=\mathbf{A}_{\parallel}(\mathbf{r},t)=0$. Thus, the transverse and longitudinal components of the electric field in the real-space representation become

$$\mathbf{E}_{\perp}(\mathbf{r},t)=-\frac{\partial}{\partial t}\mathbf{A}(\mathbf{r},t)=-\frac{\partial}{\partial t}\mathbf{A}_{\perp}(\mathbf{r},t), \tag{1.76a}$$

$$\mathbf{E}_{\parallel}(\mathbf{r},t)=-\boldsymbol{\nabla}\phi(\mathbf{r},t). \tag{1.76b}$$

Last, substituting Eq. (1.73) into Eq. (1.76b), we obtain

$$\phi(\mathbf{r},t)=\frac{1}{4\pi\varepsilon_0}\int d\mathbf{r}'\varrho(\mathbf{r}',t)\frac{1}{|\mathbf{r}-\mathbf{r}'|}, \tag{1.77}$$

which reveals that, in the Coulomb gauge, the scalar potential is equivalent to the Coulomb potential of the charge distribution.

1.2.2 Periodic boundary conditions

In this section, we impose periodic boundary conditions on the electromagnetic field in the presence of radiation sources, in a similar way to the procedure described in Section 1.1.3. These periodic boundary conditions facilitate the quantization of the field. First, we recall that in free space a homogeneous wave equation can be derived for the vector potential $\mathbf{A}(\mathbf{r},t) = \mathbf{A}_\perp(\mathbf{r},t)$ in the Coulomb gauge [Eq. (1.16)]. In the presence of radiation sources, this wave equation becomes inhomogeneous. To show this, we substitute the expressions relating the vector potential with the magnetic field [Eq. (1.7)] and with the electric field [Eq. (1.9)] into the Maxwell's equation (1.1d) and decompose the resulting expression into transverse and longitudinal components. In this way, we obtain

$$\nabla^2 \mathbf{A}_\perp(\mathbf{r},t) - \frac{1}{c^2}\frac{\partial^2}{\partial t^2}\mathbf{A}_\perp(\mathbf{r},t) = \frac{1}{\varepsilon_0 c^2}\boldsymbol{j}_\perp(\mathbf{r},t), \tag{1.78}$$

$$\frac{\partial}{\partial t}\mathbf{E}_\parallel(\mathbf{r},t) = \frac{1}{\varepsilon}\boldsymbol{j}_\parallel(\mathbf{r},t). \tag{1.79}$$

On the one hand, Eq. (1.78) is the inhomogeneous wave equation for the vector potential, with driving proportional to $\boldsymbol{j}_\perp(\mathbf{r},t)$. On the other hand, Eq. (1.79) can be related with the continuity equation [Eq. (1.2)], as the longitudinal electric field is determined by the charge density $\varrho(\mathbf{r},t)$ in the Coulomb gauge [Eq. (1.73)].

Next, we impose periodic boundary conditions by considering again that the electromagnetic field is contained in a box of side L. As discussed for the free-space electromagnetic field in Section 1.1.3, these periodic boundary conditions yield $\mathbf{k} = 2\pi(m_x, m_y, m_z)/L$, with m_x, m_y and m_z integer numbers. In this way, the vector potential can be written as a Fourier series

$$\mathbf{A}_\perp(\mathbf{r},t) = \sum_{\mathbf{k},s} \mathbf{e}_{\mathbf{k}s}[A_{\mathbf{k}s}(t)e^{i\mathbf{k}\cdot\mathbf{r}} + A^*_{\mathbf{k}s}(t)e^{-i\mathbf{k}\cdot\mathbf{r}}]. \tag{1.80}$$

Notably, in the presence of radiation sources $A_{\mathbf{k}s}(t)$ follows the equation of motion of a driven harmonic oscillator, according to the inhomogeneous wave equation given in Eq. (1.78). This contrasts with the simple equation of motion of an undriven harmonic oscillator that $A_{\mathbf{k}s}(t)$ follows in the absence of radiation sources [Eq. (1.23)]. Consequently, in the presence of radiation sources, $\mathbf{A}_\perp(\mathbf{r},t)$ no longer corresponds to a simple expansion of plane waves (see Ref. [120] for further information).

Moreover, substituting the above Fourier series into the expressions relating the vector potential with the transverse electric field [Eq. (1.76a)] and with the

magnetic field [Eq. (1.7)], we obtain

$$\mathbf{E}_{\perp}(\mathbf{r},t) = i\sum_{\mathbf{k},s}\omega_{\mathrm{k}}\mathbf{e}_{\mathbf{k}s}[A_{\mathbf{k}s}(t)e^{i\mathbf{k}\cdot\mathbf{r}} - A^{*}_{\mathbf{k}s}(t)e^{-i\mathbf{k}\cdot\mathbf{r}}], \tag{1.81}$$

$$\mathbf{B}(\mathbf{r},t) = i\sum_{\mathbf{k},s}(\mathbf{k}\times\mathbf{e}_{\mathbf{k}s})[A_{\mathbf{k}s}(t)e^{i\mathbf{k}\cdot\mathbf{r}} - A^{*}_{\mathbf{k}s}(t)e^{-i\mathbf{k}\cdot\mathbf{r}}]. \tag{1.82}$$

These expressions, valid in the Coulomb gauge, are identical to the free-space expressions in Eqs. (1.25a)–(1.25b), except for the different time evolution of $A_{\mathbf{k}s}(t)$ in both cases.

1.2.3 Quantization of the electromagnetic field in the presence of radiation sources

We describe in this section the canonical quantization of the electromagnetic field in the presence of radiation sources. With this purpose, we first derive the energy of the electromagnetic field H_F, which can be decomposed into transverse $H_{F\perp}$ and longitudinal $H_{F\parallel}$ components [Eqs. (1.29a)–(1.29b)].

On the one hand, to obtain $H_{F\perp}$ we follow an analogous procedure to the one described in Section 1.1.4. Substituting the expressions of the transverse electric and magnetic fields in the presence of radiation sources [Eqs. (1.81) and (1.82)] into the expression of the transverse electromagnetic energy in Eq. (1.29a), we obtain

$$H_{F\perp} = \varepsilon_0\mathcal{V}\sum_{\mathbf{k},s}\omega_{\mathrm{k}}^2\left(A^{*}_{\mathbf{k}s}A_{\mathbf{k}s} + A_{\mathbf{k}s}A^{*}_{\mathbf{k}s}\right), \tag{1.83}$$

which is formally identical to the expression of $H_{F\perp}$ in free space [Eq. (1.35)]. Thus, we can introduce the canonical position and momentum variables as in Section 1.1.4 and promote them to quantum-mechanical operators that satisfy the canonical commutation relations given in Eqs. (1.39a)–(1.39b). Consequently, the annihilation and creation operators can be introduced from $\hat{q}_{\mathbf{k}s}$ and $\hat{p}_{\mathbf{k}s}$ again through Eqs. (1.41a)–(1.41b), with commutation relations given in Eqs. (1.42a)–(1.42b). Therefore, we obtain that the quantum-mechanical Hamiltonian of the transverse electromagnetic field is formally identical to the free-space Hamiltonian [Eq. (1.43)], namely

$$\hat{H}_{F\perp} = \sum_{\mathbf{k},s}\hbar\omega_{\mathrm{k}}(\hat{a}^{\dagger}_{\mathbf{k}s}\hat{a}_{\mathbf{k}s} + \frac{1}{2}). \tag{1.84}$$

Thus, the eigenstates of this Hamiltonian are again the product of Fock states $|\{n_{\mathbf{k}s}\}\rangle$, with $n_{\mathbf{k}s}$ the occupation number of photons in mode ($\mathbf{k}$,s). In the Schrödinger picture, the transverse vector potential, the transverse electric field and the magnetic field operators are also formally identical to that obtained in free

space [Eqs. (1.45), (1.46) and (1.47), respectively]. Therefore,

$$\hat{\mathbf{A}}(\mathbf{r}) = \hat{\mathbf{A}}_{\perp}(\mathbf{r}) = \sum_{\mathbf{k},s} \sqrt{\frac{\hbar}{2\omega_{\mathrm{k}}\varepsilon_0 \mathcal{V}}} \mathbf{e}_{\mathbf{k}s} [\hat{a}_{\mathbf{k}s} e^{i\mathbf{k}\cdot\mathbf{r}} + \hat{a}^{\dagger}_{\mathbf{k}s} e^{-i\mathbf{k}\cdot\mathbf{r}}], \tag{1.85}$$

$$\hat{\mathbf{E}}_{\perp}(\mathbf{r}) = i \sum_{\mathbf{k},s} \sqrt{\frac{\hbar\omega_{\mathrm{k}}}{2\varepsilon_0 \mathcal{V}}} \mathbf{e}_{\mathbf{k}s} [\hat{a}_{\mathbf{k}s} e^{i\mathbf{k}\cdot\mathbf{r}} - \hat{a}^{\dagger}_{\mathbf{k}s} e^{-i\mathbf{k}\cdot\mathbf{r}}], \tag{1.86}$$

$$\hat{\mathbf{B}}(\mathbf{r}) = i \sum_{\mathbf{k},s} \sqrt{\frac{\hbar}{2\varepsilon_0 \mathcal{V}\omega_{\mathrm{k}}}} (\mathbf{k} \times \mathbf{e}_{\mathbf{k}s}) [\hat{a}_{\mathbf{k}s} e^{i\mathbf{k}\cdot\mathbf{r}} - \hat{a}^{\dagger}_{\mathbf{k}s} e^{-i\mathbf{k}\cdot\mathbf{r}}]. \tag{1.87}$$

However, we emphasize that the time evolution of $\hat{a}_{\mathbf{k}s}(t)$ and $\hat{a}^{\dagger}_{\mathbf{k}s}(t)$ in the Heisenberg picture is no longer described by the free-space expressions given in Eqs. (1.49a)–(1.49b), as in the presence of radiation sources these operators correspond to driven harmonic oscillators rather than to simple harmonic oscillators (see Ref. [120] for further information).

On the other hand, the presence of radiation sources becomes explicit in the longitudinal electromagnetic energy $H_{F\parallel}$, which vanishes in free space. According to Eq. (1.70), the longitudinal electric field (in the reciprocal space) is related to the charge density, resulting in

$$H_{F\parallel} = \frac{\varepsilon_0}{2} \int_{\mathcal{V}} d\mathbf{k} \breve{\mathbf{E}}^2_{\parallel}(\mathbf{k}, t) = \frac{1}{2\varepsilon_0} \int_{\mathcal{V}} d\mathbf{k} \frac{\breve{\varrho}^*(\mathbf{k}, t)\breve{\varrho}(\mathbf{k}, t)}{|\mathbf{k}|^2}. \tag{1.88}$$

Using Eq. (1.72) and the *Parseval-Plancherel identity*, given by

$$\int d\mathbf{r} F^*(\mathbf{r}, t) G(\mathbf{r}, t) = \int d\mathbf{k} \breve{F}^*(\mathbf{k}, t) \breve{G}(\mathbf{k}, t), \tag{1.89}$$

we can rewrite the longitudinal electromagnetic energy in the real-space representation as

$$H_{F\parallel} = \frac{1}{8\pi\varepsilon_0} \int_{\mathcal{V}} \int_{\mathcal{V}} d\mathbf{r} d\mathbf{r}' \frac{\varrho(\mathbf{r}, t)\varrho(\mathbf{r}', t)}{|\mathbf{r} - \mathbf{r}'|}. \tag{1.90}$$

Therefore, the longitudinal electromagnetic energy corresponds to the Coulomb electrostatic energy of the system of charges [121]. In Section 1.2.6, we discuss the quantization of $H_{F\parallel}$ in the case of a set of charged particles corresponding to a two-level quantum emitter.

1.2.4 Interaction between the electromagnetic field and a system of moving charged particles

We derive in this section the quantum-mechanical Hamiltonian describing the interaction between the electromagnetic field and N charged and moving particles. We consider that these particles are indexed by $i = 1, \ldots, N$ and that particle i has mass m_i and charge q_i. Additionally, this particle has time-dependent canonical

position $\mathbf{r}_i = \mathbf{r}_i(t)$ and velocity $\dot{\mathbf{r}}_i = \dot{\mathbf{r}}_i(t)$, although we do not explicitly write the time dependence of these quantities, for simplicity. This system of radiation sources is described by the charge density

$$\varrho(\mathbf{r}, t) = \sum_i q_i \delta(\mathbf{r} - \mathbf{r}_i), \tag{1.91}$$

and by the current density

$$\boldsymbol{j}(\mathbf{r}, t) = \sum_i q_i \dot{\mathbf{r}}_i \delta(\mathbf{r} - \mathbf{r}_i). \tag{1.92}$$

The total energy H of the system can be decomposed into the electromagnetic energy H_F and the kinetic energy H_K of the particles. Thus,

$$H = H_F + H_K = H_F + \sum_i \frac{1}{2} m_i \dot{\mathbf{r}}_i^2, \tag{1.93}$$

with the kinetic energy determined by the mass and velocity of the particles.

Next, we derive the expression of the canonical momenta of the particles $\mathbf{p}_i$, which allows us to quantize the kinetic Hamiltonian in Eq. (1.93) by promoting $\mathbf{r}_i$ and $\mathbf{p}_i$ to Hilbert-space operators. In general, the α-Cartesian component of the canonical momentum $\mathbf{p}_i$ (with $\alpha = x, y, z$) can be obtained from the Lagrangian $\mathcal{L}$ of the system and the canonical position as $p_{i,\alpha} = (\partial \mathcal{L})/(\partial \dot{r}_{i,\alpha})$. One can show that a suitable Lagrangian describing the classical dynamics of the moving particles and the electromagnetic field is given by [119, 120]

$$\mathcal{L} = \frac{1}{2} \int_{\mathcal{V}} \left[\varepsilon_0 \mathbf{E}^2(\mathbf{r}, t) - \frac{1}{\mu_0} \mathbf{B}^2(\mathbf{r}, t) \right] d\mathbf{r} + \sum_i \left[\frac{1}{2} m_i \dot{\mathbf{r}}_i^2 + q_i \mathbf{A}(\mathbf{r}_i, t) \cdot \dot{\mathbf{r}}_i - q_i \phi(\mathbf{r}_i) \right]. \tag{1.94}$$

This Lagrangian satisfies the principle of least action, is consistent with the Lorentz force, and is also consistent with the classical Hamiltonian in Eq. (1.93). From this Lagrangian, we find that the canonical momentum of particle i, in the Coulomb gauge [Eq. (1.11)], is given by

$$\mathbf{p}_i = m_i \dot{\mathbf{r}}_i + q_i \mathbf{A}_\perp(\mathbf{r}_i, t), \tag{1.95}$$

where the first term on the right-hand side corresponds to the *kinetic momentum* in Newtonian mechanics. In this way, the kinetic energy of the charged particles [last term on the right-hand side of Eq. (1.93)] can be rewritten as

$$H_K = \sum_i \frac{1}{2m_i} \Big(\mathbf{p}_i - q_i \mathbf{A}_\perp(\mathbf{r}_i, t) \Big)^2. \tag{1.96}$$

We now promote the canonical position and momentum of each particle to Hilbert-

space operators $\hat{\mathbf{r}}_i$ and $\hat{\mathbf{p}}_i$ that satisfy the canonical commutation relation

$$[\hat{r}_{i,\alpha}, \hat{\mathrm{p}}_{j,\beta}] = i\hbar\delta_{i,j}\delta_{\alpha,\beta}. \tag{1.97}$$

Moreover, we decompose the quantum-mechanical Hamiltonian of the electromagnetic field $\hat{H}_F$ into its transverse component $\hat{H}_{F\perp}$ [Eq. (1.84)] and its longitudinal component $\hat{H}_{F\parallel}$ [given by the quantized Coulomb electrostatic energy of the system of charges in Eq. (1.90)]. In this way, we obtain the total quantum-mechanical Hamiltonian (in the Schrödinger picture)

$$\hat{H}^{mc} = \sum_{\mathbf{k},s} \hbar\omega_{\mathrm{k}}(\hat{a}^{\dagger}_{\mathbf{k}s}\hat{a}_{\mathbf{k}s} + \frac{1}{2}) + \hat{H}_{F\parallel} + \sum_i \frac{1}{2m_i}\left(\hat{\mathbf{p}}_i - q_i\hat{\mathbf{A}}(\hat{\mathbf{r}}_i)\right)^2, \tag{1.98}$$

which is called the *minimal coupling form* of the Hamiltonian. The first term on the right-hand side of Eq. (1.98) is formally identical to the quantum-mechanical Hamiltonian of the free-space electromagnetic field, as discussed above. Additionally, the quantum-mechanical Hamiltonian

$$\hat{H}^{mc}_P = \sum_i \frac{\hat{\mathbf{p}}_i^2}{2m_i} + \hat{H}_{F\parallel} \tag{1.99}$$

involves only the degrees of freedom of the charged particles and, thus, is usually identified as the Hamiltonian of the set of particles. More specifically, the first term on the right-hand side of this equation involves only the degrees of freedom of the motion of the particles, whereas $\hat{H}_{F\parallel}$ corresponds to the quantized Coulomb electrostatic energy of the charged particles [Eq. (1.90)]. Last, the remaining terms in Eq. (1.98), namely

$$\hat{H}^{mc}_I = -\sum_i \frac{q_i}{2m_i}\left(\hat{\mathbf{p}}_i \cdot \hat{\mathbf{A}}(\hat{\mathbf{r}}_i) + \hat{\mathbf{A}}(\hat{\mathbf{r}}_i) \cdot \hat{\mathbf{p}}_i\right) + \sum_i \frac{q_i^2}{2m_i}\mathbf{A}^2(\hat{\mathbf{r}}_i), \tag{1.100}$$

are interpreted as the interaction Hamiltonian (as they involve degrees of freedom of the particle and of the field), written in the minimal coupling form.

1.2.5 Power-Zienau transformation

In this section, we present the *Power-Zienau transformation*, which leads to a more familiar form of the interaction Hamiltonian than that in Eq. (1.100). To this end, we assume that the total charge of the system of particles vanishes (i.e., $\sum_i q_i = 0$), as in the case of neutral atoms or molecules. Additionally, we denote by $R_{\max}$ the largest distance of the charged particles from the center of mass $\mathbf{r}_0$ and assume that the particles couple significantly only to electromagnetic modes of wavelength larger than $R_{\max}$, which is known as the *long-wavelength approximation*. As a consequence, we can replace the Schrödinger picture operator $\hat{\mathbf{A}}(\hat{\mathbf{r}}_i)$ by $\hat{\mathbf{A}}(\mathbf{r}_0)$ [116], which is identified as the electromagnetic vacuum field. The total Hamiltonian in

the minimal coupling form then becomes

$$\hat{H}^{mc} = \sum_{\mathbf{k},s} \hbar\omega_{\mathrm{k}} \left(\hat{a}^{\dagger}_{\mathbf{k}s} \hat{a}_{\mathbf{k}s} + \frac{1}{2} \right) + \hat{H}_{F\parallel} + \sum_i \frac{1}{2m_i} \left(\hat{\mathbf{p}}_i - q_i \hat{\mathbf{A}}(\mathbf{r}_0) \right)^2 . \tag{1.101}$$

Next, we introduce the unitary operator governing the Power-Zienau transformation (see Appendix C for a review of unitary transformations in quantum mechanics). This operator is given by

$$\hat{T} = \exp\left[-\frac{i}{\hbar} \hat{\boldsymbol{\mu}} \cdot \hat{\mathbf{A}}(\mathbf{r}_0) \right] = \exp\left[\sum_{\mathbf{k},s} \hat{\lambda}^{\dagger}_{\mathbf{k}s} \hat{a}_{\mathbf{k}s} - \hat{\lambda}_{\mathbf{k}s} \hat{a}^{\dagger}_{\mathbf{k}s} \right], \tag{1.102}$$

where we have introduced the electric dipole moment of the system of charges

$$\hat{\boldsymbol{\mu}} = \sum_i q_i \hat{\mathbf{r}}_i, \tag{1.103}$$

and we have defined

$$\hat{\lambda}_{\mathbf{k}s} = \frac{i}{\sqrt{2\hbar\omega_{\mathrm{k}}\varepsilon_0 \mathcal{V}}} e^{-i\mathbf{k}\cdot\mathbf{r}_0} \hat{\boldsymbol{\mu}} \cdot \boldsymbol{e}_{\mathbf{k}s}. \tag{1.104}$$

The Hamiltonian is transformed as

$$\begin{aligned} \hat{H}^{mp} &= \hat{T} \hat{H}^{mc} \hat{T}^{\dagger} \\ &= \hat{T} \sum_{\mathbf{k},s} \hbar\omega_{\mathrm{k}} (\hat{a}^{\dagger}_{\mathbf{k}s} \hat{a}_{\mathbf{k}s} + \frac{1}{2}) \hat{T}^{\dagger} + \hat{T} \hat{H}_{F\parallel} \hat{T}^{\dagger} + \hat{T} \sum_i \frac{1}{2m_i} \left(\hat{\mathbf{p}}_i - q_i \hat{\mathbf{A}}(\mathbf{r}_0) \right)^2 \hat{T}^{\dagger}, \end{aligned} \tag{1.105}$$

where *mp* stands for *multipolar form*.

In the following, we compute each of the terms in the last equality of Eq. (1.105) separately. To this end, we use the *expansion theorem*

$$e^{x\hat{O}} \hat{Q} e^{-x\hat{O}} = \hat{Q} + x[\hat{O}, \hat{Q}] + \frac{x^2}{2!} [\hat{O}, [\hat{O}, \hat{Q}]] + \dots \tag{1.106}$$

First, we find

$$\hat{T} \hat{a}_{\mathbf{k}s} \hat{T}^{\dagger} = \hat{a}_{\mathbf{k}s} + \hat{\lambda}_{\mathbf{k}s}, \tag{1.107a}$$

$$\hat{T} \hat{a}^{\dagger}_{\mathbf{k}s} \hat{T}^{\dagger} = \hat{a}^{\dagger}_{\mathbf{k}s} + \hat{\lambda}^{\dagger}_{\mathbf{k}s}. \tag{1.107b}$$

As a consequence, the first term in the second line of Eq. (1.105) becomes

$$\begin{aligned}\hat{T}\sum_{\mathbf{k},s}\hbar\omega_{\mathrm{k}}(\hat{a}^{\dagger}_{\mathbf{k}s}\hat{a}_{\mathbf{k}s}+\frac{1}{2})\hat{T}^{\dagger}&=\sum_{\mathbf{k},s}\hbar\omega_{\mathrm{k}}\left[(\hat{a}^{\dagger}_{\mathbf{k}s}+\hat{\lambda}^{\dagger}_{\mathbf{k}s})(\hat{a}_{\mathbf{k}s}+\hat{\lambda}_{\mathbf{k}s})+\frac{1}{2}\right]\\ =\sum_{\mathbf{k},s}\hbar\omega_{\mathrm{k}}(\hat{a}^{\dagger}_{\mathbf{k}s}\hat{a}_{\mathbf{k}s}+\frac{1}{2})&+\sum_{\mathbf{k},s}\hbar\omega_{\mathrm{k}}(\hat{a}^{\dagger}_{\mathbf{k}s}\hat{\lambda}_{\mathbf{k}s}+\hat{a}_{\mathbf{k}s}\hat{\lambda}^{\dagger}_{\mathbf{k}s})+\sum_{\mathbf{k},s}\hbar\omega_{\mathrm{k}}\hat{\lambda}^{\dagger}_{\mathbf{k}s}\hat{\lambda}_{\mathbf{k}s},\end{aligned} \tag{1.108}$$

where we have used that the Power-Zienau transformation is unitary and thus

$$\hat{T}\hat{O}\hat{Q}\hat{T}^{\dagger}=\hat{T}\hat{O}\hat{T}^{\dagger}\hat{T}\hat{Q}\hat{T}^{\dagger}, \tag{1.109}$$

with $\hat{O}$ and $\hat{Q}$ arbitrary operators. Crucially, using Eq. (1.102), we can rewrite the second term in the second line of Eq. (1.108) as

$$\begin{aligned}\sum_{\mathbf{k},s}\hbar\omega_{\mathrm{k}}(\hat{a}^{\dagger}_{\mathbf{k}s}\hat{\lambda}_{\mathbf{k}s}+\hat{a}_{\mathbf{k}s}\hat{\lambda}^{\dagger}_{\mathbf{k}s})&=-\sum_{\mathbf{k},s}i\sqrt{\frac{\hbar\omega_{\mathrm{k}}}{2\varepsilon_0\mathcal{V}}}\hat{\boldsymbol{\mu}}\cdot\boldsymbol{e}_{\mathbf{k}s}(\hat{a}^{\dagger}_{\mathbf{k}s}e^{-i\mathbf{k}\cdot\mathbf{r}_0}-\hat{a}_{\mathbf{k}s}e^{i\mathbf{k}\cdot\mathbf{r}_0})\\ &=-\hat{\boldsymbol{\mu}}\cdot\hat{\mathbf{E}}_{\perp}(\mathbf{r}_0).\end{aligned} \tag{1.110}$$

Here, we have used the expression of the transverse electric field operator [Eq. (1.86)] in the long-wavelength approximation. Moreover, the last term in the second line of Eq. (1.108) does not depend on photon annihilation or creation operators. Instead, this term depends on the dipole operator $\hat{\boldsymbol{\mu}}$, namely

$$\hat{\varepsilon}_{\mu}\equiv\sum_{\mathbf{k},s}\hbar\omega_{\mathrm{k}}\hat{\lambda}^{\dagger}_{\mathbf{k}s}\hat{\lambda}_{\mathbf{k}s}=\sum_{\mathbf{k},s}\frac{1}{2\varepsilon_0\mathcal{V}}(\hat{\boldsymbol{\mu}}\cdot\boldsymbol{e}_{\mathbf{k}s})^2, \tag{1.111}$$

which can be interpreted as the *dipole self-energy* of the system [120].

Next, we compute the second term in the second line of Eq. (1.105). Since $\hat{H}_{F\parallel}$ depends only on the quantum-mechanical position operators of the charged particles, it follows that $[\hat{H}_{F\parallel},\hat{T}]=0$. Thus, we find

$$\hat{T}\hat{H}_{F\parallel}\hat{T}^{\dagger}=\hat{H}_{F\parallel}. \tag{1.112}$$

Last, we analyze the third term in the second line of Eq. (1.105). The canonical momentum of particle i is transformed as

$$\hat{T}\hat{\mathbf{p}}_i\hat{T}^{\dagger}=\hat{\mathbf{p}}_i-\frac{iq_i}{\hbar}[\hat{\mathbf{r}}_i\cdot\hat{\mathbf{A}}(\mathbf{r}_0),\hat{\mathbf{p}}_i]=\hat{\mathbf{p}}_i+q_i\hat{\mathbf{A}}(\mathbf{r}_0). \tag{1.113}$$

Additionally, $[\hat{T},\hat{\mathbf{A}}(\mathbf{r}_0)]=0$. Thus, $\hat{\mathbf{A}}(\mathbf{r}_0)$ remains invariant under the Power-Zienau transformation:

$$\hat{T}\hat{\mathbf{A}}(\mathbf{r}_0)\hat{T}^{\dagger}=\hat{\mathbf{A}}(\mathbf{r}_0). \tag{1.114}$$

As a consequence, we obtain that the third term in the second line of Eq. (1.105)

becomes

$$\hat{T}\sum_i \frac{1}{2m_i}\left(\hat{\mathbf{p}}_i - q_i\hat{\mathbf{A}}(\mathbf{r}_0)\right)^2\hat{T}^\dagger = \sum_i \frac{1}{2m_i}\hat{\mathbf{p}}_i^2, \tag{1.115}$$

where we have used again that the Power-Zienau transformation is unitary [Eq. (1.109)].

Therefore, the transformed Hamiltonian becomes

$$\hat{H}^{mp} = \hat{T}\hat{H}^{mc}\hat{T}^\dagger = \sum_{\mathbf{k},s}\hbar\omega_{\mathrm{k}}\left(\hat{a}^\dagger_{\mathbf{k}s}\hat{a}_{\mathbf{k}s} + \frac{1}{2}\right) + \hat{H}_P^{mp} - \hat{\boldsymbol{\mu}}\cdot\hat{\mathbf{E}}_\perp(\mathbf{r}_0), \tag{1.116}$$

which is known as *the multipolar form* of the Hamiltonian. Here, we have defined the multipolar form of the Hamiltonian of the charged particles as

$$\hat{H}_P^{mp} = \sum_i \frac{1}{2m_i}\hat{\mathbf{p}}_i^2 + \hat{H}_{F\parallel} + \hat{\varepsilon}_\mu, \tag{1.117}$$

which depends uniquely on particle operators and not on photon creation or annihilation operators. Crucially, the interaction Hamiltonian in the multipolar form is given directly by the scalar product of the dipole moment operator of the system of charges and the transverse electric field operator:

$$\hat{H}_I^{mp} = -\hat{\boldsymbol{\mu}}\cdot\hat{\mathbf{E}}_\perp(\mathbf{r}_0). \tag{1.118}$$

Thus, this form of the interaction Hamiltonian is formally analogous to the potential energy of an electric point dipole in the presence of an external electric field [121]. In this thesis, we generally prefer to use the multipolar form of the interaction Hamiltonian over the minimal coupling form.

1.2.6 Interaction between the vacuum field and a two-level quantum emitter

Next, we consider that the system of N charged particles (with center of mass at $\boldsymbol{r}_0$) corresponds to a quantum emitter (QE) whose electronic dynamics can be described well by only two states (ground and excited). This *two-level approximation* is usually well justified for describing the dynamics and light emission from a QE (such as an atom or a molecule) that is driven near resonance to its lower-energy electronic excited state, with the higher electronic excited states being far off resonance with this external driving [124]. This approximation is well suited to the QEs that we consider in this thesis.

We call *ground state* to the lower energy electronic state $|g\rangle$ of the QE, while the higher energy electronic state $|e\rangle$ is called *excited state*. We consider that the transition frequency between these two states is ω_0, as shown in the schematic representation in Fig. 1.1. Under this two-level approximation, the Hamiltonian in

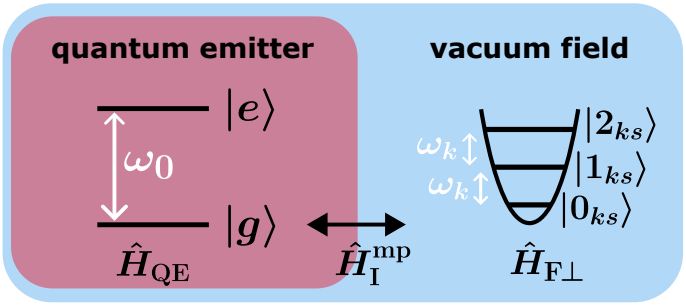

Figure 1.1: Schematic representation of the interaction between a quantum emitter (QE) and the electromagnetic vacuum field. The electronic dynamics of the QE is assumed to be well described by two states. The lower energy state is called (electronic) ground state $|g\rangle$, whereas the higher energy one is named excited state $|e\rangle$. These two states have transition frequency ω_0 and, thus, the Hamiltonian of the QE is $\hat{H}_{\mathrm{QE}} = \frac{\hbar\omega_0}{2}\hat{\sigma}_z$. The electromagnetic vacuum field, with Hamiltonian $\hat{H}_{F\perp} = \sum_{\mathbf{k},s} \hbar\omega_{\mathrm{k}}(\hat{a}^\dagger_{\mathbf{k}s}\hat{a}_{\mathbf{k}s} + 1/2)$, consists of an infinite collection of quantum harmonic oscillators of frequency ω_{k}, with $\hat{a}^\dagger_{\mathbf{k}s}$ and $\hat{a}_{\mathbf{k}s}$ the creation and annihilation operators of photons with wavevector $\mathbf{k}$ and polarization mode s. The Hamiltonian describing the interaction between the quantum emitter and the vacuum field in the multipolar form is $\hat{H}_{\mathrm{I}}^{mp} = -\hat{\boldsymbol{\mu}}\cdot\hat{\mathbf{E}}_\perp(\mathbf{r}_0)$, with $\hat{\boldsymbol{\mu}}$ the electric dipole moment operator of the QE, $\hat{\mathbf{E}}_\perp(\mathbf{r}_0)$ the transverse electric field operator, and $\mathbf{r}_0$ the position of the QE.

Eq. (1.117) becomes

$$\hat{H}_P^{mp} \to \hat{H}_{\mathrm{QE}} = \hbar\frac{\omega_0}{2}|e\rangle\langle e| - \hbar\frac{\omega_0}{2}|g\rangle\langle g| = \hbar\frac{\omega_0}{2}\hat{\sigma}_z, \tag{1.119}$$

with $\hat{\sigma}_z = |e\rangle\langle e| - |g\rangle\langle g|$ the z-Pauli matrix and the level of zero energy fixed at half the energy between $|g\rangle$ and $|e\rangle$. The fermionic lowering and raising operators of the two-level electronic dynamics are $\hat{\sigma} = |g\rangle\langle e|$ and $\hat{\sigma}^\dagger = |e\rangle\langle g|$, respectively. The commutation relations of these fermionic operators are given as

$$[\hat{\sigma}, \hat{\sigma}^\dagger] = -\hat{\sigma}_z, \tag{1.120a}$$
$$[\hat{\sigma}_z, \hat{\sigma}] = -2\hat{\sigma}, \tag{1.120b}$$
$$[\hat{\sigma}_z, \hat{\sigma}^\dagger] = 2\hat{\sigma}^\dagger. \tag{1.120c}$$

Additionally, the time evolution of the lowering and raising operators in the Heisenberg picture is obtained using the Heisenberg equation [Eq. (1.48)]. Ignoring the interaction of the emitter with the electromagnetic field (whose influence is latter discussed), we obtain

$$\frac{d}{dt}\hat{\sigma}(t) = -\frac{i}{\hbar}[\hat{\sigma}(t), \hat{H}_{\mathrm{QE}}] = -i\omega_0\hat{\sigma}(t), \tag{1.121a}$$
$$\frac{d}{dt}\hat{\sigma}^\dagger(t) = -\frac{i}{\hbar}[\hat{\sigma}^\dagger(t), \hat{H}_{\mathrm{QE}}] = i\omega_0\hat{\sigma}^\dagger(t). \tag{1.121b}$$

As a consequence, these operators are given in the Heisenberg picture by

$$\hat{\sigma}(t) = \hat{\sigma}(0)e^{-i\omega_0 t}, \tag{1.122a}$$

$$\hat{\sigma}^\dagger(t) = \hat{\sigma}^\dagger(0)e^{i\omega_0 t}. \tag{1.122b}$$

Since the Heisenberg and Schrödinger pictures coincide at the initial time, we have $\hat{\sigma}(0) = \hat{\sigma}$ and $\hat{\sigma}^\dagger(0) = \hat{\sigma}^\dagger$ (see Appendix B).

Next, we derive the Hamiltonian $\hat{H}_I^{mp}$ describing the interaction between the QE and the vacuum field in the multipolar form. To this end, we first analyze the dipole moment operator $\hat{\boldsymbol{\mu}}$ of a general two-level QE. On the one hand, the diagonal elements of this operator, $\langle g|\,\hat{\boldsymbol{\mu}}\,|g\rangle$ and $\langle e|\,\hat{\boldsymbol{\mu}}\,|e\rangle$, are related to the presence of permanent dipole moments in the emitter [125–130], as is the case for polar molecules [127, 128] or asymmetric quantum dots [130]. However, in this thesis, we are interested in QEs that do not have permanent dipole moments, and thus these diagonal elements vanish. On the other hand, the off-diagonal element $\boldsymbol{\mu} = \langle g|\,\hat{\boldsymbol{\mu}}\,|e\rangle$ of this operator couples the electronic ground and excited states of the QE. $\boldsymbol{\mu}$ is known as *transition dipole moment*, and its value can be related to the spontaneous decay rate of the QE, which is discussed in Section 1.3. Thus,

$$\hat{\boldsymbol{\mu}} = \boldsymbol{\mu}\hat{\sigma} + \boldsymbol{\mu}^*\hat{\sigma}^\dagger. \tag{1.123}$$

Substituting this expression into Eq. (1.118), we obtain

$$\hat{H}_I^{mp} = -\left(\boldsymbol{\mu}\hat{\sigma} + \boldsymbol{\mu}^*\hat{\sigma}^\dagger\right)\cdot\sum_{\mathbf{k},s} i\sqrt{\frac{\hbar\omega_{\mathrm{k}}}{2\varepsilon_0\mathcal{V}}}\mathbf{e}_{\mathbf{k}s}[\hat{a}_{\mathbf{k}s}e^{i\mathbf{k}\cdot\mathbf{r}_0} - \hat{a}_{\mathbf{k}s}^\dagger e^{-i\mathbf{k}\cdot\mathbf{r}_0}], \tag{1.124}$$

where we have also used the expression of the transverse electromagnetic field operator $\hat{\mathbf{E}}_\perp(\mathbf{r}_0)$ given in Eq. (1.86).

Last, according to the expression of the total Hamiltonian in Eq. (1.116), the Hamiltonian describing only electromagnetic degrees of freedom is $\hat{H}_{F\perp}$ [Eq. (1.84)]. The total Hamiltonian (in the multipolar form) describing the interaction between the electromagnetic field and the two-level quantum emitter thus becomes

$$\begin{aligned}\hat{H}^{mp} = \hat{H}_{F\perp} + \hat{H}_{\mathrm{QE}} + \hat{H}_I^{mp} &= \sum_{\mathbf{k},s}\hbar\omega_{\mathrm{k}}\left(\hat{a}_{\mathbf{k}s}^\dagger\hat{a}_{\mathbf{k}s} + \frac{1}{2}\right) + \hbar\frac{\omega_0}{2}\hat{\sigma}_z \\ &-\left(\boldsymbol{\mu}\hat{\sigma} + \boldsymbol{\mu}^*\hat{\sigma}^\dagger\right)\cdot\sum_{\mathbf{k},s} i\sqrt{\frac{\hbar\omega_{\mathrm{k}}}{2\varepsilon_0\mathcal{V}}}\mathbf{e}_{\mathbf{k}s}[\hat{a}_{\mathbf{k}s}e^{i\mathbf{k}\cdot\mathbf{r}_0} - \hat{a}_{\mathbf{k}s}^\dagger e^{-i\mathbf{k}\cdot\mathbf{r}_0}].\end{aligned} \tag{1.125}$$

This Hamiltonian facilitates the analysis of light emission from a quantum emitter and, thus, is crucial in this thesis. For example, it facilitates (i) to obtain the Heisenberg picture of the transverse electric field operator $\hat{\mathbf{E}}_\perp$, as shown in Section 1.2.7, and (ii) to introduce the concept of spontaneous emission, as shown in Sections 1.3 and 1.4.5.

1.2.7 Electric field emitted from a two-level quantum emitter

In this section, we derive the electric field emitted from a quantum emitter (QE) using a fundamental approach based on the interaction between the QE and the vacuum field. We begin by recalling that, in the Schrödinger picture, the transverse electric field operator $\hat{\mathbf{E}}_\perp(\mathbf{r})$ is given by a sum of annihilation $\hat{a}_{\mathbf{k}s}$ and creation $\hat{a}^\dagger_{\mathbf{k}s}$ operators and it is formally identical in both free space [Eq. (1.46)] and in the presence of radiation sources [Eq. (1.86)]. However, as discussed in Section 1.2.3, the time evolution of $\hat{a}_{\mathbf{k}s}$ and $\hat{a}^\dagger_{\mathbf{k}s}$ is influenced by the presence of radiation sources. Indeed, we next show that by deriving the Heisenberg evolution of the electric field operator $\hat{\mathbf{E}}_\perp(\mathbf{r},t)$ in the presence of a QE, we can determine how the QE affects the total electric field and extract the expression of the electric field radiated from the QE.

To facilitate the derivation of the Heisenberg-picture operator $\hat{\mathbf{E}}_\perp(\mathbf{r},t)$, we first consider the usual decomposition into two adjoint operators that are known as *positive-frequency* transverse electric field operator $\hat{\mathbf{E}}^{(+)}_\perp(\mathbf{r},t)$ and *negative-frequency* transverse electric field operator $\hat{\mathbf{E}}^{(-)}_\perp(\mathbf{r},t)$. In the Schrödinger picture, this decomposition can be expressed as

$$\hat{\mathbf{E}}_\perp(\mathbf{r}) = \hat{\mathbf{E}}^{(+)}_\perp(\mathbf{r}) + \hat{\mathbf{E}}^{(-)}_\perp(\mathbf{r}), \tag{1.126}$$

where

$$\hat{\mathbf{E}}^{(+)}_\perp(\mathbf{r}) = i\sum_{\mathbf{k},s}\sqrt{\frac{\hbar\omega_\mathrm{k}}{2\varepsilon_0\mathcal{V}}}\hat{a}_{\mathbf{k}s}e^{i\mathbf{k}\cdot\mathbf{r}}\mathbf{e}_{\mathbf{k}s}, \tag{1.127a}$$

$$\hat{\mathbf{E}}^{(-)}_\perp(\mathbf{r}) = -i\sum_{\mathbf{k},s}\sqrt{\frac{\hbar\omega_\mathrm{k}}{2\varepsilon_0\mathcal{V}}}\hat{a}^\dagger_{\mathbf{k}s}e^{-i\mathbf{k}\cdot\mathbf{r}}\mathbf{e}_{\mathbf{k}s}. \tag{1.127b}$$

We recall that, throughout this thesis, the polarization unit vector $\mathbf{e}_{\mathbf{k}s}$ is chosen to be real. The operators $\hat{\mathbf{E}}^{(+)}_\perp(\mathbf{r})$ and $\hat{\mathbf{E}}^{(-)}_\perp(\mathbf{r})$ are referred to as positive-frequency and negative-frequency operators because in free space the former rotates at 'positive frequencies' [proportional to $\exp(-i\omega_\mathrm{k}t)$], whereas the latter does it at 'negative frequencies' [proportional to $\exp(i\omega_\mathrm{k}t)$]. As these operators are adjoint to each other (which is preserved by the time evolution), we focus here on the calculation of $\hat{\mathbf{E}}^{(+)}_\perp(\mathbf{r},t)$.

Moreover, the calculation of $\hat{\mathbf{E}}^{(+)}_\perp(\mathbf{r},t)$ is further simplified by performing the *rotating-wave approximation* (RWA) in the Hamiltonian that describes the interaction between the QE and the electromagnetic vacuum field [Eq. (1.124)]. The RWA consists in neglecting the terms that simultaneously involve (i) a photon creation operator $\hat{a}^\dagger_{\mathbf{k}s}$ and the raising fermionic operator $\hat{\sigma}^\dagger$, and (ii) a photon annihilation operator $\hat{a}_{\mathbf{k}s}$ and the lowering fermionic operator $\hat{\sigma}$. These terms do not conserve the total number of excitations in the full system (including photons

and emitter excitations). The Schrödinger-picture interaction Hamiltonian under the RWA thus becomes

$$\hat{H}_I^{\mathrm{RWA}} = \hbar \sum_{\mathbf{k},s} \left[g_{\mathbf{k}s}(\mathbf{r}_0)\hat{\sigma}^\dagger \hat{a}_{\mathbf{k}s} + g_{\mathbf{k}s}^*(\mathbf{r}_0)\hat{\sigma}\hat{a}_{\mathbf{k}s}^\dagger \right], \tag{1.128}$$

where we have defined the coupling coefficient

$$g_{\mathbf{k}s}(\mathbf{r}) = -i\sqrt{\frac{\omega_{\mathrm{k}}}{2\varepsilon_0 \hbar \mathcal{V}}}\boldsymbol{\mu}^* \cdot \mathbf{e}_{\mathbf{k}s} e^{i\mathbf{k}\cdot\mathbf{r}}. \tag{1.129}$$

As already mentioned, we focus on deriving the Heisenberg picture of $\hat{\mathbf{E}}_\perp^{(+)}(\mathbf{r})$, which is proportional to the operators $\hat{a}_{\mathbf{k}s}$. The equation of motion of $\hat{a}_{\mathbf{k}s}$ is given by the Heisenberg equation [Eq. (1.48)], which yields

$$\begin{aligned} \frac{d}{dt}\hat{a}_{\mathbf{k}s} &= -\frac{i}{\hbar}[\hat{a}_{\mathbf{k}s}, \hat{H}_{\mathrm{QE}} + \hat{H}_{\mathrm{F}\perp} + \hat{H}_{\mathrm{I}}^{\mathrm{RWA}}] \\ &= -i\left[\hat{a}_{\mathbf{k}s}, \omega_{\mathrm{k}'}\hat{a}_{\mathbf{k}'s'}^\dagger \hat{a}_{\mathbf{k}'s'} + g_{\mathbf{k}s}^*(\mathbf{r}_0)\hat{\sigma}\hat{a}_{\mathbf{k}'s'}^\dagger\right] \\ &= -i\omega_{\mathrm{k}}\hat{a}_{\mathbf{k}s} - ig_{\mathbf{k}s}^*(\mathbf{r}_0)\hat{\sigma}, \end{aligned} \tag{1.130}$$

where we have used the commutation relations of the annihilation and creation photonic operators [Eqs. (1.42a)–(1.42b)]. In the last line of Eq. (1.130), we can identify a term that is proportional to $\hat{a}_{\mathbf{k}s}$, which comes from the Hamiltonian $\hat{H}_{F\perp}$ in the commutator in the first line and, provides the free-space contribution to the positive-frequency electric field operator. Additionally, another term appears in the last line of this equation, which is proportional to the lowering operator $\hat{\sigma}$ of the QE and emerges from the contribution from the interaction Hamiltonian $\hat{H}_{\mathrm{I}}^{\mathrm{RWA}}$ in the commutator in the first line. Integrating in time Eq. (1.130), we obtain

$$\hat{a}_{\mathbf{k}s}(t) = e^{-i\omega_{\mathrm{k}}t}\hat{a}_{\mathbf{k}s} - ie^{-i\omega_{\mathrm{k}}t}g_{\mathbf{k}s}^*(\mathbf{r}_0)\int_0^t d\tau \hat{\sigma}(\tau)e^{i\omega_{\mathrm{k}}\tau}. \tag{1.131}$$

Next, substituting Eq. (1.131) into Eq. (1.127a), we find

$$\hat{\mathbf{E}}_\perp^{(+)}(\mathbf{r},t) = \hat{\mathbf{E}}_{\perp,\mathrm{free}}^{(+)}(\mathbf{r},t) + \sum_{\mathbf{k},s}\sqrt{\frac{\hbar\omega_{\mathrm{k}}}{2\varepsilon_0\mathcal{V}}}\boldsymbol{e}_{\mathbf{k}s}e^{i\mathbf{k}\cdot\mathbf{r}}g_{\mathbf{k}s}^*(\mathbf{r}_0)e^{-i\omega_{\mathrm{k}}t}\int_0^t d\tau\hat{\sigma}(\tau)e^{i\omega_{\mathrm{k}}\tau}, \tag{1.132}$$

with $\hat{\mathbf{E}}_{\perp,\mathrm{free}}^{(+)}(\mathbf{r})$ the free-space contribution, which is given by

$$\hat{\mathbf{E}}_{\perp,\mathrm{free}}^{(+)}(\mathbf{r},t) = i\sum_{\mathbf{k},s}\sqrt{\frac{\hbar\omega_{\mathrm{k}}}{2\varepsilon_0\mathcal{V}}}\hat{a}_{\mathbf{k}s}e^{i(\mathbf{k}\cdot\mathbf{r}-\omega_{\mathrm{k}}t)}\mathbf{e}_{\mathbf{k}s}. \tag{1.133}$$

Additionally, the last term in Eq. (1.132) can be identified with the electric field operator (evaluated at position $\mathbf{r}$) of light emitted from the QE, which in the

following we denote as $\hat{\mathbf{E}}^{(+)}_{\perp,\mathrm{QE}}(\mathbf{r},t)$.

Next, we focus on simplifying the expression of $\hat{\mathbf{E}}^{(+)}_{\perp,\mathrm{QE}}(\mathbf{r},t)$. To this end, we transform the summation over $\mathbf{k}$ into an integral, according to

$$\sum_{\mathbf{k},s} \to \frac{\mathcal{V}}{(2\pi)^3}\sum_s \int_0^{2\pi} d\phi \int_0^{\pi} d\theta \sin\theta \int_0^{\infty} d\mathrm{k}\, \mathrm{k}^2. \tag{1.134}$$

This transformation is well justified because we assume very large quantization volumes ($\mathcal{V}\to\infty$), as discussed in Section 1.1.3. θ and ϕ are the polar and azimuthal angles of the wavevector

$$\mathbf{k} = \mathrm{k}(\sin\theta\cos\phi\boldsymbol{e}_x + \sin\theta\sin\phi\boldsymbol{e}_y + \cos\theta\boldsymbol{e}_z). \tag{1.135}$$

Furthermore, we assume that $\mathbf{r}-\mathbf{r}_0$ is aligned along the z-axis, without loss of generality. In this way,

$$\begin{aligned}\hat{\mathbf{E}}^{(+)}_{\perp,\mathrm{QE}}(\mathbf{r},t) &= \sum_{\mathbf{k},s}\sqrt{\frac{\hbar\omega_{\mathrm{k}}}{2\varepsilon_0\mathcal{V}}}\boldsymbol{e}_{\mathbf{k}s}e^{i\mathbf{k}\cdot\mathbf{r}}g^*_{\mathbf{k}s}(\mathbf{r}_0)e^{-i\omega_{\mathrm{k}}t}\int_0^t d\tau\hat{\sigma}(\tau)e^{i\omega_{\mathrm{k}}\tau}\\ &= \frac{ic}{16\pi^3\varepsilon_0}\int_0^{\infty} d\mathrm{k}\,\mathrm{k}^3\int_0^t d\tau\hat{\sigma}(\tau)e^{i\mathrm{k}c\tau}\int_0^{2\pi}d\phi\int_0^{\pi}d\theta\sin\theta e^{i\mathrm{k}R\cos\theta}\sum_s(\boldsymbol{\mu}^*\cdot\mathbf{e}_{\mathbf{k}s})^*\mathbf{e}_{\mathbf{k}s},\end{aligned} \tag{1.136}$$

with $R=|\mathbf{r}-\mathbf{r}_0|$. To compute the integral in $\mathbf{k}$-space we need to choose some polarization unit vectors $\boldsymbol{e}_{\mathbf{k}s}$ fulfilling the transversality condition in Eq. (1.20) and the orthonormality condition in Eq. (1.21). Here, we select

$$\hat{e}_{\mathbf{k}1} = -\cos\theta\cos\phi\boldsymbol{e}_x - \cos\theta\sin\phi\boldsymbol{e}_y + \sin\theta\boldsymbol{e}_z, \tag{1.137a}$$

$$\hat{e}_{\mathbf{k}2} = \sin\phi\boldsymbol{e}_x - \cos\phi\boldsymbol{e}_y. \tag{1.137b}$$

In this way, we find that the integrals over the angles θ and ϕ become

$$\begin{aligned}&\frac{1}{4\pi}\int_0^{2\pi}d\phi\int_0^{\pi}d\theta\sin\theta\sum_s(\boldsymbol{\mu}^*\cdot\mathbf{e}_{\mathbf{k}s})^*e^{i\mathrm{k}R\cos\theta}\\ &= \frac{1}{4\pi}\int_0^{2\pi}d\phi\int_0^{\pi}d\theta\sin\theta e^{i\mathrm{k}R\cos\theta}\Big[\Big(\sin\phi\mathbf{e}_x-\cos\phi\mathbf{e}_y\Big)\Big(\sin\phi\mu_x-\cos\phi\mu_y\Big)\\ &+\Big(-\cos\theta(\cos\phi\mathbf{e}_x+\sin\phi\mathbf{e}_y)+\sin\theta\mathbf{e}_z\Big)\Big(-\cos\theta(\cos\phi\mu_x+\sin\phi\mu_y)+\sin\theta\mu_z\Big)\Big]\\ &= \mathbf{e}_z\mu_z 2\frac{\sin(\mathrm{k}R)-\mathrm{k}R\cos(\mathrm{k}R)}{(\mathrm{k}R)^3}+(\mathbf{e}_x\mu_x+\mathbf{e}_y\mu_y)\frac{[(\mathrm{k}R)^2-1]\sin(\mathrm{k}R)+\mathrm{k}R\cos(\mathrm{k}R)}{(\mathrm{k}R)^3}.\end{aligned} \tag{1.138}$$

This expression can be further simplified in the far-field limit ($\mathrm{k}R\gg 1$), where the

properties of light emitted from the QE are typically measured. In this limit, we obtain

$$\frac{1}{4\pi}\int_0^{2\pi} d\phi \int_0^{\pi} d\theta \sin\theta \sum_s (\boldsymbol{\mu}^* \cdot \mathbf{e}_{\mathbf{k}s})^* e^{i\mathrm{k}R\cos\theta} \xrightarrow{\mathrm{k}R\gg 1} (\mathbf{e}_x\mu_x + \mathbf{e}_y\mu_y)\frac{\sin(\mathrm{k}R)}{\mathrm{k}R}, \tag{1.139}$$

which have vanishing contribution in the z-direction, as we have assumed $\boldsymbol{R} = \mathbf{r} - \mathbf{r}_0 = R\mathbf{e}_z$. We note that $\mathbf{e}_x\mu_x + \mathbf{e}_y\mu_y = -\boldsymbol{R}\times(\boldsymbol{R}\times\boldsymbol{\mu})/R^2$, which can be used to generalize Eq. (1.139) to arbitrary orientations of $\boldsymbol{R}$. Thus, the positive-frequency transverse electric field operator in the far-field limit becomes

$$\begin{aligned}\hat{\mathbf{E}}^{(+)}_{\perp,\mathrm{QE}}(\mathbf{r},t) &\xrightarrow{\mathrm{k}R\gg 1} -\frac{ic\boldsymbol{R}\times(\boldsymbol{R}\times\boldsymbol{\mu})}{4\pi^2\varepsilon_0 R^2}\int_0^{\infty} d\mathrm{k}\,\mathrm{k}^3 \int_0^t d\tau\hat{\sigma}(\tau)e^{i\mathrm{k}c(\tau-t)}\frac{\sin(\mathrm{k}R)}{\mathrm{k}R} \\ &= -\frac{\boldsymbol{\mathcal{E}}_{\boldsymbol{\mu}}(\mathbf{r})c^3}{2\pi\omega_0^2}\int_0^{\infty} d\mathrm{k}\,\mathrm{k}^2 \int_0^t d\tau\hat{\sigma}(\tau)\left(e^{i\mathrm{k}[R+c(\tau-t)]} - e^{i\mathrm{k}[-R+c(\tau-t)]}\right).\end{aligned} \tag{1.140}$$

Here, we have introduced

$$\boldsymbol{\mathcal{E}}_{\boldsymbol{\mu}}(\mathbf{r}) = \frac{\omega_0^2|\boldsymbol{\mu}|}{4\pi\varepsilon_0 Rc^2}\boldsymbol{e}_{\boldsymbol{R}}\times(\boldsymbol{e}_{\boldsymbol{R}}\times\boldsymbol{e}_{\boldsymbol{\mu}}), \tag{1.141}$$

where $\boldsymbol{e}_{\boldsymbol{R}} = \boldsymbol{R}/|\boldsymbol{R}|$ and $\boldsymbol{e}_{\boldsymbol{\mu}} = \boldsymbol{\mu}/|\boldsymbol{\mu}|$ are the unit vectors along the directions of $\boldsymbol{R}$ and $\boldsymbol{\mu}$, respectively. Notably, the positive-frequency electric field radiated from a classical point dipole, with dipole moment $\boldsymbol{\mu}$ and rotating at frequency ω_0, is [124]

$$\mathbf{E}^{(+)}_{\perp,\boldsymbol{\mu}}(\mathbf{r},t) = \frac{\omega_0^2|\boldsymbol{\mu}|}{4\pi\varepsilon_0 Rc^2}\boldsymbol{e}_{\boldsymbol{R}}\times(\boldsymbol{e}_{\boldsymbol{R}}\times\boldsymbol{e}_{\boldsymbol{\mu}})e^{-i(\omega_0 t-\mathbf{k}\cdot\boldsymbol{R})} = \boldsymbol{\mathcal{E}}_{\boldsymbol{\mu}}(\mathbf{r})e^{-i(\omega_0 t-\mathbf{k}\cdot\boldsymbol{R})}. \tag{1.142}$$

Thus, $\boldsymbol{\mathcal{E}}_{\boldsymbol{\mu}}(\mathbf{r})$ corresponds to the positive-frequency electric field radiated from this classical point dipole, except for the phase $e^{-i(\omega_0 t-\mathbf{k}\cdot\boldsymbol{R})}$. Within the quantum-mechanical description, this phase is encoded in the Heisenberg-picture evolution of the operator $\hat{\sigma}$, as shown below [Eq. (1.147)]. Hereafter, we refer to $\boldsymbol{\mathcal{E}}_{\boldsymbol{\mu}}(\mathbf{r})$ as the *vector amplitude* of the (positive-frequency) electric field operator radiated from a classical dipole in the far-field zone.

We recall at this point that the interaction Hamiltonian is considered under the RWA, which neglects the terms proportional to $\hat{a}_{\mathbf{k}s}\hat{\sigma}$ and $\hat{a}^\dagger_{\mathbf{k}s}\hat{\sigma}^\dagger$. If these terms were considered, a term proportional to $\hat{\sigma}^\dagger$ would emerge in Eq. (1.130) and the whole derivation would become more intricate. However, the effect of these terms can be compensated within the RWA by extending the lower limit of the k-integral

from 0 to $-\infty$, see Ref. [117]. In this way, we obtain

$$\begin{aligned}\hat{\mathbf{E}}^{(+)}_{\perp,\mathrm{QE}}(\mathbf{r},t) &\xrightarrow{\mathrm{k}R\gg 1} -\frac{\boldsymbol{\mathcal{E}}_{\boldsymbol{\mu}}(\mathbf{r})c^3}{2\pi\omega_0^2}\int_0^t d\tau\hat{\sigma}(\tau)\int_{-\infty}^{\infty} d\mathrm{k}\,\mathrm{k}^2\left(e^{i\mathrm{k}[R+c(\tau-t)]}-e^{i\mathrm{k}[-R+c(\tau-t)]}\right)\\ &= -\frac{\boldsymbol{\mathcal{E}}_{\boldsymbol{\mu}}(\mathbf{r})c^3}{2\pi\omega_0^2}\int_0^t d\tau\hat{\sigma}(\tau)\frac{1}{c^2}\frac{d^2}{d\tau^2}\int_{-\infty}^{\infty} d\mathrm{k}\left(e^{i\mathrm{k}[R+c(\tau-t)]}-e^{i\mathrm{k}[-R+c(\tau-t)]}\right)\\ &= -\frac{\boldsymbol{\mathcal{E}}_{\boldsymbol{\mu}}(\mathbf{r})}{\omega_0^2}\int_0^t d\tau\hat{\sigma}(\tau)\frac{d^2}{d\tau^2}\left(\delta(\frac{R}{c}+\tau-t)-\delta(-\frac{R}{c}+\tau-t)\right),\end{aligned} \tag{1.143}$$

where, to obtain the equality in the second line, we have used the Leibniz integral rule, and to obtain the equality in the third line, we have used

$$\int_{-\infty}^{\infty} d\tau e^{i\tau x} = 2\pi\delta(x). \tag{1.144}$$

Using the properties of the Dirac delta distribution and again the Leibniz integral rule, one can show for an arbitrary function $f(x)$ that [131]

$$\int_a^b dx f(x)\frac{d^2\delta(x-x_0)}{dx^2} = \begin{cases} -\frac{d^2f(x)}{dx^2}\Big|_{x=x_0} & \text{if } x_0\in[a,b] \\ 0 & \text{if } x_0\notin[a,b]\end{cases}. \tag{1.145}$$

In this way, the electric field operator in Eq. (1.2.7) becomes

$$\hat{\mathbf{E}}^{(+)}_{\perp,\mathrm{QE}}(\mathbf{r},t) \xrightarrow{\mathrm{k}R\gg 1} -\frac{\boldsymbol{\mathcal{E}}_{\boldsymbol{\mu}}(\mathbf{r})}{\omega_0^2}\frac{d^2}{d\tau^2}\hat{\sigma}(\tau)\Big|_{\tau=t-\frac{R}{c}}. \tag{1.146}$$

To solve the time derivative of $\hat{\sigma}(\tau)$ in this expression, the usual approximation consists in neglecting the interaction of the QE with the electromagnetic field [117]. From Eq. (1.121a), this approximation yields $\frac{d}{d\tau}\hat{\sigma}(\tau) = -i\omega_0\hat{\sigma}(\tau)$. We find

$$\hat{\mathbf{E}}^{(+)}_{\perp,\mathrm{QE}}(\mathbf{r},t) \xrightarrow{\mathrm{k}R\gg 1} \boldsymbol{\mathcal{E}}_{\boldsymbol{\mu}}(\mathbf{r})\hat{\sigma}(t-\frac{R}{c}). \tag{1.147}$$

Therefore, we have demonstrated that, in the far-field limit, the positive-frequency electric field operator (evaluated at position $\mathbf{r}$ and time t) of light radiated from the QE is given by the product of (i) the vector amplitude $\boldsymbol{\mathcal{E}}_{\boldsymbol{\mu}}(\mathbf{r})$ of the field radiated from a classical electric point dipole, and (ii) the lowering operator $\hat{\sigma}(t-R/c)$ evaluated at the retarded time $t-R/c$ [121, 132].

In summary, the total transverse electric field operator in the Heisenberg picture is obtained as the sum of the free-field operator and the field radiated from the QE

$$\hat{\mathbf{E}}_{\perp}(\mathbf{r},t) = \hat{\mathbf{E}}_{\perp,\mathrm{free}}(\mathbf{r},t) + \hat{\mathbf{E}}_{\perp,\mathrm{QE}}(\mathbf{r},t), \tag{1.148}$$

where the second term is given in the far-field limit as

$$\hat{\mathbf{E}}_{\perp,\mathrm{QE}}(\mathbf{r},t) \xrightarrow{\mathrm{k}R\gg 1} \boldsymbol{\mathcal{E}}_{\boldsymbol{\mu}}(\mathbf{r})\hat{\sigma}(t-\frac{R}{c}) + \boldsymbol{\mathcal{E}}^{*}_{\boldsymbol{\mu}}(\mathbf{r})\hat{\sigma}^{\dagger}(t-\frac{R}{c}). \tag{1.149}$$

1.3 Wigner-Weisskopf approximation and spontaneous emission from a single quantum emitter

We introduce in this section the concept of spontaneous emission of photons from the QE. To this end, we assume that the QE is initially inverted (which means that the electronic excited state $|e\rangle$ is totally populated at time $t = 0$) and that the electromagnetic field is in the vacuum state $|\mathrm{vac}\rangle$. Thus, at time $t = 0$, the complete system is in the product state $|\psi(0)\rangle = |e\rangle\,|\mathrm{vac}\rangle$. Next, we compute the time evolution of the quantum state $|\psi(t)\rangle$ using the *Wigner-Weisskopf approximation* (WWA), which was originally introduced in Ref. [16]. In this way, we show that the population of the electronic excited state decays exponentially in time due to the interaction with the electromagnetic modes of the vacuum field. We mainly follow the procedure described in Refs. [119, 124].

In a nutshell, the WWA relies on proposing an ansatz for $|\psi(t)\rangle$, whose equation of motion is then derived using the Schrödinger equation and solved assuming that the dynamics of the system is Markovian. The full derivation is facilitated by considering the interaction Hamiltonian under the rotating-wave approximation (RWA). Importantly, the RWA does not affect the spontaneous emission rate of photons from the QE, which is shown in Section 1.4.5. Additionally, the application of the WWA is simplified in the interaction picture, where the interaction Hamiltonian (under the RWA) is given by

$$\begin{aligned}\hat{H}_I^{\mathrm{RWA}}(t) &= \exp\left[\frac{i}{\hbar}(\hat{H}_{\mathrm{QE}}+\hat{H}_{F\perp})t\right]\hat{H}_I^{\mathrm{RWA}}\exp\left[-\frac{i}{\hbar}(\hat{H}_{\mathrm{QE}}+\hat{H}_{F\perp})t\right]\\ &= \hbar\sum_{\mathbf{k},s}\left[g_{\mathbf{k}s}(\mathbf{r}_0)\hat{\sigma}^{\dagger}\hat{a}_{\mathbf{k}s}e^{i(\omega_0-\omega_{\mathrm{k}})t} + g^{*}_{\mathbf{k}s}(\mathbf{r}_0)\hat{\sigma}\hat{a}^{\dagger}_{\mathbf{k}s}e^{-i(\omega_0-\omega_{\mathrm{k}})t}\right].\end{aligned} \tag{1.150}$$

In the interaction picture, the dynamics of the quantum state is governed by the *Schrödinger equation*

$$i\frac{d}{dt}\,|\psi(t)\rangle = \frac{1}{\hbar}\hat{H}_{\mathrm{I}}^{\mathrm{RWA}}(t)\,|\psi(t)\rangle\,. \tag{1.151}$$

The interaction picture is discussed in more detail in Appendix B.

The next step consists in proposing an ansatz for $|\psi(t)\rangle$. Taking into account that, under the RWA, the interaction Hamiltonian conserves the total number of excitations of the system (between photons and emitter excitations) and that we assume that the initial state is $|\psi(0)\rangle = |e\rangle\,|\mathrm{vac}\rangle$ (i.e., with one excitation in total),

we propose

$$|\psi(t)\rangle = c^e(t)\,|e\rangle\,|\mathrm{vac}\rangle + \sum_{\mathbf{k},s} c^g_{\mathbf{k}s}(t)\,|g\rangle\,\hat{a}^\dagger_{\mathbf{k}s}\,|\mathrm{vac}\rangle\,. \tag{1.152}$$

The first term on the right-hand side of Eq. (1.152) corresponds to the electronic excited state still being populated at time t, with probability amplitude $c^e(t)$. In contrast, the emitter is in the electronic ground state $|g\rangle$ in each term in the sum over $(\mathbf{k}, s)$ in Eq. (1.152). Each of the states in this summation thus corresponds to the emitter having already relaxed at time t via a radiative decay from the excited state to the ground state, which leads to the emission of a photon in electromagnetic mode $(\mathbf{k}, s)$ and has probability amplitude $c^g_{\mathbf{k}s}(t)$. The equations of motion of the probability amplitudes are obtained by substituting the proposed ansatz into the Schrödinger equation in Eq. (1.151). In this way, we find

$$i\frac{d}{dt}c^e(t) = \sum_{\mathbf{k},s} c^g_{\mathbf{k}s}(t) g_{\mathbf{k}s}(\mathbf{r}_0) e^{i(\omega_0-\omega_\mathrm{k})t}, \tag{1.153a}$$

$$i\frac{d}{dt}c^g_{\mathbf{k}s}(t) = c^e(t) g^*_{\mathbf{k}s}(\mathbf{r}_0) e^{-i(\omega_0-\omega_\mathrm{k})t}. \tag{1.153b}$$

Moreover, we formally integrate in time both sides of Eq. (1.153b), which yields

$$ic^g_{\mathbf{k}s}(t) = g^*_{\mathbf{k}s}(\mathbf{r}_0)\int_0^t dt' c^e(t') e^{-i(\omega_0-\omega_\mathrm{k})t'}. \tag{1.154}$$

Substituting this expression into Eq. (1.153a), we obtain

$$\frac{d}{dt}c^e(t) = -\int_0^t dt' \sum_{\mathbf{k},s} |g_{\mathbf{k}s}(\mathbf{r}_0)|^2 c^e(t') e^{i(\omega_0-\omega_\mathrm{k})(t-t')}. \tag{1.155}$$

We now introduce the change of integration variable $\tau = t - t'$ and, additionally, transform the summation over $\mathbf{k}$ into an integral by using Eq. (1.134). In this way, we find

$$\begin{aligned}\frac{d}{dt}c^e(t) = &-\frac{1}{(2\pi c)^3 2\varepsilon_0\hbar}\sum_s \int_0^{2\pi} d\phi \int_0^{\pi} d\theta \sin\theta |\boldsymbol{\mu}\cdot\mathbf{e}_{\mathbf{k}s}|^2 \\ &\times \int_0^t d\tau c^e(t-\tau) e^{i\omega_0\tau} \int_0^\infty d\omega_\mathrm{k}\omega_\mathrm{k}^3 e^{-i\omega_\mathrm{k}\tau}.\end{aligned} \tag{1.156}$$

Here, we have used the expression for $g_{\mathbf{k}s}(\mathbf{r}_0)$ given in Eq. (1.129). The frequency integral in Eq. (1.156) diverges at $\tau = 0$, whereas for increasing values of τ it decays rapidly due to the oscillations provided by $\exp(-i\omega_\mathrm{k}\tau)$ (see Refs. [124, 133] for further discussion). Consequently, we assume that $c^e(t-\tau)$ evolves much slower than the other terms inside the τ-integral in Eq. (1.156), which allows us to replace $c^e(t-\tau)$ by $c^e(t)$. Additionally, the contribution to this integral for increasing values of τ becomes negligible compared to the divergent contribution at

$\tau = 0$, allowing us to extend the upper limit of the τ-integral from t to ∞. These approximations result in

$$\frac{d}{dt}c^e(t) = -c^e(t)\frac{1}{(2\pi c)^3 2\varepsilon_0\hbar}\sum_s \int_0^{2\pi} d\phi \int_0^{\pi} d\theta \sin\theta |\boldsymbol{\mu}\cdot\mathbf{e}_{\mathbf{k}s}|^2 \\ \times \int_0^{\infty} d\omega_{\mathrm{k}}\omega_{\mathrm{k}}^3 \int_0^{\infty} d\tau e^{i(\omega_0-\omega_{\mathrm{k}})\tau}. \tag{1.157}$$

On the right-hand side of this equation, only $c^e(t)$ depends on time. Thus, with the approximations introduced above, $c^e(t)$ necessarily follows an exponential decay in time, which agrees very well with the experimental measurements for the type of QEs in which we are interested in this thesis. Small deviations from this exponential decay can be obtained going beyond these approximations [119, 134, 135], which is beyond our scope.

In the following, we derive the expression of the rate of the exponential decay of $c^e(t)$ by solving all the integrals in Eq. (1.157). To evaluate the time integral, we apply the *Sokhotski-Plemelj theorem* from complex analysis [136–138], which yields

$$\int_0^{\infty} d\omega f(\omega) \int_0^{\infty} dt' e^{i(\omega_0-\omega)(t-t')} = \int_0^{\infty} d\omega f(\omega)\left[\pi\delta(\omega_0-\omega) + i\,\mathrm{p.v.}\frac{1}{\omega_0-\omega}\right], \tag{1.158}$$

where $f(\omega)$ is a function of ω, and p.v. denotes the Cauchy principal value of the ω-integral. Consequently, we obtain

$$\frac{d}{dt}c^e(t) = -c^e(t)\frac{1}{(2\pi c)^3 2\varepsilon_0\hbar}\sum_s \int_0^{2\pi} d\phi \int_0^{\pi} d\theta \sin\theta \\ \times \int_0^{\infty} d\omega_{\mathrm{k}}|\boldsymbol{\mu}\cdot\mathbf{e}_{\mathbf{k}s}|^2\omega_{\mathrm{k}}^3\left[\pi\delta(\omega_0-\omega_{\mathrm{k}}) + i\,\mathrm{p.v.}\frac{1}{\omega_0-\omega_{\mathrm{k}}}\right]. \tag{1.159}$$

The contribution from the principal value integral yields a shift in the transition frequency of the QE, known as *Lamb shift*. This perturbation in the transition frequency can be better understood taking into account that the quantum emitter is not an isolated system, but it interacts with the electromagnetic field, which has non-zero energy even in its ground state $|\mathrm{vac}\rangle$ [Eq. (1.61)]. Importantly, this frequency shift is typically very small for QEs with optical transition frequencies and, additionally, the frequency value that can be measured in experiments (for example, via the emission spectrum described in Section 2.1.5) contains the effect of this shift. Thus, we ignore in the following the effect of such principal value integral and consider that ω_0 already includes the Lamb shift induced by the vacuum field (see Refs. [119, 124] for further discussion).

Additionally, to compute the integral proportional to $\delta(\omega_0-\omega_{\mathrm{k}})$, we use the units vectors $\boldsymbol{e}_{\mathbf{k}s}$ in Eqs. (1.137a)–(1.137b). In this way, we can solve the integrals

in the polar and azimuthal angles in Eq. (1.159), which yields

$$\begin{aligned}
&\sum_s \int_0^{2\pi} d\phi \int_0^{\pi} d\theta \sin\theta |\boldsymbol{\mu}\cdot\boldsymbol{e}_{\mathbf{k}s}|^2 = \sum_s \int_0^{2\pi} d\phi \int_0^{\pi} d\theta \sin\theta \\
&\times\Big[\mu_x^2(\cos^2\theta\cos^2\phi+\sin^2\phi)+\mu_y^2(\cos^2\theta\sin^2\phi+\cos^2\phi)+\mu_z^2\sin^2\theta \\
&+\mu_x\mu_y(\cos^2\theta-1)\cos\phi\sin\phi-\mu_x\mu_z\cos\theta\sin\theta\cos\phi-\mu_y\mu_z\cos\theta\sin\theta\sin\phi\Big] \\
&=|\boldsymbol{\mu}|^2\frac{8\pi}{3}.
\end{aligned} \tag{1.160}$$

Substituting this result into Eq. (1.159) and using the properties of the Dirac delta distribution to evaluate the k-integral, we find

$$\begin{aligned}
\frac{d}{dt}c^e(t) &= -c^e(t)\frac{c}{2\varepsilon_0\hbar(2\pi)^3}|\boldsymbol{\mu}|^2\frac{8\pi}{3}\int_0^{\infty} d\mathrm{k}\mathrm{k}^3\pi\delta(\omega_0-\mathrm{k}c) \\
&= -c^e(t)\frac{\omega_0^3|\boldsymbol{\mu}|^2}{6\varepsilon_0\hbar\pi c^3}.
\end{aligned} \tag{1.161}$$

Finally, by integrating both sides of this equation over time and imposing the initial condition $c^e(0)=1$, we find that the population of the electronic excited state $|e\rangle$ at time t is given by

$$|\langle e|\psi(t)\rangle|^2 = |c^e(t)|^2 = \exp\Big[-\frac{\omega_0^3|\boldsymbol{\mu}|^2}{3\pi\varepsilon_0 n^2\hbar c^3}t\Big] = \exp\Big[-\gamma_0 t\Big], \tag{1.162}$$

where we have defined

$$\gamma_0 = \frac{\omega_0^3|\boldsymbol{\mu}|^2}{3\pi\varepsilon_0\hbar c^3}. \tag{1.163}$$

The population of the electronic excited state $|e\rangle$ of the QE decays exponentially in time with rate γ_0, which thus corresponds to the spontaneous emission rate of the QE. We emphasize that the loss of population of the QE is balanced with the increase of population of the modes ($\mathbf{k}$,s) of the vacuum field and, thus, spontaneous emission can be interpreted as induced by vacuum fluctuations [119]. Additionally, substituting

$$c^e(t) = \exp\Big[-\frac{\gamma_0}{2}t\Big] \tag{1.164}$$

into Eq. (1.153b), and solving the time integral, we find

$$c^g_{\mathbf{k}s}(t) = -i\frac{g^*_{\mathbf{k}s}(\mathbf{r}_0)}{\gamma_0/2+i(\omega_0-\omega_k)}\Big[1-\exp\Big(-[\frac{\gamma_0}{2}+i(\omega_0-\omega_k)]t\Big)\Big]. \tag{1.165}$$

Thus, the probability that the radiative decay of the QE leads to the emission of a

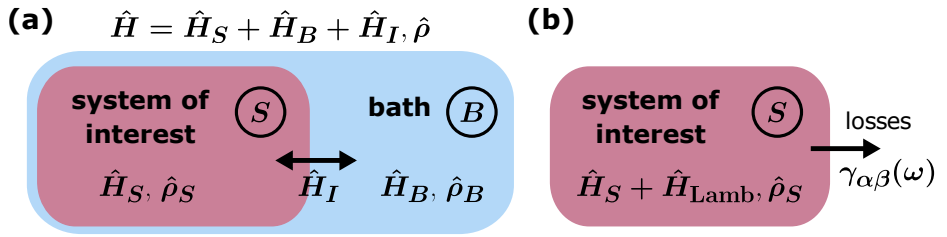

Figure 1.2: Schematic representation of an open quantum system. (a) A system of interest S (red box) interacts with a bath B (blue box). The system of interest is described by the Hamiltonian $\hat{H}_S$ and its dynamics by the density matrix $\hat{\rho}_S = \text{Tr}_B(\hat{\rho})$, with $\hat{\rho}$ the density matrix of the global system $S + B$ and Tr_B the partial trace over the Hilbert space of B. On the other hand, the bath is described by the Hamiltonian $\hat{H}_B$ and its dynamics by the density matrix $\hat{\rho}_B = \text{Tr}_S(\hat{\rho})$. The interaction is governed by the Hamiltonian $\hat{H}_I$. (b) The application of the Markovian master equation (MME) reduces the Hilbert space to that of the system of interest alone. The Hamiltonian of S is transformed to $\hat{H}_S + \hat{H}_{\text{Lamb}}$, where $\hat{H}_{\text{Lamb}}$ is the Lamb-shift Hamiltonian. Additionally, the MME governing the reduced dynamics of S includes incoherent terms (losses), with decay rates represented by $\gamma_{\alpha\beta}(\omega)$.

photon in mode ($\mathbf{k}$,s) is

$$|\langle \text{vac}| \hat{a}_{\mathbf{k}s} |\psi(t)\rangle|^2 = |c^g_{\mathbf{k}s}(t)|^2 = \frac{|g_{\mathbf{k}s}(\mathbf{r}_0)|^2}{(\gamma_0/2)^2 + (\omega_0 - \omega_k)^2} \left[1 - e^{-[\frac{\gamma_0}{2} + i(\omega_0 - \omega_k)]t}\right]^2, \tag{1.166}$$

which has a Lorentzian distribution with central frequency ω_0 and linewidth γ_0.

1.4 Markovian master equation

We introduce in this section the Markovian master equation (MME), which is a useful tool to address the dynamics of open quantum systems and plays an important role in this thesis. For example, the MME can be used to trace out the electromagnetic degrees of freedom in the description of the interaction of a quantum emitter with the vacuum field, obtaining an alternative derivation of the spontaneous decay rate γ_0 to that presented in the previous section. To introduce the MME, we first present the concept of open quantum system.

1.4.1 Open quantum systems

An *open quantum system* is any system of interest S (for instance, a quantum emitter) that interacts with another quantum system B that is not of interest. The latter system is often called *bath*, *reservoir* or simply *environment* and can involve a finite number of degrees of freedom (e.g., particular modes of an optical cavity) or an infinite number of degrees of freedom (e.g., the vacuum field). The Hilbert space of the total system $S + B$ is given by the tensor product $\mathcal{H}_S \otimes \mathcal{H}_B$, with $\mathcal{H}_S$

the Hilbert space of S and $\mathcal{H}_B$ the Hilbert space of B, as schematically depicted in Fig. 1.2a. Additionally, we denote by $\hat{H}_S$ the Hamiltonian of the system of interest, by $\hat{H}_B$ the Hamiltonian of the bath and by $\hat{H}_I(t)$ the interaction Hamiltonian, so that the total Hamiltonian (in the Schrödinger picture) is given by

$$\hat{H}(t) = \hat{H}_S + \hat{H}_B + \hat{H}_I(t). \tag{1.167}$$

Further, the state of the total system can be described in general by a density matrix $\hat{\rho}$ (see Appendix A for a review of the density matrix formalism). The time evolution of $\hat{\rho}$ is governed the *von Neumann equation*

$$\frac{d}{dt}\hat{\rho}(t) = -\frac{i}{\hbar}[\hat{H}(t), \hat{\rho}(t)], \tag{1.168}$$

as described in Appendix B. Solving this equation can be very complicated. However, taking into account that only the subsystem S is considered of interest, different techniques can be applied to trace out the degrees of freedom of the bath and solve the *reduced density matrix* $\hat{\rho}_S = \mathrm{Tr}_B(\hat{\rho})$, with Tr_B the partial trace over the Hilbert space of the bath (see Appendix A). These techniques rely on different assumptions regarding the system and the reservoir [139]. In particular, the *Markovian master equation* (MME) that we use in this thesis is mainly based on assuming that the interaction between S and B is weak, and that the decay time of B is much faster than the decay time of S. Applying the MME reduces Eq. (1.168) to the Hilbert space $\mathcal{H}_S$. In this way, the Hamiltonian in the commutator does not include the bath Hamiltonian and neither the interaction Hamiltonian. In contrast, this commutator includes only the original system Hamiltonian $\hat{H}_S$ and an additional Hamiltonian $\hat{H}_{\mathrm{Lamb}}$, called Lamb-shift Hamiltonian, which accounts for the effect of the bath on the coherent dynamics of S. Apart from the commutator, additional terms emerge in the equation that governs the dynamics of the reduced density matrix $\hat{\rho}_S = \mathrm{Tr}_B(\hat{\rho})$ resulting from the application of the MME. These latter terms make the time evolution of the reduced system non-unitary and describe the incoherent dynamics of the system, which can be a consequence of the transfer (loss) of energy from S into B, see Fig. 1.2b.

1.4.2 Microscopic derivation of the Markovian master equation

The derivation of the MME that we present here is based on the procedure described in Ref. [139]. This derivation is facilitated by the use of the interaction picture (see Appendix B for a brief introduction to the interaction picture). Once the final form of the MME is obtained, we then come back to the Schrödinger picture.

The starting point to derive the MME is the von Neumann equation in the interaction picture [labeled with the superscript (I)], which is given by

$$\frac{d}{dt}\hat{\rho}^{(I)}(t) = -\frac{i}{\hbar}[\hat{H}_I^{(I)}(t), \hat{\rho}^{(I)}(t)]. \tag{1.169}$$

Here, we have introduced the density matrix in the interaction picture

$$\hat{\rho}^{(I)}(t) = \exp\left[\frac{it}{\hbar}(\hat{H}_S + \hat{H}_B)\right]\hat{\rho}(t)\exp\left[-\frac{it}{\hbar}(\hat{H}_S + \hat{H}_B)\right], \tag{1.170}$$

as well as the interaction Hamiltonian in the same picture

$$\hat{H}_I^{(I)}(t) = \exp\left[\frac{it}{\hbar}(\hat{H}_S + \hat{H}_B)\right]\hat{H}_I(t)\exp\left[-\frac{it}{\hbar}(\hat{H}_S + \hat{H}_B)\right], \tag{1.171}$$

with the initial time fixed at $t_0 = 0$. This derivation assumes that both the system and bath Hamiltonians are time-independent, as otherwise the calculation of the interaction picture density matrix $\hat{\rho}^{(I)}(t)$ and interaction Hamiltonian $\hat{H}_I^{(I)}(t)$ become more complicated [139–141].

Next, integrating both sides of Eq. (1.169) results in

$$\hat{\rho}^{(I)}(t) = \hat{\rho}^{(I)}(0) - \frac{i}{\hbar}\int_0^t dt'[\hat{H}_I^{(I)}(t'), \hat{\rho}^{(I)}(t')]. \tag{1.172}$$

This expression can be inserted again into Eq. (1.169) to obtain

$$\frac{d}{dt}\hat{\rho}^{(I)}(t) = -\frac{i}{\hbar}\left[\hat{H}_I^{(I)}(t), \hat{\rho}^{(I)}(0) - \frac{i}{\hbar}\int_0^t dt'[\hat{H}_I^{(I)}(t'), \hat{\rho}^{(I)}(t')]\right]. \tag{1.173}$$

Taking the partial trace over the bath Hilbert space (Appendix A) on both sides of this equation leads to

$$\frac{d}{dt}\hat{\rho}_S^{(I)}(t) = -\frac{i}{\hbar}\mathrm{Tr}_B[\hat{H}_I^{(I)}(t), \hat{\rho}^{(I)}(0)] - \frac{1}{\hbar^2}\int_0^t dt'\mathrm{Tr}_B\left[\hat{H}_I^{(I)}(t), [\hat{H}_I^{(I)}(t'), \hat{\rho}^{(I)}(t')]\right]. \tag{1.174}$$

At this point we introduce the key assumptions that are made to derive the MME. First, we note that without loss of generality, the interaction Hamiltonian (in the Schrödinger picture) can be written as

$$\hat{H}_I = \sum_\alpha \hat{S}_\alpha \otimes \hat{B}_\alpha, \tag{1.175}$$

with $\hat{S}_\alpha = \hat{S}_\alpha^\dagger$ and $\hat{B}_\alpha = \hat{B}_\alpha^\dagger$ Hermitian operators acting on $\mathcal{H}_S$ and $\mathcal{H}_B$ Hilbert spaces, respectively. The first assumption consists in considering that the expectation values of the bath operators vanish at all times (see Appendix B), such that

$$\langle \hat{B}_\alpha \rangle (t) = 0. \tag{1.176}$$

As a result, the first term on the right-hand side of Eq. (1.174) vanishes.

The second assumption is known as the *Born approximation* and is based on considering that the coupling between the system of interest and the bath is very weak, such that the effect of the interaction on the reduced density matrix of

the bath $\hat{\rho}_B^{(I)} = \mathrm{Tr}_S[\hat{\rho}^{(I)}(t)]$ can be neglected. This approximation allows us to approximate the total density matrix as a tensor product:

$$\hat{\rho}^{(I)}(t) = \hat{\rho}_S^{(I)}(t) \otimes \hat{\rho}_B^{(I)}, \tag{1.177}$$

where $\hat{\rho}_B^{(I)}$ is time-independent (e.g., a thermal state). The first two approximations together simplify Eq. (1.174) to

$$\frac{d}{dt}\hat{\rho}_S^{(I)}(t) = -\frac{1}{\hbar^2}\int_0^t dt' \mathrm{Tr}_B\left[\hat{H}_I^{(I)}(t), [\hat{H}_I^{(I)}(t'), \hat{\rho}_S^{(I)}(t') \otimes \hat{\rho}_B^{(I)}]\right], \tag{1.178}$$

which is known as *Redfield equation*.

The third assumption is known as *Markovian approximation* and consists in assuming that the dynamics of the system does not depend on the state at past times. More technically, this assumption requires that the time scale over which $\hat{\rho}_S^{(I)}(t)$ varies appreciably is much larger than the decay time of the two-time *bath correlation functions* $\langle \hat{B}_\alpha^{(I)}(t)\hat{B}_\beta^{(I)}(t')\rangle$ and, thus, than the time in which the integrand on the right-hand side of Eq. (1.178) vanishes. Thus, $\hat{\rho}_S^{(I)}(t')$ inside the integral on the right-hand side of Eq. (1.174) can be replaced by $\hat{\rho}_S^{(I)}(t)$. Further, introducing the change of integral variable $\tau = t - t'$, we obtain

$$\frac{d}{dt}\hat{\rho}_S^{(I)}(t) = -\frac{1}{\hbar^2}\int_0^t d\tau \mathrm{Tr}_B\left[\hat{H}_I^{(I)}(t), [\hat{H}_I^{(I)}(t-\tau), \hat{\rho}_S^{(I)}(t) \otimes \hat{\rho}_B^{(I)}]\right]. \tag{1.179}$$

The fast decay assumed for the bath correlations additionally allows for extending the upper integral limit from t to ∞, which finally yields the Markovian master equation

$$\frac{d}{dt}\hat{\rho}_S^{(I)}(t) = -\frac{1}{\hbar^2}\int_0^\infty d\tau \mathrm{Tr}_B\left[\hat{H}_I^{(I)}(t), [\hat{H}_I^{(I)}(t-\tau), \hat{\rho}_S^{(I)}(t) \otimes \hat{\rho}_B^{(I)}]\right]. \tag{1.180}$$

We emphasize that, as a consequence of the Markov approximation, the MME cannot be used to resolve the dynamics of $\hat{\rho}_S^{(I)}(t)$ over times in the order of the decay rate of the bath correlation functions. Equation (1.180) enables to address the reduced dynamics of the system of interest via the interaction Hamiltonian in the interaction picture.

Furthermore, the application of the MME to each particular scenario can be facilitated by rewriting the general form in Eq. (1.180) in terms of the eigenoperators of the system of interest. To this end, we again use the expression of the interaction Hamiltonian in Eq. (1.175) and the spectral decomposition of the system Hamiltonian (in the Schrödinger picture), which is given by

$$\hat{H}_S = \sum_\epsilon \epsilon \left|\epsilon\right\rangle \left\langle\epsilon\right|. \tag{1.181}$$

The set of differences between eigenenergies of the system Hamiltonian $\{\hbar\omega = \epsilon' - \epsilon\}$ is known as *Bohr frequencies* of the system. For each system operator $\hat{S}_\alpha$ and Bohr frequency ω, we define the operator

$$\hat{S}_\alpha(\omega) = \sum_{\epsilon,\epsilon'} |\epsilon\rangle \langle\epsilon| \hat{S}_\alpha |\epsilon'\rangle \langle\epsilon'| \delta_{\epsilon',\epsilon+\omega\hbar}, \tag{1.182}$$

where the expression inside the summation on the right-hand side is nonzero only for those pairs of eigenstates $|\epsilon'\rangle$ and $|\epsilon\rangle$ whose eigenvalues yield a Bohr frequency $\omega = (\epsilon' - \epsilon)/\hbar$. Importantly, $\hat{S}_\alpha(\omega)$ is an eigenoperator of the system Hamiltonian, meaning that $[\hat{H}_S, \hat{S}_\alpha(\omega)] = -\omega\hat{S}_\alpha(\omega)$. These operators satisfy

$$\hat{S}_\alpha = \sum_\omega \hat{S}_\alpha(\omega), \tag{1.183}$$

which is a consequence of the completeness relation of the eigenstates of $\hat{H}_S$.

The operator $\hat{S}_\alpha(\omega)$ in the interaction picture becomes

$$\hat{S}^{(I)}_\alpha(\omega;t) = \exp\Big[it(\hat{H}_S + \hat{H}_B)\Big]\hat{S}_\alpha(\omega)\exp\Big[-it(\hat{H}_S + \hat{H}_B)\Big] = e^{-i\omega t}\hat{S}_\alpha(\omega), \tag{1.184}$$

which can be obtained using the expansion theorem in Eq. (1.106). Thus, the interaction Hamiltonian in the interaction picture can be written as

$$\hat{H}^{(I)}_I(t) = \sum_{\alpha,\omega} \hat{S}^{(I)}_\alpha(\omega;t) \otimes \hat{B}^{(I)}_\alpha(t) = \sum_{\alpha,\omega} e^{-i\omega t}\hat{S}_\alpha(\omega) \otimes \hat{B}^{(I)}_\alpha(t). \tag{1.185}$$

Next, we substitute the expression of $\hat{H}^{(I)}_I(t)$ into the MME [Eq. (1.180)], which yields

$$\begin{aligned}\frac{d}{dt}\hat{\rho}^{(I)}_S(t) = &\sum_{\omega,\omega'}\sum_{\alpha,\beta} e^{i(\omega-\omega')t}\Gamma_{\alpha\beta}(\omega)\Big(\hat{S}_\beta(\omega)\hat{\rho}^{(I)}_S(t)\hat{S}^\dagger_\alpha(\omega') - \hat{S}^\dagger_\alpha(\omega')\hat{S}_\beta(\omega)\hat{\rho}^{(I)}_S(t)\Big) \\ &+ \text{h.c.},\end{aligned} \tag{1.186}$$

where h.c. represents the Hermitian conjugated expression. Additionally, we have defined

$$\Gamma_{\alpha\beta}(\omega) = \int_0^\infty d\tau e^{i\omega\tau}\left\langle \hat{B}^{(I)}_\alpha(t)\hat{B}^{(I)}_\beta(t-\tau)\right\rangle, \tag{1.187}$$

corresponding to the Fourier transform of the bath correlation function. If $[\hat{H}_B, \hat{\rho}_B] = 0$ (meaning that $\hat{\rho}_B$ is a bath stationary state), we can simplify

$$\langle \hat{B}^{(I)}_\alpha(t)\hat{B}^{(I)}_\beta(t-\tau)\rangle = \langle \hat{B}^{(I)}_\alpha(\tau)\hat{B}^{(I)}_\beta(0)\rangle, \tag{1.188}$$

which ensures that $\Gamma_{\alpha\beta}(\omega)$ becomes time-independent.

The MME [Eq. (1.186)] can thus be rewritten as

$$\frac{d}{dt}\hat{\rho}_S^{(I)}(t) = -\frac{i}{\hbar}\left[\hat{H}_{\text{Lamb}}, \hat{\rho}_S^{(I)}(t)\right] + \sum_{\omega,\omega'}\sum_{\alpha,\beta} e^{i(\omega-\omega')t}\frac{\Gamma_{\alpha\beta}(\omega)+\Gamma^*_{\beta\alpha}(\omega')}{2}\mathcal{D}[\hat{S}_\beta(\omega), \hat{S}_\alpha(\omega')]\hat{\rho}_S^{(I)}(t), \tag{1.189}$$

where we have introduced the *Lamb-shift Hamiltonian*

$$\hat{H}_{\text{Lamb}} = \sum_{\omega,\omega'}\sum_{\alpha,\beta} e^{i(\omega-\omega')t}\frac{\Gamma_{\alpha\beta}(\omega)-\Gamma^*_{\beta\alpha}(\omega')}{2i}\hat{S}^\dagger_\alpha(\omega')\hat{S}_\beta(\omega), \tag{1.190}$$

as well as the *dissipator* superoperator $\mathcal{D}$, whose action is defined as

$$\mathcal{D}[\hat{O}_1, \hat{O}_2]\hat{\rho} = 2\hat{O}_1\hat{\rho}\hat{O}_2^\dagger - \hat{O}_2^\dagger\hat{O}_1\hat{\rho} - \hat{\rho}\hat{O}_2^\dagger\hat{O}_1. \tag{1.191}$$

The Lamb-shift Hamiltonian $\hat{H}_{\text{Lamb}}$ describes the effect induced by the bath in the coherent dynamics of S. In contrast, the second line in Eq. (1.189) corresponds to the incoherent dynamics induced by the bath in S, which can be due to the loss of energy from S to the bath and that implies that the evolution of the open system is non-unitary.

Importantly, the MME does not guarantee the complete positivity of the reduced density matrix at any time t [139, 142, 143], which could yield eigenstates with unphysical negative populations. To solve this problem, an additional assumption is required, which is known as *rotating-wave approximation* (RWA)[1]. The RWA consists in neglecting the rapidly oscillating terms in Eq. (1.189), which are those at $\omega \neq \omega'$. This approximation is valid as long as the relaxation time of S is much faster than $1/(\omega-\omega')$. The master equation thus reduces to

$$\frac{d}{dt}\hat{\rho}_S^{(I)}(t) = -\frac{i}{\hbar}\left[\hat{H}^{\text{RWA}}_{\text{Lamb}}, \hat{\rho}_S^{(I)}(t)\right] + \sum_{\omega}\sum_{\alpha,\beta}\frac{\gamma_{\alpha\beta}(\omega)}{2}\mathcal{D}[\hat{S}_\beta(\omega), \hat{S}_\alpha(\omega)]\hat{\rho}_S^{(I)}(t), \tag{1.192}$$

where we have introduced the decay rates

$$\gamma_{\alpha\beta}(\omega) = \Gamma_{\alpha\beta}(\omega) + \Gamma^*_{\beta\alpha}(\omega), \tag{1.193}$$

and the Lamb-shift Hamiltonian under the RWA

$$\hat{H}^{\text{RWA}}_{\text{Lamb}} = \sum_{\omega}\sum_{\alpha,\beta}\Delta_{\alpha\beta}(\omega)\hat{S}^\dagger_\alpha(\omega)\hat{S}_\beta(\omega), \tag{1.194}$$

[1] This is the second rotating-wave approximation (RWA) introduced in this thesis. On the one hand, we have applied the RWA to the Hamiltonian describing the interaction between the QE and the electromagnetic vacuum field [Eqs. (1.128) and (1.150)] in Sections 1.2.7 and 1.3, which neglects terms that do not conserve the total number of excitations. On the other hand, the RWA applied here consists in neglecting fast oscillatory terms induced by the bath in the reduced dynamics of the open system, both in the Lamb-shift Hamiltonian and in the dissipators.

with frequency shifts given by

$$\Delta_{\alpha\beta}(\omega) = \frac{\Gamma_{\alpha\beta}(\omega) - \Gamma^*_{\beta\alpha}(\omega)}{2i}. \tag{1.195}$$

The master equation in Eq. (1.192) is written in the interaction picture. Coming back to the Schrödinger picture, we obtain

$$\frac{d}{dt}\hat{\rho}_S(t) = -\frac{i}{\hbar}\left[\hat{H}_S + \hat{H}^{\mathrm{RWA}}_{\mathrm{Lamb}}, \hat{\rho}_S(t)\right] + \sum_{\omega}\sum_{\alpha,\beta}\frac{\gamma_{\alpha\beta}(\omega)}{2}\mathcal{D}[\hat{S}_\beta(\omega), \hat{S}_\alpha(\omega)]\hat{\rho}_S(t). \tag{1.196}$$

The Lamb-shift Hamiltonian (before and after the RWA) is equal in the interaction picture and in the Schrödinger picture because $[\hat{H}_{\mathrm{Lamb}}, \hat{H}_S] = 0$. Finally, we note that the Schrödinger-picture evolution of the density matrix $\hat{\rho}_S(t)$ allows for deriving time evolution of the expectation value $\langle\hat{O}\rangle(t) = \mathrm{Tr}\{\hat{O}\hat{\rho}_S(t)\}$ of any operator $\hat{O}$ in $\mathcal{H}_S$. Specifically, using Eq. (1.196), we obtain

$$\begin{aligned}\frac{d}{dt}\langle\hat{O}\rangle(t) = \frac{i}{\hbar}\mathrm{Tr}\Big\{[\hat{H}_S + \hat{H}^{\mathrm{RWA}}_{\mathrm{Lamb}}, \hat{O}]\hat{\rho}_S(t)\Big\} \\ + \sum_{\omega}\sum_{\alpha,\beta}\frac{\gamma_{\alpha\beta}(\omega)}{2}\Big(\mathrm{Tr}\Big\{[\hat{S}^\dagger_\alpha(\omega), \hat{O}]\hat{S}_\beta(\omega)\hat{\rho}_S(t)\Big\} + \mathrm{Tr}\Big\{\hat{S}^\dagger_\alpha(\omega)[\hat{O}, \hat{S}_\beta(\omega)]\hat{\rho}_S(t)\Big\}\Big).\end{aligned} \tag{1.197}$$

1.4.3 Lindblad master equation

In this section, we present the *Lindblad master equation*, which is an alternative form of the MME in Eq. (1.196). This equation provides further insights into the dynamics of open quantum systems.

To derive the Lindblad master equation, we first construct a set of matrices $[\gamma(\omega)]$, each with elements $\gamma_{\alpha\beta}(\omega)$ [Eq. (1.193)]. We then diagonalize the transpose of each of these matrices. In particular, we express the unitary transformation that brings $[\gamma(\omega)]^T$ into diagonal form as $[U(\omega)][\gamma(\omega)]^T[U(\omega)]^\dagger$ and denote the resulting eigenvalues as $\gamma_\alpha(\omega)$. We then use the unitary matrix $[U(\omega)]$ to compute the set of operators

$$\hat{L}_\alpha(\omega) = \sum_\beta U^*_{\alpha\beta}(\omega)\hat{S}_\beta(\omega), \tag{1.198}$$

which are called *Lindblad operators* .

Importantly, this unitary transformation enables to rewrite the MME in Eq. (1.196) as

$$\frac{d}{dt}\hat{\rho}_S(t) = -\frac{i}{\hbar}\left[\hat{H}_S + \hat{H}^{\mathrm{RWA}}_{\mathrm{Lamb}}, \hat{\rho}_S(t)\right] + \sum_{\omega}\sum_{\alpha}\frac{\gamma_\alpha(\omega)}{2}\mathcal{D}[\hat{L}_\alpha(\omega)]\hat{\rho}_S(t), \tag{1.199}$$

which is called Lindblad master equation. Here, we have introduced the *Lindblad dissipator*

$$\begin{aligned}\mathcal{D}[\hat{L}_\alpha(\omega)]\hat{\rho}_S &= \mathcal{D}[\hat{L}_\alpha(\omega), \hat{L}_\alpha(\omega)]\hat{\rho}_S \\ &= 2\hat{L}_\alpha(\omega)\hat{\rho}_S\hat{L}_\alpha^\dagger(\omega) - \hat{L}_\alpha^\dagger(\omega)\hat{L}_\alpha(\omega)\hat{\rho}_S - \hat{\rho}_S\hat{L}_\alpha^\dagger(\omega)\hat{L}_\alpha(\omega).\end{aligned} \tag{1.200}$$

We emphasize that Eq. (1.199) involves a single summation over α (apart from the summation over the Bohr frequencies), instead of the double summation over α and β in Eq. (1.196).

Last, we discuss two interesting properties of the Lindblad master equation:

- The quantities $\gamma_\alpha(\omega)$ are non-negative, as the matrices $[\gamma(\omega)]$ can be shown to be positive [139]. This property reinforces the interpretation of $\gamma_\alpha(\omega)$ as decay relaxation rates, corresponding to the inverse of some relaxation time.

- The dynamics of the system is invariant under inhomogeneous transformations of the form [139]

$$\hat{L}_\alpha(\omega) \to \hat{L}_\alpha(\omega) + l_\alpha(\omega), \tag{1.201a}$$

$$\begin{aligned}\hat{H}_S + \hat{H}_{\text{Lamb}}^{\text{RWA}} \to \hat{H}_S + \hat{H}_{\text{Lamb}}^{\text{RWA}} \\ + \frac{\hbar}{2i}\sum_\omega\sum_\alpha \gamma_\alpha(\omega)\left(l_\alpha^*(\omega)\hat{L}_\alpha(\omega) - l_\alpha(\omega)\hat{L}_\alpha^\dagger(\omega)\right),\end{aligned} \tag{1.201b}$$

  with $l_\alpha(\omega)$ a complex number. This property allows for choosing traceless Lindblad operators, which eventually can help to simplify the analytical calculation of the time evolution of $\hat{\rho}_S(t)$.

1.4.4 Adjoint master equation

In this section, we introduce the extension of the Heisenberg equation [Eq. (1.48)] to the case of open quantum systems. To this end, we consider an open system whose Schrödinger-picture dynamics is governed by the Markovian master equation in Eq. (1.196). The Heisenberg-picture evolution of an arbitrary operator $\hat{O}$ in $\mathcal{H}_S$ can be obtained as [139]

$$\begin{aligned}\frac{d}{dt}\hat{O}(t) = -\frac{i}{\hbar}[\hat{O}(t), \hat{H}_S + \hat{H}_{\text{Lamb}}^{\text{RWA}}] \\ + \sum_\omega\sum_{\alpha,\beta}\frac{\gamma_{\alpha\beta}(\omega)}{2}\left([\hat{S}_\alpha^\dagger(\omega), \hat{O}(t)]\hat{S}_\beta(\omega) + \hat{S}_\alpha^\dagger(\omega)[\hat{O}(t), \hat{S}_\beta(\omega)]\right),\end{aligned} \tag{1.202}$$

which is known as *adjoint master equation*. From this equation, we can derive the time evolution of the expectation value of $\hat{O}$ as

$$\frac{d}{dt}\langle\hat{O}\rangle(t) = \frac{i}{\hbar}\mathrm{Tr}\Big\{[\hat{H}_S + \hat{H}^{\mathrm{RWA}}_{\mathrm{Lamb}}, \hat{O}(t)]\rho_S\Big\} + \sum_{\omega}\sum_{\alpha,\beta}\frac{\gamma_{\alpha\beta}(\omega)}{2}\Big(\mathrm{Tr}\Big\{[\hat{S}^{\dagger}_{\alpha}(\omega), \hat{O}(t)]\hat{S}_{\beta}(\omega)\rho_S\Big\} + \mathrm{Tr}\Big\{\hat{S}^{\dagger}_{\alpha}(\omega)[\hat{O}(t), \hat{S}_{\beta}(\omega)]\rho_S\Big\}\Big). \tag{1.203}$$

We emphasize that the time evolution of $\langle\hat{O}\rangle(t)$ can be obtained either using the Heisenberg picture, through Eq. (1.203), or using the Schrödinger picture, through Eq. (1.197), with identical results.

1.4.5 Spontaneous emission from a single quantum emitter

We use in this section the Markovian approximation to trace out the electromagnetic degrees of freedom and derive a MME that describes the reduced dynamics of a QE. Thus, the QE plays the role of system of interest here, whereas the electromagnetic vacuum field is considered as a thermal bath at temperature T. In this way, we obtain an alternative derivation of the spontaneous decay rate γ_0 of the QE to that derived using the WWA in Section 1.3.

The first step to derive the MME consists in decomposing the Hamiltonian (in the Schrödinger picture) describing the interaction between the QE and the electromagnetic vacuum field as a summation of Hermitian system (QE) operators $\hat{S}_{\alpha}$ and bath (field) operators $\hat{B}_{\alpha}$, as described in Eq. (1.175). Importantly, we consider here the complete interaction Hamiltonian $\hat{H}^{mp}_I$ [Eq. (1.124)], without applying the RWA that neglects the terms that do not conserve the number of excitations ($\hat{\sigma}\hat{a}_{\mathbf{k}s}$ and $\hat{\sigma}^{\dagger}\hat{a}^{\dagger}_{\mathbf{k}s}$). In particular, we use the decomposition

$$\hat{H}^{mp}_I = \hbar\sum_{\mathbf{k},s}\hat{S}_{\mathbf{k}s}\otimes\hat{B}_{\mathbf{k}s}, \tag{1.204}$$

where the system and bath operators are given as

$$\hat{S}_{\mathbf{k}s} = \hat{S}^{\dagger}_{\mathbf{k}s} = \boldsymbol{\mu}\cdot\boldsymbol{e}_{\mathbf{k}s}\hat{\sigma} + \boldsymbol{\mu}^{*}\cdot\boldsymbol{e}_{\mathbf{k}s}\hat{\sigma}^{\dagger}, \tag{1.205a}$$

$$\hat{B}_{\mathbf{k}s} = \hat{B}^{\dagger}_{\mathbf{k}s} = -i\sqrt{\frac{\omega_{\mathrm{k}}}{2\varepsilon_0\hbar\mathcal{V}}}\Big[\hat{a}_{\mathbf{k}s}e^{i\mathbf{k}\cdot\mathbf{r}_0} - \hat{a}^{\dagger}_{\mathbf{k}s}e^{-i\mathbf{k}\cdot\mathbf{r}_0}\Big]. \tag{1.205b}$$

Notably, as the electromagnetic field is assumed to be at thermal equilibrium (at temperature T), the bath is here in the stationary state

$$\hat{\rho}^{th}_B = \frac{\exp(-\hat{H}_{F\perp}/k_BT)}{\mathrm{Tr}[\exp(-\hat{H}_{F\perp}/k_BT)]}, \tag{1.206}$$

$\omega = (\epsilon' - \epsilon)/\hbar$	$\epsilon/\hbar$	$\epsilon'/\hbar$	$\lvert\epsilon\rangle$	$\lvert\epsilon'\rangle$
ω_0	$-\omega_0/2$	$\omega_0/2$	$\lvert g\rangle$	$\lvert e\rangle$
$-\omega_0$	$\omega_0/2$	$-\omega_0/2$	$\lvert e\rangle$	$\lvert g\rangle$
0	$-\omega_0/2$	$-\omega_0/2$	$\lvert g\rangle$	$\lvert g\rangle$
0	$\omega_0/2$	$\omega_0/2$	$\lvert e\rangle$	$\lvert e\rangle$

Table 1.1: Bohr frequencies ω of the Hamiltonian $\hat{H}_{\rm QE} = \frac{\omega_0}{2}\hat{\sigma}_z$ of the QE considered as the system of interest. $|\epsilon\rangle$ and $|\epsilon'\rangle$ are eigenstates of $\hat{H}_{\rm QE}$, whereas ϵ and ϵ' are its eigenvalues.

which is a thermal state, with k_B the Boltzmann constant and $\hat{H}_{F\perp}$ given in Eq. (1.84). The bath operators satisfy $\langle \hat{B}_{\mathbf{k}s}\rangle(t) = \mathrm{Tr}[\hat{B}^{(I)}_{\mathbf{k}s}(t)\hat{\rho}^{th}_B] = 0$, as required to apply the MME [see Eq. (1.176)].

Next, we compute the set of Bohr frequencies of $\hat{H}_{\rm QE} = \frac{\omega_0}{2}\hat{\sigma}_z$. This Hamiltonian has eigenstates $|g\rangle$ and $|e\rangle$, with eigenvalues $-\hbar\omega_0/2$ and $\hbar\omega_0/2$, respectively. Thus, the Bohr frequencies are ω_0, $-\omega_0$, and 0, as summarized in Table 1.1. In this way, the eigenoperators of the Hamiltonian of the system of interest [Eq. (1.182)] become

$$\hat{S}_{\mathbf{k}s}(\omega_0) = |g\rangle\langle g|\hat{S}_{\mathbf{k}s}|e\rangle\langle e| = \boldsymbol{\mu}\cdot\boldsymbol{e}_{\mathbf{k}s}\hat{\sigma}, \tag{1.207a}$$

$$\hat{S}_{\mathbf{k}s}(-\omega_0) = |e\rangle\langle e|\hat{S}_{\mathbf{k}s}|g\rangle\langle g| = \boldsymbol{\mu}^*\cdot\boldsymbol{e}_{\mathbf{k}s}\hat{\sigma}^\dagger, \tag{1.207b}$$

$$\hat{S}_{\mathbf{k}s}(0) = |g\rangle\langle g|\hat{S}_{\mathbf{k}s}|g\rangle\langle g| + |e\rangle\langle e|\hat{S}_{\mathbf{k}s}|e\rangle\langle e| = 0. \tag{1.207c}$$

Moreover, we compute the bath correlation functions

$$\begin{aligned}\langle \hat{B}^{(I)}_{\mathbf{k}s}(\tau)\hat{B}^{(I)}_{\mathbf{k}'s'}(0)\rangle &= \frac{\sqrt{\omega_{\rm k}\omega_{k'}}}{2\varepsilon_0\mathcal{V}\hbar} \\ &\times\left\langle\left[\hat{a}_{\mathbf{k}s}e^{i(\mathbf{k}\cdot\mathbf{r}_0-\omega_{\rm k}\tau)} - \hat{a}^\dagger_{\mathbf{k}s}e^{-i(\mathbf{k}\cdot\mathbf{r}_0-\omega_{\rm k}\tau)}\right]\left[\hat{a}^\dagger_{\mathbf{k}'s'}e^{-i\mathbf{k}'\cdot\mathbf{r}_0} - \hat{a}_{\mathbf{k}'s'}e^{i\mathbf{k}'\cdot\mathbf{r}_0}\right]\right\rangle \\ &= \delta^3_{\mathbf{k},\mathbf{k}'}\delta_{s,s'}\frac{\omega_{\rm k}}{2\varepsilon_0\mathcal{V}\hbar}\left[n^{\rm th}_{\mathbf{k}s}e^{i\omega_{\rm k}\tau} + (1+n^{\rm th}_{\mathbf{k}s})e^{-i\omega_{\rm k}\tau}\right],\end{aligned} \tag{1.208}$$

where, in the last line, we have used the commutation relations in Eqs. (1.42a)–(1.42b). Additionally, we have introduced the electromagnetic thermal population in mode ($\mathbf{k}$,s) as

$$n^{\rm th}_{\mathbf{k}s} = \mathrm{Tr}(\hat{a}^\dagger_{\mathbf{k}s}\hat{a}_{\mathbf{k}s}\hat{\rho}^{th}_B) = \frac{\exp\left[-\frac{\hbar\omega_{\rm k}}{k_BT}\right]}{1-\exp\left[-\frac{\hbar\omega_{\rm k}}{k_BT}\right]}. \tag{1.209}$$

As a consequence, the decay rates in Eq. (1.193), which are given by the Fourier

transform of the bath correlation functions [Eq. (1.208)], become

$$\begin{aligned}\gamma_{\mathbf{k}s,\mathbf{k}'s'}(\omega) &= \int_{-\infty}^{\infty} d\tau e^{i\omega\tau}\,\langle \hat{B}^{(I)}_{\mathbf{k}s}(\tau)\hat{B}^{(I)}_{\mathbf{k}'s'}(0)\rangle \\ &= \delta^3_{\mathbf{k},\mathbf{k}'}\delta_{s,s'}\frac{\omega_{\mathrm{k}}}{\varepsilon_0\mathcal{V}\hbar}\Big[n^{\mathrm{th}}_{\mathbf{k}s}\delta(\omega+\omega_{\mathrm{k}}) + (1+n^{\mathrm{th}}_{\mathbf{k}s})\delta(\omega-\omega_{\mathrm{k}})\Big],\end{aligned} \tag{1.210}$$

where we have used $\int_{-\infty}^{\infty} dx e^{ix} = 2\pi\delta(x)$ [138].

At this point, we have all the ingredients necessary to compute the MME in the Schrödinger picture, which is given in Eq. (1.196). Indeed, ignoring again the Lamb shift induced by the vacuum field in the transition frequency of the QE [encoded in the Lamb-shift Hamiltonian], we obtain

$$\begin{aligned}\frac{d}{dt}\hat{\rho}_{\mathrm{QE}} &= -\frac{i}{\hbar}[\hat{H}_{\mathrm{QE}},\hat{\rho}_{\mathrm{QE}}] + \sum_{\mathbf{k},s}\frac{\gamma_{\mathbf{k}s,\mathbf{k}s}(\omega_0)}{2}\mathcal{D}[\hat{S}_{\mathbf{k}s}(\omega_0),\hat{S}_{\mathbf{k}s}(\omega_0)]\hat{\rho}_{\mathrm{QE}} \\ &\quad + \sum_{\mathbf{k},s}\frac{\gamma_{\mathbf{k}s,\mathbf{k}s}(-\omega_0)}{2}\mathcal{D}[\hat{S}_{\mathbf{k}s}(-\omega_0),\hat{S}_{\mathbf{k}s}(-\omega_0)]\hat{\rho}_{\mathrm{QE}} \\ &= -\frac{i}{\hbar}[\hat{H}_{\mathrm{QE}},\hat{\rho}_{\mathrm{QE}}] + \frac{\sum_{\mathbf{k},s}\gamma_{\mathbf{k}s,\mathbf{k}s}(\omega_0)|\boldsymbol{\mu}\cdot\boldsymbol{e}_{\mathbf{k}s}|^2}{2}\mathcal{D}[\hat{\sigma},\hat{\sigma}]\hat{\rho}_{\mathrm{QE}} \\ &\quad + \frac{\sum_{\mathbf{k},s}\gamma_{\mathbf{k}s,\mathbf{k}s}(-\omega_0)|\boldsymbol{\mu}\cdot\boldsymbol{e}_{\mathbf{k}s}|^2}{2}\mathcal{D}[\hat{\sigma}^\dagger,\hat{\sigma}^\dagger]\hat{\rho}_{\mathrm{QE}}.\end{aligned} \tag{1.211}$$

Here, we have defined $\hat{\rho}_{\mathrm{QE}}$ as the reduced density matrix of the QE.

Finally, taking into account that the electromagnetic modes at the frequencies of typical optical transitions in QEs have negligible thermal populations even at room temperature, we can assume $n^{\mathrm{th}}_{\mathbf{k}s} \to 0$. This thermal population also vanishes for any QE assuming $T = 0$. As a consequence, we find

$$\begin{aligned}\sum_{\mathbf{k},s}\gamma_{\mathbf{k}s,\mathbf{k}s}(\omega_0)|\boldsymbol{\mu}\cdot\boldsymbol{e}_{\mathbf{k}s}|^2 &\to \frac{\mathcal{V}}{(2\pi)^3}\sum_s\int_0^{2\pi}d\phi\int_0^{\pi}d\theta\sin\theta\int_0^{\infty}d\mathrm{k}\,\mathrm{k}^2 \\ &\quad\times\frac{\omega_{\mathrm{k}}}{\varepsilon_0\mathcal{V}\hbar}\delta(\omega_0-\omega_{\mathrm{k}})|\boldsymbol{\mu}\cdot\boldsymbol{e}_{\mathbf{k}s}|^2 \\ &= \frac{1}{(2\pi)^3c^3\varepsilon_0\hbar}|\boldsymbol{\mu}|^2\frac{8\pi}{3}\int_0^{\infty}d\omega_{\mathrm{k}}\omega_{\mathrm{k}}^3\delta(\omega_0-\omega_{\mathrm{k}}) = \gamma_0,\end{aligned} \tag{1.212}$$

where we have converted the sum over $\mathbf{k}$ into an integral [Eq. (1.134)] and used Eq. (1.160) to perform the resulting solid-angle integral. Importantly, we have also identified the expression of the spontaneous emission rate γ_0 [Eq. (1.163)] obtained

by using the WWA in Section 1.3. On the other hand,

$$\sum_{\mathbf{k},s}\gamma_{\mathbf{k}s,\mathbf{k}s}(-\omega_0)|\boldsymbol{\mu}\cdot\boldsymbol{e}_{\mathbf{k}s}|^2 \to \frac{\mathcal{V}}{(2\pi)^3}\sum_s\int_0^{2\pi}d\phi\int_0^{\pi}d\theta\sin\theta\int_0^{\infty}d\mathrm{k}\,\mathrm{k}^2 \times\frac{\omega_\mathrm{k}}{\varepsilon_0\mathcal{V}\hbar}\delta(\omega_0-\omega_\mathrm{k})|\boldsymbol{\mu}\cdot\boldsymbol{e}_{\mathbf{k}s}|^2 = \frac{1}{(2\pi)^3c^3\varepsilon_0\hbar}|\boldsymbol{\mu}|^2\frac{8\pi}{3}\int_0^{\infty}d\omega_\mathrm{k}\omega_\mathrm{k}^3\delta(\omega_0+\omega_\mathrm{k})=0. \tag{1.213}$$

In this way, we arrive to the MME (in the Schrödinger picture) that governs the dynamics of the QE

$$\frac{d}{dt}\hat{\rho}_\mathrm{QE}=-\frac{i}{\hbar}[\hat{H}_\mathrm{QE},\hat{\rho}_\mathrm{QE}]+\frac{\gamma_0}{2}\mathcal{D}[\hat{\sigma}]\hat{\rho}_\mathrm{QE}, \tag{1.214}$$

where the Lindblad dissipator $\mathcal{D}[\hat{\sigma}]\hat{\rho}_\mathrm{QE}$ is defined according to Eq. (1.200).

We conclude that the coherent dynamics of the reduced density matrix $\hat{\rho}_\mathrm{QE}$ of the QE is governed by the Hamiltonian $\hat{H}_\mathrm{QE}=\frac{\omega_0}{2}\hat{\sigma}_z$, where ω_0 is the transition frequency obtained from experiments and that includes the Lamb shift induced by the vacuum field, as discussed in Section 1.3. The spontaneous emission of the QE (with rate γ_0) is accounted for through the Lindblad dissipator $\mathcal{D}[\hat{\sigma}]\hat{\rho}_\mathrm{QE}$. Notably, the spontaneous emission rate has been derived in this section by using the MME and considering the complete expression of the multipolar form of the interaction Hamiltonian. The spontaneous emission rate obtained here is the same than as that derived in Section 1.3 using the WWA and the multipolar form of the interaction Hamiltonian under the RWA. Thus, the spontaneous emission rate is not affected by simplifying the multipolar form of the Hamiltonian through the RWA.

1.5 Interaction of a quantum emitter with a laser

At this point, we have reached the fundamental formulation of the interaction between the vacuum field and a QE with two-level behaviour. We have also shown that the vacuum field induces the spontaneous emission of photons from the excited state of the QE. Moreover, the description of light emission from quantum emitters illuminated by a continuous-wave laser is also of considerable interest for this thesis. In this section, we derive the Hamiltonian that describes the interaction between such an external illumination and the QE. Further, we introduce the concepts of dressed states and of saturation of the QE. To this end, we mainly follow the procedure described in Ref. [124].

1.5.1 Interaction Hamiltonian

The electric field generated by a laser can be described classically. We consider that this classical field has frequency ω_L, wavevector $\mathbf{k}_L$, polarization $\boldsymbol{e}_L$ and amplitude $\mathcal{E}_L(\mathbf{r})$. Under the long-wavelength approximation described in Section 1.2.5, such electric field can be assumed to be constant within the spatial extension of the QE. At the position of the center of mass of the QE, $\mathbf{r}_0$, the laser electric field can be written as

$$\boldsymbol{E}_L(\mathbf{r}_0,t) = \mathcal{E}_L(\mathbf{r}_0)\cos(\omega_L t)\boldsymbol{e}_L = \frac{\mathcal{E}_L(\mathbf{r}_0)}{2}(e^{i\omega_L t}+e^{-i\omega_L t})\boldsymbol{e}_L. \tag{1.215}$$

The interaction between the QE and the laser can thus be described, in the multipolar form, by the Schrödinger-picture interaction Hamiltonian

$$\hat{H}_L(t) = -\hat{\boldsymbol{\mu}}\cdot\boldsymbol{E}_L(\mathbf{r}_0,t) = -(\boldsymbol{\mu}\hat{\sigma}+\boldsymbol{\mu}^*\hat{\sigma}^\dagger)\cdot\frac{\mathcal{E}_L(\mathbf{r}_0)}{2}(e^{i\omega_L t}+e^{-i\omega_L t})\boldsymbol{e}_L. \tag{1.216}$$

Moreover, the lowering and raising operators evolve [in the Heisenberg picture] as $\hat{\sigma}(t) = \exp(-i\omega_0 t)\hat{\sigma}(0)$ and $\hat{\sigma}^\dagger(t) = \exp(i\omega_0 t)\hat{\sigma}^\dagger(0)$ in the absence of driving [Eqs. (1.122a)–(1.122b)]. Thus, the terms $\hat{\sigma}e^{-i\omega_L t}$ and $\hat{\sigma}^\dagger e^{i\omega_L t}$ in $\hat{H}_L(t)$ provide much faster oscillations than $\hat{\sigma}e^{i\omega_L t}$ and $\hat{\sigma}^\dagger e^{-i\omega_L t}$. The terms $\hat{\sigma}e^{-i\omega_L t}$ and $\hat{\sigma}^\dagger e^{i\omega_L t}$ can then be neglected under the RWA, so that the Hamiltonian describing the interaction between the QE and the laser reduces to

$$\hat{H}_L^{\mathrm{RWA}}(t) = -\frac{\hbar}{2}\left(\Omega\hat{\sigma}e^{i\omega_L t}+\Omega^*\hat{\sigma}^\dagger e^{-i\omega_L t}\right). \tag{1.217}$$

Here, we have defined

$$\Omega = \frac{\mathcal{E}_L(\mathbf{r}_0)\boldsymbol{\mu}\cdot\boldsymbol{e}_L}{\hbar}, \tag{1.218}$$

which is called *Rabi frequency*. Further, the laser intensity I_L and the field amplitude $\mathcal{E}_L(\mathbf{r}_0)$ are related as [121, 124]

$$I_L = \frac{1}{2}\varepsilon_0 c|\mathcal{E}_L(\mathbf{r}_0)|^2. \tag{1.219}$$

Thus, the norm of the Rabi frequency Ω is proportional to the square root of the laser intensity. More specifically, $|\Omega|$ and I_L are related by

$$|\Omega| = \sqrt{\frac{I_L 6\pi c^2\gamma_0}{\hbar\omega_0^3}}. \tag{1.220}$$

Finally, the total Hamiltonian describing the interaction between the QE and the electromagnetic field (including both the vacuum field and the laser) is given by the sum of the Hamiltonian in Eq. (1.116), corresponding to the interaction between the QE and the vacuum field, and $\hat{H}_L^{\mathrm{RWA}}(t)$. Notably, $\hat{H}_L^{\mathrm{RWA}}(t)$ is time-dependent

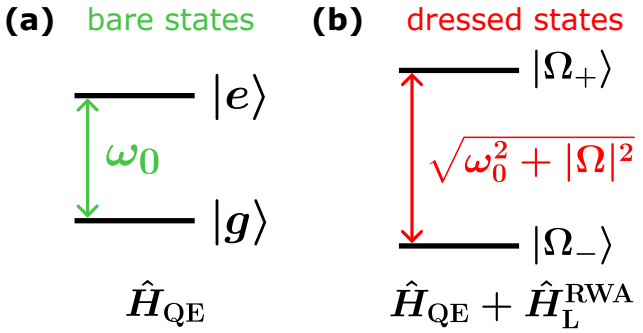

Figure 1.3: Schematic representation of the bare and dressed states. (a) The *bare states* correspond to the eigenstates of the Hamiltonian $\hat{H}_{\mathrm{QE}}$, which describes the coherent dynamics of the QE in the absence of laser driving. These states are thus the electronic ground state $|g\rangle$ and the electronic excited state $|e\rangle$. The difference of energy between the bare states is $\hbar\omega_0$. (b) The *dressed states*, which are denoted by $|\Omega_+\rangle$ (higher energy) and $|\Omega_-\rangle$ (lower energy), correspond to the eigenstates of $\hat{H}_{\mathrm{QE}} + \hat{H}_{\mathrm{L}}^{\mathrm{RWA}}$, describing the coherent dynamics of the QE under laser driving. The dressed states are given as linear combinations of the bare states, as shown in Eqs. (1.223a)–(1.223b), and the difference of energy between them is $\hbar\sqrt{\omega_0^2 + |\Omega|^2}$.

in the Schrödinger picture, which complicates the exact derivation of the MME describing the reduced dynamics of the driven QE (Section 1.4.2). However, to the best of our knowledge, the laser driving affects the spontaneous emission of the QE only under very extreme conditions, such as when the laser frequency is comparable to γ_0 and the laser intensity is very high [144, 145]. Thus, for the type of QE and illumination conditions considered in this thesis, it works extremely well to directly incorporate the driving Hamiltonian $\hat{H}_L^{\mathrm{RWA}}(t)$ into the MME in Eq. (1.214) (derived in Section 1.4.5 considering no driving). This approach leads to the effective MME

$$\frac{d}{dt}\hat{\rho}_{\mathrm{QE}} = -\frac{i}{\hbar}\left[\hbar\frac{\omega_0}{2}\hat{\sigma}_z - \frac{\hbar}{2}\left(\Omega\hat{\sigma}e^{i\omega_L t} + \Omega^*\hat{\sigma}^\dagger e^{-i\omega_L t}\right), \hat{\rho}_{\mathrm{QE}}\right] + \frac{\gamma_0}{2}\mathcal{D}[\hat{\sigma}]\hat{\rho}_{\mathrm{QE}}. \quad (1.221)$$

1.5.2 Bare states and dressed states

We show in this section that the laser driving can modify the eigenstates of the QE. We first recall that, in the absence of laser illumination, the eigenstates of the two-level QE are the electronic ground state $|g\rangle$ and the electronic excited state $|e\rangle$, with energies $-\hbar\omega_0/2$ and $\hbar\omega_0/2$, respectively. These states are usually referred to as *bare states* and schematically represented in Fig. 1.3a. However, under laser driving, the total Hamiltonian describing the dynamics of the QE is diagonalized as

$$\hat{H}_{\mathrm{QE}} + \hat{H}_L^{\mathrm{RWA}} = \hbar\frac{\sqrt{\omega_0^2 + |\Omega|^2}}{2}|\Omega_+\rangle\langle\Omega_+| - \hbar\frac{\sqrt{\omega_0^2 + |\Omega|^2}}{2}|\Omega_-\rangle\langle\Omega_-|. \quad (1.222)$$

The eigenstates of the driven QE are known as *dressed states* and are given by

$$|\Omega_+\rangle = \sin\Theta\,|g\rangle + \cos\Theta\,|e\rangle\,, \tag{1.223a}$$
$$|\Omega_-\rangle = \cos\Theta\,|g\rangle - \sin\Theta\,|e\rangle\,, \tag{1.223b}$$

where $\Theta \in [0, \pi/2]$ is called *Stückelberg angle*. This angle is defined by the ratio of the Rabi frequency Ω (proportional to $\sqrt{I_L}$) to the transition frequency of the QE. More specifically,

$$\tan(2\Theta) = |\Omega|/\omega_0. \tag{1.224}$$

The energies of the dressed states $|\Omega_\pm\rangle$ are $\pm\hbar\sqrt{\omega_0^2 + |\Omega|^2}/2$. Thus, the energy splitting between the dressed states is $\hbar\sqrt{\omega_0^2 + |\Omega|^2}$, as depicted in Fig. 1.3b. This energy splitting increases with the Rabi frequency. One can check that, in the limit of no driving, the dressed states become again the bares states, as $|\Omega_+\rangle \to |e\rangle$ and $|\Omega_-\rangle \to |g\rangle$, and $\pm\hbar\sqrt{\omega_0^2 + |\Omega|^2}/2 \to \pm\hbar\omega_0/2$.

1.5.3 Rotating frame at the laser frequency

As pointed out in Section 1.5.1, the Hamiltonian describing the laser driving is time-dependent even in the Schrödinger picture. This time-dependency complicates any analytical or numerical calculation and, thus, the analysis and characterization of light emission from the QE. We show in this section that a unitary transformation can be performed to obtain a time-independent Hamiltonian.

The effect of a general unitary transformation $\hat{\hat{T}}$ in an arbitrary Hamiltonian $\hat{H}$ is discussed in detail in Appendix C. In a nutshell, the Hamiltonian is transformed according to

$$\hat{\hat{H}} = i\hbar\frac{d\hat{\hat{T}}}{dt}\hat{\hat{T}}^\dagger + \hat{\hat{T}}\hat{H}\hat{\hat{T}}^\dagger. \tag{1.225}$$

We emphasize that the measurable quantities in experiments, which correspond to the expectation values of Hermitian operators (observables), are not affected by unitary transformations, just as they are independent of whether the Heisenberg or Schrödinger picture is used in the calculations.

In particular, we consider in this section the unitary transformation

$$\hat{\hat{T}} = \exp\left(it\frac{\omega_L}{2}\hat{\sigma}_z\right), \tag{1.226}$$

which can be interpreted as a change of reference frame. More specifically, it can be interpreted as moving to the reference frame that rotates in time at the frequency ω_L of the laser. Using the expansion theorem in Eq. (1.106), we find

$$\hat{\hat{T}}\hat{\sigma}\hat{\hat{T}}^\dagger = \hat{\sigma}e^{-i\omega_L t}, \tag{1.227a}$$
$$\hat{\hat{T}}\hat{\sigma}^\dagger\hat{\hat{T}}^\dagger = \hat{\sigma}^\dagger e^{i\omega_L t}, \tag{1.227b}$$
$$\hat{\hat{T}}\hat{\sigma}_z\hat{\hat{T}}^\dagger = \hat{\sigma}_z. \tag{1.227c}$$

In this way, $\hat{H}_{\mathrm{QE}} + \hat{H}_L^{\mathrm{RWA}}(t)$ is transformed to

$$\hat{\tilde{H}}_{\mathrm{QE}} + \hat{\tilde{H}}_L^{\mathrm{RWA}} = \hbar\frac{\Delta_0}{2}\hat{\sigma}_z - \frac{\hbar}{2}(\Omega\hat{\sigma} + \Omega^*\hat{\sigma}^\dagger), \tag{1.228}$$

where we have defined the frequency detuning between the transition frequency of the QE and the laser frequency as

$$\Delta_0 = \omega_0 - \omega_L. \tag{1.229}$$

Therefore, the Hamiltonian in Eq. (1.228) is time-independent and the MME governing the dynamics in such rotating frame becomes

$$\frac{d}{dt}\hat{\tilde{\rho}}_{\mathrm{QE}} = -\frac{i}{\hbar}\left[\hbar\frac{\Delta_0}{2}\hat{\sigma}_z - \frac{\hbar}{2}(\Omega\hat{\sigma} + \Omega^*\hat{\sigma}^\dagger)\right] + \frac{\gamma_0}{2}\mathcal{D}[\hat{\sigma}]\hat{\tilde{\rho}}_{\mathrm{QE}}. \tag{1.230}$$

Notably, the new dressed states (i.e., the eigenstates of $\hat{\tilde{H}}_{\mathrm{QE}} + \hat{\tilde{H}}_L^{\mathrm{RWA}}$) are formally identical to the ones given in Eqs. (1.223a)–(1.223b), but with the Stückelberg angle redefined as $\tan(2\Theta) = |\Omega|/\Delta_0$. Additionally, the frequency splitting between the dressed states in the rotating frame becomes

$$\Omega_R = \sqrt{\Delta_0^2 + |\Omega|^2}, \tag{1.231}$$

which is known as *generalized Rabi frequency* and is responsible for the emergence of oscillations in the populations of the bare states, as discussed below.

In the following, we use the Python package QuTiP [146] to numerically solve the MME in Eq. (1.230) and analyze the dynamics of the driven emitter. To this end, we fix the decay rate at $\gamma_0/(2\pi) = 21.5$ MHz and ω_0 at a value corresponding to a vacuum wavelength of 618 nm. These parameters are based on experiments performed with dibenzanthanthrene (DBATT) organic molecules in Ref. [1]. These molecules are taken as a reference throughout this thesis. We assume that the emitter is initially inverted (equivalently, the state $|e\rangle$ is initially excited). We first plot in Fig. 1.4a the time evolution of the population of $|e\rangle$ (solid blue line) and of $|g\rangle$ (dashed grey line) under no driving ($\Omega = 0$). We find that the population of the excited state decays exponentially to zero with rate γ_0, as expected from the analysis in Section 1.3. In contrast, the population of the ground state increases exponentially, becoming equal to 1 at sufficiently long time. Next, we analyze how the dynamics of the populations of $|e\rangle$ and $|g\rangle$ are affected by the driving of a resonant laser ($\omega_L = \omega_0$). In Fig. 1.4b, we fix $\Omega/\gamma_0 = 1$ and omit the dissipator $\mathcal{D}[\hat{\sigma}]\hat{\tilde{\rho}}_{\mathrm{QE}}$ in the simulation of the dynamics to more clearly reveal the influence of the driving on the dynamics of the QE (without the influence of the spontaneous emission). We find that the populations of the two bare states oscillate in time between 0 and 1 with a period of $2\pi/\Omega_R$. These oscillations are commonly referred to as *Rabi oscillations*. We include the dissipator $\mathcal{D}[\hat{\sigma}]\hat{\tilde{\rho}}_{\mathrm{QE}}$ again in the simulations in Fig. 1.4c and fix $\Omega/\gamma_0 = 1$. In this case, the population of $|e\rangle$ decays exponentially in time and, in addition, exhibits Rabi oscillations. Importantly, at

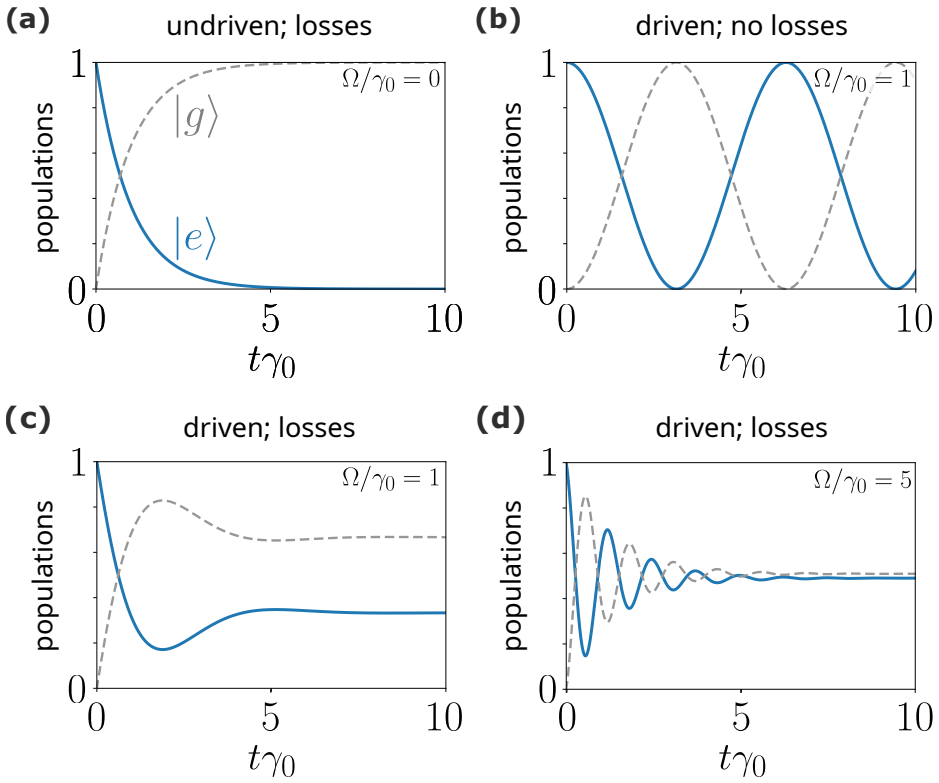

Figure 1.4: Time evolution of the populations of the bare states of the QE. We take a DBATT molecule as a reference QE, with $\gamma_0/(2\pi) = 21.5$ MHz and ω_0 corresponding to a vacuum wavelength of 618 nm. The dashed grey lines correspond to the population of the ground state $|g\rangle$ and the solid blue lines to that of the excited state $|e\rangle$. The emitter is undriven in (a) and driven resonantly in (b)-(d). The losses are artificially set to zero in the simulation in (b) to highlight the effect of the laser driving in the time evolution of the populations of the bare states. The driving strength is fixed at $\Omega/\gamma_0 = 1$ in (b) and (c), and at $\Omega/\gamma_0 = 5$ in (d).

long times, the population of the excited state becomes non-zero in contrast to the case of no driving in Fig. 1.4a. Last, we increase the driving strength to $\Omega/\gamma_0 = 5$ in Fig. 1.4d and find more pronounced oscillations of the populations. Additionally, at long times the population of $|e\rangle$ reaches a larger value than in Fig. 1.4c, which is analyzed in the next section.

1.5.4 Saturation of a quantum emitter

In this section, we analyze the behaviour of the population of $|e\rangle$ at the steady state ($t \to \infty$) for increasing values of driving strength. We show that this population cannot be larger than 1/2, which enables to introduce the concept

of saturation of the QE. To this end, we first derive the equation of motion of $\hat{\sigma}^\dagger\hat{\sigma} = |e\rangle\langle e|$, which gives the time evolution of the population of $|e\rangle$ because, in the Schrödinger picture, $\langle\hat{\sigma}^\dagger\hat{\sigma}\rangle(t) = \mathrm{Tr}[\hat{\sigma}^\dagger\hat{\sigma}\hat{\tilde{\rho}}_{\mathrm{QE}}(t)] = \langle e|\hat{\tilde{\rho}}_{\mathrm{QE}}(t)|e\rangle$. We also calculate the equation of motion of the off-diagonal element of the density matrix $\langle e|\hat{\tilde{\rho}}_{\mathrm{QE}}(t)|g\rangle = \mathrm{Tr}[\hat{\sigma}\hat{\tilde{\rho}}_{\mathrm{QE}}(t)] = \langle\hat{\sigma}\rangle(t)$. Using Eq. (1.197), we find

$$\frac{d}{dt}\langle\hat{\sigma}^\dagger\hat{\sigma}\rangle(t) = -\gamma_0\langle\hat{\sigma}^\dagger\hat{\sigma}\rangle(t) - i\left[\frac{\Omega}{2}\langle\hat{\sigma}\rangle(t) - \frac{\Omega^*}{2}\langle\hat{\sigma}^\dagger\rangle(t)\right], \tag{1.232a}$$

$$\frac{d}{dt}\langle\hat{\sigma}\rangle(t) = -\left[\frac{\gamma_0}{2} + i\Delta_0\right]\langle\hat{\sigma}\rangle(t) - i\Omega^*\langle\hat{\sigma}^\dagger\hat{\sigma}\rangle(t) + i\frac{\Omega^*}{2}. \tag{1.232b}$$

Next, the steady-state population of $|e\rangle$ can be obtained taking into account that the time-derivatives of all the elements of the density matrix vanish in the steady state [139]. In this way, we obtain

$$0 = -\gamma_0\langle\hat{\sigma}^\dagger\hat{\sigma}\rangle_{\mathrm{ss}} - i\left[\frac{\Omega}{2}\langle\hat{\sigma}\rangle_{\mathrm{ss}} - \frac{\Omega^*}{2}\langle\hat{\sigma}^\dagger\rangle_{\mathrm{ss}}\right], \tag{1.233a}$$

$$0 = -\left[\frac{\gamma_0}{2} + i\Delta_0\right]\langle\hat{\sigma}\rangle_{\mathrm{ss}} - i\Omega^*\langle\hat{\sigma}^\dagger\hat{\sigma}\rangle_{\mathrm{ss}} + i\frac{\Omega^*}{2}, \tag{1.233b}$$

where the expectation values are evaluated in the steady state (indicated by the subscript 'ss'). Solving this system of equations, we find

$$\langle\hat{\sigma}^\dagger\hat{\sigma}\rangle_{\mathrm{ss}} = \frac{1}{2}\frac{|\Omega|^2}{|\Omega|^2 + 2[(\gamma_0/2)^2 + \Delta_0^2]} = \frac{1}{2}\frac{s_L}{1+s_L}, \tag{1.234}$$

where we have introduced the *saturation parameter*

$$s_L = \frac{1}{2}\frac{|\Omega|^2}{(\gamma_0/2)^2 + \Delta_0^2}, \tag{1.235}$$

which is proportional to $|\Omega|^2$ and, thus, to the laser intensity I_L [see Eq. (1.220)]. Equation (1.234) indicates that the steady-state population of the excited state of a QE driven by a laser is smaller or equal than 1/2. Thus, the steady-state population of $|e\rangle$ cannot be larger than the steady population of $|g\rangle$, but they become equal at very strong laser driving ($s_L \to \infty$). Additionally, the value of laser intensity I_L for which $s_L = 1$ (i.e., $\langle\hat{\sigma}^\dagger\hat{\sigma}\rangle = 1/4$) at resonant driving ($\Delta_0 = 0$) is referred to as *saturation intensity*, I_{sat}. Using Eq. (1.220), we obtain

$$I_{\mathrm{sat}} = \frac{\hbar\omega_0^3\gamma_0}{12\pi c^2}. \tag{1.236}$$

Accurately calibrating the laser intensity at the position of the QE is often challenging in experiments, and so is estimating the Rabi frequency directly through Eq. (1.220). However, the comparison between experimental results and theoretical

predictions can be facilitated by expressing the Rabi frequency in terms of the ratio

$$\frac{I_L}{I_{\text{sat}}} = \frac{2|\Omega|^2}{\gamma_0^2}. \tag{1.237}$$

CHAPTER 2

QUANTUM OPTICAL COHERENCE AND LIGHT STATISTICS

In classical optics, coherence describes the ability of light to interfere [147]. In the 1960s, Roy J. Glauber revisited the concept of optical coherence and extended it to the quantum realm [111–114], an achievement widely recognized as the foundation of quantum optics. In this chapter, we review the n^{th}-order coherence function introduced by Glauber, which has become an essential tool for characterizing quantum light. We place particular emphasis on the second-order coherence function, which plays a key role in Chapters 3 and 4 of this thesis.

We first present the first-order coherence function, both the classical formulation and the quantum-mechanical formulation. Additionally, the first-order coherence function allows us to introduce the usual emission spectrum. We then generalize the coherence function to second and higher orders. Afterwards, we describe the working principles of the Hanbury-Brown Twiss interferometer that measures the second-order coherence function of light from the correlation of the intensities detected by two separate detectors, and analyze the insights that this function provides into the statistical properties of light. We also describe a modification of the standard Hanbury-Brown Twiss interferometer that enables the measurement of the second-order coherence function for photon pairs at specific frequencies. This approach reveals additional information about the emission mechanisms of a system. Moreover, we analyze the second-order correlation of light emitted from a single quantum emitter and measured in the standard Hanbury-Brown Twiss interferometer, as well as the behaviour of this correlation when it is measured in the modified Hanbury-Brown Twiss interferometer.

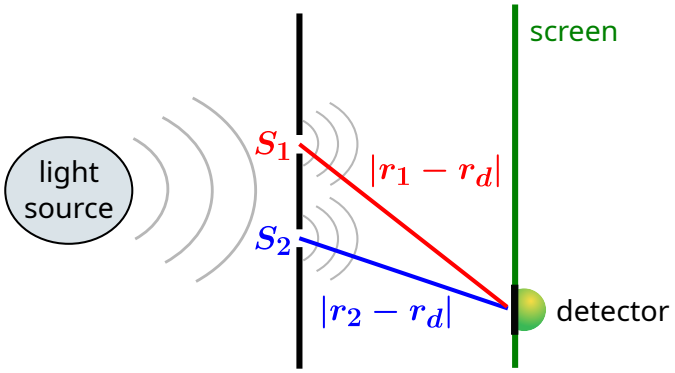

Figure 2.1: Schematic representation of the Young's interference experiment. Light emitted from a source impinges into two slits S_1 (red) and S_2 (blue), at positions $\mathbf{r}_1$ and $\mathbf{r}_2$, respectively. Light is then scattered from the slits and arrives to a screen (green), where a detector is located at position $\mathbf{r}_d$. The optical path from slit S_j to the detector is $|\mathbf{r}_j - \mathbf{r}_d|$.

2.1 First-order coherence and emission spectrum

In this section, we first analyze the concept of classical optical coherence by addressing the Young's interference experiment. Afterwards, we present a quantum description of the process of photodetection, which enables an intuitive introduction of the first-order coherence tensor and function in the quantum realm. Additionally, we present the usual emission spectrum, which can be obtained from the first-order coherence function and serves to characterize the spectral properties of light. We mainly follow Refs. [111, 114, 117, 120, 148] in this section.

2.1.1 Young's interference experiment from a classical perspective

An illustrative example of the ability of classical light to interfere is provided by the *Young's interference experiment* [147, 149]. In this experiment, light emitted from a source impinges into two slits, S_1 and S_2, at positions $\mathbf{r}_1$ and $\mathbf{r}_2$, respectively. We consider that both slits have identical geometry and size. Light is then scattered from the slits according to Huygen's principle [147], as schematically represented in Fig. 2.1. Last, scattered light arrives at a screen in the far-field region, where a detector at position $\mathbf{r}_d$ is used to measure light intensity. The total electric field at the position of the detector can be expressed as

$$\mathbf{E}(\mathbf{r}_d, t) = K\mathbf{E}(\mathbf{r}_1, t - \Delta t_1) + K\mathbf{E}(\mathbf{r}_2, t - \Delta t_2), \tag{2.1}$$

where $\mathbf{E}(\mathbf{r}_j, t - \Delta t_j)$ is the electric field scattered from slit S_j, with $\Delta t_j = |\mathbf{r}_j - \mathbf{r}_d|/c$ the time that light takes to travel from this slit to the detector. Additionally, K is

a complex coefficient that depends on the size and geometry of the slits, as well as on the distance between the slits and the detectors.

In general, the intensity of a classical electromagnetic field is defined as the rate of energy carried by the electromagnetic field per unit of time and area. For propagating electromagnetic fields, the intensity is proportional to the square of the magnitude of the electric field [121, 147]. Thus, the average intensity measured by the detector for very long times can be obtained as

$$I(\mathbf{r}_d) \propto \langle |\mathbf{E}(\mathbf{r}_d, t)|^2 \rangle_c \,. \tag{2.2}$$

Here, we have introduced the classical temporal average of an arbitrary function of time $f(t)$ as [116, 147]

$$\langle f(t) \rangle_c = \lim_{T\to\infty} \frac{1}{T} \int_0^T f(t) dt, \tag{2.3}$$

where the subscript c emphasizes that $\langle f(t) \rangle_c$ is a classical average, instead of the expectation value of a quantum-mechanical operator. This average is stationary, as it is independent of the origin of the time axis [116, 118, 147]. By substituting Eq. (2.1) into Eq. (2.2), we obtain that the average intensity at the position of the detector is

$$I(\mathbf{r}_d) = I_1(\mathbf{r}_d) + I_2(\mathbf{r}_d) + 2\sqrt{I_1(\mathbf{r}_d) I_2(\mathbf{r}_d)} \mathrm{Re}[g_c^{(1)}(\mathbf{r}_1, t - \Delta t_1; \mathbf{r}_2, t - \Delta t_2)], \tag{2.4}$$

with $I_1(\mathbf{r}_d)$ and $I_2(\mathbf{r}_d)$ the average intensities of light scattered independently from slit S_1 and S_2, as if the other slit did not exist. Further, we have introduced in Eq. (2.4) the complex function

$$g_c^{(1)}(\mathbf{r}_1, t - \Delta t_1; \mathbf{r}_2, t - \Delta t_2) = \frac{\langle \mathbf{E}(\mathbf{r}_1, t - \Delta t_1) \cdot \mathbf{E}(\mathbf{r}_2, t - \Delta t_2) \rangle_c}{\sqrt{\langle |\mathbf{E}(\mathbf{r}_1, t - \Delta t_1)|^2 \rangle_c \langle |\mathbf{E}(\mathbf{r}_2, t - \Delta t_2)|^2 \rangle_c}}, \tag{2.5}$$

which is determined by the average of the product of the electric field scattered from both slits and normalized by the squared roots of the intensities of light emitted from each slit. The average $\langle \mathbf{E}(\mathbf{r}_1, t - \Delta t_1) \cdot \mathbf{E}(\mathbf{r}_2, t - \Delta t_2) \rangle_c$ in the numerator of Eq. (2.5) is usually referred to as *mutual coherence function* or *first-order correlation* of the electric fields, while $g_c^{(1)}(\mathbf{r}_1, t - \Delta t_1; \mathbf{r}_2, t - \Delta t_2)$ is known as *normalized first-order classical correlation function*. Equation (2.4) indicates that the light scattered from the two slits interferes if $g_c^{(1)}(\mathbf{r}_1, t - \Delta t_1; \mathbf{r}_2, t - \Delta t_2)$ does not vanish. As a consequence, this function can be used to quantify the degree of coherence between both classical light beams, as discussed below.

In the Young's experiment, the interference between light scattered from both slits is reflected by the emergence of fringes on the screen. The contrast of the fringes is given by the difference between light intensity of the minima and maxima in the pattern [147, 150]. Specifically, the contrast of the fringes around the position

$\mathbf{r}_d$ of the detector can be quantified through

$$V(\mathbf{r}_d) = \frac{\max\{I(\mathbf{r}_d)\} - \min\{I(\mathbf{r}_d)\}}{\max\{I(\mathbf{r}_d)\} + \min\{I(\mathbf{r}_d)\}}, \tag{2.6}$$

which is known as *visibility*. Here, $\max\{I(\mathbf{r}_d)\}$ and $\min\{I(\mathbf{r}_d)\}$ are the maximum and minimum values, respectively, that the average intensity takes around the position of the detector $\mathbf{r}_d$. The intensity $I(\mathbf{r}_d)$ given in Eq. (2.4) results in

$$\max\{I(\mathbf{r}_d)\} = I_1(\mathbf{r}_d) + I_2(\mathbf{r}_d) + 2\sqrt{I_1(\mathbf{r}_d)I_2(\mathbf{r}_d)}|g_c^{(1)}(\mathbf{r}_1, t-\Delta t_1; \mathbf{r}_2, t-\Delta t_2)|, \tag{2.7a}$$

$$\min\{I(\mathbf{r}_d)\} = I_1(\mathbf{r}_d) + I_2(\mathbf{r}_d) - 2\sqrt{I_1(\mathbf{r}_d)I_2(\mathbf{r}_d)}|g_c^{(1)}(\mathbf{r}_1, t-\Delta t_1; \mathbf{r}_2, t-\Delta t_2)|. \tag{2.7b}$$

As a result, the visibility becomes

$$V(\mathbf{r}_d) = \frac{2\sqrt{I_1(\mathbf{r}_d)I_2(\mathbf{r}_d)}}{I_1(\mathbf{r}_d) + I_2(\mathbf{r}_d)}|g_c^{(1)}(\mathbf{r}_1, t-\Delta t_1; \mathbf{r}_2, t-\Delta t_2)|. \tag{2.8}$$

Thus, the contrast of the fringes in the Young's experiment is determined by the norm of $g_c^{(1)}(\mathbf{r}_1, t-\Delta t_1; \mathbf{r}_2, t-\Delta t_2)$ and by the ratio between the intensities of light scattered from each slit. Notably, if $I_1(\mathbf{r}_d) = I_2(\mathbf{r}_d)$, the visibility thus reduces directly to $V(\mathbf{r}_d) = |g_c^{(1)}(\mathbf{r}_1, t-\Delta t_1; \mathbf{r}_2, t-\Delta t_2)|$.

We conclude that the normalized first-order classical correlation function $g_c^{(1)}(\mathbf{r}_1, t-\Delta t_1; \mathbf{r}_2, t-\Delta t_2)$ describes the emergence of the interference between light emitted from the two slits in the Young's interference experiment. More generally, this quantity can be used to quantify the degree of coherence between light emitted from two arbitrary sources. Notably, the normalization of $g_c^{(1)}(\mathbf{r}_1, t-\Delta t_1; \mathbf{r}_2, t-\Delta t_2)$ in Eq. (2.5) is chosen such that $|g_c^{(1)}(\mathbf{r}_1, t-\Delta t_1; \mathbf{r}_2, t-\Delta t_2)|$ is bounded as [116]

$$0 \leq |g_c^{(1)}(\mathbf{r}_1, t-\Delta t_1; \mathbf{r}_2, t-\Delta t_2)| \leq 1. \tag{2.9}$$

If $|g_c^{(1)}(\mathbf{r}_1, t-\Delta t_1; \mathbf{r}_2, t-\Delta t_2)| = 1$, we say that classical light is *completely coherent*. In contrast, if $|g_c^{(1)}(\mathbf{r}_1, t-\Delta t_1; \mathbf{r}_2, t-\Delta t_2)| = 0$, light is said to be *completely incoherent*. For intermediate values, classical light is *partially coherent*. As an example, we consider a monochromatic electromagnetic plane wave, with frequency ω and linear polarization along some direction $\boldsymbol{e}_\alpha$. In this case, $\mathbf{E}(\mathbf{r}, t) = |\mathbf{E}(\mathbf{r}, t)|\boldsymbol{e}_\alpha \exp[i(\omega t - \mathbf{k}\cdot\mathbf{r})]$ and, as a consequence, $g_c^{(1)}(\mathbf{r}_1, t-\Delta t_1; \mathbf{r}_2, t-\Delta t_2) = \exp[i(\omega(\Delta t_1 - \Delta t_2) - \mathbf{k}\cdot(\mathbf{r}_1 - \mathbf{r}_2))]$. Thus, this electromagnetic plane wave is completely coherent because $|g_c^{(1)}(\mathbf{r}_1, t-\Delta t_1; \mathbf{r}_2, t-\Delta t_2)| = 1$.

2.1.2 Photodetection

We describe in this section the process of photodetection using the *atom detector model*, which facilitates the introduction of the first-order coherence function in the quantum realm. In experiments, the detection of photons typically relies on the absorption of photons by some system. Within the atom detector model, the detection system is a two-level atom, which allows for describing the fundamental aspects of photodetection in a simple way.

First, the atom in the detector is typically described as a two-level system, with ground state $|g_d\rangle$, excited state $|e_d\rangle$ and transition frequency ω_d. The Hamiltonian of this atom detector (in the Schrödinger picture) can be written as

$$\hat{H}_d = \hbar\frac{\omega_d}{2}(\hat{\zeta}^\dagger\hat{\zeta} - \hat{\zeta}\hat{\zeta}^\dagger), \tag{2.10}$$

with $\hat{\zeta} = |g_d\rangle\langle e_d|$ and $\hat{\zeta}^\dagger = |e_d\rangle\langle d_d|$ the lowering and raising operators in the Hilbert space of the two-level atom detector. Additionally, the probability of photon absorption by this atom is independent of the photon frequency or, in other words, the atom detector is *color-blind*. (This model is extended to the case of frequency-resolved detection in Section 2.4.) Further, the atom is assumed to have negligible size in comparison to the wavelength of light and, thus, its interaction with the electromagnetic field can be described by the Hamiltonian

$$\hat{H}_{d,F} = -\hat{\boldsymbol{\mu}}_d \cdot \hat{\mathbf{E}}_\perp(\mathbf{r}_d), \tag{2.11}$$

which corresponds to the interaction Hamiltonian in the multipolar form described in Sections 1.2.5 and 1.2.6. Here, $\mathbf{r}_d$ is the position of the detector and

$$\hat{\boldsymbol{\mu}}_d = \boldsymbol{\mu}_d\hat{\zeta} + \boldsymbol{\mu}_d^*\hat{\zeta}^\dagger \tag{2.12}$$

is the dipole moment operator of the atom detector, with $\boldsymbol{\mu}_d$ the corresponding transition dipole moment. Moving to the Heisenberg picture (see Appendix B), we thus obtain

$$\hat{H}_{d,F}(t) = -\left(\boldsymbol{\mu}_d\hat{\zeta}(t) + \boldsymbol{\mu}_d^*\hat{\zeta}^\dagger(t)\right)\cdot\left(\hat{\mathbf{E}}_\perp^{(-)}(\mathbf{r}_d,t) + \hat{\mathbf{E}}_\perp^{(+)}(\mathbf{r}_d,t)\right), \tag{2.13}$$

where the operators $\hat{\zeta}(t)$ and $\hat{\zeta}^\dagger(t)$ correspond to the Heisenberg picture representation of the lowering and raising operators of the atom detector, and $\hat{\mathbf{E}}_\perp^{(+)}(\mathbf{r}_d,t)$ and $\hat{\mathbf{E}}_\perp^{(-)}(\mathbf{r}_d,t)$ are the positive-frequency and negative-frequency electric field operators (see Section 1.2.7), respectively. These operators are written also in the Heisenberg picture and evaluated at the position of the detector. By applying the rotating-wave approximation (RWA) (Section 1.2.7), this Hamiltonian becomes

$$\hat{H}_{d,F}^{\mathrm{RWA}}(t) = -\boldsymbol{\mu}_d\hat{\zeta}(t)\hat{\mathbf{E}}_\perp^{(-)}(\mathbf{r}_d,t) - \boldsymbol{\mu}_d^*\hat{\zeta}^\dagger(t)\hat{\mathbf{E}}_\perp^{(+)}(\mathbf{r}_d,t). \tag{2.14}$$

We consider that initially the atom detector is in the ground state $|g_d\rangle$ and the

electromagnetic field is in some pure state $|i\rangle$. According to perturbation theory in quantum mechanics [122, 151, 152], the atom detector becomes excited (i.e., a photon from the field is absorbed) with a probability proportional to

$$\sum_f |\langle e_d, f|\hat{H}_{d,F}(t)|g_d, i\rangle|^2 = |\langle e_d|\boldsymbol{\mu}_d^*\hat{\zeta}^\dagger(t)|g_d\rangle\langle f|\hat{\mathbf{E}}_\perp^{(+)}(\mathbf{r}_d,t)|i\rangle|^2. \tag{2.15}$$

Here, $\{|f\rangle\}$ is the set of final states of the electromagnetic field, which is complete ($\mathbb{1} = \sum_f |f\rangle\langle f|$). We remark that quantifying the absolute transition probability is not needed because the first-order correlation of the electric field operators is normalized in practice, in such a way that it does not depend on the absolute value of this transition probability, which is discussed in Section 2.1.4.

We next assume that the coupling between the field and the detector is sufficiently weak such that: (i) the time evolution of the lowering operator of the atom can be approximated as $\hat{\zeta}^\dagger(t) = \exp(i\omega_d t)\hat{\zeta}^\dagger$, implying that $|\langle e_d|\hat{\zeta}^\dagger(t)|g_d\rangle|^2 = 1$; and (ii) the time evolution of $\hat{\mathbf{E}}_\perp^{(+)}(\mathbf{r}_d,t)$ is not affected by the atom detector. As a consequence, the probability of absorbing a single photon becomes proportional to

$$P_1 = \sum_f \langle i|\hat{\mathbf{E}}_\perp^{(-)}(\mathbf{r}_d,t)|f\rangle\cdot\langle f|\hat{\mathbf{E}}_\perp^{(+)}(\mathbf{r}_d,t)|i\rangle = \langle i|\hat{\mathbf{E}}_\perp^{(-)}(\mathbf{r}_d,t)\cdot\hat{\mathbf{E}}_\perp^{(+)}(\mathbf{r}_d,t)|i\rangle\,, \tag{2.16}$$

where we have taken into account that $\langle f|\hat{\mathbf{E}}_\perp^{(+)}(\mathbf{r}_d,t)|i\rangle^* = \langle i|\hat{\mathbf{E}}_\perp^{(-)}(\mathbf{r}_d,t)|f\rangle$ and that the set of final states $|f\rangle$ is complete. The expectation value of the operator

$$\hat{I}(\mathbf{r}_d,t) = \hat{\mathbf{E}}_\perp^{(-)}(\mathbf{r}_d,t)\cdot\hat{\mathbf{E}}_\perp^{(+)}(\mathbf{r}_d,t) \tag{2.17}$$

in the last equality of Eq. (2.16) is proportional to the average intensity of light arriving to the detector located at position $\mathbf{r}_d$ at time t (equivalently, to the number of photons counted by the detector). $\hat{I}(\mathbf{r}_d,t)$ is sometimes simply referred to as *intensity operator*, although we emphasize that its expectation value is proportional (not equal) to the light intensity at the detector. Therefore, Eq. (2.16) indicates that the probability of absorbing a single photon is proportional to the expectation value of this intensity operator, evaluated at the position of the detector $\mathbf{r}_d$ and at the initial field state $|i\rangle$.

In the more general case, where the electromagnetic field is in a mixed state, described by a density matrix $\hat{\rho}_F$ (see Appendix A), the photodetection probability is again proportional to the expectation value of $\hat{I}(\mathbf{r}_d,t)$. In this case, we obtain

$$P_1 = \langle\hat{I}(\mathbf{r}_d,t)\rangle = \mathrm{Tr}[\hat{I}(\mathbf{r}_d,t)\hat{\rho}_F]. \tag{2.18}$$

2.1.3 Young's interference experiment from a quantum perspective

We next revisit the Young's interference experiment described in Section 2.1.1 using now the quantum description of photodetection presented in Section 2.1.2. At the position $\mathbf{r}_d$ of the detector (see Fig. 2.1), the positive-frequency and negative-frequency electric field operators can be decomposed into contributions from the field scattered by the two slits S_1 and S_2, at positions $\mathbf{r}_1$ and $\mathbf{r}_2$, similarly to the classical electric field in Eq. (2.1). More specifically,

$$\hat{\mathbf{E}}_{\perp}^{(+)}(\mathbf{r}_d,t) = K\hat{\mathbf{E}}_{\perp}^{(+)}(\mathbf{r}_1,t-\Delta t_1) + K\hat{\mathbf{E}}_{\perp}^{(+)}(\mathbf{r}_2,t-\Delta t_2), \tag{2.19a}$$

$$\hat{\mathbf{E}}_{\perp}^{(-)}(\mathbf{r}_d,t) = K^*\hat{\mathbf{E}}_{\perp}^{(-)}(\mathbf{r}_1,t-\Delta t_1) + K^*\hat{\mathbf{E}}_{\perp}^{(-)}(\mathbf{r}_2,t-\Delta t_2), \tag{2.19b}$$

with K a factor that depends again on the size and geometry of the slits and with $\Delta t_j = |\mathbf{r}_j - \mathbf{r}_d|/c$.

The expectation value of the intensity operator $\hat{I}(\mathbf{r}_d,t)$ at the position of the detector can thus be expressed as

$$\begin{aligned}\langle\hat{I}(\mathbf{r}_d,t)\rangle \propto\ & \langle\hat{\mathbf{E}}_{\perp}^{(-)}(\mathbf{r}_1,t-\Delta t_1)\cdot\hat{\mathbf{E}}_{\perp}^{(+)}(\mathbf{r}_1,t-\Delta t_1)\rangle \\ &+ \langle\hat{\mathbf{E}}_{\perp}^{(-)}(\mathbf{r}_2,t-\Delta t_2)\cdot\hat{\mathbf{E}}_{\perp}^{(+)}(\mathbf{r}_2,t-\Delta t_2)\rangle \\ &+ \langle\hat{\mathbf{E}}_{\perp}^{(-)}(\mathbf{r}_1,t-\Delta t_1)\cdot\hat{\mathbf{E}}_{\perp}^{(+)}(\mathbf{r}_2,t-\Delta t_2)\rangle \\ &+ \langle\hat{\mathbf{E}}_{\perp}^{(-)}(\mathbf{r}_2,t-\Delta t_2)\cdot\hat{\mathbf{E}}_{\perp}^{(+)}(\mathbf{r}_1,t-\Delta t_1)\rangle\,,\end{aligned} \tag{2.20}$$

where the proportionality constant is simply $|K|^2$. The first two terms on the right-hand side of Eq. (2.20) are proportional to the intensity of light arriving from each slit independently to the detector, as if the other slit did not exist. In contrast, the last two terms correspond to the contribution from the correlation between the light emitted from the two slits and give rise to interference effects. More specifically, these latter terms can lead to oscillations in the light intensity on the screen and, thus, to the emergence of fringes. Notably, the form of Eq. (2.20) is analogous to the form of the classical expression in Eq. (2.4), which allows for the extension of the normalized correlation $g_c^{(1)}(\mathbf{r}_1,t_1;\mathbf{r}_2,t_2)$ to the quantum realm, as we discuss in the following section.

2.1.4 First-order correlation tensor and function

In this section, we introduce the concept of first-order coherence following the procedure discussed by Glauber in Ref. [111]. This procedure accounts for the effect of polarization of light, which is often ignored in textbooks by assuming scalar electric fields.

We first define the *first-order correlation tensor* $\boldsymbol{G}^{(1)}(\mathbf{r}_1,t_1;\mathbf{r}_2,t_2)$, whose

elements are given by

$$G^{(1)}_{\alpha\beta}(\mathbf{r}_1,t_1;\mathbf{r}_2,t_2)=\langle \hat{E}^{(-)}_{\perp,\alpha}(\mathbf{r}_1,t_1)\hat{E}^{(+)}_{\perp,\beta}(\mathbf{r}_2,t_2)\rangle\,. \tag{2.21}$$

Here, α and β label three-dimensional spatial coordinates (e.g., Cartesian coordinates). $G^{(1)}_{\alpha\beta}(\mathbf{r}_1,t_1;\mathbf{r}_2,t_2)$ measures the correlation between the α-component of the negative-frequency electric field at position $\mathbf{r}_1$ and time t_1 and the β-component of the positive-frequency electric field at position $\mathbf{r}_2$ and time t_2. This correlation could be analyzed, for example, in the Young's interference experiment including polarizers to select the photons emitted with α-polarization from one slit and with β-polarization from the other. By normalizing the correlation tensor $\boldsymbol{G}^{(1)}(\mathbf{r}_1,t_1;\mathbf{r}_2,t_2)$, we obtain the *normalized first-order correlation tensor* $\boldsymbol{g}^{(1)}(\mathbf{r}_1,t_1;\mathbf{r}_2,t_2)$, whose elements are given by

$$g^{(1)}_{\alpha\beta}(\mathbf{r}_1,t_1;\mathbf{r}_2,t_2)=\frac{G^{(1)}_{\alpha\beta}(\mathbf{r}_1,t_1;\mathbf{r}_2,t_2)}{\sqrt{G^{(1)}_{\alpha\alpha}(\mathbf{r}_1,t_1;\mathbf{r}_1,t_1)G^{(1)}_{\beta\beta}(\mathbf{r}_2,t_2;\mathbf{r}_2,t_2)}}. \tag{2.22}$$

Further, since the density matrix is a positive semi-definite and Hermitian operator (see Appendix A), a large number of inequalities for the correlation tensor can be derived [111, 114]. Notably, $G^{(1)}_{\alpha\beta}(\mathbf{r}_1,t_1;\mathbf{r}_2,t_2)$ satisfies the *Cauchy-Schwarz inequality*

$$G^{(1)}_{\alpha\beta}(\mathbf{r}_1,t_1;\mathbf{r}_1,t_1)G^{(1)}_{\alpha\beta}(\mathbf{r}_2,t_2;\mathbf{r}_2,t_2)\geq |G^{(1)}_{\alpha\beta}(\mathbf{r}_1,t_1;\mathbf{r}_2,t_2)|^2. \tag{2.23}$$

As a consequence, the norm of the elements of the normalized first-order correlation tensor is bounded by

$$0\leq |g^{(1)}_{\alpha\beta}(\mathbf{r}_1,t_1;\mathbf{r}_2,t_2)|\leq 1. \tag{2.24}$$

If all the elements of the normalized first-order correlation tensor satisfy $|g^{(1)}_{\alpha\beta}(\mathbf{r}_1,t_1;\mathbf{r}_2,t_2)| = 1$ for any choice of basis of three-dimensional spatial coordinates for α and β (i.e., for any choice of reference frame), we say that light is *completely first-order coherent*. Crucially, complete first-order coherence is obtained if and only if all the tensor elements $G^{(1)}_{\alpha\beta}(\mathbf{r}_1,t_1;\mathbf{r}_2,t_2)$ factorize into a product of expectation values of the field at $\mathbf{r}_1$ and $\mathbf{r}_2$, such that $G^{(1)}_{\alpha\beta}(\mathbf{r}_1,t_1;\mathbf{r}_2,t_2) = \langle \hat{E}^{(-)}_{\perp,\alpha}(\mathbf{r}_1,t_1)\rangle \langle \hat{E}^{(+)}_{\perp,\beta}(\mathbf{r}_2,t_2)\rangle$. Importantly, complete first-order coherence leads to maximum interference. Conversely, if $|g^{(1)}_{\alpha\beta}(\mathbf{r}_1,t_1;\mathbf{r}_2,t_2)| = 0$ for all components α and β we say that light is *incoherent*, which yields no interference. For intermediate values of $|g^{(1)}_{\alpha\beta}(\mathbf{r}_1,t_1;\mathbf{r}_2,t_2)|$, light is *first-order partially coherent*.

Furthermore, we can define a scalar quantity that measures the correlation between the total electric field, without discriminating on the polarization of the photons, which is known as *normalized first-order correlation function*

$g^{(1)}(\mathbf{r}_1, t_1; \mathbf{r}_2, t_2)$. This quantity can be obtained as

$$\begin{aligned} g^{(1)}(\mathbf{r}_1, t_1; \mathbf{r}_2, t_2) &= \frac{\langle \hat{\mathbf{E}}_\perp^{(-)}(\mathbf{r}_1, t_1) \cdot \hat{\mathbf{E}}_\perp^{(+)}(\mathbf{r}_2, t_2) \rangle}{\sqrt{\langle \hat{I}(\mathbf{r}_1, t_1) \rangle \langle \hat{I}(\mathbf{r}_2, t_2) \rangle}} \\ &= \frac{\sum_\alpha G^{(1)}_{\alpha\alpha}(\mathbf{r}_1, t_1; \mathbf{r}_2, t_2)}{\sqrt{\sum_\alpha G^{(1)}_{\alpha\alpha}(\mathbf{r}_1, t_1; \mathbf{r}_1, t_1) \sum_\beta G^{(1)}_{\beta\beta}(\mathbf{r}_2, t_2; \mathbf{r}_2, t_2)}}. \end{aligned} \tag{2.25}$$

This expression extends the normalized first-order classical correlation function $g_c^{(1)}(\mathbf{r}_1, t_1; \mathbf{r}_2, t_2)$ [Eq. (2.5)] to the quantum realm. Therefore, first-order coherence provides again information about interference and, its interpretation is closely related to the traditional notion of optical coherence discussed in Section 2.1.1. We anticipate that higher-order coherence serves to further characterize light (e.g., second-order coherence provides information on the statistical properties of light, as discussed in Section 2.3).

2.1.5 Emission spectrum

We introduce in this section the usual *emission spectrum* $S(\omega)$ that provides information on the frequency distribution of light emitted from any source.

In classical optics, the *Wiener-Khintchine theorem* shows that the classical emission spectrum $S_c(\omega)$ can be obtained from the Fourier transform of the classical temporal average correlation $\langle \mathbf{E}(\mathbf{r}_d, t_1) \cdot \mathbf{E}(\mathbf{r}_d, t_2) \rangle_c$ [116, 153], with $\mathbf{r}_d$ again the position of the detector. Equivalently, $S_c(\omega)$ can be obtained from the Fourier transform of the normalized first-order classical correlation function $g_c^{(1)}(\mathbf{r}_d, t_1; \mathbf{r}_d, t_2)$ [Eq. (2.5)]. Notably, if the electric field is stationary, as it is the case when the light source is in the steady state, $g_c^{(1)}(\mathbf{r}_d, t_1; \mathbf{r}_d, t_2)$ depends only on the time difference $\tau = t_2 - t_1$ and the detection position $\mathbf{r}_d$. As a result, the stationary emission spectrum can be calculated as

$$S_c(\omega) = \frac{1}{2\pi} \int_{-\infty}^{\infty} d\tau e^{i\omega\tau} \langle \mathbf{E}(\mathbf{r}_d, 0) \cdot \mathbf{E}(\mathbf{r}_d, \tau) \rangle_c . \tag{2.26}$$

We show next that the direct extension of this classical emission spectrum to the quantum realm, where the classical electric fields are replaced by quantized electric fields, carries information on the frequency distribution of photons emitted from the source. To this end, we note that the negative-frequency and positive-frequency free-space electric field operators [Eq. (1.133)] satisfy

$$\langle \hat{\mathbf{E}}_\perp^{(-)}(\mathbf{r}_d, t_1) \cdot \hat{\mathbf{E}}_\perp^{(+)}(\mathbf{r}_d, t_2) \rangle = \sum_{\mathbf{k},s} \frac{\hbar\omega_\mathbf{k}}{2\mathcal{V}\varepsilon_0} n_{\mathbf{k}s} e^{i\omega_\mathbf{k}(t_1 - t_2)}, \tag{2.27}$$

with $n_{\mathbf{k}s} = \langle \hat{a}^\dagger_{\mathbf{k}s} \hat{a}_{\mathbf{k}s} \rangle$ the average number of photons in electromagnetic mode ($\mathbf{k}$, s). According to Eq. (1.134), the summation over $\mathbf{k}$ can be transformed into an

integral, which yields

$$\langle \hat{\mathbf{E}}_{\perp}^{(-)}(\mathbf{r}_d, t_1) \cdot \hat{\mathbf{E}}_{\perp}^{(+)}(\mathbf{r}_d, t_2) \rangle = \frac{1}{2} \int_0^{\infty} S(\omega_{\mathrm{k}}) e^{i\omega_{\mathrm{k}}(t_1 - t_2)} d\omega_{\mathrm{k}}. \tag{2.28}$$

Here, we have introduced the function

$$S(\omega_{\mathrm{k}}) = \frac{\hbar \omega_{\mathrm{k}}}{(2\pi)^3 \varepsilon_0} \sum_s \int_0^{\pi} d\phi \int_0^{2\pi} d\theta \sin\theta \, n_{\mathbf{k}s}, \tag{2.29}$$

which gives information about the frequency distribution of light, as its value at ω_{k} is determined by the number of photons $n_{\mathbf{k}s}$ of frequency ω_{k} in the vacuum field, propagating from the source to the detector.

We now consider that the light source is in the steady state (ss), which is reached at very long times t_1 and t_2. As in the classical case discussed above, the correlation $\langle \hat{\mathbf{E}}_{\perp}^{(-)}(\mathbf{r}_d, t_1) \cdot \hat{\mathbf{E}}_{\perp}^{(+)}(\mathbf{r}_d, t_2) \rangle$ thus depends only on the time difference $\tau \equiv t_2 - t_1$, apart from the detection position $\mathbf{r}_d$. Additionally, taking into account that no photons are emitted at $\omega < 0$ (i.e., $n_{\mathbf{k}s}$ vanishes for $\omega < 0$), we can extend the frequency integral in Eq. (2.28) from 0 to $-\infty$. In this way, by inverting Eq. (2.28), we find that the emission spectrum $S(\omega)$ can be obtained from the Fourier transform of $\langle \hat{\mathbf{E}}_{\perp}^{(-)}(\mathbf{r}_d, 0) \cdot \hat{\mathbf{E}}_{\perp}^{(+)}(\mathbf{r}_d, \tau) \rangle_{\mathrm{ss}}$. Equivalently, $S(\omega)$ can be obtained from the Fourier transform of the first-order correlation $G^{(1)}_{\alpha\alpha}(\mathbf{r}_d, 0; \mathbf{r}_d, \tau)$ [Eq. (2.21)], so that

$$\begin{aligned} S(\omega) &= \frac{1}{\pi} \int_{-\infty}^{\infty} d\tau e^{i\omega\tau} \langle \hat{\mathbf{E}}_{\perp}^{(-)}(\mathbf{r}_d, 0) \cdot \hat{\mathbf{E}}_{\perp}^{(+)}(\mathbf{r}_d, \tau) \rangle_{\mathrm{ss}} \\ &= \frac{1}{\pi} \int_{-\infty}^{\infty} d\tau e^{i\omega\tau} \sum_{\alpha} G^{(1)}_{\alpha\alpha}(\mathbf{r}_d, 0; \mathbf{r}_d, \tau). \end{aligned} \tag{2.30}$$

The field correlation $\langle \hat{\mathbf{E}}_{\perp}^{(-)}(\mathbf{r}_d, 0) \cdot \hat{\mathbf{E}}_{\perp}^{(+)}(\mathbf{r}_d, \tau) \rangle_{\mathrm{ss}}$ can be measured in experiments using different interferometer setups [116, 154, 155]. By performing then the Fourier transform to this correlation, the emission spectrum can be obtained. Last, we note that time-dependent emission spectra can be also defined for non-stationary states of the system [156–159], but this is beyond the scope of this thesis.

2.1.6 First-order coherence and light emission spectrum from a single quantum emitter

In this section, we characterize the normalized first-order correlation function $g^{(1)}(\mathbf{r}_d, 0; \mathbf{r}_d, \tau)$ and the emission spectrum $S(\omega)$ of light emitted from a single QE in the steady state. Under weak driving, $g^{(1)}(\mathbf{r}_d, 0; \mathbf{r}_d, \tau)$ and $S(\omega)$ indicate that photons are emitted via radiative decay from the bare excited state $|e\rangle$ to the bare ground state $|g\rangle$. In contrast, under strong driving, these quantities reveal the emergence of a wider variety of emission processes, which are related to radiative decays between the dressed states introduced in Section 1.5.2. We focus directly on

$g^{(1)}(\mathbf{r}_d, 0; \mathbf{r}_d, \tau)$, instead of analyzing the two-times evolution of $g^{(1)}(\mathbf{r}_d, t_1; \mathbf{r}_d, t_2)$, because in the steady state the temporal evolution of the normalized first-order correlation function depends only on the time difference $\tau = t_2 - t_1$.

According to Eq. (2.25), $g^{(1)}(\mathbf{r}_d, 0; \mathbf{r}_d, \tau)$ is determined by the electric field operators $\hat{\mathbf{E}}^{(-)}_{\perp,\mathrm{QE}}(\mathbf{r}_d, 0)$ and $\hat{\mathbf{E}}^{(+)}_{\perp,\mathrm{QE}}(\mathbf{r}_d, \tau)$ of light scattered from the emitter. As discussed in Section 1.2.7, the positive-frequency transverse electric field operator describing the light emission from the QE is $\hat{\mathbf{E}}^{(+)}_{\perp,\mathrm{QE}}(\mathbf{r}_d, t) = \boldsymbol{\mathcal{E}}_{\boldsymbol{\mu}}(\mathbf{r}_d)\hat{\sigma}(t - |\mathbf{r}_d - \mathbf{r}_0|/c)$, where $\boldsymbol{\mathcal{E}}_{\boldsymbol{\mu}}(\mathbf{r}_d)$ is the vector amplitude of the positive-frequency electric field radiated by a classical electric point dipole, and $\hat{\sigma}(t - |\mathbf{r}_d - \mathbf{r}_0|/c)$ is the lowering operator of the QE in the Heisenberg picture, evaluated at the retarded time $|\mathbf{r}_d - \mathbf{r}_0|/c$. In the steady state, the time evolution of the normalized first-order correlation function depends only on the time difference τ between the evaluation times of the negative-frequency and positive-frequency electric field operators. Thus, the effects of the retardation time in the two operators cancel out and can be directly ignored in the calculation. Additionally, the contributions from $\boldsymbol{\mathcal{E}}_{\boldsymbol{\mu}}(\mathbf{r}_d)$ in the numerator and in the denominator of $g^{(1)}(\mathbf{r}_d, 0; \mathbf{r}_d, \tau)$ [Eq. (2.25)] also cancel each other. As a result, $g^{(1)}(\mathbf{r}_d, 0; \mathbf{r}_d, \tau)$ becomes also independent of the detection position in this case. (We remark that the detection position $\mathbf{r}_d$ may become significant when analyzing light emission from more complex systems, such as two QEs.) Therefore, we conclude that the normalized first-order correlation function [Eq. (2.25)] of light emitted from a single QE becomes

$$g^{(1)}(\tau) \equiv g^{(1)}(\mathbf{r}_d, 0; \mathbf{r}_d, \tau) = \frac{\langle \hat{\sigma}^\dagger(0)\hat{\sigma}(\tau)\rangle_{\mathrm{ss}}}{\langle \hat{\sigma}^\dagger(0)\hat{\sigma}(0)\rangle_{\mathrm{ss}}}. \tag{2.31}$$

Further, only a single matrix element of the normalized first-order correlation tensor $\boldsymbol{g}^{(1)}(\mathbf{r}_d, 0; \mathbf{r}_d, \tau)$ [Eq. (2.22)] becomes non-zero when using a basis of spatial coordinates that includes the unit vector of $\boldsymbol{\mathcal{E}}_{\boldsymbol{\mu}}(\mathbf{r}_d)$. This non-zero element is equal to the first-order correlation function $g^{(1)}(\mathbf{r}_d, 0; \mathbf{r}_d, \tau)$ in Eq. (2.31).

The emission spectrum $S(\omega)$ of light scattered from the QE can next be obtained from the Fourier transform of $\langle \mathbf{E}^{(-)}_{\perp,\mathrm{QE}}(\mathbf{r}_d, 0) \cdot \mathbf{E}^{(+)}_{\perp,\mathrm{QE}}(\mathbf{r}_d, \tau)\rangle$ [Eq. (2.30)]. Specifically, we find

$$\begin{aligned} S(\omega) &= \frac{|\boldsymbol{\mathcal{E}}_{\boldsymbol{\mu}}(\mathbf{r}_d)|^2}{\pi} \int_{-\infty}^{\infty} d\tau e^{i\omega\tau} \langle \hat{\sigma}^\dagger(0)\hat{\sigma}(\tau)\rangle_{\mathrm{ss}} \,. \\ &= \frac{3\hbar\omega_0\gamma_0}{(4\pi)^2\varepsilon_0 c} \frac{|\boldsymbol{e}_{\boldsymbol{R}} \times (\boldsymbol{e}_{\boldsymbol{R}} \times \boldsymbol{e}_{\boldsymbol{\mu}})|^2}{R^2} \int_{-\infty}^{\infty} d\tau e^{i\omega\tau} \langle \hat{\sigma}^\dagger(0)\hat{\sigma}(\tau)\rangle_{\mathrm{ss}} \,, \end{aligned} \tag{2.32}$$

where we have used the expression for $\boldsymbol{\mathcal{E}}_{\boldsymbol{\mu}}(\mathbf{r}_d)$ given in Eq. (1.141), and the expression of γ_0 given in Eq. (1.163). Additionally, $\boldsymbol{R} = \mathbf{r}_d - \mathbf{r}_0$ is the relative position vector between the emitter and the detector in the far-field region, with unit vector $\boldsymbol{e}_{\boldsymbol{R}} = \boldsymbol{R}/R$ and norm $R = |\boldsymbol{R}|$. The factors outside the integral in Eq. (2.32) are typically ignored, and arbitrary units are adopted.

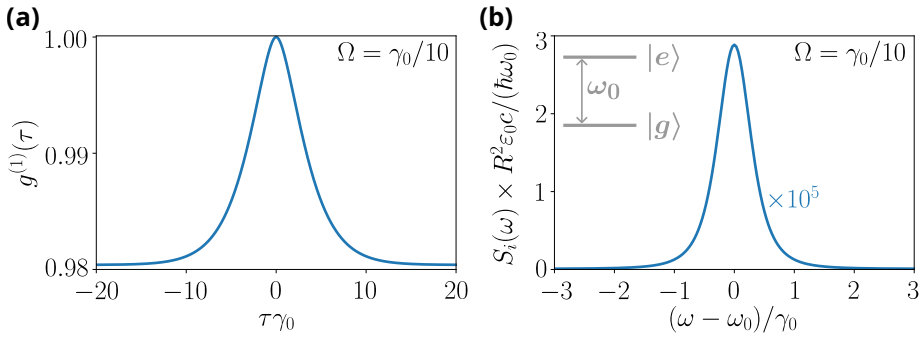

Figure 2.2: Normalized first-order correlation function and incoherent emission spectrum of light emitted from a single QE under weak driving strength. The QE is modeled as a two-level system, as schematically represented in the inset in (b), with transition frequency ω_0 and spontaneous emission rate γ_0. The laser resonantly drives the emitter ($\omega_L = \omega_0$), with Rabi frequency $\Omega = \gamma_0/10$. (a) Dependence on τ of the normalized first-order correlation function $g^{(1)}(\tau) = g^{(1)}(\mathbf{r}_d, 0; \mathbf{r}_d, \tau)$. (b) Incoherent emission spectrum $S_i(\omega)$ scaled by $R^2\varepsilon_0 c/(\hbar\omega_0)$, so that the results are independent of the specific value of distance R to the detector in the far-field region, and by 10^5.

Moreover, we can rewrite the lowering and raising operators of the QE as

$$\hat{\sigma}(t) = \langle\hat{\sigma}\rangle_{\rm ss} + \delta\hat{\sigma}(t), \tag{2.33a}$$

$$\hat{\sigma}^\dagger(t) = \langle\hat{\sigma}^\dagger\rangle_{\rm ss} + \delta\hat{\sigma}^\dagger(t), \tag{2.33b}$$

where $\delta\hat{\sigma}(t)$ and $\delta\hat{\sigma}^\dagger(t)$ are called *fluctuation lowering operator* and *fluctuation raising operator*, respectively. These fluctuation operators have vanishing steady-state expectation values by definition. Notably, the contribution from $\langle\hat{\sigma}^\dagger\rangle_{\rm ss}\langle\hat{\sigma}\rangle_{\rm ss}$ in Eq. (2.32) yields a Dirac delta peak in the emission spectrum $S(\omega)$. Thus, it is often useful to focus on the contribution of the fluctuations operators to the emission spectrum, which is referred to as *incoherent emission spectrum* and is given by

$$S_i(\omega) = \frac{3\hbar\omega_0\gamma_0}{(4\pi)^2\varepsilon_0 c}\frac{|\boldsymbol{e_R}\times(\boldsymbol{e_R}\times\boldsymbol{e_\mu})|^2}{R^2}\int_{-\infty}^{\infty} d\tau e^{i\omega\tau}\,\langle\delta\hat{\sigma}^\dagger(0)\delta\hat{\sigma}(\tau)\rangle_{\rm ss}\,. \tag{2.34}$$

The incoherent emission spectrum $S_i(\omega)$ is identical to $S(\omega)$, apart from the absence of the Dirac delta peak.

We now analyze $g^{(1)}(\tau)$ and $S(\omega)$ of light emitted from a single quantum emitter. We compute these quantities by solving numerically (with the Python package QuTiP [146]) the Markovian master equation (MME) in Eq. (1.230), which includes the effect of laser driving (treated classically) and is written in the rotating frame at the laser frequency ω_L. We first consider the emission of the QE under weak driving, fixing $\Omega = \gamma_0/10$, with γ_0 the spontaneous emission rate of the emitter [Eq. (1.163)]. Additionally, we consider that the laser is resonantly tuned to the

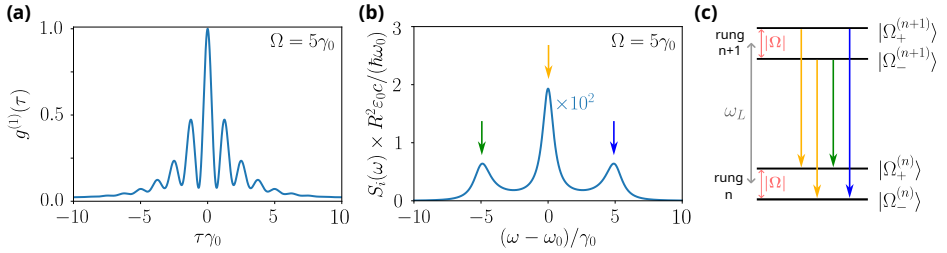

Figure 2.3: Normalized first-order correlation function and incoherent emission spectrum of light emitted from a single QE under strong driving. The two-level QE (with transition frequency ω_0 and spontaneous emission rate γ_0) is driven resonantly with Rabi frequency $\Omega = 5\gamma_0$. (a) Dependence on time delay τ of the normalized first-order correlation function $g^{(1)}(\tau) = g^{(1)}(\mathbf{r}_d, 0; \mathbf{r}_d, \tau)$. (b) Incoherent emission spectrum $S_i(\omega_0)$ scaled by $R^2\varepsilon_0 c/(\hbar\omega_0)$, so that the results are independent of the specific value of distance R to the detector in the far-field region, and by 10^2. This spectrum shows a three-peaks structure known as Mollow triplet. The arrows indicate the transitions between dressed states in (c) that give rise to each of the Mollow peaks. (c) Schematic representation of the dressed states in the rungs n and $n+1$ and the one-photon transitions that lead to the emission of photons at frequencies ω_0 (orange arrows), $\omega_0 - |\Omega|$ (green arrow) and $\omega_0 + |\Omega|$ (blue arrow).

transition frequency of the QE ($\omega_L = \omega_0$). Figure 2.2a shows the dependence of the normalized first-order correlation function $g^{(1)}(\tau)$ on the time delay τ. We find that $g^{(1)}(\tau = 0) = 1$, which means that at $\tau = 0$ light is first-order coherent. At increasing delay times τ, $g^{(1)}(\tau)$ decays exponentially to approximately ≈ 0.98, without exhibiting oscillations. Additionally, we plot the incoherent emission spectrum $S_i(\omega)$ in Fig. 2.2b and find that it exhibits a single peak centered at $\omega = \omega_0$. Therefore, the scattering of light from the QE under weak driving is due to the radiative decay from the bare excited state $|e\rangle$ to the bare ground state $|g\rangle$, see the inset of Fig. 2.2b.

We next analyze the normalized first-order correlation function under strong driving strength, again at $\omega_L = \omega_0$. As discussed in Section 1.5.2, the eigenstates of the system are modified from the bare states $|g\rangle$ and $|e\rangle$ under strong driving. The new eigenstates, $|\Omega_+\rangle$ and $|\Omega_-\rangle$, are known as dressed states and correspond to linear combinations of $|g\rangle$ and $|e\rangle$ [Eqs. (1.223a)–(1.223b)]. In the rotating frame at the laser frequency, the frequency splitting between $|\Omega_+\rangle$ and $|\Omega_-\rangle$ is given by the generalized Rabi frequency $\Omega_R = \sqrt{\Delta_0^2 + \Omega^2}$, where $\Delta_0 = \omega_0 - \omega_L$ vanishes under resonant driving. Further, we discussed in Section 1.5.3 the emergence of oscillations of frequency Ω_R in the populations of the bare states when the QE is strongly driven (Fig. 1.3). Such oscillations are known as Rabi oscillations. Figure 2.3a shows the normalized first-order correlation function $g^{(1)}(\tau)$ at $\Omega = 5\gamma_0$, which also exhibits Rabi oscillations, indicating that the intensity of light at the detector oscillates when the emitter is strongly driven. Further, $g^{(1)}(\tau)$ again reaches the maximum value of 1 at $\tau = 0$, as under weak driving, but its minimum value is significantly lower (approximately 0).

Finally, we plot in Fig. 2.3b the incoherent emission spectrum $S_i(\omega)$ under

strong laser driving ($\Omega = 5\gamma_0$). After moving back to the original, non-rotated frame, $S_i(\omega)$ exhibits two new peaks at $\omega = \omega_0 \pm \Omega = \omega_0 \pm 5\gamma_0$ (indicated by green and blue arrows), in addition to the peak at the resonance frequency $\omega = \omega_0$ (indicated with an orange arrow and found also at weak laser driving). This triple-peak structure is known as *Mollow triplet* and can be interpreted more intuitively by considering the quantum nature of the laser field illuminating the system [160, 161]. In the following, we briefly discuss the form of the Hamiltonian describing the interaction between the quantum emitter and the quantized laser field.

The Hamiltonian of the laser is given as $\hbar\omega_L \hat{a}_L^\dagger \hat{a}_L$, with $\hat{a}_L^\dagger$ and $\hat{a}_L$ creation and annihilation operators of photons of frequency ω_L, wavevector $\mathbf{k}_L$ and polarization $\boldsymbol{e}_L$. The Hamiltonian describing the interaction between the laser field and the QE can thus be written as

$$\hat{H}_L = -\hat{\boldsymbol{\mu}} \cdot \hat{\boldsymbol{E}}_L(\mathbf{r}_0, t) \xrightarrow{\text{RWA}} -g_L \hat{\sigma} \hat{a}_L^\dagger - g_L^* \hat{\sigma}^\dagger \hat{a}_L, \tag{2.35}$$

where in the last equality we have performed the RWA and introduced the coupling coefficient g_L. This Hamiltonian is equivalent to that in Eq. (1.217), where the laser field is described classically, because the laser field is completely coherent to all orders, which we discuss in Section 2.2.3. As a consequence, $\hat{a}_L$ can be replaced by $\sqrt{\langle \hat{a}_L^\dagger \hat{a}_L \rangle}$, with the number of photons in the laser field $n \equiv \langle \hat{a}_L^\dagger \hat{a}_L \rangle$ being very large [124].

The total Hamiltonian of the emitter interacting with the laser can thus be rewritten as

$$\hat{H} = \hbar \frac{\omega_0}{2} \hat{\sigma}_z + \hbar\omega_L \hat{a}_L^\dagger \hat{a}_L - g_L \hat{\sigma} \hat{a}_L^\dagger - g_L^* \hat{\sigma}^\dagger \hat{a}_L. \tag{2.36}$$

The eigenstates of this Hamiltonian are infinite and can be distributed in sets of states having the same number of total excitations (adding up photon and emitter excitations). These sets are usually referred to as *rungs* or *manifolds*. If the laser field and the emitter do not interact ($g_L = 0$), the eigenstates in the rung n (with n excitations) are $|g, n\rangle$ and $|e, n-1\rangle$. These states are equivalent to the bare states $|g\rangle$ and $|e\rangle$ discussed in Section 1.5.2, obtained by treating the illumination classically and by considering very weak illumination. Moreover, we also discussed in Section 1.5.2 (again by treating the laser illumination classically) that the laser driving can modify the eigenstates of the system, leading to the emergence of the dressed states $|\Omega_+\rangle$ and $|\Omega_-\rangle$ [Eqs. (1.223a)–(1.223b)]. We now analyze the form of the dressed states when the laser is considered as quantized. To this end, we derive the eigenstates of the full Hamiltonian in Eq. (2.36). The eigenstates in the rung n are

$$|\Omega_+^{(n)}\rangle = \sin\Theta_n |g, n\rangle + \cos\Theta_n |e, n-1\rangle, \tag{2.37a}$$

$$|\Omega_-^{(n)}\rangle = \cos\Theta_n |g, n\rangle - \sin\Theta_n |e, n-1\rangle, \tag{2.37b}$$

where the Stückelberg angle Θ_n is given by $\tan(2\Theta_n) = 2n|g_L|/\Delta_0$. The

eigenenergies of $|\Omega_+^{(n)}\rangle$ and $|\Omega_-^{(n)}\rangle$ are

$$E(|\Omega_+^{(n)}\rangle) = \hbar(n-\frac{1}{2})\omega_L + \hbar\frac{\sqrt{\Delta_0^2+4n|g_L|^2}}{2}, \tag{2.38a}$$

$$E(|\Omega_-^{(n)}\rangle) = \hbar(n-\frac{1}{2})\omega_L - \hbar\frac{\sqrt{\Delta_0^2+4n|g_L|^2}}{2}, \tag{2.38b}$$

respectively. Thus, the energy splitting between $|\Omega_+^{(n)}\rangle$ and $|\Omega_-^{(n)}\rangle$ is given by

$$\Omega_R^{(n)} \equiv E(|\Omega_+^{(n)}\rangle) - E(|\Omega_-^{(n)}\rangle) = \hbar\sqrt{\Delta_0^2+4n|g_L|^2}. \tag{2.39}$$

For a very large number n of photons in the laser field, the value of $\Omega_R^{(n)}$ becomes nearly identical for subsequent rungs. As a result, by comparing this energy splitting with the generalized Rabi frequency $\Omega_R = \sqrt{\Delta_0^2+|\Omega|^2}$, which gives the energy splitting between the dressed states under classical laser illumination [Eqs. (1.223a)–(1.223b)], we obtain the correspondence $|g_L|^2 4n = |\Omega|^2$.

Figure 2.3 shows a schematic representation of the dressed states in rungs n and $n+1$ obtained under resonant driving ($\Delta_0 = 0$). The one-photon transitions $|\Omega_+^{(n+1)}\rangle \to |\Omega_+^{(n)}\rangle$ and $|\Omega_-^{(n+1)}\rangle \to |\Omega_-^{(n)}\rangle$ (indicated by orange arrows in Fig. 2.3c) give rise to the emission of photons of frequency $\omega_L = \omega_0$ and, thus, to the central peak in the Mollow triplet. Remarkably, additional transitions are allowed, which are responsible for the emission of photons at $\omega_0 \pm |\Omega|$ and, thus, of the two side peaks in the Mollow triplet. In particular, the one-photon transition $|\Omega_+^{(n+1)}\rangle \to |\Omega_-^{(n)}\rangle$ (blue arrow) leads to the emission of a photon of frequency $\omega_0 + |\Omega|$ and the one photon transition $|\Omega_-^{(n+1)}\rangle \to |\Omega_+^{(n)}\rangle$ (green arrow) leads to the emission of a photon of frequency $\omega_0 - |\Omega|$. We emphasize that, although the emission spectrum in Fig. 2.3b is better understood from this picture where the laser field is quantized, this spectrum has been numerically calculated using the MME in Eq. (1.230), where the laser illumination is described classically, as both descriptions of the laser illumination are equivalent.

2.2 Second-order and higher-order coherence

We have shown in Section 2.1 that first-order coherence is connected to the photodetection of photons by a single detector. In this section, we introduce the concept of coincident photodetection by two detectors. This approach allows us to better interpret the normalized second-order correlation tensor and the normalized second-order correlation function, the latter of which plays a key role in this thesis. Additionally, we present the generalization to the n$^{\text{th}}$-order correlation function and tensor. We mainly follow Refs. [111, 114, 117, 120, 148].

2.2.1 Coincident photodetection by two detectors

To describe the process of coincident photodetection, we consider two atom detectors (labeled by $j = 1, 2$) at positions $\mathbf{r}_d^{(j)}$, with electronic ground states $|g_d^{(j)}\rangle$, electronic excited states $|e_d^{(j)}\rangle$, transition frequencies $\omega_d^{(j)}$, and dipole moment operators $\hat{\boldsymbol{\mu}}_d^{(j)}$. These detectors are again color-blind. The interaction Hamiltonian in the multipolar form can thus be written as

$$\hat{H}_{d,F} = -\sum_j \hat{\boldsymbol{\mu}}_d^{(j)} \cdot \hat{\mathbf{E}}_\perp(\mathbf{r}_d^{(j)}, t). \tag{2.40}$$

We focus first on describing the case in which a photon with polarization α arrives to detector $j = 1$ at time t and, additionally, a photon with polarization β arrives to detector $j = 2$ at time $t' \geq t$. We recall that α and β represent three-dimensional spatial coordinates, such as Cartesian coordinates. In experiments, polarizers can be used to distinguish the directions in which the photons are polarized. Assuming again that the electric field is initially in some pure state $|i\rangle$ and that the detectors are in their ground states, perturbation theory [151, 152, 162] yields that the probability of such double (coincident) photodetection is proportional to

$$\begin{aligned}
&\sum_{f,m} |\, \langle e_d^{(1)}, e_d^{(2)}, f|\, \hat{H}_I(t')\, |g_d^{(1)}, e_d^{(2)}, m\rangle\, \langle g_d^{(1)}, e_d^{(2)}, m|\, \hat{H}_I(t)\, |g_d^{(1)}, g_d^{(2)}, i\rangle\, |^2 \\
&= \sum_{f,m} |\mu_{d,\alpha}^{(1)}(t)\mu_{d,\beta}^{(2)}(t')\, \langle f|\, \hat{E}_{\perp,\beta}^{(+)}(\mathbf{r}_d^{(2)}, t')\, |m\rangle\, \langle m|\, \hat{E}_{\perp,\alpha}^{(+)}(\mathbf{r}_d^{(1)}, t)\, |i\rangle\, |^2 \\
&\approx |\mu_{d,\alpha}^{(1)}\mu_{d,\beta}^{(2)}|^2\, \langle i|\, \hat{E}_{\perp,\alpha}^{(-)}(\mathbf{r}_d^{(1)}, t)\hat{E}_{\perp,\beta}^{(-)}(\mathbf{r}_d^{(2)}, t')\hat{E}_{\perp,\beta}^{(+)}(\mathbf{r}_d^{(2)}, t')\hat{E}_{\perp,\alpha}^{(+)}(\mathbf{r}_d^{(1)}, t)\, |i\rangle\,,
\end{aligned} \tag{2.41}$$

where $|m\rangle$ is an intermediate state of the electromagnetic field and $\mu_{d,\alpha}^{(j)}$ is the α-component of $\langle e_d^{(j)}|\, \hat{\boldsymbol{\mu}}_d^{(j)}\, |g_d^{(j)}\rangle$. To obtain the equality in the third line we have taken into account that the set of intermediate states $|m\rangle$ is complete and, additionally, we have assumed that the coupling between the field and detector is weak enough, as we did in Section 2.1.2. The latter assumption allows for approximating $\hat{\zeta}_j^\dagger(t) \approx \exp(i\omega_d^{(j)}t)\hat{\zeta}_j^\dagger$, with $\zeta_j^\dagger = |e_d^{(j)}\rangle\, \langle g_d^{(j)}|$ the raising operators of detector j.

Therefore, we obtain that the probability of such coincident detection becomes proportional to

$$P_{\alpha\beta}^{(2)}(t, t') = \langle \hat{E}_{\perp,\alpha}^{(-)}(\mathbf{r}_d^{(1)}, t)\hat{E}_{\perp,\beta}^{(-)}(\mathbf{r}_d^{(2)}, t')\hat{E}_{\perp,\beta}^{(+)}(\mathbf{r}_d^{(2)}, t')\hat{E}_{\perp,\alpha}^{(+)}(\mathbf{r}_d^{(1)}, t)\rangle\,. \tag{2.42}$$

This expression is also valid if the electric field is in some mixed state. Further, the total probability of two-photon detection at times t and t', without discriminating

in polarization, is proportional to

$$P^{(2)}(t,t') = \sum_{\alpha,\beta} P^{(2)}_{\alpha\beta}(t,t') = \langle \mathcal{T} : \hat{I}(\mathbf{r}_d^{(1)},t)\hat{I}(\mathbf{r}_d^{(2)},t') : \rangle \,, \tag{2.43}$$

where we have used the expression of the intensity operator $\hat{I}(\mathbf{r}_d^{(1)},t)$ in Eq. (2.17) and we have introduced the *time-ordering superoperator* $\mathcal{T}$, as well as the *normal-ordering superoperator* ::. On the one hand, $\mathcal{T}$ orders negative-frequency operators (e.g., creation operators) in forward time. For example, $\mathcal{T}[\hat{a}^\dagger(t)\hat{a}^\dagger(t')] = \hat{a}^\dagger(t')\hat{a}^\dagger(t)$ whether $t' < t$. Further, $\mathcal{T}$ orders positive-frequency operators (e.g., annihilation operators) in backward time. For instance, $\mathcal{T}[\hat{a}(t)\hat{a}(t')] = \hat{a}(t')\hat{a}(t)$ if $t' > t$. Notably, $\mathcal{T}$ guarantees that Eq. (2.43) is valid also at $t' < t$. On the other hand, the normal-ordering superoperator orders negative-frequency operators to the left and positive-frequency operators to the right. For example, $:\hat{a}\hat{a}^\dagger := \hat{a}^\dagger\hat{a}$. Therefore, we conclude that the probability of double photodetection is proportional to the correlation between the intensity of light arriving at each of the detectors.

2.2.2 Second-order coherence

The expression for $P^{(2)}_{\alpha\beta}(t,t')$ in Eq. (2.42) can be mathematically generalized to the case in which each electric field operator is evaluated at a different time, position and polarization, which gives rise to the *second-order correlation tensor* $\boldsymbol{G}^{(2)}(x_1;x_2;x_3;x_4)$, with $x_j \equiv \mathbf{r}_j, t_j$. The elements of this tensor are given by

$$G^{(2)}_{\alpha_1\alpha_2\alpha_3\alpha_4}(x_1;x_2;x_3;x_4) = \langle \hat{E}^{(-)}_{\perp,\alpha_1}(x_1)\hat{E}^{(-)}_{\perp,\alpha_2}(x_2)\hat{E}^{(+)}_{\perp,\alpha_3}(x_3)\hat{E}^{(+)}_{\perp,\alpha_4}(x_4)\rangle \,. \tag{2.44}$$

The normalization of $\boldsymbol{G}^{(2)}(x_1;x_2;x_3;x_4)$ facilitates the comparison between experiments and theoretical calculations. The elements of the *normalized second-order correlation tensor* $\boldsymbol{g}^{(2)}(x_1;x_2;x_3;x_4)$ are

$$g^{(2)}_{\alpha_1\alpha_2\alpha_3\alpha_4}(x_1;x_2;x_3;x_4) = \frac{G^{(2)}_{\alpha_1\alpha_2\alpha_3\alpha_4}(x_1;x_2;x_3;x_4)}{\Pi_{j=1}^4 \sqrt{G^{(1)}_{\alpha_j\alpha_j}(x_j;x_j)}}. \tag{2.45}$$

The condition for complete first-order coherence discussed in Section 2.1.4 can be extended to second order [111]. In this case, light is said to be *completely second-order coherent* if all the elements of the second-order correlation tensor factorize as $G^{(2)}_{\alpha_1\alpha_2\alpha_3\alpha_4}(x_1;x_2;x_3;x_4) = \langle \hat{E}^{(-)}_{\perp,\alpha_1}(x_1)\rangle \langle \hat{E}^{(-)}_{\perp,\alpha_2}(x_2)\rangle \langle \hat{E}^{(+)}_{\perp,\alpha_3}(x_3)\rangle \langle \hat{E}^{(+)}_{\perp,\alpha_4}(x_4)\rangle$, which yields $|g^{(2)}_{\alpha_1\alpha_2\alpha_3\alpha_4}(x_1;x_2;x_3;x_4)| = 1$ for all elements of the normalized second-order correlation tensor and for any choice of reference frame [111].

Furthermore, from the total probability of double photodetection $P^{(2)}(t,t')$ at two detectors at positions $\mathbf{r}_d^{(1)}$ and $\mathbf{r}_d^{(2)}$ [Eq. (2.43)], we can define the *normalized*

second-order correlation function as

$$g^{(2)}(\mathbf{r}_d^{(1)}, t_1; \mathbf{r}_d^{(2)}, t_2) = \frac{\langle \mathcal{T} : \hat{I}(\mathbf{r}_d^{(1)}, t_1)\hat{I}(\mathbf{r}_d^{(2)}, t_2) : \rangle}{\langle \hat{I}(\mathbf{r}_d^{(1)}, t_1)\rangle \langle \hat{I}(\mathbf{r}_d^{(2)}, t_2)\rangle}. \tag{2.46}$$

This quantity corresponds to the normalized correlation of the intensities measured by the two detectors, taking into account all the photons arriving to the detectors (independently of their polarization directions). Thus, $g^{(2)}(\mathbf{r}_d^{(1)}, t_1; \mathbf{r}_d^{(2)}, t_2)$ is often referred to as *intensity correlation*. In practice, second-order coherence is more usually quantified through this normalized second-order correlation function, instead of by measuring all the elements of the tensor $\boldsymbol{g}^{(2)}(x_1; x_2; x_3; x_4)$. Light is then usually said to be completely second-order coherent if $g^{(2)}(\mathbf{r}_d^{(1)}, t_1; \mathbf{r}_d^{(2)}, t_2) = 1$ at all t_1 and t_2 times. The latter only occurs if the numerator in Eq. (2.46) factorizes as $\langle \mathcal{T} : \hat{I}(\mathbf{r}_d^{(1)}, t_1)\hat{I}(\mathbf{r}_d^{(2)}, t_2) : \rangle = \langle \hat{I}(\mathbf{r}_d^{(1)}, t_1)\rangle \langle \hat{I}(\mathbf{r}_d^{(2)}, t_2)\rangle$ at all t_1 and t_2 times. Notably, this factorization always holds at very large time differences ($|t_2 - t_1| \to \infty$), which yields

$$g^{(2)}(\mathbf{r}_d^{(1)}, t_1; \mathbf{r}_d^{(2)}, t_2) \xrightarrow{|t_2 - t_1| \to \infty} 1. \tag{2.47}$$

In the steady state, the temporal evolution of the above expression depends only on the time delay $\tau = t_2 - t_1$. Thus, in the steady state, the normalized second-order correlation function can be simplified to

$$g^{(2)}(\mathbf{r}_d^{(1)}, 0; \mathbf{r}_d^{(2)}, \tau) = \frac{\langle \mathcal{T} : \hat{I}(\mathbf{r}_d^{(1)}, 0)\hat{I}(\mathbf{r}_d^{(2)}, \tau) : \rangle_{\text{ss}}}{\langle \hat{I}(\mathbf{r}_d^{(1)}, 0)\rangle_{\text{ss}} \langle \hat{I}(\mathbf{r}_d^{(2)}, \tau)\rangle_{\text{ss}}}. \tag{2.48}$$

Interestingly, both the normalized second-order correlation function and the normalized second-order correlation tensor provide information on the statistical properties of light, which is discussed in Section 2.3.

2.2.3 Higher-order coherence

In this section, we briefly present the generalization of the correlation tensor and correlation function to higher orders. In the general case, n detectors are considered, each at position $\mathbf{r}_j^{(d)}$ (with $j = 1, 2, \ldots, n$) and with dipole moment operator $\hat{\boldsymbol{\mu}}_d^{(j)}$. The probability of n-photon detection, with each detector capturing a photon at time t_j, is proportional to

$$P^{(n)}(t_1, \ldots, t_n) = \langle \mathcal{T} : \hat{I}(\mathbf{r}_d^{(1)}, t_1)\hat{I}(\mathbf{r}_d^{(2)}, t_2) \ldots \hat{I}(\mathbf{r}_d^{(n)}, t_n) : \rangle . \tag{2.49}$$

Additionally, the second-order correlation tensor $\boldsymbol{G}^{(2)}(x_1; x_2; x_3; x_4)$ [Eq. (2.44)] can be generalized to the n$^{\text{th}}$-order correlation tensor $\boldsymbol{G}^{(n)}(x_1; \ldots; x_{2n})$, with elements

$$G^{(n)}_{\alpha_1 \ldots \alpha_{2n}}(x_1; \ldots; x_{2n}) = \langle \hat{E}^{(-)}_{\alpha_1}(x_1) \ldots \hat{E}^{(-)}_{\alpha_n}(x_n)\hat{E}^{(+)}_{\alpha_{n+1}}(x_{n+1}) \ldots \hat{E}^{(+)}_{\alpha_{2n}}(x_{2n})\rangle . \tag{2.50}$$

Moreover, the elements of the normalized n$^{\text{th}}$-order correlation tensor $\boldsymbol{g}^{(n)}(x_1;\ldots;x_{2n})$ are then given by

$$g^{(n)}_{\alpha_1\ldots\alpha_{2n}}(x_1;\ldots;x_{2n}) = \frac{G^{(n)}_{\alpha_1\ldots\alpha_{2n}}(x_1;\ldots;x_{2n})}{\prod_{j=1}^{2n}\sqrt{G^{(1)}_{\alpha_j\alpha_j}(x_j,x_j)}}. \tag{2.51}$$

This quantity measures the normalized correlation of photons with specific polarization directions. In contrast, the normalized correlation of all photons arriving at the detectors, independently of their polarization directions, is given by the normalized n$^{\text{th}}$-order correlation function, defined as

$$g^{(n)}(\mathbf{r}_d^{(1)},t_1;\ldots;\mathbf{r}_d^{(n)},t_n) = \frac{\langle \mathcal{T} : \hat{I}(\mathbf{r}_d^{(1)},t_1)\ldots\hat{I}(\mathbf{r}_d^{(n)},t_n) :\rangle}{\langle \hat{I}(\mathbf{r}_d^{(1)},t_1)\rangle\ldots\langle \hat{I}(\mathbf{r}_d^{(n)},t_n)\rangle}. \tag{2.52}$$

Notably, as the density matrix is a positive semi-definite operator, $g^{(n)}(\mathbf{r}_d^{(1)},t_1;\ldots;\mathbf{r}_d^{(n)},t_n)$ is always non-negative [111, 114].

Furthermore, light is said to be *completely n^{th}-order coherent* if the numerator in Eq. (2.52) factorizes as

$$\langle \mathcal{T} : \hat{I}(\mathbf{r}_d^{(1)},t_1)\ldots\hat{I}(\mathbf{r}_d^{(n)},t_n) :\rangle = \langle \hat{I}(\mathbf{r}_d^{(1)},t_1)\rangle\ldots\langle \hat{I}(\mathbf{r}_d^{(n)},t_n)\rangle\,. \tag{2.53}$$

In such a case, $g^{(n)}(\mathbf{r}_d^{(1)},t_1;\ldots;\mathbf{r}_d^{(n)},t_n) = 1$ for all $t_1,t_2,\ldots,t_n$. Importantly, we say that light is coherent to all orders if $g^{(n)}(\mathbf{r}_d^{(1)},t_1;\ldots;\mathbf{r}_d^{(n)},t_n) = 1$ for every order n. The states of light that are completely coherent to any order correspond to eigenstates of the positive-frequency electric field operator $\hat{\boldsymbol{E}}^{(+)}_{\perp}(\mathbf{r},t)$, and are simply referred to as *coherent states*. The expression of the free-space electric field operator in Eq. (1.133) allows us to express these states as

$$|\alpha\rangle = \otimes_{\mathbf{k},s}\,|\alpha_{\mathbf{k}s}\rangle\,, \tag{2.54}$$

where $|\alpha_{\mathbf{k}s}\rangle$ is an eigenstate of the operator $\hat{a}_{\mathbf{k}s}$, such that

$$\hat{a}_{\mathbf{k}s}\,|\alpha_{\mathbf{k}s}\rangle = \alpha_{\mathbf{k}s}\,|\alpha_{\mathbf{k}s}\rangle\,. \tag{2.55}$$

By using Eq. (1.56) and the normalization condition $\langle\alpha_{\mathbf{k}s}|\alpha_{\mathbf{k}s}\rangle = 1$, we obtain

$$|\alpha_{\mathbf{k}s}\rangle = \sum_{n}^{\infty}\frac{\alpha^n_{\mathbf{k}s}}{\sqrt{n!}}e^{-\alpha_{\mathbf{k}s}/2}\,|n_{\mathbf{k}s}\rangle\,, \tag{2.56}$$

with $|n_{\mathbf{k},s}\rangle$ the Fock states introduced in Section 1.1.6. In this way, the action the electromagnetic vacuum field in Eq. (1.133) into the coherent state $|\alpha\rangle$ yields

$$\hat{\mathbf{E}}_{\perp,\text{free}}(\mathbf{r},t)\,|\alpha\rangle = i\sum_{\mathbf{k},s}\sqrt{\frac{\hbar\omega_{\text{k}}}{2\varepsilon_0\mathcal{V}}}\mathbf{e}_{\mathbf{k}s}[\alpha_{\mathbf{k}s}e^{i(\mathbf{k}\cdot\mathbf{r}-\omega_{\text{k}}t)} - \alpha^*_{\mathbf{k}s}e^{-(i\mathbf{k}\cdot\mathbf{r}-\omega_{\text{k}}t)}]\,|\alpha\rangle\,. \tag{2.57}$$

By matching the eigenvalue of $\hat{\mathbf{E}}_{\perp,\text{free}}(\mathbf{r},t)$ on the right-hand side of this equation with the Fourier expansion of the classical electric field that we discussed in Section 1.1.3 [Eq. (1.25a)], we find

$$A_{\mathbf{k}s} = \sqrt{\frac{\hbar\omega_{\text{k}}}{2\varepsilon_0\mathcal{V}}}\alpha_{\mathbf{k}s}, \tag{2.58}$$

where $A_{\mathbf{k}s}$ is the complex amplitude of the classical transverse vector potential [Eq. (1.18)]. Therefore, we conclude that classical electromagnetic fields are characterized by large values of $\alpha_{\mathbf{k}s}$ because in the classical limit we take $\hbar \to 0$, which must be compensated by a value of $\alpha_{\mathbf{k}s}$ comparable to $1/\sqrt{\hbar}$ [114]. This large value of $\alpha_{\mathbf{k}s}$ in the classical limit is the reason why we assumed a large value of $\langle \hat{a}_L^\dagger \hat{a}_L \rangle$ in the description of the quantized laser field in Section 2.1.6.

2.3 Light statistics and color-blind intensity correlation

In this section, we discuss how the intensity correlation $g^{(2)}(\mathbf{r}_d^{(1)},0;\mathbf{r}_d^{(2)},\tau)$, introduced in Section 2.2.2, can reveal information about the statistical properties of light. To this end, we first describe the usual Hanbury-Brown Twiss interferometer and then introduce the concepts of antibunching and bunching. Finally, we analyze the intensity correlation of light emitted from a single quantum emitter and show that this system represents an ideal single-photon source. The analysis of light statistics plays a key role in Chapters 3 and 4 of this thesis.

2.3.1 Hanbury-Brown Twiss interferometer

We introduce in this section the Hanbury-Brown Twiss (HBT) interferometer, which is typically used in experiments to measure the intensity correlation of light. This interferometer is based on the pioneering work of Hanbury-Brown and Twiss in the 1950s, which aimed to quantify the angular diameter of the star Sirius through the measurement of the intensity correlation of light emitted from this star [163–165].

In the HBT interferometer, light emitted in some particular direction from a light source impinges on one of the input ports of a 50:50 beam splitter, as schematically represented in Fig. 2.4. The light then has an equal probability of being reflected or transmitted through the two output ports of the beam splitter. Additionally, a detector is placed on each of the two paths that the light can follow after the beam splitter. These two detectors are placed symmetrically with respect to the beam splitter, leading to $\mathbf{r}_d \equiv \mathbf{r}_d^{(1)} = \mathbf{r}_d^{(2)}$ in the expression of the intensity correlation in Eq. (2.48). Light intensity is then measured at both detectors over a time interval. By using a correlator [166], the HBT intensity correlation can be finally obtained as the product of the intensities arriving at each of the detectors with some time delay τ. This product is normalized by the light intensities arriving

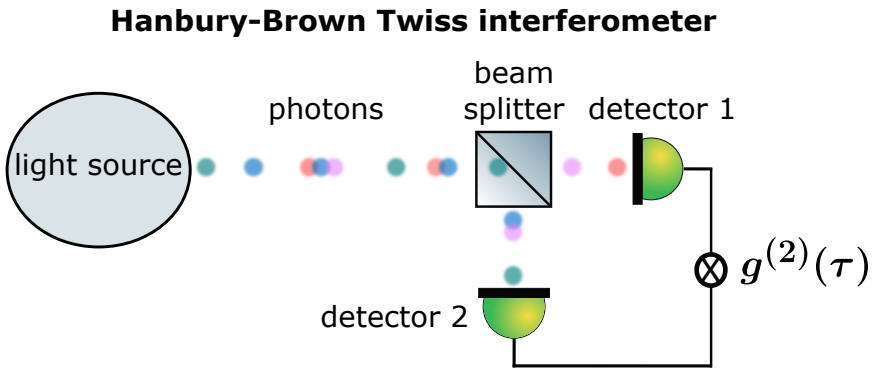

Figure 2.4: Schematic representation of the Hanbury-Brown Twiss (HBT) interferometer, which is typically used to measure the color-blind intensity correlation $g^{(2)}(\tau)$ of photons emitted from any given source. The light emitted in some particular direction impinges on a 50:50 beam splitter and then can be either reflected or transmitted, with equal probability, from it. Two detectors are symmetrically located from each of the output ports of the beam splitter. The intensities of the light beams arriving at the two detectors are measured during a certain time interval, which enables the measurement of the intensity correlation $g^{(2)}(\tau)$ by using a correlator. Circles of different colors represent photons with different frequencies.

at each of the detectors. In this way, the HBT intensity correlation is given by

$$g^{(2)}(\mathbf{r}_d, 0; \mathbf{r}_d, \tau) = \frac{\langle \mathcal{T} : \hat{I}(\mathbf{r}_d, 0)\hat{I}(\mathbf{r}_d, \tau) : \rangle_{\text{ss}}}{\langle \hat{I}(\mathbf{r}_d, 0) \rangle_{\text{ss}} \langle \hat{I}(\mathbf{r}_d, \tau) \rangle_{\text{ss}}}. \tag{2.59}$$

We note that $\mathbf{r}_d$ can be simply interpreted as the position of the beam splitter, as detection takes place in the far-field region and the two detectors are symmetrically arranged around it [i.e., only the direction of $\mathbf{r}_d$ affects the spatial dependence of $g^{(2)}(\mathbf{r}_d, 0; \mathbf{r}_d, \tau)$].

Further, the elements $g^{(2)}_{\alpha\alpha\beta\beta}(\mathbf{r}_d, 0; \mathbf{r}_d, \tau)$ of the normalized second-order correlation tensor can be measured with the HBT interferometer by placing a polarizer in each of the two possible paths that light can follow after the beam splitter (one polarized in the α-direction and the other in the β-direction). If the electric field scattered from the light source is a scalar field (as typically assumed in the literature), then the normalized second-order correlation tensor has a single non-zero element under the proper choice for the basis (reference frame) of polarization unit vectors. This single non-zero element of the tensor is equal to the normalized second-order correlation function.

In this thesis, we focus on the intensity correlation measured using an HBT interferometer and adopt the simpler notation

$$g^{(2)}(\tau) \equiv g^{(2)}(\mathbf{r}_d, 0; \mathbf{r}_d, \tau), \tag{2.60}$$

where the dependence on the detection direction is implicit. Additionally, we emphasize that $g^{(2)}(\tau)$ measures the correlation between all the photons emitted from the light source towards the beam splitter, without discriminating in polarization and, importantly, neither in frequency. Thus, this quantity is sometimes referred to as *color-blind intensity correlation*. In Section 2.4, we discuss a modification of the usual HBT interferometer that can be used to measure the intensity-correlation of photons emitted at specific frequencies, the so-called *frequency-resolved intensity correlation*.

2.3.2 Bunching and antibunching

We describe in this section the connection between the color-blind intensity correlation $g^{(2)}(\tau)$ and the statistical properties of light. To this end, we first consider a source of light emitting photons only in electromagnetic mode ($\mathbf{k}$, s). In this case, the positive-frequency and negative-frequency transverse electric field operators are $\hat{\mathbf{E}}_{\perp}^{(+)}(\mathbf{r}_d, 0) \propto \hat{a}_{\mathbf{k}s}$ and $\hat{\mathbf{E}}_{\perp}^{(-)}(\mathbf{r}_d, 0) \propto \hat{a}_{\mathbf{k}s}^{\dagger}$, according to Eqs. (1.127a)–(1.127b). Thus, the color-blind intensity correlation at delay $\tau = 0$ becomes

$$g^{(2)}(0) = \frac{\langle \hat{a}_{\mathbf{k}s}^{\dagger} \hat{a}_{\mathbf{k}s}^{\dagger} \hat{a}_{\mathbf{k}s} \hat{a}_{\mathbf{k}s} \rangle_{\mathrm{ss}}}{\langle \hat{a}_{\mathbf{k}s}^{\dagger} \hat{a}_{\mathbf{k}s} \rangle_{\mathrm{ss}}^2} = 1 + \frac{\langle (\Delta \hat{n}_{\mathbf{k}s})^2 \rangle_{\mathrm{ss}} - \langle \hat{n}_{\mathbf{k}s} \rangle_{\mathrm{ss}}}{\langle \hat{n}_{\mathbf{k}s} \rangle_{\mathrm{ss}}^2}. \tag{2.61}$$

To derive the last equality in the above equation, we have used $\hat{n}_{\mathbf{k}s} = \hat{a}_{\mathbf{k}s}^{\dagger} \hat{a}_{\mathbf{k}s}$ and the commutation relations in Eqs. (1.42a)–(1.42b). Additionally, we have introduced the variance of the number operator (Appendix A), which is given by

$$\langle (\Delta \hat{n}_{\mathbf{k}s})^2 \rangle_{\mathrm{ss}} = \langle \hat{n}_{\mathbf{k}s}^2 \rangle_{\mathrm{ss}} - \langle \hat{n}_{\mathbf{k}s} \rangle_{\mathrm{ss}}^2 . \tag{2.62}$$

Therefore, the color-blind intensity correlation $g^{(2)}(0)$ is determined by the expectation value and the variance of the photon number operator. We next show that $g^{(2)}(0)$ allows for distinguishing between different types of statistical distributions that can be followed by the number of photons emitted by the source.

We first take into account that the equality between the expectation value and the variance is a fundamental characteristic of a *Poissonian distribution*. According to Eq. (2.61), the number of photons emitted by the source follows a Poissonian distribution if, and only if, $g^{(2)}(0) = 1$. Thus, the following two conditions are equivalent:

$$\langle \hat{n}_{\mathbf{k}s} \rangle_{\mathrm{ss}} = \langle (\Delta \hat{n}_{\mathbf{k}s})^2 \rangle_{\mathrm{ss}} \Leftrightarrow g^{(2)}(0) = 1. \tag{2.63}$$

Notably, one can show that the coherent state $|\alpha_{\mathbf{k}s}\rangle$ in Eq. (2.56) results in a Poissonian photon distribution. More specifically, the probability of finding n photons in mode ($\mathbf{k}$, s) provided by the coherent state $|\alpha_{\mathbf{k}s}\rangle$ is given by

$$|\langle n_{\mathbf{k}s} | \alpha_{\mathbf{k}s} \rangle|^2 = e^{-|\alpha_{\mathbf{k}s}|^2} \frac{|\alpha_{\mathbf{k}s}|^{2n_{\mathbf{k}s}}}{n_{\mathbf{k}s}!}, \tag{2.64}$$

which is exactly a Poissonian distribution with $|\alpha_{\mathbf{k}s}|^2 = \langle n_{\mathbf{k}s}\rangle_{\text{ss}} = \langle(\Delta\hat{n}_{\mathbf{k}s})^2\rangle_{\text{ss}}$. Crucially, Poissonian distributions are characteristic of statistical processes where events occur independently of each other, or, in other words, where the occurrence of an event is not influenced by the timing of past events. Therefore, we reach an important conclusion: the number of photons emitted from a source of coherent light at a given time is completely independent of the number of photons emitted at past times and satisfies $g^{(2)}(0) = 1$. Further, a coherent source of light has intensity correlation $g^{(2)}(\tau)$ equal to 1 at all time delays [116]. This is the case for laser light.

Furthermore, Eq. (2.61) also indicates that the following conditions are equivalent:

$$\langle(\Delta\hat{n}_{\mathbf{k}s})^2\rangle_{\text{ss}} > \langle\hat{n}_{\mathbf{k}s}\rangle_{\text{ss}} \Leftrightarrow g^{(2)}(0) > 1. \tag{2.65}$$

Thus, if the intensity correlation of light emitted from a certain source yields $g^{(2)}(0) > 1$, the probability of emitting n photons follows a *super-Poissonian distribution* [$\langle(\Delta\hat{n}_{\mathbf{k}s})^2\rangle_{\text{ss}} > \langle\hat{n}_{\mathbf{k}s}\rangle_{\text{ss}}$]. This source then has a greater tendency to emit photons in bunches than a source of coherent light (i.e., a laser). A notable example is thermal light, which yields $g^{(2)}(0) = 2$ [118, 167]. In the opposite case, we obtain

$$\langle(\Delta\hat{n}_{\mathbf{k}s})^2\rangle_{\text{ss}} < \langle\hat{n}_{\mathbf{k}s}\rangle_{\text{ss}} \Leftrightarrow g^{(2)}(0) < 1. \tag{2.66}$$

Thus, if $g^{(2)}(0) < 1$, the photon distribution is *sub-Poissonian* [$\langle(\Delta\hat{n}_{\mathbf{k}s})^2\rangle_{\text{ss}} < \langle\hat{n}_{\mathbf{k}s}\rangle_{\text{ss}}$]. In this case, the source exhibits a lower tendency to emit photons in bunches compared to a coherent light source. Importantly, $g^{(2)}(0) < 1$ is a signature of quantum light, as classical light obeys the inequality $\langle I(t)^2\rangle \geq \langle I(t)\rangle^2$, implying $g^{(2)}(0) \geq 1$ [118]. The lowest limit $g^{(2)}(0) = 0$ is characteristic of single-photon sources [31], which emit one photon at a time, with no possible coincident detection at $\tau = 0$. We show in Section 2.3.3 that QEs with two-level behaviour are ideal single-photon sources.

In this thesis, we follow a common convention and refer to light as *bunched* if it follows a super-Poissonian distribution, and as *antibunched* if it follows a sub-Poissonian distribution, as it has a larger or smaller tendency, respectively, to emit photons in bunches than coherent light. However, the rigorous definitions of bunching and antibunching rely on comparing the value of the normalized second-order correlation function at $\tau = 0$ with its value at $\tau \neq 0$. More specifically, light is said to be bunched if $g^{(2)}(0) > g^{(2)}(\tau)$, and antibunched if $g^{(2)}(0) < g^{(2)}(\tau)$ [118, 168]. Typically, the practical convention that we use in this thesis and the rigorous definitions of bunching and antibunching agree because $g^{(2)}(\tau \to \infty) = 1$ [which is a consequence of Eq. (2.47)].

The connection between light statistics and the normalized second-order correlation function discussed above is based on a single electromagnetic mode ($\mathbf{k}$, s). Next, we briefly describe how this connection can be generalized to the case of an infinite number of modes. To this end, we substitute the complete expressions of the positive-frequency and negative-frequency transverse electric field operators [Eqs. (1.127a)–(1.127b)] into the expression for the color-blind intensity correlation

[Eq. (2.59)]. In this way, we obtain

$$g^{(2)}(0) = \frac{\sum_{\mathbf{k},s}\sum_{\mathbf{k}',s'}\omega_{\mathrm{k}}\omega_{\mathrm{k}'}\langle\hat{a}^{\dagger}_{\mathbf{k}s}\hat{a}^{\dagger}_{\mathbf{k}'s'}\hat{a}_{\mathbf{k}'s'}\hat{a}_{\mathbf{k}s}\rangle_{\mathrm{ss}}}{\sum_{\mathbf{k},s}\sum_{\mathbf{k}',s'}\omega_{\mathrm{k}}\omega_{\mathrm{k}'}\langle\hat{a}^{\dagger}_{\mathbf{k}s}\hat{a}_{\mathbf{k}s}\rangle_{\mathrm{ss}}\langle\hat{a}^{\dagger}_{\mathbf{k}'s'}\hat{a}_{\mathbf{k}'s'}\rangle_{\mathrm{ss}}}$$
$$= 1 + \frac{\sum_{\mathbf{k},s}\sum_{\mathbf{k}',s'}\omega_{\mathrm{k}}\omega_{\mathrm{k}'}\langle\hat{n}_{\mathbf{k}s}\hat{n}_{\mathbf{k}'s'}\rangle_{\mathrm{ss}} - \left(\sum_{\mathbf{k},s}\omega_{\mathrm{k}}\langle\hat{n}_{\mathbf{k}s}\rangle_{\mathrm{ss}}\right)^2 - \sum_{\mathbf{k},s}\omega_{\mathrm{k}}^2\langle\hat{n}_{\mathbf{k}s}\rangle_{\mathrm{ss}}}{\left(\sum_{\mathbf{k},s}\omega_{\mathrm{k}}\langle\hat{n}_{\mathbf{k}s}\rangle_{\mathrm{ss}}\right)^2}, \tag{2.67}$$

where we have used again the commutation relations in Eqs. (1.42a)–(1.42b). Thus, in the general case we find again a connection between the number of photons in each mode and the color-blind intensity correlation. Additionally, assuming that only electromagnetic modes of very similar frequency contribute significantly to the summations in the above expression, we find

$$g^{(2)}(0) = 1 + \frac{\langle(\Delta\hat{n})^2\rangle_{\mathrm{ss}} - \langle\hat{n}\rangle_{\mathrm{ss}}}{\langle\hat{n}\rangle^2_{\mathrm{ss}}}, \tag{2.68}$$

where $\hat{n} = \sum_{\mathbf{k},s}\hat{n}_{\mathbf{k}s}$ is the total number operator. The above expression is formally identical to the one in Eq. (2.61) obtained for a single electromagnetic mode. Therefore, the conditions in Eqs. (2.63), (2.65) and (2.66) are also valid for the total number operator.

2.3.3 Color-blind intensity correlation from a single quantum emitter

In this section, we investigate the HBT intensity correlation of light emitted from a resonantly driven QE and show that this system constitutes an ideal single-photon source. Additionally, we show that Rabi oscillations emerge in the time evolution of $g^{(2)}(\tau)$ for increasing driving strength.

As shown in Section 1.2.7, the positive-frequency electric field operator of light scattered from a QE is $\hat{\mathbf{E}}^{(+)}_{\perp,\mathrm{QE}}(\mathbf{r}_d,\tau) = \boldsymbol{\mathcal{E}}_{\boldsymbol{\mu}}(\mathbf{r}_d)\hat{\sigma}(\tau - |\mathbf{r}_d - \mathbf{r}_0|/c)$, where $\boldsymbol{\mathcal{E}}_{\boldsymbol{\mu}}(\mathbf{r}_d)$ is the vector amplitude of the positive-frequency electric field radiated at $\mathbf{r}_d$ from a classical electric point dipole at $\mathbf{r}_0$. The contributions from $\boldsymbol{\mathcal{E}}_{\boldsymbol{\mu}}(\mathbf{r}_d)$ in the numerator and in the denominator of $g^{(2)}(\tau)$ [Eq. (2.59)] cancel out. Additionally, the retardation time $|\mathbf{r}_d - \mathbf{r}_0|/c$ in the intensity operators $\hat{I}(\mathbf{r}_d,\tau) \propto \hat{\sigma}^{\dagger}(\tau - |\mathbf{r}_d - \mathbf{r}_0|/c)\hat{\sigma}(\tau - |\mathbf{r}_d - \mathbf{r}_0|/c)$ and $\hat{I}(\mathbf{r}_d,0) \propto \hat{\sigma}^{\dagger}(-|\mathbf{r}_d - \mathbf{r}_0|/c)\hat{\sigma}(-|\mathbf{r}_d - \mathbf{r}_0|/c)$ that appear in the numerator of $g^{(2)}(\tau)$ also cancel each other, as we focus on the steady state, which only depends on the time difference at which these two operators are evaluated [similarly to the cancellation of the retardation times in the normalized first-order correlation function $g^{(1)}(\mathbf{r}_d,0;\mathbf{r}_d,\tau)$, see Section 2.1.6]. Thus, the retardation times can also be ignored in the calculation of the color-blind

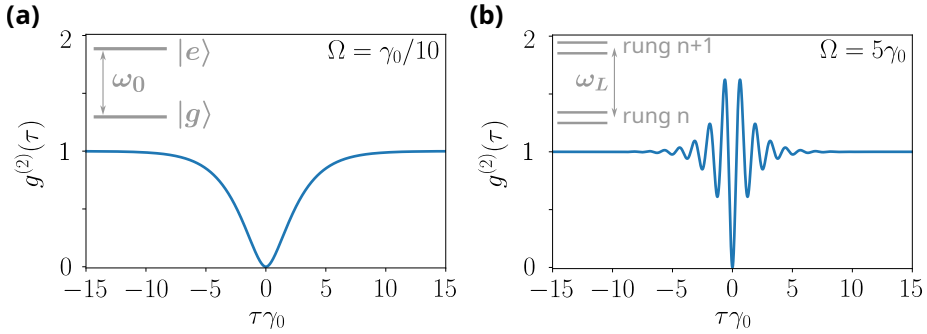

Figure 2.5: Color-blind intensity correlation $g^{(2)}(\tau) = g^{(2)}(\mathbf{r}_d, 0; \mathbf{r}_d, \tau)$ of light emitted from a driven QE. The QE has two-level-system behaviour, as schematically represented in the inset in (a), with transition frequency ω_0 and spontaneous decay rate γ_0. Additionally, the QE is driven resonantly ($\omega_L = \omega_0$), with Rabi frequency Ω. (a) The QE is weakly driven at $\Omega = \gamma_0/10$. A clear minima is obtained at short delay times, with $g^{(2)}(\tau = 0) = 0$, characteristic of single-photon emission. (b) The QE is strongly driven at $\Omega = 5\gamma_0$. Rabi oscillations emerge in the time evolution of the intensity correlation due to the dressing of the states, which is represented in the inset.

intensity correlation of light emitted from a single QE. We obtain

$$g^{(2)}(\tau) = \frac{\langle \hat{\sigma}^\dagger(0)\hat{\sigma}^\dagger(\tau)\hat{\sigma}(\tau)\hat{\sigma}(0)\rangle_{\rm ss}}{\langle \hat{\sigma}^\dagger(0)\hat{\sigma}(0)\rangle^2_{\rm ss}}. \tag{2.69}$$

Importantly, the numerator vanishes at $\tau = 0$ and, thus, $g^{(2)}(0) = 0$, independently of the strength of the driving. Therefore, two-level QEs are ideal single-photon sources. This can be easily understood by taking into account that the relaxation from $|e\rangle$ to $|g\rangle$ leads to the emission of a single photon, and the QE cannot be reexcited to emit another photon faster than the lifetime of the excited state $|e\rangle$, which is given by $1/\gamma_0$. Thus, at $\tau = 0$, coincident detection of photons is not possible.

The expression of the color-blind intensity correlation in Eq. (2.69) can be evaluated using the Markovian master equation in Eq. (1.230), which includes the laser driving. We plot in Fig. 2.5a the time evolution of $g^{(2)}(\tau)$ of light emitted from a resonantly driven QE at weak driving strength, $\Omega = \gamma_0/10$. We find a dip at $\tau = 0$, with no oscillations as $|\tau|$ increases because the eigenstates of the system can be well approximated as the bare states $|g\rangle$ and $|e\rangle$ (see the inset in Fig. 2.5a), and thus Rabi oscillations are not expected. We next increase the driving strength to $\Omega = 5\gamma_0$ (Fig. 2.5b), which is sufficient to modify the eigenstates of the emitters. Specifically, the eigenstates are distributed in infinite rungs, as described in Section 2.1.6 and schematically represented in the inset of Fig. 2.5. We find that the intensity correlation vanishes again at $\tau = 0$ and, importantly, we observe the emergence of Rabi oscillations due to the modification of the eigenstates induced by the strong driving.

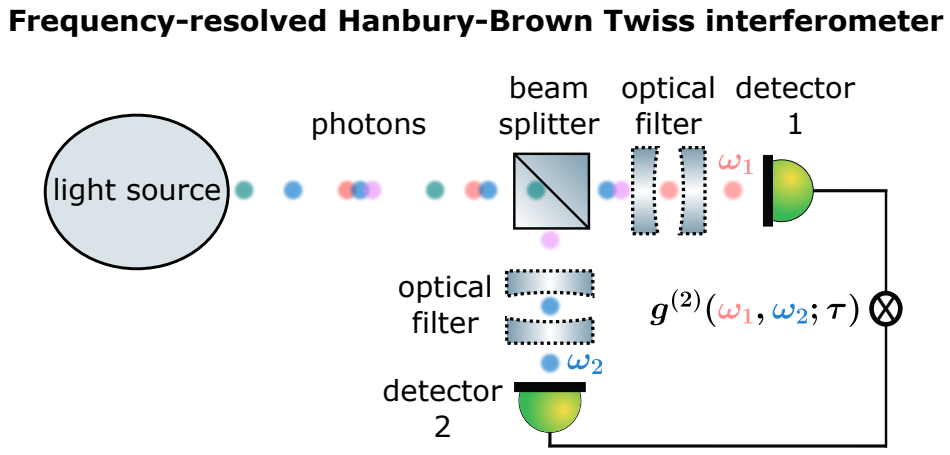

Figure 2.6: Schematic representation of the frequency-resolved Hanbury-Brown Twiss interferometer, which can be used to measure the frequency-resolved intensity correlation $g^{(2)}(\omega_1, \omega_2; \tau)$ of photons emitted from any source with delay τ and specific frequencies ω_1 and ω_2. Optical filters with mean frequencies ω_1 and ω_2 are used, so that the photons of frequency ω_1 (red circles) arrive at one of the detector and the photons of frequency ω_2 (blue circles) arrive at the other detector. The measurement of the intensities at each of the detectors enables to finally obtain the frequency-resolved intensity correlation $g^{(2)}(\omega_1, \omega_2; \tau)$, for example, by using a correlator. Circles of different colors represent photons with different frequencies.

2.4 Frequency-resolved intensity correlation

In this section, we include optical filters in the setup of the HBT interferometer to analyze the intensity correlation of photon pairs at specific frequencies, which is known as *frequency-resolved intensity correlation* (FRIC). The analysis of the FRIC provides great information about the emission processes of the system. In addition to gathering information about one-photon emission processes [which is typically also provided by the emission spectrum $S(\omega)$ discussed in Section 2.1.5], the FRIC can also unveil complex two-photon emission processes.

2.4.1 Frequency-resolved Hanbury-Brown Twiss interferometer

The FRIC can be obtained experimentally including an optical filter in each of the two paths that light can follow after passing through the beam splitter in the standard Hanbury-Brown Twiss interferometer, as depicted in Fig. 2.6. In this thesis, we consider that the filters have a Lorentzian profile with mean frequency ω_j and linewidth Γ_j (here $j = 1, 2$ labels each of the two filters), which is the case, for example, of Fabry-Pérot cavities with reflection coefficient tending to one [147, 158]. The positive-frequency and negative-frequency transverse electric field

operators, including the effect of filter j, are given by [158]

$$\hat{\mathbf{E}}^{(\pm)}_{\perp,fl}(\omega_j,\Gamma_j;t)=\frac{\Gamma_j}{2}\int_0^\infty dt' e^{-(i\omega_j+\Gamma_j/2)t'}\hat{\mathbf{E}}^{(\pm)}_{\perp}(t-t'), \tag{2.70}$$

where *fl* stands for *filter*. These filtered electric field operators allow for introducing the filtered intensity operator as

$$\hat{I}_{fl}(\omega_j,\Gamma_j;\mathbf{r}_d,\tau)=\hat{\mathbf{E}}^{(-)}_{\perp,fl}(\omega_j,\Gamma_j;t)\cdot\hat{\mathbf{E}}^{(+)}_{\perp,fl}(\omega_j,\Gamma_j;t). \tag{2.71}$$

The FRIC can then be obtained in an analogous way to the color-blind intensity correlation $g^{(2)}(\tau)$ in Eq. (2.59), but replacing the intensity operators $\hat{I}(\mathbf{r}_d,0)$ and $\hat{I}(\mathbf{r}_d,\tau)$ by the filtered intensity operators $\hat{I}_{fl}(\omega_1,\Gamma_1;\mathbf{r}_d,0)$ and $\hat{I}_{fl}(\omega_2,\Gamma_2;\mathbf{r}_d,\tau)$, respectively. Thus, the FRIC is defined as

$$g^{(2)}(\omega_1,\omega_2;\tau)=\frac{\langle\mathcal{T}:\hat{I}_{fl}(\omega_1,\Gamma_1;\mathbf{r}_d,0)\hat{I}_{fl}(\omega_2,\Gamma_2;\mathbf{r}_d,\tau):\rangle_{\rm ss}}{\langle\hat{I}_{fl}(\omega_1,\Gamma_1;\mathbf{r}_d,0)\rangle_{\rm ss}\langle\hat{I}_{fl}(\omega_2,\Gamma_2;\mathbf{r}_d,\tau)\rangle_{\rm ss}}. \tag{2.72}$$

We emphasize that $g^{(2)}(\omega_1,\omega_2;\tau)$ depends on the linewidth of the filters Γ_j and also on the detection direction $\mathbf{r}_d$. In the limit of infinitely large linewidth of the filters ($\Gamma_j\to\infty$), the value of the FRIC $g^{(2)}(\omega_1,\omega_2;\tau)$ tends to the value of the color-blind intensity correlation $g^{(2)}(\tau)$ [169].

The direct calculation of the FRIC through the rigorous expression in Eq. (2.72) requires to compute complicated four-dimensional time integrals, which have been solved for the case of resonance fluorescence of a single two-level quantum emitter [159, 170, 171]. However, the calculation of these time integrals for more complex systems usually becomes unpractical. We discuss an alternative approach in the next section.

2.4.2 Sensor method

We describe in this section a formalism that can be used to obtain the FRIC of complex systems. This formalism is known as *sensor method* and was introduced in Ref. [169]. It considers two two-level atoms that act as detectors (indexed by $j=1,2$), as in Section 2.2.1. The raising and lowering operators of these atom detectors are denoted $\hat{\zeta}^\dagger_j=|e^{(j)}_d\rangle\langle g^{(j)}_d|$ and $\hat{\zeta}_j=|g^{(j)}_d\rangle\langle e^{(j)}_d|$, respectively. The Hamiltonian of these atom detectors is given by $\hat{H}_{fl}=\sum_j\omega_j\hat{\zeta}^\dagger_j\hat{\zeta}_j$. The sensor method relies on an effective Hamiltonian that describes the interaction between the detectors and the electromagnetic field scattered from the system S, whose FRIC is of interest. Taking into account that the positive-frequency component of the dipole moment operator of atom detector j is proportional to $\hat{\zeta}^\dagger_j$, and the the negative-frequency component is proportional to $\hat{\zeta}_j$, the multipolar form of this

effective interaction can be written under the RWA as

$$\hat{H}_{S-fl} = \hbar \sum_j \epsilon_{fl} (\hat{\zeta}_j^\dagger \hat{s}_j + \hat{\zeta}_j \hat{s}_j^\dagger), \tag{2.73}$$

where ϵ_{fl} is the effective coupling strength. ϵ_{fl} is considered identical for the two detectors, for simplicity, and small enough compared to any decay rate of S and to the linewidth Γ_j, so that the atom detectors do not influence the dynamics of S. Additionally, $\hat{s}_j$ and $\hat{s}_j^\dagger$ are lowering/annihilation and raising/creation operators in the Hilbert space of S that describe the positive-frequency and negative-frequency electric field operators of light scattered from S, respectively. For example, in the case of a single two-level quantum emitter $\hat{s}_j = \hat{\sigma}$, as we showed in Section 1.2.7 that the positive-frequency electric field scattered from the QE is proportional to the lowering operator $\hat{\sigma}$ [Eq. (1.147)].

Moreover, the dynamics of the entire system is governed by the Markovian master equation

$$\frac{d}{dt}\hat{\rho} = \mathcal{L}\hat{\rho} = -\frac{i}{\hbar}[\hat{H}_S + \hat{H}_{fl} + \hat{H}_{S-fl}, \hat{\rho}] + \mathcal{L}_S^{(in)}\hat{\rho} + \mathcal{L}_{fl}^{(in)}\hat{\rho}, \tag{2.74}$$

where $\hat{\rho}$ is the density matrix of the entire system (comprising the complete Hilbert space given by the tensor product of the Hilbert space of S and the Hilbert space of the two-level detectors) and $\hat{H}_S$ is the Hamiltonian of the system of interest. Additionally, we have defined the superoperator $\mathcal{L}$, which provides the full time evolution of $\hat{\rho}$ and is known as *Liouville superoperator*. Further, $\mathcal{L}_S^{(in)}$ accounts for the incoherent dynamics of S, which can emerge from tracing out the degrees of freedom of the electromagnetic field (as well as possible additional reservoirs), whereas

$$\mathcal{L}_{fl}^{(in)} = \sum_j \frac{\Gamma_j}{2} \mathcal{D}[\hat{\zeta}_j] \tag{2.75}$$

accounts for the losses of the atom detectors, with $\mathcal{D}[\hat{\zeta}_j]$ the Lindblad dissipator defined in Eq. (1.200) and Γ_j the linewidth of the filters. We emphasize that within the formalism presented in this section, the probability of photon absorption by the atom detectors is no longer independent of the photon frequency (as in Sections 2.1.2 and 2.2.1), but it obeys a Lorentzian distribution, with linewidth Γ_j and central frequency ω_j.

The sensor method enables to calculate $g^{(2)}(\omega_1, \omega_2; \tau)$ from the two-time correlation of the operators $\hat{\zeta}_j^\dagger \hat{\zeta}_j(t) = |e_d^{(j)}\rangle \langle e_d^{(j)}|\,(t)$ of the two atom detectors. More specifically,

$$g^{(2)}(\omega_1, \omega_2; \tau) = \lim_{\epsilon_{fl} \to 0} \frac{\langle \mathcal{T} : \hat{\zeta}_1^\dagger \hat{\zeta}_1(0) \hat{\zeta}_2^\dagger \hat{\zeta}_2(\tau) : \rangle_{\rm ss}}{\langle \hat{\zeta}_1^\dagger \hat{\zeta}_1(0) \rangle_{\rm ss} \langle \hat{\zeta}_2^\dagger \hat{\zeta}_2(\tau) \rangle_{\rm ss}}. \tag{2.76}$$

Equation (2.76) resembles the original expression of $g^{(2)}(\omega_1, \omega_2; \tau)$ in Eq. (2.72), but the filtered intensity operators $\hat{I}_{fl}(\omega_j, \Gamma_j; \mathbf{r}_d, t)$ are replaced by the operator

$\hat{\zeta}_j^\dagger \hat{\zeta}_j(t)$ of the atom detector j, which corresponds to the projector onto the excited state of this detector. Equation (2.76) can be intuitively understood taking into account that the population of each detector can be expected to be proportional to the number of photons that would be detected after the filtering process. A demonstration of the mathematical equivalence between Eqs. (2.72) and (2.76) can be found in Ref. [169].

Therefore, we conclude that the sensor method allows us to compute the FRIC without the necessity of solving complicated four-dimensional integrals at the price, in principle, of enlarging the Hilbert space. This drawback is completely relaxed in the following section.

2.4.3 Sophistication of the sensor method

We describe in this section an approach based on the sensor method that allows for computing the FRIC within the Hilbert space of the system of interest S. This approach was introduced in Ref. [172]. We first rewrite the MME in Eq. (2.74) as

$$\mathcal{L}\hat{\rho} = \mathcal{L}_S\hat{\rho} + \mathcal{L}_{fl}\hat{\rho} - \frac{i}{\hbar}[\hat{H}_{S-fl}, \hat{\rho}], \tag{2.77}$$

where the Liouville superoperator

$$\mathcal{L}_S\hat{\rho} = -\frac{i}{\hbar}[\hat{H}_S, \hat{\rho}] + \mathcal{L}_S^{(in)}\hat{\rho} \tag{2.78}$$

acts only on the Hilbert space of S, whereas the Liouville superoperator

$$\mathcal{L}_{fl}\hat{\rho} = -\frac{i}{\hbar}[\hat{H}_{fl}, \hat{\rho}] + \mathcal{L}_{fl}^{(in)}\hat{\rho} \tag{2.79}$$

acts only on the Hilbert space of the atom detectors. Additionally, we decompose the steady-state density matrix as

$$\hat{\rho}_{ss} = \sum_{k\in\{g,e\}} \sum_{l\in\{g,e\}} \sum_{m\in\{g,e\}} \sum_{n\in\{g,e\}} \hat{\rho}_{k,m}^{l,n} \otimes |k_d^{(1)}\rangle \langle l_d^{(1)}| \otimes |m_d^{(2)}\rangle \langle n_d^{(2)}|, \tag{2.80}$$

where we have defined the steady-state reduced density matrix

$$\hat{\rho}_{k,m}^{l,n} = (\hat{\rho}_{l,n}^{k,m})^* = \langle k_d^{(1)}, m_d^{(2)}| \hat{\rho}_{ss} |l_d^{(1)}, n_d^{(2)}\rangle, \tag{2.81}$$

which belongs to the Hilbert space of S, with $k, l, m, n \in \{g, e\}$.

In the following, we focus on the case of zero delay time $\tau = 0$. (The extension of this procedure to $\tau \neq 0$ has been derived in Ref. [172], but it is not used in this thesis). The numerator of $g^{(2)}(\omega_1, \omega_2; 0)$ in Eq. (2.76) can be obtained from the trace of one of the reduced density matrices in Eq. (2.81) as

$$\langle \hat{\zeta}_1^\dagger \hat{\zeta}_1(0) \hat{\zeta}_2^\dagger \hat{\zeta}_2(0)\rangle_{\text{ss}} = \text{Tr}\hat{\rho}_{e,e}^{e,e}. \tag{2.82}$$

Similarly, the denominator of $g^{(2)}(\omega_1,\omega_2;0)$ in Eq. (2.76) can be calculated from

$$\langle\hat{\zeta}_1^\dagger\hat{\zeta}_1(0)\rangle_{\rm ss} = {\rm Tr}\hat{\rho}^{e,g}_{e,g}, \tag{2.83a}$$
$$\langle\hat{\zeta}_2^\dagger\hat{\zeta}_2(0)\rangle_{\rm ss} = {\rm Tr}\hat{\rho}^{g,e}_{g,e}. \tag{2.83b}$$

We next describe how to compute the reduced density matrices $\hat{\rho}^{l,n}_{k,m}$ within the Hilbert space of S.

First, we compute separately the action of the full Liouville superoperator $\mathcal{L}$ in Eq. (2.77) on each of the sixteen terms in the summation on the right-hand side of Eq. (2.80), which yields:

$$\begin{aligned}
&\mathcal{L}\left(\hat{\rho}^{g,g}_{g,g}\otimes|g_d^{(1)}\rangle\langle g_d^{(1)}|\otimes|g_d^{(2)}\rangle\langle g_d^{(2)}|\right) = \mathcal{L}_S\left(\hat{\rho}^{g,g}_{g,g}\otimes|g_d^{(1)}\rangle\langle g_d^{(1)}|\otimes|g_d^{(2)}\rangle\langle g_d^{(2)}|\right)\\
&-i\epsilon_{fl}\left(\hat{s}_1\hat{\rho}^{g,g}_{g,g}\otimes|e_d^{(1)}\rangle\langle g_d^{(1)}|\otimes|g_d^{(2)}\rangle\langle g_d^{(2)}| - \hat{\rho}^{g,g}_{g,g}\hat{s}_1^\dagger\otimes|g_d^{(1)}\rangle\langle e_d^{(1)}|\otimes|g_d^{(2)}\rangle\langle g_d^{(2)}|\right)\\
&-i\epsilon_{fl}\left(\hat{s}_2\hat{\rho}^{g,g}_{g,g}\otimes|g_d^{(1)}\rangle\langle g_d^{(1)}|\otimes|e_d^{(2)}\rangle\langle g_d^{(2)}| - \hat{\rho}^{g,g}_{g,g}\hat{s}_2^\dagger\otimes|g_d^{(1)}\rangle\langle g_d^{(1)}|\otimes|g_d^{(2)}\rangle\langle e_d^{(2)}|\right),
\end{aligned} \tag{2.84a}$$

$$\begin{aligned}
&\mathcal{L}\left(\hat{\rho}^{g,g}_{e,g}\otimes|e_d^{(1)}\rangle\langle g_d^{(1)}|\otimes|g_d^{(2)}\rangle\langle g_d^{(2)}|\right) =\\
&\left(\mathcal{L}_S - \frac{\Gamma_1}{2} - i\omega_1\right)\left(\hat{\rho}^{g,g}_{e,g}\otimes|e_d^{(1)}\rangle\langle g_d^{(1)}|\otimes|g_d^{(2)}\rangle\langle g_d^{(2)}|\right)\\
&-i\epsilon_{fl}\left(\hat{s}_1^\dagger\hat{\rho}^{g,g}_{e,g}\otimes|g_d^{(1)}\rangle\langle g_d^{(1)}|\otimes|g_d^{(2)}\rangle\langle g_d^{(2)}| - \hat{\rho}^{g,g}_{e,g}\hat{s}_1^\dagger\otimes|e_d^{(1)}\rangle\langle e_d^{(1)}|\otimes|g_d^{(2)}\rangle\langle g_d^{(2)}|\right)\\
&-i\epsilon_{fl}\left(\hat{s}_2\hat{\rho}^{g,g}_{e,g}\otimes|e_d^{(1)}\rangle\langle g_d^{(1)}|\otimes|e_d^{(2)}\rangle\langle g_d^{(2)}| - \hat{\rho}^{g,g}_{e,g}\hat{s}_2^\dagger\otimes|e_d^{(1)}\rangle\langle g_d^{(1)}|\otimes|g_d^{(2)}\rangle\langle e_d^{(2)}|\right),
\end{aligned} \tag{2.84b}$$

$$\begin{aligned}
&\mathcal{L}\left(\hat{\rho}^{e,g}_{g,g}\otimes|g_d^{(1)}\rangle\langle e_d^{(1)}|\otimes|g_d^{(2)}\rangle\langle g_d^{(2)}|\right) =\\
&\left(\mathcal{L}_S - \frac{\Gamma_1}{2} + i\omega_1\right)\left(\hat{\rho}^{e,g}_{g,g}\otimes|g_d^{(1)}\rangle\langle e_d^{(1)}|\otimes|g_d^{(2)}\rangle\langle g_d^{(2)}|\right)\\
&-i\epsilon_{fl}\left(\hat{s}_1\hat{\rho}^{e,g}_{g,g}\otimes|e_d^{(1)}\rangle\langle e_d^{(1)}|\otimes|g_d^{(2)}\rangle\langle g_d^{(2)}| - \hat{\rho}^{e,g}_{g,g}\hat{s}_1\otimes|g_d^{(1)}\rangle\langle g_d^{(1)}|\otimes|g_d^{(2)}\rangle\langle g_d^{(2)}|\right)\\
&-i\epsilon_{fl}\left(\hat{s}_2\hat{\rho}^{e,g}_{g,g}\otimes|g_d^{(1)}\rangle\langle e_d^{(1)}|\otimes|e_d^{(2)}\rangle\langle g_d^{(2)}| - \hat{\rho}^{e,g}_{g,g}\hat{s}_2^\dagger\otimes|g_d^{(1)}\rangle\langle e_d^{(1)}|\otimes|g_d^{(2)}\rangle\langle e_d^{(2)}|\right),
\end{aligned} \tag{2.84c}$$

$$\begin{aligned}
&\mathcal{L}\left(\hat{\rho}^{g,g}_{g,e}\otimes|g_d^{(1)}\rangle\langle g_d^{(1)}|\otimes|e_d^{(2)}\rangle\langle g_d^{(2)}|\right) =\\
&\left(\mathcal{L}_S - \frac{\Gamma_2}{2} - i\omega_2\right)\left(\hat{\rho}^{g,g}_{g,e}\otimes|g_d^{(1)}\rangle\langle g_d^{(1)}|\otimes|e_d^{(2)}\rangle\langle g_d^{(2)}|\right)
\end{aligned}$$

$$- i\epsilon_{fl}\Big(\hat{s}_1\hat{\rho}^{g,g}_{g,e}\otimes|e^{(1)}_d\rangle\langle g^{(1)}_d|\otimes|e^{(2)}_d\rangle\langle g^{(2)}_d| - \hat{\rho}^{g,g}_{g,e}\hat{s}^\dagger_1\otimes|g^{(1)}_d\rangle\langle e^{(1)}_d|\otimes|e^{(2)}_d\rangle\langle g^{(2)}_d|\Big)$$
$$- i\epsilon_{fl}\Big(\hat{s}^\dagger_2\hat{\rho}^{g,g}_{g,e}\otimes|g^{(1)}_d\rangle\langle g^{(1)}_d|\otimes|g^{(2)}_d\rangle\langle g^{(2)}_d| - \hat{\rho}^{g,g}_{g,e}\hat{s}^\dagger_2\otimes|g^{(1)}_d\rangle\langle g^{(1)}_d|\otimes|e^{(2)}_d\rangle\langle e^{(2)}_d|\Big), \tag{2.84d}$$

$$\mathcal{L}\Big(\hat{\rho}^{g,e}_{g,g}\otimes|g^{(1)}_d\rangle\langle g^{(1)}_d|\otimes|g^{(2)}_d\rangle\langle e^{(2)}_d|\Big) =$$
$$\Big(\mathcal{L}_S - \frac{\Gamma_2}{2} + i\omega_2\Big)\Big(\hat{\rho}^{g,e}_{g,g}\otimes|g^{(1)}_d\rangle\langle g^{(1)}_d|\otimes|g^{(2)}_d\rangle\langle e^{(2)}_d|\Big)$$
$$- i\epsilon_{fl}\Big(\hat{s}_1\hat{\rho}^{g,e}_{g,g}\otimes|e^{(1)}_d\rangle\langle g^{(1)}_d|\otimes|g^{(2)}_d\rangle\langle e^{(2)}_d| - \hat{\rho}^{g,e}_{g,g}\hat{s}^\dagger_1\otimes|g^{(1)}_d\rangle\langle e^{(1)}_d|\otimes|g^{(2)}_d\rangle\langle e^{(2)}_d|\Big)$$
$$- i\epsilon_{fl}\Big(\hat{s}_2\hat{\rho}^{g,e}_{g,g}\otimes|g^{(1)}_d\rangle\langle g^{(1)}_d|\otimes|e^{(2)}_d\rangle\langle e^{(2)}_d| - \hat{\rho}^{g,e}_{g,g}\hat{s}_2\otimes|g^{(1)}_d\rangle\langle g^{(1)}_d|\otimes|g^{(2)}_d\rangle\langle g^{(2)}_d|\Big), \tag{2.84e}$$

$$\mathcal{L}\Big(\hat{\rho}^{g,g}_{e,e}\otimes|e^{(1)}_d\rangle\langle g^{(1)}_d|\otimes|e^{(2)}_d\rangle\langle g^{(2)}_d|\Big) =$$
$$\Big(\mathcal{L}_S - \frac{\Gamma_1+\Gamma_2}{2} - i(\omega_1+\omega_2)\Big)\Big(\hat{\rho}^{g,g}_{e,e}\otimes|e^{(1)}_d\rangle\langle g^{(1)}_d|\otimes|e^{(2)}_d\rangle\langle g^{(2)}_d|\Big)$$
$$- i\epsilon_{fl}\Big(\hat{s}^\dagger_1\hat{\rho}^{g,g}_{e,e}\otimes|g^{(1)}_d\rangle\langle g^{(1)}_d|\otimes|e^{(2)}_d\rangle\langle g^{(2)}_d| - \hat{\rho}^{g,g}_{e,e}\hat{s}^\dagger_1\otimes|e^{(1)}_d\rangle\langle e^{(1)}_d|\otimes|e^{(2)}_d\rangle\langle g^{(2)}_d|\Big)$$
$$- i\epsilon_{fl}\Big(\hat{s}^\dagger_2\hat{\rho}^{g,g}_{e,e}\otimes|e^{(1)}_d\rangle\langle g^{(1)}_d|\otimes|g^{(2)}_d\rangle\langle g^{(2)}_d| - \hat{\rho}^{g,g}_{e,e}\hat{s}^\dagger_2\otimes|e^{(1)}_d\rangle\langle g^{(1)}_d|\otimes|e^{(2)}_d\rangle\langle e^{(2)}_d|\Big), \tag{2.84f}$$

$$\mathcal{L}\Big(\hat{\rho}^{e,e}_{g,g}\otimes|g^{(1)}_d\rangle\langle e^{(1)}_d|\otimes|g^{(2)}_d\rangle\langle e^{(2)}_d|\Big) =$$
$$\Big(\mathcal{L}_S - \frac{\Gamma_1+\Gamma_2}{2} + i(\omega_1+\omega_2)\Big)\Big(\hat{\rho}^{e,e}_{g,g}\otimes|g^{(1)}_d\rangle\langle e^{(1)}_d|\otimes|g^{(2)}_d\rangle\langle e^{(2)}_d|\Big)$$
$$- i\epsilon_{fl}\Big(\hat{s}_1\hat{\rho}^{e,e}_{g,g}\otimes|e^{(1)}_d\rangle\langle e^{(1)}_d|\otimes|g^{(2)}_d\rangle\langle e^{(2)}_d| - \hat{\rho}^{e,e}_{g,g}\hat{s}_1\otimes|g^{(1)}_d\rangle\langle g^{(1)}_d|\otimes|g^{(2)}_d\rangle\langle e^{(2)}_d|\Big)$$
$$- i\epsilon_{fl}\Big(\hat{s}_2\hat{\rho}^{e,e}_{g,g}\otimes|g^{(1)}_d\rangle\langle e^{(1)}_d|\otimes|e^{(2)}_d\rangle\langle e^{(2)}_d| - \hat{\rho}^{e,e}_{g,g}\hat{s}_2\otimes|g^{(1)}_d\rangle\langle e^{(1)}_d|\otimes|g^{(2)}_d\rangle\langle g^{(2)}_d|\Big), \tag{2.84g}$$

$$\mathcal{L}\Big(\hat{\rho}^{g,e}_{e,g}\otimes|e^{(1)}_d\rangle\langle g^{(1)}_d|\otimes|g^{(2)}_d\rangle\langle e^{(2)}_d|\Big) =$$
$$\Big(\mathcal{L}_S - \frac{\Gamma_1+\Gamma_2}{2} - i(\omega_1-\omega_2)\Big)\Big(\hat{\rho}^{g,e}_{e,g}\otimes|e^{(1)}_d\rangle\langle g^{(1)}_d|\otimes|g^{(2)}_d\rangle\langle e^{(2)}_d|\Big)$$
$$- i\epsilon_{fl}\Big(\hat{s}^\dagger_1\hat{\rho}^{g,e}_{e,g}\otimes|g^{(1)}_d\rangle\langle g^{(1)}_d|\otimes|g^{(2)}_d\rangle\langle e^{(2)}_d| - \hat{\rho}^{g,e}_{e,g}\hat{s}^\dagger_1\otimes|e^{(1)}_d\rangle\langle e^{(1)}_d|\otimes|g^{(2)}_d\rangle\langle e^{(2)}_d|\Big)$$

$$- i\epsilon_{fl}\Big(\hat{s}_2\hat{\rho}^{g,e}_{e,g}\otimes|e^{(1)}_d\rangle\langle g^{(1)}_d|\otimes|e^{(2)}_d\rangle\langle e^{(2)}_d| - \hat{\rho}^{g,e}_{e,g}\hat{s}_2\otimes|e^{(1)}_d\rangle\langle g^{(1)}_d|\otimes|g^{(2)}_d\rangle\langle g^{(2)}_d|\Big), \tag{2.84h}$$

$$\begin{aligned}\mathcal{L}\Big(\hat{\rho}^{e,g}_{g,e}\otimes|g^{(1)}_d\rangle\langle e^{(1)}_d|\otimes|e^{(2)}_d\rangle\langle g^{(2)}_d|\Big) &= \\ \Big(\mathcal{L}_S - \frac{\Gamma_1+\Gamma_2}{2} + i(\omega_1-\omega_2)\Big)\Big(\hat{\rho}^{e,g}_{g,e}\otimes|g^{(1)}_d\rangle\langle e^{(1)}_d|\otimes|e^{(2)}_d\rangle\langle g^{(2)}_d|\Big) &\\ - i\epsilon_{fl}\Big(\hat{s}_1\hat{\rho}^{e,g}_{g,e}\otimes|e^{(1)}_d\rangle\langle e^{(1)}_d|\otimes|e^{(2)}_d\rangle\langle g^{(2)}_d| - \hat{\rho}^{e,g}_{g,e}\hat{s}_1\otimes|g^{(1)}_d\rangle\langle g^{(1)}_d|\otimes|e^{(2)}_d\rangle\langle g^{(2)}_d|\Big) &\\ - i\epsilon_{fl}\Big(\hat{s}^\dagger_2\hat{\rho}^{e,g}_{g,e}\otimes|g^{(1)}_d\rangle\langle e^{(1)}_d|\otimes|g^{(2)}_d\rangle\langle g^{(2)}_d| - \hat{\rho}^{e,g}_{g,e}\hat{s}^\dagger_2\otimes|g^{(1)}_d\rangle\langle e^{(1)}_d|\otimes|e^{(2)}_d\rangle\langle e^{(2)}_d|\Big),\end{aligned} \tag{2.84i}$$

$$\begin{aligned}\mathcal{L}\Big(\hat{\rho}^{e,g}_{e,g}\otimes|e^{(1)}_d\rangle\langle e^{(1)}_d|\otimes|g^{(2)}_d\rangle\langle g^{(2)}_d|\Big) &= \Gamma_1\hat{\rho}^{e,g}_{e,g}\otimes|g^{(1)}_d\rangle\langle g^{(1)}_d|\otimes|g^{(2)}_d\rangle\langle g^{(2)}_d| \\ +\Big(\mathcal{L}_S-\Gamma_1\Big)\Big(\hat{\rho}^{e,g}_{e,g}\otimes|e^{(1)}_d\rangle\langle e^{(1)}_d|\otimes|g^{(2)}_d\rangle\langle g^{(2)}_d|\Big) &\\ - i\epsilon_{fl}\Big(\hat{s}^\dagger_1\hat{\rho}^{e,g}_{e,g}\otimes|g^{(1)}_d\rangle\langle e^{(1)}_d|\otimes|g^{(2)}_d\rangle\langle g^{(2)}_d| - \hat{\rho}^{e,g}_{e,g}\hat{s}_1\otimes|e^{(1)}_d\rangle\langle g^{(1)}_d|\otimes|g^{(2)}_d\rangle\langle g^{(2)}_d|\Big) &\\ - i\epsilon_{fl}\Big(\hat{s}_2\hat{\rho}^{e,g}_{e,g}\otimes|e^{(1)}_d\rangle\langle e^{(1)}_d|\otimes|e^{(2)}_d\rangle\langle g^{(2)}_d| - \hat{\rho}^{e,g}_{e,g}\hat{s}^\dagger_2\otimes|e^{(1)}_d\rangle\langle e^{(1)}_d|\otimes|g^{(2)}_d\rangle\langle e^{(2)}_d|\Big),\end{aligned} \tag{2.84j}$$

$$\begin{aligned}\mathcal{L}\Big(\hat{\rho}^{g,e}_{g,e}\otimes|g^{(1)}_d\rangle\langle g^{(1)}_d|\otimes|e^{(2)}_d\rangle\langle e^{(2)}_d|\Big) &= \Gamma_2\hat{\rho}^{g,e}_{g,e}\otimes|g^{(1)}_d\rangle\langle g^{(1)}_d|\otimes|g^{(2)}_d\rangle\langle g^{(2)}_d| \\ +\Big(\mathcal{L}_S-\Gamma_2\Big)\Big(\hat{\rho}^{g,e}_{g,e}\otimes|g^{(1)}_d\rangle\langle g^{(1)}_d|\otimes|e^{(2)}_d\rangle\langle e^{(2)}_d|\Big) &\\ - i\epsilon_{fl}\Big(\hat{s}_1\hat{\rho}^{g,e}_{g,e}\otimes|e^{(1)}_d\rangle\langle g^{(1)}_d|\otimes|e^{(2)}_d\rangle\langle e^{(2)}_d| - \hat{\rho}^{g,e}_{g,e}\hat{s}^\dagger_1\otimes|g^{(1)}_d\rangle\langle e^{(1)}_d|\otimes|e^{(2)}_d\rangle\langle e^{(2)}_d|\Big) &\\ - i\epsilon_{fl}\Big(\hat{s}^\dagger_2\hat{\rho}^{g,e}_{g,e}\otimes|g^{(1)}_d\rangle\langle g^{(1)}_d|\otimes|g^{(2)}_d\rangle\langle e^{(2)}_d| - \hat{\rho}^{g,e}_{g,e}\hat{s}_2\otimes|g^{(1)}_d\rangle\langle g^{(1)}_d|\otimes|e^{(2)}_d\rangle\langle g^{(2)}_d|\Big),\end{aligned} \tag{2.84k}$$

$$\begin{aligned}\mathcal{L}\Big(\hat{\rho}^{g,e}_{e,e}\otimes|e^{(1)}_d\rangle\langle g^{(1)}_d|\otimes|e^{(2)}_d\rangle\langle e^{(2)}_d|\Big) &= \Gamma_2\hat{\rho}^{g,e}_{e,e}\otimes|e^{(1)}_d\rangle\langle g^{(1)}_d|\otimes|g^{(2)}_d\rangle\langle g^{(2)}_d| \\ +\Big(\mathcal{L}_S-(\frac{\Gamma_1}{2}+\Gamma_2)-i\omega_1\Big)\Big(\hat{\rho}^{g,e}_{e,e}\otimes|e^{(1)}_d\rangle\langle g^{(1)}_d|\otimes|e^{(2)}_d\rangle\langle e^{(2)}_d|\Big) &\\ - i\epsilon_{fl}\Big(\hat{s}^\dagger_1\hat{\rho}^{g,e}_{e,e}\otimes|g^{(1)}_d\rangle\langle g^{(1)}_d|\otimes|e^{(2)}_d\rangle\langle e^{(2)}_d| - \hat{\rho}^{g,e}_{e,e}\hat{s}^\dagger_1\otimes|e^{(1)}_d\rangle\langle e^{(1)}_d|\otimes|e^{(2)}_d\rangle\langle e^{(2)}_d|\Big) &\\ - i\epsilon_{fl}\Big(\hat{s}^\dagger_2\hat{\rho}^{g,e}_{e,e}\otimes|e^{(1)}_d\rangle\langle g^{(1)}_d|\otimes|g^{(2)}_d\rangle\langle e^{(2)}_d| - \hat{\rho}^{g,e}_{e,e}\hat{s}_2\otimes|e^{(1)}_d\rangle\langle g^{(1)}_d|\otimes|e^{(2)}_d\rangle\langle g^{(2)}_d|\Big),\end{aligned} \tag{2.84l}$$

$$\mathcal{L}\left(\hat{\rho}^{e,e}_{g,e}\otimes|g^{(1)}_d\rangle\langle e^{(1)}_d|\otimes|e^{(2)}_d\rangle\langle e^{(2)}_d|\right)=\Gamma_2\hat{\rho}^{e,e}_{g,e}\otimes|g^{(1)}_d\rangle\langle e^{(1)}_d|\otimes|g^{(2)}_d\rangle\langle g^{(2)}_d|$$
$$+\left(\mathcal{L}_S-(\frac{\Gamma_1}{2}+\Gamma_2)+i\omega_1\right)\left(\hat{\rho}^{e,e}_{g,e}\otimes|g^{(1)}_d\rangle\langle e^{(1)}_d|\otimes|e^{(2)}_d\rangle\langle e^{(2)}_d|\right)$$
$$-i\epsilon_{fl}\left(\hat{s}_1\hat{\rho}^{e,e}_{g,e}\otimes|e^{(1)}_d\rangle\langle e^{(1)}_d|\otimes|e^{(2)}_d\rangle\langle e^{(2)}_d|-\hat{\rho}^{e,e}_{g,e}\hat{s}_1\otimes|g^{(1)}_d\rangle\langle g^{(1)}_d|\otimes|e^{(2)}_d\rangle\langle e^{(2)}_d|\right)$$
$$-i\epsilon_{fl}\left(\hat{s}^\dagger_2\hat{\rho}^{e,e}_{g,e}\otimes|g^{(1)}_d\rangle\langle e^{(1)}_d|\otimes|g^{(2)}_d\rangle\langle e^{(2)}_d|-\hat{\rho}^{e,e}_{g,e}\hat{s}_2\otimes|g^{(1)}_d\rangle\langle e^{(1)}_d|\otimes|e^{(2)}_d\rangle\langle g^{(2)}_d|\right), \tag{2.84m}$$

$$\mathcal{L}\left(\hat{\rho}^{e,g}_{e,e}\otimes|e^{(1)}_d\rangle\langle e^{(1)}_d|\otimes|e^{(2)}_d\rangle\langle g^{(2)}_d|\right)=\Gamma_1\hat{\rho}^{e,g}_{e,e}\otimes|g^{(1)}_d\rangle\langle g^{(1)}_d|\otimes|e^{(2)}_d\rangle\langle g^{(2)}_d|$$
$$+\left(\mathcal{L}_S-(\Gamma_1+\frac{\Gamma_2}{2})-i\omega_2\right)\left(\hat{\rho}^{e,g}_{e,e}\otimes|e^{(1)}_d\rangle\langle e^{(1)}_d|\otimes|e^{(2)}_d\rangle\langle g^{(2)}_d|\right)$$
$$-i\epsilon_{fl}\left(\hat{s}^\dagger_1\hat{\rho}^{e,g}_{e,e}\otimes|g^{(1)}_d\rangle\langle e^{(1)}_d|\otimes|e^{(2)}_d\rangle\langle g^{(2)}_d|-\hat{\rho}^{e,g}_{e,e}\hat{s}_1\otimes|e^{(1)}_d\rangle\langle g^{(1)}_d|\otimes|e^{(2)}_d\rangle\langle g^{(2)}_d|\right)$$
$$-i\epsilon_{fl}\left(\hat{s}^\dagger_2\hat{\rho}^{e,g}_{e,e}\otimes|e^{(1)}_d\rangle\langle e^{(1)}_d|\otimes|g^{(2)}_d\rangle\langle g^{(2)}_d|-\hat{\rho}^{e,g}_{e,e}\hat{s}^\dagger_2\otimes|e^{(1)}_d\rangle\langle e^{(1)}_d|\otimes|e^{(2)}_d\rangle\langle e^{(2)}_d|\right), \tag{2.84n}$$

$$\mathcal{L}\left(\hat{\rho}^{e,e}_{e,g}\otimes|e^{(1)}_d\rangle\langle e^{(1)}_d|\otimes|g^{(2)}_d\rangle\langle e^{(2)}_d|\right)=\Gamma_1\hat{\rho}^{e,e}_{e,g}\otimes|g^{(1)}_d\rangle\langle g^{(1)}_d|\otimes|g^{(2)}_d\rangle\langle e^{(2)}_d|$$
$$+\left(\mathcal{L}_S-(\Gamma_1+\frac{\Gamma_2}{2})+i\omega_2\right)\left(\hat{\rho}^{e,e}_{e,g}\otimes|e^{(1)}_d\rangle\langle e^{(1)}_d|\otimes|g^{(2)}_d\rangle\langle e^{(2)}_d|\right)$$
$$-i\epsilon_{fl}\left(\hat{s}^\dagger_1\hat{\rho}^{e,e}_{e,g}\otimes|g^{(1)}_d\rangle\langle e^{(1)}_d|\otimes|g^{(2)}_d\rangle\langle e^{(2)}_d|-\hat{\rho}^{e,e}_{e,g}\hat{s}_1\otimes|e^{(1)}_d\rangle\langle g^{(1)}_d|\otimes|g^{(2)}_d\rangle\langle e^{(2)}_d|\right)$$
$$-i\epsilon_{fl}\left(\hat{s}_2\hat{\rho}^{e,e}_{e,g}\otimes|e^{(1)}_d\rangle\langle e^{(1)}_d|\otimes|e^{(2)}_d\rangle\langle e^{(2)}_d|-\hat{\rho}^{e,e}_{e,g}\hat{s}_2\otimes|e^{(1)}_d\rangle\langle e^{(1)}_d|\otimes|g^{(2)}_d\rangle\langle e^{(2)}_d|\right), \tag{2.84o}$$

$$\mathcal{L}\left(\hat{\rho}^{e,e}_{e,e}\otimes|e^{(1)}_d\rangle\langle e^{(1)}_d|\otimes|e^{(2)}_d\rangle\langle e^{(2)}_d|\right)=\Gamma_1\hat{\rho}^{g,e}_{g,e}\otimes|g^{(1)}_d\rangle\langle g^{(1)}_d|\otimes|e^{(2)}_d\rangle\langle e^{(2)}_d|$$
$$+\Gamma_2\hat{\rho}^{e,e}_{e,e}\otimes|e^{(1)}_d\rangle\langle e^{(1)}_d|\otimes|g^{(2)}_d\rangle\langle g^{(2)}_d|$$
$$+\left(\mathcal{L}_S-\Gamma_1-\Gamma_2\right)\left(\hat{\rho}^{e,e}_{e,e}\otimes|e^{(1)}_d\rangle\langle e^{(1)}_d|\otimes|e^{(2)}_d\rangle\langle e^{(2)}_d|\right)$$
$$-i\epsilon_{fl}\left(\hat{s}^\dagger_1\hat{\rho}^{e,e}_{e,e}\otimes|g^{(1)}_d\rangle\langle e^{(1)}_d|\otimes|e^{(2)}_d\rangle\langle e^{(2)}_d|-\hat{\rho}^{e,e}_{e,e}\hat{s}_1\otimes|e^{(1)}_d\rangle\langle g^{(1)}_d|\otimes|e^{(2)}_d\rangle\langle e^{(2)}_d|\right)$$
$$-i\epsilon_{fl}\left(\hat{s}^\dagger_2\hat{\rho}^{e,e}_{e,e}\otimes|g^{(1)}_d\rangle\langle g^{(1)}_d|\otimes|g^{(2)}_d\rangle\langle e^{(2)}_d|-\hat{\rho}^{e,e}_{e,e}\hat{s}_2\otimes|g^{(1)}_d\rangle\langle g^{(1)}_d|\otimes|e^{(2)}_d\rangle\langle g^{(2)}_d|\right). \tag{2.84p}$$

The summation over the right-hand sides of the sixteen expressions in Eqs. (2.84a)–

(2.84p) vanishes, as $\mathcal{L}\hat{\rho}_{ss} = 0$. As a consequence, we can reorder this summation into sixteen vanishing terms, each one proportional to a different product of the form $|k_d^{(1)}\rangle\langle l_d^{(1)}| \otimes |m_d^{(2)}\rangle\langle n_d^{(2)}|$. We obtain the following hierarchy of coupled equations:

$$0 = \mathcal{L}_S\hat{\rho}^{g,g}_{g,g} - i\epsilon_{fl}\Big(\hat{s}_1^\dagger\hat{\rho}^{g,g}_{e,g} - \hat{\rho}^{e,g}_{g,g}\hat{s}_1 + \hat{s}_2^\dagger\hat{\rho}^{g,g}_{g,e} - \hat{\rho}^{g,e}_{g,g}\hat{s}_2\Big), \tag{2.85a}$$

$$0 = (\mathcal{L}_S - \frac{\Gamma_1}{2} - i\omega_1)\hat{\rho}^{g,g}_{e,g} + \Gamma_2\hat{\rho}^{g,e}_{e,e} - i\epsilon_{fl}\Big(\hat{s}_1\hat{\rho}^{g,g}_{g,g} - \hat{\rho}^{e,g}_{e,g}\hat{s}_1 + \hat{s}_2^\dagger\hat{\rho}^{g,g}_{e,e} - \hat{\rho}^{g,e}_{e,g}\hat{s}_2\Big), \tag{2.85b}$$

$$0 = (\mathcal{L}_S - \frac{\Gamma_1}{2} + i\omega_1)\hat{\rho}^{e,g}_{g,g} + \Gamma_2\hat{\rho}^{e,e}_{g,e} - i\epsilon_{fl}\Big(\hat{s}_1^\dagger\hat{\rho}^{e,g}_{e,g} - \hat{\rho}^{g,g}_{g,g}\hat{s}_1^\dagger + \hat{s}_2^\dagger\hat{\rho}^{e,g}_{g,e} - \hat{\rho}^{e,e}_{g,g}\hat{s}_2\Big), \tag{2.85c}$$

$$0 = (\mathcal{L}_S - \frac{\Gamma_2}{2} - i\omega_2)\hat{\rho}^{g,g}_{g,e} + \Gamma_1\hat{\rho}^{e,g}_{e,e} - i\epsilon_{fl}\Big(\hat{s}_2\hat{\rho}^{g,g}_{g,g} - \hat{\rho}^{g,e}_{g,e}\hat{s}_2 + \hat{s}_1^\dagger\hat{\rho}^{g,g}_{e,e} - \hat{\rho}^{e,g}_{g,e}\hat{s}_1\Big), \tag{2.85d}$$

$$0 = (\mathcal{L}_S - \frac{\Gamma_2}{2} + i\omega_2)\hat{\rho}^{g,e}_{g,g} + \Gamma_1\hat{\rho}^{e,e}_{e,g} - i\epsilon_{fl}\Big(\hat{s}_2^\dagger\hat{\rho}^{g,e}_{e,g} - \hat{\rho}^{g,g}_{g,g}\hat{s}_2^\dagger + \hat{s}_1^\dagger\hat{\rho}^{g,e}_{e,g} - \hat{\rho}^{e,e}_{g,g}\hat{s}_1\Big), \tag{2.85e}$$

$$0 = \Big(\mathcal{L}_S - \frac{\Gamma_1+\Gamma_2}{2} - i(\omega_1+\omega_2)\Big)\hat{\rho}^{g,g}_{e,e} - i\epsilon_{fl}\Big(\hat{s}_1\hat{\rho}^{g,g}_{g,e} + \hat{s}_2\hat{\rho}^{g,g}_{e,g} - \hat{\rho}^{e,g}_{e,e}\hat{s}_1 - \hat{\rho}^{g,e}_{e,e}\hat{s}_2\Big), \tag{2.85f}$$

$$0 = \Big(\mathcal{L}_S - \frac{\Gamma_1+\Gamma_2}{2} + i(\omega_1+\omega_2)\Big)\hat{\rho}^{e,e}_{g,g} - i\epsilon_{fl}\Big(\hat{s}_1^\dagger\hat{\rho}^{e,e}_{e,g} + \hat{s}_2^\dagger\hat{\rho}^{e,e}_{g,e} - \hat{\rho}^{g,e}_{g,g}\hat{s}_1^\dagger - \hat{\rho}^{e,g}_{g,g}\hat{s}_2^\dagger\Big), \tag{2.85g}$$

$$0 = \Big(\mathcal{L}_S - \frac{\Gamma_1+\Gamma_2}{2} - i(\omega_1-\omega_2)\Big)\hat{\rho}^{g,e}_{e,g} - i\epsilon_{fl}\Big(\hat{s}_1\hat{\rho}^{g,e}_{g,g} + \hat{s}_2^\dagger\hat{\rho}^{g,e}_{e,e} - \hat{\rho}^{e,e}_{e,g}\hat{s}_1 - \hat{\rho}^{g,g}_{e,g}\hat{s}_2^\dagger\Big), \tag{2.85h}$$

$$0 = \Big(\mathcal{L}_S - \frac{\Gamma_1+\Gamma_2}{2} + i(\omega_1-\omega_2)\Big)\hat{\rho}^{e,g}_{g,e} - i\epsilon_{fl}\Big(\hat{s}_1^\dagger\hat{\rho}^{e,g}_{e,e} + \hat{s}_2\hat{\rho}^{e,g}_{g,g} - \hat{\rho}^{g,g}_{g,e}\hat{s}_1^\dagger - \hat{\rho}^{e,e}_{g,e}\hat{s}_2\Big), \tag{2.85i}$$

$$0 = \Big(\mathcal{L}_S - \Gamma_1\Big)\hat{\rho}^{e,g}_{e,g} + \Gamma_2\hat{\rho}^{e,e}_{e,e} - i\epsilon_{fl}\Big(\hat{s}_1\hat{\rho}^{e,g}_{g,g} + \hat{s}_2^\dagger\hat{\rho}^{e,g}_{e,e} - \hat{\rho}^{g,g}_{e,g}\hat{s}_1^\dagger - \hat{\rho}^{e,g}_{e,e}\hat{s}_2\Big), \tag{2.85j}$$

$$0 = \Big(\mathcal{L}_S - \Gamma_2\Big)\hat{\rho}^{g,e}_{g,e} + \Gamma_1\hat{\rho}^{e,e}_{e,e} - i\epsilon_{fl}\Big(\hat{s}_1^\dagger\hat{\rho}^{g,e}_{e,e} + \hat{s}_2\hat{\rho}^{g,e}_{g,g} - \hat{\rho}^{e,e}_{g,e}\hat{s}_1 - \hat{\rho}^{g,g}_{g,e}\hat{s}_2^\dagger\Big), \tag{2.85k}$$

$$0 = \Big(\mathcal{L}_S - (\frac{\Gamma_1}{2}+\Gamma_2) - i\omega_1\Big)\hat{\rho}^{g,e}_{e,e} - i\epsilon_{fl}\Big(\hat{s}_1\hat{\rho}^{g,e}_{g,e} + \hat{s}_2\hat{\rho}^{g,e}_{e,g} - \hat{\rho}^{e,e}_{e,e}\hat{s}_1 - \hat{\rho}^{g,g}_{e,e}\hat{s}_2^\dagger\Big), \tag{2.85l}$$

$$0 = \Big(\mathcal{L}_S - (\frac{\Gamma_1}{2}+\Gamma_2) + i\omega_1\Big)\hat{\rho}^{e,e}_{g,e} - i\epsilon_{fl}\Big(\hat{s}_1^\dagger\hat{\rho}^{e,e}_{e,e} + \hat{s}_2\hat{\rho}^{e,e}_{g,g} - \hat{\rho}^{g,e}_{g,e}\hat{s}_1^\dagger - \hat{\rho}^{e,g}_{g,e}\hat{s}_2^\dagger\Big), \tag{2.85m}$$

$$0 = \left(\mathcal{L}_S - (\Gamma_1 + \frac{\Gamma_2}{2}) - i\omega_2\right)\hat{\rho}^{e,g}_{e,e} - i\epsilon_{fl}\left(\hat{s}_1\hat{\rho}^{e,g}_{g,e} + \hat{s}_2\hat{\rho}^{e,g}_{e,g} - \hat{\rho}^{g,g}_{e,e}\hat{s}^\dagger_1 - \hat{\rho}^{e,e}_{e,e}\hat{s}_2\right), \tag{2.85n}$$

$$0 = \left(\mathcal{L}_S - (\Gamma_1 + \frac{\Gamma_2}{2}) + i\omega_2\right)\hat{\rho}^{e,e}_{e,g} - i\epsilon_{fl}\left(\hat{s}_1\hat{\rho}^{e,e}_{g,g} + \hat{s}^\dagger_2\hat{\rho}^{e,e}_{e,e} - \hat{\rho}^{g,e}_{e,g}\hat{s}^\dagger_1 - \hat{\rho}^{e,g}_{e,g}\hat{s}^\dagger_2\right), \tag{2.85o}$$

$$0 = \left(\mathcal{L}_S - (\Gamma_1 + \Gamma_2)\right)\hat{\rho}^{e,e}_{e,e} - i\epsilon_{fl}\left(\hat{s}_1\hat{\rho}^{e,e}_{g,e} + \hat{s}_2\hat{\rho}^{e,e}_{e,g} - \hat{\rho}^{g,e}_{e,e}\hat{s}^\dagger_1 - \hat{\rho}^{e,g}_{e,e}\hat{s}^\dagger_2\right). \tag{2.85p}$$

Solving this system of equations would provide the sixteen density matrices $\hat{\rho}^{l,n}_{k,m}$. However, the direct resolution of such a system of equations is not simple. In the limit of weak coupling ϵ_{fl} in which we are interested, these equations can be simplified by neglecting some terms. More specifically, we take into account that the density matrix $\hat{\rho}^{l,n}_{k,m}$ scales as ϵ^N_{fl}, with N the number of indices k, l, m, n that corresponds to an excited state [172]. We then approximate all the above equations to leading order in ϵ_{fl}. In this way, we first approximate Eq. (2.85a) up to ϵ^0_{fl} order, which yields

$$\mathcal{L}_S\hat{\rho}^{g,g}_{g,g} \approx 0. \tag{2.86}$$

Thus, $\hat{\rho}^{g,g}_{g,g}$ is an eigenoperator of $\mathcal{L}_S$ with vanishing eigenvalue. As a result, $\hat{\rho}^{g,g}_{g,g}$ corresponds to the steady state of S in the absence of the atom detectors.

Moreover, approximating Eqs. (2.85b)–(2.85e) up to ϵ^1_{fl} order leads to

$$(\mathcal{L}_S - \frac{\Gamma_1}{2} - i\omega_1)\hat{\rho}^{g,g}_{e,g} \approx i\epsilon_{fl}\hat{s}_1\hat{\rho}^{g,g}_{g,g}, \tag{2.87a}$$

$$(\mathcal{L}_S - \frac{\Gamma_1}{2} + i\omega_1)\hat{\rho}^{e,g}_{g,g} \approx -i\epsilon_{fl}\hat{\rho}^{g,g}_{g,g}\hat{s}^\dagger_1, \tag{2.87b}$$

$$(\mathcal{L}_S - \frac{\Gamma_2}{2} - i\omega_2)\hat{\rho}^{g,g}_{g,e} \approx i\epsilon_{fl}\hat{s}_2\hat{\rho}^{g,g}_{g,g}, \tag{2.87c}$$

$$(\mathcal{L}_S - \frac{\Gamma_2}{2} + i\omega_2)\hat{\rho}^{g,e}_{g,g} \approx -i\epsilon_{fl}\hat{\rho}^{g,g}_{g,g}\hat{s}^\dagger_2. \tag{2.87d}$$

Thus, the density matrices $\hat{\rho}^{g,g}_{e,g}$, $\hat{\rho}^{e,g}_{g,g}$, $\hat{\rho}^{g,g}_{g,e}$, and $\hat{\rho}^{g,e}_{g,g}$ can be calculated from $\hat{\rho}^{g,g}_{g,g}$. This calculation is performed directly in the Hilbert space of S. Further, we approximate Eqs. (2.85f)–(2.85k) up to ϵ^2_{fl} order and obtain

$$\left(\mathcal{L}_S - \frac{\Gamma_1+\Gamma_2}{2} - i(\omega_1+\omega_2)\right)\hat{\rho}^{g,g}_{e,e} \approx i\epsilon_{fl}\left(\hat{s}_1\hat{\rho}^{g,g}_{g,e} + \hat{s}_2\hat{\rho}^{g,g}_{e,g}\right), \tag{2.88a}$$

$$\left(\mathcal{L}_S - \frac{\Gamma_1+\Gamma_2}{2} + i(\omega_1+\omega_2)\right)\hat{\rho}^{e,e}_{g,g} \approx -i\epsilon_{fl}\left(\hat{\rho}^{g,e}_{g,g}\hat{s}^\dagger_1 + \hat{\rho}^{e,g}_{g,g}\hat{s}^\dagger_2\right), \tag{2.88b}$$

$$\left(\mathcal{L}_S - \frac{\Gamma_1+\Gamma_2}{2} - i(\omega_1-\omega_2)\right)\hat{\rho}^{g,e}_{e,g} \approx i\epsilon_{fl}\left(\hat{s}_1\hat{\rho}^{g,e}_{g,g} - \hat{\rho}^{g,g}_{e,g}\hat{s}^\dagger_2\right), \tag{2.88c}$$

$$\left(\mathcal{L}_S - \frac{\Gamma_1+\Gamma_2}{2} + i(\omega_1-\omega_2)\right)\hat{\rho}^{e,g}_{g,e} \approx -i\epsilon_{fl}\left(\hat{\rho}^{g,g}_{g,e}\hat{s}^\dagger_1 - \hat{s}_2\hat{\rho}^{e,g}_{g,g}\right), \tag{2.88d}$$

$$\Big(\mathcal{L}_S - \Gamma_1\Big)\hat{\rho}^{e,g}_{e,g} \approx i\epsilon_{fl}\Big(\hat{s}_1\hat{\rho}^{e,g}_{g,g} - \hat{\rho}^{g,g}_{e,g}\hat{s}_1^\dagger\Big), \tag{2.88e}$$

$$\Big(\mathcal{L}_S - \Gamma_2\Big)\hat{\rho}^{g,e}_{g,e} \approx i\epsilon_{fl}\Big(\hat{s}_2\hat{\rho}^{g,e}_{g,g} - \hat{\rho}^{g,g}_{g,e}\hat{s}_2^\dagger\Big). \tag{2.88f}$$

These equations allow us to solve the density matrices $\hat{\rho}^{g,g}_{e,e}$, $\hat{\rho}^{e,e}_{g,g}$, $\hat{\rho}^{g,e}_{e,g}$, $\hat{\rho}^{e,g}_{g,e}$, $\hat{\rho}^{e,g}_{e,g}$, and $\hat{\rho}^{g,e}_{g,e}$ from the density matrices that have been previously calculated using Eqs. (2.86) and (2.87a)–(2.87d). The calculation is again carried out in the Hilbert space of S. Importantly, we recall that the density matrices $\hat{\rho}^{e,g}_{e,g}$ and $\hat{\rho}^{g,e}_{g,e}$ give the denominator of $g^{(2)}(\omega_1,\omega_2;0)$ [Eqs. (2.83a)–(2.83b)]. Furthermore, approximating Eqs. (2.85l)–(2.85o) to ϵ^3_{fl} order yields

$$\Big(\mathcal{L}_S - (\frac{\Gamma_1}{2}+\Gamma_2) - i\omega_1\Big)\hat{\rho}^{g,e}_{e,e} \approx i\epsilon_{fl}\Big(\hat{s}_1\hat{\rho}^{g,e}_{g,e} + \hat{s}_2\hat{\rho}^{g,e}_{e,g} - \hat{\rho}^{g,g}_{e,e}\hat{s}_2^\dagger\Big), \tag{2.89a}$$

$$\Big(\mathcal{L}_S - (\frac{\Gamma_1}{2}+\Gamma_2) + i\omega_1\Big)\hat{\rho}^{e,e}_{g,e} \approx i\epsilon_{fl}\Big(\hat{s}_2\hat{\rho}^{e,e}_{g,g} - \hat{\rho}^{g,e}_{g,e}\hat{s}_1^\dagger - \hat{\rho}^{e,g}_{g,e}\hat{s}_2^\dagger\Big), \tag{2.89b}$$

$$\Big(\mathcal{L}_S - (\Gamma_1+\frac{\Gamma_2}{2}) - i\omega_2\Big)\hat{\rho}^{e,g}_{e,e} \approx i\epsilon_{fl}\Big(\hat{s}_1\hat{\rho}^{e,g}_{g,e} + \hat{s}_2\hat{\rho}^{e,g}_{e,g} - \hat{\rho}^{e,e}_{e,e}\hat{s}_2\Big), \tag{2.89c}$$

$$\Big(\mathcal{L}_S - (\Gamma_1+\frac{\Gamma_2}{2}) + i\omega_2\Big)\hat{\rho}^{e,e}_{e,g} \approx i\epsilon_{fl}\Big(\hat{s}_1\hat{\rho}^{e,e}_{g,g} - \hat{\rho}^{g,e}_{e,g}\hat{s}_1^\dagger - \hat{\rho}^{e,g}_{e,g}\hat{s}_2^\dagger\Big). \tag{2.89d}$$

These equations enable to obtain $\hat{\rho}^{g,e}_{e,e}$, $\hat{\rho}^{e,e}_{g,e}$, $\hat{\rho}^{e,g}_{e,e}$, and $\hat{\rho}^{e,e}_{e,g}$. The latter density matrices can be substituted in Eq. (2.85p), which finally allows us to compute $\hat{\rho}^{e,e}_{e,e}$ and, thus, the numerator $\langle\hat{\zeta}_1^\dagger\hat{\zeta}_1(0)\hat{\zeta}_2^\dagger\hat{\zeta}_2(0)\rangle_{\rm ss}$ of $g^{(2)}(\omega_1,\omega_2;0)$ [Eq. (2.82)].

In summary, the procedure described in this section allows us to calculate in succession the sixteen density matrices $\hat{\rho}^{l,n}_{k,m}$, starting from $\hat{\rho}^{g,g}_{g,g}$, which describes the steady state density matrix of S in the absence of detectors. Importantly, the calculation of these matrices can be done directly in the Hilbert space of S. $g^{(2)}(\omega_1,\omega_2;0)$ can then be obtained from the traces of three of these matrices (namely, of $\hat{\rho}^{e,g}_{e,g}$, $\hat{\rho}^{g,e}_{g,e}$, and $\hat{\rho}^{e,e}_{e,e}$) using Eqs. (2.72), (2.82), (2.83a) and (2.83b). Last, we note that the resulting $g^{(2)}(\omega_1,\omega_2;0)$ is independent of the specific value of ϵ_{fl}, as the dependence on ϵ_{fl} of the numerator [$\propto\epsilon^4_{fl}$] and of the denominator [$\propto\epsilon^4_{fl}$] of $g^{(2)}(\omega_1,\omega_2;0)$ cancel out.

2.4.4 Frequency-resolved intensity correlation of light emitted from a single quantum emitter

In this section, we calculate the FRIC of light emitted from a single QE and show that the analysis of $g^{(2)}(\omega_1,\omega_2;0)$ as a function of ω_1 and ω_2 provides useful information on the emission mechanisms of the system.

We first analyze the FRIC for relatively weak laser intensity, so that the eigenstates of the driven QE correspond to the bare states (as described in Section 1.5.2). In particular, we consider a laser resonantly tuned to the transition frequency

of the QE ($\omega_L = \omega_0$) with Rabi frequency fixed at $\Omega = \gamma_0/10$. We recall that the dynamics of the driven QE in the rotating frame at the laser frequency is governed by the MME in Eq. (1.230). We use this MME to compute $g^{(2)}(\omega_1, \omega_2; 0)$ using the procedure described in Section 2.4.3, with the effective Hamiltonian describing the interaction between the QE and the detectors given as

$$\hat{H}_{S-fl} = \hbar \sum_j \epsilon_{fl}(\hat{\zeta}_j^\dagger \hat{\sigma} + \hat{\zeta}_j \hat{\sigma}^\dagger). \tag{2.90}$$

Thus, the system operators in Eq. (2.73) are $\hat{s}_j = \hat{\sigma}$ and $\hat{s}_j^\dagger = \hat{\sigma}^\dagger$. Additionally, we fix the linewidth of the filters at $\Gamma_j = \gamma_0/10$.

The top panel of Fig. 2.7a shows the incoherent emission spectrum $S_i(\omega)$ of the single quantum emitter [Eq. (2.34)], which is the same as in Fig. 2.2b and is discussed in Section 2.1.6. In the bottom panel of Fig. 2.7a, we plot a map showing the dependence of $g^{(2)}(\omega_1, \omega_2; 0)$ on ω_1 and ω_2. The x-axis in this map corresponds to the normalized laser detuning of the photons arriving at detector $j = 1$, $(\omega_1 - \omega_L)/\gamma_0 = (\omega_1 - \omega_0)/\gamma_0$, while the y-axis corresponds to the normalized laser detuning of the photons arriving at detector $j = 2$, $(\omega_2 - \omega_L)/\gamma_0 = (\omega_2 - \omega_0)/\gamma_0$. In the FRIC map, we use the standard color convention [173–178], where the blue color corresponds to antibunched emission [$g^{(2)}(\omega_1, \omega_2; 0) < 1$], red to bunched emission [$g^{(2)}(\omega_1, \omega_2; 0) > 1$], and white to Poissonian statistics [$g^{(2)}(\omega_1, \omega_2; 0) = 1$]. To improve the visibility of both the antibunched and bunched emissions, we additionally make use of a linear scale in the range $0 \leq g^{(2)}(\omega_1, \omega_2; 0) \leq 1$ and a logarithmic scale in the range $1 \leq g^{(2)}(\omega_1, \omega_2; 0) \leq 50$.

We find that the FRIC map in Fig. 2.7a exhibits a strongly antibunched background, which can be understood from the value of the color-blind intensity correlation $g^{(2)}(0) = 0$ provided by a single QE (see Section 2.3.3). On top of this strongly antibunched background, different lines emerge, which constitute a signature of the different mechanisms of photon emission from the driven QE. To analyze these lines, it is convenient to consider the laser field to be quantized, so that the eigenstates of the system are distributed in infinite rungs, each rung with a fixed number of total excitations (including photons, see Section 2.1.6). Under weak enough laser driving, we recall that the eigenstates in the rung n (with n excitations) correspond to the bare states $|g, n\rangle$ and $|e, n-1\rangle$, which are schematically represented in Fig. 2.7b. As $|g, n\rangle$ and $|e, n-1\rangle$ are degenerate in energy (for $\omega_L = \omega_0$, as chosen here), the one-photon transitions from eigenstates of subsequent rungs (e.g., from $|e, n\rangle$ to $|g, n\rangle$) leads to the emission of photons of frequency $\omega_L = \omega_0$, which is represented by a solid orange arrow in Fig. 2.7b. Notably, the emission of one photon due to such a one-photon transition does not influence the frequency of the next emitted photon. As a consequence, the correlations $g^{(2)}(\omega_1 = \omega_0, \omega_2 = \omega'; 0)$ and $g^{(2)}(\omega_1 = \omega', \omega_2 = \omega_0; 0)$ are mostly independent of ω', which gives rise to a vertical line and a horizontal line at $\omega_1 = \omega_0$ and $\omega_2 = \omega_0$, respectively. These one-photon transitions can also be identified by the peaks in the emission spectrum of the system, shown on top of Fig. 2.7a.

Moreover, the FRIC map in Fig. 2.7a also exhibits an antidiagonal line at

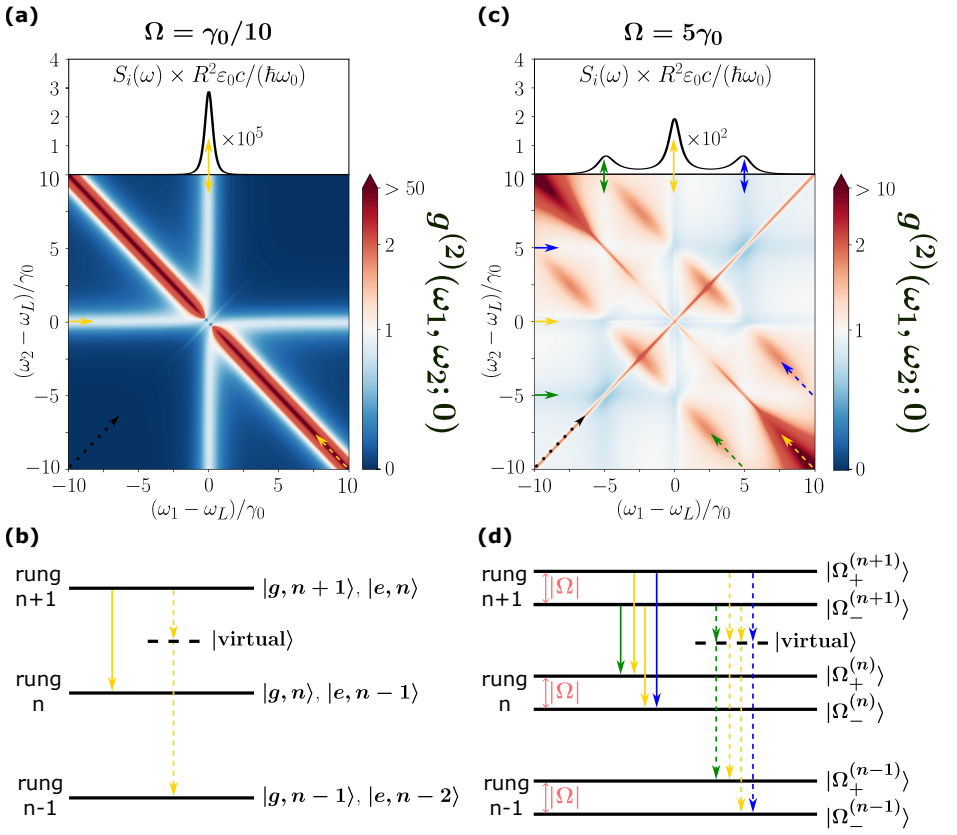

Figure 2.7: FRIC for a resonantly driven two-level QE. [(a),(c)] Incoherent emission spectra (top panels) and FRIC maps (bottom panels) for Rabi frequency (a) $\Omega = \gamma_0/10$, and (c) $\Omega = 5\gamma_0$. The incoherent emission spectra $S_i(\omega)$ are scaled by $R^2\varepsilon_0 c/(\hbar\omega_0)$, with R the distance to the detector in the far-field region, and additionally by 10^5 in (a) and by 10^2 in (c). In the FRIC maps, we follow the standard color convention, where blue color means antibunched emission, red color bunched emission, and white Poissonian statistics. In the color bar, we use a linear scale in the interval $0 \leq g^{(2)}(\omega_1, \omega_2; 0) \leq 1$ and a logarithmic scale for $g^{(2)}(\omega_1, \omega_2; 0) \geq 1$. Solid arrows are used to mark the horizontal and vertical lines in the FRIC maps, while dashed arrows are used for the antidiagonal lines related to two-photon processes through intermediate virtual states. Black dotted arrows indicate the diagonal line at $\omega_1 = \omega_2$, corresponding to the detection of two photons of identical frequency. We consider filters with linewidth $\Gamma_j = \gamma_0/10$. [(b),(d)] Schematic representations of the eigenstates in rungs $n-1$, n, and $n+1$, together with the corresponding one-photon transitions between eigenstates (solid arrows) and two-photon transitions through intermediate virtual states (dashed arrows). In (b) the eigenstates in rung n correspond to the bare states $|g, n\rangle$ and $|e, n-1\rangle$, whereas in (d) the eigenstates in rung n correspond to the dressed states $|\Omega_+^{(n)}\rangle$ and $|\Omega_-^{(n)}\rangle$.

$\omega_1+\omega_2 = 2\omega_L$ (indicated by a dashed orange arrow), which reveals the emergence of two-photon transitions through intermediate virtual states, called *leapfrog processes* [173]. More specifically, antidiagonal lines unveil the emission of a photon of frequency ω_1 (ω_2) due to a transition from an initial eigenstate in the rung $n+1$ to a virtual state, followed by the emission of a photon of frequency ω_2 (ω_1) due to relaxation from the virtual state to another eigenstate in the rung $n-1$ (see the dashed orange arrow in Fig. 2.7b). The frequency difference between the initial and final eigenstates determines the value of $\omega_1+\omega_2$ satisfied along the antidiagonal line. Throughout this thesis, dashed arrows in FRIC maps indicate leapfrog processes, while solid arrows indicate one-photon emission processes. Additionally, as these antidiagonal lines correspond to the correlated emission of two photons, they are usually characterized by strong bunching. Importantly, these two-photon processes cannot be identified in the emission spectrum, nor in the color-blind intensity correlation, which highlights the advantages of the FRIC in providing additional information about the emission mechanisms of the system.

We next explore in Fig. 2.7c the incoherent emission spectrum (top panel) and the FRIC map (bottom panel) of the QE under strong driving. We fix $\Omega = 5\gamma_0$, so that the eigenstates of the system are modified by the laser driving and correspond to the dressed states described in Sections 1.5.2 and 2.1.6. Specifically, the two eigenstates in the rung n are the dressed states $|\Omega_+^{(n)}\rangle$ and $|\Omega_-^{(n)}\rangle$ [Eqs. (2.37a)–(2.37b)], with frequency splitting $|\Omega|$, as schematically represented in Fig. 2.7d. As discussed in Section 2.1.6, the frequency splitting between the dressed states enables the emission of photons at frequencies $\omega_L - \Omega = \omega_0 - \Omega$ (marked with solid green arrows in Figs. 2.7c and 2.7d) and $\omega_L + \Omega = \omega_0 + \Omega$ (solid blue arrows), in addition to the photons emitted at $\omega_L = \omega_0$ (solid orange arrows). As a consequence, the Mollow triplet emerges in the incoherent emission spectrum on top of Fig. 2.7c. Importantly, the large variety of one-photon emission processes under strong driving also gives rise to the emergence of three horizontal lines and three vertical lines in the FRIC map on the bottom panel of Fig. 2.7c. Similarly, the FRIC map in Fig. 2.7c exhibits two additional antidiagonal lines (compared to the FRIC map in Fig. 2.7a), one corresponding to a leapfrog process with $|\Omega_+^{(n+1)}\rangle$ as initial state and $|\Omega_-^{(n-1)}\rangle$ as final state [which fulfills $\omega_1+\omega_2 = 2\omega_L + |\Omega|$ and is represented with a dashed blue arrow in Fig. 2.7b] and another antidiagonal line corresponding to a leapfrog process with $|\Omega_-^{(n+1)}\rangle$ as initial state and with $|\Omega_+^{(n-1)}\rangle$ as final state [which fulfills $\omega_1+\omega_2 = 2\omega_L - |\Omega|$ and is represented with a dashed green arrow in Fig. 2.7b].

Finally, we note that diagonal lines at $\omega_1 = \omega_2$ can be observed in the FRIC maps shown in Figs. 2.7a and 2.7c (hardly observable in Fig. 2.7a), which are marked with dotted black arrows. These lines correspond to the simultaneous detection of two identical photons. The intensity correlation along this diagonal line is twice that at the nearby points in the map [173, 174]. The reason is that a coincidence is counted no matter which photon arrives at detector $j=1$ and which one arrives at the detector $j=2$, in contrast to the case in which $\omega_1 \neq \omega_2$, which doubles the probability of a coincidence in the detectors.

CHAPTER 3

INTENSITY CORRELATION OF ZERO-PHONON-LINE PHOTONS FROM TWO INTERACTING QUANTUM EMITTERS

We analyze in this chapter the statistical properties of the light emitted into the Zero-Phonon Line (ZPL) from two quantum emitters separated by short distances. To this end, we first derive the Hamiltonian that describes the interaction between the electromagnetic vacuum field and the quantum emitters. We then trace out the degrees of freedom of the electromagnetic vacuum field using the Markovian master equation formalism, revealing that the vacuum field mediates the dipole-dipole interaction between the two emitters. Additionally, we discuss how the dipole-dipole interaction can modify the eigenstates of the emitters, as well as their energies and lifetimes. Notably, we introduce in this analysis the combined Debye-Waller/Franck-Condon factor, which effectively accounts for the influence of the internal vibrations of the emitters and the phonons of the host medium on the dipole-dipole interaction.

Afterwards, we perform a systematic analysis of both the color-blind intensity correlation and the frequency-resolved intensity correlation (FRIC) of light emitted into the ZPL from two interacting quantum emitters. On the one hand, we find that the color-blind intensity correlation can be tailored from strong antibunching to strong bunching by tuning the laser frequency and intensity. On the other hand, the analysis of the FRIC provides further information about the different relaxation processes underlying photon emission, allowing us to unveil one-photon and two-photon emission processes that cannot be retrieved from either the emission spectrum nor the color-blind intensity correlation. These results show that two

interacting emitters are a versatile and practical source of quantum light and highlight the usefulness of the intensity correlation in unveiling complex dynamics in this system.

3.1 Dynamics of two interacting quantum emitters

We show in this section that the electromagnetic vacuum field mediates the dipole-dipole interaction between two quantum emitters. Our starting point is the minimal coupling form of the Hamiltonian that describes the interaction between the electromagnetic field and a set of charged particles (Section 1.2.4). We consider that these charged particles are distributed into two separated space regions, representing two different neutral systems (e.g., two atoms). We then apply the Power-Zienau transformation (Section 1.2.5) and derive the multipolar form of the Hamiltonian. This latter Hamiltonian is used to trace out the Hilbert space of the electromagnetic vacuum field and derive the Markovian master equation (MME) that governs the reduced dynamics of the emitters. This MME includes a term in the Hamiltonian that describes the coherent dipole-dipole interaction, as well as dissipators that capture the incoherent dipole-dipole interaction. The emergence of these terms thus shows that the emitter-emitter interaction is mediated by the electromagnetic vacuum field.

3.1.1 Minimal coupling form of the Hamiltonian for two separated systems of charges

In this section, we present the minimal coupling form of the Hamiltonian describing the interaction between the electromagnetic field and two separated systems of charged particles. The general form of the minimal coupling Hamiltonian $\hat{H}^{mc}$ has been derived in Section 1.2.4 and is given in Eq. (1.98). In general, this Hamiltonian can be decomposed into three terms, namely $\hat{H}^{mc} = \hat{H}_{F\perp} + \hat{H}_{F\parallel} + \hat{H}_K$. Here, $\hat{H}_{F\perp}$ corresponds to the contribution from the transverse electromagnetic vacuum field and is formally identical to the Hamiltonian of the electromagnetic field in the absence of radiation sources (Section 1.1.5), whereas $\hat{H}_{F\parallel}$ accounts for the contribution from the longitudinal electromagnetic field and can be identified as the quantized Coulomb electrostatic energy of the charges [Eq. (1.90)]. Additionally, $\hat{H}_K$ corresponds to the kinetic Hamiltonian of the particles and accounts for the interaction of the particles with the electromagnetic field.

We now consider two systems, labeled by $j = 1, 2$, of separated charged particles. Each of these two systems has center of mass at $\mathbf{r}_0^{(j)}$ and neutral global charge. Under the long-wavelength approximation (Section 1.2.5), the Hamiltonian of the

two separated systems of charges can be written in the minimal coupling form as

$$\begin{aligned}\hat{H}^{mc} &= \hat{H}_{F\perp} + \hat{H}_K + \hat{H}_{F\parallel} \\ &= \sum_{\mathbf{k},s} \hbar\omega_{\mathrm{k}}(\hat{a}^\dagger_{\mathbf{k}s}\hat{a}_{\mathbf{k}s} + \frac{1}{2}) + \sum_j \sum_i \frac{1}{2m_i^{(j)}}\left(\hat{\mathbf{p}}_i^{(j)} - q_i^{(j)}\hat{\mathbf{A}}(\mathbf{r}_0^{(j)})\right)^2 + \hat{H}_{F\parallel},\end{aligned} \tag{3.1}$$

where $m_i^{(j)}$ and $q_i^{(j)}$ represents the mass and charge, respectively, of the particle i of system j, whereas $\hat{\mathbf{p}}_i^{(j)}$ is the canonical momentum operator of the same particle. The first term in the second line of Eq. (3.1) corresponds to $\hat{H}_{F\perp}$, whereas the second term corresponds to $\hat{H}_K$. Importantly, the contribution from the longitudinal electromagnetic field can be decomposed as

$$\hat{H}_{F\parallel} = \hat{H}_{F\parallel}^{(1)} + \hat{H}_{F\parallel}^{(2)} + \hat{H}_{F\parallel}^{(12)}, \tag{3.2}$$

where $\hat{H}_{F\parallel}^{(1)}$ and $\hat{H}_{F\parallel}^{(2)}$ are the Hamiltonian resulting from the quantization of the Coulomb electrostatic energy of each of the system of charges (as if the other system were not present), whereas $\hat{H}_{F\parallel}^{(12)}$ is given by the quantization of the electrostatic interaction energy between the two system of charges. More specifically, $\hat{H}_{F\parallel}^{(12)}$ can be obtained by taking the classical expression describing the electrostatic interaction energy between two dipoles (each representing the net dipole moment of each system of charges) [121, 132] and promoting the classical dipole moments $\boldsymbol{\mu}^{(1)}$ and $\boldsymbol{\mu}^{(2)}$ to quantum-mechanical operators $\hat{\boldsymbol{\mu}}^{(1)}$ and $\hat{\boldsymbol{\mu}}^{(2)}$. We obtain

$$\hat{H}_{F\parallel}^{(12)} = \frac{1}{4\pi\varepsilon_0 r_{12}^3}\left(\hat{\boldsymbol{\mu}}^{(1)}\cdot\hat{\boldsymbol{\mu}}^{(2)} - 3(\hat{\boldsymbol{\mu}}^{(1)}\cdot\boldsymbol{e}_{\mathbf{r}_{12}})(\hat{\boldsymbol{\mu}}^{(2)}\cdot\boldsymbol{e}_{\mathbf{r}_{12}})\right), \tag{3.3}$$

where r_{12} and $\boldsymbol{e}_{\mathbf{r}_{12}}$ denote the norm and unit vector, respectively, of $\mathbf{r}_{12} = \mathbf{r}_0^{(1)} - \mathbf{r}_0^{(2)}$. Thus, r_{12} represents the distance between the two dipoles.

The electric dipole moment operator of each system is given by

$$\hat{\boldsymbol{\mu}}^{(j)} = \sum_i q_i^{(j)}\hat{\mathbf{r}}_i^{(j)}, \tag{3.4}$$

as in Section 1.2.4. Here, $\hat{\mathbf{r}}_i^{(j)}$ is the canonical position operator of the particle i of system j. The dipole moment operators satisfy two relevant properties: (i) they are Hermitian operators, since the operators $\hat{\mathbf{r}}_i^{(j)}$ are also Hermitian; and (ii) they commute with each other,

$$[\hat{\boldsymbol{\mu}}^{(1)}, \hat{\boldsymbol{\mu}}^{(2)}] = 0, \tag{3.5}$$

which is a direct consequence of the commutation relations of the position operators [Eq. (1.97)].

3.1.2 Multipolar form of the Hamiltonian for two separated systems of charges

In this section, we derive the multipolar form of the Hamiltonian describing the interaction between the electromagnetic vacuum field and the two separated systems of charges. To this end, we apply the Power-Zienau transformation introduced in Section 1.2.5. For two separated system of charges, the unitary operator governing this transformation is given by

$$\hat{T} = \exp\left[-\frac{i}{\hbar} \sum_j \hat{\boldsymbol{\mu}}^{(j)} \cdot \hat{\mathbf{A}}(\mathbf{r}_0^{(j)}) \right] = \exp\left[\sum_j \sum_{\mathbf{k},s} \hat{\lambda}_{\mathbf{k}s}^{(j)\dagger} \hat{a}_{\mathbf{k}s} - \hat{\lambda}_{\mathbf{k}s}^{(j)} \hat{a}_{\mathbf{k}s}^{\dagger} \right], \tag{3.6}$$

where we have introduced

$$\hat{\lambda}_{\mathbf{k}s}^{(j)} = \frac{i}{\sqrt{2\hbar\omega_{\mathrm{k}}\varepsilon_0 \mathcal{V}}} e^{-i\mathbf{k}\cdot\mathbf{r}_0^{(j)}} \hat{\boldsymbol{\mu}}^{(j)} \cdot \boldsymbol{e}_{\mathbf{k}s}. \tag{3.7}$$

The multipolar form of the Hamiltonian can then be obtained as

$$\hat{H}^{mp} = \hat{T}\hat{H}^{mc}\hat{T}^{\dagger} = \hat{T}\hat{H}_{F\parallel}\hat{T}^{\dagger} + \hat{T}\hat{H}_K\hat{T}^{\dagger} + \hat{T}\hat{H}_{F\perp}\hat{T}^{\dagger}. \tag{3.8}$$

We next compute each term on the right-hand side of this equation separately.

First, we recall that $\hat{H}_{F\parallel}$ ultimately depends only on the canonical position operators of the particles (Section 1.2.5). As a consequence, $[\hat{H}_{F\parallel}, \hat{T}] = 0$, and thus,

$$\hat{T}\hat{H}_{F\parallel}\hat{T}^{\dagger} = \hat{H}_{F\parallel}. \tag{3.9}$$

Moreover, using the expansion theorem in Eq. (1.106), we find $[\hat{T}, \hat{\mathbf{A}}(\mathbf{r}_0^{(j)})] = 0$. Additionally, as $[\hat{\mathbf{r}}_i^{(j)} \cdot \hat{\mathbf{A}}(\mathbf{r}_0^{(j)}), \hat{\mathbf{p}}_i^{(j)}] = i\hbar\hat{\mathbf{A}}(\mathbf{r}_0^{(j)})$ (Section 1.2.5), we obtain

$$\hat{T}\hat{H}_K\hat{T}^{\dagger} = \hat{T}\sum_j\sum_i \frac{1}{2m_i^{(j)}} \left(\hat{\mathbf{p}}_i^{(j)} - q_i^{(j)}\hat{\mathbf{A}}(\mathbf{r}_0^{(j)}) \right)^2 \hat{T}^{\dagger} = \sum_j\sum_i \left(\frac{\hat{\mathbf{p}}_i^{(j)}}{2m_i^{(j)}} \right)^2. \tag{3.10}$$

We next compute $\hat{T}\hat{H}_{F\perp}\hat{T}^{\dagger}$. To this end, we use again the expansion theorem [Eq. (1.106)], which yields

$$\hat{T}\hat{a}_{\mathbf{k}s}\hat{T}^{\dagger} = \hat{a}_{\mathbf{k}s} + \hat{\lambda}_{\mathbf{k}s}^{(1)} + \hat{\lambda}_{\mathbf{k}s}^{(2)}, \tag{3.11a}$$

$$\hat{T}\hat{a}_{\mathbf{k}s}^{\dagger}\hat{T}^{\dagger} = \hat{a}_{\mathbf{k}s}^{\dagger} + \hat{\lambda}_{\mathbf{k}s}^{(1)\dagger} + \hat{\lambda}_{\mathbf{k}s}^{(2)\dagger}. \tag{3.11b}$$

Taking into account that the Power-Zienau transformation is unitary (i.e., $\hat{T}^{\dagger}\hat{T} = \mathbb{1}$),

we obtain

$$\begin{aligned}\hat{T}\hat{H}_{F\perp}\hat{T}^\dagger = &\sum_{\mathbf{k},s}\hbar\omega_{\mathrm{k}}(\hat{a}^\dagger_{\mathbf{k}s}\hat{a}_{\mathbf{k}s}+\frac{1}{2})+\sum_j\sum_{\mathbf{k},s}\hbar\omega_{\mathrm{k}}(\hat{a}^\dagger_{\mathbf{k}s}\hat{\lambda}^{(j)}_{\mathbf{k}s}+\hat{a}_{\mathbf{k}s}\hat{\lambda}^{(j)\dagger}_{\mathbf{k}s})\\ &+\sum_j\sum_{\mathbf{k},s}\hbar\omega_{\mathrm{k}}\hat{\lambda}^{(j)\dagger}_{\mathbf{k}s}\hat{\lambda}^{(j)}_{\mathbf{k}s}+\sum_{\mathbf{k},s}\hbar\omega_{\mathrm{k}}\left(\hat{\lambda}^{(1)\dagger}_{\mathbf{k}s}\hat{\lambda}^{(2)}_{\mathbf{k}s}+\hat{\lambda}^{(2)\dagger}_{\mathbf{k}s}\hat{\lambda}^{(1)}_{\mathbf{k}s}\right).\end{aligned} \tag{3.12}$$

The first term on the right-hand side of this equation is again $\hat{H}_{F\perp}$, whereas the second term gives rise to the multipolar form of the interaction Hamiltonian between the electromagnetic field and the charges. Namely,

$$\begin{aligned}\sum_{\mathbf{k},s}\hbar\omega_{\mathrm{k}}(\hat{a}^\dagger_{\mathbf{k}s}\hat{\lambda}^{(j)}_{\mathbf{k}s}+\hat{a}_{\mathbf{k}s}\hat{\lambda}^{(j)\dagger}_{\mathbf{k}s}) &= -\sum_{\mathbf{k},s}i\sqrt{\frac{\hbar\omega_{\mathrm{k}}}{2\varepsilon_0\mathcal{V}}}\hat{\boldsymbol{\mu}}^{(j)}\cdot\boldsymbol{e}_{\mathbf{k}s}(\hat{a}^\dagger_{\mathbf{k}s}e^{-i\mathbf{k}\cdot\mathbf{r}_0^{(j)}}-\hat{a}_{\mathbf{k}s}e^{i\mathbf{k}\cdot\mathbf{r}_0^{(j)}})\\ &= -\hat{\boldsymbol{\mu}}^{(j)}\cdot\hat{\mathbf{E}}_\perp(\mathbf{r}_0^{(j)}),\end{aligned} \tag{3.13}$$

where $\hat{\mathbf{E}}_\perp(\mathbf{r}_0^{(j)})$ is the transverse component of the electromagnetic field evaluated at $\mathbf{r}_0^{(j)}$ [Eq. (1.86)]. Further, the third term on the right-hand side of Eq. (3.12) yields the dipole self-energies $\hat{\varepsilon}_\mu^{(j)}$ of each of the emitters [Eq. (1.111)]. Specifically,

$$\sum_j\sum_{\mathbf{k},s}\hbar\omega_{\mathrm{k}}\hat{\lambda}^{(j)\dagger}_{\mathbf{k}s}\hat{\lambda}^{(j)}_{\mathbf{k}s}=\sum_j\sum_{\mathbf{k},s}\frac{1}{2\varepsilon_0\mathcal{V}}(\hat{\boldsymbol{\mu}}^{(j)}\cdot\boldsymbol{e}_{\mathbf{k}s})^2=\sum_j\hat{\varepsilon}_\mu^{(j)}. \tag{3.14}$$

So far, the application of the Power-Zienau transformation to each of the terms of the minimal coupling form of the Hamiltonian in Eq. (3.1) is a direct generalization of the transformation of the single-emitter Hamiltonian (Section 1.2.5), except for one important difference. This difference lies on the last term in Eq. (3.12), which consists of cross terms between the two systems of charges. We show next that this term is opposite to $\hat{H}^{(12)}_{F\parallel}$ [Eq. (3.3)] and, thus, the two terms cancel each other out. To show this, we first use the expressions of the operators $\hat{\lambda}^{(j)}_{\mathbf{k}s}$ given in Eq. (3.7) and find

$$\begin{aligned}&\sum_{\mathbf{k},s}\hbar\omega_{\mathrm{k}}\left(\hat{\lambda}^{(1)\dagger}_{\mathbf{k}s}\hat{\lambda}^{(2)}_{\mathbf{k}s}+\hat{\lambda}^{(2)\dagger}_{\mathbf{k}s}\hat{\lambda}^{(1)}_{\mathbf{k}s}\right)\\ &=\sum_{\mathbf{k},s}\hbar\omega_{\mathrm{k}}\left(\frac{e^{ir_{12}\mathbf{k}\cdot\boldsymbol{e}_{\mathbf{r}_{12}}}}{2\hbar\varepsilon_0\omega_{\mathrm{k}}\mathcal{V}}(\hat{\boldsymbol{\mu}}^{(1)}\cdot\boldsymbol{e}_{\mathbf{k}s})(\hat{\boldsymbol{\mu}}^{(2)}\cdot\boldsymbol{e}_{\mathbf{k}s})+\frac{e^{-ir_{12}\mathbf{k}\cdot\boldsymbol{e}_{\mathbf{r}_{12}}}}{2\hbar\varepsilon_0\omega_{\mathrm{k}}\mathcal{V}}(\hat{\boldsymbol{\mu}}^{(2)}\cdot\boldsymbol{e}_{\mathbf{k}s})(\hat{\boldsymbol{\mu}}^{(1)}\cdot\boldsymbol{e}_{\mathbf{k}s})\right).\end{aligned} \tag{3.15}$$

We next transform the summation over $\mathbf{k}$ into an integral [Eq. (1.134)], which

yields

$$\sum_{\mathbf{k},s}\hbar\omega_{\mathrm{k}}\left(\hat{\lambda}^{(1)\dagger}_{\mathbf{k}s}\hat{\lambda}^{(2)}_{\mathbf{k}s}+\hat{\lambda}^{(2)\dagger}_{\mathbf{k}s}\hat{\lambda}^{(1)}_{\mathbf{k}s}\right)=\lim_{\omega\to 0}\frac{1}{2\varepsilon_0(2\pi)^3c^3}\sum_s\int_0^{\pi}d\theta\sin\theta\int_0^{2\pi}d\phi$$
$$\times\Bigg(-\mathrm{p.v.}\int_0^{\infty}d\omega_{\mathrm{k}}\frac{\omega_{\mathrm{k}}^3}{\omega-\omega_{\mathrm{k}}}e^{ir_{12}\mathbf{k}\cdot\boldsymbol{e}_{\mathbf{r}_{12}}}(\hat{\boldsymbol{\mu}}^{(1)}\cdot\boldsymbol{e}_{\mathbf{k}s})(\hat{\boldsymbol{\mu}}^{(2)}\cdot\boldsymbol{e}_{\mathbf{k}s}) \tag{3.16}$$
$$+\mathrm{p.v.}\int_0^{\infty}d\omega_{\mathrm{k}}\frac{\omega_{\mathrm{k}}^3}{\omega+\omega_{\mathrm{k}}}e^{-ir_{12}\mathbf{k}\cdot\boldsymbol{e}_{\mathbf{r}_{12}}}(\hat{\boldsymbol{\mu}}^{(2)}\cdot\boldsymbol{e}_{\mathbf{k}s})(\hat{\boldsymbol{\mu}}^{(1)}\cdot\boldsymbol{e}_{\mathbf{k}s})\Bigg).$$

Here, we have additionally introduced the parameter ω in the denominators to facilitate the calculation of the integrals, as discussed below. Once the integrals are solved, the limit of this parameter to 0 is taken. Next, we perform the change of variable $\omega_{\mathrm{k}}\to-\omega_{\mathrm{k}}$ in the frequency integral appearing in the last line of the above equation. Additionally, taking into account that $\hat{\boldsymbol{\mu}}^{(1)}$ and $\hat{\boldsymbol{\mu}}^{(2)}$ commute [Eq. (3.5)], we find

$$\sum_{\mathbf{k},s}\hbar\omega_{\mathrm{k}}\left(\hat{\lambda}^{(1)\dagger}_{\mathbf{k}s}\hat{\lambda}^{(2)}_{\mathbf{k}s}+\hat{\lambda}^{(2)\dagger}_{\mathbf{k}s}\hat{\lambda}^{(1)}_{\mathbf{k}s}\right)=-\lim_{\omega\to 0}\frac{1}{2\varepsilon_0(2\pi)^3c^3}\,\mathrm{p.v.}\int_{-\infty}^{\infty}d\omega_{\mathrm{k}}\frac{\omega_{\mathrm{k}}^3}{\omega-\omega_{\mathrm{k}}}$$
$$\times\int_0^{\pi}d\theta\sin\theta\int_0^{2\pi}d\phi\sum_s e^{ir_{12}\mathbf{k}\cdot\boldsymbol{e}_{\mathbf{r}_{12}}}(\hat{\boldsymbol{\mu}}^{(1)}\cdot\boldsymbol{e}_{\mathbf{k}s})(\hat{\boldsymbol{\mu}}^{(2)}\cdot\boldsymbol{e}_{\mathbf{k}s}). \tag{3.17}$$

To further facilitate the evaluation of the integrals, we consider $\boldsymbol{e}_{\mathbf{r}_{12}}=\boldsymbol{e}_z$ (that is, the vector pointing from one center of mass to the other is oriented along the z-axis). Using the expressions for the polarization unit vectors $\boldsymbol{e}_{\mathbf{k}s}$ in Eqs. (1.137a)–(1.137b), we carry out the solid angle integral and obtain

$$\sum_{\mathbf{k},s}\hbar\omega_{\mathrm{k}}\left(\hat{\lambda}^{(1)\dagger}_{\mathbf{k}s}\hat{\lambda}^{(2)}_{\mathbf{k}s}+\hat{\lambda}^{(2)\dagger}_{\mathbf{k}s}\hat{\lambda}^{(1)}_{\mathbf{k}s}\right)=-\lim_{\omega\to 0}\frac{2\pi}{\varepsilon_0(2\pi)^3c^3}\,\mathrm{p.v.}\int_{-\infty}^{\infty}d\omega_{\mathrm{k}}\frac{\omega_{\mathrm{k}}^3}{\omega-\omega_{\mathrm{k}}}$$
$$\times\Bigg[\left(\hat{\boldsymbol{\mu}}^{(1)}_x\hat{\boldsymbol{\mu}}^{(2)}_x+\hat{\boldsymbol{\mu}}^{(1)}_y\hat{\boldsymbol{\mu}}^{(2)}_y\right)\left(\frac{\sin(\mathrm{k}r_{12})}{\mathrm{k}r_{12}}-\frac{\sin(\mathrm{k}r_{12})}{(\mathrm{k}r_{12})^3}+\frac{\cos(\mathrm{k}r_{12})}{(\mathrm{k}r_{12})^2}\right) \tag{3.18}$$
$$+2\hat{\boldsymbol{\mu}}^{(1)}_z\hat{\boldsymbol{\mu}}^{(2)}_z\left(\frac{\sin(\mathrm{k}r_{12})}{(\mathrm{k}r_{12})^3}-\frac{\cos(\mathrm{k}r_{12})}{(\mathrm{k}r_{12})^2}\right)\Bigg].$$

Furthermore, to solve the frequency integral we take into account that [179]

$$\mathrm{p.v.}\int_{-\infty}^{\infty}d\omega_{\mathrm{k}}\frac{\omega_{\mathrm{k}}^3}{\omega-\omega_{\mathrm{k}}}\left(a\frac{\sin(\omega_{\mathrm{k}}r_{12}/c)}{\omega_{\mathrm{k}}r_{12}/c}-a\frac{\cos(\omega_{\mathrm{k}}r_{12}/c)}{(\omega_{\mathrm{k}}r_{12}/c)^2}+b\frac{\sin(\omega_{\mathrm{k}}r_{12}/c)}{(\omega_{\mathrm{k}}r_{12}/c)^3}\right)$$
$$=-\pi\omega^3\left(a\frac{\cos(\omega_{\mathrm{k}}r_{12}/c)}{\omega_{\mathrm{k}}r_{12}/c}+a\frac{\sin(\omega_{\mathrm{k}}r_{12}/c)}{(\omega_{\mathrm{k}}r_{12}/c)^2}+b\frac{\cos(\omega_{\mathrm{k}}r_{12}/c)}{(\omega_{\mathrm{k}}r_{12}/c)^3}\right). \tag{3.19}$$

Taking the limit $\omega \to 0$, we finally obtain

$$\sum_{\mathbf{k},s} \hbar\omega_{\mathrm{k}} \left(\hat{\lambda}^{(1)\dagger}_{\mathbf{k}s} \hat{\lambda}^{(2)}_{\mathbf{k}s} + \hat{\lambda}^{(2)\dagger}_{\mathbf{k}s} \hat{\lambda}^{(1)}_{\mathbf{k}s} \right) = - \frac{\hat{\boldsymbol{\mu}}^{(1)} \cdot \hat{\boldsymbol{\mu}}^{(2)} - 3(\hat{\boldsymbol{\mu}}^{(1)} \cdot \boldsymbol{e}_{\mathbf{r}_{12}})(\hat{\boldsymbol{\mu}}^{(2)} \cdot \boldsymbol{e}_{\mathbf{r}_{12}})}{4\pi\varepsilon_0 r_{12}^3}. \tag{3.20}$$

This term is identical to $-\hat{H}^{(12)}_{F\parallel}$ [Eqs. (3.3) and (3.9)], so the two terms cancel each other out.

Therefore, the multipolar form of the Hamiltonian of two separated systems of charges becomes

$$\hat{H}^{mp} = \hat{T}\hat{H}^{mc}\hat{T}^{\dagger} = \sum_{\mathbf{k},s} \hbar\omega_{\mathrm{k}} (\hat{a}^{\dagger}_{\mathbf{k}s}\hat{a}_{\mathbf{k}s} + \frac{1}{2}) + \sum_j \hat{H}^{mp}_{P,j} + \sum_j \hat{H}^{mp}_{I,j}, \tag{3.21}$$

where we have defined

$$\hat{H}^{mp}_{P,j} = \sum_i \left(\frac{\hat{\mathbf{p}}^{(j)}_i}{2m^{(j)}_i} \right)^2 + \hat{H}^{(j)}_{F\parallel} + \hat{\varepsilon}^{(j)}_{\mu}, \tag{3.22}$$

and

$$\hat{H}^{mp}_{I,j} = -\hat{\boldsymbol{\mu}}^{(j)} \cdot \hat{\mathbf{E}}_{\perp}(\mathbf{r}^{(j)}_0). \tag{3.23}$$

We have grouped the terms in this way so that $\hat{H}^{mp}_{P,j}$ and $\hat{H}^{mp}_{I,j}$ are direct generalizations of the multipolar Hamiltonians in Eqs. (1.117) and (1.118), which were derived in Section 1.2.5 for a single system of charged particles.

We emphasize that the interaction between the two systems of charges is mediated by the electromagnetic field. To illustrate how this interaction is mediated, we note that the Hamiltonian $\hat{H}^{mp}_{I,1}$ is given by the product of the dipole moment operator $\hat{\boldsymbol{\mu}}^{(1)}$ of the system of charges $j = 1$ and the electric field operator $\hat{\mathbf{E}}_{\perp}(\mathbf{r}^{(1)}_0)$, which is evaluated at the center of mass of this same system of charges. Crucially, $\hat{\mathbf{E}}_{\perp}(\mathbf{r}^{(1)}_0)$ includes the influence of the field radiated by the system of particles $j = 2$, giving rise to the interaction between the two system of charges. Similarly, $\hat{H}^{mp}_{I,2}$ is given by the product of $\hat{\boldsymbol{\mu}}^{(2)}$ and the electric field operator $\hat{\mathbf{E}}_{\perp}(\mathbf{r}^{(2)}_0)$, which is evaluated at the center of mass of the system of charges $j = 2$ and accounts for the field radiated by the system of charges $j = 1$.

3.1.3 Multipolar form of the Hamiltonian for two quantum emitters

In this section, we derive the multipolar form of the Hamiltonian when considering that each system of charges represents a quantum emitter (QE) with two-level system behaviour. We label the QEs by $j = 1, 2$, in the same way as the systems of charged particles. Each QE has electronic ground state $|g_j\rangle$ and electronic excited state $|e_j\rangle$, with transition frequency $\omega_{e,j}$, as schematically represented in Fig. 3.1. Similar to the case of a single QE (Section 1.2.6), we identify the multipolar form

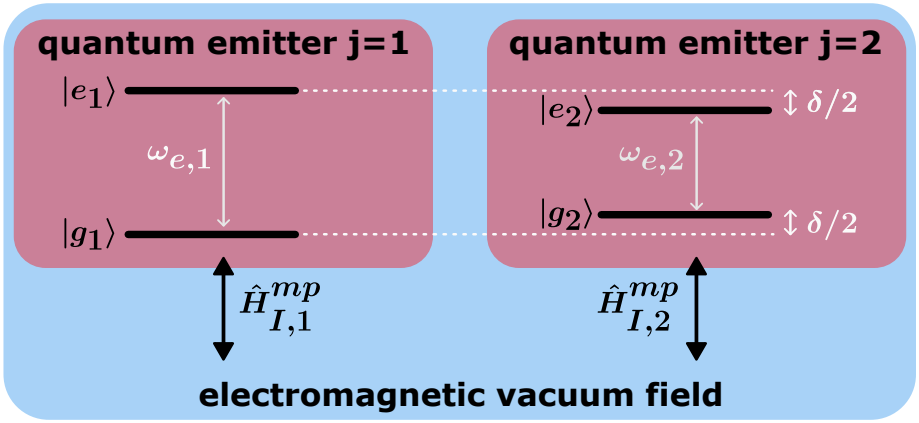

Figure 3.1: Schematic representation of the interaction between two quantum emitters and the electromagnetic vacuum field. The emitters are labeled by $j = 1, 2$. Emitter j has electronic ground state $|g_j\rangle$ and excited state $|e_j\rangle$, with transition frequency $\omega_{e,j}$. The transition frequencies can be different, with detuning $\delta = \omega_{e,1} - \omega_{e,2}$. The interaction of emitter j with the electromagnetic vacuum field is described by the multipolar interaction Hamiltonian $\hat{H}^{mp}_{I,j}$ [Eq. (3.26)].

of the Hamiltonian of the system of charges j with the Hamiltonian of the emitter j. Namely,

$$\hat{H}^{mp}_{P,j} \to \hat{H}^{(j)}_{\mathrm{QE}} = \hbar \frac{\omega_{e,j}}{2} \hat{\sigma}_{z,j}, \tag{3.24}$$

where $\hat{\sigma}_{z,j} = |e_j\rangle\langle e_j| - |g_j\rangle\langle g_j|$ is the z-Pauli matrix in the Hilbert space of the emitter j.

Moreover, we consider again that the QEs have no permanent dipole moments. Thus, the dipole moment operator of emitter j can be expressed as

$$\hat{\boldsymbol{\mu}}^{(j)} = \boldsymbol{\mu}_j \hat{\sigma}_j + \boldsymbol{\mu}_j^* \hat{\sigma}_j^\dagger, \tag{3.25}$$

with $\boldsymbol{\mu}^{(j)}$ the transition dipole moment between the electronic excited state $|e_j\rangle$ and the ground state $|g_j\rangle$, and $\hat{\sigma}_j = |g_j\rangle\langle e_j|$ and $\hat{\sigma}_j^\dagger = |e_j\rangle\langle g_j|$ the corresponding lowering and raising operators, respectively. Substituting this dipole moment operator into the multipolar form of the interaction Hamiltonian $\hat{H}^{mp}_{I,j}$ [Eq. (3.23)] and using the expression for the transverse electric field operator in Eq. (1.86), we find

$$\hat{H}^{mp}_I \to \sum_j \hat{H}^{mp}_{I,j} = -\sum_j \left(\boldsymbol{\mu}_j \hat{\sigma} + \boldsymbol{\mu}_j^* \hat{\sigma}^\dagger \right) \cdot \sum_{\mathbf{k},s} i \sqrt{\frac{\hbar \omega_{\mathrm{k}}}{2\varepsilon_0 \mathcal{V}}} \mathbf{e}_{\mathbf{k}s} [\hat{a}_{\mathbf{k}s} e^{i\mathbf{k}\cdot\mathbf{r}_j} - \hat{a}^\dagger_{\mathbf{k}s} e^{-i\mathbf{k}\cdot\mathbf{r}_j}]. \tag{3.26}$$

For simplicity, we have replaced the notation of the center of mass of $\mathbf{r}_0^{(j)}$ by $\mathbf{r}_j$.

Therefore, we find that the complete Hamiltonian (in the multipolar form)

describing the interaction between the electromagnetic vacuum field and two quantum emitters is given by

$$\begin{aligned}\hat{H}^{mp} &= \sum_{\mathbf{k},s} \hbar\omega_{\mathrm{k}}(\hat{a}^{\dagger}_{\mathbf{k}s}\hat{a}_{\mathbf{k}s} + \frac{1}{2}) + \sum_{j} \hbar\frac{\omega_{e,j}}{2}\hat{\sigma}_{z,j} \\ &- \sum_{j}\left(\boldsymbol{\mu}_j\hat{\sigma}_j + \boldsymbol{\mu}_j^{*}\hat{\sigma}_j^{\dagger}\right)\cdot\sum_{\mathbf{k},s} i\sqrt{\frac{\hbar\omega_{\mathrm{k}}}{2\varepsilon_0\mathcal{V}}}\mathbf{e}_{\mathbf{k}s}[\hat{a}_{\mathbf{k}s}e^{i\mathbf{k}\cdot\mathbf{r}_j} - \hat{a}^{\dagger}_{\mathbf{k}s}e^{-i\mathbf{k}\cdot\mathbf{r}_j}].\end{aligned} \tag{3.27}$$

We emphasize that this Hamiltonian does not include any direct coupling between the emitters. This interaction is mediated by the vacuum field, as we show in the following section.

3.1.4 Markovian master equation: dipole-dipole interaction induced by the vacuum field

We derive in this section the Markovian master equation (MME) that describes the reduced dynamics of the two quantum emitters. To this end, we apply the formalism described in Section 1.4 to trace out the degrees of freedom of the electromagnetic vacuum field, which extends the derivation in Section 1.4.5 from one to two QEs. The resulting MME shows that the electromagnetic field is responsible for mediating the dipole-dipole interaction between the emitters, in addition to inducing their spontaneous emission of photons.

Bohr frequencies, eigenoperators and bath correlation functions

We first derive the elements required for the calculation of the Lamb-shift Hamiltonian and the dissipators arising from tracing out the electromagnetic vacuum field. We consider that the entire system is divided into a system of interest, consisting of the two emitters, and a bath, corresponding to the electromagnetic vacuum field. More specifically, the electromagnetic vacuum field acts as a thermal bath at temperature T, with Hamiltonian $\hat{H}_{F\perp}$ [first term on the right-hand side of Eq. (3.27)] and in the stationary thermal state

$$\hat{\rho}_B^{th} = \frac{\exp(-\hat{H}_{F\perp}/k_BT)}{\mathrm{Tr}[\exp(-\hat{H}_{F\perp}/k_BT)]}. \tag{3.28}$$

On the other hand, the system of interest is described by the Hamiltonian $\hat{H}_0 = \hat{H}^{(1)}_{\mathrm{QE}} + \hat{H}^{(2)}_{\mathrm{QE}} = \hbar\sum_j \frac{\omega_{e,j}}{2}\hat{\sigma}_{z,j}$. The eigenstates $|\epsilon\rangle$ of this Hamiltonian are $|g_1g_2\rangle$, $|g_1e_2\rangle$, $|e_1g_2\rangle$, and $|e_1e_2\rangle$, with spectral decomposition given as

$$\hat{H}_0 = \hbar\omega_0\Big(|e_1e_2\rangle\langle e_1e_2| - |g_1g_2\rangle\langle g_1g_2|\Big) + \hbar\frac{\delta}{2}\Big(|e_1g_2\rangle\langle e_1g_2| - |g_1e_2\rangle\langle g_1e_2|\Big). \tag{3.29}$$

$\omega = (\epsilon' - \epsilon)/\hbar$	$\epsilon/\hbar$	$\epsilon'/\hbar$	$\lvert\epsilon\rangle$	$\lvert\epsilon'\rangle$
$\omega_{e,1}$	$-\omega_0$	$\delta/2$	$\lvert g_1 g_2\rangle$	$\lvert e_1 g_2\rangle$
$\omega_{e,1}$	$-\delta/2$	ω_0	$\lvert g_1 e_2\rangle$	$\lvert e_1 e_2\rangle$
$-\omega_{e,1}$	$\delta/2$	$-\omega_0$	$\lvert e_1 g_2\rangle$	$\lvert g_1 g_2\rangle$
$-\omega_{e,1}$	ω_0	$-\delta/2$	$\lvert e_1 e_2\rangle$	$\lvert g_1 e_2\rangle$
$\omega_{e,2}$	$-\omega_0$	$-\delta/2$	$\lvert g_1 g_2\rangle$	$\lvert g_1 e_2\rangle$
$\omega_{e,2}$	$\delta/2$	ω_0	$\lvert e_1 g_2\rangle$	$\lvert e_1 e_2\rangle$
$-\omega_{e,2}$	$-\delta/2$	$-\omega_0$	$\lvert g_1 e_2\rangle$	$\lvert g_1 g_2\rangle$
$-\omega_{e,2}$	ω_0	$\delta/2$	$\lvert e_1 e_2\rangle$	$\lvert e_1 g_2\rangle$
δ	$-\delta/2$	$\delta/2$	$\lvert g_1 e_2\rangle$	$\lvert e_1 g_2\rangle$
$-\delta$	$\delta/2$	$-\delta/2$	$\lvert e_1 g_2\rangle$	$\lvert g_1 e_2\rangle$
$2\omega_0$	ω_0	$-\omega_0$	$\lvert g_1 g_2\rangle$	$\lvert e_1 e_2\rangle$
$-2\omega_0$	ω_0	$-\omega_0$	$\lvert e_1 e_2\rangle$	$\lvert g_1 g_2\rangle$
0	$-\omega_0$	$-\omega_0$	$\lvert g_1 g_2\rangle$	$\lvert g_1 g_2\rangle$
0	$-\delta/2$	$-\delta/2$	$\lvert g_1 e_2\rangle$	$\lvert g_1 e_2\rangle$
0	$\delta/2$	$\delta/2$	$\lvert e_1 g_2\rangle$	$\lvert e_1 g_2\rangle$
0	ω_0	ω_0	$\lvert e_1 e_2\rangle$	$\lvert e_1 e_2\rangle$

Table 3.1: Bohr frequencies ω of the Hamiltonian $\hat{H}_0 = \hat{H}_{\mathrm{QE}}^{(1)} + \hat{H}_{\mathrm{QE}}^{(2)} = \sum_j \frac{\omega_{e,j}}{2}\hat{\sigma}_{z,j}$ of the QEs, which are considered as the system of interest. $|\epsilon\rangle$ and $|\epsilon'\rangle$ are eigenstates of $\hat{H}_0$, whereas ϵ and ϵ' are their corresponding eigenvalues. $\delta = \omega_{e,1} - \omega_{e,2}$ is the frequency detuning between both emitters, and $\omega_0 = (\omega_{e,1} + \omega_{e,2})/2$ is the arithmetic average frequency.

Here, we have introduced the arithmetic average transition frequency

$$\omega_0 = \frac{\omega_{e,1} + \omega_{e,2}}{2}, \tag{3.30}$$

as well as the detuning

$$\delta = \omega_{e,1} - \omega_{e,2} \tag{3.31}$$

between the two transition frequencies. The spectral decomposition of $\hat{H}_0$ in Eq. (3.29) yields that the Bohr frequencies of the system of interest are $\pm\omega_{e,1}$, $\pm\omega_{e,2}$, $\pm\delta$, $\pm 2\omega_0$ and 0, with corresponding eigenstates given in Table 3.1. The Bohr frequencies are required later in this derivation.

Next, we rewrite the interaction Hamiltonian $\hat{H}_I^{mp}$ [Eq. (3.26)] as a summation of Hermitian operators $\hat{S}_{j,\mathbf{k}s}$ and $\hat{B}_{j,\mathbf{k}s}$ that belongs to the Hilbert space of the system of interest and to the Hilbert space of the bath, respectively. We find

$$\hat{H}_I^{mp} = \hbar \sum_j \sum_{\mathbf{k},s} \hat{S}_{j,\mathbf{k}s} \otimes \hat{B}_{j,\mathbf{k}s}, \tag{3.32}$$

with

$$\hat{S}_{j,\mathbf{k}s} = \boldsymbol{\mu}_j \cdot \boldsymbol{e}_{\mathbf{k}s}(\hat{\sigma}_j + \hat{\sigma}_j^\dagger), \tag{3.33a}$$

$$\hat{B}_{j,\mathbf{k}s} = -i\sqrt{\frac{\omega_{\mathrm{k}}}{2\varepsilon_0\hbar\mathcal{V}}}\left[\hat{a}_{\mathbf{k}s}e^{i\mathbf{k}\cdot\mathbf{r}_j} - \hat{a}^{\dagger}_{\mathbf{k}s}e^{-i\mathbf{k}\cdot\mathbf{r}_j}\right]. \tag{3.33b}$$

Here and in the rest of this thesis, we assume that $\boldsymbol{\mu}_j$ is real, for simplicity. On the one hand, $\hat{S}_{j,\mathbf{k}s}$ allows us to compute the eigenoperators $\hat{S}_{j,\mathbf{k}s}(\omega)$ of $\hat{H}_0$ [Eq. (1.182)], with ω any Bohr frequency. We find that the only non-vanishing eigenoperators are

$$\hat{S}_{j,\mathbf{k}s}(\omega_{e,j}) = \boldsymbol{\mu}_j \cdot \boldsymbol{e}_{\mathbf{k}s}\hat{\sigma}_j, \tag{3.34a}$$

$$\hat{S}_{j,\mathbf{k}s}(-\omega_{e,j}) = \boldsymbol{\mu}_j \cdot \boldsymbol{e}_{\mathbf{k}s}\hat{\sigma}^{\dagger}_j, \tag{3.34b}$$

which are key elements in the derivation of the MME. On the other hand, the operators $\hat{B}_{j,\mathbf{k}s}$ allows us to compute the bath correlation function $\langle\hat{B}^{(I)}_{j,\mathbf{k}s}(\tau)\hat{B}^{(I)}_{j',\mathbf{k}'s'}(0)\rangle$, whose Fourier transformation also play a critical role in this derivation. Here, $\hat{B}^{(I)}_{j,\mathbf{k}s}$ is the interaction-picture representation of $\hat{B}_{j,\mathbf{k}s}$ (Appendix B), and it is given by

$$\begin{aligned}\hat{B}^{(I)}_{j,\mathbf{k}s}(\tau) &= \exp[it(\hat{H}_{F\perp}+\hat{H}_0)]\hat{B}_{j,\mathbf{k}s}\exp[-it(\hat{H}_{F\perp}+\hat{H}_0)] \\ &= i\sqrt{\frac{\omega_{\mathrm{k}}}{2\varepsilon_0\hbar\mathcal{V}}}\left[\hat{a}_{\mathbf{k}s}e^{i(\mathbf{k}\cdot\mathbf{r}_j-\omega_{\mathrm{k}}\tau)} - \hat{a}^{\dagger}_{\mathbf{k}s}e^{-(i\mathbf{k}\cdot\mathbf{r}_j-\omega_{\mathrm{k}}\tau)}\right].\end{aligned} \tag{3.35}$$

Thus, the bath correlation function becomes

$$\begin{aligned}&\langle\hat{B}^{(I)}_{j,\mathbf{k}s}(\tau)\hat{B}^{(I)}_{j',\mathbf{k}'s'}(0)\rangle = \frac{\sqrt{\omega_{\mathrm{k}}\omega_{\mathrm{k}'}}}{2\varepsilon_0\mathcal{V}\hbar} \\ &\times\left\langle\left[\hat{a}_{\mathbf{k}s}e^{i(\mathbf{k}\cdot\mathbf{r}_j-\omega_{\mathrm{k}}\tau)} - \hat{a}^{\dagger}_{\mathbf{k}s}e^{-i(\mathbf{k}\cdot\mathbf{r}_j-\omega_{\mathrm{k}}\tau)}\right]\left[\hat{a}^{\dagger}_{\mathbf{k}'s'}e^{-i\mathbf{k}'\cdot\mathbf{r}_{j'}} - \hat{a}_{\mathbf{k}'s'}e^{i\mathbf{k}'\cdot\mathbf{r}_{j'}}\right]\right\rangle \\ &\approx \delta^3_{\mathbf{k},\mathbf{k}'}\delta_{s,s'}\frac{\omega_{\mathrm{k}}}{2\varepsilon_0\mathcal{V}\hbar}\exp\left[i\mathbf{k}\cdot(\mathbf{r}_j-\mathbf{r}_{j'}) - i\omega_{\mathrm{k}}\tau\right],\end{aligned} \tag{3.36}$$

where we have used the commutation relations in Eqs. (1.42a)–(1.42b). Additionally, in the last line of Eq. (3.36), we have assumed that the thermal populations of the modes of the electromagnetic vacuum field excited by the QEs are negligible (as it is the case for QEs with transition frequencies near the visible range), as in Section 1.4.5. The Fourier transform of this bath correlation function results in

$$\begin{aligned}\Gamma_{j\mathbf{k}s,j'\mathbf{k}'s'}(\omega) &= \int_0^{\infty} d\tau e^{i\omega\tau}\,\langle\hat{B}^{(I)}_{j,\mathbf{k}s}(\tau)\hat{B}^{(I)}_{j',\mathbf{k}'s'}(0)\rangle \\ &\approx \delta^3_{\mathbf{k},\mathbf{k}'}\delta_{s,s'}\frac{\omega_{\mathrm{k}}}{2\varepsilon_0\mathcal{V}\hbar}e^{i\mathbf{k}\cdot(\mathbf{r}_j-\mathbf{r}_{j'})}\left[\pi\delta(\omega-\omega_{\mathrm{k}}) + i\,\mathrm{p.v.}\frac{1}{\omega-\omega_{\mathrm{k}}}\right],\end{aligned} \tag{3.37}$$

where we have used Eq. (1.158) to compute the time integral.

So far, we have derived the non-vanishing eigenoperators $\hat{S}_{j,\mathbf{k}s}(\pm\omega_{e,j})$ and the Fourier transform of the bath correlation functions $\Gamma_{j\mathbf{k}s,j'\mathbf{k}'s'}(\omega)$. In the following,

we substitute these quantities into the MME in Eq. (1.189), which does not consider the effect of the rotating-wave approximation (RWA). We choose this form of the MME because the terms neglected by the RWA are crucial to capture the coherent interaction between emitters, as we show next.

Coherent dipole-dipole coupling

We now focus on deriving the Lamb-shift Hamiltonian in Eq. (1.190), which gives rise to the coherent dipole-dipole interaction between the emitters. We obtain

$$\begin{aligned}
\hat{H}^{(I)}_{\text{Lamb}} &= \sum_{\omega,\omega'}\sum_{j,\mathbf{k},s}\sum_{j',\mathbf{k}',s'} e^{i(\omega-\omega')t}\frac{\Gamma_{j\mathbf{k}s,j'\mathbf{k}'s'}(\omega)-\Gamma^{*}_{j'\mathbf{k}'s',j\mathbf{k}s}(\omega')}{2i}\hat{S}^{\dagger}_{j\mathbf{k}s}(\omega')\hat{S}_{j'\mathbf{k}'s'}(\omega)\\
&= \sum_{j,\mathbf{k},s}\sum_{j',\mathbf{k}',s'} e^{i(\omega_{e,j}-\omega_{e,j'})t}\frac{\Gamma_{j\mathbf{k}s,j'\mathbf{k}'s'}(\omega_{e,j})-\Gamma^{*}_{j'\mathbf{k}'s',j\mathbf{k}s}(\omega_{e,j'})}{2i}\\
&\times \hat{S}^{\dagger}_{j\mathbf{k}s}(\omega_{e,j'})\hat{S}_{j'\mathbf{k}'s'}(\omega_{e,j})\\
&+ \sum_{j,\mathbf{k},s}\sum_{j',\mathbf{k}',s'} e^{-i(\omega_{e,j}-\omega_{e,j'})t}\frac{\Gamma_{j\mathbf{k}s,j'\mathbf{k}'s'}(-\omega_{e,j})-\Gamma^{*}_{j'\mathbf{k}'s',j\mathbf{k}s}(-\omega_{e,j'})}{2i}\\
&\times \hat{S}^{\dagger}_{j\mathbf{k}s}(-\omega_{e,j'})\hat{S}_{j'\mathbf{k}'s'}(-\omega_{e,j}).
\end{aligned} \tag{3.38}$$

The terms in the last equality of this equation for which the eigenoperators are evaluated at the same frequencies [i.e., at $\omega_{e,j'}=\omega_{e,j}$ and at $-\omega_{e,j'}=-\omega_{e,j}$] give rise to the Lamb shift induced by the vacuum field in the transition frequency of each emitter. As discussed in Section 1.3, the values of these shifts are very small for QEs with optical transition frequencies and, additionally, they are already accounted for in the values of transition frequencies measured in experiments. We thus neglect such terms, which yields

$$\begin{aligned}
\hat{H}^{(I)}_{\text{Lamb}} &= \hat{\sigma}^{\dagger}_2\hat{\sigma}_1 e^{i\delta t}\sum_{\mathbf{k},s}\sum_{\mathbf{k}',s'}(\boldsymbol{\mu}_2\cdot\boldsymbol{e}_{\mathbf{k}s})^{*}(\boldsymbol{\mu}_1\cdot\boldsymbol{e}_{\mathbf{k}'s'})\frac{\Gamma_{1\mathbf{k}s,2\mathbf{k}'s'}(\omega_{e,1})-\Gamma^{*}_{2\mathbf{k}'s',1\mathbf{k}s}(\omega_{e,2})}{2i}\\
&+ \hat{\sigma}^{\dagger}_2\hat{\sigma}_1 e^{i\delta t}\sum_{\mathbf{k},s}\sum_{\mathbf{k}',s'}(\boldsymbol{\mu}_2\cdot\boldsymbol{e}_{\mathbf{k}'s'})^{*}(\boldsymbol{\mu}_1\cdot\boldsymbol{e}_{\mathbf{k}s})\frac{\Gamma_{2\mathbf{k}s,1\mathbf{k}'s'}(-\omega_{e,2})-\Gamma^{*}_{1\mathbf{k}'s',2\mathbf{k}s}(-\omega_{e,1})}{2i}\\
&+ \hat{\sigma}^{\dagger}_1\hat{\sigma}_2 e^{-i\delta t}\sum_{\mathbf{k},s}\sum_{\mathbf{k}',s'}(\boldsymbol{\mu}_1\cdot\boldsymbol{e}_{\mathbf{k}s})^{*}(\boldsymbol{\mu}_2\cdot\boldsymbol{e}_{\mathbf{k}'s'})\frac{\Gamma_{2\mathbf{k}s,1\mathbf{k}'s'}(\omega_{e,2})-\Gamma^{*}_{1\mathbf{k}'s',2\mathbf{k}s}(\omega_{e,1})}{2i}\\
&+ \hat{\sigma}^{\dagger}_1\hat{\sigma}_2 e^{-i\delta t}\sum_{\mathbf{k},s}\sum_{\mathbf{k}',s'}(\boldsymbol{\mu}_1\cdot\boldsymbol{e}_{\mathbf{k}'s'})^{*}(\boldsymbol{\mu}_2\cdot\boldsymbol{e}_{\mathbf{k}s})\frac{\Gamma_{1\mathbf{k}s,2\mathbf{k}'s'}(-\omega_{e,1})-\Gamma^{*}_{2\mathbf{k}'s',1\mathbf{k}s}(-\omega_{e,2})}{2i}\\
&\equiv \hat{\sigma}_1\hat{\sigma}^{\dagger}_2 e^{i\delta t}V + \hat{\sigma}^{\dagger}_1\hat{\sigma}_2 e^{-i\delta t}V^{*}.
\end{aligned} \tag{3.39}$$

Notably, this Hamiltonian contains terms proportional to the operators $\hat{\sigma}_1^\dagger\hat{\sigma}_2$ and $\hat{\sigma}_1\hat{\sigma}_2^\dagger$, which represent the excitation of one emitter and the relaxation of the other one. Thus, this Hamiltonian describes the coherent transfer of energy between the emitters. Importantly, as this Hamiltonian emerges in the reduced Hilbert space of the emitters after tracing out the degrees of freedom of the electromagnetic vacuum field, the vacuum field can thus be interpreted as responsible of mediating such transfer of energy or, equivalently, as responsible of mediating the coherent interaction between the emitters.

Next, we develop the expression of the coupling coefficient V in Eq. (3.39) by using the expressions of $\Gamma_{j\mathbf{k}s,j'\mathbf{k}'s'}(\omega)$ in Eq. (3.37) and considering $\delta \ll \omega_0$. The latter allows us to substitute $\omega_{e,1}$ and $\omega_{e,2}$ by the arithmetic average transition frequency ω_0. In this way, we obtain

$$\begin{aligned}
V &= \frac{1}{2i}\sum_{\mathbf{k},s}\sum_{\mathbf{k}',s'}(\boldsymbol{\mu}_2\cdot\boldsymbol{e}_{\mathbf{k}s})^*(\boldsymbol{\mu}_1\cdot\boldsymbol{e}_{\mathbf{k}'s'})\Big[\Gamma_{1\mathbf{k}s,2\mathbf{k}'s'}(\omega_{e,1})-\Gamma^*_{2\mathbf{k}'s',1\mathbf{k}s}(\omega_{e,2})\Big]\\
&+\frac{1}{2i}\sum_{\mathbf{k},s}\sum_{\mathbf{k}',s'}(\boldsymbol{\mu}_2\cdot\boldsymbol{e}_{\mathbf{k}'s'})^*(\boldsymbol{\mu}_1\cdot\boldsymbol{e}_{\mathbf{k}s})\Big[\Gamma_{2\mathbf{k}s,1\mathbf{k}'s'}(-\omega_{e,2})-\Gamma^*_{1\mathbf{k}'s',2\mathbf{k}s}(-\omega_{e,1})\Big]\\
&=\sum_{\mathbf{k},s}\frac{\omega_\mathrm{k}}{2\varepsilon_0\mathcal{V}\hbar}(\boldsymbol{\mu}_2\cdot\boldsymbol{e}_{\mathbf{k}s})^*(\boldsymbol{\mu}_1\cdot\boldsymbol{e}_{\mathbf{k}s})\\
&\times\left[e^{i\mathbf{k}\cdot(\mathbf{r}_1-\mathbf{r}_2)}\,\mathrm{p.v.}\frac{1}{\omega_0-\omega_\mathrm{k}}+e^{-i\mathbf{k}\cdot(\mathbf{r}_1-\mathbf{r}_2)}\,\mathrm{p.v.}\frac{1}{-\omega_0-\omega_\mathrm{k}}\right].
\end{aligned}\tag{3.40}$$

We now transform the summations over $\mathbf{k}$ into an integral [Eq. (1.134)], which results in

$$\begin{aligned}
V &= \frac{\mathcal{V}}{(2\pi)^3}\sum_s\int_0^\infty d\mathrm{k}\,\mathrm{k}^2\int_0^\pi d\theta\sin\theta\int_0^{2\pi}d\phi\frac{\omega_\mathrm{k}}{2\varepsilon_0\mathcal{V}\hbar}(\boldsymbol{\mu}_2\cdot\boldsymbol{e}_{\mathbf{k}s})^*(\boldsymbol{\mu}_1\cdot\boldsymbol{e}_{\mathbf{k}s})\\
&\times\left[e^{i\mathbf{k}\cdot(\mathbf{r}_1-\mathbf{r}_2)}\,\mathrm{p.v.}\frac{1}{\omega_0-\omega_\mathrm{k}}-e^{-i\mathbf{k}\cdot(\mathbf{r}_1-\mathbf{r}_2)}\,\mathrm{p.v.}\frac{1}{\omega_0+\omega_\mathrm{k}}\right]\\
&=\frac{1}{(2\pi c)^3 2\varepsilon_0\hbar}\,\mathrm{p.v.}\int_{-\infty}^\infty d\omega_\mathrm{k}\frac{\omega_\mathrm{k}^3}{\omega_0-\omega_\mathrm{k}}\int_0^\pi d\theta\sin\theta\int_0^{2\pi}d\phi e^{i\mathbf{k}\cdot(\mathbf{r}_1-\mathbf{r}_2)}\\
&\times\sum_s(\boldsymbol{\mu}_2\cdot\boldsymbol{e}_{\mathbf{k}s})^*(\boldsymbol{\mu}_1\cdot\boldsymbol{e}_{\mathbf{k}s}).
\end{aligned}\tag{3.41}$$

To integrate over the solid angle, we assume $\mathbf{r}_1-\mathbf{r}_2=r_{12}\boldsymbol{e}_z$ and, additionally, we use the expressions of the polarization unit vectors $\boldsymbol{e}_{\mathbf{k}s}$ in Eqs. (1.137a)–(1.137b).

We find

$$\begin{aligned}
V &= \frac{1}{(2\pi c)^3 2\varepsilon_0 \hbar}\,\mathrm{p.v.}\int_{-\infty}^{\infty} d\omega_\mathrm{k}\frac{\omega_\mathrm{k}^3}{\omega_0-\omega_\mathrm{k}}\int_0^\pi d\theta\sin\theta e^{i\omega_\mathrm{k} r_{12}\cos\theta/c}\int_0^{2\pi} d\phi \\
&\times\sum_s(\boldsymbol{\mu}_2\cdot\boldsymbol{e}_{\mathbf{k}s})(\boldsymbol{\mu}_1\cdot\boldsymbol{e}_{\mathbf{k}s}) \\
&= \frac{\pi}{(2\pi c)^3 2\varepsilon_0\hbar}\,\mathrm{p.v.}\int_{-\infty}^{\infty} d\omega_\mathrm{k}\frac{\omega_\mathrm{k}^3}{\omega_0-\omega_\mathrm{k}}\int_0^\pi d\theta\sin\theta e^{i\omega_\mathrm{k} r_{12}\cos\theta/c} \\
&\times\left[\left(\mu_{1,x}\mu_{2,x}+\mu_{1,y}\mu_{2,y}\right)(1+\cos^2\theta)+\mu_{1,z}\mu_{2,z}2\sin^2\theta\right] \\
&= \frac{2\pi}{(2\pi c)^3\varepsilon_0\hbar}\,\mathrm{p.v.}\int_{-\infty}^{\infty} d\omega_\mathrm{k}\frac{\omega_\mathrm{k}^3}{\omega_0-\omega_\mathrm{k}}\left[2\mu_{1,z}\mu_{2,z}\left(\frac{\sin(\mathrm{k}r_{12})}{(\mathrm{k}r_{12})^3}-\frac{\cos(\mathrm{k}r_{12})}{(\mathrm{k}r_{12})^2}\right)\right. \\
&\left.+\left(\mu_{1,x}\mu_{2,x}+\mu_{1,y}\mu_{2,y}\right)\left(-\frac{\sin(\mathrm{k}r_{12})}{(\mathrm{k}r_{12})^3}+\frac{\cos(\mathrm{k}r_{12})}{(\mathrm{k}r_{12})^2}+\frac{\sin(\mathrm{k}r_{12})}{\mathrm{k}r_{12}}\right)\right].
\end{aligned} \tag{3.42}$$

The frequency integral can be solved using Eq. (3.19), which yields

$$\begin{aligned}
V &= \frac{\omega_0^3}{4\pi c^3\varepsilon_0\hbar}\left[-2\mu_{1,z}\mu_{2,z}\left(\frac{\cos(\mathrm{k}_0 r_{12})}{(\mathrm{k}_0 r_{12})^3}-\frac{\sin(\mathrm{k}_0 r_{12})}{(\mathrm{k}_0 r_{12})^2}\right)\right. \\
&\left.+\left(\mu_{1,x}\mu_{2,x}+\mu_{1,y}\mu_{2,y}\right)\left(\frac{\cos(\mathrm{k}_0 r_{12})}{(\mathrm{k}_0 r_{12})^3}+\frac{\sin(\mathrm{k}_0 r_{12})}{(\mathrm{k}_0 r_{12})^2}-\frac{\cos(\mathrm{k}_0 r_{12})}{\mathrm{k}_0 r_{12}}\right)\right],
\end{aligned} \tag{3.43}$$

with $\mathrm{k}_0=\omega_0/c$ the wavenumber corresponding to the arithmetic average transition frequency ω_0. Finally, using the expression of the decay rate γ_0 of a two-level QE with transition frequency ω_0 [Eq. (1.163)] and taking into account that we considered $\mathbf{r}_1-\mathbf{r}_2$ to be aligned in the z-axis, we obtain

$$\begin{aligned}
V &= \frac{3\gamma_0}{4}\left[\left(-\boldsymbol{e}_{\boldsymbol{\mu}_1}\cdot\boldsymbol{e}_{\boldsymbol{\mu}_2}+(\boldsymbol{e}_{\boldsymbol{\mu}_1}\cdot\boldsymbol{e}_{\mathbf{r}_{12}})(\boldsymbol{e}_{\boldsymbol{\mu}_2}\cdot\boldsymbol{e}_{\mathbf{r}_{12}})\right)\frac{\cos(\mathrm{k}_0 r_{12})}{\mathrm{k}_0 r_{12}}\right. \\
&\left.+\left(\boldsymbol{e}_{\boldsymbol{\mu}_1}\cdot\boldsymbol{e}_{\boldsymbol{\mu}_2}-3(\boldsymbol{e}_{\boldsymbol{\mu}_1}\cdot\boldsymbol{e}_{\mathbf{r}_{12}})(\boldsymbol{e}_{\boldsymbol{\mu}_2}\cdot\boldsymbol{e}_{\mathbf{r}_{12}})\right)\left(\frac{\cos(\mathrm{k}_0 r_{12})}{(\mathrm{k}_0 r_{12})^3}+\frac{\sin(\mathrm{k}_0 r_{12})}{(\mathrm{k}_0 r_{12})^2}\right)\right],
\end{aligned} \tag{3.44}$$

where $\boldsymbol{e}_{\boldsymbol{\mu}_j}$ corresponds to the unit vector of $\boldsymbol{\mu}_j$ and $\boldsymbol{e}_{\mathbf{r}_{12}}$ to the unit vector of $\mathbf{r}_1-\mathbf{r}_2$. The expression for the dipole-dipole coupling strength V in Eq. (3.44) is identical to the expression of the electromagnetic interaction between two classical electric point dipoles, including retardation effects [121, 132].

Dissipative dipole-dipole coupling

We focus next on the calculation of the second line in Eq. (1.189), which corresponds to the dissipators describing the losses of the quantum emitters. We obtain

$$\begin{aligned}
&\sum_{\omega,\omega'}\sum_{j,\mathbf{k},s}\sum_{j',\mathbf{k}',s'} e^{i(\omega-\omega')t}\frac{\Gamma_{j\mathbf{k}s,j'\mathbf{k}'s'}(\omega)+\Gamma^*_{j'\mathbf{k}'s',j\mathbf{k}s}(\omega')}{2}\mathcal{D}[\hat{S}_{j'\mathbf{k}'s'}(\omega),\hat{S}_{j\mathbf{k}s}(\omega')]\\
&=\sum_{\mathbf{k},s}\sum_{\mathbf{k}',s'}\frac{\Gamma_{1\mathbf{k}s,1\mathbf{k}'s'}(\omega_{e,1})+\Gamma^*_{1\mathbf{k}'s',1\mathbf{k}s}(\omega_{e,1})}{2}\mathcal{D}[\hat{S}_{1\mathbf{k}'s'}(\omega_{e,1}),\hat{S}_{1\mathbf{k}s}(\omega_{e,1})]\\
&+\sum_{\mathbf{k},s}\sum_{\mathbf{k}',s'}\frac{\Gamma_{2\mathbf{k}s,2\mathbf{k}'s'}(\omega_{e,2})+\Gamma^*_{2\mathbf{k}'s',2\mathbf{k}s}(\omega_{e,2})}{2}\mathcal{D}[\hat{S}_{2\mathbf{k}'s'}(\omega_{e,2}),\hat{S}_{2\mathbf{k}s}(\omega_{e,2})]\\
&+\sum_{\mathbf{k},s}\sum_{\mathbf{k}',s'}e^{i\delta t}\frac{\Gamma_{2\mathbf{k}s,1\mathbf{k}'s'}(\omega_{e,1})+\Gamma^*_{1\mathbf{k}'s',2\mathbf{k}s}(\omega_{e,2})}{2}\mathcal{D}[\hat{S}_{1\mathbf{k}'s'}(\omega_{e,1}),\hat{S}_{2\mathbf{k}s}(\omega_{e,2})]\\
&+\sum_{\mathbf{k},s}\sum_{\mathbf{k}',s'}e^{-i\delta t}\frac{\Gamma_{1\mathbf{k}s,2\mathbf{k}'s'}(\omega_{e,2})+\Gamma^*_{2\mathbf{k}'s',1\mathbf{k}s}(\omega_{e,1})}{2}\mathcal{D}[\hat{S}_{2\mathbf{k}'s'}(\omega_{e,2}),\hat{S}_{1\mathbf{k}s}(\omega_{e,1})].
\end{aligned}\tag{3.45}$$

Substituting the expression for $\Gamma_{j\mathbf{k}s,j'\mathbf{k}'s'}(\omega)$ from Eq. (3.37), we find

$$\begin{aligned}
&\sum_{\omega,\omega'}\sum_{j,\mathbf{k},s}\sum_{j',\mathbf{k}',s'} e^{i(\omega-\omega')t}\frac{\Gamma_{j\mathbf{k}s,j'\mathbf{k}'s'}(\omega)+\Gamma^*_{j'\mathbf{k}'s',j\mathbf{k}s}(\omega')}{2}\mathcal{D}[\hat{S}_{j'\mathbf{k}'s'}(\omega),\hat{S}_{j\mathbf{k}s}(\omega')]\\
&=\frac{1}{2}\mathcal{D}[\hat{\sigma}_1]\sum_{\mathbf{k},s}\frac{|\boldsymbol{\mu}_1\cdot\boldsymbol{e}_{\mathbf{k}s}|^2\omega_{\mathrm{k}}}{\varepsilon_0\mathcal{V}\hbar}\pi\delta(\omega_{e,1}-\omega_{\mathrm{k}})\\
&+\frac{1}{2}\mathcal{D}[\hat{\sigma}_2]\sum_{\mathbf{k},s}\frac{|\boldsymbol{\mu}_2\cdot\boldsymbol{e}_{\mathbf{k}s}|^2\omega_{\mathrm{k}}}{\varepsilon_0\mathcal{V}\hbar}\pi\delta(\omega_{e,2}-\omega_{\mathrm{k}})\\
&+e^{i\delta t}\frac{1}{2}\mathcal{D}[\hat{\sigma}_1,\hat{\sigma}_2]\sum_{\mathbf{k},s}\frac{(\boldsymbol{\mu}_2\cdot\boldsymbol{e}_{\mathbf{k}s})(\boldsymbol{\mu}_1\cdot\boldsymbol{e}_{\mathbf{k}s})^*\omega_{\mathrm{k}}}{\varepsilon_0\mathcal{V}\hbar}e^{-i\mathbf{k}\cdot(\mathbf{r}_1-\mathbf{r}_2)}\pi\delta(\omega_0-\omega_{\mathrm{k}})\\
&+e^{-i\delta t}\frac{1}{2}\mathcal{D}[\hat{\sigma}_2,\hat{\sigma}_1]\sum_{\mathbf{k},s}\frac{(\boldsymbol{\mu}_1\cdot\boldsymbol{e}_{\mathbf{k}s})(\boldsymbol{\mu}_2\cdot\boldsymbol{e}_{\mathbf{k}s})^*\omega_{\mathrm{k}}}{\varepsilon_0\mathcal{V}\hbar}e^{i\mathbf{k}\cdot(\mathbf{r}_1-\mathbf{r}_2)}\pi\delta(\omega_0-\omega_{\mathrm{k}}).
\end{aligned}\tag{3.46}$$

In the summations in the last two lines of this equation we have assumed again $\delta \ll \omega_0$ and replaced $\omega_{e,j}$ by ω_0.

We now compute separately each of the summations on the right-hand side of Eq. (3.46). On the one hand, the decay rate associated with the dissipator $\mathcal{D}[\hat{\sigma}_j]$

becomes

$$\begin{aligned}
&\sum_{\mathbf{k},s} \frac{|\boldsymbol{\mu}_j \cdot \boldsymbol{e}_{\mathbf{k}s}|^2 \omega_{\mathrm{k}}}{\varepsilon_0 \mathcal{V} \hbar} \pi \delta(\omega_{e,j} - \omega_{\mathrm{k}}) = \frac{\pi}{(2\pi c)^3 \varepsilon_0 \hbar} \\
&\times \int_0^\infty d\omega_{\mathrm{k}} \omega_{\mathrm{k}}^3 \delta(\omega_{e,j} - \omega_{\mathrm{k}}) \sum_s \int_0^{2\pi} d\phi \int_0^\pi d\theta \sin\theta |\boldsymbol{\mu_j} \cdot \boldsymbol{e_{\mathbf{k}s}}|^2 \\
&= \frac{\omega_{e,j}^3 |\boldsymbol{\mu}_j|^2}{3\pi \varepsilon_0 \hbar c^3}.
\end{aligned} \tag{3.47}$$

Here, we have used Eq. (1.160) to solve the solid angle integrals. Notably, the resulting expression in the third line of this equation corresponds to the spontaneous emission rate of a two-level emitter with transition frequency $\omega_{e,j}$ and transition dipole moment $\boldsymbol{\mu}_j$ [Eq. (1.163)], which we denote by γ_j. Specifically,

$$\gamma_j = \frac{\omega_{e,j}^3 |\boldsymbol{\mu}_j|^2}{3\pi \varepsilon_0 \hbar c^3} = \sum_{\mathbf{k},s} \frac{|\boldsymbol{\mu}_j \cdot \boldsymbol{e}_{\mathbf{k}s}|^2 \omega_{\mathrm{k}}}{\varepsilon_0 \mathcal{V} \hbar} \pi \delta(\omega_{e,j} - \omega_{\mathrm{k}}). \tag{3.48}$$

On the other hand, to compute the decay rate associated with $\mathcal{D}[\hat{\sigma}_1, \hat{\sigma}_2]$ in Eq. (3.46), we consider again that $\boldsymbol{e}_{\mathbf{r}_{12}}$ is aligned along the z-axis and use the expressions of the polarization unit vectors in Eqs. (1.137a)–(1.137b). We obtain

$$\begin{aligned}
&\sum_{\mathbf{k},s} \frac{(\boldsymbol{\mu}_2 \cdot \boldsymbol{e}_{\mathbf{k}s})(\boldsymbol{\mu}_1 \cdot \boldsymbol{e}_{\mathbf{k}s})^* \omega_{\mathrm{k}}}{\varepsilon_0 \mathcal{V} \hbar} e^{-i\mathbf{k}\cdot(\mathbf{r}_1 - \mathbf{r}_2)} \pi \delta(\omega_0 - \omega_{\mathrm{k}}) = \frac{\pi}{(2\pi c)^3 \varepsilon_0 \hbar} \\
&\times \int_0^\infty d\omega_{\mathrm{k}} \omega_{\mathrm{k}}^3 \delta(\omega_0 - \omega_{\mathrm{k}}) \int_0^\pi d\theta \sin\theta e^{-i\omega_{\mathrm{k}} r_{12} \cos\theta / c} \int_0^{2\pi} d\phi \sum_s (\boldsymbol{\mu}_2 \cdot \boldsymbol{e}_{\mathbf{k}s})(\boldsymbol{\mu}_1 \cdot \boldsymbol{e}_{\mathbf{k}s})^* \\
&= \frac{\pi^2}{(2\pi c)^3 \varepsilon_0 \hbar} \int_0^\infty d\omega_{\mathrm{k}} \omega_{\mathrm{k}}^3 \delta(\omega_0 - \omega_{\mathrm{k}}) \int_0^\pi d\theta \sin\theta \\
&\times \Big((\mu_{1,x}\mu_{2,x} + \mu_{1,y}\mu_{2,y})(1 + \cos^2\theta) + \mu_{1,z}\mu_{2,z} 2\sin\theta \Big) \\
&= \frac{1}{2\pi \varepsilon_0 \hbar c^3} \int_0^\infty d\omega_{\mathrm{k}} \omega_{\mathrm{k}}^3 \delta(\omega_0 - \omega_{\mathrm{k}}) \Bigg[2\mu_{1,z}\mu_{2,z} \left(\frac{\sin(\mathrm{k}r_{12})}{(\mathrm{k}r_{12})^3} - \frac{\cos(\mathrm{k}r_{12})}{(\mathrm{k}r_{12})^2} \right) \\
&+ \Big(\mu_{1,x}\mu_{2,x} + \mu_{1,y}\mu_{2,y} \Big) \left(- \frac{\sin(\mathrm{k}r_{12})}{(\mathrm{k}r_{12})^3} + \frac{\cos(\mathrm{k}r_{12})}{(\mathrm{k}r_{12})^2} + \frac{\sin(\mathrm{k}r_{12})}{\mathrm{k}r_{12}} \right) \Bigg].
\end{aligned} \tag{3.49}$$

As $\boldsymbol{e}_{\mathbf{r}_{12}}$ has been fixed along the z-axis, we can now rewrite this expression as

$$\begin{aligned}\tilde{\gamma} \equiv & \sum_{\mathbf{k},s} \frac{(\boldsymbol{\mu}_2 \cdot \boldsymbol{e}_{\mathbf{k}s})(\boldsymbol{\mu}_1 \cdot \boldsymbol{e}_{\mathbf{k}s})^* \omega_{\mathrm{k}}}{\varepsilon_0 \mathcal{V} \hbar} e^{-i\mathbf{k}\cdot(\mathbf{r}_1-\mathbf{r}_2)} \pi \delta(\omega_0 - \omega_{\mathrm{k}}) = \\ & = \frac{3\gamma_0}{2}\Bigg[\bigg(\boldsymbol{e}_{\boldsymbol{\mu}_1}\cdot\boldsymbol{e}_{\boldsymbol{\mu}_2} - (\boldsymbol{e}_{\boldsymbol{\mu}_1}\cdot\boldsymbol{e}_{\mathbf{r_{12}}})(\boldsymbol{e}_{\boldsymbol{\mu}_2}\cdot\boldsymbol{e}_{\mathbf{r_{12}}})\bigg)\frac{\sin(\mathrm{k}_0 r_{12})}{\mathrm{k}_0 r_{12}} \\ & + \bigg(\boldsymbol{e}_{\boldsymbol{\mu}_1}\cdot\boldsymbol{e}_{\boldsymbol{\mu}_2} - 3(\boldsymbol{e}_{\boldsymbol{\mu}_1}\cdot\boldsymbol{e}_{\mathbf{r_{12}}})(\boldsymbol{e}_{\boldsymbol{\mu}_2}\cdot\boldsymbol{e}_{\mathbf{r_{12}}})\bigg)\bigg(-\frac{\sin(\mathrm{k}_0 r_{12})}{(\mathrm{k}_0 r_{12})^3} + \frac{\cos(\mathrm{k}_0 r_{12})}{(\mathrm{k}_0 r_{12})^2}\bigg)\Bigg],\end{aligned} \tag{3.50}$$

where we have defined this decay rate as $\tilde{\gamma}$. In a similar way, one can show that the decay rate associated with dissipator $\mathcal{D}[\hat{\sigma}_2, \hat{\sigma}_1]$ is again $\tilde{\gamma}$ [Eq. (3.50)].

Therefore, we conclude that, in addition to the spontaneous emission of each emitter (with rate γ_j), the electromagnetic vacuum field also mediates an incoherent or dissipative dipole-dipole interaction between the emitters, with rate $\tilde{\gamma}$. This interaction is accounted for in the MME through dissipators that mix lowering and raising operators of both emitters.

Final form of the MME

The Lamb-shift Hamiltonian and dissipators derived above by tracing out the degrees of freedom of the electromagnetic vacuum field lead to the interaction-picture MME

$$\begin{aligned}\frac{d}{dt}\hat{\rho}^{(I)} = & -\frac{i}{\hbar}[\hbar V(e^{i\delta t}\hat{\sigma}_1\hat{\sigma}_2^\dagger + e^{-i\delta t}\hat{\sigma}_1^\dagger\hat{\sigma}_2), \hat{\rho}^{(I)}] + \sum_j \frac{\gamma_j}{2}\mathcal{D}[\hat{\sigma}_j]\hat{\rho}^{(I)} \\ & + \frac{\tilde{\gamma}e^{i\delta t}}{2}\mathcal{D}[\hat{\sigma}_1, \hat{\sigma}_2]\hat{\rho}^{(I)} + \frac{\tilde{\gamma}e^{-i\delta t}}{2}\mathcal{D}[\hat{\sigma}_2, \hat{\sigma}_1]\hat{\rho}^{(I)},\end{aligned} \tag{3.51}$$

where $\hat{\rho}^{(I)}$ is the reduced density matrix of the emitters in the interaction picture. Transforming this MME to the Schrödinger picture yields

$$\frac{d}{dt}\hat{\rho} = -\frac{i}{\hbar}[\hat{H}_0 + \hat{H}_{\mathrm{int}}, \hat{\rho}] + \sum_j \frac{\gamma_j}{2}\mathcal{D}[\hat{\sigma}_j]\hat{\rho} + \frac{\tilde{\gamma}}{2}\Big(\mathcal{D}[\hat{\sigma}_1, \hat{\sigma}_2]\hat{\rho} + \mathcal{D}[\hat{\sigma}_2, \hat{\sigma}_1]\hat{\rho}\Big), \tag{3.52}$$

where we recall that $\hat{H}_0 = \hat{H}_{\mathrm{QE}}^{(1)} + \hat{H}_{\mathrm{QE}}^{(2)} = \hbar\sum_j \frac{\omega_{e,j}}{2}\hat{\sigma}_{z,j}$ is the unperturbed Hamiltonian of the quantum emitters, and

$$\hat{H}_{\mathrm{int}} = \hbar V(\hat{\sigma}_1\hat{\sigma}_2^\dagger + \hat{\sigma}_1^\dagger\hat{\sigma}_2) \tag{3.53}$$

corresponds to the Lamb-shift Hamiltonian in the Schrödinger picture, which is identified as the interaction Hamiltonian between the two emitters mediated by the electromagnetic vacuum field. This interaction Hamiltonian can modify the eigenstates of the quantum emitters, which we discuss in detail in Section 3.2.1.

3.1.5 Effective description of the electronic dynamics of two interacting solid-state quantum emitters

In the previous section, we have derived the Markovian master equation (MME) governing the reduced dynamics of two quantum emitters in vacuum [Eq. (3.52)], assuming that they behave as ideal two-level systems. This two-level description can be directly applied to model the dynamics of atomic systems. However, in this thesis, we focus on characterizing light emission from solid-state quantum emitters, which can support internal vibrational modes. Additionally, these emitters are embedded in a host matrix with refractive index $n \neq 1$, supporting phononic modes that also affect the emitter dynamics. In this section, we adapt the MME in Eq. (3.52) to effectively incorporate the impact of the vibrational and phononic modes in the dynamics of the pure (0-phonon) electronic states, so that the emitters can be treated as perfect two-level systems after modifying appropriately the value of different parameters.

The interaction of the electronic states $|e_j\rangle$ and $|g_j\rangle$ with internal vibrational modes and with phononic modes of the host matrix results in additional decay channels for the emitters. Specifically, in addition to the purely electronic transition $|e_j\rangle \to |g_j\rangle$, known as *Zero-Phonon Line* (ZPL), the electronic excited state $|e_j\rangle$ can also relax to vibrational or phononic levels in the electronic ground state. The probability that the relaxation of the electronic excited state occurs via the ZPL is quantified by the *combined Debye-Waller/Franck-Condon factor* α_{DW} [1, 180]. This factor is bounded between 0 ($|e_j\rangle$ always decays to vibrational or phononic levels) and 1 ($|e_j\rangle$ always decays into the ZPL).

Hereafter, we consider that γ_j corresponds to the total emission rate from the pure electronic excited state $|e_j\rangle$, which includes the decay into the ZPL and also the decay to the vibrational and phononic levels in the electronic ground state. γ_j thus corresponds to the inverse of the lifetime of $|e_j\rangle$. As a result, the effective decay rate into the ZPL is obtained from γ_j and α_{DW} as

$$\gamma_j^{\mathrm{ZPL}} = \alpha_{\mathrm{DW}}\gamma_j. \tag{3.54}$$

Using Eq. (3.48), the ZPL transition dipole moment of emitter j is thus given by

$$|\boldsymbol{\mu}_j^{\mathrm{ZPL}}| = \sqrt{\frac{\gamma_j^{\mathrm{ZPL}} 3\pi\varepsilon_0\hbar c^3}{\omega_{e,j}^3 n}} = \sqrt{\frac{\alpha_{\mathrm{DW}}\gamma_j 3\pi\varepsilon_0\hbar c^3}{\omega_{e,j}^3 n}}, \tag{3.55}$$

where we have also included the influence of the refractive index $n \neq 1$ of the host medium (which can differ from that of vacuum), by replacing $c \to c/n$ and $\varepsilon_0 \to \varepsilon_0 n^2$ [31, 181]. Importantly, within the framework adopted in this chapter, the emitters are always treated as two-level systems and no vibrational or phononic states are directly included in the MME. As a consequence, we consider that the decay rate associated with the Lindblad dissipators $\mathcal{D}[\hat{\sigma}_j]\hat{\rho}$ in the MME [Eq. (3.52)] is the total emission rate γ_j (instead of γ_j^{ZPL}, which would yield an incorrect lifetime for $|e_j\rangle$).

Furthermore, we consider in this thesis situations in which the coherent dipole-dipole coupling is much weaker than the decay rates of the vibrational or phononic modes that can couple to the electronic states. As a result, the coupling mediated by vibrational or phononic levels can be neglected, and we consider that the emitters interact only through the ZPL. We thus modify the expressions for the coherent dipole-dipole coupling [Eq. (3.44)] and the dissipative dipole-dipole coupling [Eq. (3.50)], replacing the total dipole moments by $\boldsymbol{\mu}_j^{\mathrm{ZPL}}$. In this way, we obtain that the effective expressions for the coherent and dissipative dipole-dipole couplings become

$$V_{\mathrm{DW}} = \alpha_{\mathrm{DW}} V = \alpha_{\mathrm{DW}} \frac{3\gamma_0}{4}\left[\left(- \boldsymbol{e}_{\boldsymbol{\mu}_1}\cdot\boldsymbol{e}_{\boldsymbol{\mu}_2} + (\boldsymbol{e}_{\boldsymbol{\mu}_1}\cdot\boldsymbol{e}_{\mathbf{r}_{12}})(\boldsymbol{e}_{\boldsymbol{\mu}_2}\cdot\boldsymbol{e}_{\mathbf{r}_{12}})\right)\frac{\cos(\mathrm{k}_0 r_{12})}{\mathrm{k}_0 r_{12}} + \left(\boldsymbol{e}_{\boldsymbol{\mu}_1}\cdot\boldsymbol{e}_{\boldsymbol{\mu}_2} - 3(\boldsymbol{e}_{\boldsymbol{\mu}_1}\cdot\boldsymbol{e}_{\mathbf{r}_{12}})(\boldsymbol{e}_{\boldsymbol{\mu}_2}\cdot\boldsymbol{e}_{\mathbf{r}_{12}})\right)\left(\frac{\cos(\mathrm{k}_0 r_{12})}{(\mathrm{k}_0 r_{12})^3} + \frac{\sin(\mathrm{k}_0 r_{12})}{(\mathrm{k}_0 r_{12})^2}\right)\right], \tag{3.56a}$$

$$\tilde{\gamma}_{\mathrm{DW}} = \alpha_{\mathrm{DW}} \tilde{\gamma} = \alpha_{\mathrm{DW}} \frac{3\gamma_0}{2}\left[\left(\boldsymbol{e}_{\boldsymbol{\mu}_1}\cdot\boldsymbol{e}_{\boldsymbol{\mu}_2} - (\boldsymbol{e}_{\boldsymbol{\mu}_1}\cdot\boldsymbol{e}_{\mathbf{r_{12}}})(\boldsymbol{e}_{\boldsymbol{\mu}_2}\cdot\boldsymbol{e}_{\mathbf{r_{12}}})\right)\frac{\sin(\mathrm{k}_0 r_{12})}{\mathrm{k}_0 r_{12}} + \left(\boldsymbol{e}_{\boldsymbol{\mu}_1}\cdot\boldsymbol{e}_{\boldsymbol{\mu}_2} - 3(\boldsymbol{e}_{\boldsymbol{\mu}_1}\cdot\boldsymbol{e}_{\mathbf{r_{12}}})(\boldsymbol{e}_{\boldsymbol{\mu}_2}\cdot\boldsymbol{e}_{\mathbf{r_{12}}})\right)\left(- \frac{\sin(\mathrm{k}_0 r_{12})}{(\mathrm{k}_0 r_{12})^3} + \frac{\cos(\mathrm{k}_0 r_{12})}{(\mathrm{k}_0 r_{12})^2}\right)\right], \tag{3.56b}$$

where $\mathrm{k}_0 = n\omega_0/c$ corresponds to the wavevector in the homogeneous medium, with refractive index $n \neq 1$. Therefore, the key change with respect to the MME derived for ideal two-level quantum emitters is a decrease in the coherent and dissipative couplings by a factor of α_{DW}, as V is replaced by V_{DW} and $\tilde{\gamma}$ by $\tilde{\gamma}_{\mathrm{DW}}$.

Finally, at very short separation distances between the emitters ($\mathrm{k}_0 r_{12} \ll 1$), the expressions of the coherent and dissipative couplings are substantially simplified. Taking the limit $\mathrm{k}_0 r_{12} \to 0$ in Eqs. (3.56a)–(3.56b), we find

$$V_{\mathrm{DW}} \xrightarrow{\mathrm{k}_0 r_{12}\to 0} \alpha_{\mathrm{DW}} \frac{3\gamma_0}{4(\mathrm{k}_0 r_{12}^3)}\left(\boldsymbol{e}_{\boldsymbol{\mu}_1}\cdot\boldsymbol{e}_{\boldsymbol{\mu}_2} - 3(\boldsymbol{e}_{\boldsymbol{\mu}_1}\cdot\boldsymbol{e}_{\mathbf{r}_{12}})(\boldsymbol{e}_{\boldsymbol{\mu}_2}\cdot\boldsymbol{e}_{\mathbf{r}_{12}})\right), \tag{3.57a}$$

$$\tilde{\gamma}_{\mathrm{DW}} \xrightarrow{\mathrm{k}_0 r_{12}\to 0} \alpha_{\mathrm{DW}}\gamma_0 \boldsymbol{e}_{\boldsymbol{\mu}_1}\cdot\boldsymbol{e}_{\boldsymbol{\mu}_2}. \tag{3.57b}$$

We emphasize that the effective MME introduced in this section works well to describe the dynamics of the pure electronic states $|e_j\rangle$ and $|g_j\rangle$ and, thus, to characterize the light emission into the ZPL. In Sections 3.3 and 3.4, we use this framework to analyze the statistics of the light emitted into the ZPL from two strongly interacting emitters under different illumination schemes. In Chapter 4, we present a refined model that allows us to additionally analyze the statistics of light emitted due to the decay from the electronic excited state to vibrational or phononic levels in the electronic ground state.

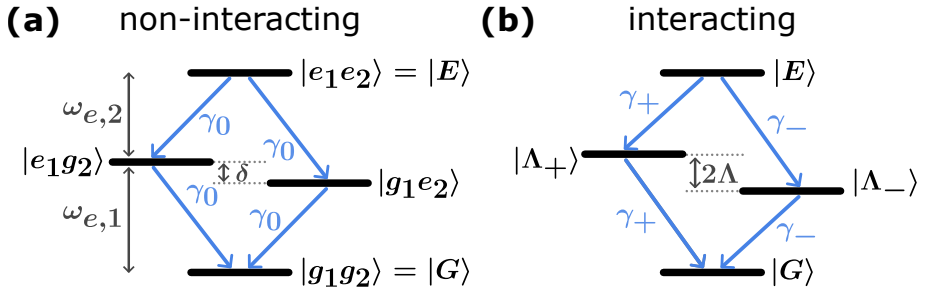

Figure 3.2: Schematic representation of the eigenstates of two quantum emitters. (a) In the absence of dipole-dipole interaction, the eigenstates are $|g_1g_2\rangle$, $|g_1e_2\rangle$, $|e_1g_2\rangle$, and $|e_1e_2\rangle$. The emitters have transition frequencies $\omega_{e,1}$ and $\omega_{e,2}$, with detuning $\delta = \omega_{e,1} - \omega_{e,2}$. Blue arrows represent the one-photon transitions, with γ_0 the total spontaneous emission rate of each emitter (assumed to be identical for both of them). (b) Under dipole-dipole interaction, the eigenstates of the system become $|G\rangle = |g_1g_2\rangle$, $|\Lambda_-\rangle$, $|\Lambda_+\rangle$, and $|E\rangle = |e_1e_2\rangle$. The transition frequencies from $|G\rangle$ to $|\Lambda_\pm\rangle$ are $\omega_\pm = \omega_0 \pm \Lambda$, with $\omega_0 = (\omega_{e,1} + \omega_{e,2})/2$ and $\Lambda = \sqrt{V_{\mathrm{DW}}^2 + (\delta/2)^2}$. The decay rate of the one-photon transitions $|E\rangle \to |\Lambda_\pm\rangle$ and $|\Lambda_\pm\rangle \to |G\rangle$ is $\gamma_\pm$ [Eq. (3.64)].

3.2 Dynamics of the superradiant and subradiant states under laser driving

We show in this section that the dipole-dipole interaction between the two emitters can result in the emergence of new eigenstates with modified energies, lifetimes, and coupling strengths to the driving laser. Notably, we discuss the emergence of superradiant and subradiant states when the transition dipole moments of the two emitters are not perpendicular. Moreover, we describe the interaction between the emitters and a laser, which leads to the emergence of the dressed eigenstates. Finally, we derive the equations of motion for all the elements of the density matrix, which are then used in Section 3.3 to gain analytical insights into the behaviour of the color-blind intensity correlation.

3.2.1 Superradiant and subradiant states

In this section, we show that the dipole-dipole interaction can significantly impact the eigenstates of the emitters. To this end, we first recall that, in the absence of the dipole-dipole interaction, the emitters are described by the Hamiltonian $\hat{H}_0 = \hat{H}_{\mathrm{QE}}^{(1)} + \hat{H}_{\mathrm{QE}}^{(2)} = \sum_j \hbar \frac{\omega_{e,j}}{2} \hat{\sigma}_{z,j}$, whose eigenstates are $|e_1e_2\rangle$, $|e_1g_2\rangle$, $|g_1e_2\rangle$, and $|g_1g_2\rangle$, as schematically represented in Fig. 3.2a. Additionally, the coherent dipole-dipole interaction between the emitters is described by the Hamiltonian $\hat{H}_{\mathrm{int}} = \hbar V_{\mathrm{DW}}(\hat{\sigma}_1^\dagger \hat{\sigma}_2 + \hat{\sigma}_1 \hat{\sigma}_2^\dagger)$ (Sections 3.1.4 and 3.1.5). Under dipole-dipole interaction, the eigenstates of the emitters are thus obtained by diagonalizing

the total Hamiltonian $\hat{H}_0 + \hat{H}_{\text{int}}$. By doing this, we find

$$\hat{H}_0 + \hat{H}_{\text{int}} = \hbar\omega_0(|E\rangle\langle E| - |G\rangle\langle G|) + \hbar\Lambda(|\Lambda_+\rangle\langle\Lambda_+| - |\Lambda_-\rangle\langle\Lambda_-|), \tag{3.58}$$

where $\omega_0 = (\omega_{e,1} + \omega_{e,2})/2$ is again the arithmetic average transition frequency and, additionally, we have introduced the ground state $|G\rangle = |g_1 g_2\rangle$, the doubly-excited state $|E\rangle = |e_1 e_2\rangle$, and the single-excitation states

$$|\Lambda_+\rangle = \cos\Theta_\Lambda\,|g_1 e_2\rangle + \sin\Theta_\Lambda\,|e_1 g_2\rangle\,, \tag{3.59a}$$
$$|\Lambda_-\rangle = -\sin\Theta_\Lambda\,|g_1 e_2\rangle + \cos\Theta_\Lambda\,|e_1 g_2\rangle\,. \tag{3.59b}$$

Here, the angle Θ_Λ fulfills

$$\sin(2\Theta_\Lambda) = V_{\text{DW}}/\Lambda, \tag{3.60a}$$
$$\cos(2\Theta_\Lambda) = -\delta/(2\Lambda), \tag{3.60b}$$

with $\delta = \omega_{e,1} - \omega_{e,2}$ the detuning between the two transition frequencies. The states $|\Lambda_+\rangle$ and $|\Lambda_+\rangle$ are quantum superpositions of the states $|g_1 e_2\rangle$ and $|e_1 g_2\rangle$, for which one of the emitters is in the excited state and the other one is in the ground state. Thus, $|\Lambda_+\rangle$ and $|\Lambda_-\rangle$ are usually referred to as *delocalized* states. The energy difference between $|\Lambda_+\rangle$ (higher energy) and $|\Lambda_-\rangle$ (lower energy) is given by

$$2\Lambda = \sqrt{4V_{\text{DW}}^2 + \delta^2}. \tag{3.61}$$

The transition frequency from the state $|G\rangle$ to $|\Lambda_\pm\rangle$ is given by

$$\omega_\pm = \omega_0 \pm \Lambda, \tag{3.62}$$

as schematically represented in Fig. 3.2b.

Next, we derive the decay rates for the delocalized states $|\Lambda_+\rangle$ and $|\Lambda_-\rangle$. To this end, we rewrite the dissipators in Eq. (3.52) using the new basis of eigenstates $|E\rangle$, $|\Lambda_+\rangle$, $|\Lambda_-\rangle$, and $|G\rangle$. Assuming $\gamma_0 \equiv \gamma_1 = \gamma_2$, we obtain

$$\begin{aligned}
&\sum_j \frac{\gamma_j}{2}\mathcal{D}[\hat{\sigma}_j]\hat{\rho} + \frac{\tilde{\gamma}_{\text{DW}}}{2}\Big(\mathcal{D}[\hat{\sigma}_1,\hat{\sigma}_2]\hat{\rho} + \mathcal{D}[\hat{\sigma}_2,\hat{\sigma}_1]\hat{\rho}\Big)\\
&= \frac{\gamma_+}{2}\big(\mathcal{D}[\hat{\sigma}_{G+}]\hat{\rho} + \mathcal{D}[\hat{\sigma}_{+E}]\hat{\rho}\big) + \frac{\gamma_-}{2}\big(\mathcal{D}[\hat{\sigma}_{G-}]\hat{\rho} + \mathcal{D}[\hat{\sigma}_{-E}]\hat{\rho}\big)\\
&+ \frac{\tilde{\gamma}_+}{2}\big(\mathcal{D}[\hat{\sigma}_{G+},\hat{\sigma}_{+E}]\hat{\rho} + \mathcal{D}[\hat{\sigma}_{+E},\hat{\sigma}_{G+}]\hat{\rho}\big) + \frac{\tilde{\gamma}_-}{2}\big(\mathcal{D}[\hat{\sigma}_{G-},\hat{\sigma}_{-E}]\hat{\rho} + \mathcal{D}[\hat{\sigma}_{-E},\hat{\sigma}_{G-}]\hat{\rho}\big)\\
&+ \frac{\tilde{\gamma}_0}{2}\big(\mathcal{D}[\hat{\sigma}_{G-},\hat{\sigma}_{+E}]\hat{\rho} + \mathcal{D}[\hat{\sigma}_{+E},\hat{\sigma}_{G-}]\hat{\rho}\big) + \frac{\tilde{\gamma}_0}{2}\big(\mathcal{D}[\hat{\sigma}_{G+},\hat{\sigma}_{-E}]\hat{\rho} + \mathcal{D}[\hat{\sigma}_{-E},\hat{\sigma}_{G+}]\hat{\rho}\big)\\
&+ \frac{\tilde{\gamma}_{12}}{2}\big(\mathcal{D}[\hat{\sigma}_{G+},\hat{\sigma}_{G-}]\hat{\rho} + \mathcal{D}[\hat{\sigma}_{G-},\hat{\sigma}_{G+}]\hat{\rho}\big) + \frac{\tilde{\gamma}_{12}}{2}\big(\mathcal{D}[\hat{\sigma}_{+E},\hat{\sigma}_{-E}]\hat{\rho} + \mathcal{D}[\hat{\sigma}_{-E},\hat{\sigma}_{+E}]\hat{\rho}\big).
\end{aligned} \tag{3.63}$$

Here, $\hat{\sigma}_{ab} = |a\rangle\langle b|$, where the subscripts $a, b = E, G$ refer to the states $|E\rangle$ and

$|G\rangle$, and the subscripts $a, b = \pm$ refer to $|\Lambda_\pm\rangle$. Additionally, in Eq. (3.63), we have defined the decay rates $\tilde{\gamma}_\pm = \tilde{\gamma}_{\rm DW} \pm \gamma_0 \sin(2\Theta_\Lambda)$, $\tilde{\gamma}_0 = \gamma_0 \cos(2\Theta_\Lambda)$, $\tilde{\gamma}_{12} = \tilde{\gamma}_{\rm DW} \cos(2\Theta_\Lambda)$ and

$$\gamma_\pm = \gamma_0 \pm \tilde{\gamma}_{\rm DW} \sin(2\Theta_\Lambda) = \gamma_0 \pm \tilde{\gamma}_{\rm DW} \frac{V_{\rm DW}}{\Lambda}. \tag{3.64}$$

Notably, the dissipators in Eq. (3.63) with decay rates $\gamma_\pm$ correspond to one-photon transitions between states of the interacting basis (see Fig. 3.2b). In contrast, the rest of the dissipators in Eq. (3.63) (with decay rates denoted with tilde symbol) represent incoherent cross processes in the interacting basis. Crucially, Eq. (3.64) indicates that the decay rates γ_+ and γ_- of the delocalized Λ_+ and Λ_- are different to each other when both the coherent dipole-dipole coupling $V_{\rm DW}$ and the dissipative dipole-dipole coupling $\tilde{\gamma}_{\rm DW}$ are not negligible. These conditions are well satisfied when the emitters are separated by short distances ($k_0 r_{12} \ll 1$) and their transition dipole moments are not oriented perpendicularly [Eq. (3.57b)]. In this case, the delocalized state with larger decay rate is called *superradiant state*, whereas the delocalized state with smaller decay rate is known as *subradiant state*. As the subradiant state has a longer coherence time, it could turn into a good candidate for applications in quantum information storage [85–87]. The specific configuration of transition dipole moments (relative orientation) determines which delocalized state ($|\Lambda_+\rangle$ or $|\Lambda_-\rangle$) is the superradiant state and which one is the subradiant state.

Finally, we note that for short separation distances between the emitters and parallel transition dipole moments, the decay rates of the delocalized states become $\gamma_\pm = \gamma_0(1 \pm \alpha_{\rm DW} V_{\rm DW}/\Lambda)$ [from Eq. (3.57b)]. Additionally, if the emitters are identical ($\delta = 0$, yielding $\Lambda = |V_{\rm DW}|$), the decay rates of the superradiant and subradiant states become $\gamma_0(1 + \alpha_{\rm DW})$ and $\gamma_0(1 - \alpha_{\rm DW})$, respectively. This result highlights the strong impact of the combined Debye-Waller/Franck-Condon factor on the dynamics of the system.

3.2.2 Interaction of two quantum emitters with a laser

We introduce the Hamiltonian that describes the interaction of the two emitters with a laser, as well as the final form of the master equation that we use to analyze the intensity correlation of the Zero-Phonon-Line photons emitted from two strongly interacting emitters in Sections 3.3 and 3.4. To this end, we consider that the two quantum emitters are illuminated by a laser of frequency ω_L and intensity I_L. The Hamiltonian describing this driving laser is obtained straightforwardly from the discussion in Section 1.5.1, and it is given by

$$\hat{H}_L = -\hbar \sum_{j=1}^{2} \frac{\boldsymbol{\mu_j} \cdot \boldsymbol{\mathcal{E}}_L}{2\hbar} (\hat{\sigma}_j e^{i\omega_L t} + \hat{\sigma}_j^\dagger e^{-i\omega_L t}), \tag{3.65}$$

where $\boldsymbol{\mathcal{E}}_L = \mathcal{E}_L \boldsymbol{e}_L$ [Eq. (1.215)], with $\boldsymbol{e}_L$ the polarization unit vector of the laser field and $\mathcal{E}_L = \mathcal{E}_L(\mathbf{r}_1) = \mathcal{E}_L(\mathbf{r}_2)$ the amplitude of the laser field at the position of the emitters (assumed to be the same at both positions). Notably, Eq. (3.65) does not include any relative spatial phase because we consider that the laser impinges normally to the plane in which the emitters are located (i.e., the laser wavevector $\mathbf{k}_L$ is perpendicular to $\mathbf{r}_1 - \mathbf{r}_2$).

Furthermore, we assume that both emitters have identical transition dipole moments ($\boldsymbol{\mu}_1 = \boldsymbol{\mu}_2$) and that the electric field is linearly polarized in the same direction than the transition dipole moments. In this configuration, both Rabi frequencies become equal to $\Omega = \boldsymbol{\mu}_1 \cdot \boldsymbol{\mathcal{E}}_L/\hbar = \boldsymbol{\mu}_2 \cdot \boldsymbol{\mathcal{E}}_L/\hbar$. Further, including the influence of the refractive index ($n \neq 1$) of the host in Eq. (1.220), Ω can be related to the laser intensity I_L as

$$|\Omega| = \sqrt{\frac{I_L 6\pi c^2 \gamma_0}{\hbar \omega_0^3 n^2}} = \sqrt{\frac{I_L \gamma_0^2}{2 I_{\text{sat}}}}, \tag{3.66}$$

where the saturation intensity of each emitter is given by

$$I_{\text{sat}} = \frac{\hbar \omega_0^3 \gamma_0 n^2}{12\pi c^2}. \tag{3.67}$$

To gain insights into the effect of the excitation laser on the delocalized states, we rewrite $\hat{H}_L$ [Eq. (3.65)] in the interacting basis $\{|E\rangle, |\Lambda_+\rangle, |\Lambda_-\rangle, |G\rangle\}$. We find

$$\hat{H}_L = -\hbar \sum_{k\in\{+,-\}} \frac{\Omega_k}{2} \left[(\hat{\sigma}_{Gk} + \hat{\sigma}_{kE}) e^{i\omega_L t} + (\hat{\sigma}_{kG} + \hat{\sigma}_{Ek}) e^{-i\omega_L t} \right]. \tag{3.68}$$

Here, we have introduced the effective pumping rates

$$\Omega_\pm = \Omega(\cos\Theta_\Lambda \pm \sin\Theta_\Lambda), \tag{3.69}$$

with Ω_+ the driving strength of the transitions $|G\rangle \to |\Lambda_+\rangle$ and $|\Lambda_+\rangle \to |E\rangle$, and Ω_- the driving strength of the transitions $|G\rangle \to |\Lambda_-\rangle$ and $|\Lambda_-\rangle \to |E\rangle$. These effective pumping rates can be related to the laser intensity as

$$\Omega_\pm^2 = \Omega^2[1 \pm \sin(2\Theta_\Lambda)] = \gamma_0^2 \frac{I_L}{2 I_{\text{sat}}} (1 \pm \frac{V_{\text{DW}}}{\Lambda}). \tag{3.70}$$

We move next to the rotating frame at the laser frequency ω_L by applying the unitary transformation $\hat{U}_L = \exp[i\omega_L t(|E\rangle\langle E| - |G\rangle\langle G|)]$ (the effect of unitary transformations is discussed in Appendix C). In this way, the full Hamiltonian becomes

$$\begin{aligned} \hat{H} = {} & \hbar\Delta_0(|E\rangle\langle E| - |G\rangle\langle G|) + \hbar\Lambda(|\Lambda_+\rangle\langle\Lambda_+| - |\Lambda_-\rangle\langle\Lambda_-|) \\ & - \hbar \sum_{k\in\{+,-\}} \frac{\Omega_k}{2} (\hat{\sigma}_{Gk} + \hat{\sigma}_{kE} + \hat{\sigma}_{kG} + \hat{\sigma}_{Ek}), \end{aligned} \tag{3.71}$$

where $\Delta_0 = \omega_0 - \omega_L$ is the laser detuning with respect to the mean frequency ω_0. The terms in the first line of Eq. (3.71) represent the undriven Hamiltonian, including the dipole-dipole interaction between the two emitters, while the terms in the second line account for the laser driving. In this rotating frame, the dynamics of the interacting emitters is finally governed by the Markovian master equation

$$\frac{d}{dt}\hat{\rho} = -\frac{i}{\hbar}[\hat{H},\hat{\rho}] + \sum_j \frac{\gamma_j}{2}\mathcal{D}[\hat{\sigma}_j]\hat{\rho} + \frac{\tilde{\gamma}_{\mathrm{DW}}}{2}\Big(\mathcal{D}[\hat{\sigma}_1,\hat{\sigma}_2]\hat{\rho} + \mathcal{D}[\hat{\sigma}_2,\hat{\sigma}_1]\hat{\rho}\Big). \tag{3.72}$$

The full Hamiltonian $\hat{H}$ [Eq. (3.71)] in this MME is time-independent, which facilitates the numerical calculation of the dynamics of the emitters, as well as the derivation of the analytical equations of motion of the elements of the density matrix, as we show next.

The expectation values of the operators $\hat{\sigma}_{aa} = |a\rangle\langle a|$ give the populations of the states of the interacting basis (i.e., the diagonal elements of the density matrix). In contrast, the expectation values of the operators $\hat{\sigma}_{ab}$ $(a \neq b)$ correspond to the off-diagonal elements of the density matrix and correspond to the coherence between difference states of the basis (Appendix A). To derive the time evolution of these expectation values, we apply Eq. (1.197), which yields

$$\frac{d}{dt}\langle\hat{\sigma}_{EE}\rangle = -2\gamma_0\langle\hat{\sigma}_{EE}\rangle + i\frac{\Omega_+}{2}\Big[\langle\hat{\sigma}_{E+}\rangle - \langle\hat{\sigma}_{+E}\rangle\Big] + i\frac{\Omega_-}{2}\Big[\langle\hat{\sigma}_{E-}\rangle - \langle\hat{\sigma}_{-E}\rangle\Big], \tag{3.73a}$$

$$\begin{aligned}\frac{d}{dt}\langle\hat{\sigma}_{++}\rangle = &-\gamma_+\Big[\langle\hat{\sigma}_{++}\rangle - \langle\hat{\sigma}_{EE}\rangle\Big] - \frac{\tilde{\gamma}_{12}}{2}\Big[\langle\hat{\sigma}_{-+}\rangle + \langle\hat{\sigma}_{+-}\rangle\Big] \\ &+ i\frac{\Omega_+}{2}\Big[\langle\hat{\sigma}_{+E}\rangle - \langle\hat{\sigma}_{E+}\rangle + \langle\hat{\sigma}_{+G}\rangle - \langle\hat{\sigma}_{G+}\rangle\Big],\end{aligned} \tag{3.73b}$$

$$\begin{aligned}\frac{d}{dt}\langle\hat{\sigma}_{--}\rangle = &-\gamma_-\Big[\langle\hat{\sigma}_{--}\rangle - \langle\hat{\sigma}_{EE}\rangle\Big] - \frac{\tilde{\gamma}_{12}}{2}\Big[\langle\hat{\sigma}_{-+}\rangle + \langle\hat{\sigma}_{+-}\rangle\Big] \\ &+ i\frac{\Omega_-}{2}\Big[\langle\hat{\sigma}_{-E}\rangle - \langle\hat{\sigma}_{E-}\rangle + \langle\hat{\sigma}_{-G}\rangle - \langle\hat{\sigma}_{G-}\rangle\Big],\end{aligned} \tag{3.73c}$$

$$\frac{d}{dt}\langle\hat{\sigma}_{EG}\rangle = \langle\hat{\sigma}_{EG}\rangle(i2\Delta_0 - \gamma_0) + i\frac{\Omega_+}{2}\Big[\langle\hat{\sigma}_{E+}\rangle - \langle\hat{\sigma}_{+G}\rangle\Big] + i\frac{\Omega_-}{2}\Big[\langle\hat{\sigma}_{E-}\rangle - \langle\hat{\sigma}_{-G}\rangle\Big], \tag{3.73d}$$

$$\begin{aligned}\frac{d}{dt}\langle\hat{\sigma}_{E+}\rangle = &-i\frac{\Omega_+}{2}\Big[-\langle\hat{\sigma}_{EE}\rangle + \langle\hat{\sigma}_{++}\rangle - \langle\hat{\sigma}_{EG}\rangle\Big] - i\frac{\Omega_-}{2}\langle\hat{\sigma}_{-+}\rangle \\ &+ \langle\hat{\sigma}_{E+}\rangle\Big[i(\Delta_0 - \Lambda) - \gamma_0 - \gamma_+/2\Big] - \frac{\tilde{\gamma}_{12}}{2}\langle\hat{\sigma}_{E-}\rangle,\end{aligned} \tag{3.73e}$$

$$\frac{d}{dt}\langle\hat{\sigma}_{E-}\rangle = -i\frac{\Omega_-}{2}\Big[-\langle\hat{\sigma}_{EE}\rangle + \langle\hat{\sigma}_{--}\rangle - \langle\hat{\sigma}_{EG}\rangle\Big] - i\frac{\Omega_+}{2}\langle\hat{\sigma}_{+-}\rangle$$

$$+\langle\hat{\sigma}_{E-}\rangle\left[i(\Delta_0+\Lambda)-\gamma_0-\gamma_-/2\right]-\frac{\tilde{\gamma}_{12}}{2}\langle\hat{\sigma}_{E+}\rangle\,, \tag{3.73f}$$

$$\frac{d}{dt}\langle\hat{\sigma}_{+G}\rangle=-i\frac{\Omega_+}{2}\left[-\langle\hat{\sigma}_{++}\rangle+\langle\hat{\sigma}_{GG}\rangle+\langle\hat{\sigma}_{EG}\rangle\right]+i\frac{\Omega_-}{2}\langle\hat{\sigma}_{+-}\rangle$$
$$+\left[i(\Delta_0+\Lambda)-\gamma_+/2\right]\langle\hat{\sigma}_{+G}\rangle-\frac{\tilde{\gamma}_{12}}{2}\langle\hat{\sigma}_{-G}\rangle+\tilde{\gamma}_+\langle\hat{\sigma}_{E+}\rangle+\tilde{\gamma}_0\langle\hat{\sigma}_{E-}\rangle\,, \tag{3.73g}$$

$$\frac{d}{dt}\langle\hat{\sigma}_{-G}\rangle=-i\frac{\Omega_-}{2}\left[-\langle\hat{\sigma}_{--}\rangle+\langle\hat{\sigma}_{GG}\rangle+\langle\hat{\sigma}_{EG}\rangle\right]+i\frac{\Omega_+}{2}\langle\hat{\sigma}_{-+}\rangle$$
$$+\left[i(\Delta_0-\Lambda)-\gamma_-/2\right]\langle\hat{\sigma}_{-G}\rangle-\frac{\tilde{\gamma}_{12}}{2}\langle\hat{\sigma}_{+G}\rangle+\tilde{\gamma}_-\langle\hat{\sigma}_{E-}\rangle+\tilde{\gamma}_0\langle\hat{\sigma}_{E+}\rangle\,, \tag{3.73h}$$

$$\frac{d}{dt}\langle\hat{\sigma}_{+-}\rangle=-i\frac{\Omega_+}{2}\left[\langle\hat{\sigma}_{E-}\rangle+\langle\hat{\sigma}_{G-}\rangle\right]+i\frac{\Omega_-}{2}\left[\langle\hat{\sigma}_{+E}\rangle+\langle\hat{\sigma}_{+G}\rangle\right]$$
$$+(i2\Lambda-\gamma_0)\langle\hat{\sigma}_{+-}\rangle+\frac{\tilde{\gamma}_{12}}{2}\left[2\langle\hat{\sigma}_{EE}\rangle-\langle\hat{\sigma}_{++}\rangle-\langle\hat{\sigma}_{--}\rangle\right]. \tag{3.73i}$$

This system of equations is valid for arbitrary laser intensity and frequency, but its exact analytical resolution leads to very complex expressions. In Section 3.3.1, we discuss some approximations that allows us to solve this system of equations in the steady state.

3.2.3 Dressed states of the interacting emitters under laser driving

We discuss in this section two different approximations for deriving the eigenstates and eigenenergies of the full Hamiltonian $\hat{H}$ in Eq. (3.71), which is written in the rotating frame at the laser frequency. Diagonalizing the total Hamiltonian helps to understand the emission mechanisms of the system and is particularly valuable for interpreting the frequency-resolved intensity correlation in Section 3.4. To diagonalize the Hamiltonian, we consider specifically that the dipole moments are parallel and aligned in the same direction as $\mathbf{r}_{12}=\mathbf{r}_1-\mathbf{r}_2$, which is called J-configuration, as schematically represented in Fig. 3.3a. In this configuration, the coherent dipole-dipole coupling V_{DW} is negative [Eq. (3.56a)], the lower-energy delocalized state $|\Lambda_-\rangle$ corresponds to the superradiant state, and the higher-energy delocalized state $|\Lambda_+\rangle$ to the subradiant state. In Sections 3.3 and 3.4, we analyze the intensity correlation of light emitted into the ZPL from two interacting emitters in a J-configuration.

Laser resonantly tuned to the superradiant or subradiant states

We first introduce an approximation valid under weak enough illumination and when the laser is resonantly tuned either to the transition frequency of the

superradiant state ($\omega_L = \omega_0 - \Lambda$) or to the transition frequency of the subradiant state ($\omega_L = \omega_0 + \Lambda$). Under these laser frequencies and intensities, the Hamiltonian in Eq. (3.71) has two pairs of degenerate eigenstates at energies $\pm\Lambda$ (in the rotating frame at the laser frequency ω_L). Namely, if the laser is tuned to the transition frequency of the superradiant state $|\Lambda_-\rangle$ ($\Delta_0 = \Lambda$), the states $|G\rangle$ and $|\Lambda_-\rangle$ become degenerate (with energy $-\Lambda$) and the states $|E\rangle$ and $|\Lambda_+\rangle$ become degenerate (with energy Λ). In contrast, if the laser is tuned to the transition frequency of the subradiant state $|\Lambda_+\rangle$ ($\Delta_0 = -\Lambda$), the states $|E\rangle$ and $|\Lambda_-\rangle$ become degenerate (with energy $-\Lambda$) and the states $|G\rangle$ and $|\Lambda_+\rangle$ become degenerate (with energy Λ).

We then neglect the driving terms in the second line of Eq. (3.71) that connect states that are not degenerate under weak enough illumination. As a consequence, if the laser is tuned to the transition frequency of the superradiant state $|\Lambda_-\rangle$, the driving Hamiltonian becomes $\hat{H}_L = -\hbar\frac{\Omega_+}{2}\hat{\sigma}_{E+} - \hbar\frac{\Omega_-}{2}\hat{\sigma}_{G-} + \text{h.c.}$. In contrast, if the laser is tuned to the transition frequency of the subradiant state $|\Lambda_+\rangle$, the laser Hamiltonian is approximated as $\hat{H}_L = -\hbar\frac{\Omega_+}{2}\hat{\sigma}_{G+} - \hbar\frac{\Omega_-}{2}\hat{\sigma}_{E-} + \text{h.c.}$ The resulting total Hamiltonian (in the rotating frame at the laser frequency ω_L) can then be analytically diagonalized in both cases. Notably, we find that the eigenstates correspond to symmetric and antisymmetric combinations of the pairs of degenerate states. Specifically, the eigenstates can be written as

$$|A_{X+}\rangle = (|X\rangle - |\Lambda_+\rangle)/\sqrt{2}, \tag{3.74a}$$

$$|S_{X+}\rangle = (|X\rangle + |\Lambda_+\rangle)/\sqrt{2}, \tag{3.74b}$$

$$|S_{Y-}\rangle = (|Y\rangle + |\Lambda_-\rangle)/\sqrt{2}, \tag{3.74c}$$

$$|A_{Y-}\rangle = (|Y\rangle - |\Lambda_-\rangle)/\sqrt{2}, \tag{3.74d}$$

where $X = E$ and $Y = G$ if the laser is tuned to the transition frequency of the superradiant state $|\Lambda_-\rangle$, whereas $X = G$ and $Y = E$ if the laser is tuned to the transition frequency of the subradiant state $|\Lambda_+\rangle$. The corresponding eigenenergies are equal to

$$E(|A_{X+}\rangle) = \Lambda + \frac{\Omega}{2}(\cos\Theta_\Lambda + \sin\Theta_\Lambda), \tag{3.75a}$$

$$E(|S_{X+}\rangle) = \Lambda - \frac{\Omega}{2}(\cos\Theta_\Lambda + \sin\Theta_\Lambda), \tag{3.75b}$$

$$E(|S_{Y-}\rangle) = -\Lambda - \frac{\Omega}{2}(\cos\Theta_\Lambda - \sin\Theta_\Lambda), \tag{3.75c}$$

$$E(|A_{Y-}\rangle) = -\Lambda + \frac{\Omega}{2}(\cos\Theta_\Lambda - \sin\Theta_\Lambda). \tag{3.75d}$$

The energy splitting between the two higher-energy states $|A_{X+}\rangle$ and $|S_{X+}\rangle$ is equal to $|\Omega(\cos\Theta_\Lambda + \sin\Theta_\Lambda)|$, while the energy splitting between the lower-energy states $|S_{Y-}\rangle$ and $|A_{Y-}\rangle$ is equal to $|\Omega(\cos\Theta_\Lambda - \sin\Theta_\Lambda)|$.

Next, we compare the eigenenergies obtained analytically in Eqs. (3.75a)–(3.75d) with the eigenenergies E_i ($i \in \{1, 2, 3, 4\}$) of the exact eigenstates $|E_i\rangle$ obtained

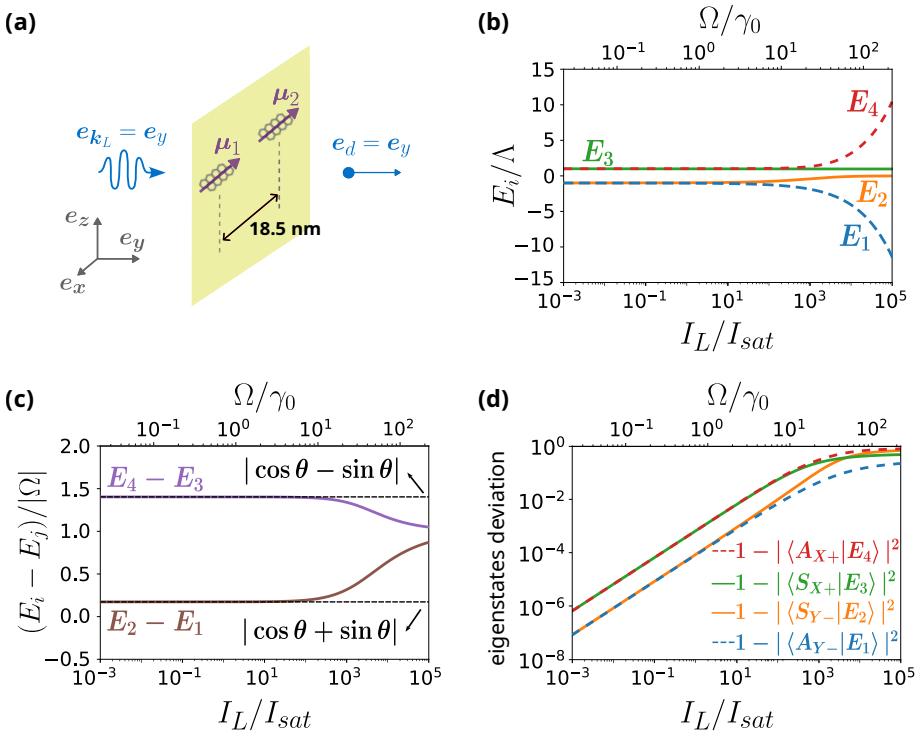

Figure 3.3: Eigenenergies and eigenstates of two interacting emitters when the laser is tuned resonantly to the transition frequency of one of the delocalized states. (a) Schematic representation of the two emitters in a J-configuration. The transition dipole moments are aligned along the x-axis, and the emitters are separated by 18.5 nm along this same axis. The combined Debye-Waller/Franck-Condon factor is $\alpha_{\mathrm{DW}} = 0.3$, yielding $V_{\mathrm{DW}} = -20\gamma_0$, and the detuning between the emitters is $\delta = 10\gamma_0$. The laser wavevector $\mathbf{k}_L$ and the detection direction $\mathbf{r}_d$ are aligned along the y-axis, such that their corresponding unit vectors are $\boldsymbol{e}_{\mathbf{k}_L} = \mathbf{k}_L/|\mathbf{k}_L| = \boldsymbol{e}_y$ and $\boldsymbol{e}_d = \mathbf{r}_{\boldsymbol{d}}/|\mathbf{r}_{\boldsymbol{d}}| = \boldsymbol{e}_y$, respectively. (b) Eigenenergies E_i (normalized by Λ and obtained numerically) of the Hamiltonian in Eq. (3.71) as a function of the laser intensity I_L, with the laser tuned either to the transition frequency of the superradiant state or to that of the subradiant state (E_i are identical for both laser frequencies). (c) Energy splitting (normalized by $|\Omega|$) obtained numerically, between the more energetic eigenstates $|E_3\rangle$ and $|E_4\rangle$ (purple line) and energy splitting between the less energetic eigenstates $|E_1\rangle$ and $|E_2\rangle$ (brown line). Horizontal black dashed lines represent the same energy splittings calculated using the analytical expressions in Eqs. (3.75a)–(3.75d). (d) Deviation of the eigenstates $|A_{Y-}\rangle, |S_{Y-}\rangle, |S_{X+}\rangle, |A_{X+}\rangle$ (obtained analytically) from the exact eigenstates $|E_1\rangle, |E_2\rangle, |E_3\rangle, |E_4\rangle$ (obtained numerically) as a function of the laser intensity I_L. The deviation is estimated as the difference between 1 and the squared overlap of the analytical eigenstate and the corresponding numerical eigenstate. For the case in which the laser is tuned to the transition frequency of the superradiant state $|\Lambda_-\rangle$ then $X = E$ and $Y = G$, whereas if the laser is tuned to the transition frequency of the subradiant $|\Lambda_+\rangle$ state then $X = G$ and $Y = E$.

numerically. To this end, we consider as a reference two DBATT molecules with

dipole-dipole coupling $V_{\mathrm{DW}} = -20\gamma_0$, molecular detuning $\delta = 10\gamma_0$, and combined Debye-Waller/Franck-Condon factor $\alpha_{\mathrm{DW}} = 0.3$ (see Section 3.3). We plot in Fig. 3.3b the exact numerical eigenenergies E_i (normalized by Λ) and in Fig. 3.3c the numerical energy splitting (normalized by the absolute value of the Rabi frequency $|\Omega|$) between the two higher-energy states (purple line), as well as between the two lower-energy states (brown line). Figure 3.3c shows that the energy splittings obtained numerically (solid lines) are in excellent agreement with that obtained by using the analytical expressions in Eqs. (3.75a)–(3.75d) (horizontal dashed black lines) up to a laser intensity $I_L \approx 100 I_{\mathrm{sat}}$.

Last, we test the accuracy of the analytical eigenstates in Eqs. (3.74a)–(3.74d) by computing the difference between 1 and the squared overlap of the numerical and analytical eigenstates. For example, for the lowest-energy state, the deviation of the eigenstate $|A_{Y-}\rangle$ (obtained analytically) from the exact eigenstate $|E_1\rangle$ (calculated numerically) is given by $1 - |\langle A_{Y-}|E_1\rangle|^2$. We plot these deviations in Fig. 3.3d, which shows that these analytical eigenstates are a very accurate approximation of the exact eigenstates of the system under weak and moderate laser intensities. These approximate eigenstates are therefore used in Sections 3.4.1 and 3.4.2 to develop a better understanding of the FRIC maps obtained for these laser frequencies.

Laser tuned to the two-photon resonance

We now describe an approximate diagonalization of the Hamiltonian in Eq. (3.71), which is written in the rotating frame at the laser frequency ω_L, for a laser tuned to half the frequency between $|G\rangle$ and $|E\rangle$ ($\omega_L = \omega_0$). We refer to this laser excitation as *two-photon resonance*, because it enables the resonant excitation of the doubly-excited state $|E\rangle$ through a two-photon process.

To diagonalize the Hamiltonian in Eq. (3.71), we neglect the terms that are proportional to Ω_+ in this case. The reason is that both the superradiant state $|\Lambda_-\rangle$ and the subradiant state $|\Lambda_+\rangle$ are non-resonantly driven and, additionally, the effective pumping Ω_+ through the subradiant state is considered to be much smaller than the effective pumping Ω_- through the superradiant state. Specifically, for the two interacting DBATT molecules considered here (with $V_{\mathrm{DW}} = -20\gamma_0$ and $\delta = 10\gamma_0$), Ω_+ is approximately one order of magnitude smaller than Ω_- [Eq. (3.69)]. By neglecting these terms and fixing the laser tuned to the two-photon resonance ($\Delta_0 = 0$), the Hamiltonian in Eq. (3.71) becomes $\hat{H} = \hbar\Lambda(|\Lambda_+\rangle\langle\Lambda_+| - |\Lambda_-\rangle\langle\Lambda_-|) - \hbar\frac{\Omega_-}{2}(\hat{\sigma}_{G-} + \hat{\sigma}_{-E} + \hat{\sigma}_{-G} + \hat{\sigma}_{E-})$. This Hamiltonian can be diagonalized analytically, which yields that the eigenenergies are given by

$$E_1 = -\frac{\Lambda}{2} - \sqrt{\left(\frac{\Lambda}{2}\right)^2 + \left(\frac{\Omega_-}{\sqrt{2}}\right)^2}, \tag{3.76a}$$

$$E_2 = 0, \tag{3.76b}$$

$$E_3 = -\frac{\Lambda}{2} + \sqrt{\left(\frac{\Lambda}{2}\right)^2 + \left(\frac{\Omega_-}{\sqrt{2}}\right)^2}, \tag{3.76c}$$

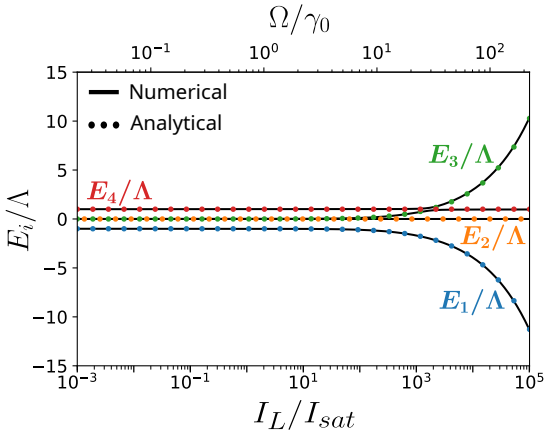

Figure 3.4: Dependence of the eigenenergies of two interacting emitters on the laser intensity for a laser tuned to the two-photon resonance ($\omega_L = \omega_0$). Solid lines represent the eigenenergies (normalized by Λ) of the full Hamiltonian in Eq. (3.71), obtained numerically. Dots represent the eigenenergies obtained using the analytical approximations given in Eqs. (3.76a)–(3.76d). The dipole-dipole coupling is $V_{\mathrm{DW}} = -20\gamma_0$, the detuning between the emitters is $\delta = 10\gamma_0$, and the combined Debye-Waller/Franck-Condon factor is $\alpha_{\mathrm{DW}} = 0.3$.

$$E_4 = \Lambda. \tag{3.76d}$$

We plot in Fig. 3.4 the eigenenergies obtained analytically (dots) and numerically (solid lines), which shows that they are in very good agreement. The corresponding analytical eigenstates result in:

$$|E_1\rangle = \frac{1}{\sqrt{(\frac{\Omega_-}{\sqrt{2}})^2 + E_3^2}}\left(\frac{\Omega_-}{\sqrt{2}}|\Lambda_-\rangle + E_3|S_{EG}\rangle\right), \tag{3.77a}$$

$$|E_2\rangle = |A_{EG}\rangle, \tag{3.77b}$$

$$|E_3\rangle = \frac{1}{\sqrt{(\frac{\Omega_-}{\sqrt{2}})^2 + E_1^2}}\left(-\frac{\Omega_-}{\sqrt{2}}|\Lambda_-\rangle - E_1|S_{EG}\rangle\right), \tag{3.77c}$$

$$|E_4\rangle = |\Lambda_+\rangle, \tag{3.77d}$$

where $|S_{EG}\rangle = (|E\rangle + |G\rangle)/\sqrt{2}$ and $|A_{EG}\rangle = (|E\rangle - |G\rangle)/\sqrt{2}$. Equations (3.77a)–(3.77d) show that $|A_{EG}\rangle$ and $|\Lambda_+\rangle$ are eigenstates of the system for any laser intensity, whereas the other two dressed eigenstates ($|E_1\rangle$ and $|E_3\rangle$) are superpositions of $|S_{EG}\rangle$ and $|\Lambda_-\rangle$, with coefficients that depend on the laser intensity. Additionally, we note that under weak enough illumination, the eigenstates $|E_2\rangle = |A_{EG}\rangle$ and $|E_3\rangle = |S_{EG}\rangle$ become degenerate in energy (in the rotating frame at the laser frequency).

3.3 Color-blind intensity correlation

We perform in this section a systematic analysis of the color-blind intensity correlation $g^{(2)}_{\mathrm{ZPL}}(0)$ of Zero-Phonon-Line (ZPL) photons emitted from two strongly interacting emitters. Specifically, we investigate the dependence of $g^{(2)}_{\mathrm{ZPL}}(0)$ on the laser intensity I_L and detuning δ between the transition frequencies of the emitters for different values of laser frequency ω_L. This analysis shows that the statistics of light emitted into the ZPL from these two emitters can be tailored over a very large range of values, from strong antibunching to strong bunching. Additionally, we also discuss the impact of the combined Debye-Waller/Franck-Condon factor α_{DW} on the color blind-intensity correlation. Thus, the systematic analysis presented in this section extends previous theoretical studies of the color-blind intensity correlation of light emitted by two interacting quantum emitters, which have primarily focused on atomic systems (with $\alpha_{\mathrm{DW}} = 1$) and on the case where the laser is tuned to the two-photon resonance ($\omega_L = \omega_0$) [182–190].

As an example of application of our system, we focus on two dibenzanthanthrene (DBATT) molecules embedded in a naphthalene film with $n = 1.5$. We consider that $\boldsymbol{r}_{12} = \mathbf{r}_1 - \mathbf{r}_2$ is oriented parallel to the transition dipole moments (J-configuration), with both $\boldsymbol{r}_{12}$ and the dipole moments aligned along the x-axis, as schematically represented in Fig. 3.3a. The laser is incident along the direction normal to the dipole orientation, and the emitted light is detected along the same direction. More specifically, the laser wavevector $\mathbf{k}_L$ and the detection direction $\mathbf{r}_{\boldsymbol{d}}$ are aligned along the y-axis, such that $\boldsymbol{e}_{\mathbf{k}_L} = \mathbf{k}_L/|\mathbf{k}_L| = \boldsymbol{e}_y$ and $\boldsymbol{e}_d = \mathbf{r}_{\boldsymbol{d}}/|\mathbf{r}_{\boldsymbol{d}}| = \boldsymbol{e}_y$. In this J-configuration, the lower-energy delocalized state $|\Lambda_-\rangle$ is the superradiant state and the higher-energy delocalized state $|\Lambda_+\rangle$ is the subradiant state. We also assume the following parameters, based on the experiments in Ref. [1]: (i) the mean frequency ω_0 corresponds to a vacuum wavelength of $\lambda_0 = 618$ nm; (ii) the spontaneous decay rate is $\gamma_0/(2\pi) = 21.5$ MHz; (iii) the combined Debye-Waller/Franck-Condon factor is $\alpha_{\mathrm{DW}} = 0.3$; and (iv) the dipole-dipole coupling is $V_{\mathrm{DW}} = -20\gamma_0$, as provided by a separation distance $r_{12} \approx 18.5$ nm. We emphasize that the results in this section are also valid for any other pair of quantum emitters having the same coupling strength V_{DW} and combined Debye-Waller/Franck-Condon factor α_{DW}. Additionally, equivalent results are obtained for the case of a molecular H-aggregate configuration ($\boldsymbol{r}_{12}$ is perpendicular to the transition dipole moments), with the only difference that in this case the superradiant state is the higher-energy delocalized state $|\Lambda_+\rangle$ and the subradiant state is the lower-energy delocalized state $|\Lambda_-\rangle$.

3.3.1 Color-blind intensity correlation for parallel dipole moments

We derive in this section the expression for the color-blind intensity correlation $g^{(2)}_{\mathrm{ZPL}}(0)$ of ZPL photons emitted from two interacting emitters with parallel transition dipole moments. The resulting expression can be directly used to perform numerical calculations, as well as to develop deeper analytical insights

into the behaviour of $g^{(2)}_{\mathrm{ZPL}}(0)$ under various illumination conditions, which we also discuss in this section.

In general, the color-blind intensity correlation can be obtained from the positive-frequency and negative-frequency transverse electric field operators $\hat{\mathbf{E}}^{(+)}_{\perp}(\mathbf{r}_d,t)$ and $\hat{\mathbf{E}}^{(-)}_{\perp}(\mathbf{r}_d,t)$ (Section 2.3). These two operators are Hermitian conjugate of each other. In the far-field region, the positive-frequency electric field operator of ZPL light scattered from emitter j (Section 1.2.7) is given by the product of (i) the vector amplitude $\boldsymbol{\mathcal{E}}_{\boldsymbol{\mu}_j^{\mathrm{ZPL}}}(\mathbf{r}_d)$ of the positive-frequency electric field radiated by a classical point dipole $\boldsymbol{\mu}_j^{\mathrm{ZPL}}$ at the position $\mathbf{r}_j$ of the emitter [see Eqs. (1.141) and (3.55)], with $\mathbf{r}_d$ the detection position, and (ii) the lowering operator $\hat{\sigma}_j(t-|\mathbf{r}_j-\mathbf{r}_d|n/c)$, with $|\mathbf{r}_j-\mathbf{r}_d|n/c$ the retardation time experienced by a photon propagating from the emitter to the detector through a host medium of refractive index n. As a result, the positive-frequency electric field operator of light emitted from the two emitters into the ZPL becomes

$$\hat{\mathbf{E}}^{(+)}_{\perp,\mathrm{ZPL}}(\mathbf{r}_d,t)=\boldsymbol{\mathcal{E}}_{\boldsymbol{\mu}_1^{\mathrm{ZPL}}}(\mathbf{r}_d)\hat{\sigma}_1(t-|\mathbf{r}_1-\mathbf{r}_d|n/c)+\boldsymbol{\mathcal{E}}_{\boldsymbol{\mu}_2^{\mathrm{ZPL}}}(\mathbf{r}_d)\hat{\sigma}_2(t-|\mathbf{r}_2-\mathbf{r}_d|n/c). \tag{3.78}$$

Notably, the color-blind intensity correlation of ZPL photons emitted from two emitters depends on the detection position $\mathbf{r}_d$ [191], in contrast to the case of a single quantum emitter discussed in Section 2.3.3. This dependence arises because (i) $\boldsymbol{\mathcal{E}}_{\boldsymbol{\mu}_1^{\mathrm{ZPL}}}(\mathbf{r}_d)$ and $\boldsymbol{\mathcal{E}}_{\boldsymbol{\mu}_2^{\mathrm{ZPL}}}(\mathbf{r}_d)$ can be different in general, and (ii) the operators $\hat{\sigma}_1(t-|\mathbf{r}_1-\mathbf{r}_d|n/c)$ and $\hat{\sigma}_2(t-|\mathbf{r}_2-\mathbf{r}_d|n/c)$ have different time arguments, with their difference depending on the detection position. We next introduce an approximation that allows us to evaluate the operators $\hat{\sigma}_1(t-|\mathbf{r}_1-\mathbf{r}_d|n/c)$ and $\hat{\sigma}_2(t-|\mathbf{r}_2-\mathbf{r}_d|n/c)$ at the same time argument.

In the far-field region, the distance between emitter j and the detector can be approximated as $|\mathbf{r}_j-\mathbf{r}_d|\approx|\mathbf{r}_d|-\boldsymbol{e}_d\cdot\mathbf{r}_j$ [192], with $\boldsymbol{e}_d=\mathbf{r}_d/|\mathbf{r}_d|$ the unit vector of the detection position. This approximation holds as long as the origin of the coordinate system is close to the positions of the quantum emitters. As a result, we obtain

$$\hat{\sigma}_j(t-|\mathbf{r}_j-\mathbf{r}_d|n/c)\approx\hat{\sigma}_j(t-|\mathbf{r}_d|n/c+\boldsymbol{e}_d\cdot\mathbf{r}_jn/c). \tag{3.79}$$

Additionally, we consider that the evolution of this operator during the time $\boldsymbol{e}_d\cdot\mathbf{r}_jn/c$ is not perturbed by the electromagnetic vacuum field, and thus simply follows an oscillatory behaviour, according to Eqs. (1.122a)–(1.122b). Consequently, this approximation yields

$$\hat{\sigma}_j(t-|\mathbf{r}_d|n/c+\boldsymbol{e}_d\cdot\mathbf{r}_dn/c)\approx\hat{\sigma}_j(t-|\mathbf{r}_d|n/c)\exp(-i\omega_{e,j}\boldsymbol{e}_d\cdot\mathbf{r}_jn/c), \tag{3.80}$$

with $\omega_{e,j}$ the transition frequency of emitter j. Substituting Eqs. (3.79) and (3.80) into Eq. (3.78), we find

$$\begin{aligned}\hat{\mathbf{E}}^{(+)}_{\perp,\mathrm{ZPL}}(\mathbf{r}_d,t)=&\boldsymbol{\mathcal{E}}_{\boldsymbol{\mu}_1^{\mathrm{ZPL}}}(\mathbf{r}_d)\hat{\sigma}_1(t-|\mathbf{r}_d|n/c)\exp(-i\omega_0\boldsymbol{e}_d\cdot\mathbf{r}_1n/c)\\&+\boldsymbol{\mathcal{E}}_{\boldsymbol{\mu}_2^{\mathrm{ZPL}}}(\mathbf{r}_d)\hat{\sigma}_2(t-|\mathbf{r}_d|n/c)\exp(-i\omega_0\boldsymbol{e}_d\cdot\mathbf{r}_2n/c).\end{aligned} \tag{3.81}$$

For simplicity, we have taken into account here that the transition frequencies $\omega_{e,1}$ and $\omega_{e,2}$ are almost identical and, thus we have replaced them by the arithmetic average transition frequency ω_0. This approximation is valid as long as $\delta = \omega_{e,1} - \omega_{e,2} \ll \omega_0$. Importantly, the operators $\hat{\sigma}_1(t-|\mathbf{r}_d|n/c)$ and $\hat{\sigma}_2(t-|\mathbf{r}_d|n/c)$ in Eq. (3.81) are now evaluated at the same time argument.

We consider next that the transition dipole moments are identical ($\boldsymbol{\mu}_1 = \boldsymbol{\mu}_2$). As a consequence, $\boldsymbol{\mathcal{E}}_{\boldsymbol{\mu}_1^{\mathrm{ZPL}}}(\mathbf{r}_d) = \boldsymbol{\mathcal{E}}_{\boldsymbol{\mu}_2^{\mathrm{ZPL}}}(\mathbf{r}_d)$, as long as the distance to the detector is much larger than the separation distance $r_{12} = |\mathbf{r}_1 - \mathbf{r}_2|$ between the emitters [Eq. (1.141)]. The positive-frequency electric field operator in Eq. (3.81) then reduces to

$$\hat{\mathbf{E}}^{(+)}_{\perp,\mathrm{ZPL}}(\mathbf{r}_d,t) = \boldsymbol{e}_{\boldsymbol{\mathcal{E}}_{\boldsymbol{\mu}}} \hat{E}^{(+)}_{\perp,\mathrm{ZPL}}(\mathbf{r}_d,t), \tag{3.82}$$

where we have defined $\boldsymbol{e}_{\boldsymbol{\mathcal{E}}_{\boldsymbol{\mu}}} = \boldsymbol{\mathcal{E}}_{\boldsymbol{\mu}_1^{\mathrm{ZPL}}}(\mathbf{r}_d)/|\boldsymbol{\mathcal{E}}_{\boldsymbol{\mu}_1^{\mathrm{ZPL}}}(\mathbf{r}_d)| = \boldsymbol{\mathcal{E}}_{\boldsymbol{\mu}_2^{\mathrm{ZPL}}}(\mathbf{r}_d)/|\boldsymbol{\mathcal{E}}_{\boldsymbol{\mu}_2^{\mathrm{ZPL}}}(\mathbf{r}_d)|$ and the scalar positive-frequency electric field operator

$$\hat{E}^{(+)}_{\perp,\mathrm{ZPL}}(\mathbf{r}_d,t) = \xi_{\mathrm{ZPL}} \cdot \left(\hat{\sigma}_1(t-|\mathbf{r}_d|n/c) + \hat{\sigma}_2(t-|\mathbf{r}_d|n/c) e^{i\varphi_{\mathrm{ZPL}}} \right), \tag{3.83}$$

with

$$\xi_{\mathrm{ZPL}} = \exp(-i\omega_0 \boldsymbol{e}_d \cdot \mathbf{r}_1 n/c) |\boldsymbol{\mathcal{E}}_{\boldsymbol{\mu}_1^{\mathrm{ZPL}}}(\mathbf{r}_d)|, \tag{3.84}$$

and

$$\varphi_{\mathrm{ZPL}} = \omega_0 \boldsymbol{e}_d \cdot (\mathbf{r}_1 - \mathbf{r}_2) n/c. \tag{3.85}$$

Additionally, we consider that light is detected in the normal direction to the plane in which the dipoles are contained (i.e., $\boldsymbol{e}_{\mathbf{r}_d}$ is orthogonal to $\boldsymbol{\mu}_1 = \boldsymbol{\mu}_2$ and to $\mathbf{r}_1 - \mathbf{r}_2$). For this detection direction, $\varphi_{\mathrm{ZPL}} = 0$ [Eq. (3.85)]. Thus, the scalar positive-frequency electric field operator simplifies to

$$\hat{E}^{(+)}_{\perp,\mathrm{ZPL}}(t) \equiv \hat{E}^{(+)}_{\perp,\mathrm{ZPL}}(\mathbf{r}_d,t)\Big|_{\varphi_{\mathrm{ZPL}}=0} = \xi_{\mathrm{ZPL}} \cdot \left(\hat{\sigma}_1(t-|\mathbf{r}_d|n/c) + \hat{\sigma}_2(t-|\mathbf{r}_d|n/c) \right). \tag{3.86}$$

We now focus on the expression of the color-blind intensity correlation [Eq. (2.60)]. As the positive-frequency and negative-frequency electric field operators have the same polarization at all times [Eq. (3.82)], the intensity correlation of ZPL photons at delay τ can be directly calculated from the scalar electric field operators [Eq. (3.86)] as

$$g^{(2)}_{\mathrm{ZPL}}(\tau) = \frac{\langle \hat{E}^{(-)}_{\perp,\mathrm{ZPL}}(0) \hat{E}^{(-)}_{\perp,\mathrm{ZPL}}(\tau) \hat{E}^{(+)}_{\perp,\mathrm{ZPL}}(\tau) \hat{E}^{(+)}_{\perp,\mathrm{ZPL}}(0) \rangle_{ss}}{\langle E^{(-)}_{\perp,\mathrm{ZPL}}(0) E^{(+)}_{\perp,\mathrm{ZPL}}(0) \rangle_{ss} \langle E^{(-)}_{\perp,\mathrm{ZPL}}(\tau) E^{(+)}_{\perp,\mathrm{ZPL}}(\tau) \rangle_{ss}}, \tag{3.87}$$

where the expectation values are calculated in the steady state (ss). We emphasize that the retardation times $|\mathbf{r}_d|/c$ on the right-hand side of the expression of the scalar electric field operators in Eq. (3.86) do not influence the value of $g^{(2)}_{\mathrm{ZPL}}(\tau)$, as their contribution to the positive-frequency electric field operators cancel with their contribution to the negative-frequency electric field operator (see Section 2.3.3).

As a consequence, the intensity correlation at delay $\tau = 0$, which is given by

$$g^{(2)}_{\mathrm{ZPL}}(0) = \frac{\langle \hat{E}^{(-)}_{\perp,\mathrm{ZPL}}(0)\hat{E}^{(-)}_{\perp}(0)\hat{E}^{(+)}_{\perp,\mathrm{ZPL}}(0)\hat{E}^{(+)}_{\perp,\mathrm{ZPL}}(0)\rangle_{ss}}{\langle E^{(-)}_{\perp,\mathrm{ZPL}}(0)E^{(+)}_{\perp,\mathrm{ZPL}}(0)\rangle^{2}_{ss}}, \tag{3.88}$$

can be obtained using directly the electric field operators

$$\hat{E}^{(+)}_{\perp,\mathrm{ZPL}}(0) = \xi_{\mathrm{ZPL}}\Big(\hat{\sigma}_1(0) + \hat{\sigma}_2(0)\Big), \tag{3.89a}$$

$$\hat{E}^{(-)}_{\perp,\mathrm{ZPL}}(0) = \xi_{\mathrm{ZPL}}\Big(\hat{\sigma}^{\dagger}_1(0) + \hat{\sigma}^{\dagger}_2(0)\Big). \tag{3.89b}$$

Further, by substituting Eqs. (3.89a)–(3.89b) into Eq. (3.88), one can obtain after some algebra

$$g^{(2)}_{\mathrm{ZPL}}(0) = \frac{4p_E}{\Big[2p_E + (1+\sin(2\Theta_\Lambda))p_{\Lambda_+} + (1-\sin(2\Theta_\Lambda))p_{\Lambda_-} - \cos(2\Theta_\Lambda)\mathrm{Re}\rho_{+-}\Big]^2}, \tag{3.90}$$

where $p_k = \langle k|\,\hat{\rho}_{ss}\,|k\rangle$ are steady-state populations (with $|k\rangle$ a state of the interacting basis $\{|E\rangle, |\Lambda_+\rangle, |\Lambda_-\rangle, |G\rangle\}$), and $\rho_{+-} = \langle\Lambda_+|\,\hat{\rho}_{ss}\,|\Lambda_-\rangle$ is the steady-state coherence between the delocalized states. Therefore, Eq. (3.90) indicates that the behaviour of $g^{(2)}_{\mathrm{ZPL}}(0)$ can be completely understood from the steady state of the system. However, the exact solution of the steady state of the interacting molecules is very intricate in general, as it requires to solve the complete set of equations in Eqs. (3.73a)–(3.73i). In the following, we discuss different approximations to obtain further analytical insights into this steady state and, thus, into $g^{(2)}_{\mathrm{ZPL}}(0)$.

Weak and intense laser intensities

First, under weak laser intensity ($I_L \lesssim I_{\mathrm{sat}}$), we find numerically that p_E and ρ_{+-} are much smaller than the population of (at least) one of the delocalized states $|\Lambda_\pm\rangle$. Thus, the intensity correlation can be approximated under weak illumination as

$$g^{(2)}_{\mathrm{ZPL}}(0)\Big|_{I_L\lesssim I_{\mathrm{sat}}} = \frac{4p_E}{[(1+\sin(2\Theta_\Lambda))p_{\Lambda_+} + (1-\sin(2\Theta_\Lambda))p_{\Lambda_-}]^2}. \tag{3.91}$$

The numerator in Eq. (3.91) accounts for the probability of emitting two photons, which is proportional to the steady-state population p_E of the doubly-excited state $|E\rangle$. In contrast, the denominator is related the probability of single-photon emission and is given by the steady-state populations p_{Λ_-} and $p_{\Lambda_+}$of the single-excitation delocalized states $|\Lambda_-\rangle$ and $|\Lambda_+\rangle$. Equation (3.91) indicates that, if the population of the doubly-excited state is much smaller than the square of the steady-state populations of the delocalized states, then the intensity correlation becomes strongly antibunched. In the opposite limit, strong bunching occurs.

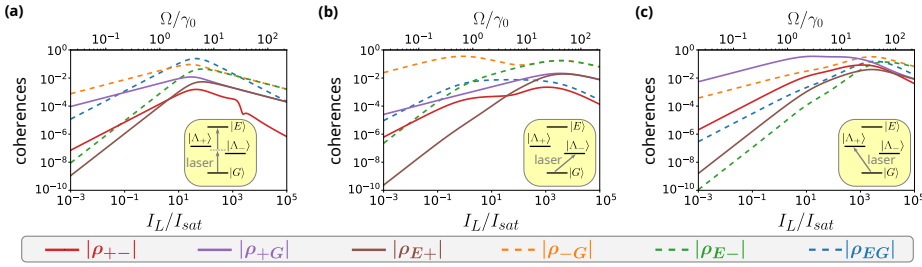

Figure 3.5: Absolute value of the steady-state coherences as a function of the laser intensity for different laser detunings. The laser is tuned to: (a) the two-photon resonance, (b) the transition frequency of the superradiant state $|\Lambda_-\rangle$, and (c) the transition frequency of the subradiant state $|\Lambda_+\rangle$. The insets in (a)-(c) illustrate the different resonant excitation processes promoted by the different laser frequencies. Solid lines represent the coherences that involve the subradiant state $|\Lambda_+\rangle$, namely (red) $\rho_{+-} = \langle\Lambda_+|\,\hat{\rho}_{ss}\,|\Lambda_-\rangle$, (purple) $\rho_{+G} = \langle\Lambda_+|\,\hat{\rho}_{ss}\,|G\rangle$ and (brown) $\rho_{E+} = \langle E|\,\hat{\rho}_{ss}\,|\Lambda_+\rangle$. Dashed lines represent the coherences that do not involve the subradiant state, namely (orange) $\rho_{-G} = \langle\Lambda_-|\,\hat{\rho}_{ss}\,|G\rangle$, (green) $\rho_{E-} = \langle E|\,\hat{\rho}_{ss}\,|\Lambda_-\rangle$ and (blue) $\rho_{EG} = \langle E|\,\hat{\rho}_{ss}\,|G\rangle$. The dipole-dipole coupling is $V_{\rm DW} = -20\gamma_0$, the combined Debye-Waller/Franck-Condon factor is $\alpha_{\rm DW} = 0.3$, and the molecular detuning is $\delta = 10\gamma_0$.

On the other hand, under very intense laser intensity ($I_L \gg I_{\rm sat}$), the populations of the molecular excited states saturate and become equal to 1/2 (Section 1.5.4). In this limit, the populations of the interacting system becomes $p_E, p_{\Lambda_+}, p_{\Lambda_-}, p_G \to 1/4$, whereas $\rho_{+-} \to 0$. Substituting these values into Eq. (3.90), we find

$$g^{(2)}_{\rm ZPL}(0)\Big|_{I_L \gg I_{\rm sat}} = 1. \tag{3.92}$$

Laser tuned to the two-photon resonance and to the superradiant state

We describe next an approximation that relies on the value of the laser frequency and that is valid for all laser intensities. Specifically, when the laser is either tuned to the two-photon resonance ($\omega_L = \omega_0$) or to the transition frequency of the superradiant state $|\Lambda_-\rangle$ ($\omega_L = \omega_0 - \Lambda$), the steady-state coherences between the subradiant state $|\Lambda_+\rangle$ and any other state are much smaller than the largest coherence of the system (in the interacting basis). We have verified the validity of this approximation by computing numerically the steady-state populations and coherences as a function of the laser intensity and frequency, with molecular detuning fixed at $\delta = 10\gamma_0$. The resulting coherences $\rho_{ab} = {\rm Tr}(\hat{\sigma}_{ab}\hat{\rho}_{ss})$ are plotted in Fig. 3.5, which confirms that we can neglect the steady-state coherences related to the subradiant state (ρ_{+-}, ρ_{+G}, ρ_{E+}) for these two laser detunings ($\Delta_0 = 0$ and $\Delta_0 = \Lambda$). In this way, the set of Eqs. (3.73a)–(3.73i) is reduced in the steady-state to

$$0 = -2\gamma_0 p_E - \Omega_- {\rm Im}\rho_{E-}, \tag{3.93a}$$

$$0 = -\gamma_+(p_{\Lambda_+} - p_E), \tag{3.93b}$$
$$0 = -\gamma_-(p_{\Lambda_-} - p_E) + \Omega_-(\mathrm{Im}\rho_{E-} - \mathrm{Im}\rho_{-G}), \tag{3.93c}$$
$$0 = (i2\Delta_0 - \gamma_0)\rho_{EG} + i\frac{\Omega_-}{2}(\rho_{E-} - \rho_{-G}), \tag{3.93d}$$
$$0 = -i\frac{\Omega_-}{2}(-p_E + p_{\Lambda_-} - \rho_{EG}) + [i(\Delta_0 + \Lambda) - \gamma_0 - \gamma_-/2]\rho_{E-}, \tag{3.93e}$$
$$0 = -i\frac{\Omega_-}{2}(-p_{\Lambda_-} + p_G + \rho_{EG}) + [i(\Delta_0 - \Lambda) - \gamma_-/2]\rho_{-G} + \tilde{\gamma}_-\rho_{E-}. \tag{3.93f}$$

Notably, Eq. (3.93b) yields $p_E = p_{\Lambda_+}$. We use Eqs. (3.93a)–(3.93f) in Sections 3.3.3 and 3.3.4 to derive analytical expressions for the steady-state populations and for the color-blind intensity correlation $g^{(2)}_{\mathrm{ZPL}}(0)$.

3.3.2 Color-blind intensity correlation under different laser frequencies

In this section, we provide a general overview of the rich landscape of values that $g^{(2)}_{\mathrm{ZPL}}(0)$ can exhibit for the pair of quantum emitters with parallel transition dipole moments studied here, from almost perfect antibunching [$g^{(2)}_{\mathrm{ZPL}}(0) \approx 0$] to extreme bunching [$g^{(2)}_{\mathrm{ZPL}}(0) \gg 1$]. To this end, we compute numerically $g^{(2)}_{\mathrm{ZPL}}(0)$, using Eq. (3.88), for three different laser frequencies, namely: (i) half the frequency between $|G\rangle$ and $|E\rangle$ (two-photon resonance); (ii) the transition frequency of the superradiant state $|\Lambda_-\rangle$; and (iii) the transition frequency of the subradiant state $|\Lambda_+\rangle$.

We first fix the laser frequency at the two photon resonance ($\omega_L = \omega_0$), which enables to resonantly excite the doubly-excited state $|E\rangle$ through a two-photon process. In Fig. 3.6a, we plot the dependence of $g^{(2)}_{\mathrm{ZPL}}(0)$ on the laser intensity I_L and the molecular detuning δ for this laser frequency. We note that δ can be tuned in experiments, for instance, via the Stark effect [1, 99, 100, 105]. Under weak illumination, we find that $g^{(2)}_{\mathrm{ZPL}}(0)$ is strongly bunched, which reveals that the emission of photons in cascade is strongly enhanced with respect to light emission obeying Poissonian statistics. Additionally, the difference between the laser frequency $\omega_L = \omega_0$ and the resonance frequencies $\omega_\pm = \omega_0 \pm \Lambda$ of the single-excitation states $|\Lambda_\pm\rangle$ increases with the molecular detuning. Thus, the ratio between two-photon emission processes and single-photon emission processes grows with the molecular detuning. As a consequence, $g^{(2)}_{\mathrm{ZPL}}(0)$ also increases with the molecular detuning δ, as shown in Fig. 3.6a. In Section 3.3.3, we analyze in more detail the light statistics for this laser frequency.

Next, we fix the laser frequency at $\omega_L = \omega_0 - \Lambda$, for which the laser is resonantly tuned to the superradiant state $|\Lambda_-\rangle$. Figure 3.6b shows the behaviour of $g^{(2)}_{\mathrm{ZPL}}(0)$ for this laser frequency, revealing that the emission is strongly antibunched under weak illumination. Consequently, the two coupled molecules act as a single-photon source for this laser frequency, as it occurs for a single molecule with two-level-system

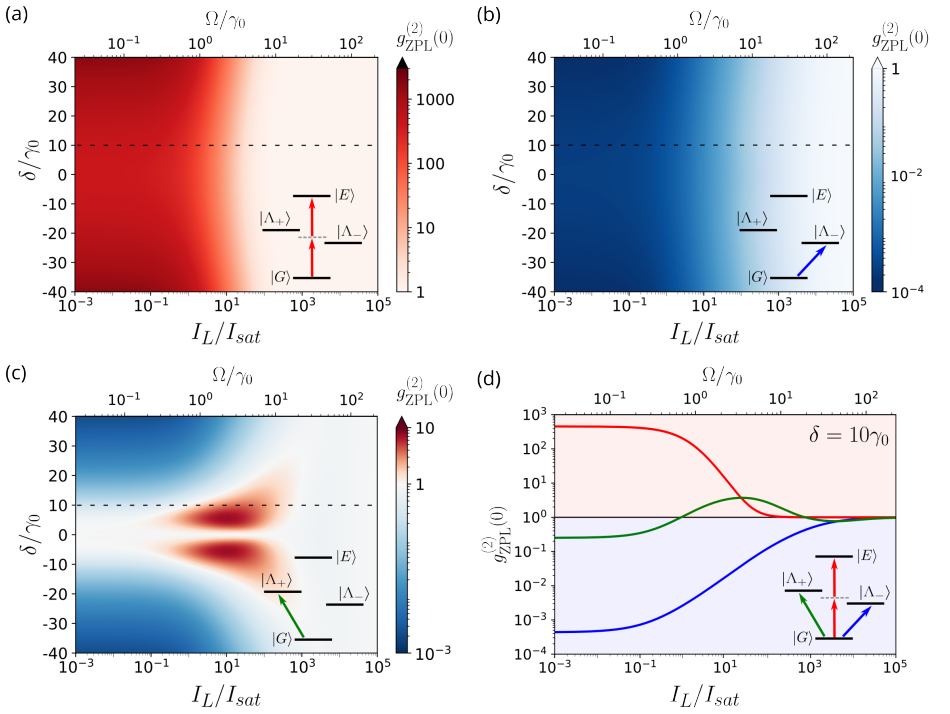

Figure 3.6: Color-blind intensity correlation $g^{(2)}_{\mathrm{ZPL}}(0)$ of light emitted into the ZPL from two interacting emitters with parallel transition dipole moments, as a function of the laser intensity I_L and molecular detuning δ. In (a) the laser is tuned to the two-photon resonance ($\omega_L = \omega_0$), which leads to bunched emission. In (b) the laser excites resonantly the superradiant state $|\Lambda_-\rangle$ ($\omega_L = \omega_0 - \Lambda$) giving rise to antibunched emission. In (c) the laser is tuned to the transition frequency of the subradiant state $|\Lambda_+\rangle$ ($\omega_L = \omega_0 + \Lambda$) and $g^{(2)}_{\mathrm{ZPL}}(0)$ shows a more complex dependence on the laser intensity and molecular detuning. In (a)-(c), color blue represents antibunched emission [$g^{(2)}_{\mathrm{ZPL}}(0) < 1$], red bunched emission [$g^{(2)}_{\mathrm{ZPL}}(0) > 1$], and white Poissonian statistics [$g^{(2)}_{\mathrm{ZPL}}(0) = 1$]. Cuts of the results in (a)-(c) for $\delta = 10\gamma_0$ (along the dashed black lines) are plotted in (d), where the red line corresponds to a laser tuned to the two-photon resonance, the blue line is obtained for a laser tuned to the superradiant state and the green line corresponds to a laser tuned to the subradiant state. In (d), red and blue shaded background corresponds to bunched and antibunched emission, respectively. The insets illustrate the different laser detunings considered. The dipole-dipole coupling is $V_{\mathrm{DW}} = -20\gamma_0$ and the combined Debye-Waller/Franck-Condon factor is $\alpha_{\mathrm{DW}} = 0.3$.

behaviour (Section 2.3.3), but with a larger decay rate $\gamma_0(1 + \alpha_{\mathrm{DW}}|V_{\mathrm{DW}}|/\Lambda)$ and larger transition dipole moment. Thus, the emission of single photons is accelerated by a factor $1 + \alpha_{\mathrm{DW}}|V_{\mathrm{DW}}|/\Lambda$ with respect to the case of a single emitter. In Section 3.3.4, we quantify analytically the small deviation of the light statistics from that of an ideal single photon source [with $g^{(2)}_{\mathrm{ZPL}}(0) = 0$] for this laser detuning, as well as the increase of $g^{(2)}_{\mathrm{ZPL}}(0)$ observed in Fig. 3.6b for increasing laser intensities.

Moreover, Fig. 3.6c shows that a more complex dependence of $g^{(2)}_{\mathrm{ZPL}}(0)$ on the laser intensity and on the molecular detuning is found when the laser is tuned to the transition frequency of the subradiant state $|\Lambda_+\rangle$ ($\omega_L = \omega_0 + \Lambda$). In this case, if the two molecules are very far from resonance ($|\delta| \gg 30\gamma_0$), the system behaves again similar to a single TLS and the emission is strongly antibunched under weak illumination. In the opposite case, if the molecules are identical ($\delta = 0$) the light emitted has approximately Poissonian statistics [$g^{(2)}_{\mathrm{ZPL}}(0) \approx 1$]. Interestingly, if the molecules are slightly off-resonance, then both bunched and antibunched emission can be obtained for resonant excitation of the subradiant state, depending on the value of laser intensity I_L. The complex behaviour of $g^{(2)}_{\mathrm{ZPL}}(0)$ for this laser frequency is analyzed in detail in Section 3.3.5.

Notably, Fig. 3.6 indicates different ways to tune the emission from antibunching to bunching. For example, for two slightly detuned emitters and a laser tuned to the transition frequency of the subradiant state, we can obtain both types of light statistics by modifying the laser intensity. As another example, we can use weak illumination and tune the laser either to the two-photon resonance or to the superradiant state in order to obtain extreme values of bunching and antibunching, respectively. This level of controlled cross-over between bunched and antibunched emission depending on a reasonable variation of experimental parameters can be of potential technological interest in engineering photon sources. Alternative physical configurations to achieve this cross-over include tuning the relative phase between the light scattered coherently and incoherently by an ensemble of trapped ions in a nanofiber [193], manipulating the position of the detector for the case of two trapped ions [191], controlling the temperature of a thermal atomic vapor in a cell [194] or tailoring the laser polarization and the material gain of a plasmonic nanosphere close to two quantum emitters [195].

To summarize the broad range of color-blind intensity correlations that can be obtained by tuning the laser frequency and intensity, we fix $\delta = 10\gamma_0$ in Fig. 3.6d and plot the dependence of $g^{(2)}_{\mathrm{ZPL}}(0)$ on the laser intensity for a laser tuned to (red line) the two-photon resonance, (blue line) the transition frequency of the superradiant state and (green line) the transition frequency of the subradiant state. For this value of molecular detuning, $\sin(2\Theta_\Lambda) = -0.97$ and $\cos(2\Theta_\Lambda) = -0.24$ in Eqs. (3.90) and (3.91). In Sections 3.3.3–3.3.5, we analyze more extensively the behaviour of $g^{(2)}_{\mathrm{ZPL}}(0)$ shown in Fig. 3.6d for the three laser frequencies and with support of analytical equations.

3.3.3 Laser resonantly tuned to the two-photon resonance

In this section, we consider that the molecules are driven by a laser tuned to the two-photon resonance ($\omega_L = \omega_0$, which yields $\Delta_0 = 0$) and discuss in detail the dependence of $g^{(2)}_{\mathrm{ZPL}}(0)$ on the laser intensity at $\delta = 10\gamma_0$ (red line in Fig. 3.6d and black solid line in Fig. 3.7a). To this end, we first derive analytical expressions for the steady-state populations using Eqs. (3.93a)–(3.93f).

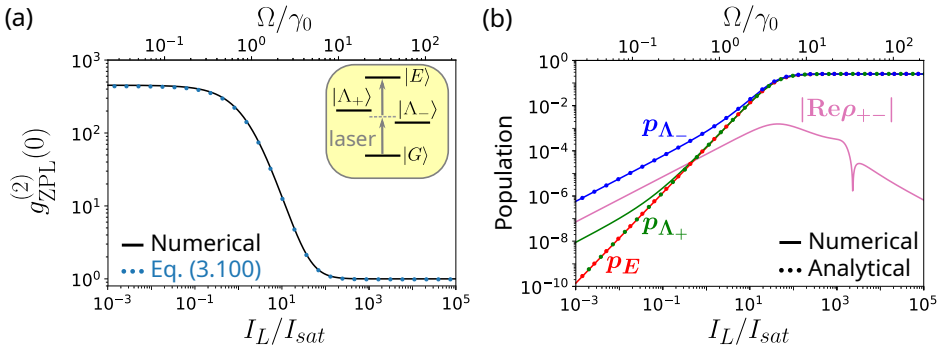

Figure 3.7: Dependence on the laser intensity of (a) $g^{(2)}_{\mathrm{ZPL}}(0)$ and (b) the steady-state populations when the laser is tuned resonantly to the two-photon resonance. In (a), the solid black line is obtained numerically using Eq. (3.90), whereas blue dots are calculated with the full analytical expression in Eq. (3.100). The inset in (a) represents the excitation at the two-photon resonance ($\omega_L = \omega_0$). In (b), blue corresponds to the steady-state population of the superradiant state $|\Lambda_-\rangle$, green to that of the subradiant state $|\Lambda_+\rangle$, red to that of the doubly-excited state $|E\rangle$ and pink to absolute value of the real part of the steady-state coherence $\rho_{+-} = \langle\Lambda_+|\hat{\rho}_{ss}|\Lambda_-\rangle$. Solid lines correspond to the numerical calculations, whereas dots represent the analytical results obtained from the expressions in Eqs. (3.94) and (3.95). We consider $V_{\mathrm{DW}} = -20\gamma_0$, $\alpha_{\mathrm{DW}} = 0.3$ and $\delta = 10\gamma_0$.

Derivation of the analytical steady-state populations

We first substitute $\Delta_0 = 0$ into Eqs. (3.93a)–(3.93f). By solving the resulting set of equations, we find that the populations of $|E\rangle$ and $|\Lambda_+\rangle$ are equal and given by

$$p_E\Big|^{\mathrm{2PR}} = p_{\Lambda_+}\Big|^{\mathrm{2PR}} = \frac{\Omega_-^4}{4\Omega_-^4 + 2\Omega_-^2\gamma_0(4\gamma_0 + 3\gamma_- - 4\tilde{\gamma}_-) + (4\gamma_0\Lambda)^2}, \tag{3.94}$$

with 2PR standing for *two-photon resonance*. These populations converge to 1/4 for sufficiently strong laser intensities (Ω_- much larger than all the other parameters). On the other hand, the population of the superradiant state $|\Lambda_-\rangle$ becomes related to the populations in Eq. (3.94) as

$$p_{\Lambda_-}\Big|^{\mathrm{2PR}} = p_E\Big|^{\mathrm{2PR}}\left[1+\left(\frac{2\gamma_0}{\Omega_-}\right)^2\right]. \tag{3.95}$$

This expression also converges to 1/4 for sufficiently strong laser intensities. Additionally, Eq. (3.95) indicates that the population of the superradiant state is much larger than the population of the subradiant state and of the doubly-excited state under weak laser intensities.

The steady-state populations obtained in Eqs. (3.94) and (3.95) are plotted with dots in Fig. 3.7b, showing a good agreement with the numerical results that we discuss below (solid lines in Fig. 3.7b).

Color-blind intensity correlation under weak illumination

Under weak laser intensity ($I_L \ll I_{\text{sat}}$), the analytical expression in Eq. (3.95) for the population p_{Λ_-} reduces to

$$p_{\Lambda_-}\Big|_{I_L \ll I_{\text{sat}}}^{\text{2PR}} = \left(\frac{\Omega_-}{2\Lambda}\right)^2 = \frac{I_L}{I_{\text{sat}}}\frac{1-\sin(2\Theta_\Lambda)}{2\varsigma^2}, \tag{3.96}$$

where we have used Eq. (3.70) to relate Ω_-^2 with the laser intensity. Further, we have defined

$$\varsigma \equiv \frac{2\Lambda}{\gamma_0}. \tag{3.97}$$

Equation (3.96) reveals that the superradiant state is excited through single-photon processes in this intensity regime ($I_L \ll I_{\text{sat}}$), as its steady-state population increases linearly with the laser intensity. Further, for the same intensity range, we obtain that the doubly-excited state $|E\rangle$ is excited through two-photon processes because its population depends quadratically on the laser intensity

$$p_E\Big|_{I_L \ll I_{\text{sat}}}^{\text{2PR}} = \left(\frac{\Omega_-^2}{4\gamma_0\Lambda}\right)^2 = \frac{I_L^2}{I_{\text{sat}}^2}\frac{(1-\sin(2\Theta_\Lambda))^2}{16\varsigma^2}, \tag{3.98}$$

which is obtained from Eq. (3.94).

Additionally, within this intensity range ($I_L \ll I_{\text{sat}}$), we observe in Fig. 3.7b that the population p_{Λ_+} of the subradiant state $|\Lambda_+\rangle$ is two orders of magnitude smaller than the population p_{Λ_-} of the superradiant state $|\Lambda_-\rangle$. As a consequence, p_{Λ_+} can be neglected in the calculation of the intensity correlation in Eq. (3.91). Both the numerator $[4p_E]$ and the denominator $[p_{\Lambda_-}^2(1-\sin(2\Theta_\Lambda))^2]$ in Eq. (3.91) thus scale quadratically with the laser intensity and $g^{(2)}_{\text{ZPL}}(0)$ becomes independent of the specific value of I_L/I_{sat}. The resulting expression is given by

$$g^{(2)}_{\text{ZPL}}(0)\Big|_{I_L \ll I_{\text{sat}}}^{\text{2PR}} = \left(\frac{\varsigma}{1-\sin(2\Theta_\Lambda)}\right)^2, \tag{3.99}$$

which agrees with the numerical results in Fig. 3.7a and becomes equal to 439.5 in our configuration. Equation (3.99) shows that the emission is strongly bunched if the splitting 2Λ is much larger than the spontaneous emission rate γ_0 (as it occurs when $V_{\text{DW}} \gg \gamma_0$), so that $\varsigma \gg 1$. Interestingly, Eq. (3.99) can be used to estimate molecular parameters in experiments. For example, the distance between the two emitters r_{12} and the molecular detuning δ could be simultaneously estimated through the measurement of $g^{(2)}_{\text{ZPL}}(0)|^{\text{2PR}}_{I_L \ll I_{\text{sat}}}$ and the splitting $2\Lambda = \sqrt{4V_{\text{DW}}^2 + \delta^2}$ between the transition frequencies of the superradiant and subradiant states. Alternatives to extract r_{12} are based on superresolution imaging techniques [1, 92], which are time demanding.

Color-blind intensity correlation for increasing laser intensities

For increasing laser intensities ($I_L \gtrsim 10^{-1} I_{\text{sat}}$), the intensity correlation strongly decreases. Figure 3.7b shows that the population p_E of the doubly-excited state $|E\rangle$ becomes comparable to the population p_{Λ_-} of the superradiant state $|\Lambda_-\rangle$ in this case. As a consequence, Eq. (3.91) is no longer a good approximation. By substituting the analytical populations in Eqs. (3.94) and (3.95) into the expression of the color-blind intensity correlation in Eq. (3.90), with $\text{Re}\rho_{+-} = 0$, we obtain

$$\begin{aligned} g^{(2)}_{\text{ZPL}}(0)\Big|^{\text{2PR}} &= \frac{\Omega_-^4 + \Omega_-^2\gamma_0(2\gamma_0 + 3\gamma_-/2 - 2\tilde{\gamma}_-) + (2\gamma_0\Lambda)^2}{[\Omega_-^2 + \gamma_0^2(1-\sin(2\Theta_\Lambda))]^2} \\ &= \frac{1}{[(2+I_L/I_{\text{sat}})(1-\sin(2\Theta_\Lambda))\gamma_0]^2} \times \Big[(1-\sin(2\Theta_\Lambda))^2\gamma_0^2(I_L/I_{\text{sat}})^2 \\ &+ (4\Lambda)^2 + 2\gamma_0(1-\sin(2\Theta_\Lambda))(2\gamma_0 + 3\gamma_-/2 - 2\tilde{\gamma}_-)(I_L/I_{\text{sat}})\Big], \end{aligned} \tag{3.100}$$

with $\tilde{\gamma}_- = \tilde{\gamma} - \gamma_0 \sin(2\Theta_\Lambda)$. Figure 3.7a shows the excellent agreement between Eq. (3.100) (blue dots) and the numerical results (black solid line) for any laser intensity, including the convergence to $g^{(2)}_{\text{ZPL}}(0) = 1$ for strong enough laser intensities.

3.3.4 Laser resonantly tuned to the superradiant state

We examine in this section the color-blind intensity correlation $g^{(2)}_{\text{ZPL}}(0)$ of light emitted into the ZPL when the laser is tuned to the transition frequency of the superradiant state $|\Lambda_-\rangle$ ($\omega_L = \omega_0 - \Lambda$). In this case, the single-excitation delocalized state $|\Lambda_-\rangle$ (which couples more efficiently to light than $|\Lambda_+\rangle$ and, additionally, is excited resonantly) dominates the response under weak enough illumination, with negligible effect of the doubly-excited state $|E\rangle$ and of the subradiant state $|\Lambda_+\rangle$. The system thus behaves in close analogy to a resonantly driven TLS, with strongly antibunched emission, as shown by the solid black line in Fig. 3.8a (corresponding to the blue line in Fig. 3.6d). To gain analytical insights into the behaviour of $g^{(2)}_{\text{ZPL}}(0)$, we first derive the expressions of the steady-state populations for arbitrary laser intensity, as we did in Section 3.3.3 for the case of two-photon resonance illumination. We then use these expressions to discuss the behaviour of the color-blind intensity correlation at weak and increasing laser intensities.

Derivation of the analytical steady-state populations

To derive the analytical expressions of the steady-state populations, we solve the set of Eqs. (3.93a)–(3.93f) with $\Delta_0 = \Lambda$. The resulting populations of the doubly excited state and the subradiant state are given as

$$p_E\Big|^{|\Lambda_-\rangle} = p_{\Lambda_+}\Big|^{|\Lambda_-\rangle} = \frac{\Omega_-^4}{4\Omega_-^4 + 2\Omega_-^2[(2\kappa)^2 + \gamma_0(\gamma_- - 4\tilde{\gamma}_-)] + (2\kappa\gamma_-)^2}, \tag{3.101}$$

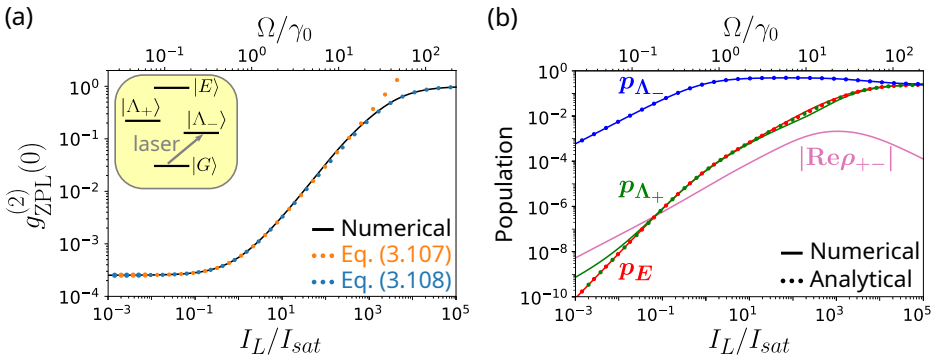

Figure 3.8: Dependence on the laser intensity of (a) $g^{(2)}_{\mathrm{ZPL}}(0)$ and (b) the steady-state populations when the laser is tuned resonantly to the superradiant state $|\Lambda_-\rangle$. In (a), the solid black line is obtained numerically using Eq. (3.90), while orange dots are calculated with the analytical expression in Eq. (3.107) and blue dots with the analytical expression in Eq. (3.108). The resonant excitation at the transition frequency of the superradiant state is illustrated in the inset in (a). In (b), blue corresponds to the steady-state population of the superradiant state $|\Lambda_-\rangle$, green to that of the subradiant state $|\Lambda_+\rangle$, red to that of the doubly-excited state $|E\rangle$, and pink to the absolute value of the real part of the steady-state coherence $\rho_{+-} = \langle\Lambda_+|\hat{\rho}_{ss}|\Lambda_-\rangle$. Solid lines correspond to the numerical calculations, whereas dots represent the analytical results obtained from the expressions in Eqs. (3.101) and (3.103). We consider $V_{\mathrm{DW}} = -20\gamma_0$, $\alpha_{\mathrm{DW}} = 0.3$ and $\delta = 10\gamma_0$.

with

$$\kappa = \sqrt{(2\Lambda)^2 + (\gamma_0 + \gamma_-/2)^2}. \tag{3.102}$$

These populations converge to 1/4 for strong laser intensities. Additionally, the population of the superradiant state is

$$p_{\Lambda_-}\Big|^{|\Lambda_-\rangle} = p_E\Big|^{|\Lambda_-\rangle} + \frac{\Omega_-^2\,(2\kappa)^2}{4\Omega_-^4 + 2\Omega_-^2[(2\kappa)^2 + \gamma_0(\gamma_- - 4\tilde{\gamma}_-)] + (2\kappa\gamma_-)^2}. \tag{3.103}$$

These analytical steady-state populations are plotted with dots in Fig. 3.8b, showing an excellent agreement with the numerical results (solid lines).

Color-blind intensity correlation under weak illumination

In the laser intensity range $I_L \ll I_{\mathrm{sat}}$, the analytical expressions in Eqs. (3.101) and (3.103) reduce to

$$p_E\Big|^{|\Lambda_-\rangle}_{I_L \ll I_{\mathrm{sat}}} = p_{\Lambda_+}\Big|^{|\Lambda_-\rangle}_{I_L \ll I_{\mathrm{sat}}} = \left(\frac{\Omega_-^2}{2\kappa\gamma_-}\right)^2 = \frac{I_L^2}{I_{\mathrm{sat}}^2}\left(\frac{\gamma_0^2(1-\sin(2\Theta_\Lambda))}{4\kappa\gamma_-}\right)^2, \tag{3.104}$$

and

$$p_{\Lambda_-}\Big|^{|\Lambda_-\rangle}_{I_L\ll I_{\rm sat}} = \left(\frac{\Omega_-}{\gamma_-}\right)^2 = \frac{I_L}{I_{\rm sat}}\frac{\gamma_0^2(1-\sin(2\Theta_\Lambda))}{2\gamma_-^2}. \tag{3.105}$$

Thus, the population p_{Λ_-} of the superradiant state $|\Lambda_-\rangle$ depends linearly on the laser intensity, and the population p_E of the doubly-excited $|E\rangle$ does it quadratically, as in the case of weak laser intensity and illumination tuned to the two-photon resonance (Section 3.3.3). The population of the subradiant state $|\Lambda_+\rangle$, which can be safely neglected in the denominator of Eq. (3.91), also depends quadratically on the laser intensity, because it is populated through the relaxation of the doubly-excited state $|E\rangle$ for these laser intensities. Thus, both the numerator and the denominator scale quadratically in Eq. (3.91) and, as a result, the intensity correlation $g^{(2)}_{\rm ZPL}(0)$ becomes independent of the laser intensity:

$$g^{(2)}_{\rm ZPL}(0)\Big|^{|\Lambda_-\rangle}_{I_L\ll I_{\rm sat}} = \left[\frac{\gamma_-}{\kappa(1-\sin(2\Theta_\Lambda))}\right]^2. \tag{3.106}$$

Equation (3.106) becomes equal to 2.5×10^{-4} for our molecular configuration. Crucially, this equation shows that, as long as the losses are much smaller than κ (e.g., strong dipole-dipole coupling), the intensity correlation is characterized by strong antibunching (in contrast to the bunching obtained when the laser is tuned to the two-photon resonance). Thus, the coupled emitters behave in this case as a single-photon source with larger emission rate and transition dipole moment than a single emitter.

Color-blind intensity correlation for increasing laser intensities

The value of $g^{(2)}_{\rm ZPL}(0)$ increases for stronger laser intensities ($I_L \gtrsim 10^{-1}I_{\rm sat}$). This increase is due to the fact that the population p_{Λ_-} of the superradiant state $|\Lambda_-\rangle$ reaches a maximum value of 0.49 (which is very close to the excited-state population of a saturated TLS, see Section 1.5.4) and remains almost constant, while the population of the doubly-excited state $|E\rangle$ now increases linearly with the laser intensity due to the large and constant population of the superradiant state. As a consequence, $g^{(2)}_{\rm ZPL}(0)$ also increases linearly with the laser intensity. Specifically, it is given by

$$g^{(2)}_{\rm ZPL}(0)\Big|^{|\Lambda_-\rangle}_{I_L\lesssim I_{\rm sat}} = \frac{\gamma_-^2+(1-\sin(2\Theta_\Lambda))\gamma_0^2 I_L/I_{\rm sat}}{\kappa^2(1-\sin(2\Theta_\Lambda))^2}. \tag{3.107}$$

We plot the dependence of $g^{(2)}_{\rm ZPL}(0)$ on the laser intensity according to this equation (orange dots) in Fig. 3.8a, which shows an excellent agreement with the numerical results (solid black line) up to $I_L \approx 10^3 I_{\rm sat}$.

For even stronger laser intensities, Eq. (3.91) is no longer a good approximation because the contributions of the population of the doubly-excited state and subradiant state to the denominator of Eq. (3.90) need to be accounted for. By substituting the expressions of the steady-state populations in Eqs. (3.101) and

(3.103) into Eq. (3.90), we obtain

$$g^{(2)}_{\mathrm{ZPL}}(0)\Big|^{|\Lambda_-\rangle} = \frac{4\Omega_-^4 + 2\Omega_-^2\left[(2\kappa)^2 + \gamma_0(\gamma_- - 4\tilde{\gamma}_-)\right] + (2\kappa\gamma_-)^2}{4[\Omega_-^2 + (1-\sin(2\Theta_\Lambda))\kappa^2]^2}$$
$$= \frac{1}{(1-\sin(2\Theta_\Lambda))^2[(I_L/I_{\mathrm{sat}})\gamma_0^2 + 2\kappa^2]^2}\cdot\Big[(I_L/I_{\mathrm{sat}})^2\gamma_0^4(1-\sin(2\Theta_\Lambda))^2$$
$$+ (I_L/I_{\mathrm{sat}})\gamma_0^2(1-\sin(2\Theta_\Lambda))[(2\kappa)^2 + \gamma_0(\gamma_- - 4\tilde{\gamma}_-)] + (2\kappa\gamma_-)^2\Big]. \tag{3.108}$$

This expression reproduces the numerical results for arbitrary laser intensity (compare blue dots and black line in Fig. 3.8a), including the saturation to $g^{(2)}_{\mathrm{ZPL}}(0) = 1$ for very large intensities.

3.3.5 Laser resonantly tuned to the subradiant state

In this section, we analyze the complex behaviour of the color-blind intensity correlation when the laser is tuned to the transition frequency of the subradiant state. We show that this behaviour is due to the competition between two excitation mechanisms: (i) the resonant excitation of the subradiant state $|\Lambda_+\rangle$, a state that couples very inefficiently to light; and (ii) the non-resonant excitation of the superradiant state $|\Lambda_-\rangle$, which couples very well to light. We first develop an analytical model to derive the steady state under weak illumination and, afterwards, we investigate numerically the behaviour of $g^{(2)}_{\mathrm{ZPL}}(0)$ at increasing laser intensities.

Weak illumination

To derive the steady-state populations under weak illumination and for a laser tuned to the transition frequency of the subradiant state $|\Lambda_+\rangle$, we calculate the populations of two independent three-level systems. One of these three-level systems consists of the states $\{|G\rangle, |\Lambda_+\rangle, |E\rangle\}$, corresponding to the excitation of the doubly-excited state via the resonantly pumped subradiant state. The second three-level system is composed by the states $\{|G\rangle, |\Lambda_-\rangle, |E\rangle\}$ and represents the excitation of the doubly-excited state via the non-resonantly driven superradiant state $|\Lambda_-\rangle$. The pumping rates for the transitions $|G\rangle \to |\Lambda_\pm\rangle$ and $|\Lambda_\pm\rangle \to |E\rangle$ are $\Omega_\pm$ and the decay rates of the transitions $|E\rangle \to |\Lambda_\pm\rangle$ and $|\Lambda_\pm\rangle \to |G\rangle$ are $\gamma_\pm$.

The dynamics equations of the elements of the density matrix for the first three-level system $\{|G\rangle, |\Lambda_+\rangle, |E\rangle\}$ are given by:

$$\frac{d}{dt}\langle\hat{\sigma}_{EE}\rangle = -\gamma_+\langle\hat{\sigma}_{EE}\rangle + i\frac{\Omega_+}{2}\Big[\langle\hat{\sigma}_{E+}\rangle - \langle\hat{\sigma}_{+E}\rangle\Big], \tag{3.109a}$$

$$\frac{d}{dt}\langle\hat{\sigma}_{++}\rangle = -\gamma_+\Big[\langle\hat{\sigma}_{++}\rangle - \langle\hat{\sigma}_{EE}\rangle\Big] + i\frac{\Omega_+}{2}\Big[\langle\hat{\sigma}_{+E}\rangle - \langle\hat{\sigma}_{E+}\rangle + \langle\hat{\sigma}_{+G}\rangle - \langle\hat{\sigma}_{G+}\rangle,\Big] \tag{3.109b}$$

$$\frac{d}{dt}\langle\hat{\sigma}_{+G}\rangle = -i\frac{\Omega_+}{2}\Big[-\langle\hat{\sigma}_{++}\rangle + \langle\hat{\sigma}_{GG}\rangle + \langle\hat{\sigma}_{EG}\rangle\Big] - \frac{\gamma_+}{2}\langle\hat{\sigma}_{+G}\rangle\,, \tag{3.109c}$$

$$\frac{d}{dt}\langle\hat{\sigma}_{E+}\rangle = i\frac{\Omega_+}{2}\Big[\langle\hat{\sigma}_{EE}\rangle - \langle\hat{\sigma}_{++}\rangle + \langle\hat{\sigma}_{EG}\rangle\Big] - (i2\Lambda + \gamma_+/2)\langle\hat{\sigma}_{E+}\rangle\,,$$

$$\frac{d}{dt}\langle\hat{\sigma}_{EG}\rangle = i\frac{\Omega_+}{2}\Big[\langle\hat{\sigma}_{E+}\rangle - \langle\hat{\sigma}_{+G}\rangle\Big] - (i2\Lambda + \gamma_+/2)\langle\hat{\sigma}_{EG}\rangle\,. \tag{3.109d}$$

Next, by neglecting the steady-state coherence $\rho_{EG} = \langle E|\hat{\rho}_{ss}|G\rangle$ between the ground state $|G\rangle$ and the doubly-excited state $|E\rangle$, we solve the steady-state density matrix. The resulting steady-state populations can be additionally simplified assuming $\Lambda \gg \gamma_0$, which leads to the steady-state population of the subradiant state $|\Lambda_+\rangle$

$$p_{\Lambda_+}\Big|^{|\Lambda_+\rangle} = \frac{1 + (\Omega_+/4\Lambda)^2}{2 + 3(\Omega_+/4\Lambda)^2 + (\gamma_+/\Omega_+)^2}, \tag{3.110}$$

and to the steady-state population of the doubly-excited state $|E\rangle$

$$p_E^{(+)}\Big|^{|\Lambda_+\rangle} = \frac{(\Omega_+/4\Lambda)^2}{2 + 3(\Omega_+/4\Lambda)^2 + (\gamma_+/\Omega_+)^2}. \tag{3.111}$$

Here, we have introduced the superscript $(+)$ to stress that $p_E^{(+)}|^{|\Lambda_+\rangle}$ corresponds to the contribution to the total steady-state population of the doubly excited state arising from excitation via $|\Lambda_+\rangle$.

We follow the same procedure with the three-level system $\{|G\rangle, |\Lambda_-\rangle, |E\rangle\}$. The transition $|G\rangle \to |\Lambda_-\rangle$ is non-resonantly pumped (with detuning 2Λ), whereas the transition $|\Lambda_+\rangle \to |E\rangle$ is resonantly driven. The dynamics equations are then given by:

$$\frac{d}{dt}\langle\hat{\sigma}_{EE}\rangle = -\gamma_-\langle\hat{\sigma}_{EE}\rangle + i\frac{\Omega_-}{2}\Big[\langle\hat{\sigma}_{E-}\rangle - \langle\hat{\sigma}_{-E}\rangle\Big], \tag{3.112a}$$

$$\frac{d}{dt}\langle\hat{\sigma}_{--}\rangle = -\gamma_-\Big[\langle\hat{\sigma}_{--}\rangle - \langle\hat{\sigma}_{EE}\rangle\Big] + i\frac{\Omega_-}{2}\Big[\langle\hat{\sigma}_{-E}\rangle - \langle\hat{\sigma}_{E-}\rangle + \langle\hat{\sigma}_{-G}\rangle - \langle\hat{\sigma}_{G-}\rangle\Big], \tag{3.112b}$$

$$\frac{d}{dt}\langle\hat{\sigma}_{-G}\rangle = -i\frac{\Omega_-}{2}\Big[-\langle\hat{\sigma}_{--}\rangle + \langle\hat{\sigma}_{GG}\rangle + \langle\hat{\sigma}_{EG}\rangle\Big] - (i2\Lambda + \gamma_-/2)\langle\hat{\sigma}_{-G}\rangle\,, \tag{3.112c}$$

$$\frac{d}{dt}\langle\hat{\sigma}_{E-}\rangle = i\frac{\Omega_-}{2}\Big[\langle\hat{\sigma}_{EE}\rangle - \langle\hat{\sigma}_{--}\rangle + \langle\hat{\sigma}_{EG}\rangle\Big] - \frac{\gamma_-}{2}\langle\hat{\sigma}_{E-}\rangle\,, \tag{3.112d}$$

$$\frac{d}{dt}\langle\hat{\sigma}_{EG}\rangle = i\frac{\Omega_-}{2}\Big[\langle\hat{\sigma}_{E-}\rangle - \langle\hat{\sigma}_{-G}\rangle\Big] - (i2\Lambda + \gamma_-/2)\langle\hat{\sigma}_{EG}\rangle\,. \tag{3.112e}$$

In this case, we do not neglect any coherence and only assume that $\Lambda \gg \gamma_0$. The

steady-state population of the superradiant state $|\Lambda_-\rangle$ is thus given by

$$p_{\Lambda_-}\Big|^{|\Lambda_+\rangle} = \frac{1}{1+(4\Lambda/\Omega_-)^2}, \tag{3.113}$$

and the population of the doubly-excited state $|E\rangle$ by

$$p_E^{(-)}\Big|^{|\Lambda_+\rangle} = \frac{2(\Omega_-/4\Lambda)^4}{2+3(\Omega_-/4\Lambda)^2+(\Omega_-/4\Lambda)^4}. \tag{3.114}$$

Here, the superscript $(-)$ is introduced to remark that $p_E^{(-)}|^{|\Lambda_+\rangle}$ corresponds to the contribution to the steady-state population of $|E\rangle$ that is excited via $|\Lambda_-\rangle$.

Therefore, the total population p_E of the doubly-excited state $|E\rangle$ is understood as the sum of the population $p_E^{(+)}$ excited via the resonantly driven subradiant state $|\Lambda_+\rangle$ and the population $p_E^{(-)}$ excited via the non-resonantly driven superradiant state $|\Lambda_-\rangle$. Thus, this population is given by

$$p_E\Big|^{|\Lambda_+\rangle} = p_E^{(+)}\Big|^{|\Lambda_+\rangle} + p_E^{(-)}\Big|^{|\Lambda_+\rangle}. \tag{3.115}$$

We now take the weak intensity limit ($I_L \ll I_{\text{sat}}$) in these expressions. In this way, we find that the populations p_{Λ_+} and p_{Λ_-} of the single-excitation delocalized states $|\Lambda_+\rangle$ and $|\Lambda_-\rangle$ scale linearly with the laser intensity. Specifically, we find

$$p_{\Lambda_+}\Big|^{|\Lambda_+\rangle}_{I_L\ll I_{\text{sat}}} = \frac{I_L}{I_{\text{sat}}}\frac{\gamma_0^2(1+\sin(2\Theta_\Lambda))}{\gamma_+^2}, \tag{3.116}$$

$$p_{\Lambda_-}\Big|^{|\Lambda_+\rangle}_{I_L\ll I_{\text{sat}}} = \frac{I_L}{I_{\text{sat}}}\frac{\gamma_0^2(1-\sin(2\Theta_\Lambda))}{2(4\Lambda)^2}, \tag{3.117}$$

where we have assumed $\Lambda \gg \gamma_0$, for simplicity. Notably, the population of the subradiant state $|\Lambda_+\rangle$ (green line in Fig. 3.9b) is two orders of magnitude larger than that of the superradiant state $|\Lambda_-\rangle$ (blue line), since the former is driven resonantly and the later non-resonantly (with laser detuning equal to 2Λ). On the other hand, in the denominator of $g^{(2)}_{\text{ZPL}}(0)$ in Eq. (3.91) the population p_{Λ_-} of the superradiant state $|\Lambda_-\rangle$ is multiplied by a factor $1-\sin(2\Theta_\Lambda) \approx 1.97$, which is two orders of magnitude larger than the factor $1+\sin(2\Theta_\Lambda) \approx 0.03$ multiplying the population p_{Λ_+} of the subradiant state $|\Lambda_+\rangle$, since the superradiant state couples much more efficiently to light. Both delocalized states thus contribute comparably to the denominator of Eq. (3.91) and need to be taken into account in the calculation of $g^{(2)}_{\text{ZPL}}(0)$.

Further, taking the limit $I_L \ll I_{\text{sat}}$ in Eq. (3.115), we obtain

$$p_E\Big|_{I_L \ll I_{\text{sat}}}^{|\Lambda_+\rangle} = \frac{I_L^2}{I_{\text{sat}}^2}\left[\frac{(1+\sin(2\Theta_\Lambda))\gamma_0^2}{8\Lambda\gamma_+}\right]^2 + \frac{I_L^2}{I_{\text{sat}}^2}\left[\frac{(1-\sin(2\Theta_\Lambda))\gamma_0^2}{2(4\Lambda)^2}\right]^2, \tag{3.118}$$

where the first term of the right-hand side accounts for the population excited via the subradiant state $|\Lambda_+\rangle$ (through a two-photon process) and the second term via the superradiant state $|\Lambda_-\rangle$ (through a two-photon process as well). According to Eq. (3.91), $g^{(2)}_{\text{ZPL}}(0)$ therefore becomes independent of the laser intensity under weak illumination and can be obtained as

$$g^{(2)}_{\text{ZPL}}(0)\Big|_{I_L \ll I_{\text{sat}}}^{|\Lambda_+\rangle} = 4\frac{\left(\frac{1-\sin(2\Theta_\Lambda)}{(4\Lambda)^2}\right)^2 + \left(\frac{1+\sin(2\Theta_\Lambda)}{4\Lambda\gamma_+}\right)^2}{\left[\left(\frac{1-\sin(2\Theta_\Lambda)}{4\Lambda}\right)^2 + \left(\frac{1+\sin(2\Theta_\Lambda)}{\gamma_+}\right)^2\right]^2}. \tag{3.119}$$

Notably, the intensity correlation under weak illumination can reach a much larger value [$g^{(2)}_{\text{ZPL}}(0)|^{|\Lambda_+\rangle}_{I_L \ll I_{\text{sat}}} \approx 0.25$ for our specific molecular parameters] than when the laser is tuned to the transition frequency of the superradiant state [$g^{(2)}_{\text{ZPL}}(0)|^{|\Lambda_-\rangle}_{I_L \ll I_{\text{sat}}} \approx 2.5 \times 10^{-4}$], which emphasizes that the dynamics of the coupled molecules is now more complex than that of a single TLS-like emitter. The simple expression of $g^{(2)}_{\text{ZPL}}(0)$ in Eq. (3.119) can also be used for the experimental estimation of molecular parameters, in a similar way to the analytical expression in Eq. (3.99) of $g^{(2)}_{\text{ZPL}}(0)$ for a weak laser tuned resonantly to the two-photon resonance.

Increasing laser intensities

We now analyze the behaviour of $g^{(2)}_{\text{ZPL}}(0)$ for increasing laser intensities by using numerical calculations. In the range of laser intensity $10^{-1} \lesssim I_L/I_{\text{sat}} \lesssim 10^1$, Fig. 3.9b shows that the slope of the population p_E of the doubly-excited state $|E\rangle$ scales superquadratically, which indicates that the excitation of the doubly-excited state $|E\rangle$ can no longer be understood as resulting from two independent two-photon processes (i.e., p_E does not correspond to the sum of the populations provided by two independent three-level systems). In contrast, the excitation of $|E\rangle$ via the resonantly driven subradiant state $|\Lambda_+\rangle$ and via the non-resonantly driven superradiant state $|\Lambda_-\rangle$ coherently interfere. This effect is revealed, on the one hand, in the increase in the slope of the real part of the coherence $\rho_{+-} = \langle\Lambda_+|\hat{\rho}_{ss}|\Lambda_-\rangle$ between the superradiant and subradiant states (represented with a pink solid line in Fig. 3.9b). On the other hand, the interference between the excitation of the doubly-excited state from the superradiant state and from the subradiant state also has an effect in the complex interplay between the imaginary part of the coherence $\rho_{E+} = \langle E|\hat{\rho}_{ss}|\Lambda_+\rangle$ (related to the excitation of the doubly-excited state via the subradiant state $|\Lambda_+\rangle$) and the imaginary part of the coherence $\rho_{E-} = \langle E|\hat{\rho}_{ss}|\Lambda_-\rangle$ (related to the excitation via the superradiant state $|\Lambda_-\rangle$). These latter coherences

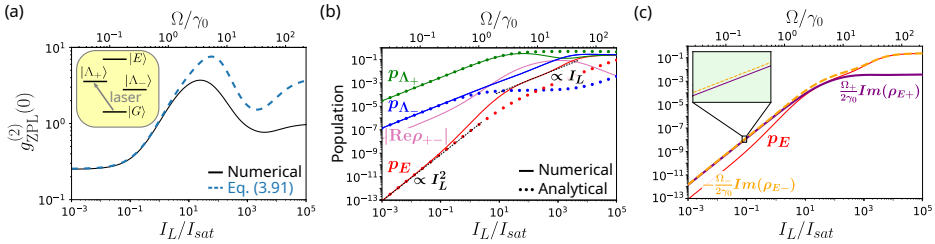

Figure 3.9: Color-blind intensity correlation $g^{(2)}_{\rm ZPL}(0)$ and steady-state populations and coherences when the laser is tuned resonantly to the subradiant state $|\Lambda_+\rangle$. (a) Dependence on the laser intensity of the color-blind intensity correlation $g^{(2)}_{\rm ZPL}(0)$ of ZPL photons. The solid black line is obtained numerically using the exact expression in Eq. (3.90), whereas the dashed blue line is calculated numerically using the approximate Eq. (3.91). The inset illustrates the laser frequency used. (b) Dependence on I_L of the steady-state populations of (blue) the superradiant state $|\Lambda_-\rangle$, (green) the subradiant state $|\Lambda_+\rangle$, (red) the doubly-excited state $|E\rangle$, and (pink) the absolute value of the real part of the steady-state coherence $\rho_{+-} = \langle\Lambda_+|\hat{\rho}_{ss}|\Lambda_-\rangle$. Solid lines correspond to the exact numerical calculations, whereas dots represent the analytical results obtained using Eqs. (3.110), (3.113) and (3.115). Black dashed lines represent the linear and quadratic scaling of p_E with laser intensity. (c) Dependence on the laser intensity of the coherences (dashed orange line) $-\frac{\Omega_-}{2\gamma_0}{\rm Im}\rho_{E-}$ and (solid purple line) $\frac{\Omega_+}{2\gamma_0}{\rm Im}\rho_{E+}$, whose difference corresponds to (red solid line) the population of the doubly-excited state according to Eq. (3.120). The inset corresponds to a zoom (within the interval from $I_L/I_{\rm sat} = 7\times10^{-2}$ to $I_L/I_{\rm sat} = 10^{-1}$) showing that $-\frac{\Omega_-}{2\gamma_0}{\rm Im}\rho_{E-}$ is slightly larger than $\frac{\Omega_+}{2\gamma_0}{\rm Im}\rho_{E+}$. We consider $V_{\rm DW} = -20\gamma_0$, $\alpha_{\rm DW} = 0.3$ and $\delta = 10\gamma_0$ in all panels.

contribute to the population of the doubly-excited state as

$$p_E = -\frac{\Omega_+}{2\gamma_0}{\rm Im}\rho_{E+} - \frac{\Omega_-}{2\gamma_0}{\rm Im}\rho_{E-}, \tag{3.120}$$

obtained from the exact expression in Eq. (3.73a) by taking $\frac{d}{dt}\langle\hat{\sigma}_{EE}\rangle = 0$. Figure 3.9c shows that the two terms on the right-hand side of Eq. (3.120) are of opposite sign and are comparable in magnitude. Under very weak illumination, both terms scale quadratically with the intensity and thus so does p_E, as the negative term is slightly smaller in magnitude than the positive one (see inset in Fig. 3.9c). For increasing laser intensities the slope of the negative term starts to decrease and thus its cancellation with the larger positive term is reduced, which leads to the superquadratic behaviour of p_E with the laser intensity. Additionally, the populations of the single-excitation delocalized states $|\Lambda_+\rangle$ and $|\Lambda_-\rangle$ still depend linearly on the laser intensity (see Fig. 3.9b) and thus the superquadratic scaling of the doubly-excited state leads to an increase in the intensity correlation (see Fig. 3.9a), according to Eq. (3.91). Importantly, $g^{(2)}_{\rm ZPL}(0)$ eventually crosses from antibunching to bunching, which indicates that the correlation can be of either one type or the other for this laser frequency and molecular detuning ($\delta = 10\gamma_0$),

depending on the intensity of the laser. This cross-over is also captured by the simplified Eq. (3.91) (dashed blue line in Fig. 3.9a), which shows a good agreement with the results obtained with the exact Eq. (3.90) for $I_L \lesssim I_{\text{sat}}$.

For laser intensities larger than $10I_{\text{sat}}$, the population p_{Λ_+} of the subradiant state $|\Lambda_+\rangle$ reaches a maximum value of 0.33. Additionally, the population of the doubly-excited state $|E\rangle$ becomes linearly dependent on the laser intensity due to the large population of the subradiant state for these laser intensities. The intensity correlation then reaches a maximum value of 3.71. For even larger laser intensities ($I_L \gtrsim 10^3 I_{\text{sat}}$), all populations converge to 0.25 (i.e., both molecules become saturated and thus uncorrelated) and, as a result, the intensity correlation converges to $g^{(2)}_{\text{ZPL}}(0) = 1$. Notably, the evolution of $g^{(2)}_{\text{ZPL}}(0)$ from its maximum value to 1 is not a simple decay, but it reaches a minimum before growing again, which highlights the complexity of the excitation and emission processes between states for this laser detuning.

3.3.6 Influence of the combined Debye-Waller/Franck-Condon factor

In this section, we analyze the impact of the combined Debye-Waller/Franck-Condon factor α_{DW} on the color-blind intensity correlation $g^{(2)}_{\text{ZPL}}(0)$ of light emitted into the ZPL from the two interacting emitters with parallel transition dipole moments. Figure 3.10 shows the dependence of $g^{(2)}_{\text{ZPL}}(0)$ on the laser intensity I_L and α_{DW}, calculated at $\delta = 10\gamma_0$. We fix the dipole-dipole coupling at $V_{\text{DW}} = -20\gamma_0$ [i.e., the intermolecular distance r_{12} is modified simultaneously with α_{DW} according to Eq. (3.56a)] to focus on the impact of α_{DW} on the decay rates γ_- and γ_+ of the superradiant state $|\Lambda_-\rangle$ and the subradiant state $|\Lambda_+\rangle$, respectively. For identical emitters ($\delta = 0$) and $\alpha_{\text{DW}} = 1$, as often assumed in the literature, the decay rate of the superradiant state yields $\gamma_- = 2\gamma_0$ at very short distances, while the decay rate of the subradiant state vanishes (i.e., infinite long lifetime). In contrast, smaller values of α_{DW} reduces considerably the difference between γ_- and γ_+ according to $\gamma_\pm = \gamma_0(1 \pm \alpha_{\text{DW}} \sin(2\Theta_\Lambda))$. Here, $\sin(2\Theta_\Lambda) = V_{\text{DW}}/\Lambda = -0.97$.

We find that the modification of $\gamma_\pm$ through α_{DW} does not significantly impact on the color-blind intensity correlation $g^{(2)}_{\text{ZPL}}(0)$ when the laser is tuned to the two-photon resonance (Fig. 3.10a) or to the transition frequency of the superradiant state $|\Lambda_-\rangle$ (Fig. 3.10b). In contrast, when the laser is tuned resonantly to the subradiant state $|\Lambda_+\rangle$, Fig. 3.10c shows that the minimum and maximum values of $g^{(2)}_{\text{ZPL}}(0)$ can be notably modified by α_{DW}. However, the qualitative behavior, including the presence of a cross-over from antibunched emission (for weak enough laser intensities) to bunched emission (for increasing laser intensities), is maintained when α_{DW} is changed.

To emphasize this behaviour, we plot in Fig. 3.10d cuts of the results in Figs. 3.10a–3.10c at $I_L = 10^{-3} I_{\text{sat}}$. $g^{(2)}_{\text{ZPL}}(0)$ is almost constant when the laser is tuned to the two-photon resonance (red solid line) and increases slightly with α_{DW} [from $g^{(2)}_{\text{ZPL}}(0) \approx 1.5 \times 10^{-4}$ when $\alpha_{\text{DW}} \to 0$ to $g^{(2)}_{\text{ZPL}}(0) \approx 6 \times 10^{-4}$ at $\alpha_{\text{DW}} = 1$] if the

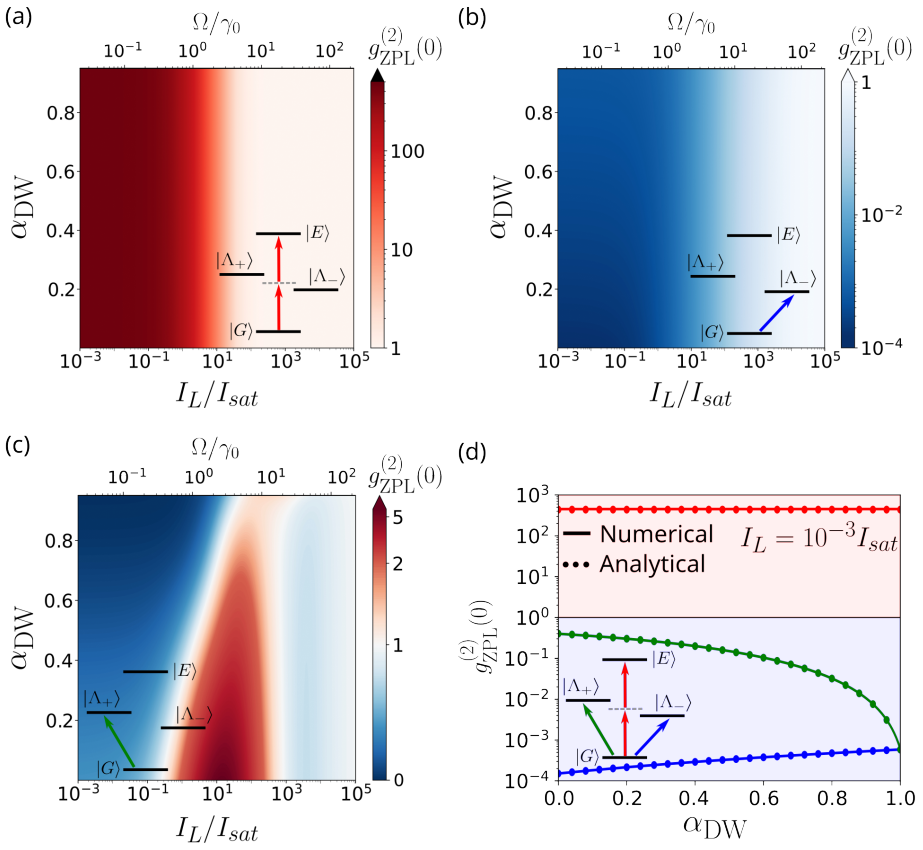

Figure 3.10: Dependence of the color-blind intensity correlation $g^{(2)}_{\rm ZPL}(0)$ of a pair of interacting emitters on the combined Debye-Waller/Franck-Condon factor $\alpha_{\rm DW}$ and on the laser intensity I_L. The laser is tuned to (a) the two-photon resonance ($\omega_L = \omega_0$), (b) the transition frequency of the superradiant state $|\Lambda_-\rangle$ ($\omega_L = \omega_0 - \Lambda$) and (c) the transition frequency of the subradiant state $|\Lambda_+\rangle$ ($\omega_L = \omega_0 + \Lambda$). In (a)-(c), color blue represents antibunched emission [$g^{(2)}_{\rm ZPL}(0) < 1$], red bunched emission [$g^{(2)}_{\rm ZPL}(0) > 1$] and white Poissonian statistics [$g^{(2)}_{\rm ZPL}(0) = 1$]. We use a logarithmic scale in the color bars in (a)-(b). We use a linear scale in the interval $0 \leq g^{(2)}_{\rm ZPL}(0) \leq 1$ and a logarithmic scale for $g^{(2)}_{\rm ZPL}(0) > 1$ in (c). Cuts of the numerical results in (a)-(c) for $I_L = 10^{-3} I_{\rm sat}$ are plotted in (d), where the red line corresponds to a laser tuned to the two-photon resonance, the blue line is obtained for a laser tuned to the superradiant state and the green line corresponds to a laser tuned to the subradiant state. Dots in (d) correspond to analytical results obtained with (red) Eq. (3.99), (blue) Eq. (3.106) and (green) Eq. (3.119). In (d), red and blue shaded backgrounds represent bunched and antibunched statistics, respectively. The insets illustrate the different laser detunings considered. The molecular detuning considered is $\delta = 10\gamma_0$ and the dipole-dipole coupling is $V_{\rm DW} = -20\gamma_0$ [i.e., the modification of $\alpha_{\rm DW}$ is accompanied by a modification of the distance between the emitters according to Eq. (3.56a)].

laser is tuned resonantly to the superradiant state $|\Lambda_-\rangle$ (blue solid line). More significantly, when the laser is tuned to the transition frequency of the subradiant state $|\Lambda_+\rangle$ (green solid line), $g^{(2)}_{\mathrm{ZPL}}(0)$ decreases considerably with α_{DW} [from ≈ 0.4 when $\alpha_{\mathrm{DW}} \to 0$ down to $\approx \gamma_0^2/(2\Lambda)^2 \approx 6 \times 10^{-4}$ at $\alpha_{\mathrm{DW}} = 1$]. The analytical results (dots in Fig. 3.10d) obtained with (red) Eq. (3.99), (blue) Eq. (3.106) and (green) Eq. (3.119) show an excellent agreement with the numerical results for all values of α_{DW}. Therefore, these results show that the color-blind intensity correlation of light emitted into the ZPL from two interacting emitters can be especially sensitive to the combined Debye-Waller/Franck-Condon factor when the laser is tuned resonantly to the subradiant state.

3.4 Frequency-resolved intensity correlation

In this section, we investigate the frequency-resolved intensity correlation (FRIC) of photons emitted into the ZPL from two strongly interacting emitters at delay $\tau = 0$ and detected along the direction normal to the plane in which the emitters are located. In contrast to the color-blind intensity correlation examined in Section 3.3, the FRIC measures the correlation between pairs of photons of specific frequencies ω_1 and ω_2, providing great information on the emission mechanisms of the system (Section 2.4). We take as reference emitters the same pair of interacting DBATT molecules as in Section 3.3, and focus again on analyzing the role of the laser frequency and intensity, thus complementing previous studies of FRIC from interacting emitters, which have focused either on excitation at the two-photon resonance [178] or on emitters under incoherent pumping [173].

The numerical calculations of the FRIC $g^{(2)}_{\mathrm{ZPL}}(\omega_1, \omega_2; 0)$ in this section are performed following the approach described in Section 2.4.3. As the positive-frequency electric field operator of light scattered from the two emitters in the normal direction to the plane in which thy are located is proportional to $\hat{\sigma}_1 + \hat{\sigma}_2$ [Eq. (3.86)], the system operator that describes the interaction of the emitters with the n-th detector is $\hat{s}_n = \hat{\sigma}_1 + \hat{\sigma}_2$, with $n \in \{1, 2\}$ [Eq. (2.73)]. Additionally, we fix the linewidth of the two filters at $\Gamma = \gamma_0/10$, as we did in Section 2.4.4.

3.4.1 FRIC when the laser is resonantly tuned to the superradiant state

In this section, we analyze the FRIC when the laser frequency corresponds to the transition frequency of the superradiant state $|\Lambda_-\rangle$ ($\omega_L = \omega_0 - \Lambda$), for weak, moderate and strong laser intensities.

Weak laser intensity

We first examine the FRIC at $I_L = 0.1 I_{\mathrm{sat}}$. Figure 3.11a shows the normalized incoherent emission spectrum (top) and the FRIC map (bottom). As in Section 2.4.4, the x-axis and y-axis of the FRIC map correspond to the normalized laser

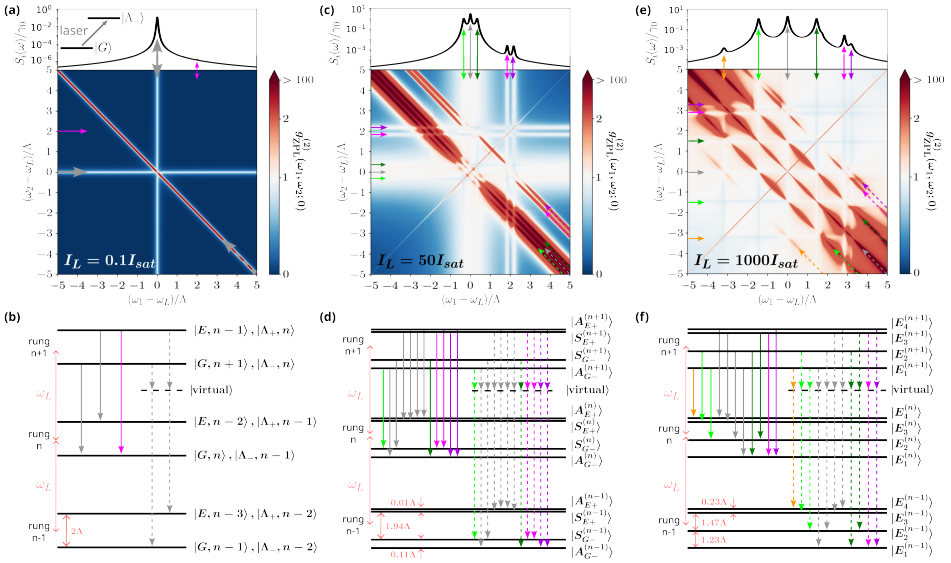

Figure 3.11: FRIC for a laser tuned to the transition frequency of the superradiant state $|\Lambda_-\rangle$, $\omega_L = \omega_0 - \Lambda$. [(a),(c),(e)] Normalized incoherent emission spectra (top panel) and FRIC maps (bottom panel) for laser intensity (a) $I_L = 0.1I_{\rm sat}$, (c) $I_L = 50I_{\rm sat}$ and (e) $I_L = 1000I_{\rm sat}$. The inset in (a) illustrates the molecular energy levels $|G\rangle$ and $|\Lambda_-\rangle$ and the resonant excitation of the superradiant state. In the FRIC maps the standard color convention is used, where blue color represents antibunched emission, while red color bunched emission and white Poissonian statistics. In the color bar, we use a linear scale in the interval $0 \leq g^{(2)}_{\rm ZPL}(\omega_1, \omega_2; 0) \leq 1$ and a logarithmic scale in the range $1 \leq g^{(2)}_{\rm ZPL}(\omega_1, \omega_2; 0) \leq 100$. We consider a filter of linewidth $\Gamma = \gamma_0/10$. [(b),(d),(f)] Schematic representation of the eigenstates (accounting for the quantum nature of the laser field) in rungs $n-1$, n and $n+1$ for laser intensity (b) $I_L = 0.1I_{\rm sat}$, (d) $I_L = 50I_{\rm sat}$ and (f) $I_L = 1000I_{\rm sat}$. Each rung contains four eigenstates with equal number of excitations. Solid arrows are used to mark the horizontal and vertical lines in the FRIC maps, the peaks in the incoherent emission spectra and the one-photon transitions in the diagram of the eigenstates, whereas dashed arrows are used for the antidiagonal lines and the two-photon processes through virtual states. The dipole-dipole coupling is $V_{\rm DW} = -20\gamma_0$, the combined Debye-Waller/Franck-Condon factor is $\alpha_{\rm DW} = 0.3$ and the molecular detuning is $\delta = 10\gamma_0$.

detuning of the photons arriving at detector 1, $(\omega_1 - \omega_L)/\Lambda$, and at detector 2, $(\omega_2 - \omega_L)/\Lambda$, respectively. Additionally, we use again the standard color convention [173, 175–178], where the blue color represents antibunched emission $[g^{(2)}_{\rm ZPL}(\omega_1, \omega_2; 0) < 1]$, red bunched emission $[g^{(2)}_{\rm ZPL}(\omega_1, \omega_2; 0) > 1]$ and white Poissonian statistics $[g^{(2)}_{\rm ZPL}(\omega_1, \omega_2; 0) = 1]$. To improve the visibility of the antibunched emission as well as of the bunched emission, we use of a linear scale in the range $0 \leq g^{(2)}_{\rm ZPL}(\omega_1, \omega_2; 0) \leq 1$ and a logarithmic scale in the range $1 \leq g^{(2)}_{\rm ZPL}(\omega_1, \omega_2; 0) \leq 100$. Regarding the incoherent emission spectrum (Section

2.1.6), it is computed as

$$\bar{S}_i(\omega) \propto \int_{-\infty}^{\infty} d\tau \left\langle \delta\hat{E}^{(-)}_{\perp,\mathrm{ZPL}}(\tau)\delta\hat{E}^{(+)}_{\perp,\mathrm{ZPL}}(0)\right\rangle_{ss} e^{-i\omega t}, \tag{3.121}$$

and it is normalized in such a way that [196]

$$\int_0^{\infty} d\omega \bar{S}_i(\omega) = \gamma_0 \left\langle \delta\hat{\sigma}_1^{\dagger}\delta\hat{\sigma}_1 + \delta\hat{\sigma}_2^{\dagger}\delta\hat{\sigma}_2\right\rangle_{ss} + \tilde{\gamma}_{\mathrm{DW}} \left\langle \delta\hat{\sigma}_1^{\dagger}\delta\hat{\sigma}_2 + \delta\hat{\sigma}_2^{\dagger}\delta\hat{\sigma}_1\right\rangle_{ss}. \tag{3.122}$$

We use the bar symbol to stress that this incoherent spectrum is normalized. This normalization facilitates the comparison between the peak amplitudes of different incoherent emission spectra.

The FRIC map in Fig. 3.11a is characterized by a strongly antibunched background, which can be understood from the very small value of the color-blind intensity correlation for these laser parameters [$g^{(2)}_{\mathrm{ZPL}}(0) \approx 10^{-4}$, Fig. 3.8a]. On top of this strongly antibunched background we observe a vertical line at $\omega_1 = \omega_L$, a horizontal line at $\omega_2 = \omega_L$ (marked by solid grey arrows) and a bunched antidiagonal line (dashed grey arrow) at $\omega_1 + \omega_2 = 2\omega_L$. These lines constitute a signature of the mechanisms of photon emission and to analyze them is convenient to account for the quantum nature of the illumination, as discussed in Section 2.4.4. The eigenstates of the full quantized system are distributed in infinite rungs, with the eigenstates that belongs to the same rung having equal number of total excitations (i.e., molecular excitations plus photons in the laser field). For example, the eigenstates in the rung with n excitations (rung n) under weak illumination are the hybrid states $\{|G,n\rangle, |\Lambda_-,n-1\rangle, |\Lambda_+,n-1\rangle, |E,n-2\rangle\}$, with $|n\rangle$ the n-Fock state of the laser field. Notably, for this laser frequency and intensity, the states $|\Lambda_-,n-1\rangle$ and $|G,n\rangle$ become degenerate in energy, as well as the states $|E,n-2\rangle$ and $|\Lambda_+,n-1\rangle$ are also degenerate. These two pairs of degenerate states are analogous to those obtained by treating the laser excitation classically and moving to the rotating frame at the laser frequency (namely, in this case $|\Lambda_-\rangle$ and $|G\rangle$ are degenerate in energy, and so are $|E\rangle$ and $|\Lambda_+\rangle$, see Section 3.2.3). Further, for these laser parameters, each rung is composed by two doubly degenerate states. The eigenstates of three subsequent rungs are depicted in the level scheme in Fig. 3.11b.

On the one hand, the frequencies at which the horizontal and vertical lines emerge in the FRIC map correspond to the frequencies of the one-photon transitions between eigenstates of the system (Section 2.4.4), such as the transition from the superradiant state $|\Lambda_-,n\rangle$ in the rung $n+1$ to the ground state $|G,n\rangle$ in the rung n. Like in all FRIC maps in this thesis, we use solid arrows in Figs. 3.11a and 3.11b to represent these one-photon transitions in the level scheme as well as to mark the corresponding horizontal and vertical lines. These one-photon transitions can also be identified by the peaks in the emission spectrum of the system, shown on top of Fig. 3.11a.

On the other hand, the antidiagonal line in the FRIC map at $\omega_1 + \omega_2 = 2\omega_L$ is

a signature of relaxation processes known as leapfrog process, which consists in the emission of a photon of frequency ω_1 (ω_2) due to the transition from an initial eigenstate in the rung $n+1$ to a virtual state and the emission of a photon of frequency ω_2 (ω_1) due to the relaxation from the virtual state to another eigenstate in the rung $n-1$ (Section 2.4.4). The energy difference between the initial and final eigenstates determines the value of $\omega_1+\omega_2$ satisfied along the antidiagonal line. This antidiagonal line and the corresponding two-photon transition are marked with dashed arrows in Figs. 3.11a and 3.11b, and throughout this thesis. Additionally, as these antidiagonal lines correspond to the correlated emission of two photons, they are usually characterized by strong bunching. Importantly, these two-photon processes cannot be unveiled in the emission spectrum, and neither in the color-blind intensity correlation, which stresses the advantages of the FRIC to gain additional information about the transitions in the system.

Comparing these results with those in Section 2.4.4, we thus find that the FRIC map of the two coupled molecules when the laser is tuned to the superradiant state (Fig. 3.11a) resembles that of a TLS (Fig. 2.7a) when both are under weak illumination. For these laser parameters, the two interacting molecules thus behave almost as a single TLS, with a very low impact of the subradiant state and the doubly-excited state on the FRIC map in Fig. 3.11a. For example, the horizontal and vertical lines related to the decay from the weakly populated subradiant state $|\Lambda_+,n\rangle$ to the ground state $|G,n\rangle$ (marked with pink arrows) are not appreciated in the FRIC map because the associated increase of $g^{(2)}_{\mathrm{ZPL}}(\omega_1,\omega_2;0)$ is too small.

Moderate laser intensity

We next plot the FRIC map for $I_L = 50I_{\mathrm{sat}}$ in Fig. 3.11c. Under this laser intensity, the eigenstates of the emitters become appreciably dressed and they are described as different linear combinations of the bare states $\{|G,n\rangle, |\Lambda_-,n-1\rangle, |\Lambda_+,n-1\rangle, |E,n-2\rangle\}$. Specifically, the eigenstates can be accurately described by antisymmetric and symmetric states analogous to those in Eqs. (3.74a)–(3.74d), with $X=E$ and $Y=G$. Namely, the dressed states in the n$^{\mathrm{th}}$-rung are given by

$$|A^{(n)}_{E+}\rangle = (|E,n-2\rangle - |\Lambda_+,n-1\rangle)/\sqrt{2}, \tag{3.123a}$$

$$|S^{(n)}_{E+}\rangle = (|E,n-2\rangle + |\Lambda_+,n-1\rangle)/\sqrt{2}, \tag{3.123b}$$

$$|S^{(n)}_{G-}\rangle = (|G,n\rangle + |\Lambda_-,n-1\rangle)/\sqrt{2}, \tag{3.123c}$$

$$|A^{(n)}_{G-}\rangle = (|G,n\rangle - |\Lambda_-,n-1\rangle)/\sqrt{2}, \tag{3.123d}$$

and they are schematically represented in Fig. 3.11d. At this laser intensity, the dressed states $|S^{(n)}_{G-}\rangle$ and $|A^{(n)}_{G-}\rangle$ have a significant energy splitting equal to $|(\cos\Theta_\Lambda - \sin\Theta_\Lambda)\Omega| \approx 0.11\Lambda$ [Eqs. (3.75a)–(3.75d)], in contrast to the case of weak illumination where they are degenerate in energy. The one-photon transitions $|S^{(n)}_{G-}\rangle \to |S^{(n-1)}_{G-}\rangle$ and $|A^{(n)}_{G-}\rangle \to |A^{(n-1)}_{G-}\rangle$ (marked with solid grey arrows in Fig.

3.11d) lead to the emission of photons of frequency $\omega_L = \omega_0 - \Lambda$, whereas the one-photon transitions $|S_{G-}^{(n)}\rangle \rightarrow |A_{G-}^{(n-1)}\rangle$ and $|A_{G-}^{(n)}\rangle \rightarrow |S_{G-}^{(n-1)}\rangle$ give rise to the emission of photons of frequencies $\omega_L + |(\cos\Theta_\Lambda - \sin\Theta_\Lambda)\Omega| \approx \omega_L + 0.11\Lambda$ (dark green arrow) and $\omega_L - |(\cos\Theta_\Lambda - \sin\Theta_\Lambda)\Omega| \approx \omega_L - 0.11\Lambda$ (light green arrow), respectively. As a consequence, three peaks emerge near $\omega_L = \omega_0$ in the emission spectrum on top of Fig. 3.11c, which are analogous to the Mollow triplet in the emission spectrum of a single TLS under strong enough illumination (Section 2.1.6). In the FRIC map, these one-photon transitions lead to a broad vertical line and a broad horizontal line, which emerge due to the overlapping of three vertical and horizontal lines at frequencies ω_L and $\omega_L \pm |(\cos\Theta_\Lambda - \sin\Theta_\Lambda)\Omega| \approx \omega_L \pm 0.11\Lambda$.

Moreover, new antidiagonal lines emerge in the FRIC map satisfying $\omega_1 + \omega_2 = 2\omega_L \pm |(\cos\Theta_\Lambda - \sin\Theta_\Lambda)\Omega|$ (see the light green and dark green dashed arrows in Fig. 3.11c). These new lines unveil additional two-photon transitions through virtual states and emerge due to the energy splitting between the dressed states $|S_{G-}^{(n)}\rangle$ and $|A_{G-}^{(n)}\rangle$, which are linear combinations of the superradiant and ground molecular states. These lines are also analogous to the ones emerging in a single TLS under the same laser intensity (Section 2.4.4).

On the other hand, we observe additional lines in the FRIC map that are due to the non-negligible effect of the subradiant state and of the doubly-excited state for this laser intensity. First, we observe two horizontal and vertical lines centered at frequency $\omega_L + 2\Lambda$, which corresponds to the one-photon transitions from one of the dressed states $|A_{E+}^{(n)}\rangle$ and $|S_{E+}^{(n)}\rangle$ to one of the dressed states $|S_{G-}^{(n-1)}\rangle$ and $|A_{G-}^{(n-1)}\rangle$ in a lower rung. The FRIC map also exhibits two additional antidiagonal lines corresponding to the two-photon transitions from $|A_{E+}^{(n+1)}\rangle$ and $|S_{E+}^{(n+1)}\rangle$ to one of the dressed states $|S_{G-}^{(n-1)}\rangle$ and $|A_{G-}^{(n-1)}\rangle$ through an intermediate virtual state. In summary, the FRIC map in Fig. 3.11c mostly resembles the FRIC map of a TLS consisting of the ground and the superradiant state, driven resonantly under the same laser intensity, but with additional lines accounting for the impact of the subradiant state and the doubly-excited state on the light emission.

Interestingly, not all the transitions between eigenstates are reflected in the FRIC map. In particular, we do not observe horizontal and vertical lines centered at frequency $\omega_L - 2\Lambda = \omega_0 - 3\Lambda$, corresponding to the one-photon transitions from $|S_{G-}^{(n)}\rangle$ or $|A_{G-}^{(n)}\rangle$ to $|A_{E+}^{(n-1)}\rangle$ or $|S_{E+}^{(n-1)}\rangle$. Similarly, no peak appears at frequency $\omega_L - 2\Lambda = \omega_0 - 3\Lambda$ in the emission spectrum on top of Fig. 3.11c. To understand this effect, we calculate the probability of these transitions using Fermi's golden rule [151, 162], which states that the transition probability between an initial eigenstate $|i\rangle$ and a final eigenstate $|f\rangle$ is proportional to $|\langle f|(\hat{\sigma}_1 + \hat{\sigma}_2)|i\rangle|^2$. The emission operator can be written in the interacting basis as

$$\begin{aligned}\hat{\sigma}_1 + \hat{\sigma}_2 = &(\cos\Theta_\Lambda + \sin\Theta_\Lambda)(|G\rangle\langle\Lambda_+| + |\Lambda_+\rangle\langle E|) \\ &+ (\cos\Theta_\Lambda - \sin\Theta_\Lambda)(|G\rangle\langle\Lambda_-| + |\Lambda_-\rangle\langle E|).\end{aligned} \tag{3.124}$$

As a consequence, $\langle S_{E+}^{(n-1)}|(\hat{\sigma}_1 + \hat{\sigma}_2)|S_{G-}^{(n)}\rangle = \langle A_{E+}^{(n-1)}|(\hat{\sigma}_1 + \hat{\sigma}_2)|S_{G-}^{(n)}\rangle =$

$\langle S_{E+}^{(n-1)}| (\hat{\sigma}_1 + \hat{\sigma}_2) |A_{G-}^{(n)}\rangle = \langle A_{E+}^{(n-1)}| (\hat{\sigma}_1 + \hat{\sigma}_2) |A_{G-}^{(n)}\rangle = 0$, which means that all the one-photon transitions with energy difference $\omega_L - 2\Lambda = \omega_0 - 3\Lambda$ are forbidden. Finally, we note that the FRIC map does not show antidiagonal lines corresponding to two-photon transitions from the states $|S_{G-}^{(n+1)}\rangle$ or $|A_{G-}^{(n+1)}\rangle$ to any of the states $|S_{E+}^{(n-1)}\rangle$ or $|A_{E+}^{(n-1)}\rangle$, which indicates that these transitions are also forbidden.

Strong laser intensity

Last, we plot in Fig. 3.11e the FRIC map for intense laser illumination, $I_L = 10^3 I_{\text{sat}}$. For this laser intensity, we obtain the dressed eigenstates $|E_i^{(n)}\rangle$ numerically. One of the main differences with respect to the case of moderate laser intensity is that the three Mollow-like vertical, horizontal and antidiagonal lines (marked with light green, grey and dark green arrows) in the FRIC map do not overlap and can be clearly distinguished. This separation arises because the energy splitting between the dressed states $|E_1^{(n)}\rangle$ and $|E_2^{(n)}\rangle$ is much larger than for the case of moderate laser intensity.

Another noticeable effect of the increase of laser intensity is that we observe a wider variety of vertical, horizontal and antidiagonal lines in the FRIC map. There are two main factors involved in the emergence of new lines. The first one is the larger energy splitting between $|E_3^{(n)}\rangle$ and $|E_4^{(n)}\rangle$, which was negligible in the case of moderate intensity, and allows for resolving new transitions. The second factor responsible of the emergence of new lines in the FRIC map is that the forbidden transitions for moderate laser intensities now become allowed due to the more complex nature of the dressed eigenstates, which under strong illumination are not simple symmetric and antisymmetric combinations of two states of the interacting basis $\{|G, n\rangle, |\Lambda_-, n-1\rangle, |\Lambda_+, n-1\rangle, |E, n-2\rangle\}$.

The diagonal bunched line at $\omega_1 = \omega_2$ corresponds to the simultaneous detection of two identical photons (Section 2.4.4). The value of the intensity correlation along this diagonal is twice that at nearby points on the map [169, 173, 174]. This increase occurs because a coincidence is counted no matter which photon arrives at detector 1 and which one arrives at detector 2 (in contrast to the case in which $\omega_1 \neq \omega_2$), a situation which doubles the probability of a coincidence in the detectors.

3.4.2 FRIC when the laser is resonantly tuned to the subradiant state

Next, we analyze the FRIC for a laser tuned to the transition frequency of the subradiant state $|\Lambda_+\rangle$ ($\omega_L = \omega_0 + \Lambda$). For this laser frequency, the FRIC maps become more complex than for the previous detuning due to the emergence of additional lines and also to the possibility of having FRIC maps with both antibunched or bunched background depending on the laser intensity.

Weak laser intensity

In the same way as when the laser is resonantly tuned to the superradiant state (Section 3.4.1), the eigenstates of the full quantized system are $\{|G,n\rangle, |\Lambda_-,n-1\rangle, |\Lambda_+,n-1\rangle, |E,n-2\rangle\}$ under sufficiently weak illumination. However, when the laser is resonantly tuned to the subradiant state, the states $|G,n\rangle$ and $|\Lambda_+,n-1\rangle$ in the rung n are degenerate in energy and, in the same way, so are the states $|\Lambda_-,n-1\rangle$ and $|E,n-2\rangle$, which contrast with the pairs of degenerate states when the laser is resonantly tuned to the superradiant state (Section 3.4.1).

We plot the FRIC map at $I_L = 0.1I_{\text{sat}}$ in Fig. 3.12a, and a scheme of the energy levels in Fig. 3.12b. The background of the FRIC map is antibunched, which is consistent with the value of the color-blind intensity correlation, $g^{(2)}_{\text{ZPL}}(0) \approx 0.3$, for these laser parameters. Over this background, three horizontal, three vertical and three antidiagonal lines emerge. Thus, in contrast with the case in which the laser is resonantly tuned to the superradiant state, this FRIC map does not resemble the one of a TLS under weak illumination. The reason for this is the competition between the resonant excitation of the subradiant state and the non-resonant excitation of the superradiant state (which couples very efficiently to light), as discussed for the color-blind intensity correlation in Section 3.3.5. Both excitation pathways can lead to the emission of photons of frequency $\omega_L = \omega_0 + \Lambda$ giving rise to the central horizontal and vertical lines in the FRIC map. Additionally, the central antidiagonal line in the FRIC map corresponds to the emission of two photons of frequencies ω_1 and ω_2, via an intermediate virtual state, fulfilling $\omega_1 + \omega_2 = 2\omega_L$, so that the final state is the same as the initial one but two rungs down. Further, photons of frequency $\omega_L - 2\Lambda = \omega_0 - \Lambda$ can also be emitted (lines marked with solid red arrows in the FRIC map and also in Fig. 3.12b), as well as leapfrog processes fulfilling $\omega_1 + \omega_2 = 2\omega_L - 2\Lambda$ can take place (red dashed arrows).

Moreover, the excitation of the subradiant state $|\Lambda_+,n\rangle$ in rung n can lead to the emission of photons of frequency $\omega_L + 2\Lambda = \omega_0 + 3\Lambda$ due to the transition to any of the states $|E,n-2\rangle$ or $|\Lambda_-,n-1\rangle$ in rung $n-1$, which gives rise to the horizontal and vertical lines marked with purple solid arrows in the FRIC map in Fig. 3.12a. However, the emission of these photons is not reflected in the emission spectrum on top of Fig. 3.12a and, additionally, these lines should not appear in the FRIC map according to the Fermi's golden rule (following similar arguments than in Section 3.4.1). We attribute the emergence of these lines in the map to the very small modification of the eigenstates $\{|G,n\rangle, |\Lambda_-,n-1\rangle, |\Lambda_+,n-1\rangle, |E,n-2\rangle\}$ due to the weak illumination (Section 3.2.3), so that the transition is no longer strictly forbidden. Therefore, for this laser detuning, the FRIC map reveals one-photon transitions that occur with very low probability and which are hidden in the emission spectrum. Similarly, two-photon transitions via intermediate virtual states satisfying $\omega_1 + \omega_2 = 2\omega_L + 2\Lambda$ are also allowed due to the very small dressing of the eigenstates (marked with the dashed purple arrows).

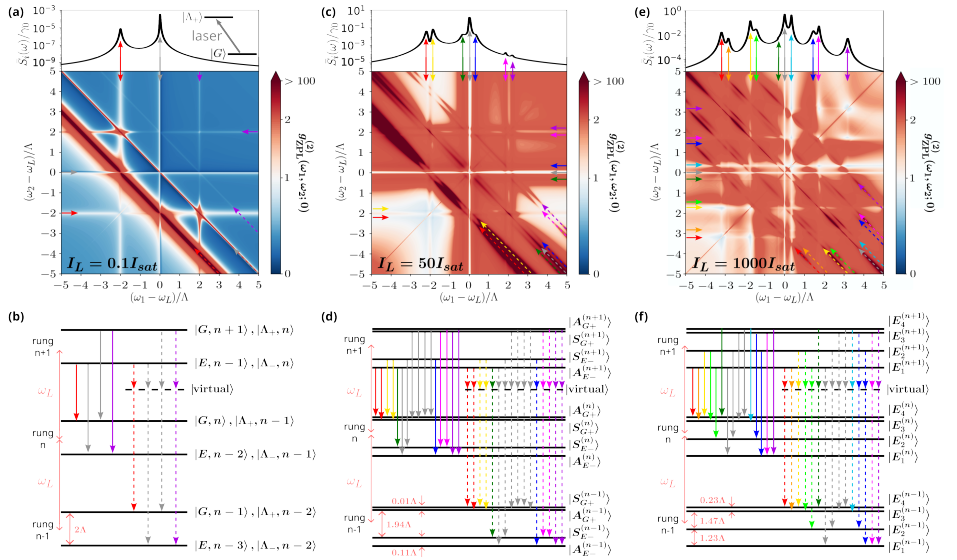

Figure 3.12: FRIC for a laser tuned to the transition frequency of the subradiant state $|\Lambda_+\rangle$, $\omega_L = \omega_0 + \Lambda$. [(a),(c),(e)] Normalized incoherent emission spectra (top panel) and FRIC maps (bottom panel) for laser intensity (a) $I_L = 0.1I_{\rm sat}$, (c) $I_L = 50I_{\rm sat}$ and (e) $I_L = 1000I_{\rm sat}$. We depict the molecular energy levels $|G\rangle$ and $|\Lambda_+\rangle$ and the resonant excitation of the subradiant state in the inset in (a). We follow the standard color convention in the FRIC maps and use blue color to represent antibunched emission, red for bunched emission and white for Poissonian statistics. In the color bar, a linear scale is used in the range $0 \leq g^{(2)}_{\rm ZPL}(\omega_1, \omega_2; 0) \leq 1$ and a logarithmic scale in the interval $1 \leq g^{(2)}_{\rm ZPL}(\omega_1, \omega_2; 0) \leq 100$. We consider a filter with linewidth $\Gamma = \gamma_0/10$. [(b),(d),(f)] Diagrams of the eigenstates, with the laser field quantized, in the rungs $n-1$, n and $n+1$ for laser intensity (b) $I_L = 0.1I_{\rm sat}$, (d) $I_L = 50I_{\rm sat}$, and (f) $I_L = 1000I_{\rm sat}$. Each of the rungs have four eigenstates with equal number of excitations. Solid arrows are used to mark the horizontal and vertical lines in the FRIC maps, the peaks in the incoherent emission spectra and the one-photon transitions in the diagrams of the eigenstates, while dashed arrows are used for antidiagonal lines related to leapfrog processes. We consider $V_{\rm DW} = -20\gamma_0$, $\alpha_{\rm DW} = 0.3$ and $\delta = 10\gamma_0$.

Moderate and strong laser intensities

We present in Fig. 3.12c the FRIC map for a moderate laser of intensity $I_L = 50I_{\rm sat}$. For these laser parameters, the dressed eigenstates can be approximated again as symmetric and antisymmetric combinations of the states that are degenerate under weak illumination, in analogous way to the dressed states obtained in Eqs. (3.74a)–(3.74d) (with $X = G$ and $Y = E$) in the rotating frame at the frequency of the laser. In this way, we obtain that the eigenstates in the rung n are

$$|A^{(n)}_{G+}\rangle = (|G, n\rangle - |\Lambda_+, n-1\rangle)/\sqrt{2}, \tag{3.125a}$$

$$|S^{(n)}_{G+}\rangle = (|G, n\rangle + |\Lambda_+, n-1\rangle)/\sqrt{2}, \tag{3.125b}$$

$$|S_{E-}^{(n)}\rangle = (|E, n-2\rangle + |\Lambda_-, n-1\rangle)/\sqrt{2}, \tag{3.125c}$$

$$|A_{E-}^{(n)}\rangle = (|E, n-2\rangle - |\Lambda_-, n-1\rangle)/\sqrt{2}. \tag{3.125d}$$

In contrast to the case in which we tune the laser to the transition frequency of the superradiant state with the same laser intensity, we observe that the FRIC map in Fig. 3.12c is bunched [$g^{(2)}_{\mathrm{ZPL}}(\omega_1, \omega_2; 0) > 1$] for most pairs of filtered frequencies ω_1 and ω_2. This general bunching can be expected from the bunched color-blind intensity correlation for these laser parameters (see Fig. 3.9a). Over this general bunched background, a variety of horizontal, vertical and antidiagonal lines are again observed. Similar to the case of moderate laser intensity in Section 3.4.1, this wide variety of lines emerge due to the significant energy splitting $|\Omega(\cos\Theta_\Lambda - \sin\Theta_\Lambda)| = 0.11\Lambda$ between the dressed states $|S_{E-}^{(n)}\rangle$ and $|A_{E-}^{(n)}\rangle$. This energy splitting increases the number of different transitions that lead to emission of photons (see Fig. 3.12d), with respect to the case of weak laser intensity.

Finally, we present in Fig. 3.12e the FRIC map for $I_L = 1000 I_{\mathrm{sat}}$, which also exhibits a significant bunching for almost every pair of filtered frequencies. For this intensity, the numerical calculation of the dressed eigenstates $|E_i^{(n)}\rangle$ in rung n is again necessary. The energy splittings between all the dressed eigenstates $|E_i^{(n)}\rangle$ become significant, as schematically represented in Fig. 3.12f. As a consequence, in the FRIC map we observe more horizontal, vertical and antidiagonal lines than in the case of moderate laser intensity, with the corresponding one-photon and two-photon transitions depicted in Fig. 3.12f.

3.4.3 FRIC when the laser is resonantly tuned to the two-photon resonance

In this section, we discuss the FRIC when the laser is tuned to the two-photon resonance ($\omega_L = \omega_0$), which has been analyzed in detail in Ref. [178]. First, we plot in Fig. 3.13a the incoherent emission spectrum $\bar{S}_i(\omega)$ and the FRIC map for $I_L = 0.1 I_{\mathrm{sat}}$. This map is in general strongly bunched, which can be expected from the strongly bunched color-blind intensity correlation for these laser parameters (see Fig. 3.7a). Over this strongly bunched background, we can distinguish two vertical and two horizontal lines, for which the correlation takes much lower values. On the one hand, the lines at $\omega_1 = \omega_L$ (here, $\omega_L = \omega_0$) and $\omega_2 = \omega_L$ (marked by grey solid arrows) are related to the one-photon transitions depicted with grey arrows Fig. 3.13b, which includes the transition from the state $|\Lambda_-, n-2\rangle$ (in the rung $n+1$) to the state $|\Lambda_-, n-1\rangle$ (in the rung n), for instance. On the other hand, the one-photon transitions related to the lines at $\omega_1 = \omega_L - \Lambda$ and $\omega_2 = \omega_L - \Lambda$ are indicated with light green solid arrows in Fig. 3.13b, as for example the transition from the state $|\Lambda_-, n-2\rangle$ to the state $|G, n-1\rangle$. Further, we observe in the incoherent emission spectrum on top of Fig. 3.13a a third peak at frequency $\omega_1 = \omega_L + \Lambda$, related to the one-photon transitions from the subradiant state $|\Lambda_+, n\rangle$ in rung $n+1$ to the ground state $|G, n\rangle$ in rung n, whose corresponding horizontal and vertical lines (marked by dark green solid arrows)

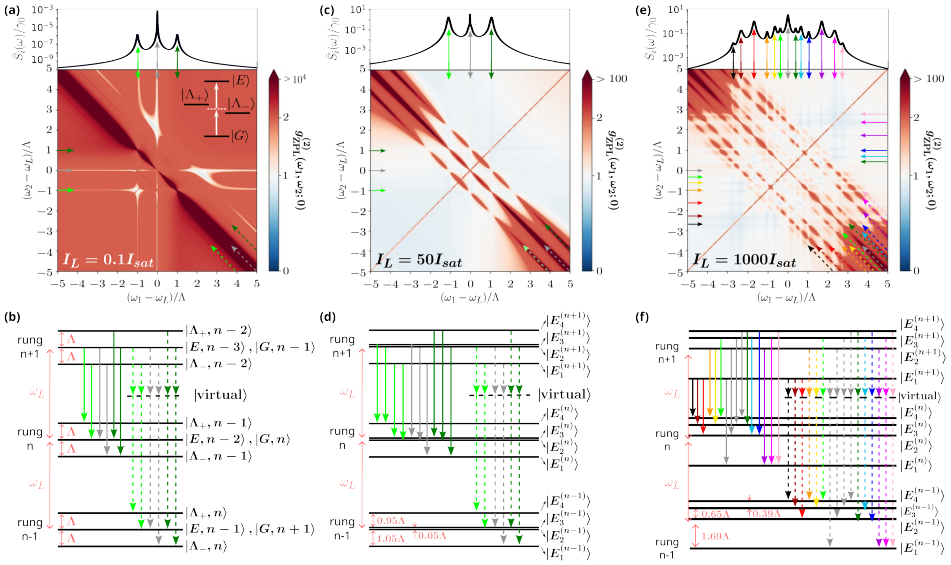

Figure 3.13: FRIC for a laser tuned to the two-photon resonance, $\omega_L = \omega_0$. [(a),(c),(e)] Normalized incoherent emission spectra (top panel) and FRIC maps (bottom panel) for laser intensity (a) $I_L = 0.1I_{\mathrm{sat}}$, (c) $I_L = 50I_{\mathrm{sat}}$ and (e) $I_L = 1000I_{\mathrm{sat}}$. The inset in (a) illustrates the molecular energy levels and the resonant excitation of the doubly-excited state $|E\rangle$ with two-photons. In the FRIC maps the standard color convention is used, where blue color represents antibunched emission, while red color bunched emission and white Poissonian statistics. In the color bar, we use a linear scale in the interval $0 \leq g^{(2)}_{\mathrm{ZPL}}(\omega_1,\omega_2;0) \leq 1$ and a logarithmic scale in the range $g^{(2)}_{\mathrm{ZPL}}(\omega_1,\omega_2;0) \geq 1$. We consider a filter linewidth $\Gamma = \gamma_0/10$. [(b),(d),(f)] Schematic representation of the eigenstates (accounting for the quantum nature of the laser field) in rungs $n-1$, n and $n+1$ for laser intensity (b) $I_L = 0.1I_{\mathrm{sat}}$, (d) $I_L = 50I_{\mathrm{sat}}$ and (f) $I_L = 1000I_{\mathrm{sat}}$. Each rung contains four eigenstates with equal number of excitations. Solid arrows are used to mark the horizontal and vertical lines in the FRIC maps, the peaks in the incoherent emission spectra and the one-photon transitions in the diagrams of the eigenstates, whereas dashed arrows are used for the antidiagonal lines related to the two-photon processes through virtual states. We consider $V_{\mathrm{DW}} = -20\gamma_0$, $\alpha_{\mathrm{DW}} = 0.3$ and $\delta = 10\gamma_0$.

cannot be distinguished in the FRIC map due to the strong background bunching. In contrast, three antidiagonal lines with stronger bunching than the background emerge in the FRIC map in Fig. 3.13a (see the broad line marked by a dashed grey arrow and the subtle lines marked by a dashed light green arrow and a dashed dark green arrow) corresponding to three different types of leapfrog processes that can take place for these laser parameters.

As the laser intensity is increased up to $I_L = 50I_{\mathrm{sat}}$, the eigenstates of the system become slightly dressed, according to Eqs. (3.77a)–(3.77d). Figure 3.13c shows the corresponding incoherent emission spectrum and the FRIC map for $I_L = 50I_{\mathrm{sat}}$, and Fig. 3.13d the energy level structure. Notably, as the value of the color-blind intensity correlation $g^{(2)}_{\mathrm{ZPL}}(0)$ decreases, the value of the frequency-

resolved intensity correlation $g^{(2)}_{\mathrm{ZPL}}(\omega_1, \omega_2; 0)$ of the background of the FRIC map also decreases and the three horizontal and three vertical lines can now be clearly distinguished. This map is very similar to the one discussed in Ref. [178] for identical emitters driven by a laser tuned to the two-photon resonance. For even stronger laser intensities, the eigenstates of the system become strongly dressed and a variety of horizontal and vertical lines emerge in the FRIC map [178]. We plot in Fig. 3.13e the emission spectrum and the FRIC map for $I_L = 1000 I_{\mathrm{sat}}$, with the corresponding one-photon transitions as well as leapfrog processes illustrated in Fig. 3.13f.

3.4.4 Influence of the combined Debye-Waller/Franck-Condon factor

Last, we analyze the impact of the combined Debye-Waller/Franck-Condon factor α_{DW} on the FRIC map for a laser tuned to the transition frequency of the subradiant state. We choose this laser frequency because of the large sensitivity of the color-blind intensity correlation to α_{DW} found in Fig. 3.10 for this laser frequency. As in Section 3.3.6, we focus on analyzing the impact of α_{DW} on the decay rates γ_- and γ_+ of the superradiant state $|\Lambda_-\rangle$ and the subradiant state $|\Lambda_+\rangle$, respectively. To this end, we fix the dipole-dipole coupling at $V_{\mathrm{DW}} = -20\gamma_0$ and modify the intermolecular distance r_{12} simultaneously with α_{DW} according to Eq. (3.56a). Additionally, we consider again weak laser intensity $I_L = 0.1 I_{\mathrm{sat}}$.

Figure 3.14a shows the FRIC map at $\alpha_{\mathrm{DW}} = 0.05$, which is very similar to the FRIC map obtained at $\alpha_{\mathrm{DW}} = 0.3$ in Fig. 3.14b, corresponding to the FRIC map in Fig. 3.12a. This large similarity is attributed to the relatively small difference between the γ_-/γ_+ ratio in both cases ($\gamma_-/\gamma_+ \approx 1.1$ when $\alpha_{\mathrm{DW}} = 0.05$, while $\gamma_-/\gamma_+ \approx 1.8$ when $\alpha_{\mathrm{DW}} = 0.3$). However, Fig. 3.14c shows that the FRIC map is substantially modified at $\alpha_{\mathrm{DW}} = 0.75$ ($\gamma_-/\gamma_+ \approx 6.3$), with a more strongly antibunched background. Most notably, neglecting the combined Debye-Waller/Franck-Condon factor ($\alpha_{\mathrm{DW}} = 1$) leads to a drastically different FRIC map (Fig. 3.14d). In this case $\gamma_-/\gamma_+ \approx 66$ and the FRIC map exhibits a single antidiagonal line (which is not bunched) and a single horizontal/vertical line. We conclude that the FRIC map can thus be drastically different when $\alpha_{\mathrm{DW}} = 1$, as typically assumed in the literature. These results emphasize the importance of accounting for α_{DW} in the description of the interacting solid-state emitters when intensity correlations are investigated.

3.5 Summary and conclusions

We have shown in this chapter that the electromagnetic vacuum field mediates the dipole-dipole interaction between two quantum emitters separated by short distances and, additionally, we have characterized the intensity correlations of light emitted into the Zero-Phonon Line from these two interacting emitters under different illumination conditions. To this end, we have first derived the multipolar

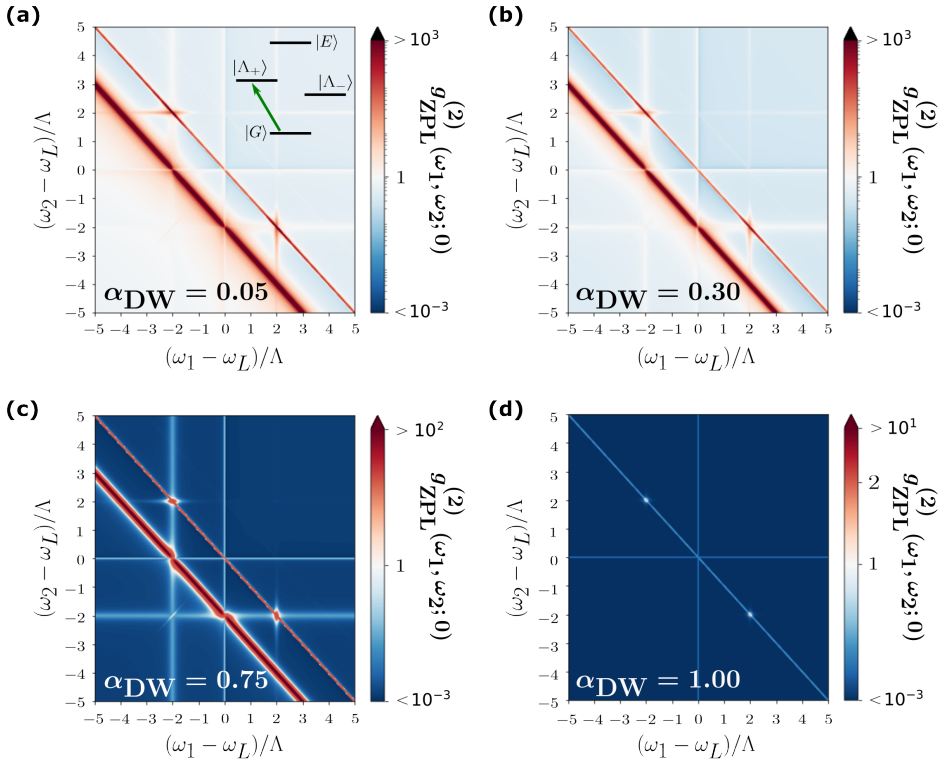

Figure 3.14: Influence of $\alpha_{\rm DW}$ on the FRIC maps when the laser is tuned to the transition frequency of the subradiant state $|\Lambda_+\rangle$. The inset in (a) illustrates the laser frequency. The combined Debye-Waller/Franck-Condon factor is fixed at (a) $\alpha_{\rm DW} = 0.05$, (b) $\alpha_{\rm DW} = 0.3$, (c) $\alpha_{\rm DW} = 0.75$, and (d) $\alpha_{\rm DW} = 1$. We follow the standard color convention in the FRIC maps. According to this convention, blue color means antibunched emission, red bunched emission and white Poissonian statistics. A logarithmic scale in the color bar is used in the complete range of values of $g^{(2)}_{\rm ZPL}(\omega_1, \omega_2; 0)$. We consider $V_{\rm DW} = -20\gamma_0$, $\delta = 10\gamma_0$, $I_L = 0.1 I_{\rm sat}$ and $\Gamma = 0.1\gamma_0$ in all the panels.

form of the Hamiltonian describing the interaction between two quantum emitters and the electromagnetic vacuum field. Then, we have derived a Markovian master equation in the reduced Hilbert space of the emitters, by tracing out the degrees of freedom of the electromagnetic vacuum field. In the resulting Markovian master equation, the coherent and dissipative dipole-dipole couplings induced by the vacuum field emerge explicitly, as well as the spontaneous emission of each emitter. Afterwards, we have introduced an effective approach to adapt this Markovian master equation for describing the electronic dynamics of solid-state emitters supporting vibrational/phononic modes. Within this effective framework, the coherent and dissipative dipole-dipole couplings are modified by the combined Debye-Waller/Franck-Condon factor.

We next have shown that, at short separation distances, the dipole-dipole interaction between the emitters is strong enough to modify their eigenstates and eigenenergies. Notably, when the transition dipole moments are not perpendicularly oriented, the dipole-dipole interaction leads to the emergence of superradiant and subradiant states. These states are single-excitation states with the electronic excitation delocalized between both emitters. The decay rates of these two states, as well as their coupling strengths to the laser field, differ from each other and from the case of no interaction.

Furthermore, we have analyzed the intensity correlations of light emitted into the Zero-Phonon Line from solid-state quantum emitters that strongly interact. We have demonstrated first that the color-blind intensity correlation can be tailored from extreme bunching to strong antibunching by modifying the laser parameters. We have also shown that this dependence can be altered by changing the frequency detuning between the two emitters. For weak enough laser intensities, the color-blind intensity correlation is characterized by an extreme bunching if the laser is tuned to the two-photon resonance. In contrast, if the laser is tuned to the transition frequency of the superradiant state, the intensity correlation becomes strongly antibunched, so that the system behaves as a single-photon source with larger decay rate than that of a single emitter. For these two laser detunings, we have derived analytical expressions, valid for non-identical molecules, $\alpha_{\mathrm{DW}} \neq 1$ and arbitrary laser intensity, which accurately reproduce the numerical intensity correlation. Further, we have shown that the combined Debye-Waller/Franck-Condon factor can influence the behaviour of the color-blind intensity correlation, specially when the laser is tuned to the transition frequency of the subradiant state.

Additionally, we have found that the color-blind intensity correlation exhibits a more complex dependence on the laser intensity and on the detuning between the emitters when the laser is tuned to the transition frequency of the subradiant state. For this laser detuning, the light emitted into the ZPL can be either bunched, antibunched or Poissonian, which is a signature of the complexity of the excitation and emission processes at this laser frequency. These emission and excitation processes may become even more complex in the presence of dephasing effects, which have been neglected in this analysis and require a more sophisticated description [197, 198]. Further, we have derived an analytical expression of $g^{(2)}_{\mathrm{ZPL}}(0)$ when the laser is tuned resonantly to the subradiant state at weak laser intensities. This expression, as well as analogous expressions for the other laser detunings, can help to experimentally determine the distance and detuning between the emitters.

Finally, we have also explored the frequency-resolved intensity correlation (FRIC) for the three laser detunings and shown that it provides further information on a variety of relaxation processes of the driven, interacting emitters. For a laser tuned to the transition frequency of the superradiant state, we have demonstrated that the FRIC generally resembles that of a resonantly driven TLS, but it also exhibits some differences due to the influence of the subradiant state and the doubly-excited state. Interestingly, for weak and moderate laser intensities, the FRIC maps indicate that some of the transitions are forbidden (absence of lines at certain frequencies), which is consistent with the peaks in the emission spectrum. On the

other hand, when the laser is tuned to the transition frequency of the subradiant state the FRIC becomes more complex due to the important competition between the resonant excitation of the subradiant state and the non-resonant excitation of the superradiant state. We have found that the FRIC can unveil one-photon transitions that occur with such low probability that they are not resolved by the emission spectrum. Thus, the FRIC manifests a stronger sensitivity to reveal transitions that occur with very low probability. Interestingly, we have shown that the FRIC can be strongly influenced by the combined Debye-Waller/Franck-Condon factor again when the laser is tuned to the transition frequency of the subradiant state. These results stress the interest of the intensity correlations to better characterize and understand the emission from interacting quantum emitters.

CHAPTER 4

INTENSITY CORRELATION OF STOKES-SHIFTED PHOTONS FROM TWO QUANTUM EMITTERS

We have analyzed in Chapter 3 the correlation of photons emitted into the Zero-Phonon Line (ZPL) from two interacting quantum emitters. In addition to the ZPL photons, solid-state quantum emitters can also scatter photons due to the radiative decay from the electronic excited state to a vibrational/phononic level in the electronic ground state. These photons are red-shifted with respect to the ZPL and are referred to as Stokes-shifted photons. We develop in this chapter a model to analyze the correlation of Stokes-shifted photons scattered from two quantum emitters. This model is of significant experimental interest, as usual experiments involving light emission from solid-state quantum emitters rely on the measurement of the Stokes-shifted emission, particularly when the emitters are driven by a laser resonantly tuned to their electronic excited state. In this case, optical filters are employed to eliminate the laser photons in the detection process, which also discard the ZPL photons because their frequency is nearly identical to that of the resonant laser. For example, available experiments on the correlation of photons emitted from two quantum emitters that interact via vacuum-induced dipole-dipole coupling rely on the detection of Stokes-shifted photons [1, 99, 199, 200].

We first provide a description of the emission of Stokes-shifted photons from solid-state emitters. Additionally, we review a method that has been used in Refs. [1, 92, 199] to obtain an approximate description of the correlation of Stokes-shifted photons emitted from two interacting emitters, which neglects the influence of the quantum coherence between the emitters, as well as the first-order coherence of light scattered from the two emitters. We next present the model that constitutes the core of this chapter, which enables a more complete description of the correlation of

Stokes-shifted photons, as it accounts for the full influence of quantum coherence. Afterwards, we use this model to demonstrate that quantum coherence can indeed play a significant role in the emission of Stokes-shifted photons from two interacting emitters, as well as from two non-interacting emitters. Further, we compare the correlation of ZPL photons (which has been already analyzed in detail in Chapter 3) and that of Stokes-shifted photons emitted from two strongly interacting emitters, revealing that they can exhibit substantial differences. Last, we analyze the impact of considering a large number of vibrational modes on the correlation of Stokes-shifted photons, and extend the model to the case of an arbitrary number of interacting emitters.

4.1 Stokes-shifted photons from solid-state quantum emitters

In this section, we describe the emission of Stokes-shifted photons from solid-state quantum emitters that support vibrational and/or phononic modes. We also review an approach that provides an approximate description of the correlation of Stokes-shifted photons emitted from two interacting quantum emitters, which relies on neglecting the influence of quantum coherence and is referred to as *conditional-probability approach*.

4.1.1 Description of the emission of Stokes-shifted photons

The electronic excited state $|e\rangle$ of solid-state quantum emitters can relax through a radiative decay, either directly to the pure (0-phonon) electronic ground state $|g\rangle$, emitting a Zero-Phonon-Line (ZPL) photon, or to a 1-phonon level in the electronic ground state, emitting a *Stokes-shifted photon*. These different relaxation processes are revealed in the emission spectrum of the quantum emitter. For example, Fig. 4.1a shows the emission spectrum of a single DBATT molecule embedded in a naphthalene crystal at a temperature of 1.7 K. This figure is adapted from Ref. [201] and reproduced with permission from Springer Nature. The spectrum of the DBATT molecule exhibits a sharp peak at $\lambda \approx 618$ nm, corresponding to the photons emitted into the Zero-Phonon Line ($|e\rangle \rightarrow |g\rangle$). This transition is marked with a blue arrow in the schematic representation of energy levels in Fig. 4.1b. Notably, the emission spectrum in Fig. 4.1a reveals additional peaks at increasing wavelengths, constituting a signature of the red-shifted emission of Stokes-shifted photons. We illustrate the corresponding transitions, from $|e\rangle$ to 1-phonon levels in the electronic ground state, with red arrows in Fig. 4.1b.

Moreover, developing a model that accurately describes the correlation of Stokes-shifted photons is of significant experimental interest. In particular, usual resonance fluorescence experiments, where the electronic excited state $|e\rangle$ of the emitter is resonantly excited, rely on the analysis of Stokes-shifted light scattered from the solid-state quantum emitters [54, 202–204]. In these experiments, optical filters are employed to remove the laser photons, ensuring that only photons scattered by

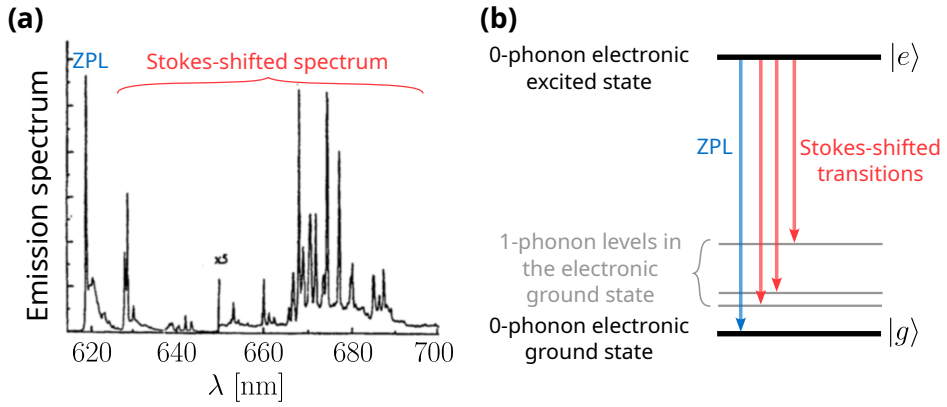

Figure 4.1: Zero-Phonon Line (ZPL) and Stokes-shifted emission from a solid-state quantum emitter. (a) Experimental emission spectrum of a single DBATT molecule embedded in a naphthalene crystal at $T = 1.7$ K. Figure adapted from Ref. [201] and reproduced with permission from Springer Nature. (b) Schematic representation of the pure (0-phonon) electronic excited state $|e\rangle$, the pure (0-phonon) electronic ground state $|g\rangle$, and three different 1-phonon levels in the electronic ground state. The ZPL corresponds to the transition from $|e\rangle$ to $|g\rangle$ and is indicated with a blue arrow. The Stokes-shifted transitions (from $|e\rangle$ to a 1-phonon level in the electronic ground state) are indicated with red arrows.

the emitters arrive to the detectors. As a consequence of this filtering, the ZPL photons are also excluded in the detection process, since their frequency closely matches that of the resonant excitation laser.

Notably, available experiments investigating the correlation of two solid-state emitters with vacuum-induced electromagnetic interaction are based on this excitation and filtering scheme [1, 92, 99, 200]. This is the case, for example, of the experiments presented in this chapter (Figs. 4.5, 4.6, and 4.8), where the correlation of Stokes-shifted light emitted from two DBATT molecules is measured. These molecules are embedded in a thin naphthalene crystal film, and the system is cooled to cryogenic temperatures ($T = 3.2$ K). In addition to the photon correlation measurements, the one-photon excitation spectra of the coupled molecules can also be recorded at various laser intensities, which enables the estimation of the molecular parameters [1]. These experiments were conducted by the Bordeaux Nanophotonics Group, led by Brahim Lounis, at the Institut d'Optique Graduate School (CNRS) in Bordeaux, France.

4.1.2 Conditional-probability approach to the Stokes-shifted correlation

We review in this section the method used in Refs. [1, 92, 199] to describe the correlation of Stokes-shifted photons emitted from two interacting emitters, referred to as *conditional-probability approach*. This approach does not take into account

the quantum coherence between the states of the two emitters, nor the influence of the first-order coherence of the light they emit (i.e., interference effects, see Section 2.1.4). As a consequence, it fails to describe experiments where these coherences become important, as we show in Section 4.3.

The calculation of the intensity correlation within the conditional-probability approach is based on the *reset matrix formalism* [187, 205], which calculates the conditional probability of emitting a photon at time $t+\tau$, assuming that the system has emitted a photon at an earlier time t. At the steady state (ss), the reset matrix formalism yields

$$g^{(2)}_{\text{reset}}(\tau) = \frac{\text{Tr}\{\hat{I}(\mathbf{r}_d,\tau)\hat{\rho}_{\text{reset}}\}}{\langle \hat{I}(\mathbf{r}_d,0)\rangle_{ss}}, \tag{4.1}$$

with $\mathbf{r}_d$ the detection direction in the far-field region. The denominator on the right-hand side of Eq. (4.1) is the steady-state expectation value of the Schrödinger-picture intensity operator $\hat{I}(\mathbf{r}_d,0)$ [Eq. (2.17)], whereas the numerator represents the expectation value of the Heisenberg-picture operator $\hat{I}(\mathbf{r}_d,\tau)$ for an initial state $\hat{\rho}_{\text{reset}}$. Importantly, $\hat{\rho}_{\text{reset}}$ is referred to as *reset density matrix* and describes the state of the system right after emitting a photon, provided that the system was in the steady state before the emission.

Further, within the conditional-probability approach, the emitters are again described as two-level systems, whose dynamics is described by the Markovian master equation derived in Sections 3.1.4 and 3.1.5. The correlation of ZPL photons can thus be obtained using the electric field operator in Eq. (3.81), as described in Section 3.3.1. Crucially, the conditional-probability approach assumes that the emission of Stokes-shifted photons is an incoherent process and obtains the correlation of Stokes-shifted photons by subtracting the influence of quantum coherence from the ZPL correlation. This quantum coherence is encoded in the off-diagonal elements of the density matrices in the uncoupled (localized) basis $\{|e_1e_2\rangle, |e_1g_2\rangle, |g_1e_2\rangle, |g_1g_2\rangle\}$, which contain the coherence between the emitters (Appendix A), as well as in the off-diagonal elements of the intensity operator in the same basis, which contain the first-order coherence of the electric field (as we discuss below).

On the one hand, by neglecting the off-diagonal elements of the steady-state density matrix in the uncoupled basis $\{|e_1e_2\rangle, |e_1g_2\rangle, |g_1e_2\rangle, |g_1g_2\rangle\}$, the steady-state density matrix results in

$$\hat{\bar{\rho}}_{ss} = p_{ee}\,|e_1e_2\rangle\langle e_1e_2| + p_{eg}\,|e_1g_2\rangle\langle e_1g_2| + p_{ge}\,|g_1e_2\rangle\langle g_1e_2| + p_{gg}\,|g_1g_2\rangle\langle g_1g_2|, \tag{4.2}$$

where the bar symbol in $\hat{\bar{\rho}}_{ss}$ is introduced to indicate the use of the conditional-probability approach, and $p_{ab} = \langle a_1b_2|\hat{\rho}_{\text{ss}}|a_1b_2\rangle$ (with $a,b \in \{e,g\}$) is the steady-state population of $|a_1b_2\rangle$. Further, to derive the reset density matrix we take into account that the doubly-excited state $|e_1e_2\rangle$ can decay either to $|e_1g_2\rangle$ or to $|e_1g_2\rangle$, which would reset the state to $p_{ee}\,|e_1g_2\rangle\langle e_1g_2|$ or to $p_{ee}\,|g_1e_2\rangle\langle g_1e_2|$, respectively. Similarly, both $|e_1g_2\rangle$ and $|g_1e_2\rangle$ can decay to the ground state $|g_1g_2\rangle$, reseting the state to $p_{eg}\,|g_1g_2\rangle\langle g_1g_2|$ and $p_{ge}\,|g_1g_2\rangle\langle g_1g_2|$, respectively. As a result, the reset

density matrix becomes [199]:

$$\hat{\tilde{\rho}}_{\text{reset}} = \frac{p_{ee}\left|e_1g_2\right\rangle\left\langle e_1g_2\right| + p_{ee}\left|g_1e_2\right\rangle\left\langle g_1e_2\right| + p_{eg}\left|g_1g_2\right\rangle\left\langle g_1g_2\right| + p_{ge}\left|g_1g_2\right\rangle\left\langle g_1g_2\right|}{2p_{ee} + p_{eg} + p_{ge}}. \tag{4.3}$$

On the other hand, the intensity operator $\hat{I}(\mathbf{r}_d, \tau)$ [Eq. (2.17)] can be obtained from the transverse electric field operators derived in Section 3.3.1. Specifically, by considering that the two emitters have identical transition dipole moments ($\boldsymbol{\mu}_1 = \boldsymbol{\mu}_2$), we obtain

$$\begin{aligned}\hat{I}_{\text{ZPL}}(\mathbf{r}_d, \tau) &= \hat{E}^{(-)}_{\perp,\text{ZPL}}(\mathbf{r}_d, \tau)\hat{E}^{(+)}_{\perp,\text{ZPL}}(\mathbf{r}_d, \tau) = \sum_{j=1}^{2}\hat{E}^{(-)}_{\perp,\text{ZPL},j}(\mathbf{r}_d, \tau)\sum_{l=1}^{2}\hat{E}^{(+)}_{\perp,\text{ZPL},l}(\mathbf{r}_d, \tau) \\ &= \hat{E}^{(-)}_{\perp,\text{ZPL},1}(\mathbf{r}_d, \tau)\hat{E}^{(+)}_{\perp,\text{ZPL},1}(\mathbf{r}_d, \tau) + \hat{E}^{(-)}_{\perp,\text{ZPL},2}(\mathbf{r}_d, \tau)\hat{E}^{(+)}_{\perp,\text{ZPL},2}(\mathbf{r}_d, \tau) \\ &+ \hat{E}^{(-)}_{\perp,\text{ZPL},1}(\mathbf{r}_d, \tau)\hat{E}^{(+)}_{\perp,\text{ZPL},2}(\mathbf{r}_d, \tau) + \hat{E}^{(-)}_{\perp,\text{ZPL},2}(\mathbf{r}_d, \tau)\hat{E}^{(+)}_{\perp,\text{ZPL},1}(\mathbf{r}_d, \tau),\end{aligned} \tag{4.4}$$

where $\hat{E}^{(+)}_{\perp,\text{ZPL}}(\mathbf{r}_d, \tau)$ is the positive-frequency scalar electric field operator of light scattered from the two emitters into the ZPL [Eq. (3.83)]. We have decomposed this operator in Eq. (4.4) as $\hat{E}^{(+)}_{\perp,\text{ZPL}}(\mathbf{r}_d, \tau) = \hat{E}^{(+)}_{\perp,\text{ZPL},1}(\mathbf{r}_d, \tau) + \hat{E}^{(+)}_{\perp,\text{ZPL},2}(\mathbf{r}_d, \tau)$, with

$$\hat{E}^{(+)}_{\perp,\text{ZPL},1}(\mathbf{r}_d, \tau) = \xi_{\text{ZPL}}\hat{\sigma}_1(\tau), \tag{4.5a}$$

$$\hat{E}^{(+)}_{\perp,\text{ZPL},2}(\mathbf{r}_d, \tau) = \xi_{\text{ZPL}}\hat{\sigma}_2(\tau)e^{i\varphi_{\text{ZPL}}}. \tag{4.5b}$$

Here, ξ_{ZPL} is the complex coefficient in Eq. (3.84) and $\varphi_{\text{ZPL}} = \omega_0\boldsymbol{e}_d \cdot (\mathbf{r}_1 - \mathbf{r}_2)n/c$ is the relative phase between the two lowering operators due to the two different positions $\mathbf{r}_1$ and $\mathbf{r}_2$ of the emitters, with $\boldsymbol{e}_d = \mathbf{r}_d/|\mathbf{r}_d|$ the unit vector along the detection direction, n the refractive index of the medium in which the emitters are embedded and c the speed of light in vacuum. Additionally, we note that the influence of the retardation time $|\mathbf{r}_d|n/c$ on the lowering and raising operators of the emitter on the right-hand sides of Eqs. (4.5a)–(4.5b) has been ignored, as it does not affect the result of the intensity correlation (Section 3.3.1). Importantly, the terms

$$\begin{aligned}\hat{E}^{(-)}_{\perp,\text{ZPL},1}(\mathbf{r}_d, \tau)\hat{E}^{(+)}_{\perp,\text{ZPL},1}(\mathbf{r}_d, \tau) + \hat{E}^{(-)}_{\perp,\text{ZPL},2}(\mathbf{r}_d, \tau)\hat{E}^{(+)}_{\perp,\text{ZPL},2}(\mathbf{r}_d, \tau) &= |\xi_{\text{ZPL}}|^2 \\ \times\Big[2\left|e_1e_2\right\rangle\left\langle e_1e_2\right|(\tau) + \left|e_1g_2\right\rangle\left\langle e_1g_2\right|(\tau) + \left|g_1e_2\right\rangle\left\langle g_1e_2\right|(\tau)\Big]&\end{aligned} \tag{4.6}$$

in Eq. (4.4) describe the intensity of light scattered independently from each emitter, as discussed in Section 2.1.3. The right-hand side of this equation indicates that these non-interfering light intensities depend only on operators that are diagonal

in the uncoupled basis. In contrast, the terms

$$\hat{E}^{(-)}_{\perp,\mathrm{ZPL},1}(\mathbf{r}_d,\tau)\hat{E}^{(+)}_{\perp,\mathrm{ZPL},2}(\mathbf{r}_d,\tau)+\hat{E}^{(-)}_{\perp,\mathrm{ZPL},2}(\mathbf{r}_d,\tau)\hat{E}^{(+)}_{\perp,\mathrm{ZPL},1}(\mathbf{r}_d,\tau)=|\xi_{\mathrm{ZPL}}|^2 \times\Big[\,|e_1g_2\rangle\langle g_1e_2|\,(\tau)e^{i\varphi_{\mathrm{ZPL}}}+|g_1e_2\rangle\langle e_1g_2|\,(\tau)e^{-i\varphi_{\mathrm{ZPL}}}\Big] \tag{4.7}$$

depend only on off-diagonal operators (in the uncoupled basis) and describe the interference of light scattered from the two emitters. Thus, Eq. (4.7) is associated with the degree of first-order coherence (Sections 2.1.3 and 2.1.4). Crucially, these terms are neglected within the conditional-probability approach. As a result, the Stokes-shifted intensity operator is identified as

$$\hat{\bar{I}}_{\mathrm{St}}(\tau)=|\xi_{\mathrm{ZPL}}|^2\Big[2\,|e_1e_2\rangle\langle e_1e_2|\,(\tau)+|e_1g_2\rangle\langle e_1g_2|\,(\tau)+|g_1e_2\rangle\langle g_1e_2|\,(\tau)\Big] \tag{4.8}$$

within the conditional-probability approach. In the steady state, the expectation value of this operator becomes

$$\langle\hat{\bar{I}}_{\mathrm{St}}(0)\rangle_{ss}=|\xi_{\mathrm{ZPL}}|^2\Big[2p_{ee}+p_{eg}+p_{ge}\Big]. \tag{4.9}$$

Finally, by substituting Eqs. (4.3), (4.8) and (4.9) into Eq. (4.1), we obtain that the Stokes-shifted correlation within the conditional-probability approach is given by

$$\bar{g}^{(2)}_{\mathrm{St}}(\tau)=\frac{p_{ee}\,\langle e_1g_2|\,\hat{\bar{I}}_{\mathrm{St}}(\tau)\,|e_1g_2\rangle}{\langle\hat{\bar{I}}_{\mathrm{St}}(0)\rangle_{ss}\,[2p_{ee}+p_{eg}+p_{ge}]}+\frac{p_{ee}\,\langle g_1e_2|\,\hat{\bar{I}}_{\mathrm{St}}(\tau)\,|g_1e_2\rangle}{\langle\hat{\bar{I}}_{\mathrm{St}}(0)\rangle_{ss}\,[2p_{ee}+p_{eg}+p_{ge}]} +\frac{p_{eg}\,\langle g_1g_2|\,\hat{\bar{I}}_{\mathrm{St}}(\tau)\,|g_1g_2\rangle}{\langle\hat{\bar{I}}_{\mathrm{St}}(0)\rangle_{ss}\,[2p_{ee}+p_{eg}+p_{ge}]}+\frac{p_{ge}\,\langle g_1g_2|\,\hat{\bar{I}}_{\mathrm{St}}(\tau)\,|g_1g_2\rangle}{\langle\hat{\bar{I}}_{\mathrm{St}}(0)\rangle_{ss}\,[2p_{ee}+p_{eg}+p_{ge}]}. \tag{4.10}$$

This expression has an intuitive statistical interpretation, associated with the contribution of each allowed one-photon transition (in the uncoupled basis) to increase the probability of having coincidences in the Hanbury-Brown Twiss interferometer used to measure the intensity correlation. More specifically, the expression on the right-hand side of Eq. (4.10) is decomposed in four terms with equal denominator and whose numerators are given by products of steady-state populations and diagonal elements of the intensity operator. In the numerator of each of these terms, the steady-state population is associated with the initial state of a one-photon transition, whereas the diagonal element of the intensity operator is associated with the final state of that same transition, as schematically represented in Fig. 4.2. For example, $p_{ee}\,\langle e_1g_2|\,\hat{\bar{I}}_{\mathrm{St}}(\tau)\,|e_1g_2\rangle$ corresponds to the contribution to the numerator of the intensity correlation from the one-photon transition $|e_1e_2\rangle\rightarrow|e_1g_2\rangle$.

In the next section, we develop a more complete model to describe the correlation

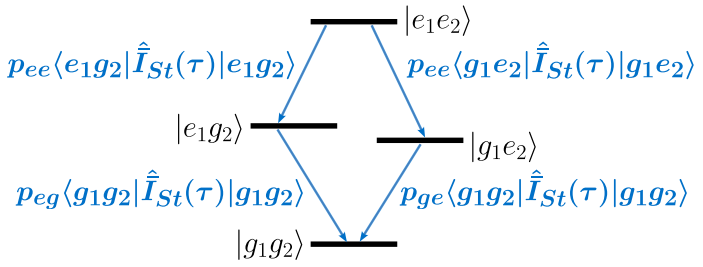

Figure 4.2: Schematic representation of the one-photon transitions and their contribution to the numerator of the Stokes-shifted correlation $\bar{g}^{(2)}_{\mathrm{St}}(\tau)$ within the conditional-probability approach. The one-photon transition $|a_1b_2\rangle \rightarrow |c_1d_2\rangle$ (with $a,b,c,d \in \{e,g\}$) contributes to the numerator of $\bar{g}^{(2)}_{\mathrm{St}}(\tau)$ as $p_{ab}\,\langle c_1d_2|\hat{\bar{I}}_{\mathrm{St}}(\tau)|c_1d_2\rangle$, with $p_{ab} = \langle a_1b_2|\hat{\rho}_{ss}|a_1b_2\rangle$ the steady-state population of $|a_1b_2\rangle$ and $\langle c_1d_2|\hat{\bar{I}}_{\mathrm{St}}(\tau)|c_1d_2\rangle$ a diagonal element of the operator $\hat{\bar{I}}_{\mathrm{St}}(\tau)$ that describes the Stokes-shifted intensity within the conditional-probability approach [Eq. (4.8)].

of Stokes-shifted photons, which incorporates the influence of quantum coherence between the state of the two emitters, as well as the coherence between the electric field scattered from the two emitters. When the effects of quantum coherence are discarded again within this more complete model, the results of the conditional-probability approach can be retrieved.

4.2 Model of the correlation of Stokes-shifted photons

We present in this section a model to describe the correlation of Stokes-shifted photons emitted from two quantum emitters, as well as the correlation of ZPL photons, which accounts for the influence of quantum coherence.

4.2.1 Markovian master equation

We consider two almost identical quantum emitters, with pure electronic ground and excited states denoted again as $|g_j\rangle$ and $|e_j\rangle$. The two emitters have equal spontaneous decay rate γ_0, identical transition dipole moments ($\boldsymbol{\mu}_1 = \boldsymbol{\mu}_2$). and slightly different electronic transition frequencies $\omega_{e,1}$ and $\omega_{e,2}$, with $\delta = \omega_{e,1} - \omega_{e,2} \ll \omega_{e,1}, \omega_{e,2}$. Crucially, we consider an additional state $|v_j\rangle$ for each emitter, which corresponds to a 1-phonon level in the electronic ground state, with vibrational mode of frequency ω_v and decay rate γ_v, see Fig. 4.3a.

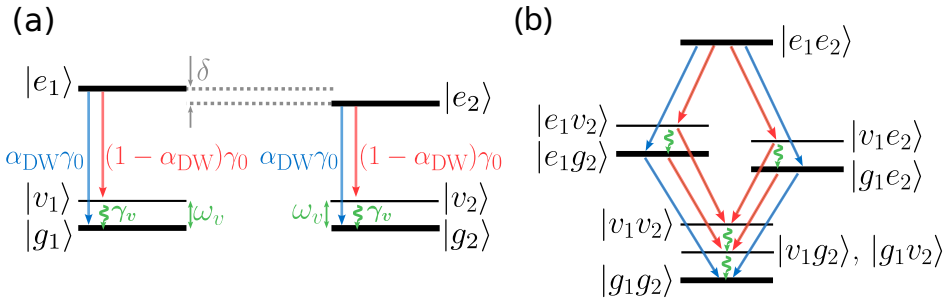

Figure 4.3: Schematic representation of the energy levels of the two quantum emitters in the absence of interaction and within the model proposed to address the correlation of Stokes-shifted photons. Blue arrows correspond to ZPL radiative transitions, red arrows to radiative Stokes-shifted transitions, and green arrows to transitions from a 1-phonon state to the pure electronic ground state. The states are represented in (a) in the reduced Hilbert space of each emitter, and in (b) in the total Hilbert space of the two emitters. $\delta = \omega_{e,1} - \omega_{e,2}$ is the frequency detuning between the electronic transition frequencies $\omega_{e,1}$ and $\omega_{e,2}$ of the two emitters. ω_v and γ_v are the frequency and decay rate of the vibrational/phononic mode analyzed. $\alpha_{\mathrm{DW}}\gamma_0$ is the decay rate of the ZPL transition of the emitter j, with γ_0 the total decay rate of the electronic excited state $|e_0\rangle$ and α_{DW} the combined Debye-Waller/Frank-Condon factor. $(1-\alpha_{\mathrm{DW}})\gamma_0$ is the decay rate of the Stokes-shifted transition within this model.

The unperturbed Hamiltonian of the system can be written as

$$\hat{H}_0 = \hbar \sum_{j=1}^{2} \left[\frac{\omega_{e,j}}{2} \left(|e_j\rangle \langle e_j| - |g_j\rangle \langle g_j| \right) + \frac{2\omega_v - \omega_{e,j}}{2} |v_j\rangle \langle v_j| \right]. \tag{4.11}$$

Further, the coherent dipole-dipole interaction between the two emitters is described again by the Hamiltonian

$$\hat{H}_{\mathrm{int}} = \hbar V_{\mathrm{DW}} (\hat{\sigma}_1^\dagger \hat{\sigma}_2 + \hat{\sigma}_1 \hat{\sigma}_2^\dagger), \tag{4.12}$$

with V_{DW} the coupling strength in Eq. (3.56a), which includes the influence of the combined Debye-Waller/Franck-Condon factor α_{DW}. Notably, this interaction Hamiltonian considers that the emitters couple only through the purely electronic states. The coupling through the 1-phonon levels is not taken into account because it does not affect the dynamics of the emitters nor their light emission, as we consider short-lived vibrations with $\omega_v, \gamma_v \gg \gamma_0, V_{\mathrm{DW}}$. Further, the Hamiltonian describing the laser excitation is again $\hat{H}_L = -\frac{\hbar}{2} \sum_{j=1}^{2} (\Omega_j^* \hat{\sigma}_j^\dagger e^{-i\omega_L t} + \Omega_j \hat{\sigma}_j e^{i\omega_L t})$, with ω_L the laser frequency and Ω_j the Rabi frequency of emitter j [Eqs. (1.218) and (3.66)]. The total Hamiltonian thus becomes

$$\hat{H} = \hat{H}_0 + \hat{H}_{\mathrm{int}} + \hat{H}_L. \tag{4.13}$$

We next move to the rotating frame at the laser frequency ω_L by using the

unitary transformation

$$\hat{U}_L = \exp\left[it\frac{\omega_L}{2}\Big(|e_j\rangle\langle e_j| - |g_j\rangle\langle g_j| - |v_j\rangle\langle v_j|\Big)\right]. \tag{4.14}$$

The total Hamiltonian $\hat{\tilde{H}}$ in this rotating frame is calculated following the general procedure described in Appendix C. We obtain

$$\hat{\tilde{H}} = \hbar\sum_{j=1}^{2}\left[\frac{\Delta_j}{2}(|e_j\rangle\langle e_j| - |g_j\rangle\langle g_j|) + \frac{2\omega_v - \Delta_j}{2}|v_j\rangle\langle v_j|\right] - \frac{\hbar}{2}\sum_{j=1}^{2}(\Omega_j^*\hat{\sigma}_j^\dagger + \Omega_j\hat{\sigma}_j) + \hat{H}_{\text{int}}, \tag{4.15}$$

with $\Delta_j = \omega_{e,j} - \omega_L$ the detuning of the electronic transition frequency of emitter j with respect to the laser frequency.

Furthermore, the dynamics of the density matrix describing the state of the two emitters is governed by the Markovian master equation

$$\begin{aligned}\frac{d}{dt}\hat{\rho} = -\frac{i}{\hbar}[\hat{\tilde{H}},\hat{\rho}] + \sum_{j=1}^{2}\Bigg(&\frac{\alpha_{\text{DW}}\gamma_0}{2}\mathcal{D}[\hat{\sigma}_j] + \frac{(1-\alpha_{\text{DW}})\gamma_0}{2}\mathcal{D}[|v_j\rangle\langle e_j|] \\ &+ \sum_{k\neq j}\frac{\tilde{\gamma}_{\text{DW}}}{2}\mathcal{D}[\hat{\sigma}_j,\hat{\sigma}_k] + \frac{\gamma_v}{2}\mathcal{D}[|g_j\rangle\langle v_j|]\Bigg)\hat{\rho},\end{aligned} \tag{4.16}$$

where γ_0 is the total decay rate from the excited state $|e_1\rangle$ and also from the state $|e_2\rangle$ (Section 3.1.5). Notably, as the combined Debye-Waller/Franck-Condon factor α_{DW} corresponds to the fraction of photons emitted into the ZPL line, we have fixed $\alpha_{\text{DW}}\gamma_0$ as the decay rate into the ZPL [first dissipator in Eq. (4.16)] and $(1-\alpha_{\text{DW}})\gamma_0$ as the decay rate into the 1-phonon level [second dissipator]. The last dissipator in Eq. (4.16) accounts for the relaxation from the vibrational state $|v_j\rangle$ to $|g_j\rangle$. Additionally, $\tilde{\gamma}_{\text{DW}}$ is again the crossed-decay rate including the effect of α_{DW} [Eq. (3.56b)].

4.2.2 Calculation of the intensity correlation

The calculation of the intensity correlation is performed through the general expression in Eq. (2.60), instead of the reset matrix formalism [Eq. (4.1)]. As the emitters have identical transition dipole moments ($\boldsymbol{\mu}_1 = \boldsymbol{\mu}_2$), the intensity correlation can be calculated using scalar electric field operators, as discussed in Section 3.3.1. Specifically, the intensity correlation can thus be obtained as

$$g_\chi^{(2)}(\tau) = \frac{\langle \hat{E}_{\perp,\chi}^{(-)}(\mathbf{r}_d,0)\hat{E}_{\perp,\chi}^{(-)}(\mathbf{r}_d,\tau)\hat{E}_{\perp,\chi}^{(+)}(\mathbf{r}_d,\tau)\hat{E}_{\perp,\chi}^{(+)}(\mathbf{r}_d,0)\rangle_{ss}}{\langle \hat{E}_{\perp,\chi}^{(-)}(\mathbf{r}_d,0)\hat{E}_{\perp,\chi}^{(+)}(\mathbf{r}_d,0)\rangle_{ss}^2}. \tag{4.17}$$

This equation can be used to compute the correlation of ZPL photons ($\chi = \text{ZPL}$), as well as the Stokes-shifted correlation ($\chi = \text{St}$). In experiments, these two situations

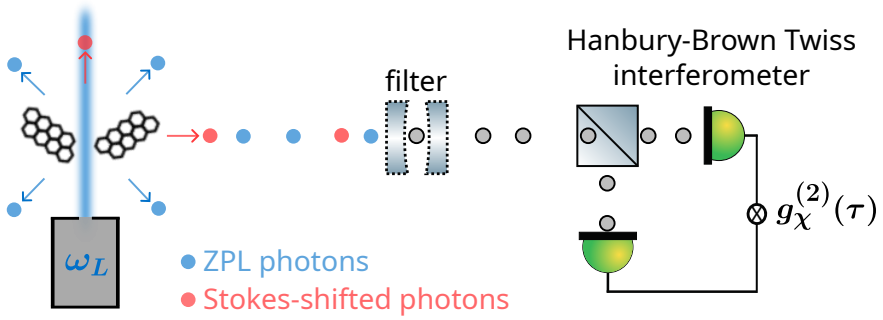

Figure 4.4: Schematic representation of light emitted from two interacting emitters, the filtering of this light and the measurement of the intensity correlation $g_\chi^{(2)}(\tau)$. A laser beam at frequency ω_L (in blue) excites resonantly the pure electronic excited state of the quantum emitters, which then can emit a photon at the same frequency (blue circles) or a Stokes-shifted photon (red circles). A filter selects either the ZPL ($\chi = \text{ZPL}$) or Stokes-shifted ($\chi = \text{St}$) light (grey circles represent these filtered photons).

correspond to the use of different optical filters before light passes through the beam splitter in the Hanbury-Brown Twiss interferometer, as schematically represented in Fig. 4.4.

On the one hand, the correlation of ZPL photons can be obtained by using the positive-frequency electric field operator

$$\hat{E}^{(+)}_{\perp,\text{ZPL}}(\mathbf{r}_d,\tau) = \xi_{\text{ZPL}}\cdot\Big(|g_1\rangle\langle e_1|\,(\tau-|\mathbf{r}_d|n/c) + e^{i\varphi_{\text{ZPL}}}|g_2\rangle\langle e_2|\,(\tau-|\mathbf{r}_d|n/c)\Big), \tag{4.18}$$

which describes the radiative transitions from the pure electronic states $|e_j\rangle$ to the pure electronic ground states $|g_j\rangle$ (Section 3.3.1), with $\xi_{\text{ZPL}} = |\boldsymbol{\mathcal{E}}_{\boldsymbol{\mu}_1^{\text{ZPL}}}(\mathbf{r}_d)|\exp(-i\omega_0\boldsymbol{e}_d\cdot\mathbf{r}_1 n/c)$ and $\varphi_{\text{ZPL}} = \omega_0\boldsymbol{e}_d\cdot(\mathbf{r}_1-\mathbf{r}_2)n/c$. Here, $\boldsymbol{e}_d = \mathbf{r}_d/|\mathbf{r}_d|$ is the unit vector along the direction of detection, and $\boldsymbol{\mathcal{E}}_{\boldsymbol{\mu}_1^{\text{ZPL}}}(\mathbf{r}_d)$ is the vector amplitude of the positive-frequency electric field [see Eq. (1.141)] radiated from a classical point dipole $\boldsymbol{\mu}_1^{\text{ZPL}}$ [Eq. (3.55)] and evaluated at position $\mathbf{r}_d$ in the far-field region. Additionally, we recall that $\boldsymbol{\mathcal{E}}_{\boldsymbol{\mu}_1^{\text{ZPL}}}(\mathbf{r}_d) = \boldsymbol{\mathcal{E}}_{\boldsymbol{\mu}_2^{\text{ZPL}}}(\mathbf{r}_d)$, as both transition dipole moments are identical. The calculation of the ZPL correlation within this model yields the same results as that obtained in Chapter 3 with the two-level description of the emitters.

On the other hand, the correlation of Stokes-shifted photons can be obtained by using instead the positive-frequency electric field operator

$$\hat{E}^{(+)}_{\perp,\text{St}}(\mathbf{r}_d,\tau) = \xi_{\text{St}}\cdot\Big(|v_1\rangle\langle e_1|\,(\tau-|\mathbf{r}_d|n/c) + e^{i\varphi_{\text{St}}}|v_2\rangle\langle e_2|\,(\tau-|\mathbf{r}_d|n/c)\Big), \tag{4.19}$$

describing the radiative transitions from the pure electronic states $|e_j\rangle$ to the vibrational/phononic states $|v_j\rangle$. The complex coefficient ξ_{St} and the phase φ_{St} can be obtained following the same procedure used to derive ξ_{ZPL} and φ_{ZPL} in Section 3.3.1, which yields

$$\xi_{\mathrm{St}} = \exp[-i(\omega_0 - \omega_v)\boldsymbol{e}_d \cdot \mathbf{r}_1 n/c]|\boldsymbol{\mathcal{E}}_{\boldsymbol{\mu}_1^{\mathrm{St}}}(\mathbf{r}_d)|, \tag{4.20a}$$

$$\varphi_{\mathrm{St}} = (\omega_0 - \omega_v)\boldsymbol{e}_d \cdot (\mathbf{r}_1 - \mathbf{r}_2)n/c. \tag{4.20b}$$

Here, $\boldsymbol{\mathcal{E}}_{\boldsymbol{\mu}_1^{\mathrm{St}}}(\mathbf{r}_d)$ is again the vector amplitude of the classical electric field radiated by a point dipole in the far-field region [Eq. (1.141)], but in this case the magnitude of the dipole moment is given by

$$|\boldsymbol{\mu}_j^{\mathrm{St}}| = \sqrt{\frac{(1-\alpha_{\mathrm{DW}})\gamma_0 3\pi\varepsilon_0\hbar c^3}{\omega_{e,j}^3 n}}. \tag{4.21}$$

We emphasize that the specific values of the coefficients ξ_{ZPL} and ξ_{St} do not affect the intensity correlations $g^{(2)}_{\mathrm{ZPL}}(\tau)$ and $g^{(2)}_{\mathrm{St}}(\tau)$, as their contribution to the numerator in Eq. (4.17) cancel out with their contribution to the denominator.

4.3 Influence of quantum coherence on the Stokes-shifted correlation

In this section, we first show that the analytical expression of the Stokes-shifted correlation provided by the model presented in Section 4.2 can be decomposed into contributions that are dependent or independent of quantum coherence. This decomposition allows us to characterize the influence of quantum coherence in the intensity correlation. We show next that the contributions that are influenced by quantum coherence can play a significant role in the correlation of Stokes-shifted photons emitted from two interacting emitters, as well as in the case in which the emitters do not interact.

4.3.1 Decomposition of the Stokes-shifted correlation

We focus in this section on the case in which light is detected in the direction $\mathbf{r}_d$ perpendicular to the plane in which the transition dipole moments and the molecules are contained. As a result, $\varphi_{\mathrm{St}} = 0$, which facilitates the analytical expressions of the contributions in which the Stokes-shifted correlation $g^{(2)}_{\mathrm{St}}(\tau)$ is decomposed in this section. These expressions can be generalized to arbitrary values of φ_{St}.

We first define the positive-frequency Stokes-shifted electric field operator at

$\varphi_{\mathrm{St}} = 0$ as

$$\hat{E}^{(+)}_{\perp,\mathrm{St}}(\tau) = \hat{E}^{(+)}_{\perp,\mathrm{St}}(\mathbf{r}_d,\tau)\Big|_{\varphi_{\mathrm{St}}=0} = \xi_{\mathrm{St}}\cdot\Big(\,|v_1\rangle\langle e_1|\,(\tau-|\mathbf{r}_d|n/c)+|v_2\rangle\langle e_2|\,(\tau-|\mathbf{r}_d|n/c)\Big). \tag{4.22}$$

By substituting this electric field operator into the expression of the intensity correlation in Eq. (4.17), we obtain

$$g^{(2)}_{\mathrm{St}}(\tau) = \frac{\langle \hat{E}^{(-)}_{\perp,\mathrm{St}}(0)\hat{E}^{(-)}_{\perp,\mathrm{St}}(\tau)\hat{E}^{(+)}_{\perp,\mathrm{St}}(\tau)\hat{E}^{(+)}_{\perp,\mathrm{St}}(0)\rangle_{ss}}{\langle \hat{E}^{(-)}_{\perp,\mathrm{St}}(0)\hat{E}^{(+)}_{\perp,\mathrm{St}}(0)\rangle^2_{ss}}. \tag{4.23}$$

Additionally, according to Eq. (2.17), the operator associated with the intensity of Stokes-shifted light can be introduced as

$$\begin{aligned}\hat{I}_{\mathrm{St}}(\tau) &= \hat{E}^{(-)}_{\perp,\mathrm{St}}(\tau)\hat{E}^{(+)}_{\perp,\mathrm{St}}(\tau)\\ &= |\xi_{\mathrm{St}}|^2\Big(\,|e_1\rangle\langle v_1|\,(\tau)+|e_2\rangle\langle v_2|\,(\tau)\Big)\Big(\,|v_1\rangle\langle e_1|\,(\tau)+|v_2\rangle\langle e_2|\,(\tau)\Big).\end{aligned} \tag{4.24}$$

We substitute now this intensity operator into Eq. (4.23), yielding that the Stokes-shifted correlation can be rewritten as

$$g^{(2)}_{\mathrm{St}}(\tau) = \frac{G^{(2)}_{\mathrm{St}}(\tau)}{\langle \hat{I}_{\mathrm{St}}(\mathbf{r}_d,0)\rangle^2}, \tag{4.25}$$

where the numerator is given by

$$\begin{aligned}G^{(2)}_{\mathrm{St}}(\tau) &= \langle \hat{E}^{(-)}_{\perp,\mathrm{St}}(0)\hat{I}_{\mathrm{St}}(\tau)\hat{E}^{(+)}_{\perp,\mathrm{St}}(0)\rangle_{ss}\\ &= |\xi_{\mathrm{St}}|^2\,\langle(|e_1\rangle\langle v_1|+|e_2\rangle\langle v_2|)\hat{I}_{\mathrm{St}}(\tau)(|v_1\rangle\langle e_1|+|v_2\rangle\langle e_2|)\rangle_{ss}\,,\end{aligned} \tag{4.26}$$

and the steady-state expectation value of the Stokes-shifted intensity in the denominator is

$$\langle \hat{I}_{\mathrm{St}}(0)\rangle = |\xi_{\mathrm{St}}|^2\Big(2p_{ee}+p_{eg}+p_{ge}+p_{ev}+p_{ve}+2\mathrm{Re}\rho_{ev,ve}\Big). \tag{4.27}$$

Here, $p_{ab} = \langle a_1b_2|\hat{\rho}_{ss}|a_1b_2\rangle$ is the population of the state $|a_1b_2\rangle$ of the uncoupled (localized) basis, with $a,b \in \{e,g,v\}$, and $\rho_{ev,ve} = \langle e_1v_2|\hat{\rho}_{ss}|v_1e_2\rangle$ is the steady-state coherence between $|e_1v_2\rangle$ and $|v_1e_2\rangle$. This coherence vanishes as long as the emitters couple only through the ZPL, as we consider in this chapter.

We next use the cyclic property of the trace to rewrite $G^{(2)}_{\mathrm{St}}(\tau)$ [the numerator in Eq. (4.25)] as a function of matrix elements of the steady-state density matrix $\hat{\rho}_{ss}$ and of the intensity operator $\hat{I}_{\mathrm{St}}(\tau)$. To this end, we choose the uncoupled basis because the first-order coherence between the light scattered by the two emitters is associated with the off-diagonal elements of the intensity operator in

this basis (Section 4.1.2). Additionally, as we consider that the emitters couple only through the ZPL, the emission of a Stokes-shifted photon projects the system into a localized state of the uncoupled basis and the coherence between the two emitters can be attributed to the off-diagonal elements of the density matrix in this basis [199]. In this way, we obtain

$$
\begin{aligned}
G^{(2)}_{\mathrm{St}}(\tau)/|\xi_{\mathrm{St}}|^4 = {} & p_{ee}\,\langle v_1e_2|\,\hat{I}_{\mathrm{St}}(\tau)\,|v_1e_2\rangle + p_{ee}\,\langle e_1v_2|\,\hat{I}_{\mathrm{St}}(\tau)\,|e_1v_2\rangle \\
& + p_{eg}\,\langle v_1g_2|\,\hat{I}_{\mathrm{St}}(\tau)\,|v_1g_2\rangle + p_{ge}\,\langle g_1v_2|\,\hat{I}_{\mathrm{St}}(\tau)\,|g_1v_2\rangle \\
& + p_{ev}\,\langle v_1v_2|\,\hat{I}_{\mathrm{St}}(\tau)\,|v_1v_2\rangle + p_{ve}\,\langle v_1v_2|\,\hat{I}_{\mathrm{St}}(\tau)\,|v_1v_2\rangle \\
& + (\langle v_1e_2|\,\hat{I}_{\mathrm{St}}(\tau)\,|e_1v_2\rangle + \langle e_1v_2|\,\hat{I}_{\mathrm{St}}(\tau)\,|v_1e_2\rangle)p_{ee} \\
& + \rho_{eg,ee}[\langle v_1e_2|\,\hat{I}_{\mathrm{St}}(\tau)\,|v_1g_2\rangle + \langle e_1v_2|\,\hat{I}_{\mathrm{St}}(\tau)\,|v_1g_2\rangle] \\
& + \rho_{ge,ee}[\langle v_1e_2|\,\hat{I}_{\mathrm{St}}(\tau)\,|g_1v_2\rangle + \langle e_1v_2|\,\hat{I}_{\mathrm{St}}(\tau)\,|g_1v_2\rangle] \\
& + \rho_{ee,eg}[\langle v_1g_2|\,\hat{I}_{\mathrm{St}}(\tau)\,|e_1v_2\rangle + \langle v_1g_2|\,\hat{I}_{\mathrm{St}}(\tau)\,|v_1e_2\rangle] \\
& + \rho_{ee,ge}[\langle g_1v_2|\,\hat{I}_{\mathrm{St}}(\tau)\,|e_1v_2\rangle + \langle g_1v_2|\,\hat{I}_{\mathrm{St}}(\tau)\,|v_1e_2\rangle] \\
& + (\rho_{ee,ve} + \rho_{ee,ev})[\langle v_1v_2|\,\hat{I}_{\mathrm{St}}(\tau)\,|v_1e_2\rangle + \langle v_1v_2|\,\hat{I}_{\mathrm{St}}(\tau)\,|e_1v_2\rangle] \\
& + (\rho_{ve,ee} + \rho_{ev,ee})[\langle e_1v_2|\,\hat{I}_{\mathrm{St}}(\tau)\,|v_1v_2\rangle + \langle v_1e_2|\,\hat{I}_{\mathrm{St}}(\tau)\,|v_1v_2\rangle] \\
& + (\rho_{eg,ev} + \rho_{eg,ve})\,\langle v_1v_2|\,\hat{I}_{\mathrm{St}}(\tau)\,|v_1g_2\rangle \\
& + (\rho_{ge,ev} + \rho_{ge,ve})\,\langle v_1v_2|\,\hat{I}_{\mathrm{St}}(\tau)\,|g_1v_2\rangle \\
& + (\rho_{ev,eg} + \rho_{ve,eg})\,\langle v_1g_2|\,\hat{I}_{\mathrm{St}}(\tau)\,|v_1v_2\rangle \\
& + (\rho_{ev,ge} + \rho_{ve,ge})\,\langle g_1v_2|\,\hat{I}_{\mathrm{St}}(\tau)\,|v_1v_2\rangle \\
& + \rho_{eg,ge}\,\langle g_1v_2|\,\hat{I}_{\mathrm{St}}(\tau)\,|v_1g_2\rangle + \rho_{ge,eg}\,\langle v_1g_2|\,\hat{I}_{\mathrm{St}}(\tau)\,|g_1v_2\rangle \\
& + (\rho_{ev,ve} + \rho_{ve,ev})\,\langle v_1v_2|\,\hat{I}_{\mathrm{St}}(\tau)\,|v_1v_2\rangle\,,
\end{aligned}
\tag{4.28}
$$

where $\rho_{ab,cd} = \langle a_1b_2|\hat{\rho}_{ss}|c_1d_2\rangle$, with $a, b, c, d \in \{e, g, v\}$. This expression can be decomposed into three different contributions

$$
G^{(2)}_{\mathrm{St}}(\tau) = G^{(2)}_{\mathrm{d}}(\tau) + G^{(2)}_{\mathrm{coh,I}}(\tau) + G^{(2)}_{\mathrm{coh},\rho}(\tau), \tag{4.29}
$$

so that the Stokes-shifted correlation becomes decomposed as well into three contributions

$$
g^{(2)}_{\mathrm{St}}(\tau) = \frac{G^{(2)}_{\mathrm{d}}(\tau)}{\langle \hat{I}_{\mathrm{St}}(0)\rangle^2} + \frac{G^{(2)}_{\mathrm{coh,I}}(\tau)}{\langle \hat{I}_{\mathrm{St}}(0)\rangle^2} + \frac{G^{(2)}_{\mathrm{coh},\rho}(\tau)}{\langle \hat{I}_{\mathrm{St}}(0)\rangle^2}. \tag{4.30}
$$

On the one hand, $G^{(2)}_{\mathrm{d}}(\tau)$ involves the terms on the right-hand side of Eq. (4.28) that involve diagonal elements of $\hat{\rho}_{ss}$ and of $\hat{I}_{\mathrm{St}}(\tau)$ in the uncoupled basis. Thus, this contribution is influenced neither by the quantum coherence between the emitters nor by the first-order coherence of the light they scatter. Specifically,

$G_{\mathrm{d}}^{(2)}(\tau)$ is given by

$$\begin{aligned} G_{\mathrm{d}}^{(2)}(\tau)/|\xi_{\mathrm{St}}|^4 = {} & p_{ee}\,\langle v_1e_2|\,\hat{I}_{\mathrm{St}}(\tau)\,|v_1e_2\rangle + p_{ee}\,\langle e_1v_2|\,\hat{I}_{\mathrm{St}}(\tau)\,|e_1v_2\rangle \\ & + p_{eg}\,\langle v_1g_2|\,\hat{I}_{\mathrm{St}}(\tau)\,|v_1g_2\rangle + p_{ge}\,\langle g_1v_2|\,\hat{I}_{\mathrm{St}}(\tau)\,|g_1v_2\rangle \\ & + p_{ev}\,\langle v_1v_2|\,\hat{I}_{\mathrm{St}}(\tau)\,|v_1v_2\rangle + p_{ve}\,\langle v_1v_2|\,\hat{I}_{\mathrm{St}}(\tau)\,|v_1v_2\rangle\,. \end{aligned} \tag{4.31}$$

The six terms on the right-hand side of this expression are products of steady-state populations p_{ab} and diagonal elements $\langle c_1d_2|\,\hat{I}_{\mathrm{St}}(\tau)\,|c_1d_2\rangle$ of the intensity operator $\hat{I}_{\mathrm{St}}(\tau)$. Thus, $G_{\mathrm{d}}^{(2)}(\tau)$ has the same intuitive interpretation as the Stokes-shifted correlation obtained using the conditional-probability approach (Section 4.1.2), with each of these six terms on the right-hand side of Eq. (4.31) being related to one of the Stokes-shifted transitions in Fig. 4.3b. For example, $p_{ee}\,\langle v_1e_2|\,\hat{I}_{\mathrm{St}}(\tau)\,|v_1e_2\rangle$ accounts for the contribution of the one-photon transition $|e_1e_2\rangle \rightarrow |v_1e_2\rangle$ to increasing the Stokes-shifted correlation. Even more, taking into account that terms in the last line of Eq. (4.31) are negligible in comparison to the other four terms (because the steady-state populations of the 1-phonon levels are much smaller than the steady-state populations of the pure electronic states), and that the 1-phonon states decay very fast to the pure ground state, we can approximate

$$\begin{aligned} G_{\mathrm{d}}^{(2)}(\tau)/|\xi_{\mathrm{St}}|^4 \approx {} & p_{ee}\,\langle g_1e_2|\,\hat{I}_{\mathrm{St}}(\tau)\,|g_1e_2\rangle + p_{ee}\,\langle e_1g_2|\,\hat{I}_{\mathrm{St}}(\tau)\,|e_1g_2\rangle \\ & + p_{eg}\,\langle g_1g_2|\,\hat{I}_{\mathrm{St}}(\tau)\,|g_1g_2\rangle + p_{ge}\,\langle g_1g_2|\,\hat{I}_{\mathrm{St}}(\tau)\,|g_1g_2\rangle\,. \end{aligned} \tag{4.32}$$

The right-hand side of this expression corresponds indeed to the numerator of the Stokes-shifted correlation $\bar{g}_{St}^{(2)}(\tau)$ obtained with the conditional-probability approach [Eq. (4.10)].

Moreover, the second term on the right-hand side of the correlation numerator in Eq. (4.29) involves diagonal elements of the density matrix (populations) and off-diagonal elements of the operator $\hat{I}_{\mathrm{St}}(\tau)$. Specifically,

$$G_{\mathrm{coh,I}}^{(2)}(\tau)/|\xi_{\mathrm{St}}|^4 = p_{ee}(\langle v_1e_2|\,\hat{I}_{\mathrm{St}}(\tau)\,|e_1v_2\rangle + \langle e_1v_2|\,\hat{I}_{\mathrm{St}}(\tau)\,|v_1e_2\rangle). \tag{4.33}$$

Interestingly, $G_{\mathrm{coh,I}}^{(2)}(\tau)$ can be interpreted as due to the quantum interference between the emission paths of the two quantum emitters, which is usually referred to as *Hanbury-Brown Twiss effect* [164, 206, 207]. Last, $G_{\mathrm{coh},\rho}^{(2)}(\tau)$ is given by the rest of terms in Eq. (4.28), which include off-diagonal elements of the steady-state

density matrix. More specifically, $G^{(2)}_{\mathrm{coh},\rho}(\tau)$ is defined as

$$\begin{aligned}
G^{(2)}_{\mathrm{coh},\rho}(\tau)/|\xi_{\mathrm{St}}|^4 = {} & \rho_{eg,ee}[\langle v_1 e_2|\,\hat{I}_{\mathrm{St}}(\tau)\,|v_1 g_2\rangle + \langle e_1 v_2|\,\hat{I}_{\mathrm{St}}(\tau)\,|v_1 g_2\rangle] \\
& + \rho_{ge,ee}[\langle v_1 e_2|\,\hat{I}_{\mathrm{St}}(\tau)\,|g_1 v_2\rangle + \langle e_1 v_2|\,\hat{I}_{\mathrm{St}}(\tau)\,|g_1 v_2\rangle] \\
& + \rho_{ee,eg}[\langle v_1 g_2|\,\hat{I}_{\mathrm{St}}(\tau)\,|e_1 v_2\rangle + \langle v_1 g_2|\,\hat{I}_{\mathrm{St}}(\tau)\,|v_1 e_2\rangle] \\
& + \rho_{ee,ge}[\langle g_1 v_2|\,\hat{I}_{\mathrm{St}}(\tau)\,|e_1 v_2\rangle + \langle g_1 v_2|\,\hat{I}_{\mathrm{St}}(\tau)\,|v_1 e_2\rangle] \\
& + (\rho_{ee,ve} + \rho_{ee,ev})[\langle v_1 v_2|\,\hat{I}_{\mathrm{St}}(\tau)\,|v_1 e_2\rangle + \langle v_1 v_2|\,\hat{I}_{\mathrm{St}}(\tau)\,|e_1 v_2\rangle] \\
& + (\rho_{ve,ee} + \rho_{ev,ee})[\langle e_1 v_2|\,\hat{I}_{\mathrm{St}}(\tau)\,|v_1 v_2\rangle + \langle v_1 e_2|\,\hat{I}_{\mathrm{St}}(\tau)\,|v_1 v_2\rangle] \\
& + (\rho_{eg,ev} + \rho_{eg,ve})\,\langle v_1 v_2|\,\hat{I}_{\mathrm{St}}(\tau)\,|v_1 g_2\rangle \\
& + (\rho_{ge,ev} + \rho_{ge,ve})\,\langle v_1 v_2|\,\hat{I}_{\mathrm{St}}(\tau)\,|g_1 v_2\rangle \\
& + (\rho_{ev,eg} + \rho_{ve,eg})\,\langle v_1 g_2|\,\hat{I}_{\mathrm{St}}(\tau)\,|v_1 v_2\rangle \\
& + (\rho_{ev,ge} + \rho_{ve,ge})\,\langle g_1 v_2|\,\hat{I}_{\mathrm{St}}(\tau)\,|v_1 v_2\rangle \\
& + \rho_{eg,ge}\,\langle g_1 v_2|\,\hat{I}_{\mathrm{St}}(\tau)\,|v_1 g_2\rangle + \rho_{ge,eg}\,\langle v_1 g_2|\,\hat{I}_{\mathrm{St}}(\tau)\,|g_1 v_2\rangle \\
& + (\rho_{ev,ve} + \rho_{ve,ev})\,\langle v_1 v_2|\,\hat{I}_{\mathrm{St}}(\tau)\,|v_1 v_2\rangle\,.
\end{aligned} \tag{4.34}$$

The contributions $G^{(2)}_{\mathrm{coh,I}}(\tau)$ and $G^{(2)}_{\mathrm{coh},\rho}(\tau)$ thus account for the influence of quantum coherence to the correlation of Stokes-shifted photons, in contrast to $G^{(2)}_{\mathrm{d}}(\tau)$. Therefore, if quantum coherence is neglected (as done within the conditional-probability approach in Section 4.1.2), $G^{(2)}_{\mathrm{coh,I}}(\tau) = G^{(2)}_{\mathrm{coh},\rho}(\tau) = 0$ and the Stokes-shifted correlation reduces to

$$g^{(2)}_{\mathrm{St,d}}(\tau) \equiv \frac{G^{(2)}_{\mathrm{d}}(\tau)}{\langle \hat{I}_{\mathrm{St}}(0)\rangle^2}. \tag{4.35}$$

To gain further insights into the three contributions in which we have decomposed $G^{(2)}_{\mathrm{St}}(\tau)$, we evaluate them at delay $\tau = 0$. On the one hand, we find that all the elements $\langle a_1 b_2|\,\hat{I}_{\mathrm{St}}(\tau)\,|c_1 d_2\rangle$ in Eq. (4.34) vanish at $\tau = 0$, which results in

$$G^{(2)}_{\mathrm{coh},\rho}(0) = 0. \tag{4.36}$$

At different delay times, $G^{(2)}_{\mathrm{coh},\rho}(\tau)$ can become nonzero and comparable to $G^{(2)}_{\mathrm{d}}(\tau)$, as we show below. On the other hand, we find that $G^{(2)}_{\mathrm{d}}(0)$ and $G^{(2)}_{\mathrm{coh,I}}(0)$ are identical and given by

$$G^{(2)}_{\mathrm{d}}(0)/|\xi_{\mathrm{St}}|^4 = G^{(2)}_{\mathrm{coh,I}}(0)/|\xi_{\mathrm{St}}|^4 = 2p_{ee}. \tag{4.37}$$

Thus, $G^{(2)}_{\mathrm{St}}(0)/|\xi_{\mathrm{St}}|^4$ is equal to $4\rho_{ee}$.

We compare in the next section the behaviour of the complete Stokes-

shifted correlation $g^{(2)}_{\mathrm{St}}(\tau)$, including the influence of quantum coherence, and the approximate Stokes-shifted correlation $g^{(2)}_{\mathrm{St,d}}(\tau)$, which neglects the influence of quantum coherence, of photons emitted from two quantum emitters at different separation distances.

4.3.2 Two emitters separated by short distances

We first consider two DBATT molecules separated by a short distance along the x-axis ($r_{12} = 27$ nm) and in a H-configuration, so that the transition dipole moments of the two molecules are oriented along the perpendicular z-axis. Additionally, we consider that the excitation laser impinges in the normal direction to the xz-plane in which the transition dipole moments and the molecules are contained, as schematically represented in Fig. 4.5a. Thus, we fix that the laser wavevector $\mathbf{k}_L$ is aligned along the y-axis, so that $\boldsymbol{e}_{\mathbf{k}_L} \equiv \mathbf{k}_L/|\mathbf{k}_L| = \boldsymbol{e}_y$. We also consider that light is detected in the normal direction to this plane, which yields $\varphi_{\mathrm{St}} = 0$. The values of V_{DW}, $\tilde{\gamma}_{\mathrm{DW}}$, and δ are obtained (with an uncertainty of approximately 2 %) through independent experimental measurements of the excitation spectra at different values of laser intensity and they are specified in the second row of Table 4.1.

We plot in Fig. 4.5b the correlation of Stokes-shifted photons for this molecular pair when the laser is resonantly tuned to the two-photon resonance ($\omega_L = \omega_0$) and in Fig. 4.5d when the laser is slightly detuned from the two-photon resonance ($\omega_L = \omega_0 - 0.93\gamma_0$), respectively. For the simulations in these two figures we consider the DBATT vibrational mode $\hbar\omega_v = 31.86$ meV [208], and $1/\gamma_v = 10$ ps based on experiments in Ref. [209]. Additionally, the values of the Rabi frequencies Ω_j are estimated from the values of the laser intensity used in the experiment ($I_L = 60$ W/cm^2) and the experimental saturation intensity ($I_{\mathrm{sat}} = 14$ W/cm^2), using Eq. (1.237).

Figure 4.5b shows that the simulated $g^{(2)}_{\mathrm{St}}(\tau)$ [Eq. (4.30), which includes the influence of quantum coherence] (red line) exhibits a very good agreement with the experimental measurements (grey line), except for the emergence of an extremely narrow peak at $\tau = 0$ in the simulation. This narrow peak cannot be resolved in the experiments due to the insufficient time resolution of the detectors, as we discuss in Section 4.3.3. Notably, the simulation obtained with $g^{(2)}_{\mathrm{St,d}}(\tau)$ [Eq. (4.35),

Figure	$\boldsymbol{\mu}_j/\lvert\boldsymbol{\mu}_j\rvert$	$\boldsymbol{r}_{12}$ [nm]	V_{DW}/γ_0	γ_{ij}/γ_0	δ/γ_0	Ω_j/γ_0	$\boldsymbol{e}_{\mathbf{k}_L}$
4.5, 4.6, 4.9a	$\boldsymbol{e}_z$	$27\boldsymbol{e}_x$	2.98	0.29	5	1.5	$\boldsymbol{e}_y$
4.7, 4.9b	$\boldsymbol{e}_z$	$400\boldsymbol{e}_x$	-0.04	-10^{-3}	5	1.5	$\boldsymbol{e}_y$
4.8	$\boldsymbol{e}_x$	$19.8\boldsymbol{e}_x$	-17	0.3	14	3.15	$\boldsymbol{e}_y$

Table 4.1: Molecular and laser parameters used in the simulations in Figs. 4.5, 4.6, and 4.9a (second row), in Figs. 4.7 and 4.9b (third row), and in Fig. 4.8 (fourth row). In all the cases $\gamma_0/(2\pi) = 21.5$ MHz, $\alpha_{\mathrm{DW}} = 0.3$, $\hbar\omega_v = 31.86$ meV, $1/\gamma_v = 10$ ps.

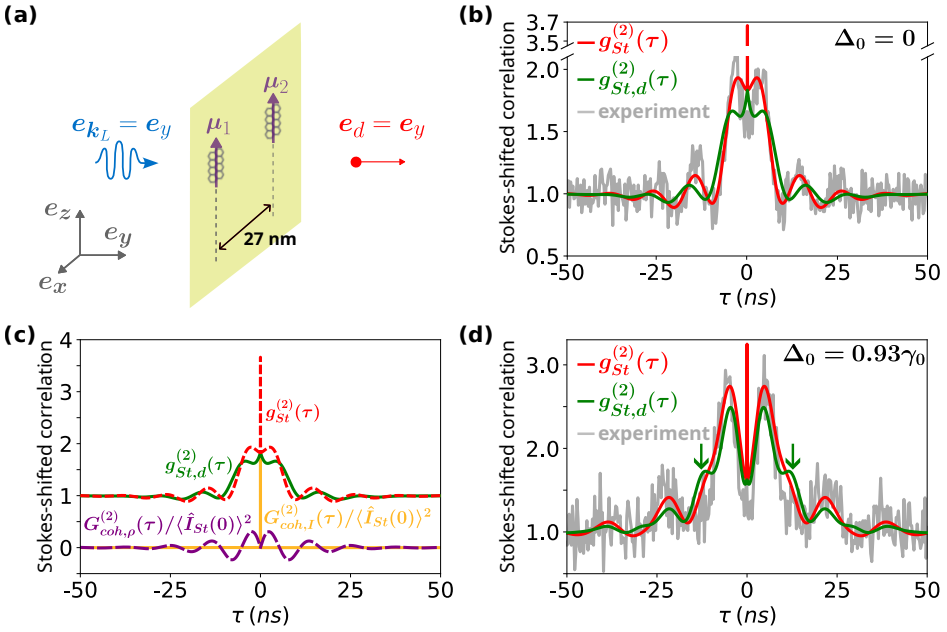

Figure 4.5: Impact of quantum coherence on the correlation of Stokes-shifted photons emitted from two interacting DBATT molecules. (a) Schematic representation of the molecular pair analyzed in (b), (c), and (d). The molecules are in a H-configuration and separated by $r_{12} = 27$ nm. The laser excitation impinges in the normal direction to the xz-plane in which the molecules are located, and light is detected also in the normal direction to this plane. The laser is tuned to the two-photon resonance ($\omega_L = \omega_0$) in (b) and (c) and slightly detuned from the two-photon resonance in (d), where $\omega_L = \omega_0 - 0.93\gamma_0$. The rest of the parameters are detailed in the second row of Table 4.1. [(b),(d)] Dependence on the time delay τ of the simulated Stokes-shifted correlation $g^{(2)}_{\rm St}(\tau)$ (red lines), which is obtained with the complete model [Eq. (4.30)] and includes the influence of quantum coherence, of the simulated Stokes-shifted correlation $g^{(2)}_{\rm St,d}(\tau)$ (green lines), which is obtained with the approximation that removes the influence of quantum coherence [Eq. (4.35)], and of the experimental Stokes-shifted correlation (grey lines). The experiments were conducted by the Bordeaux Nanophotonics Group, led by Brahim Lounis, at the Institut d'Optique Graduate School (CNRS). (c) Dependence on the time delay τ of the different contributions in which $g^{(2)}_{\rm St}(\tau)$ (red line) can be decomposed according to Eq. (4.30). Green line corresponds to $g^{(2)}_{\rm St,d}(\tau) = G^{(2)}_{\rm d}(\tau)/\langle \hat{I}_{\rm St}(0)\rangle^2$, orange line to $G^{(2)}_{\rm coh,I}(\tau)/\langle \hat{I}_{\rm St}(0)\rangle^2$, and dashed purple line to $G^{(2)}_{\rm coh,\rho}(\tau)/\langle \hat{I}_{\rm St}(0)\rangle^2$.

which neglects the influence of quantum coherence] (green line) exhibits appreciable differences with the experimental measurements. Specifically, we observe that when quantum coherence is neglected (i) the amplitude and period of the oscillations are notably modified, and (ii) a broad peak is found at delay $\tau = 0$, whereas the experiments show a dip at $\tau = 0$.

We next analyze the behaviour of the three contributions in which we have

decomposed the Stokes-shifted correlation in Eq. (4.30) to better characterize the origin of the different behaviour exhibited by the exact $g^{(2)}_{\mathrm{St}}(\tau)$ and the approximate $g^{(2)}_{\mathrm{St,d}}(\tau)$ simulations of the Stokes-shifted correlation in Fig. 4.5b. To this end, we plot in Fig. 4.5c $G^{(2)}_{\mathrm{coh,I}}(\tau)/\left\langle \hat{I}_{\mathrm{St}}(0)\right\rangle^2$ (orange line), $G^{(2)}_{\mathrm{d}}(\tau)/\left\langle \hat{I}_{\mathrm{St}}(0)\right\rangle^2 = g^{(2)}_{\mathrm{St,d}}(\tau)$ (green line), and $G^{(2)}_{\mathrm{coh},\rho}(\tau)/\left\langle \hat{I}_{\mathrm{St}}(0)\right\rangle^2$ (dashed purple line) as a function of the time delay τ. We find that $G^{(2)}_{\mathrm{coh,I}}(\tau)/\left\langle \hat{I}_{\mathrm{St}}(0)\right\rangle^2$ and $G^{(2)}_{\mathrm{coh},\rho}(\tau)/\left\langle \hat{I}_{\mathrm{St}}(0)\right\rangle^2$, which are the contributions affected by quantum coherence, vanish at large delay times. Additionally, $G^{(2)}_{\mathrm{coh,I}}(\tau)/\left\langle \hat{I}_{\mathrm{St}}(0)\right\rangle^2$ is only non-zero at very short delay times, being responsible of the extremely narrow peak exhibited by $g^{(2)}_{\mathrm{St}}(\tau)$ at $\tau = 0$. On the other hand, $G^{(2)}_{\mathrm{coh},\rho}(\tau)/\left\langle \hat{I}_{\mathrm{St}}(0)\right\rangle^2$ is zero at $\tau = 0$, but it becomes important in the timescale of the lifetime of the electronic excited states (nanoseconds) and can take either positive and negative values. Thus, accounting for the influence of the quantum coherence encoded in $G^{(2)}_{\mathrm{coh},\rho}(\tau)/\left\langle \hat{I}_{\mathrm{St}}(0)\right\rangle^2$ is crucial to capture well the experimental measurements in Fig. 4.5b.

Moreover, the results in Fig. 4.5d, which are obtained for a laser slightly detuned from the two-photon resonance ($\omega_L = \omega_0 - 0.93\gamma_0$), shows again that the experimental Stokes-shifted correlation is better reproduced by the simulation of $g^{(2)}_{\mathrm{St}}(\tau)$ obtained with the complete model. The only significant difference between $g^{(2)}_{\mathrm{St}}(\tau)$ and the experiments is again the extremely narrow peak obtained in the simulation at $\tau = 0$, which is not observed in the experiments due to the insufficient temporal resolution of the detectors. Further, when the influence of quantum coherence is neglected, two bumps emerge at $\tau \approx \pm 10$ ns (see the green arrows). These bumps are clearly not measured in experiments and are not exhibited by the complete simulation including quantum coherence, which highlights again the importance of quantum coherence in the Stokes-shifted correlation.

4.3.3 Influence of the time resolution of the detectors

We discuss in this section the influence of the detector resolution on the Stokes-shifted correlation and find that the main effect is that it prevents the experimental observation of the narrow peaks exhibited by the simulated correlations $g^{(2)}_{\mathrm{St}}(\tau)$ at $\tau = 0$ in Figs. 4.5b and 4.5d. A precise description of the influence of the two detectors in the Hanbury-Brown Twiss interferometer is complex, as it involves the independent convolution of the intensity operators associated with the light arriving at each detector. This difficulty is analogous to that encountered in the calculation of the frequency-resolved intensity correlation (FRIC), where integrated electric field operators $\hat{\mathbf{E}}^{(\pm)}_{\perp,fl}(\omega_j, \Gamma_j; t)$ [Eq. (2.70)] are required to account for the effect of the optical filters (see further discussion in Sections 2.4.1 and 2.4.2). Thus, to asses the influence of the detectors resolution on the intensity correlation, we avoid this complication by adopting a simpler, effective approach that we believe incorporates the main effect of the convolution.

To check in a simple way that the detector resolution only limits the observation

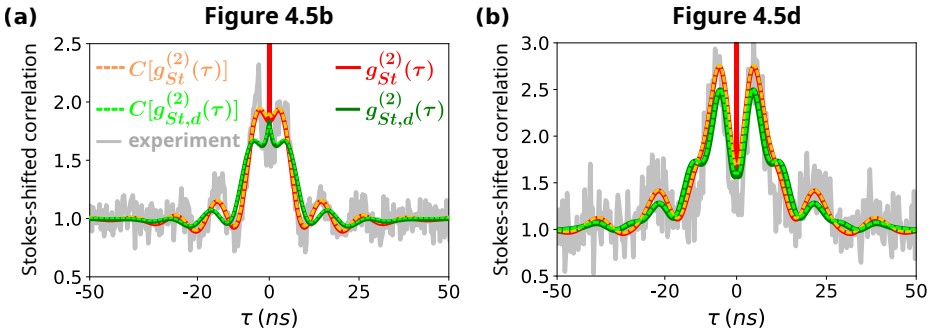

Figure 4.6: Influence of the detector resolution on the Stokes-shifted correlation. $g^{(2)}_{\mathrm{St}}(\tau)$ (solid red line) is the simulated correlation obtained with the complete model, which includes the influence of quantum coherence, while $g^{(2)}_{\mathrm{St,d}}(\tau)$ (solid dark green line) is the approximate simulated correlation obtained by removing the influence of quantum coherence and without considering the convolution. $C[g^{(2)}_{\mathrm{St}}(\tau)]$ (dashed orange line) and $C[g^{(2)}_{\mathrm{St,d}}(\tau)]$ (dashed light green line) are the corresponding convolved Stokes-shifted correlation, obtained according to Eq. (4.39) with a time resolution of the detector $\Delta t_d = 400$ ps. We consider in (a) the same molecular and laser parameters as in Fig. 4.5b, while we consider in (b) the same parameters as in Fig. 4.5d. These parameters are detailed in the second row of Table 4.1.

of the narrow peaks around $\tau = 0$, we directly calculate the convolution of the resulting intensity correlation $g^{(2)}(\tau)$ with a Gaussian function $h(t)$ having a full-width at half maximum (FWHM) of $\sqrt{2}\Delta t_d$, where $\Delta t_d = 400$ ps is the detector resolution. The factor $\sqrt{2}$ accounts for the combined effect of using two detectors in the Hanbury-Brown Twiss interferometer, since the convolution of two Gaussian functions yields another Gaussian with a FWHM scaled by $\sqrt{2}$. As a result, the function $h(t)$ is given by

$$h(t) = \exp\left[-\left(\frac{t\sqrt{2\ln 2}}{\Delta t_d}\right)^2\right], \tag{4.38}$$

and the convolution is calculated as

$$C[g^{(2)}(\tau)] = \int_{-\infty}^{\infty} h(t) g^{(2)}(\tau - t) dt. \tag{4.39}$$

We plot in Figs. 4.6a (using the same laser and molecular parameters as in Fig. 4.5b) and 4.6b (same parameters as in Fig. 4.5d) the convolved Stokes-shifted correlation $C[g^{(2)}_{\mathrm{St}}(\tau)]$ (dashed orange lines, including the influence of quantum coherence) and $C[g^{(2)}_{\mathrm{St,d}}(\tau)]$ (dashed light green lines, neglecting the influence of quantum coherence). For reference, we also plot the correlations $g^{(2)}_{\mathrm{St}}(\tau)$ (solid red lines) and $g^{(2)}_{\mathrm{St,d}}(\tau)$ (solid green lines) that do not consider the effect of the

convolution, as well as the experimental results (grey lines). Figure 4.6 shows that the only significant impact of the convolution is the disappearance of the narrow peaks predicted at $\tau = 0$ when quantum coherence is taken into account. The linewidth of these peaks is comparable to the vibrational lifetime (tens of picoseconds) and, thus, much narrower than the detector resolution (400 ps). Notably, the bumps exhibited by $g^{(2)}_{\mathrm{St,d}}(\tau)$ at $\tau \approx \pm 10$ ns in Fig. 4.5d (which are not found in the experiments nor in the simulations with the complete model including quantum coherence) are also exhibited by $C[g^{(2)}_{\mathrm{St,d}}(\tau)]$, see Fig. 4.6b. Thus, the absence of these bumps in the experimental data is not due to the detector resolution, strongly supporting that quantum coherence plays a significant role in the emission of Stokes-shifted photons.

4.3.4 Two emitters separated by large distances

We analyze in this section the correlation of Stokes-shifted photons emitted from two distant emitters and find that quantum coherence again plays an important role. This analysis is motivated by the discrepancy between the theoretical predictions and experimental measurements of the intensity correlation of light emitted from ensembles of uncorrelated emitters at delay $\tau = 0$. Specifically, theoretical descriptions of light emission from N resonantly driven uncorrelated two-level quantum emitters yield $g^{(2)}(\tau = 0) = 2(1 - 1/N)$ [210–212], as long as the emitters are almost identical and equally pumped. Thus, $g^{(2)}(\tau = 0) = 1$ is expected in the particular case of $N = 2$ uncorrelated emitters. However, as far as we know, available experiments up to date have reported $g^{(2)}(\tau = 0) \approx 0.5$ independently of the particular implementation of the two-level quantum emitters [50, 51, 213, 214]. To shed light into this discrepancy, we consider a situation where $r_{12} = 400$ nm (which yields a negligible dipole-dipole coupling). Additionally, we consider again that the laser excitation impinges perpendicularly to the plane in which the transition dipole moments and the molecules are contained, and that light is detected also in this normal direction, as sketched in Fig. 4.7a. The detuning between the transition frequencies of the two emitters is $\delta = \omega_{e,1} - \omega_{e,2} = 5\gamma_0$ and the laser frequency is fixed at $\omega_L = \omega_0 = (\omega_{e,1} + \omega_{e,2})/2$. The rest of parameters are specified in the third row of Table 4.1.

We plot in Figs. 4.7b and 4.7c the simulation of $g^{(2)}_{\mathrm{St}}(\tau)$ obtained with the complete model (red lines, including the influence of quantum coherence) and with the approximate expression $g^{(2)}_{\mathrm{St,d}}(\tau)$ (green lines, neglecting the influence of quantum coherence). The complete model yields $g^{(2)}_{\mathrm{St}}(\tau = 0) = 1$, with a fast decay in the time scale of the vibrational lifetime (tens of picoseconds) to 0.5 (i.e., to the value measured in available experiments [50, 51, 213, 214]). To better characterize the origin of this fast decay, we plot in Fig. 4.7d the behaviour of each of the contributions in which we have decomposed $g^{(2)}_{\mathrm{St}}(\tau)$ in Eq. (4.30). We obtain that $G^{(2)}_{\mathrm{coh,I}}(\tau)$ is again responsible of this fast decay. Specifically, we find that the coherence encoded in $G^{(2)}_{\mathrm{coh,I}}(\tau)$ at $\tau = 0$ [Eq. (4.37)] is lost in the timescale of the

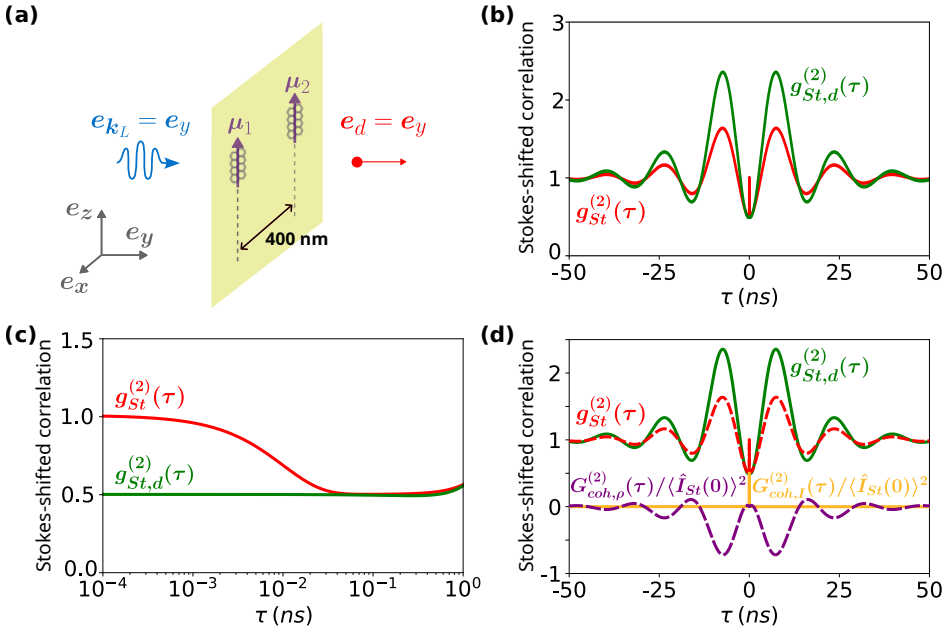

Figure 4.7: Impact of quantum coherence on the correlation of Stokes-shifted photons emitted from two distant DBATT molecules. (a) Schematic representation of the molecular pair analyzed in (b), (c) and (d). The molecules are in a H-configuration and separated by $r_{12} = 400$ nm in the x direction. The laser excitation impinges in the normal direction to the xz-plane in which the molecules are located and tuned to the two-photon resonance. Additionally, light is detected also in the normal direction to this plane. The rest of the parameters are detailed in the third row of Table 4.1. (b) Dependence on the time delay τ of the simulated Stokes-shifted correlation $g^{(2)}_{\mathrm{St}}(\tau)$ (red lines), which is obtained with the complete model [Eq. (4.30)] and includes the influence of quantum coherence, and of the simulated Stokes-shifted correlation $g^{(2)}_{\mathrm{St,d}}(\tau)$ (green lines), which is obtained with the approximation that removes the influence of quantum coherence [Eq. (4.35)]. (c) Zoom of the results in (b) from $\tau = 10^{-4}$ ns to $\tau = 10^{0}$ ns. A logarithmic scale is used in the x-axis of this figure to facilitate the analysis. (d) Dependence on the time delay τ of the different contributions in which $g^{(2)}_{\mathrm{St}}(\tau)$ (dashed red line) can be decomposed according to Eq. (4.30). The green line corresponds to $g^{(2)}_{\mathrm{St,d}}(\tau) = G^{(2)}_{\mathrm{d}}(\tau)/\langle\hat{I}_{\mathrm{St}}(0)\rangle^2$, the orange line to $G^{(2)}_{\mathrm{coh,I}}(\tau)/\langle\hat{I}_{\mathrm{St}}(0)\rangle^2$, and the dashed purple line to $G^{(2)}_{\mathrm{coh},\rho}(\tau)/\langle\hat{I}_{\mathrm{St}}(0)\rangle^2$.

vibrational lifetime, which can be attributed to the vibrational modes acting as a dephasing channel [210]. Notably, this fast decay cannot be resolved in available experiments due to the time resolution of the detectors, as discussed in Section 4.3.3. Therefore, we conclude that the discrepancy between theoretical predictions and experimental measurements of the intensity correlation of light emitted from two uncorrelated emitters at delay $\tau = 0$ is due to the insufficient time resolution of the detectors.

Furthermore, at times longer than the vibrational lifetime (on the nanosecond

timescale), the Stokes-shifted correlations shown in Fig. 4.7b exhibit pronounced oscillations at a frequency given by the generalized Rabi frequency [Eq. (1.231)], which at this laser frequency is $\Omega_R = \sqrt{(\delta/2)^2 + |\Omega_j|^2}$. Importantly, the oscillations exhibited by $g^{(2)}_{\mathrm{St}}(\tau)$ (red line) and by $g^{(2)}_{\mathrm{St,d}}(\tau)$ (green line) strongly differ in amplitude, which indicates that quantum coherence also influences the correlation of Stokes-shifted photons emitted from two non-interacting emitters at long times. Figure 4.7d shows that the coherence encoded in $G^{(2)}_{\mathrm{coh},\rho}(\tau)$ [Eq. (4.34)] is responsible for the difference at long times in the amplitudes of $g^{(2)}_{\mathrm{St}}(\tau)$ and $g^{(2)}_{\mathrm{St,d}}(\tau)$ in Fig. 4.7b.

4.4 Comparison between ZPL and Stokes-shifted correlations

So far, we have presented in Section 4.2 a model that allows us to compute the correlation of Stokes-shifted photons and that of ZPL photons emitted from solid-state quantum emitters, and we have analyzed in Section 4.3 the influence of quantum coherence in the emission of Stokes-shifted photons, which is ignored by the conditional-probability approach. In this section, we now compare the correlation of ZPL photons and of Stokes-shifted photons emitted from two interacting DBATT molecules and show that these two correlations can be drastically different. To this end, we simulate the experimental configuration in Ref. [1], which measured the statistics of the Stokes-shifted photons emitted from two strongly interacting molecules in a J-configuration, as sketched in Fig. 4.8a. Additionally, light is detected again in the normal direction to the plane in which the molecules and the transition dipole moments are contained ($\varphi_{\mathrm{ZPL}} = \varphi_{\mathrm{St}} = 0$), and the excitation laser impinges also in the normal direction to this plane. The rest of molecular and laser parameters are specified in the fourth row of Table 4.1. Notably, the Rabi frequencies Ω_j are again estimated from the value of the laser intensity used in the experiment and the experimental saturation intensity, which in this case are $I_L = 60$ W/cm^2 and $I_{\mathrm{sat}} = 14$ W/cm^2, using Eq. (1.237).

4.4.1 Laser resonantly tuned to the superradiant state

We first plot in Fig. 4.8b the intensity correlation when the laser is tuned resonantly to the superradiant state, which in the J-aggregate configuration corresponds to the delocalized state $|\Lambda_-\rangle = -\sin\Theta_\Lambda\,|g_1e_2\rangle + \cos\Theta_\Lambda\,|e_1g_2\rangle$ [Eq. (3.59b)], with the angle Θ_Λ defined in Eqs. (3.60a)–(3.60b). The transition frequency of this state is $\omega_0 - \Lambda$ (Section 3.2.1). We find that the intensity correlation of Stokes-shifted photons (dashed red line) is almost identical to the correlation of ZPL photons (solid blue line), both exhibiting antibunching and Rabi oscillations due to the approximately TLS-like behaviour of the interacting system under this laser frequency and intensity, as discussed in detail in Section 3.3.4. The intensity correlation obtained experimentally in Ref. [1] (solid grey line) is well reproduced

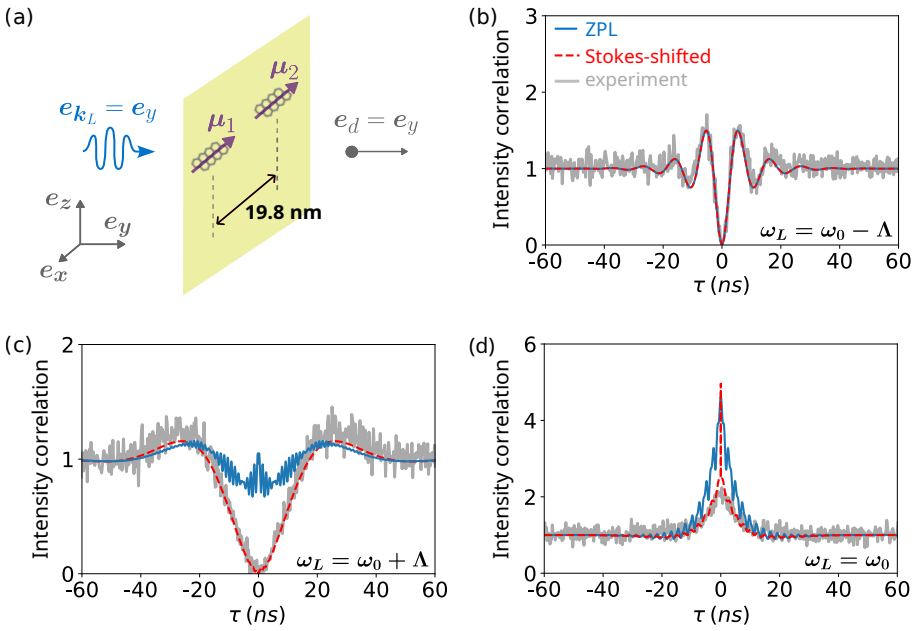

Figure 4.8: Comparison of the correlation of ZPL photons and of Stokes-shifted photons emitted from two strongly interacting DBATT molecules. (a) The two molecules are in J-configuration. The laser excitation impinges in the normal direction to the plane in which the molecules and the transition dipole moments are contained. Light is detected also in the normal direction to this plane. The laser is tuned resonantly to the (b) superradiant state $|\Lambda_-\rangle$ ($\omega_L = \omega_0 - \Lambda$), (c) subradiant state $|\Lambda_+\rangle$ ($\omega_L = \omega_0 + \Lambda$), and (d) two-photon resonance ($\omega_L = \omega_0$). The simulated intensity correlation of ZPL (solid blue line) and Stokes-shifted (dashed red line) light are plotted as a function of the time delay τ. Solid grey line corresponds to the experimental results reported in Ref. [1]. All the parameters are specified in the fourth row of Table 4.1.

by the two simulations.

4.4.2 Laser resonantly tuned to the subradiant state

We next plot in Fig. 4.8c the intensity correlation when the laser is tuned resonantly to the subradiant state $|\Lambda_+\rangle = \cos\Theta_\Lambda |g_1 e_2\rangle + \sin\Theta_\Lambda |e_1 g_2\rangle$ [Eq. (3.59a)], with transition frequency $\omega_0 + \Lambda$. In this case, the simulated correlation of ZPL photons and of Stokes-shifted photons show a very different behaviour. The correlation of Stokes-shifted photons exhibits again antibunching, Rabi oscillations and, crucially, an excellent agreement with the experimental measurements. In contrast, the correlation of ZPL photons shows $g^{(2)}_{\mathrm{ZPL}}(0) \approx 1$ and oscillations with two different timescales, one corresponding to Rabi oscillations and the other to much faster oscillations of frequency 2Λ. The faster oscillations can be attributed to the

significant interference between the superradiant and the subradiant states obtained under this laser frequency, which is discussed in detail in Section 3.3.5. These interference processes do not affect the Stokes-shifted correlation because the emitters couple only through the ZPL.

To gain further insights into the different value of the two correlations at $\tau = 0$ in Fig. 4.8c, we derive analytical expressions of the Stokes-shifted correlation and the ZPL correlation at delay $\tau = 0$. On the one hand, by rewriting Eq. (3.90) in the uncoupled basis, we obtain that the ZPL correlation at $\tau = 0$ is

$$g^{(2)}_{\mathrm{ZPL}}(0) = \frac{4p_{ee}}{\left[2p_{ee} + p_{eg} + p_{ge} + 2\mathrm{Re}\rho_{eg,ge}\right]^2}. \tag{4.40}$$

On the other hand, by using Eqs. (4.25), (4.27), (4.36), and (4.37), we obtain that the Stokes-shifted correlation at $\tau = 0$ is given by

$$g^{(2)}_{\mathrm{St}}(0) = \frac{4p_{ee}}{\left[2p_{ee} + p_{eg} + p_{ge}\right]^2}. \tag{4.41}$$

The populations p_{ev} and p_{ve} are neglected here, as they are much smaller than the populations of the pure electronic states. Importantly, the coherence between $|e_1 v_2\rangle$ and $|v_1 e_2\rangle$ does not affect the denominator in Eq. (4.41) because the emitters couple only through the purely electronic states, as discussed in Section 4.3.1. Equations (4.40) and (4.41) indicate that the correlation of ZPL and that of Stokes-shifted photons can be different at $\tau = 0$ if the coherence $\mathrm{Re}\rho_{eg,ge}$ is comparable to the value of the steady-state populations p_{eg} and p_{ge}. As discussed in Section 3.3.5, the coherence between the superradiant and subradiant states is significant when the laser is tuned resonantly to the transition frequency of the subradiant state, as it is the case in Fig. 4.8c. Particularly, for the laser parameters in this figure, $\mathrm{Re}\rho_{eg,ge}$ is negative and comparable to the values of the steady-state populations p_{eg} and p_{ge}, decreasing the denominator of the ZPL correlation in comparison to the denominator of the Stokes-shifted correlation. As a result, the value of ZPL correlation at $\tau = 0$ significantly increases with respect to the value of the Stokes-shifted correlation.

4.4.3 Laser tuned to the two-photon resonance

Last, we show in Fig. 4.8d the intensity correlation when the laser is tuned to the two-photon resonance, $\omega_L = \omega_0$. In this case, both the correlation of ZPL photons and of Stokes-shifted photons are bunched, as this laser frequency enables the resonant excitation of the doubly-excited state $|e_1 e_2\rangle$ through a two-photon process, which strongly increases the probability of emitting photons in cascade (Section 3.3.3). Additionally, the two correlations exhibit oscillations of frequency Λ, corresponding to the detuning between the laser frequency and the transition

frequency of the superradiant state. However, the ZPL correlation exhibits more pronounced oscillations and does not capture well the experimental measurements, whereas the Stokes-shifted correlation reproduces them very well. These results reveal that the correlation of Stokes-shifted photons and of ZPL photons emitted from two strongly interacting quantum emitters can be very different and emphasize the importance of an accurate description of each experimental configuration.

4.5 Extension of the model to a larger number of emitters and vibrational modes

We have analyzed so far the correlation of Stokes-shifted photons emitted from two solid-state emitters due to the decay from the electronic excited state to a specific vibrational/phononic mode. However, many vibrational/phononic modes can couple with the electronic states of solid-state emitters, giving rise to the emission of Stokes-shifted photons at different frequencies. We examine in this section the influence of a larger number of vibrational modes on the Stokes-shifted correlation of photons from two interacting emitters. Finally, we extend the model to the case of an arbitrary number of quantum emitters, each one supporting an arbitrary number of vibrational/phononic modes.

4.5.1 Influence of a larger number of vibrational modes

To illustrate the influence of a larger number of vibrational modes on the Stokes-shifted correlation we first consider two quantum emitters, each of them supporting two vibrational modes of frequencies $\omega_v^{(1)}$ and $\omega_v^{(2)}$. The corresponding 1-phonon states of these modes are denoted by $|v_j^{(m)}\rangle$, where $j = 1, 2$ labels each of the emitters and $m = 1, 2$ each of the vibrational modes. We represent an scheme of the energy levels of the uncoupled emitters in the inset of Fig. 4.9a. The Hamiltonian of the system (in the rotating frame at the laser frequency) can be written as

$$\hat{H} = \hbar \sum_{j=1}^{2} \left[\frac{\Delta_j}{2} (|e_j\rangle \langle e_j| - |g_j\rangle \langle g_j|) + \sum_{m=1}^{2} \frac{2\omega_v^{(m)} - \Delta_j}{2} |v_j^{(m)}\rangle \langle v_j^{(m)}| \right] + \hat{H}_{\text{int}} + \hat{H}_L, \tag{4.42}$$

where the interaction and laser Hamiltonians are again given as $\hat{H}_{\text{int}} = \hbar V_{\text{DW}} (\hat{\sigma}_1^\dagger \hat{\sigma}_2 + \hat{\sigma}_1 \hat{\sigma}_2^\dagger)$ and $\hat{H}_L = -\frac{\hbar}{2} \sum_{j=1}^{2} (\Omega_j \hat{\sigma}_j^\dagger + \Omega_j^* \hat{\sigma}_j)$, respectively. The Markovian master equation including the dissipative processes and governing the dynamics of the

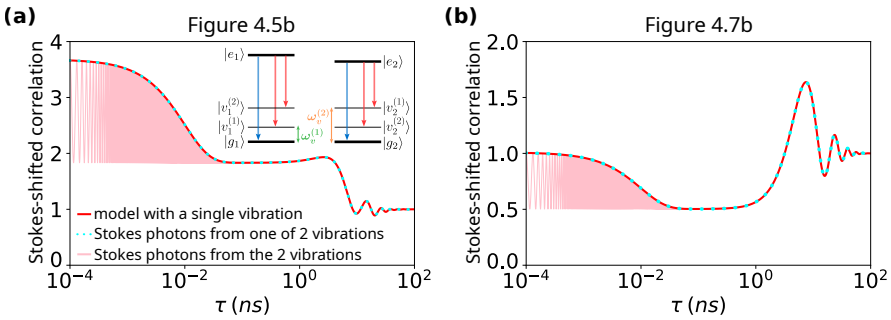

Figure 4.9: Comparison of the simulated correlation of Stokes-shifted photons emitted from two DBATT molecules when different numbers of 1-phonon states are considered. Red lines represent simulations obtained using the model presented in Section 4.2, where a single 1-phonon state is considered in each emitter (specifically, the vibrational mode at 257 cm^{-1} of the DBATT molecules). Additionally, we perform simulations using the master equation in Eq. (4.43), where two 1-phonon states are considered, $|v_j^{(1)}\rangle$ (with frequency $\omega_v^{(1)}$ corresponding to the vibrational mode at 257 cm^{-1} of the DBATT molecules) and $|v_j^{(2)}\rangle$ (with frequency $\omega_v^{(2)}$ corresponding to the vibrational mode at 1331 cm^{-1} of the DBATT molecules). In the inset in (a) we depict the energy levels, the different Stokes-shifted transitions (red arrows) and the ZPL transitions (blue arrows). We use the model that includes two 1-phonon levels for each emitter to simulate the correlation of Stokes-shifted photons in two different scenarios: (i) considering the Stokes-shifted photons emitted due to the assistance of the two vibrational levels of each emitter (solid pink lines); and (ii) considering only the Stokes-shifted photons emitted due to the assistance of the vibrational mode of frequency $\omega_v^{(1)}$ (dotted cyan lines), which experimentally corresponds to filtering only the Stokes-shifted photons from this vibrational mode. In (a) we fix the molecular configuration to that used in Fig. 4.5b, where two interacting molecules are driven by a laser tuned to the two-photon resonance $\omega_L = \omega_0$ (all the parameters are detailed in the second row of Table 4.1), and in (b) we simulate the molecular configuration used in Fig. 4.7b, where the two emitters are at very far distances and again $\omega_L = \omega_0$ (all the parameters are specified in the third row of Table 4.1).

system is given as

$$\frac{d}{dt}\hat{\rho} = -\frac{i}{\hbar}[\hat{\tilde{H}}, \hat{\rho}] + \sum_{j=1}^{2}\left(\frac{\alpha_{\text{DW}}\gamma_0}{2}\mathcal{D}[\hat{\sigma}_j]\hat{\rho} + \sum_{k\neq j}\frac{\tilde{\gamma}_{\text{DW}}}{2}\mathcal{D}[\hat{\sigma}_j, \hat{\sigma}_k]\hat{\rho}\right) + \sum_{j=1}^{2}\sum_{m=1}^{2}\left(\frac{(1-\alpha_{\text{DW}})\gamma_0}{4}\mathcal{D}[|v_j^{(m)}\rangle\langle e_j|]\hat{\rho} + \frac{\gamma_v}{2}\mathcal{D}[|g_j\rangle\langle v_j^{(m)}|]\hat{\rho}\right), \tag{4.43}$$

where we have assumed that the vibrations have identical decay rate γ_v and that the decay rate from $|e_j\rangle$ to $|v_j^{(1)}\rangle$ is $(1-\alpha_{\text{DW}})\gamma_0/2$ and identical to the decay rate from $|e_j\rangle$ to $|v_j^{(2)}\rangle$. These latter dissipation processes are represented by red arrows in the inset in Fig. 4.9a, whereas the dissipation into the Zero-Phonon Line (having decay rate $\alpha_{\text{DW}}\gamma_0$) is represented with blue arrows.

We next simulate the correlation of Stokes-shifted photons emitted from two DBATT molecules at cryogenic temperatures. We use $\hbar\omega_v^{(1)} = 31.86$ meV and $\hbar\omega_v^{(2)} = 165.02$ meV, which correspond to the DBATT vibrational modes at 257 cm^{-1} and 1331 cm^{-1} [208], respectively. In Fig. 4.9a we fix the same molecular H-configuration as in Fig. 4.5b, where the two molecules strongly interact, and in Fig. 4.9b we use the same molecular parameters as in Fig. 4.7b, where the two molecules are separated by a large distance (see the second and third rows of Table 4.1 for further details on the parameters considered). In both cases, the laser is tuned to the two-photon resonance $\omega_L = \omega_0$. We use $\hat{E}^{(+)}_{\perp,\mathrm{St}}(t)/\xi_{\mathrm{St}} = \sum_m |v_1^{(m)}\rangle \langle e_1|(t) + |v_2^{(m)}\rangle \langle e_2|(t)$ to calculate the intensity correlation of Stokes-shifted photons emitted from the two molecules due to the assistance of the two-vibrational modes. At delay times larger than the lifetime of the vibrations ($|\tau| \gg 1/\gamma_v$), the resulting intensity correlation (solid pink line) shows the same behaviour than the simulation obtained in Fig. 4.5b (red solid line), where a single vibrational mode was considered in the master equation. However, on the timescale of the vibrational lifetime, we find that the decay of the intensity correlation to half its $\tau = 0$ value (which is due to the loss of coherence, as discussed in Section 4.3) is accompanied by fast oscillations at frequency $\omega_v^{(2)} - \omega_v^{(1)}$.

Furthermore, we calculate the intensity correlation using $\hat{E}^{(+)}_{\perp,\mathrm{St}}(t)/\xi_{\mathrm{St}} = |v_1^{(1)}\rangle \langle e_1|(t) + |v_2^{(1)}\rangle \langle e_2|(t)$ (cyan dotted line), which represents the correlation of Stokes-shifted photons that are due only to the assistance of the vibrational mode at 257 cm^{-1}. We find that this latter simulated intensity correlation is identical to the one obtained in Fig. 4.5b (red solid line) using a Markovian master equation that includes a single vibrational mode. Therefore, we conclude that the Stokes-shifted correlation of light emitted from two quantum emitters is well described by using a single vibrational mode in the model (as we do in Sections 4.3 and 4.4), except for the exact behaviour of the correlation at times comparable to the lifetime of the vibrations. The behaviour at this timescale is hard to capture in experiments, due to the limitations of the time resolution of available detectors (see Section 4.3.3), and depends on the exact filtering scheme used in the experiment, as shown in Figs. 4.9a and 4.9b.

4.5.2 Extension of the model to an arbitrary number of emitters

We extend in this section the model described in Section 4.2 to the case of an arbitrary number $N \geq 2$ of almost identical emitters. Additionally, we consider that the emitter j supports an arbitrary number M_j of vibrational/phononic modes. In this case, the total Hamiltonian (in the rotating frame at the laser frequency) is

given by

$$\hat{H} = \hbar \sum_{j=1}^{N} \left[\frac{\Delta_j}{2} (|e_j\rangle \langle e_j| - |g_j\rangle \langle g_j|) + \sum_{m=1}^{M_j} \frac{2\omega_v^{(j,m)} - \Delta_j}{2} |v_j^{(m)}\rangle \langle v_j^{(m)}| \right] + \hat{H}_{\text{int}} + \hat{H}_L, \tag{4.44}$$

where $\omega_v^{(j,m)}$ is the frequency of the vibrational/phononic mode m of the emitter j. The laser Hamiltonian can be written as

$$\hat{H}_L = -\frac{\hbar}{2} \sum_{j=1}^{N} (\Omega_j \hat{\sigma}_j^\dagger + \Omega_j^* \hat{\sigma}_j). \tag{4.45}$$

Additionally, the interaction Hamiltonian $\hat{H}_{\text{int}}$ in Eq. (4.44) includes all possible dipole-dipole couplings between different emitters. Specifically,

$$\hat{H}_{\text{int}} = \hbar \sum_{i}^{N} \sum_{j<i}^{N} V_{\text{DW},ij} (\hat{\sigma}_i^\dagger \hat{\sigma}_j + \hat{\sigma}_i \hat{\sigma}_j^\dagger), \tag{4.46}$$

where

$$\begin{aligned} V_{\text{DW},ij} = \frac{3}{4} \alpha_{\text{DW}} \gamma_0 \Bigg[& -\Big(\boldsymbol{e}_{\boldsymbol{\mu}_i} \cdot \boldsymbol{e}_{\boldsymbol{\mu}_j} - (\boldsymbol{e}_{\boldsymbol{\mu}_i} \cdot \boldsymbol{e}_{\boldsymbol{r}_{ij}})(\boldsymbol{e}_{\boldsymbol{\mu}_j} \cdot \boldsymbol{e}_{\boldsymbol{r}_{ij}}) \Big) \frac{\cos(\mathrm{k}_{0,ij} r_{ij})}{\mathrm{k}_{0,ij} r_{ij}} \\ & + \Big(\boldsymbol{e}_{\boldsymbol{\mu}_i} \cdot \boldsymbol{e}_{\boldsymbol{\mu}_j} - 3(\boldsymbol{e}_{\boldsymbol{\mu}_i} \cdot \boldsymbol{e}_{\boldsymbol{r}_{ij}})(\boldsymbol{e}_{\boldsymbol{\mu}_j} \cdot \boldsymbol{e}_{\boldsymbol{r}_{ij}}) \Big) \left(\frac{\sin(\mathrm{k}_{0,ij} r_{ij})}{(\mathrm{k}_{0,ij} r_{ij})^2} + \frac{\cos(\mathrm{k}_{0,ij} r_{ij})}{(\mathrm{k}_{0,ij} r_{ij})^3} \right) \Bigg] \end{aligned} \tag{4.47}$$

is the strength of the coherent dipole-dipole coupling between emitters i and j, which have transition dipole moments $\boldsymbol{\mu}_i$ and $\boldsymbol{\mu}_j$, and are located at positions $\boldsymbol{r}_i$ and $\boldsymbol{r}_j$. In Eq. (4.47), we have also introduced the wavenumber $\mathrm{k}_{0,ij} = 2\pi/(n\omega_{0,ij})$, with $\omega_{0,ij} = (\omega_{e,i} + \omega_{e,j})/2$ the arithmetic average between the transition frequency $\omega_{e,i}$ of emitter i and the transition frequency $\omega_{e,j}$ of emitter j, as well as the unit vectors $\boldsymbol{e}_{\boldsymbol{\mu}_i} = \boldsymbol{\mu}_i/|\boldsymbol{\mu}_i|$, $\boldsymbol{e}_{\boldsymbol{\mu}_j} = \boldsymbol{\mu}_j/|\boldsymbol{\mu}_j|$, and $\boldsymbol{e}_{\boldsymbol{r}_{ij}} = (\boldsymbol{r}_i - \boldsymbol{r}_j)/r_{ij}$, with $r_{ij} = |\mathbf{r}_i - \mathbf{r}_j|$ the distance between the emitters i and j.

Moreover, the Markovian master equation in Eq. (4.43) can be directly generalized as

$$\begin{aligned} \frac{d}{dt}\hat{\rho} = & -\frac{i}{\hbar}[\hat{H}, \hat{\rho}] + \sum_{j=1}^{N} \frac{\alpha_{\text{DW}}\gamma_0}{2} \mathcal{D}[\hat{\sigma}_j]\hat{\rho} + \sum_{j=1}^{N} \sum_{i \neq j} \frac{\tilde{\gamma}_{\text{DW},ij}}{2} \mathcal{D}[\hat{\sigma}_j, \hat{\sigma}_i]\hat{\rho} \\ & + \sum_{j=1}^{N} \sum_{m=1}^{M_j} \frac{\gamma_{e-v}^{(j,m)}}{2} \mathcal{D}[|v_j^{(m)}\rangle \langle e_j|]\hat{\rho} + \sum_{j=1}^{N} \sum_{m=1}^{M_j} \frac{\gamma_v^{(j,m)}}{2} \mathcal{D}[|g_j\rangle \langle v_j^{(m)}|]\hat{\rho}, \end{aligned} \tag{4.48}$$

where the dissipative dipole-dipole coupling between emitters i and j is given by

$$\tilde{\gamma}_{\mathrm{DW},ij} = \frac{3}{2}\alpha_{\mathrm{DW}}\gamma_0\left[\left(\boldsymbol{e}_{\boldsymbol{\mu}_i}\cdot\boldsymbol{e}_{\boldsymbol{\mu}_j} - (\boldsymbol{e}_{\boldsymbol{\mu}_i}\cdot\boldsymbol{e}_{\boldsymbol{r}_{ij}})(\boldsymbol{e}_{\boldsymbol{\mu}_j}\cdot\boldsymbol{e}_{\boldsymbol{r}_{ij}})\right)\frac{\sin(\mathrm{k}_{0,ij}r_{ij})}{\mathrm{k}_{0,ij}r_{ij}} + \left(\boldsymbol{e}_{\boldsymbol{\mu}_i}\cdot\boldsymbol{e}_{\boldsymbol{\mu}_j} - 3(\boldsymbol{e}_{\boldsymbol{\mu}_i}\cdot\boldsymbol{e}_{\boldsymbol{r}_{ij}})(\boldsymbol{e}_{\boldsymbol{\mu}_j}\cdot\boldsymbol{e}_{\boldsymbol{r}_{ij}})\right)\left(\frac{\cos(\mathrm{k}_{0,ij}r_{ij})}{(\mathrm{k}_{0,ij}r_{ij})^2} - \frac{\sin(\mathrm{k}_{0,ij}r_{ij})}{(\mathrm{k}_{0,ij}r_{ij})^3}\right)\right]. \tag{4.49}$$

Further, $\gamma_v^{(j,m)}$ in Eq. (4.48) is the decay rate of the vibrational/phononic mode m of the emitter j (i.e., $1/\gamma_v^{(j,m)}$ is the lifetime of this vibrational/phononic mode), while $\gamma_{e-v}^{(j,m)}$ is the decay rate of the excited state $|e_j\rangle$ into the 1-phonon level $|v_j^{(m)}\rangle$. Notably, as the total decay rate of emitter j is γ_0 and the decay rate into the ZPL is $\alpha_{\mathrm{DW}}\gamma_0$, the set of decay rates into of 1-phonon levels satisfy

$$\sum_{m}^{M_j}\gamma_{e-v}^{(j,m)} = (1-\alpha_{\mathrm{DW}})\gamma_0. \tag{4.50}$$

Assuming again that all the molecules and their transition dipole moments are contained in the same plane and that light is detected in the normal direction to this plane, the correlation of ZPL photons can be then obtained by substituting the positive-frequency electric field operator $\hat{E}^{(+)}_{\perp,\mathrm{ZPL}}(\tau)/\xi_{\mathrm{ZPL}} = \sum_{j=1}^{N}|g_j\rangle\langle e_j|(\tau)$ into the expression for $g^{(2)}_{\mathrm{ZPL}}(\tau)$ in Eq. (4.17). In the same conditions, the positive-frequency electric field operator in Eq. (4.19), which describes the Stokes-shifted scattering from two emitters that support a vibrational mode each, can be extended to the case of an arbitrary number of emitters and vibrations as

$$\hat{E}^{(+)}_{\perp,\mathrm{St}}(\tau) \propto \sum_{j=1}^{N}\sum_{m=1}^{M_j}\sqrt{\gamma_{e-v}^{(j,m)}\left(\omega_0-\omega_v^{(j,m)}\right)}\,|v_j^{(m)}\rangle\langle e_j|(\tau). \tag{4.51}$$

Here, we have taken into account that the vector amplitude $\boldsymbol{\mathcal{E}}_{\boldsymbol{\mu}}$ of the positive-frequency electric field radiated from a classical point dipole with decay rate $\gamma_{e-v}^{(j,m)}$ and frequency $\omega_0-\omega_v^{(j,m)}$ in the far-field region is proportional to $\sqrt{\gamma_{e-v}^{(j,m)}(\omega_0-\omega_v^{(j,m)})}$ [see Eqs. (1.141) and (1.163)]. This square root factor has been neglected in Section 4.5.1 for simplicity, as its value is almost identical for the two molecular vibrations considered there and, thus, it does not notably affect the intensity correlations in Figs. 4.9a and 4.9b.

4.6 Summary and conclusions

We have analyzed in this chapter the correlation of Stokes-shifted photons emitted from two solid-state quantum emitters. The main interest of this analysis relies on the interpretation of state-of-the-art experiments with quantum emitters that

interact through vacuum-induced dipole-dipole coupling, where the emitters are excited on resonance to their electronic excited state and only the Stokes-shifted light is detected due to the use of optical filters. First, we have reviewed the conditional-probability approach used in previous works to address the correlation of Stokes-shifted photons [1, 92, 199], which does not account for the influence of quantum coherence in the Stokes-shifted emission. Afterwards, we have presented a versatile model that can be used to describe the correlation of Stokes-shifted photons and also that of ZPL photons from two quantum emitters. Importantly, this model accounts for the influence of quantum coherence.

By using this complete model, we have shown that quantum coherence can indeed significantly impact the correlation of Stokes-shifted photons emitted from two interacting quantum emitters. To this end, we have compared the results of experimental measurements of the Stokes-shifted correlation from two interacting DBATT molecules with those from the simulations of the complete model introduced here. In this way, it has been revealed that including the influence of quantum coherence provides a better agreement with experimental results. Furthermore, we have shown that quantum coherence can also impact the correlation of Stokes-shifted photons emitted from two non-interacting emitters. We have also found that the discrepancy between theoretical and experimental intensity correlations of light from two uncorrelated emitters at delay $\tau = 0$ is due to the insufficient time resolution of the detectors in available experiments.

Moreover, we have revealed that the correlation of Stokes-shifted photons scattered from interacting emitters can exhibit significant differences with respect to the correlation of ZPL photons, depending on the molecular and laser parameters. These results emphasize the importance of an accurate description of each experimental configuration.

We have also shown that when Stokes-shifted photons of different frequencies (arising from the decays into different vibrational levels) are collected, the behaviour of the intensity correlation at very short timescales (on the order of the lifetime of the vibrations) becomes more involved. Specifically, we have found fast oscillations with a period given by the difference in frequency of the different vibrational modes. In contrast, at delay times that are much larger than the lifetime of the vibrations, the Stokes-shifted correlation is unaffected if Stokes-shifted photons from a single or from several vibrational/phononic modes are measured. Last, we have presented the extension of the model to the case in which an arbitrary number of emitters and vibrational modes are considered, which can be used in future works to explore more involved experimental configurations.

CHAPTER 5

GENERATION OF ENTANGLED PHOTONS FROM TWO INTERACTING QUANTUM EMITTERS

We have analyzed the normalized second-order correlation of Zero-Phonon-Line photons (Chapter 3) and of Stokes-shifted photons (Chapter 4) emitted from two interacting quantum emitters. This analysis has demonstrated that the statistics of light emitted from this system can be tailored across a wide range of regimes. In this chapter, we expand our analysis of light emission from interacting quantum emitters and its relevance for quantum technological applications. Specifically, we show that two interacting emitters can generate entangled photons, which are crucial elements in quantum communication, quantum cryptography, and other applications in quantum technologies.

We first introduce the concept of quantum entanglement and discuss the significance of designing sources of polarization-entangled photons. Next, we provide an intuitive explanation of how polarization-entangled photons can be generated from the decay into the Zero-Phonon Line from two interacting quantum emitters with perpendicular transition dipole moments. This relative orientation between the transition dipole moments contrasts with the parallel one considered in Chapters 3 and 4. Additionally, we rigorously verify the intuitive picture of the generation of two entangled photons by deriving the exact two-photon state of the electromagnetic vacuum field provided by the relaxation of two initially excited quantum emitters. To this end, we use the Wigner-Weisskopf approximation (WWA).

Moreover, we demonstrate that a highly entangled photon pair can be post-

selected using optical filters. We verify that this high degree of entanglement is not significantly affected by small changes in the orientation of the transition dipole moments or by the influence of the combined Debye-Waller/Franck-Condon factor. Further, we also show that the photon entanglement is not significantly affected by small changes in the detection directions, which indicates that a lens can be used to improve the collection efficiency in experiments without significantly reducing the high degree of photon entanglement.

Finally, we show that entangled photons can also be generated from two non-interacting emitters with perpendicular transition dipole moments. However, in this case the two-photon entangled state is less robust against small changes in the detection direction, which reduces its practical utility as compared to the entanglement produced by interacting emitters.

5.1 Photon entanglement

We introduce in this section the concept of quantum entanglement, with a special focus on entanglement between the polarization degree of freedom of two photons. Additionally, we describe a fundamental measure of the degree of polarization entanglement in a two-photon state, which is known as *entanglement entropy*, as well as a more practical measure, so-called *concurrence*.

5.1.1 Separable and entangled states

Entanglement refers to the non-local quantum correlation between the state of $N \geq 2$ distant quantum systems. We focus here on the simplest case, provided by $N = 2$ systems. We refer to the two systems as A and B, with Hilbert spaces $\mathcal{H}_A$ and $\mathcal{H}_B$, respectively. The Hilbert space of the whole system, $\mathcal{H}_{AB}$, is given by the tensor product of $\mathcal{H}_A$ and $\mathcal{H}_B$:

$$\mathcal{H}_{AB} = \mathcal{H}_A \otimes \mathcal{H}_B. \tag{5.1}$$

Importantly, the two systems are spatially separated, so that their states can be measured independently. The observer who can measure the state of A is commonly referred to as *Alice*, while the observer who can measure the state of B is called *Bob*.

Moreover, we consider that A and B have two-dimensional Hilbert spaces. Two-dimensional quantum systems are the fundamental building blocks of quantum information and quantum computing, and they are typically referred to as *qubits*. Examples include the electronic ground and excited states of two-level quantum emitters, the spin-up and spin-down states of spin-1/2 particles, and two orthogonal polarization modes of photons. Notably, photons are promising candidates for processing and distributing entanglement, as their quantum state is not significantly altered while photons travel long distances. Thus, we consider in this section two polarization-entangled photons as a representative example of qubits to illustrate entanglement in two-qubit systems. The polarization state of each photon can be

described in the orthonormal basis $\{|H\rangle_\chi, |V\rangle_\chi\}$ (with $\chi \in \{A, B\}$), where H and V denote horizontal and vertical polarizations, respectively.

An arbitrary two-photon pure state $|\psi\rangle_{AB} \in \mathcal{H}_{AB}$ can be written as

$$\begin{aligned} |\psi\rangle_{AB} &= c_{HH}\,|H\rangle_A \otimes |H\rangle_B + c_{HV}\,|H\rangle_A \otimes |V\rangle_B \\ &\quad + c_{VH}\,|V\rangle_A \otimes |H\rangle_B + c_{VV}\,|V\rangle_A \otimes |V\rangle_B \\ &= c_{HH}\,|H_A H_B\rangle + c_{HV}\,|H_A V_B\rangle + c_{VH}\,|V_A H_B\rangle + c_{VV}\,|V_A V_B\rangle\,, \end{aligned} \tag{5.2}$$

where we have chosen the two-photon state basis $\{|H\rangle_A \otimes |H\rangle_B = |H_A H_B\rangle$, $|H\rangle_A \otimes |V\rangle_B = |H_A V_B\rangle$, $|V\rangle_A \otimes |H\rangle_B = |V_A H_B\rangle$, $|V\rangle_A \otimes |V\rangle_B = |V_A V_B\rangle\}$, and we have introduced the two-photon probability amplitudes $c_{ss'}$, with $s, s' \in \{H, V\}$ labeling the polarization mode (as in Chapters 1–3). Notably, $|\psi\rangle_{AB}$ is called *separable* if it can be written as a tensor product of two individual states $|\psi^{(A)}\rangle_A \in \mathcal{H}_A$ and $|\psi^{(B)}\rangle_B \in \mathcal{H}_B$, which belong to the individual Hilbert spaces of A and B, respectively. Thus, the following equivalence holds:

$$|\psi\rangle_{AB} \text{ is separable } \Leftrightarrow |\psi\rangle_{AB} = |\psi^{(A)}\rangle_A \otimes |\psi^{(B)}\rangle_B\,. \tag{5.3}$$

For example, $|H_A H_B\rangle = |H\rangle_A \otimes |H\rangle_B$ is a separable state. Similarly, if any one of the probability amplitudes $c_{ss'}$ in Eq. (5.2) equals 1 and the rest are zero, the state is separable. Another example of separable state occurs when all the probability amplitudes $c_{ss'}$ equal $1/2$, because in this case

$$\begin{aligned} |\psi\rangle_{AB}\Big|_{c_{HH}=c_{HV}=c_{VH}=c_{VV}=1/2} &= \frac{1}{2}\,|H_A H_B\rangle + \frac{1}{2}\,|H_A V_B\rangle + \frac{1}{2}\,|V_A H_B\rangle + \frac{1}{2}\,|V_A V_B\rangle \\ &= \frac{|H\rangle_A + |V\rangle_A}{\sqrt{2}} \otimes \frac{|H\rangle_B + |V\rangle_B}{\sqrt{2}}. \end{aligned} \tag{5.4}$$

However, $|\psi\rangle_{AB}$ cannot always be written as a tensor product of two individual states. In such a case, $|\psi\rangle_{AB}$ is said to be an *entangled state*, that is:

$$|\psi\rangle_{AB} \text{ is entangled } \Leftrightarrow |\psi\rangle_{AB} \neq |\psi^{(A)}\rangle_A \otimes |\psi^{(B)}\rangle_B\,. \tag{5.5}$$

An entangled pure state is written as a coherent superposition of separable pure states. Consequently, the measurement of the individual state of either subsystem A or B has more than one possible outcome, regardless of the measurement basis. Crucially, measuring the individual state of one subsystem leads to the collapse of the entire quantum state $|\psi\rangle_{AB}$ into a separable state. This collapse determines the state of the other subsystem, without need of an individual measurement of its state. For example, the two-photon state

$$|\psi\rangle_{AB}\Big|_{c_{HV}=c_{VH}=0} = c_{HH}\,|H_A H_B\rangle + c_{VV}\,|V_A V_B\rangle\,, \tag{5.6}$$

which has non-zero two-photon probability amplitudes c_{HH} and c_{VV}, is an entangled state because it cannot be written as tensor product of two states. In this case, the measurement of the polarization state of photon A in the basis $\{|H\rangle_A, |V\rangle_A\}$ can yield both horizontal and vertical polarizations as outcomes, and so does measuring the state of photon B. However, once a measurement is made on A, the entire two-photon state collapses, determining the outcome of a measurement of the state of B. Specifically, if the outcome of the measurement of A gives horizontal polarization, this implies that the two-photon state $|\psi\rangle_{AB}|_{c_{HV}=c_{VH}=0}$ [Eq. (5.6)] has collapsed into $|H_A H_B\rangle$, determining an horizontal-polarization outcome for a measurement on B. In contrast, if the measurement of the polarization state of photon A in the two-photon entangled state $|\psi\rangle|_{c_{HV}=c_{VH}=0}$ [Eq. (5.6)] yields vertical polarization, the two-photon state $|\psi\rangle|_{c_{HV}=c_{VH}=0}$ collapses into $|V_A V_B\rangle$ and, thus, photon B is also vertically polarized. We emphasize that the outcome of measuring B was not determined prior to the measurement on A. Thus, as the measurements on the two systems are not independent in this case, but are correlated even if A and B are far apart, we say that there exists a non-local quantum correlation between the two systems. This non-local quantum correlation is commonly referred to as *entanglement*.

5.1.2 Bell states

We show in this section that the correlation between the outcomes of individual measurements on an entangled state is not equally strong for every entangled state. Importantly, we introduce a set of orthonormal two-photon states that exhibit maximal non-local quantum correlation.

We consider again two photons in the state $|\psi\rangle_{AB}|_{c_{HV}=c_{VH}=0}$ [Eq. (5.6)]. In this case, the measurement of the individual state of photon A has a probability $|c_{HH}|^2$ of yielding horizontal-polarization for the two photons as outcome and a probability $|c_{VV}|^2$ of giving vertical-polarization as outcome (again for the two photons). Notably, as $|c_{HH}|^2$ increases and $|c_{VV}|^2$ decreases, the state $|\psi\rangle_{AB}|_{c_{HV}=c_{VH}=0}$ becomes closer to the separable state $|H_A H_B\rangle$. As a consequence, the non-local quantum correlation between the outcomes of the measurement decreases, because the repetition of the experiment will yield most of the times the same outcomes as those provided by the separable state $|H_A H_B\rangle$. In contrast, the non-local quantum correlation maximizes at $|c_{HH}|^2 = |c_{VV}|^2 = 1/2$, as in this case the probability of measuring horizontal or vertical polarization for one of the photons (which leads to the collapse and determination of the state of the other photon) are equal. Additionally, if we fix real probability amplitudes for simplicity, we find that the condition $|c_{HH}|^2 = |c_{VV}|^2 = 1/2$ can be satisfied by two orthogonal states: one with $c_{HH} = c_{VV} = 1/\sqrt{2}$ and another with $c_{HH} = -c_{VV} = 1/\sqrt{2}$. Namely, these two states can be written as

$$|\phi_+\rangle_{AB} = \frac{|H_A H_B\rangle + |V_A V_B\rangle}{\sqrt{2}}, \tag{5.7a}$$

$$|\phi_-\rangle_{AB} = \frac{|H_A H_B\rangle - |V_A V_B\rangle}{\sqrt{2}}. \tag{5.7b}$$

We emphasize that these states exhibit maximal non-local quantum correlation and, as a consequence, they are referred to as *maximally entangled states*. In contrast, any state with $|c_{HV}|^2 = |c_{VH}|^2 = 0$ and unequal non-zero probabilities $|c_{HH}|^2 \neq |c_{VV}|^2$ is called *partially entangled*.

So far, we have focused on entangled states for which the two-photon probability amplitudes c_{HV} and c_{VH} vanish. However, two-photon states involving $|H_A V_B\rangle$ and $|V_A H_B\rangle$ can also exhibit maximal entanglement. Considering again real probability amplitudes, these states are

$$|\psi_+\rangle_{AB} = \frac{|H_A V_B\rangle + |V_A H_B\rangle}{\sqrt{2}}, \tag{5.8a}$$

$$|\psi_-\rangle_{AB} = \frac{|H_A V_B\rangle - |V_A H_B\rangle}{\sqrt{2}}. \tag{5.8b}$$

For these two-photon states, the measurement of the polarization state of A can yield horizontal or vertical outcomes with equal probability again. As a result of this measurement, the two-photon state collapse and the state of B becomes determined. Therefore, the states $|\psi_+\rangle_{AB}$ and $|\psi_-\rangle_{AB}$ are maximally entangled, like $|\phi_+\rangle_{AB}$ and $|\phi_-\rangle_{AB}$. The key difference between the states $|\psi_\pm\rangle_{AB}$ and the states $|\phi_\pm\rangle_{AB}$ is that in the ϕ states, photons A and B share the same polarization outcome upon measurement, while in the ψ states, their polarization outcomes are orthogonal and thus they show different polarization upon measurement. These four maximally entangled states are known as *Bell states*.

5.1.3 Degree of entanglement of pure states

We describe in this section how to quantify the degree of entanglement of two-qubit pure states, which is of great interest for technological applications because perfect maximally entangled states do not exist in practice.

Fidelity with respect to a maximally entangled state

A simple way to gain an intuition on the degree of entanglement of a two-photon state is to evaluate its similarity with respect to a maximally entangled state. A standard measure of the similarity between two states is the so-called *fidelity* $\mathcal{F}$, which we describe in detail in Appendix A. The fidelity between two arbitrary pure states $|a\rangle$ and $|b\rangle$ is defined as

$$\mathcal{F}(|a\rangle, |b\rangle) = |\langle a|b\rangle|^2. \tag{5.9}$$

This quantity ranges from 0 to 1. It reaches its maximum value when $|a\rangle$ and $|b\rangle$ are identical up to a global phase, and equals to zero when the states are orthogonal.

The fidelity of an arbitrary two-photon state $|\psi\rangle_{AB}$ with respect to a maximally

entangled state can thus provide information about the degree of entanglement of $|\psi\rangle_{AB}$. For example, $\mathcal{F}(|\psi\rangle_{AB}, |\phi_-\rangle_{AB}) = 1$ [with $|\phi_-\rangle_{AB}$ the Bell state in Eq. (5.7b)] implies that $|\psi\rangle_{AB}$ is also a maximally entangled state. Further, if $\mathcal{F}(|\psi\rangle_{AB}, |\phi_-\rangle_{AB})$ is close to one, we can reasonably conclude that the degree of entanglement of $|\psi\rangle_{AB}$ is large. However, this approach is limited because it quantifies the similarity with respect to a single reference state. Indeed, a low value of $\mathcal{F}(|\psi\rangle_{AB}, |\phi_-\rangle_{AB})$ does not necessarily mean that the degree of entanglement of $|\psi\rangle_{AB}$ is small, as $|\psi\rangle_{AB}$ may be more similar to another maximally entangled state different from $|\phi_-\rangle_{AB}$. Therefore, fidelity alone does not constitute a complete or general measure of entanglement.

Entanglement entropy

Quantifying the degree of entanglement is a challenging task in general [63–65]. However, in the simplest case of systems composed of two qubits, well defined measures of the degree of entanglement have been established. In the case of two-qubit pure states $|\psi\rangle_{AB}$, the *entanglement entropy* $E(|\psi\rangle_{AB})$ is the standard measure of the degree of entanglement. This measure relies on the *von Neumann entropy* $\mathcal{S}$ (Appendix A), which serves to quantify the entropy of any quantum system. Specifically, this quantity is defined in general as

$$\mathcal{S}(\hat{\rho}) = -\mathrm{Tr}(\hat{\rho}\log_2\hat{\rho}) = -\sum_i \eta_i \log_2 \eta_i, \tag{5.10}$$

where $\hat{\rho}$ is an arbitrary density matrix, with eigenvalues $\{\eta_i\}$. Importantly, the von Neumann entropy vanishes for pure states and reaches its maximum value, $\log_2 \dim(\mathcal{H})$, for maximally mixed states, with $\dim(\mathcal{H})$ the dimension of the corresponding Hilbert space.

The entanglement entropy $E(|\psi\rangle_{AB})$ of a two-photon pure state $|\psi\rangle_{AB}$ is obtained as the von Neumann entropy of the reduced density matrix of any of the two photons, $\hat{\rho}_A = \mathrm{Tr}_B(|\psi\rangle_{AB}\langle\psi|_{AB})$ or $\hat{\rho}_B = \mathrm{Tr}_A(|\psi\rangle_{AB}\langle\psi|_{AB})$, with Tr_χ the partial trace over the Hilbert space $\mathcal{H}_\chi$ (Appendix A). Thus, $E(|\psi\rangle_{AB})$ is given by

$$E(|\psi\rangle_{AB}) = \mathcal{S}(\hat{\rho}_A) = \mathcal{S}(\hat{\rho}_B). \tag{5.11}$$

Importantly, the reduced density matrix of a separable state always yield a pure state. As a result, the von Neumann entropy of the reduced states vanishes, and so does the entanglement entropy. In contrast, the partial trace of a maximally entangled state [such as the Bell states in Eqs. (5.7a)–(5.7b) and Eqs. (5.8a)–(5.8b)] always yields a maximally mixed state, with von Neumann entropy $\log_2 2 = 1$ in the case of two-qubit systems. We thus obtain that the entanglement entropy is bounded in this case between 0 (separable state) and 1 (maximally entangled state). Further, $E(|\psi\rangle_{AB})$ can be intuitively interpreted by considering that Alice and Bob can use a large amount of Bell states (which have maximal degree of entanglement) and of separable states (with no entanglement), and they aim to produce N_c copies of the two-photon state $|\psi\rangle_{AB}$ by using only classical communication and performing only

local unitary transformations on each of the qubits. The entanglement entropy of $|\psi\rangle_{AB}$ gives a number $m = N_c \cdot E(|\psi\rangle_{AB})$ of Bell states needed by Alice and Bob to produce these N_c copies of $|\psi\rangle_{AB}$ [65, 215, 216]. This interpretation can be rigorously demonstrated [215], although it goes beyond the scope of this introduction.

Concurrence

The entanglement entropy in Eq. (5.11) can be written as [216–219]

$$E(|\psi\rangle_{AB}) = H_E\left(\frac{1+\sqrt{1-[\mathcal{C}(|\psi\rangle_{AB})]^2}}{2}\right). \tag{5.12}$$

Here, we have introduced the binary entropy function

$$H_E(x) = -x\log_2 x - (1-x)\log_2(1-x), \tag{5.13}$$

as well as the function

$$\mathcal{C}(|\psi\rangle_{AB}) = 2|c_{HH}c_{VV} - c_{HV}c_{VH}|. \tag{5.14}$$

This function $\mathcal{C}(|\psi\rangle_{AB})$ is bounded between 0 and 1, as $E(|\psi\rangle_{AB})$. Crucially, the entanglement entropy $E(|\psi\rangle_{AB})$ in Eq. (5.12) is monotonically related to $\mathcal{C}(|\psi\rangle_{AB})$ and, as a consequence, $\mathcal{C}(|\psi\rangle_{AB})$ can be understood as a measure of the degree of entanglement of the pure state $|\psi_{AB}\rangle$ [217, 218].

The function $\mathcal{C}(|\psi\rangle_{AB})$, which is referred to as *concurrence*, can provide further insights into the two-photon entanglement. For example, Eq. (5.14) indicates that the two-photon pure state $|\psi\rangle_{AB}$ in Eq. (5.2) is separable if, and only if, $c_{HH}c_{VV} = c_{HV}c_{VH}$. Additionally, the concurrence facilitates the quantification of the degree of polarization-entanglement for two-photon mixed states, as we show in the following section.

5.1.4 Degree of entanglement of mixed states

We have focused so far on describing entanglement in two-photon pure states. However, all quantum systems are in mixed states in practice, described by density matrices (Appendix A). In this section, we present an intuitive extension of the concurrence to the case of mixed states.

We have classified in Section 5.1.1 two-qubit pure states as separable or entangled, depending on whether they can be written as tensor products of two individual qubit states that belong to the individual Hilbert spaces of A and B. This notion of entanglement can be extended to the case of two-qubit mixed states in a straightforward manner. Specifically, a two-qubit mixed state, with density matrix $\hat{\rho}_{AB} \in \mathcal{H}_{AB}$, is separable if $\hat{\rho}_{AB}$ can be written as a summation of density matrices that are related to separable states only. Specifically, the following

condition holds:

$$\begin{aligned}\hat{\rho}_{AB} \text{ is separable } \Leftrightarrow \hat{\rho}_{AB} &= \sum_i \Upsilon_i \left|\psi_i^{(A)}\right\rangle_A \left\langle\psi_i^{(A)}\right|_A \otimes \left|\psi_i^{(B)}\right\rangle_B \left\langle\psi_i^{(B)}\right|_B \\ &= \sum_i \Upsilon_i \hat{\rho}_{i,A} \otimes \hat{\rho}_{i,B},\end{aligned} \tag{5.15}$$

where Υ_i are non-negative real coefficients, and $\left|\psi_i^{(\chi)}\right\rangle_\chi$ and $\hat{\rho}_{i,\chi}$ belong to the Hilbert space $\mathcal{H}_\chi$. In the opposite case, we can say that $\hat{\rho}_{AB}$ is entangled and the equivalence

$$\hat{\rho}_{AB} \text{ is entangled } \Leftrightarrow \hat{\rho}_{AB} \neq \sum_i \Upsilon_i \hat{\rho}_{i,A} \otimes \hat{\rho}_{i,B} \tag{5.16}$$

holds. Notably, establishing well-defined measures of the degree of entanglement for two-qubit mixed states becomes drastically more complex compared to the case of pure states [65, 216]. A very common and practical measure of the degree of entanglement of two-qubit mixed states results from extending the concurrence $\mathcal{C}$ defined in Eq. (5.14) for pure states. In the following, we present a intuitive description of the concurrence for mixed states. A rigorous derivation of this quantity can be found in Refs. [218, 219].

The expression of the concurrence $\mathcal{C}(\left|\psi\right\rangle_{AB})$ of a two-qubit pure state in Eq. (5.14) can be rewritten as

$$\mathcal{C}(\left|\psi\right\rangle_{AB}) = \sqrt{\mathcal{F}(\left|\psi\right\rangle_{AB}, \left|\tilde{\psi}\right\rangle_{AB})} = |\left\langle\psi\right|_{AB} \left|\tilde{\psi}\right\rangle_{AB}|, \tag{5.17}$$

where we have used the expression of the fidelity between two pure states in Eq. (5.9), and we have defined the state

$$\left|\tilde{\psi}\right\rangle_{AB} \equiv (\hat{\sigma}_A^y \otimes \hat{\sigma}_B^y)\hat{K} \left|\psi\right\rangle_{AB}. \tag{5.18}$$

Here, $\hat{K}$ transforms all the probability amplitudes of $\left|\psi\right\rangle_{AB}$ to their complex conjugates, with $\left|\psi\right\rangle_{AB}$ written in a basis of separable states, such as $\{|H_AH_B\rangle$, $|H_AV_B\rangle$, $|V_AH_B\rangle$, $|V_AV_B\rangle\}$ in the case of photon polarization, which we take again as a reference of qubit. Namely, the action of $\hat{K}$ on the state $\left|\psi\right\rangle_{AB}$ in Eq. (5.2) is:

$$\hat{K} \left|\psi\right\rangle_{AB} = c_{HH}^* \left|H_AH_B\right\rangle + c_{HV}^* \left|H_AV_B\right\rangle + c_{VH}^* \left|V_AH_B\right\rangle + c_{VV}^* \left|V_AV_B\right\rangle. \tag{5.19}$$

Additionally, $\hat{\sigma}_\chi^y = -i \left|H\right\rangle_\chi \left\langle H\right|_\chi + i \left|V\right\rangle_\chi \left\langle V\right|_\chi$ in Eq. (5.18) is the y-Pauli matrix in the Hilbert space $\mathcal{H}_\chi$. Interestingly, Eq. (5.17) indicates that the concurrence of $\left|\psi\right\rangle_{AB}$ is determined by how much this state is affected by the transformation $(\hat{\sigma}_A^y \otimes \hat{\sigma}_B^y)\hat{K}$. For example, if this transformation modifies $\left|\psi\right\rangle_{AB}$ only through a difference of global phase, the fidelity $\mathcal{F}(\left|\psi\right\rangle_{AB}, \left|\tilde{\psi}\right\rangle_{AB})$ is one and the state is maximally entangled. In contrast, if the transformation leads to an orthogonal state, $\left|\psi\right\rangle_{AB}$ is separable.

We now consider an arbitrary density matrix $\hat{\rho}_{AB}$ describing a general two-photon state. This matrix is transformed by $(\hat{\sigma}_A^y \otimes \hat{\sigma}_B^y)\hat{K}$ as

$$\hat{\tilde{\rho}}_{AB} = (\hat{\sigma}_A^y \otimes \hat{\sigma}_B^y)\hat{\rho}_{AB}^*(\hat{\sigma}_A^y \otimes \hat{\sigma}_B^y), \tag{5.20}$$

with $\hat{\rho}_{AB}^*$ obtained by complex conjugating all the elements of $\hat{\rho}_{AB}$ in the basis $\{|H_AH_B\rangle, |H_AV_B\rangle, |V_AH_B\rangle, |V_AV_B\rangle\}$. Further, the fidelity between two mixed states is in general defined as (Appendix A)

$$\mathcal{F}(\hat{\rho}_1, \hat{\rho}_2) = \left(\mathrm{Tr}\sqrt{\sqrt{\hat{\rho}_1}\hat{\rho}_2\sqrt{\hat{\rho}_1}}\right)^2. \tag{5.21}$$

Thus, the square root of the fidelity between $\hat{\rho}_{AB}$ and $\hat{\rho}_{AB}^*$ is given by

$$\sqrt{\mathcal{F}(\hat{\rho}_{AB}, \hat{\tilde{\rho}}_{AB})} = \mathrm{Tr}\sqrt{\sqrt{\hat{\rho}_{AB}}\hat{\tilde{\rho}}_{AB}\sqrt{\hat{\rho}_{AB}}} = \sum_{i=1}^{4}\lambda_i, \tag{5.22}$$

where $\{\lambda_i\}$ are the eigenvalues of $\sqrt{\sqrt{\hat{\rho}_{AB}}\hat{\tilde{\rho}}_{AB}\sqrt{\hat{\rho}_{AB}}}$. Importantly, the concurrence $\mathcal{C}(\hat{\rho}_{AB})$ does not directly corresponds to $\sqrt{\mathcal{F}(\hat{\rho}_{AB}, \hat{\tilde{\rho}}_{AB})}$, which would be a straightforward extension of the concurrence of two-photon pure states [Eq. (5.17)]. Instead, the concurrence of a general two-photon state is given by [218, 219]

$$\mathcal{C}(\hat{\rho}_{AB}) = \max\{0, 2\lambda_1 - \sqrt{\mathcal{F}(\hat{\rho}_{AB}, \hat{\tilde{\rho}}_{AB})}\}, \tag{5.23}$$

with $\lambda_1 = \max\{\lambda_i\}$ the largest eigenvalue of $\sqrt{\sqrt{\hat{\rho}_{AB}}\hat{\tilde{\rho}}_{AB}\sqrt{\hat{\rho}_{AB}}}$. We emphasize that if $\hat{\rho}_{AB}$ describes a two-photon pure state (i.e., $\hat{\rho}_{AB} = |\psi\rangle_{AB}\langle\psi|_{AB}$), the general expression of the concurrence in Eq. (5.23) reduces to the simpler expression for two-photon pure states in Eq. (5.17).

5.1.5 Generation of entangled photons

Early evidence for the existence of quantum entanglement was provided by a series of experiments conducted between the 1960s and 1980s [220–225], in which polarization-entangled photons were generated from the cascade emission from calcium and mercury atomic beams. These experiments spurred the development of quantum technologies, where photons play a key role in processing and distributing entanglement. The applications of entangled photons include quantum communication [34–36], quantum cryptography [66–70], and quantum sensing and imaging [71–77]. However, the atomic beams used in the pioneering experiments on quantum entanglement exhibit isotropic emission due to the randomness of the orientations of the transition dipole moments of the atoms. Further, the degree of polarization drastically decreases in this case if photons are not emitted back to back (i.e., in exact opposite directions) [226, 227]. Consequently, the collection efficiency of entangled photons from atomic beams is very low, which reduces the

technological utility of atomic beams as sources of entangled photons. Significant efforts have thus been made in the last few decades to design more practical sources of entangled photons [227–229].

Nowadays, the most common source of entangled photon pairs is based on parametric down-conversion (PDC), which is a nonlinear optical process in which a photon pumps a nonlinear crystal, leading to the scattering of two photons [42–44]. In this process, both energy and momentum are conserved, imposing constraints on the directions of the two scattered photons [227]. Two types of PDC can be distinguished depending on whether the two scattered photons have parallel (type I) or perpendicular (type II) polarization directions. The second type of PDC can be used to generate polarization-entangled photon pairs [230–234]. However, entangled photons generated from PDC suffer from several drawbacks, the main one being the intrinsic probabilistic nature of this non-linear process.

To overcome the drawbacks of PDC, biexciton quantum dots (QDs) have attracted much attention over the last two decades [235–238], as they can be used to generate entangled photons deterministically. In this case, entangled photons are generated from the cascade emission of the biexciton (doubly excited state) of the QD, in a similar manner to the cascade emission from atomic beams. However, in quantum dots, the control over the directions of emission is improved compared to atomic beams. The collection efficiency in these systems, however, often remains low, as they are typically embedded in a host medium with a high refractive index. Optical cavity structures have been shown to improve the collection efficiency of entangled photons emitted from QDs [239–242], but challenges remain, and further research is required in this regard. Additionally, the emission of entangled photons from biexciton QDs faces further challenges, such as the usual fine structure splitting that can reduce photon entanglement [242–244], and the range of operation typically limited to the infrared.

Notably, a deterministic source of entangled photons in the visible range could find applications in different contexts. In quantum communication, such a source would facilitate the interfacing between light and quantum nodes with optical transition frequencies [245, 246], and it could also facilitate the quantum-enhanced imaging of biological samples [247, 248]. However, only a few sources of entangled photons operating in the visible regime have been proposed [249–251], aside from the probabilistic PDC [230, 252, 253].

In the following, we show that pairs of photons entangled in polarization can be generated by two interacting quantum emitters with two-level-system behaviour. These emitters can represent a variety of systems, such as trapped ions, atoms and solid-state emitters, including organic molecules or defects in inorganic crystals. This variety of possible implementations offers large technological versatility, for instance, in choosing the spectral emission regime. In particular, the application of our proposal in state-of-the-art experiments with interacting organic molecules (e.g., DBATT molecules) at cryogenic temperatures would allow for the emission of entangled photons in the visible regime [1, 92, 99, 200], as these molecules have optical transition frequencies.

5.2 Analysis of the generation of entangled photons from two interacting quantum emitters

We show in this section that two interacting emitters can be used to generate a two-photon state that is entangled in frequency and polarization. To this end, we focus again on the analysis of light radiated into the Zero-Phonon Line (ZPL) from the two emitters, as in Chapter 3. We first provide an intuitive description of the generation of this two-photon state. Afterwards, we use the Wigner-Weisskopf approximation (WWA) to rigorously derive the exact two-photon state provided by the relaxation of two emitters with arbitrary relative orientation of their transition dipole moments. We then verify that this exact two-photon state is indeed entangled in frequency and polarization if the transition dipole moments are perpendicularly oriented.

5.2.1 Intuitive picture of the generation of entangled photons from two interacting quantum emitters

We consider two two-level quantum emitters (labeled by $j = 1, 2$). Emitter j is located at position $\mathbf{r}_j$ and has electronic excited state $|e_j\rangle$ and ground state $|g_j\rangle$, as in previous chapters. For simplicity, the emitters have identical transition frequencies $\omega_{e,1} = \omega_{e,2} = \omega_0$, and transition dipole moments of the same magnitude $|\boldsymbol{\mu}_1| = |\boldsymbol{\mu}_2| = \mu$. The two emitters are contained in the xz-plane, with $\mathbf{r}_{12} = \mathbf{r}_1 - \mathbf{r}_2$ aligned along the z-axis and separated by a distance $r_{12} = |\mathbf{r}_{12}|$, as schematically represented in Fig. 5.1a. The two transition dipole moments are also contained in the xz-plane, with mutually perpendicular orientation, which contrasts with the parallel dipole moments analyzed in Chapters 3 and 4. More specifically, we fix $\boldsymbol{\mu}_1 = \mu(\boldsymbol{e}_x + \boldsymbol{e}_z)/\sqrt{2}$ and $\boldsymbol{\mu}_2 = \mu(\boldsymbol{e}_x - \boldsymbol{e}_z)/\sqrt{2}$. As discussed below, this configuration of perpendicular dipoles allows for detecting photons polarized in the x-direction, as well as in the z-direction, opening up the door to generate a photon pair that is entangled in polarization.

We plot in Fig. 5.1b the dependence of the coherent dipole-dipole coupling V [black line, obtained from Eq. (3.44)] and of the dissipative dipole-dipole coupling $\tilde{\gamma}$ [brown line, Eq. (3.50)] on the distance r_{12} between the two emitters in the configuration of perpendicular transition dipole moments. We consider again two DBATT organic molecules as reference emitters and use the molecular parameters specified in Section 3.3, except for the Debye-Waller/Franck-Condon factor, which is fixed at $\alpha_{\mathrm{DW}} = 1$ here (changing the value of α_{DW} is equivalent to slightly modifying the distance, as we show in Section 5.4.2), yielding $V = V_{\mathrm{DW}}$ and $\tilde{\gamma} = \tilde{\gamma}_{\mathrm{DW}}$. Figure 5.1b shows that the dissipative coupling $\tilde{\gamma}$ is very small in comparison to the spontaneous emission rate γ_0 of each of the emitters, even at very short distances. In contrast, the coherent coupling strength V, can be significantly larger than γ_0 if the distance r_{12} between emitters is much smaller than the vacuum wavelength λ_0 associated to the transition frequency ω_0 of the emitters, $\lambda_0 = 2\pi c/\omega_0$. As we

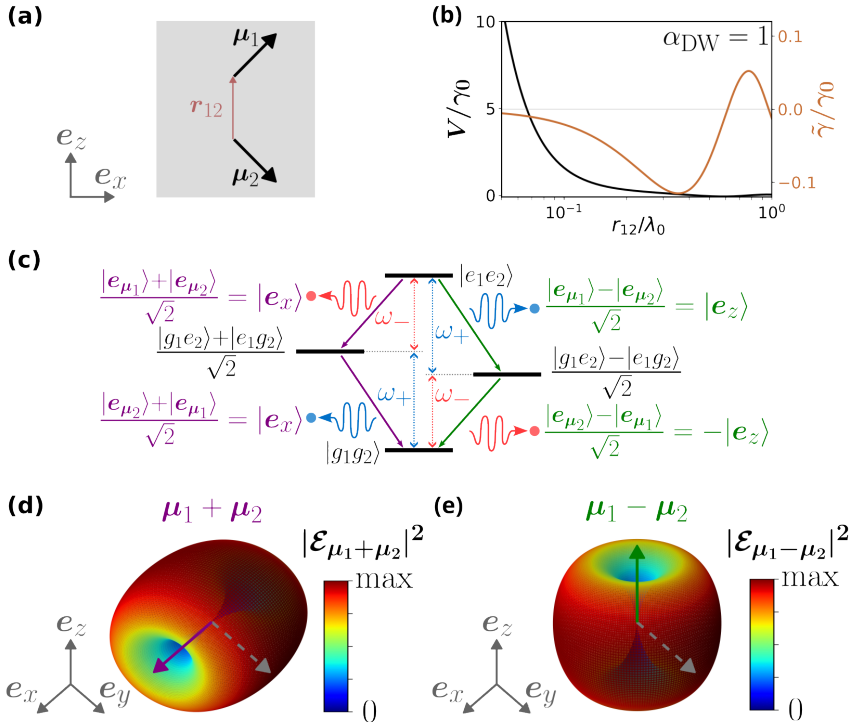

Figure 5.1: Photon emission from the symmetric and antisymmetric hybrid states of two DBATT molecules. (a) Schematic representation of two emitters located in the xz-plane, with their relative position vector $\mathbf{r}_{12}$ aligned along the z-axis. The transition dipole moments are oriented perpendicularly to each other, given by $\boldsymbol{\mu}_1 = \mu(\boldsymbol{e}_x + \boldsymbol{e}_z)/\sqrt{2}$ and $\boldsymbol{\mu}_2 = \mu(\boldsymbol{e}_x - \boldsymbol{e}_z)/\sqrt{2}$. (b) Dependence on the distance $r_{12} = |\mathbf{r}_{12}|$ between both emitters (normalized by the vacuum wavelength $\lambda_0 = 618$ nm) of the coherent dipole-dipole coupling V (black line) and of the dissipative coupling $\tilde{\gamma}$ (brown line). V and $\tilde{\gamma}$ are normalized by the spontaneous emission rate γ_0. We fix the combined Debye-Waller/Franck-Condon factor at $\alpha_{\mathrm{DW}} = 1$ and the refractive index of the surrounding medium at $n = 1.5$. (c) Schematic level structure and relaxation paths of the coupled system. The initial state $|e_1e_2\rangle$ can relax via the symmetric state $|S\rangle = (|g_1e_2\rangle + |e_1g_2\rangle)/\sqrt{2}$ (transitions indicated with purple arrows) generating two photons with polarization state $|\boldsymbol{e}_x\rangle$ (corresponding to the direction of the transition dipole moment of the symmetric state, written in purple). $|e_1e_2\rangle$ can also relax via the antisymmetric state $|A\rangle = (|g_1e_2\rangle - |e_1g_2\rangle)/\sqrt{2}$ (transitions indicated with green arrows), which leads to the emission of a photon with polarization state $|\boldsymbol{e}_z\rangle$ (corresponding to the direction of the transition dipole moment of the antisymmetric state, written in green) and another photon with polarization state $-|\boldsymbol{e}_z\rangle$ (opposite direction to the dipole moment of the antisymmetric state). [(d),(e)] Radiation patterns of electric point dipoles oriented along (d) $\boldsymbol{\mu}_1 + \boldsymbol{\mu}_2 \propto \boldsymbol{e}_x$, corresponding to the transition dipole moment of the symmetric state (marked by a purple arrow), and (e) $\boldsymbol{\mu}_1 - \boldsymbol{\mu}_2 \propto \boldsymbol{e}_z$, corresponding to that of the antisymmetric state (marked by a green arrow). The squared amplitude of the classical electric field generated by these electric point dipoles is denoted as (d) $|\boldsymbol{\mathcal{E}}_{\boldsymbol{\mu}_1+\boldsymbol{\mu}_2}|^2$ and (e) $|\boldsymbol{\mathcal{E}}_{\boldsymbol{\mu}_1-\boldsymbol{\mu}_2}|^2$, as defined in Eq. (1.142). The grey dashed arrows indicate the y-axis direction.

consider in this chapter that the emitters have identical transition frequencies (no detuning, $\delta = 0$), the coherent interaction leads to the formation of delocalized states that correspond to symmetric (S) and antisymmetric (A) superpositions of the uncoupled localized states $|e_1 g_2\rangle$ and $|g_1 e_2\rangle$ [Eqs. (3.59a)–(3.59b)], which can be written as

$$|S\rangle = \frac{|g_1 e_2\rangle + |e_1 g_2\rangle}{\sqrt{2}}, \tag{5.24a}$$

$$|A\rangle = \frac{|g_1 e_2\rangle - |e_1 g_2\rangle}{\sqrt{2}}. \tag{5.24b}$$

Crucially, these delocalized states have almost identical decay rates $\gamma_0 + \tilde{\gamma} \approx \gamma_0$ ($|S\rangle$) and $\gamma_0 - \tilde{\gamma} \approx \gamma_0$ ($|A\rangle$), as the dissipative coupling $\tilde{\gamma}$ is negligible for these perpendicular dipole moments $\boldsymbol{\mu}_1 = \mu(\boldsymbol{e}_x + \boldsymbol{e}_z)/\sqrt{2}$ and $\boldsymbol{\mu}_2 = \mu(\boldsymbol{e}_x - \boldsymbol{e}_z)/\sqrt{2}$. Thus, in contrast to Chapters 3 and 4, the hybrid states that emerge when quantum emitters with perpendicular dipole moments interact do not correspond to superradiant and subradiant states.

We now focus on analyzing the light emitted into the Zero-Phonon Line from two emitters separated by a short distance, starting from the doubly-excited state $|e_1 e_2\rangle$. The system can be prepared in this state, for example, using a pulsed laser with frequency resonantly tuned to the two-photon resonance ($\omega_L = \omega_0$), as in usual experiments with biexciton quantum dots [236, 241, 254]. As the hybrid states $|S\rangle$ and $|A\rangle$ have similar decay rate for these emitters with perpendicular transition dipole moments, the initial doubly-excited state $|e_1 e_2\rangle$ can decay with almost the same probability to $|S\rangle$ and $|A\rangle$. Notably, the radiative decay from $|e_1 e_2\rangle$ to $|S\rangle$ produces a photon of frequency $\omega_- = \omega_0 - V$ [Eqs. (3.61) and (3.62)] and polarization state $(|\boldsymbol{e}_{\boldsymbol{\mu}_1}\rangle + |\boldsymbol{e}_{\boldsymbol{\mu}_2}\rangle)/\sqrt{2} = |\boldsymbol{e}_x\rangle$, which is followed by the relaxation from $|S\rangle$ to $|g_1 g_2\rangle$ that leads to the emission of a photon of frequency $\omega_+ = \omega_0 + V$ and identical polarization state $(|\boldsymbol{e}_{\boldsymbol{\mu}_2}\rangle + |\boldsymbol{e}_{\boldsymbol{\mu}_1}\rangle)/\sqrt{2} = |\boldsymbol{e}_x\rangle$. This cascade emission is schematically indicated with purple arrows in Fig. 5.1c. On the other hand, the radiative decay from $|e_1 e_2\rangle$ to $|A\rangle$ produces a photon of frequency ω_+ and polarization $(|\boldsymbol{e}_{\boldsymbol{\mu}_1}\rangle - |\boldsymbol{e}_{\boldsymbol{\mu}_2}\rangle)/\sqrt{2} = |\boldsymbol{e}_z\rangle$, which is followed by the relaxation from $|A\rangle$ to $|g_1 g_2\rangle$ that leads to the emission of a photon of frequency ω_- and polarization $(|\boldsymbol{e}_{\boldsymbol{\mu}_2}\rangle - |\boldsymbol{e}_{\boldsymbol{\mu}_1}\rangle)/\sqrt{2} = -|\boldsymbol{e}_z\rangle$ (green arrows in Fig. 5.1c). Therefore, this intuitive analysis suggests that the two-photon state is given by

$$|\phi_-^{\text{int}}\rangle = \frac{|\boldsymbol{e}_x, \omega_+\rangle\,|\boldsymbol{e}_x, \omega_-\rangle - |\boldsymbol{e}_z, \omega_-\rangle\,|\boldsymbol{e}_z, \omega_+\rangle}{\sqrt{2}}, \tag{5.25}$$

where $|\boldsymbol{e}_\alpha, \omega\rangle$ represents the state of a photon polarized along the direction $\boldsymbol{e}_\alpha$ and of frequency ω. $|\phi_-^{\text{int}}\rangle$ is entangled in frequency and polarization. Notably, if the frequency degree of freedom is erased, $|\phi_-^{\text{int}}\rangle$ reduces to the Bell state $|\phi_-\rangle_{AB}$ in Eq. (5.7b). We emphasize that the intuitive argument on the generation of the entangled photon pair provided in this section lacks information of, for example, the directions of emission. This argument also neglects the possibility of two-photon

emission through intermediate virtual states. These aspects will be incorporated in the following sections.

We provide next a simple analysis of the directions of emission that are expected to yield higher collection efficiency. To this end, we note that an electric point dipole has a doughnut-shaped radiation pattern, with maximum (and equal) radiation strength in the plane perpendicular to the orientation of the point dipole [121, 132]. We plot in Fig. 5.1d the radiation pattern of the transition dipole moment $\boldsymbol{\mu}_1 + \boldsymbol{\mu}_2$ of the symmetric state $|S\rangle$, which is oriented along the x-direction. The radiation from this dipole is maximal in the yz-plane. Similarly, Fig. 5.1e shows the radiation pattern of the transition dipole moment $\boldsymbol{\mu}_1 - \boldsymbol{\mu}_2$ of the antisymmetric state $|A\rangle$, which is oriented along the z-direction and has maximal radiation in the xy-plane. As a consequence, $\boldsymbol{e}_y$ and $-\boldsymbol{e}_y$ can be expected to be optimal directions of photon emission because they are directions of maximal radiation for the transition dipole moments of both hybrid states $|S\rangle$ and $|A\rangle$ (see dashed grey arrows in Figs. 5.1d and 5.1e).

In the following, we derive the exact two-photon state resulting from the relaxation of the two emitters, including the photon degrees of freedom of frequency, polarization, and propagation directions. We then use the exact analytical expression obtained to rigorously verify the intuitive arguments presented in this section on the generation of entangled photons.

5.2.2 Wigner-Weisskopf approximation for two quantum emitters

We derive in this section the two-photon state provided by the relaxation of two initially excited quantum emitters. To this end, we apply the Wigner-Weisskopf approximation (WWA), which was used in Section 1.3 to derive the spontaneous emission rate γ_0 of a single emitter. We choose here the WWA over the Markovian master equation approach, employed in Chapters 3 and 4, because the WWA allows for a complete characterization of the electromagnetic vacuum field state, capturing the probabilities of photon emission at arbitrary directions, frequencies, and polarizations.

We consider that the transition dipole moments of the two emitters have the same magnitude, μ, and are contained on the xz-plane, with arbitrary orientation. More specifically, the transition dipole moments are given by

$$\boldsymbol{\mu}_j = \mu(\cos\alpha_j \boldsymbol{e}_x + \sin\alpha_j \boldsymbol{e}_z), \tag{5.26}$$

with arbitrary values of α_1 and α_2 (i.e., the transition dipole moments $\boldsymbol{\mu}_1$ and $\boldsymbol{\mu}_2$ are not necessarily orthogonal within this derivation). Further, the emitters are located at positions $\mathbf{r}_j$ within a homogeneous medium with refractive index n, with $\mathbf{r}_{12} = \mathbf{r}_1 - \mathbf{r}_2 = r_{12}\boldsymbol{e}_z$ oriented again along the z-axis, as schematically represented in Fig. 5.2. We derived in Section 3.1.3 the multipolar form of the Hamiltonian describing the dynamics of the emitters and the electromagnetic vacuum field [Eq.

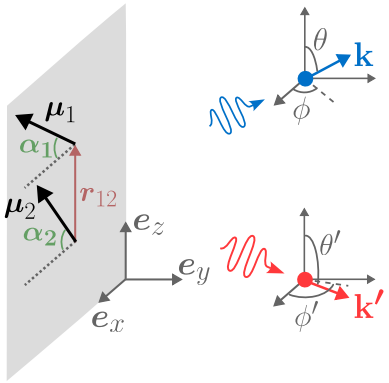

Figure 5.2: Schematic representation of the two-photon emission from two initially excited quantum emitters. The emitters (indexed by $j = 1, 2$) behave as two-level systems, with transition dipole moment $\boldsymbol{\mu}_j = \mu(\cos\alpha_j \boldsymbol{e}_x + \sin\alpha_j \boldsymbol{e}_z)$, and they are located at positions $\boldsymbol{r}_j$, with $\boldsymbol{r}_{12} = \boldsymbol{r}_1 - \boldsymbol{r}_2$ oriented in the z-direction (axis indicated at the bottom). The relaxation of the emitters generates two photons in electromagnetic modes ($\mathbf{k}$, s) and ($\mathbf{k}'$, s') with probability amplitude $c^{gg}_{\mathbf{k}s\mathbf{k}'s'}$, where s and s' are the polarization modes and $\mathbf{k}$ and $\mathbf{k}'$ are the wavevectors. Additionally, θ and ϕ represent the polar and azimuthal angles, respectively, of the wavevector $\mathbf{k}$ in spherical coordinates. In Sections 5.2.1, 5.2.3, 5.3, 5.5 and 5.6, we focus on the case of perpendicular transition dipole moments, with $\alpha_1 = -\alpha_2 = \pi/4$.

(3.27)]. Particularly, the multipolar form of the interaction Hamiltonian is given by

$$\hat{H}_I^{mp} = -\sum_j \left(\boldsymbol{\mu}_j \hat{\sigma}_j + \boldsymbol{\mu}_j^* \hat{\sigma}_j^\dagger\right) \cdot \sum_{\mathbf{k},s} i\sqrt{\frac{\hbar\omega_\mathrm{k}}{2\varepsilon_0 n^2 \mathcal{V}}} \mathbf{e}_{\mathbf{k}s} [\hat{a}_{\mathbf{k}s} e^{i\mathbf{k}\cdot\mathbf{r}_j} - \hat{a}^\dagger_{\mathbf{k}s} e^{-i\mathbf{k}\cdot\mathbf{r}_j}], \quad (5.27)$$

where we have included the influence of the refractive index $n \neq 1$ of the host medium by replacing $c \to c/n$ and $\varepsilon_0 \to \varepsilon_0 n^2$. We recall that $\hat{a}^\dagger_{\mathbf{k}s}$ and $\hat{a}_{\mathbf{k}s}$ are the creation and annihilation operators of photons in mode ($\mathbf{k}$,s), and that the wavevector can be written in spherical coordinates as

$$\begin{aligned} \mathbf{k} &= \mathrm{k}(\sin\theta\cos\phi \boldsymbol{e}_x + \sin\theta\sin\phi \boldsymbol{e}_y + \cos\theta \boldsymbol{e}_z) \\ &= \frac{n\omega_\mathrm{k}}{c}(\sin\theta\cos\phi \boldsymbol{e}_x + \sin\theta\sin\phi \boldsymbol{e}_y + \cos\theta \boldsymbol{e}_z), \end{aligned} \quad (5.28)$$

with θ and ϕ, respectively, the polar angle with respect to the z-axis and the azimuthal angle (see Fig. 5.2), and $\mathrm{k} = n\omega_\mathrm{k}/c$. Additionally, the index $s = 1, 2$ labels two orthogonal polarization modes of the wavevector $\mathbf{k}$, with unit vectors $\boldsymbol{e}_{\mathbf{k}s}$ [Eqs. (1.137a)–(1.137b)].

The Wigner-Weisskopf approximation (WWA) consists in assuming an ansatz $|\psi(t)\rangle$ for the time evolution of some initial excited state $|\psi(0)\rangle$. The ansatz is then solved by using the Schrödinger equation, as discussed in Section 1.3 for the case

of a single emitter. Here, we are interested in the initial state

$$|\psi(0)\rangle = |e_1 e_2\rangle\,|\text{vac}\rangle\,, \tag{5.29}$$

with $|\text{vac}\rangle$ the electromagnetic vacuum state [Eq. (1.60)]. Notably, considering the complete interaction Hamiltonian $\hat{H}_I^{mp}$ [Eq. (5.27)] complicates the direct application of the WWA, since this complete Hamiltonian requires a unpractical ansatz, including states with two photons in the field and the two emitters in the excited state, for example. This ansatz does not yield a closed system of coupled differential equations for the probability amplitudes. Crucially, the application of the WWA is facilitated by using the interaction Hamiltonian under the rotating-wave approximation (RWA), which neglects the terms that are proportional to $\hat{\sigma}_j\hat{a}_{\mathbf{k}s}$ and to $\hat{\sigma}_j^\dagger\hat{a}_{\mathbf{k}s}^\dagger$ in Eq. (5.27). More specifically, the interaction Hamiltonian under the RWA becomes

$$\hat{H}_I^{\text{RWA}} = \sum_{\mathbf{k},s}\sum_j \left(g_{\mathbf{k}s}^{(j)}\hat{\sigma}_j^\dagger\hat{a}_{\mathbf{k}s} + g_{\mathbf{k}s}^{(j)*}\hat{\sigma}_j\hat{a}_{\mathbf{k}s}^\dagger \right), \tag{5.30}$$

with coupling coefficient

$$g_{\mathbf{k}s}^{(j)} = g_{\mathbf{k}s}(\mathbf{r}_j) = -i\sqrt{\frac{\omega_\text{k}}{2\varepsilon_0 n^2\hbar\mathcal{V}}}\boldsymbol{\mu}_j\cdot\boldsymbol{e}_{\mathbf{k}s}e^{i\mathbf{k}\cdot\mathbf{r}_j}. \tag{5.31}$$

The RWA allows us to consider a practical ansatz $|\psi(t)\rangle$, consisting of a superposition of pure states with a fixed number of excitations (between photons and emitters excitations). Notably, the calculations in Section 3.1.4 (where we traced out the Hilbert space of the electromagnetic vacuum field and derived the Markovian master equation governing the reduced dynamics of the two emitters) showed that the RWA does not affect the spontaneous emission rate γ_0, nor the dissipative coupling $\tilde{\gamma}$. However, the terms neglected by the RWA in the interaction Hamiltonian were required to capture the right coherent dipole-dipole coupling V. Fortunately, Milonni and Knight showed a simple approach in Ref. [179] that enables the application of the WWA together with the RWA, retrieving the correct value of V, which we apply and discuss below. Thus, we use both the RWA and the WWA here.

The proposed ansatz is

$$\begin{aligned}|\psi(t)\rangle = {} & c^{ee}(t)\,|e_1e_2\rangle\,|\text{vac}\rangle + \sum_{\mathbf{k},s}\left(c_{\mathbf{k}s}^{eg}(t)\,|e_1g_2\rangle + c_{\mathbf{k}s}^{ge}(t)\,|g_1e_2\rangle \right)\hat{a}_{\mathbf{k}s}^\dagger\,|\text{vac}\rangle \\ & + \sum_{\mathbf{k},s}\sum_{\substack{(\mathbf{k}',s')\\ \geq(\mathbf{k},s)}} c_{\mathbf{k}s,\mathbf{k}'s'}^{gg}(t)\,|g_1g_2\rangle\,\hat{a}_{\mathbf{k}s}^\dagger\hat{a}_{\mathbf{k}'s'}^\dagger\,|\text{vac}\rangle\,,\end{aligned} \tag{5.32}$$

which only contains terms with two excitations in total (between photons and emitter excitations), as the RWA is considered. $c^{ee}(t)$ is the probability amplitude

of finding the system still in the initial state $|e_1e_2\rangle\,|\text{vac}\rangle$ at time t, which satisfies $c^{ee}(0) = 1$ [see Eq. (5.29)]. $c^{eg}_{\mathbf{k}s}(t)$ and $c^{ge}_{\mathbf{k}s}(t)$ are the probability amplitudes of states in which, respectively, the second or the first emitter have relaxed, leading to the generation of a photon in mode ($\mathbf{k}$, s). Last, $c^{gg}_{\mathbf{k}s,\mathbf{k}'s'}(t)$ is the probability amplitude of a state in which both emitters have relaxed, giving rise to two photons in modes ($\mathbf{k}$, s) and ($\mathbf{k}'$, s'), respectively. We are mainly interested in the analytical expression of this two-photon probability amplitude $c^{gg}_{\mathbf{k}s,\mathbf{k}'s'}(t)$, as it contains all the information of the two-photon emission. We remark that in the double summation in the second line of Eq. (5.32) each state appears and is counted only once [255], which is indicated by the compact notation $(\mathbf{k}', s') \geq (\mathbf{k}, s)$. In other words, only one of the terms $|g_1g_2\rangle\,\hat{a}^\dagger_{\mathbf{k}s}\hat{a}^\dagger_{\mathbf{k}'s'}\,|\text{vac}\rangle$ and $|g_1g_2\rangle\,\hat{a}^\dagger_{\mathbf{k}'s'}\hat{a}^\dagger_{\mathbf{k}s}\,|\text{vac}\rangle$ [with $(\mathbf{k}, s) \neq (\mathbf{k}', s')$] appear in this summation because they represent the same physical state, as $[\hat{a}^\dagger_{\mathbf{k}s}, \hat{a}^\dagger_{\mathbf{k}'s'}] = 0$.

Next, to obtain the analytical expressions of the probability amplitudes in Eq. (5.32), we use the Schrödinger equation in the interaction picture (Appendix B), which is given by

$$i\frac{d}{dt}\,|\psi(t)\rangle = \hat{H}_I^{\text{RWA}}(t)\,|\psi(t)\rangle\,, \tag{5.33}$$

with

$$\begin{aligned}\hat{H}_I^{\text{RWA}}(t) &= \exp\Big[i(\hat{H}_0 + \hat{H}_{F\perp})t/\hbar\Big]\,\hat{H}_I^{\text{RWA}}\exp\Big[-i(\hat{H}_0 + \hat{H}_{F\perp})t/\hbar\Big] \\ &= \sum_{\mathbf{k},s}\sum_j\left(g^{(j)}_{\mathbf{k}s}\hat{\sigma}^\dagger_j\hat{a}_{\mathbf{k}s}e^{i(\omega_0-\omega_\text{k})t} + g^{(j)*}_{\mathbf{k}s}\hat{\sigma}_j\hat{a}^\dagger_{\mathbf{k}s}e^{-i(\omega_0-\omega_\text{k})t}\right).\end{aligned} \tag{5.34}$$

On the one hand, the substitution of the ansatz $|\psi(t)\rangle$ [Eq. (5.32)] on the left-hand side of Eq. (5.33) yields

$$\begin{aligned}i\frac{d}{dt}\,|\psi(t)\rangle &= i\frac{d}{dt}(c^{ee})\,|e_1e_2\rangle\,|\text{vac}\rangle + \sum_{\mathbf{k},s} i\frac{d}{dt}(c^{eg}_{\mathbf{k}s})\,|e_1g_2\rangle\,\hat{a}^\dagger_{\mathbf{k}s}\,|\text{vac}\rangle \\ &+ \sum_{\mathbf{k},s} i\frac{d}{dt}(c^{ge}_{\mathbf{k}s})\,|g_1e_2\rangle\,\hat{a}^\dagger_{\mathbf{k}s}\,|\text{vac}\rangle + \sum_{\mathbf{k},s}\sum_{\substack{(\mathbf{k}',s')\\ \geq(\mathbf{k},s)}} i\frac{d}{dt}(c^{gg}_{\mathbf{k}s,\mathbf{k}'s'})\,|g_1g_2\rangle\,\hat{a}^\dagger_{\mathbf{k}s}\hat{a}^\dagger_{\mathbf{k}'s'}\,|\text{vac}\rangle\,,\end{aligned} \tag{5.35}$$

where all the probability amplitudes are evaluated at time t. On the other hand, substituting the ansatz $|\psi(t)\rangle$ [Eq. (5.32)] on the right-hand side of Eq. (5.33), we

find

$$
\begin{aligned}
H_I^{\mathrm{RWA}}(t)\,|\psi(t)\rangle &= \sum_{\mathbf{k},s} e^{i(\omega_0-\omega_{\mathrm{k}})t}\left[g^{(2)}_{\mathbf{k}s}c^{eg}_{\mathbf{k}s}+g^{(1)}_{\mathbf{k}s}c^{ge}_{\mathbf{k}s}\right]|e_1e_2\rangle\,|\mathrm{vac}\rangle \\
&+\sum_{\mathbf{k}'',s''} e^{-i(\omega_0-\omega_{\mathrm{k}''})t}\left[g^{(1)*}_{\mathbf{k}''s''}\,|g_1e_2\rangle+g^{(2)*}_{\mathbf{k}''s''}\,|e_1g_2\rangle\right]c^{ee}\hat{a}^{\dagger}_{\mathbf{k}''s''}\,|\mathrm{vac}\rangle \\
&+\sum_{\mathbf{k},s}\sum_{\substack{(\mathbf{k}',s')\\ \geq(\mathbf{k},s)}}\sum_{\mathbf{k}'',s''} e^{i(\omega_0-\omega_{\mathrm{k}''})t}\left[g^{(1)}_{\mathbf{k}s}\,|e_1g_2\rangle+g^{(2)}_{\mathbf{k}s}\,|g_1e_2\rangle\right]c^{gg}_{\mathbf{k}s\mathbf{k}'s'}\hat{a}_{\mathbf{k}''s''}\hat{a}^{\dagger}_{\mathbf{k}s}\hat{a}^{\dagger}_{\mathbf{k}'s'}\,|\mathrm{vac}\rangle \\
&+\sum_{\mathbf{k},s}\sum_{\substack{(\mathbf{k}',s')\\ \geq(\mathbf{k},s)}}\sum_{\mathbf{k}'',s''} e^{-i(\omega_0-\omega_{\mathrm{k}''})t}\left[g^{(1)*}_{\mathbf{k}s}c^{eg}_{\mathbf{k}s}+g^{(2)*}_{\mathbf{k}s}c^{ge}_{\mathbf{k}s}\right]|g_1g_2\rangle\,\hat{a}^{\dagger}_{\mathbf{k}''s''}\hat{a}^{\dagger}_{\mathbf{k}s}\,|\mathrm{vac}\rangle\,.
\end{aligned}
\tag{5.36}
$$

Matching Eqs. (5.35) and (5.36) and taking into account that $[\hat{a}^{\dagger}_{\mathbf{k}s},\hat{a}_{\mathbf{k}'s'}]=\delta_{\mathbf{k},\mathbf{k}'}\delta_{s,s'}$ and $[\hat{a}^{\dagger}_{\mathbf{k}s},\hat{a}^{\dagger}_{\mathbf{k}'s'}]=0$, we obtain the set of coupled differential equations

$$
i\frac{d}{dt}c^{ee}(t)=\sum_{\mathbf{k},s}c^{ge}_{\mathbf{k}s}(t)g^{(1)}_{\mathbf{k}s}e^{i(\omega_0-\omega_{\mathrm{k}})t}+\sum_{\mathbf{k},s}c^{eg}_{\mathbf{k}s}(t)g^{(2)}_{\mathbf{k}s}e^{i(\omega_0-\omega_{\mathrm{k}})t}, \tag{5.37a}
$$

$$
i\frac{d}{dt}c^{eg}_{\mathbf{k}s}(t)=e^{-i(\omega_0-\omega_{\mathrm{k}})t}c^{ee}(t)g^{(2)*}_{\mathbf{k}s}+\sum_{\mathbf{k}',s'}e^{i(\omega_0-\omega_{\mathrm{k}'})t}g^{(1)}_{\mathbf{k}'s'}c^{gg}_{\mathbf{k}s,\mathbf{k}'s'}(t)\epsilon(\mathbf{k}s,\mathbf{k}'s'), \tag{5.37b}
$$

$$
i\frac{d}{dt}c^{ge}_{\mathbf{k}s}(t)=e^{-i(\omega_0-\omega_{\mathrm{k}})t}c^{ee}(t)g^{(1)*}_{\mathbf{k}s}+\sum_{\mathbf{k}',s'}e^{i(\omega_0-\omega_{\mathrm{k}'})t}g^{(2)}_{\mathbf{k}'s'}c^{gg}_{\mathbf{k}s,\mathbf{k}'s'}(t)\epsilon(\mathbf{k}s,\mathbf{k}'s'), \tag{5.37c}
$$

$$
\begin{aligned}
i\frac{d}{dt}c^{gg}_{\mathbf{k}s,\mathbf{k}'s'}(t)&=\frac{1}{\epsilon(\mathbf{k}s,\mathbf{k}'s')}\left[c^{eg}_{\mathbf{k}s}(t)g^{(1)*}_{\mathbf{k}'s'}e^{-i(\omega_0-\omega_{\mathrm{k}'})t}+c^{eg}_{\mathbf{k}'s'}(t)g^{(1)*}_{\mathbf{k}s}e^{-i(\omega_0-\omega_{\mathrm{k}})t}\right]\\
&+\frac{1}{\epsilon(\mathbf{k}s,\mathbf{k}'s')}\left[c^{ge}_{\mathbf{k}s}(t)g^{(2)*}_{\mathbf{k}'s'}e^{-i(\omega_0-\omega_{\mathrm{k}'})t}+c^{ge}_{\mathbf{k}'s'}(t)g^{(2)*}_{\mathbf{k}s}e^{-i(\omega_0-\omega_{\mathrm{k}})t}\right],
\end{aligned}
\tag{5.37d}
$$

where $\epsilon(\mathbf{k}s,\mathbf{k}'s')$ is the Einstein function [255], which is equal to 2 if $\mathbf{k}=\mathbf{k}'$ and $s=s'$, whereas it becomes equal to 1 in any other case. We have checked that reducing the above system of differential equations to the case of a single polarization mode s leads to the same system of equations provided in Ref. [255].

We next formally integrate the differential equation of the two-photon probability

amplitude $c^{gg}_{\mathbf{k}s,\mathbf{k}'s'}(t)$ [Eq. (5.37d)], which yields

$$\begin{aligned} c^{gg}_{\mathbf{k}s\mathbf{k}'s'}(t) = &-\frac{i}{\epsilon(\mathbf{k}s,\mathbf{k}'s')}\int_0^t dt' e^{-i(\omega_0-\omega_{\mathrm{k}'})t'}\left[c^{eg}_{\mathbf{k}s}(t')g^{(1)*}_{\mathbf{k}'s'} + c^{ge}_{\mathbf{k}s}(t')g^{(2)*}_{\mathbf{k}'s'}\right] \\ &-\frac{i}{\epsilon(\mathbf{k}s,\mathbf{k}'s')}\int_0^t dt' e^{-i(\omega_0-\omega_{\mathrm{k}})t'}\left[c^{eg}_{\mathbf{k}'s'}(t')g^{(1)*}_{\mathbf{k}s} + c^{ge}_{\mathbf{k}'s'}(t')g^{(2)*}_{\mathbf{k}s}\right]. \end{aligned} \tag{5.38}$$

Further, we substitute this equation into the differential equations of $c^{eg}_{\mathbf{k}s}(t)$ and $c^{ge}_{\mathbf{k}s}(t)$, which are given in Eqs. (5.37b) and (5.37c), respectively. Here, we describe in detail the procedure followed after the substitution into the differential equation of $c^{eg}_{\mathbf{k}s}(t)$ [an identical procedure is followed after the substitution into the differential equation of $c^{ge}_{\mathbf{k}s}(t)$]. The result of this substitution is

$$\begin{aligned} i\frac{d}{dt}c^{eg}_{\mathbf{k}s}(t) = &\, e^{-i(\omega_0-\omega_{\mathrm{k}})t}c^{ee}(t)g^{(2)*}_{\mathbf{k}s} - i\sum_{\mathbf{k}'s'} e^{i(\omega_0-\omega_{\mathrm{k}'})t}g^{(1)}_{\mathbf{k}'s'} \\ &\times\left[\int_0^t dt' c^{eg}_{\mathbf{k}s}(t')g^{(1)*}_{\mathbf{k}'s'}e^{-i(\omega_0-\omega_{\mathrm{k}'})t'} + \int_0^t dt' c^{ge}_{\mathbf{k}s}(t')g^{(2)*}_{\mathbf{k}'s'}e^{-i(\omega_0-\omega_{\mathrm{k}'})t'}\right. \\ &\left. + \int_0^t dt' c^{eg}_{\mathbf{k}'s'}(t')g^{(1)*}_{\mathbf{k}s}e^{-i(\omega_0-\omega_{\mathrm{k}})t'} + \int_0^t dt' c^{ge}_{\mathbf{k}'s'}(t')g^{(2)*}_{\mathbf{k}s}e^{-i(\omega_0-\omega_{\mathrm{k}})t'}\right]. \end{aligned} \tag{5.39}$$

The terms in the last line of this expression vanish, as demonstrated in Ref. [256]. After this demonstration, the authors in Ref. [256] limit themselves to the case in which both transition dipole moments have identical polarization, which is not our case.

We now assume that the probability amplitudes vary much slower in time than the other terms inside the time integral in Eq. (5.39). As described in Section 1.3, this approximation works very well and, additionally, allows us (i) to replace $c^{eg}_{\mathbf{k}s}(t')$ and $c^{ge}_{\mathbf{k}s}(t')$ in Eq. (5.39) by $c^{eg}_{\mathbf{k}s}(t)$ and $c^{ge}_{\mathbf{k}s}(t)$, and (ii) to extend the upper limit of the time integral in this equation to ∞. As a consequence, Eq. (5.39) becomes

$$\begin{aligned} i\frac{d}{dt}c^{eg}_{\mathbf{k}s}(t) = &\, e^{-i(\omega_0-\omega_{\mathrm{k}})t}c^{ee}(t)g^{(2)*}_{\mathbf{k}s} \\ &- i\sum_{\mathbf{k}'s'}\int_0^\infty dt' e^{i(\omega_0-\omega_{\mathrm{k}'})(t-t')}\left[c^{eg}_{\mathbf{k}s}(t)|g^{(1)}_{\mathbf{k}'s'}|^2 + c^{ge}_{\mathbf{k}s}(t)g^{(1)}_{\mathbf{k}'s'}g^{(2)*}_{\mathbf{k}'s'}\right]. \end{aligned} \tag{5.40}$$

At this point, we transform the summation over $\mathbf{k}$ into an integral in $\mathbf{k}$-space [Eq. (1.134)]. Additionally, the calculation of the time integrals in Eq. (5.40) is

facilitated by the Sokhotski-Plemelj theorem in Eq. (1.158). In this way, we obtain

$$i\frac{d}{dt}c_{\mathbf{k}s}^{eg} = e^{-i(\omega_0-\omega_{\mathrm{k}})t}c^{ee}g_{\mathbf{k}s}^{(2)*} - i\frac{\mathcal{V}}{(2\pi)^3}\sum_{s'=1,2}\int_0^{2\pi}d\phi'\int_0^{\pi}d\theta'\sin\theta'\int_0^{\infty}d\mathrm{k}'(\mathrm{k}')^2 \times\left[\pi\delta(\omega_0-\omega_{\mathrm{k}'})+i\,\mathrm{p.v.}\frac{1}{(\omega_0-\omega_{\mathrm{k}'})}\right]\left[c_{\mathbf{k}s}^{eg}|g_{\mathbf{k}'s'}^{(1)}|^2+c_{\mathbf{k}s}^{ge}g_{\mathbf{k}'s'}^{(1)}g_{\mathbf{k}'s'}^{(2)*}\right], \tag{5.41}$$

where all the probability amplitudes are evaluated at time t. Next, we decompose the integral in the $\mathbf{k}$-space on the right-hand side of Eq. (5.41) into different contributions, which are calculated separately. Each of these contributions emerges from the multiplication of the different terms in brackets inside the integral in Eq. (5.41). First, the term proportional to $|g_{\mathbf{k}'s'}^{(1)}|^2\mathrm{p.v.}\{(\omega_0-\omega_{\mathrm{k}'})^{-1}\}$ is ignored because it provides the Lamb shift induced by the free-space electromagnetic field in the transition frequency of emitter $j=1$, as described in Section 1.3. This frequency shift is negligible for emitter transitions at optical frequencies and, additionally, the transition frequencies estimated from experiments (e.g., via a one-photon spectrum) already include this small shift. Thus, we consider that ω_0 in our model already contains the Lamb shift. Second, the term proportional to $|g_{\mathbf{k}'s'}^{(1)}|^2\delta(\omega_0-\omega_{\mathrm{k}'})$ provides the spontaneous emission rate γ_0 of emitter $j=1$. To demonstrate this, we use the general polarization vectors in Eqs. (1.137a)–(1.137b), which yields

$$\begin{aligned}
&\frac{\mathcal{V}}{(2\pi)^3}\sum_{s'=1,2}\int_0^{2\pi}d\phi'\int_0^{\pi}d\theta'\sin\theta'\int_0^{\infty}d\mathrm{k}'(\mathrm{k}')^2|g_{\mathbf{k}'s'}^{(1)}|^2\pi\delta(\omega_0-\omega_{\mathrm{k}'})\\
&=\frac{\mathcal{V}}{(2\pi)^3}\int_0^{\infty}d\mathrm{k}'(\mathrm{k}')^2\frac{\omega_{\mathrm{k}'}}{2\varepsilon_0 n^2\hbar\mathcal{V}}\pi\delta(\omega_0-\omega_{\mathrm{k}'})\int_0^{2\pi}d\phi'\int_0^{\pi}d\theta'\sin\theta'\sum_{s'=1,2}|\boldsymbol{\mu}_j\cdot\boldsymbol{e}_{\mathbf{k}'s'}|^2\\
&=\pi\frac{\mathcal{V}|\boldsymbol{\mu}_j|^2}{(2\pi)^3}\int_0^{\infty}d\mathrm{k}'(\mathrm{k}')^2\frac{\omega_{\mathrm{k}}}{2\varepsilon_0 n^2\hbar\mathcal{V}}\delta(\omega_0-\omega_{\mathrm{k}'})\int_0^{2\pi}d\phi'\int_0^{\pi}d\theta'\sin\theta'\Big[\sin^2\alpha_j\sin^2\theta'\\
&+\cos^2\alpha_j(\cos^2\theta'\cos^2\phi'+\sin^2\phi')-2\cos\alpha_j\sin\alpha_j\cos\theta'\sin\theta'\cos\phi'\Big]\\
&=\pi\frac{\mathcal{V}|\boldsymbol{\mu}_j|^2}{(2\pi)^3}\frac{8\pi}{3}\int_0^{\infty}d\mathrm{k}'(\mathrm{k}')^2\frac{\omega_{\mathrm{k}'}}{2\varepsilon_0 n^2\hbar\mathcal{V}}\delta(\omega_0-\omega_{\mathrm{k}'})=\frac{\omega_0^3|\boldsymbol{\mu}_j|^2 n}{6\pi\varepsilon_0\hbar c^3}=\frac{\gamma_0}{2}.
\end{aligned} \tag{5.42}$$

The remaining two contributions of the integral in Eq. (5.41) are obtained

integrating the term proportional to $g^{(1)}_{\mathbf{k}'s'}g^{(2)*}_{\mathbf{k}'s'}$. In this case, we find

$$\begin{aligned}
&\frac{\mathcal{V}}{(2\pi)^3}\sum_{s=1,2}\int_0^{2\pi}d\phi\int_0^{\pi}d\theta\sin\theta\int_0^{\infty}d\mathrm{k}'(\mathrm{k}')^2 g^{(1)}_{\mathbf{k}'s'}g^{(2)*}_{\mathbf{k}'s'}[\pi\delta(\omega_0-\omega_{\mathrm{k}'})+i\,\mathrm{p.v.}\frac{1}{\omega_0-\omega_{\mathrm{k}'}}]\\
&=\frac{\mathcal{V}}{(2\pi)^3}\frac{c|\boldsymbol{\mu}|^2}{2\varepsilon_0 n^3\hbar\mathcal{V}}4\pi\int_0^{\infty}d\mathrm{k}'(\mathrm{k}')^3[\pi\delta(\omega_0-\omega_{\mathrm{k}'})+i\,\mathrm{p.v.}\frac{1}{\omega_0-\omega_{\mathrm{k}'}}]\\
&\times\Bigg[\cos\alpha_1\cos\alpha_2\left(-\frac{\sin(\mathrm{k}'r_{12})}{(\mathrm{k}'r_{12})^3}+\frac{\cos(\mathrm{k}'r_{12})}{(\mathrm{k}'r_{12})^2}+\frac{\sin(\mathrm{k}'r_{12})}{(\mathrm{k}'r_{12})}\right)\\
&+2\sin\alpha_1\sin\alpha_2\left(\frac{\sin(\mathrm{k}'r_{12})}{(\mathrm{k}'r_{12})^3}-\frac{\cos(\mathrm{k}'r_{12})}{(\mathrm{k}'r_{12})^2}\right)\Bigg]\\
&=\frac{3\gamma_0}{4\pi\omega_0^3}\int_0^{\infty}d\omega_{\mathrm{k}'}\omega^3_{\mathrm{k}'}[\pi\delta(\omega_0-\omega_{\mathrm{k}'})+i\,\mathrm{p.v.}\frac{1}{\omega_0-\omega_{\mathrm{k}'}}]\\
&\times\Bigg[\cos\alpha_1\cos\alpha_2\left(-\frac{\sin(\mathrm{k}'r_{12})}{(\mathrm{k}'r_{12})^3}+\frac{\cos(\mathrm{k}'r_{12})}{(\mathrm{k}'r_{12})^2}+\frac{\sin(\mathrm{k}'r_{12})}{(\mathrm{k}'r_{12})}\right)\\
&+2\sin\alpha_1\sin\alpha_2\left(\frac{\sin(\mathrm{k}'r_{12})}{(\mathrm{k}'r_{12})^3}-\frac{\cos(\mathrm{k}'r_{12})}{(\mathrm{k}'r_{12})^2}\right)\Bigg].
\end{aligned}\tag{5.43}$$

The direct calculation of the frequency integral in this expression does not give the exact dipole-dipole coupling V [Eq. (3.44)], due to the terms ignored by the RWA in the interaction Hamiltonian (which are proportional to $\hat{\sigma}_j\hat{a}_{\mathbf{k}s}$ and to $\hat{\sigma}_j^{\dagger}\hat{a}_{\mathbf{k}s}^{\dagger}$), as described above. Milonni and Knight pointed out in Ref. [179] that extending the lower limit of the frequency integral from 0 to $-\infty$ captures in an effective way the contribution of the terms neglected by the RWA (as we did in the derivation of the electric field radiated from a quantum emitter in Section 1.2.7), leading to the rigorous expression of the coherent dipole-dipole coupling V. Following this

argument in Eq. (5.43), we obtain

$$\begin{aligned}
&\frac{3\gamma_0}{4\pi\omega_0^3}\int_{-\infty}^{\infty} d\omega_{\mathrm{k}'}\omega_{\mathrm{k}'}^3[\pi\delta(\omega_0-\omega_{\mathrm{k}'})+i\,\mathrm{p.v.}\frac{1}{\omega_0-\omega_{\mathrm{k}'}}]\\
&\times\Bigg[\cos\alpha_1\cos\alpha_2\bigg(-\frac{\sin(\mathrm{k}'r_{12})}{(\mathrm{k}'r_{12})^3}+\frac{\cos(\mathrm{k}'r_{12})}{(\mathrm{k}'r_{12})^2}+\frac{\sin(\mathrm{k}'r_{12})}{(\mathrm{k}'r_{12})}\bigg)\\
&+2\sin\alpha_1\sin\alpha_2\bigg(\frac{\sin(\mathrm{k}'r_{12})}{(\mathrm{k}'r_{12})^3}-\frac{\cos(\mathrm{k}'r_{12})}{(\mathrm{k}'r_{12})^2}\bigg)\Bigg]\\
&=\frac{3\gamma_0}{4}i\Bigg[-\cos\alpha_1\cos\alpha_2\frac{\cos(\mathrm{k}_0r_{12})}{(\mathrm{k}_0r_{12})}\\
&+(\cos\alpha_1\cos\alpha_2-2\sin\alpha_1\sin\alpha_2)\bigg(\frac{\sin(\mathrm{k}_0r_{12})}{(\mathrm{k}_0r_{12})^2}+\frac{\cos(\mathrm{k}_0r_{12})}{(\mathrm{k}_0r_{12})^3}\bigg)\Bigg]\\
&+\frac{3\gamma_0}{4}\Bigg[\cos\alpha_1\cos\alpha_2\frac{\sin(\mathrm{k}_0r_{12})}{(\mathrm{k}_0r_{12})}\\
&+(\cos\alpha_1\cos\alpha_2-2\sin\alpha_1\sin\alpha_2)\bigg(\frac{\cos(\mathrm{k}_0r_{12})}{(\mathrm{k}_0r_{12})^2}-\frac{\sin(\mathrm{k}_0r_{12})}{(\mathrm{k}_0r_{12})^3}\bigg)\Bigg]\\
&=iV+\frac{\tilde{\gamma}}{2},
\end{aligned}\tag{5.44}$$

where $\mathrm{k}_0=n\omega_0/c$ is the wavenumber at ω_0. In the evaluation of the complex integral in Eq. (5.44), we have used [179]

$$\begin{aligned}
&\int_{-\infty}^{\infty} d\omega_{\mathrm{k}}\omega_{\mathrm{k}}^3[\pi\delta(\omega_0-\omega_{\mathrm{k}})+i\,\mathrm{p.v.}\frac{1}{\omega_0-\omega_{\mathrm{k}}}]\bigg(q\frac{\sin(\mathrm{k}r_{12})}{(\mathrm{k}r_{12})^3}-q\frac{\cos(\mathrm{k}r_{12})}{(\mathrm{k}r_{12})^2}+p\frac{\sin(\mathrm{k}r_{12})}{(\mathrm{k}r_{12})}\bigg)\\
&=\pi\omega_0^3\bigg(q\frac{\sin(\mathrm{k}_0r_{12})}{(\mathrm{k}_0r_{12})^3}-q\frac{\cos(\mathrm{k}_0r_{12})}{(\mathrm{k}_0r_{12})^2}+p\frac{\sin(\mathrm{k}_0r_{12})}{(\mathrm{k}_0r_{12})}\bigg)\\
&-i\pi\omega_0^3\bigg(q\frac{\cos(\mathrm{k}_0r_{12})}{(\mathrm{k}_0r_{12})^3}+q\frac{\sin(\mathrm{k}_0r_{12})}{(\mathrm{k}_0r_{12})^2}+p\frac{\cos(\mathrm{k}_0r_{12})}{(\mathrm{k}_0r_{12})}\bigg).
\end{aligned}\tag{5.45}$$

Additionally, in Eq. (5.44) we have identified the coherent dipole-dipole coupling V [Eq. (3.44)] and the dissipative dipole-dipole coupling $\tilde{\gamma}$ [Eq. (3.50)]. Particularly, for the transition dipole moments considered in this section [Eq. (5.26)] and $\mathbf{r}_{12}=r_{12}\boldsymbol{e}_z$, the coherent dipole-dipole coupling reduces to

$$\begin{aligned}
V=\frac{3\gamma_0}{4}\Bigg[&-\cos\alpha_1\cos\alpha_2\frac{\cos(\mathrm{k}_0r_{12})}{(\mathrm{k}_0r_{12})}\\
&+(\cos\alpha_1\cos\alpha_2-2\sin\alpha_1\sin\alpha_2)\bigg(\frac{\sin(\mathrm{k}_0r_{12})}{(\mathrm{k}_0r_{12})^2}+\frac{\cos(\mathrm{k}_0r_{12})}{(\mathrm{k}_0r_{12})^3}\bigg)\Bigg],
\end{aligned}\tag{5.46}$$

and the dissipative dipole-dipole coupling to

$$\tilde{\gamma} = \frac{3\gamma_0}{2}\Bigg[\cos\alpha_1\cos\alpha_2\frac{\sin(\mathrm{k}_0 r_{12})}{(\mathrm{k}_0 r_{12})} + (\cos\alpha_1\cos\alpha_2 - 2\sin\alpha_1\sin\alpha_2)\left(\frac{\cos(\mathrm{k}_0 r_{12})}{(\mathrm{k}_0 r_{12})^2} - \frac{\sin(\mathrm{k}_0 r_{12})}{(\mathrm{k}_0 r_{12})^3}\right)\Bigg]. \tag{5.47}$$

Substituting Eqs. (5.42), (5.43) and (5.44) into Eq. (5.41) we obtain

$$i\frac{d}{dt}c^{eg}_{\mathbf{k}s}(t) = e^{-i(\omega_0-\omega_\mathrm{k})t}c^{ee}(t)g^{(2)*}_{\mathbf{k}s} - ic^{eg}_{\mathbf{k}s}(t)\frac{\gamma_0}{2} + c^{ge}_{\mathbf{k}s}(t)(V - i\frac{\tilde{\gamma}}{2}). \tag{5.48}$$

Similarly, after applying the same procedure to the differential equation of $c^{ge}_{\mathbf{k}s}(t)$ in Eq. (5.37c), we find

$$i\frac{d}{dt}c^{ge}_{\mathbf{k}s}(t) = e^{-i(\omega_0-\omega_\mathrm{k})t}c^{ee}(t)g^{(1)*}_{\mathbf{k}s} - ic^{ge}_{\mathbf{k}s}(t)\frac{\gamma_0}{2} + c^{eg}_{\mathbf{k}s}(t)(V - i\frac{\tilde{\gamma}}{2}). \tag{5.49}$$

Therefore, Eqs. (5.48) and (5.49) provide a pair of differential equations for the probability amplitudes $c^{eg}_{\mathbf{k}s}(t)$ and $c^{ge}_{\mathbf{k}s}(t)$, respectively, that depend only on these same probability amplitudes and on $c^{ee}(t)$. The coherent dipole-dipole coupling V, the dissipative coupling $\tilde{\gamma}$ and the spontaneous emission rate γ_0 appear explicitly in these differential equations.

Furthermore, we consider that the population $|c^{ee}(t)|^2$ of the doubly-excited state $|e_1e_2\rangle$ decays with rate $2\gamma_0$, which can be verified for example using the Markovian master equation to trace the electromagnetic degrees of freedom and reduce to the Hilbert space of the emitters, as done in Section 3.1.4. Specifically, this can be checked by simplifying Eq. (3.73a) to the case of no driving. We thus consider

$$c^{ee}(t) = e^{-\gamma_0 t}c^{ee}(0) = e^{-\gamma_0 t}, \tag{5.50}$$

which yields $|c^{ee}(t)|^2 = \exp(-2\gamma_0 t)$. Consequently, we obtain the set of coupled differential equations

$$\frac{d}{dt}c^{eg}_{\mathbf{k}s}(t) = -ie^{-i(\omega_0-\omega_\mathrm{k})t}e^{-\gamma_0 t}g^{(2)*}_{\mathbf{k}s} - c^{eg}_{\mathbf{k}s}(t)\frac{\gamma_0}{2} - (iV + \frac{\tilde{\gamma}}{2})c^{ge}_{\mathbf{k}s}(t), \tag{5.51a}$$

$$\frac{d}{dt}c^{ge}_{\mathbf{k}s}(t) = -ie^{-i(\omega_0-\omega_\mathrm{k})t}e^{-\gamma_0 t}g^{(1)*}_{\mathbf{k}s} - c^{ge}_{\mathbf{k}s}(t)\frac{\gamma_0}{2} - (iV + \frac{\tilde{\gamma}}{2})c^{eg}_{\mathbf{k}s}(t). \tag{5.51b}$$

These differential equations couple only a pair of probability amplitudes, $c^{eg}_{\mathbf{k}s}(t)$ and $c^{ge}_{\mathbf{k}s}(t)$, and can be solved analytically without further approximations [in contrast to the set of infinite coupled differential equations in Eqs. (5.37a)–(5.37d)]. The

solution of this system is

$$2ic^{eg}_{\mathbf{k}s}(t) = S^{(-)}_{\mathbf{k}s}\exp\Big[-(\frac{\gamma_0+\tilde{\gamma}}{2}+iV)t\Big] - \frac{i}{2}A^{(+)}_{\mathbf{k}s}\exp\Big[-(\frac{\gamma_0-\tilde{\gamma}}{2}-iV)t\Big] - (S^{(-)}_{\mathbf{k}s}-A^{(+)}_{\mathbf{k}s})\exp\Big[-(\gamma_0+i(\omega_0-\omega_\mathrm{k}))t\Big], \tag{5.52a}$$

$$2ic^{ge}_{\mathbf{k}s}(t) = S^{(-)}_{\mathbf{k}s}\exp\Big[-(\frac{\gamma_0+\tilde{\gamma}}{2}+iV)t\Big] + A^{(+)}_{\mathbf{k}s}\exp\Big[-(\frac{\gamma_0-\tilde{\gamma}}{2}-iV)t\Big] - (S^{(-)}_{\mathbf{k}s}+A^{(+)}_{\mathbf{k}s})\exp\Big[-(\gamma_0-i(\omega_0-\omega_\mathrm{k}))t\Big], \tag{5.52b}$$

where we have introduced

$$S^{(\pm)}_{\mathbf{k}s} = \frac{g^{(1)*}_{\mathbf{k}s}+g^{(2)*}_{\mathbf{k}s}}{(\gamma_0\pm\tilde{\gamma})/2+i(\omega_0\pm V-\omega_\mathrm{k})}, \tag{5.53}$$

$$A^{(\pm)}_{\mathbf{k}s} = \frac{g^{(1)*}_{\mathbf{k}s}-g^{(2)*}_{\mathbf{k}s}}{(\gamma_0\pm\tilde{\gamma})/2+i(\omega_0\pm V-\omega_\mathrm{k})}, \tag{5.54}$$

which are Lorentzian distributions related to the emission of a single photon of frequency ω_k centered around $\omega_0 \pm V$, with linewidth $\gamma_0 \pm \tilde{\gamma}$.

Finally, we substitute Eqs. (5.52a)–(5.52b) into the differential equation of $c^{gg}_{\mathbf{k}s,\mathbf{k}'s'}(t)$ [Eq. (5.37d)] and solve the resulting time integral. We find

$$\begin{aligned}2\epsilon(\mathbf{k}s\mathbf{k}'s')\dot{c}^{gg}_{\mathbf{k}s\mathbf{k}'s'}(t) = &-\Big(1-\exp\Big[-[\frac{\gamma_0+\tilde{\gamma}}{2}+i(\omega_0-\omega_{\mathrm{k}'}+V)]t\Big]\Big)S^{(-)}_{\mathbf{k}s}S^{(+)}_{\mathbf{k}'s'}\\ &-\Big(1-\exp\Big[-[\frac{\gamma_0+\tilde{\gamma}}{2}+i(\omega_0-\omega_\mathrm{k}+V)]t\Big]\Big)S^{(-)}_{\mathbf{k}'s'}S^{(+)}_{\mathbf{k}s}\\ &+\Big(1-\exp\Big[-[\frac{\gamma_0-\tilde{\gamma}}{2}+i(\omega_0-\omega_{\mathrm{k}'}-V)]t\Big]\Big)A^{(+)}_{\mathbf{k}s}A^{(-)}_{\mathbf{k}'s'}\\ &+\Big(1-\exp\Big[-[\frac{\gamma_0-\tilde{\gamma}}{2}+i(\omega_0-\omega_\mathrm{k}-V)]t\Big]\Big)A^{(+)}_{\mathbf{k}'s'}A^{(-)}_{\mathbf{k}s}\\ &+\Big(1-\exp\Big[-[\gamma_0+i(2\omega_0-\omega_\mathrm{k}-\omega_{\mathrm{k}'})]t\Big]\Big)\\ &\times\Big[S^{(-)}_{\mathbf{k}s}S^{(0)}_{\mathbf{k}'s'\mathrm{k}}+S^{(-)}_{\mathbf{k}'s'}S^{(0)}_{\mathbf{k}s\mathrm{k}'}-A^{(+)}_{\mathbf{k}s}A^{(0)}_{\mathbf{k}'s'\mathrm{k}}-A^{(+)}_{\mathbf{k}'s'}A^{(0)}_{\mathbf{k}s\mathrm{k}'}\Big].\end{aligned} \tag{5.55}$$

Here, we have introduced the Lorentzian distributions

$$S^{(0)}_{\mathbf{k}s\mathrm{k}'} = \frac{g^{(1)*}_{\mathbf{k}s}+g^{(2)*}_{\mathbf{k}s}}{\gamma_0+i(2\omega_0-\omega_\mathrm{k}-\omega_{\mathrm{k}'})}, \tag{5.56}$$

$$A^{(0)}_{\mathbf{k}s\mathrm{k}'} = \frac{g^{(1)*}_{\mathbf{k}s} - g^{(2)*}_{\mathbf{k}s}}{\gamma_0 + i(2\omega_0 - \omega_\mathrm{k} - \omega_{\mathrm{k}'})}, \tag{5.57}$$

which are related to the emission of two photons at frequencies ω_k and $\omega_{\mathrm{k}'}$ satisfying energy conservation $\omega_\mathrm{k} + \omega_{\mathrm{k}'} = 2\omega_0$. These two-photon emission processes can be mediated by intermediate virtual states rather than by real eigenstates of the system, as the leapfrog processes described in Sections 2.4.4 and 3.4.

At sufficiently long times ($t \to \infty$), we find that both emitters have relaxed [i.e., $c^{ee}(\infty) = c^{eg}_{\mathbf{k}s}(\infty) = c^{ge}_{\mathbf{k}s}(\infty) = 0$] and the two-photon state becomes

$$|\psi(\infty)\rangle = \sum_{\mathbf{k},s} \sum_{\substack{(\mathbf{k}',s') \\ \geq(\mathbf{k},s)}} c^{gg}_{\mathbf{k}s,\mathbf{k}'s'}(\infty)\, |g_1 g_2\rangle\, \hat{a}^\dagger_{\mathbf{k}s} \hat{a}^\dagger_{\mathbf{k}'s'} |\mathrm{vac}\rangle\,, \tag{5.58}$$

with the two-photon probability amplitudes given by

$$\begin{aligned} c^{gg}_{\mathbf{k}s,\mathbf{k}'s'}(\infty) = &- \frac{S^{(-)}_{\mathbf{k}s}\left[S^{(+)}_{\mathbf{k}'s'} - S^{(0)}_{\mathbf{k}'s'\mathrm{k}}\right] + S^{(-)}_{\mathbf{k}'s'}\left[S^{(+)}_{\mathbf{k}s} - S^{(0)}_{\mathbf{k}s\mathrm{k}'}\right]}{2\epsilon(\mathbf{k}s, \mathbf{k}'s')} \\ &+ \frac{A^{(+)}_{\mathbf{k}s}\left[A^{(-)}_{\mathbf{k}'s'} - A^{(0)}_{\mathbf{k}'s'\mathrm{k}}\right] + A^{(+)}_{\mathbf{k}'s'}\left[A^{(-)}_{\mathbf{k}s} - A^{(0)}_{\mathbf{k}s\mathrm{k}'}\right]}{2\epsilon(\mathbf{k}s, \mathbf{k}'s')}. \end{aligned} \tag{5.59}$$

These probability amplitudes carry all the information of the two-photon emission: directions of emission, frequencies and polarizations. As a consequence, they encode as well the information of the degree of two-photon entanglement.

In the following, we use the analytical expression of the two-photon probability amplitude $c^{gg}_{\mathbf{k}s,\mathbf{k}'s'}(\infty)$ [Eq. (5.59)] to characterize the two-photon state resulting when the emitters are perpendicularly oriented (Section 5.2.3), as well as to quantify the degree of entanglement of the two-photon post-selected state obtained after including the influence of optical filters and erasing the frequency degrees of freedom (Section 5.3).

5.2.3 Rigorous analysis of the generation of entangled photons from interacting quantum emitters

We show in this section that the two-photon steady state $|\psi(\infty)\rangle$ derived in Section 5.2.2 is consistent with that expected from the intuitive argument in Section 5.2.1, when the transition dipole moments are perpendicularly oriented.

To better characterize the two-photon state $|\psi(\infty)\rangle$ [Eq. (5.58)], we first define the probability density for each pair of frequencies, polarization modes and directions of emission. To this end, we use the normalization condition

$|\langle\psi(\infty)|\psi(\infty)\rangle|^2 = 1$, which yields

$$\begin{aligned} 1 &= \sum_{\mathbf{k},s}\sum_{\mathbf{k}',s'} |c^{gg}_{\mathbf{k}s,\mathbf{k}'s'}(\infty)|^2 \\ &= \int d\Omega \int d\Omega' \int_0^\infty d\mathrm{k} \int_0^\infty d\mathrm{k}' \sum_{s,s'} \frac{\mathrm{k}^2(\mathrm{k}')^2 |c^{gg}_{\mathbf{k}s\mathbf{k}'s'}(\infty)|^2 \mathcal{V}^2}{(2\pi)^6}, \end{aligned} \tag{5.60}$$

with $d\Omega$ and $d\Omega'$ differential solid angles that are integrated in the full space. In the second line of this expression we have transformed the summations over $\mathbf{k}$ and $\mathbf{k}'$ into integrals by using Eq. (1.134). Therefore, we can define

$$P(\mathbf{k},s;\mathbf{k}',s') = \frac{\mathrm{k}^2(\mathrm{k}')^2 |c^{gg}_{\mathbf{k}s\mathbf{k}'s'}(\infty)|^2 \mathcal{V}^2}{(2\pi)^6} \tag{5.61}$$

as the probability density of emission of two photons in modes ($\mathbf{k}$,s) and ($\mathbf{k}'$,s'). The integral of P over all degrees of freedom is one. Further, by integrating over the full range of absolute values of the wavevectors, and summing over the polarization modes, we can introduce the probability density for emission of two photons at directions (θ,ϕ) and (θ',ϕ'):

$$D(\theta,\phi;\theta',\phi') = \int_0^\infty d\mathrm{k} \int_0^\infty d\mathrm{k}' \sum_{s,s'} P(\mathbf{k},s;\mathbf{k}',s'). \tag{5.62}$$

In contrast to $P(\mathbf{k},s;\mathbf{k}',s')$, the probability density $D(\theta,\phi;\theta',\phi')$ distinguishes neither the frequencies of the photons (encoded in the absolute values of the wavevectors) nor their polarization modes.

We consider next that the transition dipole moments are perpendicularly oriented to each other and contained in the xz-plane, as in Section 5.2.1. Specifically, we fix again $\boldsymbol{\mu}_1 = \mu(\boldsymbol{e}_x + \boldsymbol{e}_z)/\sqrt{2}$ and $\boldsymbol{\mu}_2 = \mu(\boldsymbol{e}_x - \boldsymbol{e}_z)/\sqrt{2}$, which corresponds to $\alpha_1 = -\alpha_2 = \pi/4$ in Eq. (5.26). We first verify that the dominant directions of photon emission are those perpendicular to the xz-plane, as expected from the dipole radiation patterns in Figs. 5.1d and 5.1e. To this end, we fix $r_{12} = 0.075\lambda_0$, yielding $V \approx 3.5\gamma_0$, and also $\theta = \phi = \pi/2$, corresponding to the wavevector direction $\boldsymbol{e}_\mathbf{k} = \mathbf{k}/|\mathbf{k}| = \boldsymbol{e}_y$ (i.e., along the y-axis perpendicular to the xz-plane). We plot in Fig. 5.3 the resulting probability density D as a function of θ' and ϕ'. Figure 5.3 shows two regions where the probability density D becomes larger, which are around the directions $\boldsymbol{e}_{\mathbf{k}'} = \mathbf{k}'/|\mathbf{k}'| = \boldsymbol{e}_y$ (at $\theta' = \phi' = \pi/2$) and $\boldsymbol{e}_{\mathbf{k}'} = -\boldsymbol{e}_y$ ($\theta' = -\phi' = \pi/2$), as expected from the simple argument in Section 5.2.1. We emphasize that $D(\theta,\phi;\theta',\phi')$ has been defined so that integrating this function over the four angle arguments is equal to one.

Next, we analyze the two-photon state $|\psi(\infty)\rangle$ for emission directions fixed at $\boldsymbol{e}_\mathbf{k} = \boldsymbol{e}_y$ and $\boldsymbol{e}_{\mathbf{k}'} = -\boldsymbol{e}_y$, with intermolecular distance along the z-axis fixed again at $r_{12} = 0.075\lambda_0$. To this end, we plot in Fig. 5.4a the probability density P [Eq. (5.61)] as a function of the photon frequencies $\omega_\mathrm{k} = \mathrm{k}c/n$ and $\omega_{\mathrm{k}'} = \mathrm{k}'c/n$

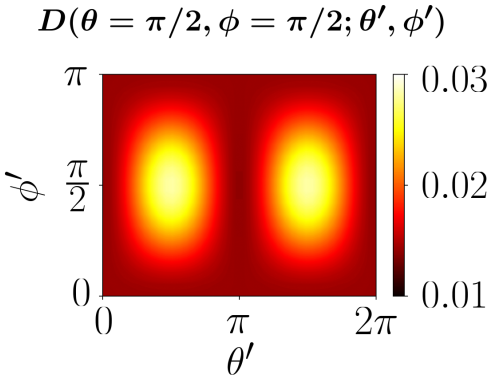

Figure 5.3: Dependence of the probability density $D(\theta = \pi/2, \phi = \pi/2; \theta', \phi')$ on θ' and ϕ' for two DBATT molecules separated by a distance $r_{12} = 0.075\lambda_0$ along the z-axis and with perpendicular transition dipole moments ($\alpha_1 = -\alpha_2 = \pi/4$ in Fig. 5.2). These molecules have spontaneous emission rate $\gamma_0/(2\pi) = 21.5$ MHz, transition frequency $\omega_0 = 2\pi c/\lambda_0$ corresponding to a vacuum wavelength $\lambda_0 = 618$ nm, and are embedded in a naphthalene crystal with $n = 1.5$. We neglect here the influence of the combined Debye-Waller/Franck-Condon by fixing $\alpha_{\rm DW} = 1$.

considering that the polarization modes s and s' of both photons are polarized along the x-axis direction. Specifically, we set $\boldsymbol{e}_{\mathbf{k}s} = \boldsymbol{e}_{\mathbf{k}'s'} = \boldsymbol{e}_x$. We find that P takes maximal values $\approx 3.5 \cdot 10^{-3}$ when one of the photons has frequency $\omega_+ = \omega_0 + V$ and the other photon $\omega_- = \omega_0 - V$, consistent with the two-photon emission via the symmetric state $|S\rangle$, see purple arrows in Fig. 5.1c. We find a similar dependence on $\omega_{\rm k}$ and $\omega_{\rm k'}$ of P for the case in which both s and s' are polarized along the z-axis (i.e., $\boldsymbol{e}_{\mathbf{k}s} = \boldsymbol{e}_{\mathbf{k}'s'} = \boldsymbol{e}_z$), which is shown in Fig. 5.4b. The maxima have again a value of $\approx 3.5 \cdot 10^{-3}$ and are found for a photon of frequency ω_+ and another photon of frequency ω_-, related in this case to the cascade emission via the antisymmetric state $|A\rangle$, which is indicated with green arrows in Fig. 5.1c.

The probability density P drastically decreases if one of the photons has x-polarization and the other photon z-polarization. To this end, we plot in Figs. 5.4c and 5.4d the dependence of P on the photon frequencies $\omega_{\rm k} = {\rm k}c/n$ and $\omega_{\rm k'} = {\rm k}'c/n$ when s is polarized along the x-axis ($\boldsymbol{e}_{\mathbf{k}s} = \boldsymbol{e}_x$), and s' along the z-axis ($\boldsymbol{e}_{\mathbf{k}'s'} = \boldsymbol{e}_z$). In Fig. 5.4c, we use a colorbar with the same scale as in Figs. 5.4a (where $\boldsymbol{e}_{\mathbf{k}s} = \boldsymbol{e}_{\mathbf{k}'s'} = \boldsymbol{e}_x$) and 5.4b (where $\boldsymbol{e}_{\mathbf{k}s} = \boldsymbol{e}_{\mathbf{k}'s'} = \boldsymbol{e}_z$). We find that the probability density P becomes negligible when s and s' are orthogonal modes, in comparison to the cases in which they are parallel. Further, we modify the scale of the colorbar in Fig. 5.4d, which allows to quantify that the maximum values of P when s and s' are orthogonal ($\boldsymbol{e}_{\mathbf{k}s} = \boldsymbol{e}_x$ and $\boldsymbol{e}_{\mathbf{k}'s'} = \boldsymbol{e}_z$) are 30 orders of magnitude smaller than the maximum values of P at parallel s and s' polarization modes (Figs. 5.4a and 5.4b). Identical behaviour of P is obtained at $\boldsymbol{e}_{\mathbf{k}s} = \boldsymbol{e}_z$ and $\boldsymbol{e}_{\mathbf{k}'s'} = \boldsymbol{e}_x$.

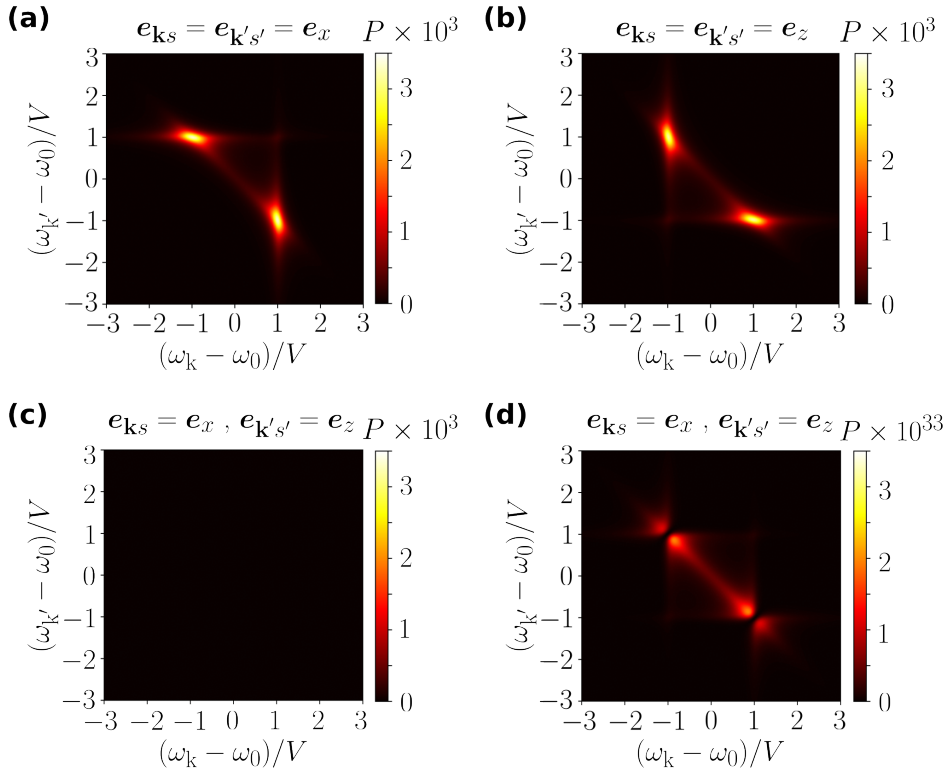

Figure 5.4: Characterization of the two-photon emission probability density P at directions $\boldsymbol{e}_{\mathbf{k}} = \boldsymbol{e}_y$ and $\boldsymbol{e}_{\mathbf{k}'} = -\boldsymbol{e}_y$. We consider two DBATT molecules with perpendicular transition dipole moments, with $\alpha_1 = -\alpha_2 = \pi/4$ in Eq. (5.26). These molecules have $\gamma_0/(2\pi) = 21.5$ MHz, vacuum wavelength $\lambda_0 = 618$ nm and they are embedded in a naphthalene crystal with refractive index $n = 1.5$. Additionally, we fix the intermolecular distance at $r_{12} = 0.075\lambda_0$, and neglect the influence of the combined Debye-Waller/Franck-Condon factor by fixing $\alpha_{\mathrm{DW}} = 1$. We plot P as a function of the photon frequencies $\omega_{\mathrm{k}} = \mathrm{k}c/n$ and $\omega_{\mathrm{k}'} = \mathrm{k}'c/n$, with the polarization modes s and s' polarized along the directions (a) $\boldsymbol{e}_{\mathbf{k}s} = \boldsymbol{e}_{\mathbf{k}'s'} = \boldsymbol{e}_x$, (b) $\boldsymbol{e}_{\mathbf{k}s} = \boldsymbol{e}_{\mathbf{k}'s'} = \boldsymbol{e}_z$, and (c,d) $\boldsymbol{e}_{\mathbf{k}s} = \boldsymbol{e}_x$ and $\boldsymbol{e}_{\mathbf{k}'s'} = \boldsymbol{e}_z$. In (c) we use a colorbar with the same scale as in (a) and (b). Panel (d) is identical to panel (c) except that we modify the scale of the colorbar 30 orders of magnitude to emphasize how small the values are.

Therefore, we conclude that two photons emitted along the directions $\boldsymbol{e}_{\mathbf{k}} = \boldsymbol{e}_y$ and $\boldsymbol{e}_{\mathbf{k}'} = -\boldsymbol{e}_y$ have negligible probability of having mutually orthogonal polarization (in the basis $\boldsymbol{e}_x$ and $\boldsymbol{e}_z$) in comparison to having parallel polarization, which is consistent with the entangled photon-state in Eq. (5.25) expected from the intuitive analysis in Section 5.2.1.

To further characterize the two-photon state $|\psi(\infty)\rangle$ at the directions of emission $\boldsymbol{e}_{\mathbf{k}} = \boldsymbol{e}_y$ and $\boldsymbol{e}_{\mathbf{k}'} = -\boldsymbol{e}_y$, we analyze the behaviour of the complex phase of

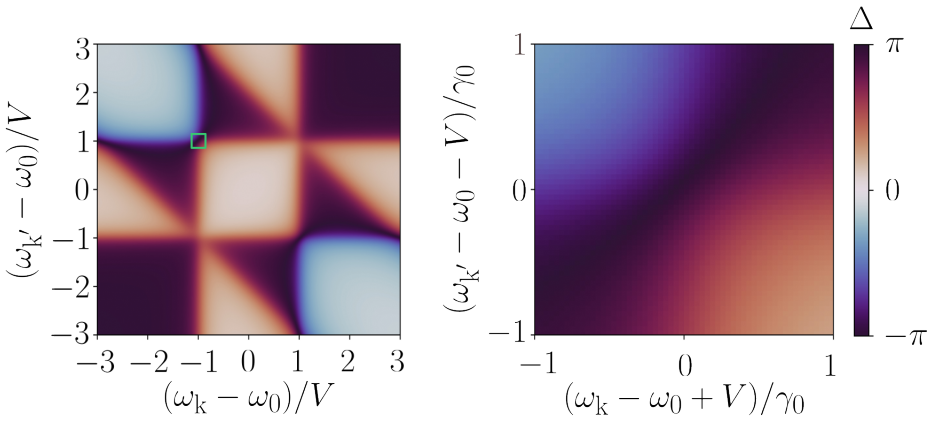

Figure 5.5: Characterization of the complex phase of the two-photon probability amplitude $c^{gg}_{\mathbf{k}s,\mathbf{k}'s'}(\infty)$. We focus on the directions of emission $\boldsymbol{e}_{\mathbf{k}} = \boldsymbol{e}_y$ and $\boldsymbol{e}_{\mathbf{k}'} = -\boldsymbol{e}_y$, and plot the relative phase Δ [Eq. (5.63)], which corresponds to the difference between the complex phase of the two-photon probability amplitude $c^{gg}_{\mathbf{k}s,\mathbf{k}'s'}(\infty)$ at $\boldsymbol{e}_{\mathbf{k}s} = \boldsymbol{e}_{\mathbf{k}'s'} = \boldsymbol{e}_x$ and the complex phase of the two-photon probability amplitude at $\boldsymbol{e}_{\mathbf{k}s} = \boldsymbol{e}_{\mathbf{k}'s'} = \boldsymbol{e}_z$. In the right panel we show a zoom of this relative phase around $\omega_{\mathrm{k}} = \omega_0 - V$ and $\omega_{\mathrm{k}'} = \omega_0 + V$ (highlighted with a green box in the left panel). The parameters used in the simulations correspond to two DBATT molecules with perpendicular transition dipole moments, $\alpha_1 = -\alpha_2 = \pi/4$ in Eq. (5.26). These molecules have $\gamma_0/(2\pi) = 21.5$ MHz, vacuum wavelength $\lambda_0 = 618$ nm and they are embedded in a naphthalene crystal with refractive index $n = 1.5$. Additionally, we fix the intermolecular distance along the z-axis at $r_{12} = 0.075\lambda_0$, and neglect the influence of the combined Debye-Waller/Franck-Condon factor by fixing $\alpha_{\mathrm{DW}} = 1$.

$c^{gg}_{\mathbf{k}s,\mathbf{k}'s'}(\infty)$. In Fig. 5.5, we plot the relative phase Δ between the two-photon probability amplitude at $\boldsymbol{e}_{\mathbf{k}s} = \boldsymbol{e}_{\mathbf{k}'s'} = \boldsymbol{e}_x$ and the two-photon probability amplitude at $\boldsymbol{e}_{\mathbf{k}s} = \boldsymbol{e}_{\mathbf{k}'s'} = \boldsymbol{e}_z$, again as a function of the frequency of the two photons. More specifically,

$$\begin{aligned}\Delta = &\ \mathrm{phase}\left[c^{gg}_{\mathbf{k}s,\mathbf{k}'s'}(\infty)\right]_{\boldsymbol{e}_{\mathbf{k}}=-\boldsymbol{e}_{\mathbf{k}'}=\boldsymbol{e}_y,\boldsymbol{e}_{\mathbf{k}s}=\boldsymbol{e}_{\mathbf{k}'s'}=\boldsymbol{e}_x} \\ &- \mathrm{phase}\left[c^{gg}_{\mathbf{k}s,\mathbf{k}'s'}(\infty)\right]_{\boldsymbol{e}_{\mathbf{k}}=-\boldsymbol{e}_{\mathbf{k}'}=\boldsymbol{e}_y,\boldsymbol{e}_{\mathbf{k}s}=\boldsymbol{e}_{\mathbf{k}'s'}=\boldsymbol{e}_z}.\end{aligned} \tag{5.63}$$

We find $\Delta \approx \pi$ near the photon frequencies that yield maximal probability density P of two-photon emission (i.e., one photon at ω_+ and another photon at ω_-), as can be more easily appreciated in the zoom in the right panel of Fig. 5.5. This difference of phase agrees with the relative phase between $|\boldsymbol{x},\omega_-\rangle\,|\boldsymbol{x},\omega_+\rangle$ and $|\boldsymbol{z},\omega_+\rangle\,|\boldsymbol{z},\omega_-\rangle$ in Eq. (5.25). However, deviations in the photon frequencies of the order of $\approx \gamma_0$ are sufficient to strongly modify the relative phase, which implies

deviating from the maximally entangled state in Eq. (5.25). Consequently, filters with very narrow linewidths are needed to post-select a highly entangled state, as we show in the next section.

5.3 Post-selection of a highly entangled two-photon state

We show in this section that a two-photon state highly entangled in polarization can be post-selected using optical filters and color-blind detectors. We consider that Alice detects light propagating in the direction $\boldsymbol{e}_y$ and Bob does it in the direction $-\boldsymbol{e}_y$, as schematically represented in Fig. 5.6. The post-selected state is based on the detection of a single ZPL photon by Alice and a single ZPL photon by Bob. Thus, this state is determined by the two-photon probability amplitudes $c^{gg}_{\mathbf{k}s\mathbf{k}'s'}(\infty)$ with $\boldsymbol{e}_{\mathbf{k}} = \boldsymbol{e}_y$ and $\boldsymbol{e}_{\mathbf{k}'} = -\boldsymbol{e}_y$. Additionally, Alice ($A$) and Bob ($B$) use optical filters with Lorentzian profiles given by

$$F_A(\omega) = \frac{\Gamma/2}{(\Gamma/2) + i(\omega - \omega_+)}, \tag{5.64a}$$

$$F_B(\omega) = \frac{\Gamma/2}{(\Gamma/2) + i(\omega - \omega_-)}. \tag{5.64b}$$

These profiles assume that both optical filters have the same linewidth Γ, but while Alice filters light around ω_+, Bob does it around ω_-.

Moreover, as the detectors are color-blind, the post-selected state has only polarization degrees of freedom and is thus properly described by a two-photon density matrix $\hat{\rho}_{\text{post}}$ (rather than by a pure state) due to the erasure of frequency information (Appendix A). To obtain the post-selected state, we follow the usual tomography procedure [257, 258]. In the orthogonal basis of polarization formed by the $\boldsymbol{e}_x$ and $\boldsymbol{e}_z$ directions (which are also orthogonal to the detection directions $\boldsymbol{e}_{\mathbf{k}} = \boldsymbol{e}_y$ and $\boldsymbol{e}_{\mathbf{k}'} = -\boldsymbol{e}_y$), the elements of the density matrix $\hat{\rho}_{\text{post}}$ are given by

$$\begin{aligned}\langle uu'|\,\hat{\rho}_{\text{post}}\,|ss'\rangle = \frac{1}{N_{\text{post}}}\int_0^\infty d\omega_{\text{k}}\int_0^\infty d\omega_{\text{k}'}\,\langle u(\omega_{\text{k}})u'(\omega_{\text{k}'})|\psi(\infty)\rangle \\ \times\,\langle\psi(\infty)|s(\omega_{\text{k}})s'(\omega_{\text{k}'})\rangle\,,\end{aligned} \tag{5.65}$$

where u, u', s, and s' are polarization modes with unit vectors $\boldsymbol{e}_x$ or $\boldsymbol{e}_z$. Additionally, $|s(\omega_{\text{k}})s'(\omega_{\text{k}'})\rangle$ is a two-photon pure state that (i) involves a photon of frequency ω_{k} propagating towards Alice ($\boldsymbol{e}_{\mathbf{k}} = \boldsymbol{e}_y$) and a photon of frequency $\omega_{\text{k}'}$ propagating towards Bob ($\boldsymbol{e}_{\mathbf{k}'} = -\boldsymbol{e}_y$), and (ii) accounts for the influence of the optical filters. More specifically, this state is given by

$$|s(\omega_{\text{k}})s'(\omega_{\text{k}'})\rangle = F_A(\omega_{\text{k}})F_B(\omega_{\text{k}'})\hat{a}^\dagger_{\mathbf{k}s}\hat{a}^\dagger_{\mathbf{k}'s'}\,|\text{vac}\rangle\Big|_{\mathbf{k}=\boldsymbol{e}_y n\omega_{\text{k}}/c,\mathbf{k}'=-\boldsymbol{e}_y n\omega_{\text{k}'}/c}. \tag{5.66}$$

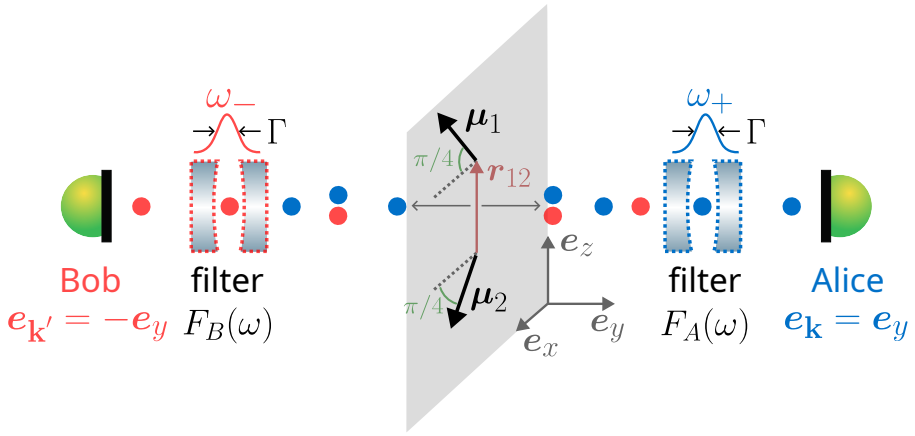

Figure 5.6: Schematic representation of the post-selection procedure. The transition dipole moments of the emitters are assumed to be contained in the xz-plane and perpendicularly oriented to each other ($\alpha_1 = -\alpha_2 = \pi/4$ in Fig. 5.2). Blue circles represent photons emitted at frequency $\approx \omega_+ = \omega_0 + V$, while red circles correspond to photons emitted from the interacting system at frequency $\approx \omega_- = \omega_0 - V$. *Alice* detects only photons emitted at $\boldsymbol{e}_{\mathbf{k}} = \boldsymbol{e}_y$ and *Bob* does it at $\boldsymbol{e}_{\mathbf{k}'} = -\boldsymbol{e}_y$. Additionally, Alice uses a filter with Lorentzian profile $F_A(\omega)$, with linewidth Γ and central frequency ω_+, whereas Bob uses a filter with Lorentzian profile $F_B(\omega)$, with linewidth Γ and central frequency ω_-.

Last, we have included in Eq. (5.65) the normalization factor

$$N_{\rm post} = \sum_{s,s'} \int_0^\infty d\omega_{\rm k} \int_0^\infty d\omega_{\rm k'} |\, \langle \psi(\infty) | s(\omega_{\rm k}) s'(\omega_{\rm k'}) \rangle \,|^2, \tag{5.67}$$

which guarantees that $\mathrm{Tr}\hat{\rho}_{\rm post} = 1$.

We quantify next the degree of entanglement of the two-photon post-selected state $\hat{\rho}_{\rm post}$ and its dependence on the separation distance r_{12} between the emitters as well as on the linewidth Γ of the filters. To this end, we compute the concurrence $\mathcal{C}(\hat{\rho}_{\rm post})$ [Eq. (5.23)], which quantifies the degree of polarization-entanglement between the two photons ($0 \leq \mathcal{C} \leq 1$, with $\mathcal{C} = 1$ for maximum entanglement, as discussed in Section 5.1). We consider again two DBATT molecules and plot in Figure 5.7a the dependence of $1 - \mathcal{C}(\hat{\rho}_{\rm post})$ on Γ (normalized by γ_0) and on r_{12} (normalized by λ_0). We find that filters with very narrow linewidth ($\Gamma/\gamma_0 \ll 0.1$) are needed to obtain a highly entangled post-selected state ($1 - \mathcal{C} \lesssim 10^{-2}$). Additionally, at $\Gamma/\gamma_0 \ll 0.1$ the dependence of the concurrence on r_{12} is very small for the range of distances analyzed here (the behaviour at larger separation distances is analyzed in Section 5.6). We attribute the necessity of very narrow filters to the high sensitivity to the frequency dispersion of the relative phase Δ between the two-photon probability amplitude $c^{gg}_{\mathbf{k}s,\mathbf{k}'s'}(\infty)$ at $s = s' = \boldsymbol{e}_x$ and the corresponding $c^{gg}_{\mathbf{k}s,\mathbf{k}'s'}(\infty)$ at $s = s' = \boldsymbol{e}_z$ [both of them evaluated at $\boldsymbol{e}_{\mathbf{k}} = -\boldsymbol{e}_{\mathbf{k}'} = \boldsymbol{e}_y$, see Eq.

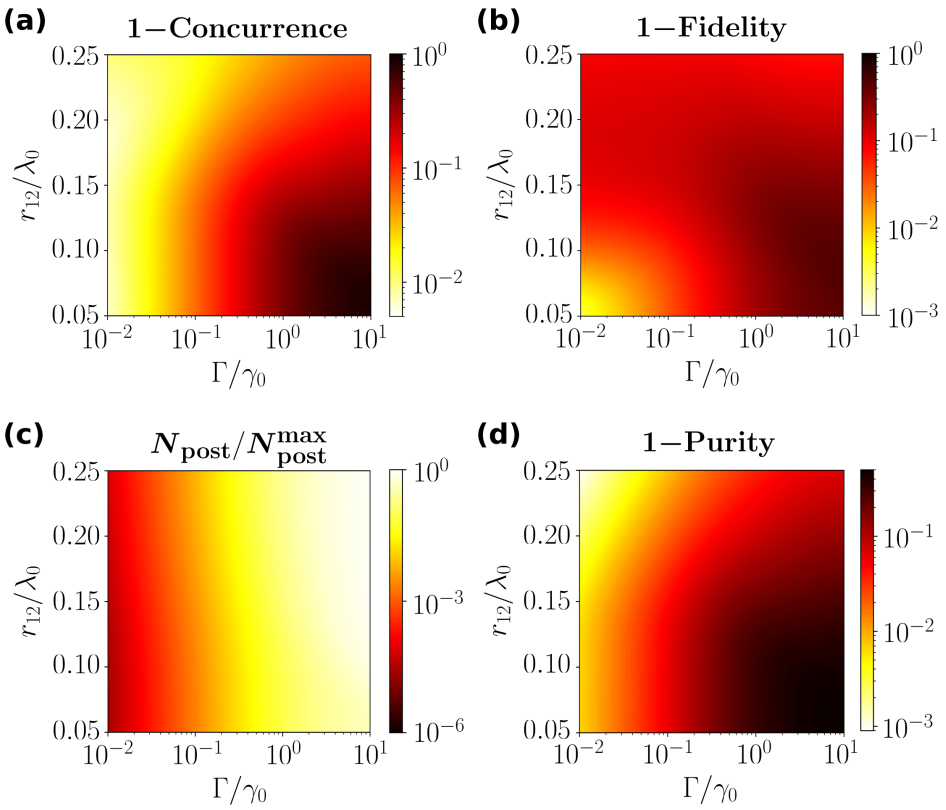

Figure 5.7: Characterization of the two-photon post-selected state $\hat{\rho}_{\rm post}$. The dependence on the linewidth Γ of the filters (normalized by the spontaneous emission rate γ_0) and on the distance r_{12} along the z-axis between the two emitters (normalized by λ_0) is plotted for (a) $1-\mathcal{C}(\hat{\rho}_{\rm post})$ [where $\mathcal{C}(\hat{\rho}_{\rm post})$ is the concurrence], (b) $1-\mathcal{F}(\hat{\rho}_{\rm post}, |\phi_-^{\rm xz}\rangle\langle\phi_-^{\rm xz}|)$ [where $\mathcal{F}(\hat{\rho}_{\rm post}, |\phi_-^{\rm xz}\rangle\langle\phi_-^{\rm xz}|)$ is the fidelity of $\hat{\rho}_{\rm post}$ with respect to the Bell state $|\phi_-^{\rm xz}\rangle = (|\boldsymbol{e}_x\boldsymbol{e}_x\rangle - |\boldsymbol{e}_z\boldsymbol{e}_z\rangle)/\sqrt{2}$], (c) the normalizing factor $N_{\rm post}$ of the density matrix divided by its maximum value $N_{\rm post}^{\rm max}$ in the Γ and r_{12} range plotted here, and (d) $1-\mathcal{P}(\hat{\rho}_{\rm post})$ [where $\mathcal{P}(\hat{\rho}_{\rm post})$ is the purity of $\hat{\rho}_{\rm post}$]. The two emitters are DBATT molecules, with $\gamma_0/(2\pi) = 21.5$ MHz, vacuum wavelength $\lambda_0 = 618$ nm, and embedded in a naphthalene crystal with refractive index $n = 1.5$. The transition dipole moments of these molecules are contained in the xz-plane and perpendicularly oriented to each other ($\alpha_1 = -\alpha_2 = \pi/4$ in Fig. 5.2). Alice detects only photons emitted at $\boldsymbol{e}_{\mathbf{k}} = \boldsymbol{e}_y$ and uses a Lorentzian filter centered around $\omega_+ = \omega_0 + V$, whereas Bob detects only photons emitted at $\boldsymbol{e}_{\mathbf{k}'} = -\boldsymbol{e}_y$ and uses a Lorentzian filter with central frequency $\omega_- = \omega_0 - V$.

(5.63)]. As discussed in Section 5.2.3 and shown in Fig. 5.5, if one of the photons has frequency ω_+ and the other one ω_- we find $\Delta \approx \pi$ (corresponding to a Bell state, with maximum entanglement), but small deviations in the photon frequencies drastically change this value of relative phase.

Moreover, to further verify the simple argument in Section 5.2.1, we analyze the similarity between the post-selected state $\hat{\rho}_{\text{post}}$ and the polarization Bell state

$$|\phi_{-}^{\text{xz}}\rangle = \frac{|\boldsymbol{e}_x\boldsymbol{e}_x\rangle - |\boldsymbol{e}_z\boldsymbol{e}_z\rangle}{\sqrt{2}}, \tag{5.68}$$

expected from Eq. (5.25) once the frequency degrees of freedom are erased. $|\phi_{-}^{\text{xz}}\rangle$ corresponds to the Bell state $|\phi_{-}\rangle$ [Eq. (5.7b)], with horizontal polarization in the x-axis ($H = \boldsymbol{e}_x$) and vertical polarization in the z-axis ($V = \boldsymbol{e}_z$). We compute the fidelity of $\hat{\rho}_{\text{post}}$ with respect to such state, which is given by

$$\mathcal{F}(\hat{\rho}_{\text{post}}, |\phi_{-}^{\text{xz}}\rangle\langle\phi_{-}^{\text{xz}}|) = |\langle\phi_{-}^{\text{xz}}|\hat{\rho}_{\text{post}}|\phi_{-}^{\text{xz}}\rangle|, \tag{5.69}$$

according to Eq. (5.21). Figure 5.7b shows the dependence on Γ/γ_0 and on r_{12}/λ_0 of $1 - \mathcal{F}(\hat{\rho}_{\text{post}}, |\phi_{-}^{\text{xz}}\rangle\langle\phi_{-}^{\text{xz}}|)$. We find again that very narrow filters are required to minimize the deviation of the post-selected state from $|\phi_{-}^{\text{xz}}\rangle$. Additionally, decreasing the intermolecular distances r_{12} for such narrow filters ($\Gamma/\gamma_0 \ll 0.1$) further minimizes the deviation of the post-selected state from $|\phi_{-}^{\text{xz}}\rangle$.

These findings indicate that filters with very narrow linewidths are required to obtain a highly polarization-entangled post-selected state. However, the probability of Alice and Bob receiving a single photon each decreases as the filters become narrower. To quantify how much this probability is reduced in comparison to the case in which broad filters are used, we analyze the factor N_{post}, given by the trace of $\hat{\rho}_{\text{post}}$ before normalization [Eq. (5.67)]. We plot in Fig. 5.7c the dependence on Γ/γ_0 and on r_{12}/λ_0 of N_{post}, divided by its maximum value $N_{\text{post}}^{\text{max}}$ obtained within the range of linewidth and intermolecular distance explored in this figure. For very narrow filters ($\Gamma \approx 10^{-2}\gamma_0$), N_{post} can be up to 6 orders of magnitude smaller than for broad filters ($\Gamma \approx 10\gamma_0$). Thus, to choose the optimal spectral widths of the filters in experiments, it is necessary to balance the degree of two-photon entanglement obtained and the probability of detecting two photons, as decreasing values of Γ increase the concurrence of the post-selected state but at the cost of lowering $N_{\text{post}}/N_{\text{post}}^{\text{max}}$.

Last, to gain additional information on the post-selected state $\hat{\rho}_{\text{post}}$, we analyze the loss of purity that occurs due to the erasure of the frequency information induced by the post-selection. To this end, we use the standard measure of purity of a quantum state (see Appendix A), which is defined as

$$\mathcal{P}(\hat{\rho}_{\text{post}}) = \text{Tr}(\hat{\rho}_{\text{post}}^2), \tag{5.70}$$

and known as *purity*. $\mathcal{P}(\hat{\rho}_{\text{post}})$ is bounded between 1/2 (maximally mixed state) and 1 (pure state). We plot in Fig. 5.7d the dependence of $1 - \mathcal{P}(\hat{\rho}_{\text{post}})$ on Γ/γ_0 and on r_{12}/λ_0. We find that the purity of the post-selected state decreases with the linewidths of the filters and that $1 - \mathcal{P}(\hat{\rho}_{\text{post}})$ exhibits a very similar behaviour to that of $1 - \mathcal{C}(\hat{\rho}_{\text{post}})$ in Fig. 5.7a.

5.4 Robustness of the photon entanglement

We have shown in Section 5.3 that a two-photon state highly entangled in polarization can be post-selected if the transition dipole moments of the emitters are perpendicularly oriented. Additionally, we have neglected the influence of the combined Debye-Waller/Franck-Condon factor in this analysis, by setting $\alpha_{\mathrm{DW}} = 1$. We now show that the high degree of photon entanglement is robust against small misalignments in the orientation of the transition dipole moments, as well as against the value of the combined Debye-Waller/Franck-Condon ($\alpha_{\mathrm{DW}} \neq 1$).

5.4.1 Misaligments in the orientation of the transition dipole moments

We first verify that the high values of concurrence and fidelity are robust against small misalignments in the orientation of the transition dipole moments. To this end, we recall the general expressions of the transition dipole moments in Eq. (5.26), where the angles α_1 and α_2 describe the orientation of the dipole moments within the xz-plane. Following the same procedure as in Section 5.3, we compute the post-selected state $\hat{\rho}_{\mathrm{post}}$ as a function of $\alpha_1 = -\alpha_2$, again at detection directions $\boldsymbol{e}_{\mathbf{k}} = \boldsymbol{e}_y$ and $\boldsymbol{e}_{\mathbf{k}'} = -\boldsymbol{e}_y$, which are perpendicular to the xz-plane in which the molecules are contained.

We plot in Fig. 5.8a the dependence on $\alpha_1 = -\alpha_2$ of $1 - \mathcal{C}(\hat{\rho}_{\mathrm{post}})$ (blue dots) and $1 - \mathcal{F}(\hat{\rho}_{\mathrm{post}}, |\phi_-^{\mathrm{xz}}\rangle\langle\phi_-^{\mathrm{xz}}|)$ (orange dots), which reach minimal values at $\alpha_1 = -\alpha_2 = \pi/4$, corresponding to perpendicular transition dipole moments. Crucially, we find very low values of $1 - \mathcal{C}(\hat{\rho}_{\mathrm{post}})$ and $1 - \mathcal{F}(\hat{\rho}_{\mathrm{post}}, |\phi_-^{\mathrm{xz}}\rangle\langle\phi_-^{\mathrm{xz}}|)$ also for moderate deviations from $\alpha_1 = -\alpha_2 = \pi/4$, which indicates that the two-photon post-selected state is highly entangled even if the dipoles are not exactly perpendicular.

5.4.2 Influence of the Debye-Waller/Franck-Condon factor

We show next that the combined Debye-Waller/Franck-Condon factor α_{DW} does not affect significantly the high values of concurrence obtained in Section 5.3. The theoretical description of the interaction between the two emitters can effectively account for the influence of α_{DW} by modifying the expressions of the coherent dipole-dipole coupling V [Eq. (5.46)] and the dissipative coupling $\tilde{\gamma}$ [Eq. (5.47)], as discussed in Section 3.1.5. More specifically, both coupling parameters are additionally multiplied by α_{DW}, so that V is replaced by $V_{\mathrm{DW}} = \alpha_{\mathrm{DW}} V$ and $\tilde{\gamma}$ is replaced by $\tilde{\gamma}_{\mathrm{DW}} = \alpha_{\mathrm{DW}}\tilde{\gamma}$. As discussed in Section 5.2.1, the dissipative coupling $\tilde{\gamma}$ is small in comparison to the spontaneous emission rate γ_0 for perpendicular transition dipole moments (see the brown line in Fig. 5.1b). As a consequence, changing α_{DW} mostly affects the coherent dipole-dipole coupling V_{DW}, in a similar way as changing the distance r_{12} between the emitters. Thus, if we consider $\alpha_{\mathrm{DW}} \neq 1$, the results obtained in previous sections can be reproduced to good accuracy by modifying r_{12} appropriately so that the coherent dipole-dipole coupling

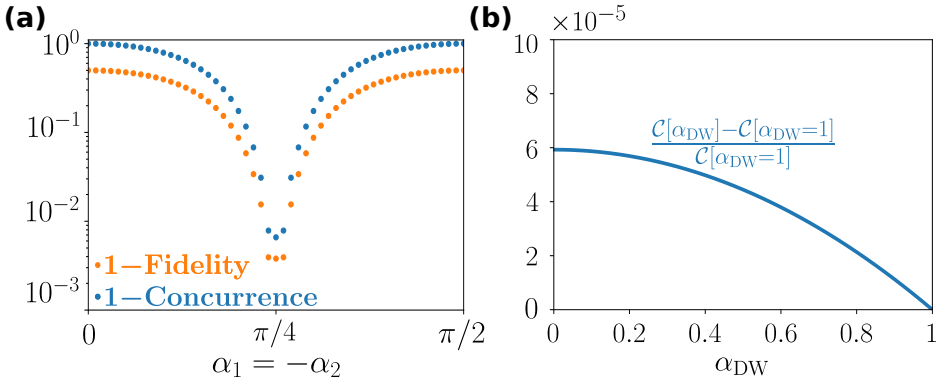

Figure 5.8: Robustness of the polarization-entanglement of the two-photon post-selected state $\hat{\rho}_{\rm post}$. The two emitters are DBATT molecules, with $\gamma_0/(2\pi) = 21.5$ MHz, vacuum wavelength $\lambda_0 = 618$ nm, and embedded in a naphthalene crystal with refractive index $n = 1.5$. The detection directions are fixed at $\boldsymbol{e}_{\mathbf{k}} = \boldsymbol{e}_y$ and $\boldsymbol{e}_{\mathbf{k}'} = -\boldsymbol{e}_y$. Filters with linewidth $\Gamma/\gamma_0 = 10^{-2}$ are considered. (a) Behaviour of $1-\mathcal{C}(\hat{\rho}_{\rm post})$ (blue dots) and $1-\mathcal{F}(\hat{\rho}_{\rm post}, |\phi_-^{\rm xz}\rangle\langle\phi_-^{\rm xz}|)$ (orange dots) as a function of the angles $\alpha_1 = -\alpha_2$, with intermolecular distance fixed at $r_{12} = 0.05\lambda_0$ and $\alpha_{\rm DW} = 1$. Here, α_j gives the orientation of the transition dipole moment $\boldsymbol{\mu}_j = \mu(\cos\alpha_j \boldsymbol{e}_x + \sin\alpha_j \boldsymbol{e}_z)$ on the xz-plane. Thus, the emitters are perpendicularly oriented at $\alpha_1 = -\alpha_2 = \pi/4$. $\mathcal{C}(\hat{\rho}_{\rm post})$ is the concurrence and $\mathcal{F}(\hat{\rho}_{\rm post}, |\phi_-^{\rm xz}\rangle\langle\phi_-^{\rm xz}|)$ is the fidelity of the post-selected state $\hat{\rho}_{\rm post}$ with respect to the maximally entangled state $|\phi_-^{\rm xz}\rangle$. (b) Dependence on $\alpha_{\rm DW}$ of $(\mathcal{C}[\alpha_{\rm DW}]-\mathcal{C}[\alpha_{\rm DW}=1])/\mathcal{C}[\alpha_{\rm DW}=1]$, corresponding to the deviation of the concurrence $\mathcal{C}(\hat{\rho}_{\rm post})$ from its value at $\alpha_{\rm DW} = 1$ [which is fixed in the rest of this chapter, including panel (a) of this figure]. The coherent dipole-dipole coupling is fixed at $V_{\rm DW} = V\alpha_{\rm DW} = 11.17\gamma_0$, which corresponds to $r_{12} = 0.05\lambda_0$ at $\alpha_{\rm DW} = 1$. Alice detects only photons emitted at $\boldsymbol{e}_{\mathbf{k}} = \boldsymbol{e}_y$ and uses a Lorentzian filter centered around $\omega_+ = \omega_0 + V_{\rm DW}$, whereas Bob detects only photons emitted at $\boldsymbol{e}_{\mathbf{k}'} = -\boldsymbol{e}_y$ and uses a Lorentzian filter with central frequency $\omega_- = \omega_0 - V_{\rm DW}$.

remains fixed according to

$$V_{\rm DW} = \alpha_{\rm DW}\frac{3\gamma_0}{4}\left[(\cos\alpha_1\cos\alpha_2 - 2\sin\alpha_1\sin\alpha_2)\left(\frac{\sin(\mathrm{k}_0 r_{12})}{(\mathrm{k}_0 r_{12})^2} + \frac{\cos(\mathrm{k}_0 r_{12})}{(\mathrm{k}_0 r_{12})^3}\right) - \cos\alpha_1\cos\alpha_2\frac{\cos(\mathrm{k}_0 r_{12})}{(\mathrm{k}_0 r_{12})}\right]. \tag{5.71}$$

To rigorously verify that the influence of $\alpha_{\rm DW}$ in $\tilde{\gamma}_{\rm DW}$ does not alter the high values of concurrence reported in Section 5.3, we plot in Fig. 5.8b the deviation of $\mathcal{C}(\hat{\rho}_{\rm post})$ from its value at $\alpha_{\rm DW} = 1$ for different values of combined Debye-Waller/Franck-Condon factor. Additionally, we have fixed $\Gamma = 10^{-2}\gamma_0$ and the dipole-dipole coupling at $V_{\rm DW} = 11.17\gamma_0$, the same as in Fig. 5.7 (where $\alpha_{\rm DW} = 1$ and $r_{12} = 0.05\lambda_0$). As $V_{\rm DW}$ is fixed, the variation of $\alpha_{\rm DW}$ in Fig. 5.8b only affects

the weak dissipative dipole-dipole coupling, according to

$$\tilde{\gamma}_{\mathrm{DW}} = \alpha_{\mathrm{DW}} \frac{3\gamma_0}{2} \left[(\cos\alpha_1 \cos\alpha_2 - 2\sin\alpha_1 \sin\alpha_2) \left(\frac{\cos(\mathrm{k}_0 r_{12})}{(\mathrm{k}_0 r_{12})^2} - \frac{\sin(\mathrm{k}_0 r_{12})}{(\mathrm{k}_0 r_{12})^3} \right) + \cos\alpha_1 \cos\alpha_2 \frac{\sin(\mathrm{k}_0 r_{12})}{(\mathrm{k}_0 r_{12})} \right]. \tag{5.72}$$

Figure 5.8b shows that the maximum deviation of the concurrence with respect to the value that it takes at $\alpha_{\mathrm{DW}} = 1$ is $\approx 6 \cdot 10^{-5}$ and occurs at $\alpha_{\mathrm{DW}} \to 0$. Thus, the only relevant effect of α_{DW} for perpendicular transition dipole moments is the scaling between V_{DW} and r_{12}, as expected from the simple arguments in Section 5.2.1.

5.5 Effect of a lens on the two-photon probability amplitudes

We have focused so far on characterizing the degree of entanglement of the post-selected state $\hat{\rho}_{\mathrm{post}}$ when Alice and Bob detect the photons emitted at directions $\boldsymbol{e}_{\mathbf{k}} = \boldsymbol{e}_y$ and $\boldsymbol{e}_{\mathbf{k}'} = -\boldsymbol{e}_y$, respectively. We have shown that a highly entangled two-photon state can be post-selected by using filters with very narrow bandwidth (Fig. 5.7a), but these narrow filters notably reduce the photon collection (Fig. 5.7c). In experiments, light is collected by a lens, whose numerical aperture is key (together with the filters width) to determine the collection efficiency. A complete analysis on the influence of lenses in the photon entanglement goes beyond the scope of this thesis. However, to gain an understanding of the expected impact of the lens on the two-photon probability amplitudes, we consider in this section the effect of deviations in the detection direction and show that moderate values of them are not expected to significantly affect the high values of fidelity $\mathcal{F}(\hat{\rho}_{\mathrm{post}}, |\phi_-^{\mathrm{xz}}\rangle \langle\phi_-^{\mathrm{xz}}|)$ of the post-selected state $\hat{\rho}_{\mathrm{post}}$ with respect to the Bell state $|\phi_-^{\mathrm{xz}}\rangle$. We focus on the analysis of the fidelity $\mathcal{F}(\hat{\rho}_{\mathrm{post}}, |\phi_-^{\mathrm{xz}}\rangle \langle\phi_-^{\mathrm{xz}}|)$ because this quantity measures the similarity between between $\hat{\rho}_{\mathrm{post}}$ and a fixed state (in our case, $|\phi_-^{\mathrm{xz}}\rangle$). Thus, we expect that if the fidelity is high over all individual angles collected by a lens of a given numerical aperture, the fidelity with respect to this same state will also be high. For example, if the state of the emitted light (after the lens) is $|\phi_-^{\mathrm{xz}}\rangle$ for all angles, we expect that the whole collected beam will be maximally entangled and that this entanglement can be easily measured by using two polarizers.

More specifically, we consider that Alice detects light propagating in some direction $\boldsymbol{e}_{\mathbf{k}} = \boldsymbol{e}_{\mathbf{k}}(\theta, \phi)$ satisfying $\boldsymbol{e}_{\mathbf{k}} \cdot \boldsymbol{e}_y > 0$, whereas the detection direction of Bob is again fixed at $\boldsymbol{e}_{\mathbf{k}'} = -\boldsymbol{e}_y$. Additionally, Alice and Bob measure the polarization of photons in the same basis $\{|\boldsymbol{e}_x\rangle, |\boldsymbol{e}_z\rangle\}$. However, the polarization directions of the photons propagating towards Alice are generally different to $\boldsymbol{e}_x$ and $\boldsymbol{e}_z$ (except at $\theta = \phi = \pi/2$, which is the case analyzed in previous sections). To collimate the photons and rotate their directions of polarization, guaranteeing

that they are polarized in the xz-plane, we consider that Alice uses a lens oriented normally to the y-axis. The effect of the lens is included through the application of a unitary transformation to the two-photon probability amplitudes of the post-selected state, as we show next.

We first recall that the probability amplitude $c^{gg}_{\mathbf{k}s\mathbf{k}'s'}(\infty)$ [Eq. (5.59)] can be obtained for any two polarization modes indexed by s, with unit vectors $\boldsymbol{e}_{\mathbf{k}s}$, as long as these unit vectors are mutually perpendicular and also perpendicular to $\boldsymbol{e}_{\mathbf{k}}$. The same holds for the two polarization modes indexed by s'. For example, in the calculations performed in Sections 5.2.3–5.4, we used $\boldsymbol{e}_x$ and $\boldsymbol{e}_z$ as the two $\boldsymbol{e}_{\mathbf{k}s}$ unit vectors, as well as the two $\boldsymbol{e}_{\mathbf{k}'s'}$ unit vectors. The reasons for this choice were that $\boldsymbol{e}_x$ and $\boldsymbol{e}_z$ are orthogonal to the propagation directions $\boldsymbol{e}_{\mathbf{k}} = -\boldsymbol{e}_{\mathbf{k}'} = \boldsymbol{e}_y$ considered in those sections, and also that Alice and Bob measured the polarization in the basis $\{|\boldsymbol{e}_x\rangle, |\boldsymbol{e}_z\rangle\}$. Here, we use again the polarization units vectors $\boldsymbol{e}_x$ and $\boldsymbol{e}_z$ in the calculation of the two-photon probability amplitudes $c^{gg}_{\mathbf{k}s\mathbf{k}'s'}(\infty)$ for the photon propagating towards Bob ($\boldsymbol{e}_{\mathbf{k}'} = -\boldsymbol{e}_y$), who does not use any lens. In contrast, regarding the photon propagating towards Alice, we choose that its polarization unit vectors are given by the usual transverse-electric (TE) and transverse-magnetic (TM) modes (before passing through the lens). Thus, these unit vectors are perpendicular ($\boldsymbol{e}_{\mathbf{k}\mathrm{TE}}$) and parallel ($\boldsymbol{e}_{\mathbf{k}\mathrm{TM}}$) to the optical plane of incidence, which is formed by the wavevector $\boldsymbol{e}_{\mathbf{k}}(\theta,\phi)$ and the direction $\boldsymbol{e}_y$, which is normal to the lens. In this way, these unit vectors are given by

$$\boldsymbol{e}_{\mathbf{k}\mathrm{TE}} \propto \cos\theta \boldsymbol{e}_x - \sin\theta\cos\phi \boldsymbol{e}_z, \tag{5.73a}$$

$$\boldsymbol{e}_{\mathbf{k}\mathrm{TM}} \propto \sin^2\theta\cos\phi\sin\phi \boldsymbol{e}_x - (\cos^2\theta + \sin^2\theta\cos^2\phi)\boldsymbol{e}_y + \sin\theta\cos\theta\sin\phi \boldsymbol{e}_z, \tag{5.73b}$$

as schematically represented in Fig. 5.9a.

This choice of polarization unit vectors for the photon propagating towards Alice facilitates the calculation of the influence of the lens on the two-photon probability amplitudes. On the one hand, the TE-mode is not affected by the lens [132]. Thus,

$$\boldsymbol{e}^{(l)}_{\mathbf{k}\mathrm{TE}} = \boldsymbol{e}_{\mathbf{k}\mathrm{TE}}, \tag{5.74}$$

where (l) is used to label the direction of the polarization after passing through the lens. On the other hand, the TM-mode becomes perpendicular to the y-axis and to the TE-mode after passing though the lens [132] and can be obtained as

$$\boldsymbol{e}^{(l)}_{\mathbf{k}\mathrm{TM}} \propto \sin\theta\cos\phi \boldsymbol{e}_x + \cos\theta \boldsymbol{e}_z. \tag{5.75}$$

Importantly, the two-photon probability amplitude $c^{gg}_{\mathbf{k}s\mathbf{k}'s'}(\infty)$ associated with the photon propagating towards Alice with polarization $s = \mathrm{TE}$ before passing through the lens coincides with the two-photon probability amplitude after the photon has passed the lens and is polarized along the direction $\boldsymbol{e}^{(l)}_{\mathbf{k}\mathrm{TE}}$. In the same way, the two-photon probability amplitude $c^{gg}_{\mathbf{k}s\mathbf{k}'s'}(\infty)$ for the photon propagating towards Alice in the TM-mode is equal to the two-photon probability amplitude of the

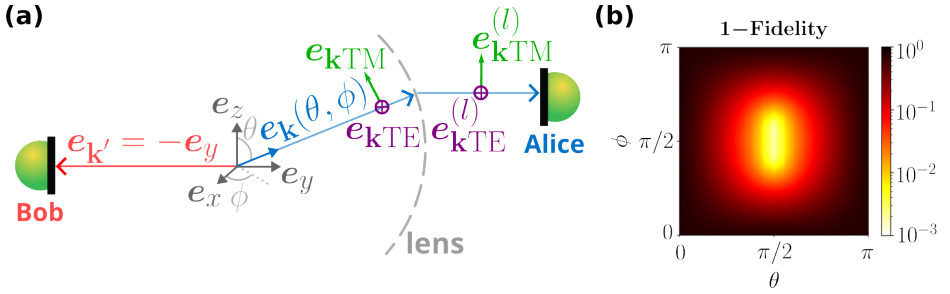

Figure 5.9: Effect of the detection direction on the two-photon post-selected state. (a) Scheme of the considered setup, including the rotations in the polarization unit vectors of the photon propagating towards Alice produced by a lens oriented perpendicular to the direction $\boldsymbol{e}_y$. The photon detected by Alice is emitted in the direction $\boldsymbol{e}_{\mathbf{k}} = \boldsymbol{e}_{\mathbf{k}}(\theta,\phi)$ (in blue), where θ and ϕ are the polar and azimuthal angles of the wavevector $\mathbf{k}$ (see the Cartesian coordinate system plotted in grey). This photon has orthogonal polarization modes TE (with unit vector perpendicular to the plane of incidence formed by $\boldsymbol{e}_{\mathbf{k}}$ and $\boldsymbol{e}_y$) and TM (with unit vector contained in the plane of incidence). The TE and TM polarization modes have unit vectors $\boldsymbol{e}_{\mathbf{k}\mathrm{TE}}$ (in purple) and $\boldsymbol{e}_{\mathbf{k}\mathrm{TM}}$ (in green), respectively. The lens (dashed grey line) rotates such unit vectors, so that the photon propagates along the y-axis and it becomes polarized in the xz-plane. The polarization unit vectors after the lens are denoted as $\boldsymbol{e}^{(l)}_{\mathbf{k}\mathrm{TE}}$ and $\boldsymbol{e}^{(l)}_{\mathbf{k}\mathrm{TM}}$. Bob detects a photon propagating in the direction $\boldsymbol{e}_{\mathbf{k}} = -\boldsymbol{e}_y$ (in red). Alice and Bob use a Lorentzian filter each, centered around $\omega_+ = \omega_0 + V$ (Alice) and $\omega_- = \omega_0 - V$ (Bob). (b) Dependence on the detection direction $\boldsymbol{e}_{\mathbf{k}} = \boldsymbol{e}_{\mathbf{k}}(\theta,\phi)$ of Alice of the deviation of the post-selected state $\hat{\rho}_{\mathrm{post}}$ from the Bell state $|\phi^{\mathrm{xz}}_-\rangle = (|\boldsymbol{e}_x\boldsymbol{e}_x\rangle - |\boldsymbol{e}_z\boldsymbol{e}_z\rangle)/\sqrt{2}$, which is quantified through $1 - \mathcal{F}(\hat{\rho}_{\mathrm{post}}, |\phi^{\mathrm{xz}}_-\rangle\langle\phi^{\mathrm{xz}}_-|)$.

photon polarized along the direction $\boldsymbol{e}^{(l)}_{\mathbf{k}\mathrm{TM}}$ after the lens.

Furthermore, as previously mentioned, Alice (and also Bob) measures the photon polarization in the basis $\{|\boldsymbol{e}_x\rangle, |\boldsymbol{e}_z\rangle\}$. To obtain the two-photon probability amplitudes in this basis, a unitary transformation is performed, which can be written as

$$\begin{bmatrix} c^{gg}_{\mathbf{k}s=\boldsymbol{e}_x,\mathbf{k}'s'} \\ c^{gg}_{\mathbf{k}s=\boldsymbol{e}_z,\mathbf{k}'s'} \end{bmatrix} = [R] \begin{bmatrix} c^{gg}_{\mathbf{k}s=\mathrm{TE},\mathbf{k}'s'} \\ c^{gg}_{\mathbf{k}s=\mathrm{TM},\mathbf{k}'s'} \end{bmatrix}. \tag{5.76}$$

The probability amplitudes on the right-hand side of this equation (values before the lens) can be calculated directly from the analytical expression in Eq. (5.59). Importantly, the unitary matrix $[R]$ is exactly the same one that transforms the unit vectors

$$\begin{bmatrix} \boldsymbol{e}_x \\ \boldsymbol{e}_z \end{bmatrix} = [R] \begin{bmatrix} \boldsymbol{e}^{(l)}_{\mathbf{k}\mathrm{TE}} \\ \boldsymbol{e}^{(l)}_{\mathbf{k}\mathrm{TM}} \end{bmatrix}. \tag{5.77}$$

Thus, this matrix is given by

$$[R] = \frac{1}{\sqrt{\cos^2\theta + \sin^2\theta\cos^2\phi}} \begin{bmatrix} \cos\theta & \sin\theta\cos\phi \\ -\sin\theta\cos\phi & \cos\theta \end{bmatrix}. \tag{5.78}$$

Therefore, the post-selected state $\hat{\rho}_{\rm post}$ can be obtained using (i) Eq. (5.65), and (ii) the two-photon probability amplitudes $c^{gg}_{\mathbf{k}s=\boldsymbol{e}_x,\mathbf{k}'s'}$ and $c^{gg}_{\mathbf{k}s=\boldsymbol{e}_z,\mathbf{k}'s'}$ obtained from application of Eq. (5.59) and Eq. (5.76).

We plot in Fig. 5.9b the dependence of $1-\mathcal{F}(\hat{\rho}_{\rm post},|\phi^{\rm xz}_-\rangle\langle\phi^{\rm xz}_-|)$ on θ and ϕ for two DBATT molecules at $r_{12}=0.05\lambda_0$ and $\Gamma=10^{-2}\gamma_0$. We find $1-\mathcal{F}(\hat{\rho}_{\rm post},|\phi^{\rm xz}_-\rangle\langle\phi^{\rm xz}_-|)\lesssim 10^{-2}$ over a range of angles covering a large solid angle. Therefore, one can conclude that collecting the light with a lens of such solid angle would increase collection while the state can still be expected to be highly entangled.

5.6 Entangled photons from two distant emitters

In this section, we analyze the fidelity and concurrence of a post-selected state for larger values of intermolecular distance r_{12} than those analyzed in previous sections. This analysis indicates that achieving large entanglement at fixed directions remains possible, but that the two-photon state is less promising for practical applications once the effect of a collecting lens is considered. This difference highlights the advantage of quantum emitters at short separation distances for practical entanglement generation.

We first give a simple argument to justify why a highly entangled two-photon state can be again post-selected from the emission of two far away emitters with orthogonal transition dipole moments $\boldsymbol{\mu}_1=\mu(\boldsymbol{e}_x+\boldsymbol{e}_z)/\sqrt{2}$ and $\boldsymbol{\mu}_2=\mu(\boldsymbol{e}_x-\boldsymbol{e}_z)/\sqrt{2}$ and identical transition frequencies. At sufficiently large separation distance r_{12} (along the z-axis), the dipole-dipole coupling becomes negligible (Fig. 5.1a). Thus, the eigenstates of the system are simply $|g_1g_2\rangle$ (with eigenvalue $-\hbar\omega_0$), $|g_1e_2\rangle$ (with eigenvalue 0), $|e_1g_2\rangle$ (with eigenvalue 0) and $|e_1e_2\rangle$ (with eigenvalue $\hbar\omega_0$), as schematically represented in Fig. 5.10a. The radiative decay from the doubly-excited state generates two-photons at frequencies ω_0, one of them with polarization $\boldsymbol{e}_{\boldsymbol{\mu}_1}$ and the other one with polarization $\boldsymbol{e}_{\boldsymbol{\mu}_2}$, as they are generated from the independent relaxation of each emitter. Thus, the post-selected state becomes a superposition of two detection possibilities: (i) the photon propagating towards Alice (in the direction $\boldsymbol{e}_y$) having polarization $\boldsymbol{e}_{\boldsymbol{\mu}_1}$ and the photon propagating towards Bob (in the direction -$\boldsymbol{e}_y$) having polarization $\boldsymbol{e}_{\boldsymbol{\mu}_2}$, and (ii) the opposite situation, in which the photon propagating towards Alice is polarized along the direction $\boldsymbol{e}_{\boldsymbol{\mu}_2}$ and the photon propagating towards Bob is polarized along the direction $\boldsymbol{e}_{\boldsymbol{\mu}_1}$. Thus, we expect that the two-photon state is given by

$$\begin{aligned}|\psi(r_{12}\to\infty)\rangle&=\frac{|\boldsymbol{e}_{\boldsymbol{\mu}_1}\rangle_A|\boldsymbol{e}_{\boldsymbol{\mu}_2}\rangle_B+|\boldsymbol{e}_{\boldsymbol{\mu}_2}\rangle_A|\boldsymbol{e}_{\boldsymbol{\mu}_1}\rangle_B}{\sqrt{2}}\\&=\frac{|\boldsymbol{e}_x\rangle_A|\boldsymbol{e}_x\rangle_B-|\boldsymbol{e}_z\rangle_A|\boldsymbol{e}_z\rangle_B}{\sqrt{2}}=|\phi^{\rm xz}_-\rangle\,,\end{aligned}\tag{5.79}$$

where in the second line we have used $|\boldsymbol{e}_{\boldsymbol{\mu}_1}\rangle_\chi=(|\boldsymbol{e}_x\rangle_\chi+|\boldsymbol{e}_z\rangle_\chi)/\sqrt{2}$ and $|\boldsymbol{e}_{\boldsymbol{\mu}_2}\rangle_\chi=(|\boldsymbol{e}_x\rangle_\chi-|\boldsymbol{e}_z\rangle_\chi)/\sqrt{2}$. We thus obtain that the state $|\psi(r_{12}\to\infty)\rangle$ expected for

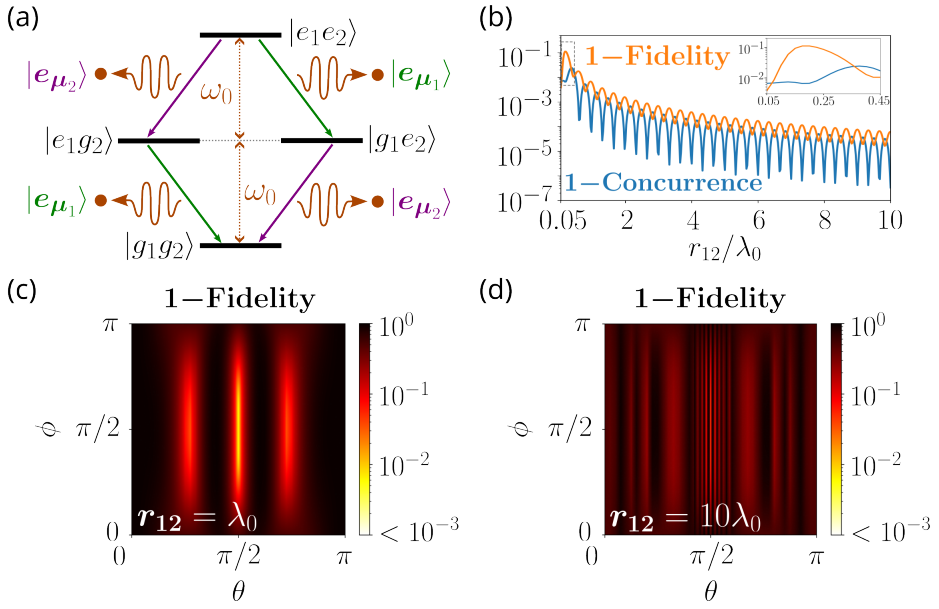

Figure 5.10: Characterization of the post-selected state for large separation distances r_{12} between the emitters. (a) Schematic representation of the energy levels and decay paths for two uncoupled emitters. The emitters are assumed to have identical transition frequencies ω_0 (in brown) and thus the relaxation of any of the emitters produces a photon with this frequency. The transition dipole moments of the emitters are perpendicularly oriented to each other, with $\boldsymbol{e}_{\boldsymbol{\mu}_1} = (\boldsymbol{e}_x + \boldsymbol{e}_z)/\sqrt{2}$ and $\boldsymbol{e}_{\boldsymbol{\mu}_2} = (\boldsymbol{e}_x - \boldsymbol{e}_z)/\sqrt{2}$. The relaxation of emitter j leads to the emission of a photon with polarization state $|\boldsymbol{e}_{\boldsymbol{\mu}_j}\rangle$. (b) Dependence on r_{12}/λ_0 of $1-\mathcal{C}(\hat{\rho}_{\rm post})$ (blue solid line) and of $1-\mathcal{F}(\hat{\rho}_{\rm post}, |\phi_-^{\rm xz}\rangle\langle\phi_-^{\rm xz}|)$ (orange solid line). In this panel we consider that Alice detects photons emitted in the direction $\boldsymbol{e}_y$ and Bob does it in the direction $-\boldsymbol{e}_y$. The inset corresponds to a zoom of $1-\mathcal{C}(\hat{\rho}_{\rm post})$ and $1-\mathcal{F}(\hat{\rho}_{\rm post}, |\phi_-^{\rm xz}\rangle\langle\phi_-^{\rm xz}|)$ at the interval $0.05\lambda_0 \leq r_{12} \leq 0.45\lambda_0$, corresponding to the dashed grey box. [(c),(d)] Dependence of $1-\mathcal{F}(\hat{\rho}_{\rm post}, |\phi_-^{\rm xz}\rangle\langle\phi_-^{\rm xz}|)$ [with $\mathcal{F}(\hat{\rho}_{\rm post}, |\phi_-^{\rm xz}\rangle\langle\phi_-^{\rm xz}|)$ the fidelity with respect to the Bell state $(|\boldsymbol{e}_x\rangle_A|\boldsymbol{e}_x\rangle_B - |\boldsymbol{e}_z\rangle_A|\boldsymbol{e}_z\rangle_B)/\sqrt{2}$] on the direction of detection $\mathbf{k} = \mathbf{k}(\theta,\phi)$ of Alice for separation distances (c) $r_{12} = \lambda_0$, and (d) $r_{12} = 10\lambda_0$. θ and ϕ are the polar and azimuthal angles of the wavevector $\mathbf{k}$ in spherical coordinates, see the sketch in Fig. 5.9a. The direction of detection of Bob is fixed at $\boldsymbol{e}_{\mathbf{k}'} = -\boldsymbol{e}_y$. The minimum value of the colormap in (d) is saturated to facilitate a better comparison with other colormaps in which the behaviour of the fidelity is also analyzed. In panels [(b),(c),(d)] we consider that the emitters are DBATT molecules, with $\gamma_0/(2\pi) = 21.5$ MHz, vacuum wavelength $\lambda_0 = 618$ nm, and they are embedded in a naphthalene crystal with refractive index $n = 1.5$. Alice and Bob use a Lorentzian filter each, centered around $\omega_+ = \omega_0 + V$ (Alice) and $\omega_- = \omega_0 - V$ (Bob).

emitters separated by very far distance is identical to the state $|\phi_-^{\rm xz}\rangle$ expected for very short separation distances r_{12} (see Sections 5.2.1 and 5.3), although the physical mechanism describing the generation of the photon pair is different, as well as the photon frequencies.

Next, following the procedure described in Section 5.3 of the main text and considering again two DBATT molecules as reference emitters, we calculate the

concurrence $\mathcal{C}(\hat{\rho}_{\rm post})$ of the post-selected state (at $\boldsymbol{e}_{\mathbf{k}} = -\boldsymbol{e}_{\mathbf{k}'} = \boldsymbol{e}_y$) for increasing separation distances, as well as the fidelity $\mathcal{F}(\hat{\rho}_{\rm post}, |\phi_-^{\rm xz}\rangle\langle\phi_-^{\rm xz}|)$ with respect to the Bell state $|\psi(r_{12}\to\infty)\rangle = |\phi_-^{\rm xz}\rangle$. Figure 5.10b shows $1-\mathcal{C}(\hat{\rho}_{\rm post})$ (solid blue line) and $1-\mathcal{F}(\hat{\rho}_{\rm post}, |\phi_-^{\rm xz}\rangle\langle\phi_-^{\rm xz}|)$ (orange blue line). We find that the concurrence and the fidelity, and thus the entanglement, can be maximized in two different ways. On the one hand, when the coherent dipole-dipole interaction between the emitters is significant (at short separation distances r_{12}), the photon entanglement increases for decreasing values of r_{12} (see the inset in Fig. 5.10b). On the other hand, if the dipole-dipole interaction is weak (at large separation distances r_{12}), the photon entanglement increases for larger values of r_{12}, which is consistent with the simple argument given in the previous paragraph. As a consequence, we observe in Fig. 5.10b that $1-\mathcal{C}(\hat{\rho}_{\rm post})$ reaches a maximum value (corresponding to lower photon entanglement) at an intermediate regime of separation distances ($r_{12}\sim 0.35\lambda_0$), where the dipole-dipole interaction is not very weak nor very strong.

However, we show next that despite the high values of concurrence obtained at large separation distances r_{12}, we do not expect such a configuration to be practical for applications in quantum technologies. To this end, we analyze the two-photon post-selected state under different detection directions at this large separation situation. As discussed in Section 5.5, we expect that the two-photon state measured in experiments including lenses is highly entangled if large values of fidelity with respect to a fixed Bell state are obtained at all directions over the solid angle of collection (given by the numerical aperture of the lens). We plot in Fig. 5.10c the dependence of $1-\mathcal{F}(\hat{\rho}_{\rm post}, |\phi_-^{\rm xz}\rangle\langle\phi_-^{\rm xz}|)$ on the detection direction of Alice at $r_{12}=\lambda_0$ (with the detection direction of Bob again fixed at $\boldsymbol{e}_{\mathbf{k}'} = -\boldsymbol{e}_y$), where the fidelity $\mathcal{F}(\hat{\rho}_{\rm post}, |\phi_-^{\rm xz}\rangle\langle\phi_-^{\rm xz}|)$ with respect to the Bell state $|\phi_-^{\rm xz}\rangle = |\psi(r_{12}\to\infty)\rangle$ is obtained following the procedure described in Section 5.5. We find that $1-\mathcal{F}(\hat{\rho}_{\rm post}, |\phi_-^{\rm xz}\rangle\langle\phi_-^{\rm xz}|)$ drastically increases [i.e., $\mathcal{F}(\hat{\rho}_{\rm post}, |\phi_-^{\rm xz}\rangle\langle\phi_-^{\rm xz}|)$ drastically decreases] under small deviations from $\theta=\pi/2$. This deviation becomes more extreme for increasing separation distances, as shown in Fig. 5.10d, where we have fixed $r_{12}=10\lambda_0$. In particular, by examining the variation of $1-\mathcal{F}(\hat{\rho}_{\rm post}, |\phi_-^{\rm xz}\rangle\langle\phi_-^{\rm xz}|)$ as a function of θ at fixed $\phi=\pi/2$ in Figs. 5.10c and 5.10d, we find that the FWHM of the central dip of $1-\mathcal{F}(\hat{\rho}_{\rm post}, |\phi_-^{\rm xz}\rangle\langle\phi_-^{\rm xz}|)$ is approximately 10 times larger at $r_{12}=\lambda_0$ (Fig. 5.10c) than at $r_{12}=10\lambda_0$ (Fig. 5.10d). Therefore, we expect that obtaining a highly entangled two-photon state from two quantum emitters separated by large distances might turn out very challenging in practice, once the collecting lens is accounted for, in contrast to the case of short separation distances discussed in Section 5.5.

5.7 Summary and conclusions

We have first introduced in this chapter the concept of quantum entanglement, focusing on the case of two qubits and taking as a reference the polarization degree of freedom of two photons. Further, we have presented the entanglement entropy and the concurrence, which serve to quantify the degree of polarization-entanglement

between two photons.

Moreover, we have provided a demonstration that two interacting quantum emitters with two-level-system behaviour can be used as a source of entangled photons. These quantum emitters can represent a variety of systems (for example, organic molecules, trapped ions, quantum dots, atoms, and diamond-color centers), which provides a large technological versatility to implement this scheme for entanglement generation. For example, emission of entangled-photon pairs in the visible range could be obtained in state-of-the-art experiments with interacting organic molecules at cryogenic temperatures [1, 92, 99, 200]. To show the robustness of the proposal, we have first derived the dynamics of the quantum state of the electromagnetic field interacting with two quantum emitters using the Wigner-Weisskopf approximation. Considering that the emitters are initially excited and have perpendicular transition dipole moments, we have demonstrated that a highly polarization-entangled two-photon state can be post-selected. More specifically, we consider that Alice and Bob are located at the normal directions to the transition dipole moments of the emitters and, additionally, each of them use an optical filter. We have found that the entanglement (quantified through the concurrence) increases with decreasing the spectral widths of the filters. Additionally, the fidelity of the post-selected state with respect to a fixed Bell state approaches the maximum value of one as the separation distance between the emitters becomes very small. We have also verified that this fidelity is high even if light is detected with some deviation from the normal direction to the dipole moments, which indicates that lenses could provide larger collection efficiencies without disturbing significantly the photon entanglement. We have also checked that the high photon entanglement is robust against misaligments in the orientation between the transition dipole moments and against the influence of the combined Debye-Waller/Franck-Condon factor.

Importantly, the optimal values of spectral widths of the filters in experiments require an appropriate balance between the degree of two-photon entanglement of the post-selected state (which increases with decreasing the bandwidth of the filters) and the probability of two-photon detection (which decreases with the bandwidth of the filters). Future theoretical analyses should address the complete impact of lenses and finite-size detectors and/or the assistance of optical cavities to improve the collection efficiency without affecting the degree of two-photon entanglement [259, 260].

These results show that interacting quantum emitters can produce highly polarization-entangled photon pairs, with large versatility and adaptability, and thus become very promising building blocks for quantum communication, cryptography, sensing and imaging.

CONCLUSIONS AND OUTLOOK

We have explored in this thesis the emission of light from two interacting quantum emitters, with the aim of achieving a more complete fundamental understanding and characterization of this phenomenon, as well as unveiling potential applications of interacting quantum emitters as light sources. To this end, we have first established a solid theoretical framework, which we summarize in the following:

- In Chapter 1, we have provided a detailed and comprehensive description of the interaction between the electromagnetic vacuum field and a single quantum emitter. In particular, we have derived the electromagnetic far-field radiated by the emitter and introduced the concept of spontaneous photon emission using two complementary approaches: the Wigner-Weisskopf approximation and the Markovian master equation.

- In Chapter 2, we have provided the normalized correlation functions introduced by Glauber to quantify the degree of optical coherence of quantum light. Special attention has been placed on the description of the second-order correlation function, or intensity correlation, and its connection with the photon emission statistics of the source. We have discussed both the color-blind and the frequency-resolved intensity correlations and illustrated their behavior for the simple case of a single quantum emitter.

- In Chapter 3, we have derived the standard Hamiltonian describing the interaction between the electromagnetic vacuum field and two quantum emitters, which has served as the key starting point for the results obtained in this thesis. By tracing out the Hilbert space of the electromagnetic vacuum field, we have obtained the usual Markovian master equation describing the reduced dynamics of the two quantum emitters. This equation reveals that the electromagnetic vacuum field can mediate the interaction between the emitters, in addition to inducing their spontaneous emission. We have also presented an effective modification of this master equation to describe the dynamics of two interacting solid-state quantum emitters, incorporating the influence of the internal vibrations of the emitters and the phonons of the environment on the emitter-emitter interaction through the combined Debye-Waller/Franck-Condon factor.

The main results of this thesis are presented in Chapters 3–5. We discuss in the following our conclusions and possible future research directions:

- In Chapter 3, we have considered two interacting solid-state emitters with parallel transition dipole moments, leading to the emergence of superradiant and subradiant states. We have then performed a systematic analysis of both the color-blind intensity correlation of Zero-Phonon-Line (ZPL) photons emitted from these emitters, as well as that of the frequency-resolved intensity correlation (FRIC).

  On the one hand, the values of the color-blind intensity correlation can range from extreme bunching to strong antibunching, depending on the laser parameters and on the detuning between the transition frequencies of the emitters. For example, tuning the laser to the two-photon resonance enhances cascade emission, resulting in strong bunching at low laser intensities. In contrast, resonant excitation of the superradiant state can lead to strong antibunching and single-photon emission, with a decay rate greater than that of a single emitter. For these two cases, we have derived analytical expressions that accurately describe the intensity correlations, valid for non-identical emitters and arbitrary laser intensities. These expressions may be used to experimentally estimate the distance between emitters. Interestingly, when the laser is tuned to the subradiant state, the color-blind intensity correlation displays more intricate behavior, ranging from bunching to antibunching or Poissonian statistics, which is attributed to the complex competition between different excitation and relaxation pathways.

  On the other hand, the FRIC offers deeper insights into the relaxation processes of the coupled emitters. When the laser is tuned to the transition frequency of the superradiant state, the FRIC resembles that of a resonantly driven two-level system at weak and moderate laser intensities, though deviations appear due to the influence of the subradiant and doubly-excited states. At strong laser intensities, the FRIC shows that the laser modifies the eigenstates of the interacting system, leading to more complex emission processes. Furthermore, the FRIC becomes even more interesting when the laser is tuned to the subradiant state. In this regime, in addition to the emergence of two-photon transitions through intermediate virtual states, the FRIC can reveal one-photon transitions occurring with extremely low probabilities, a fingerprint usually not visible in the standard emission spectrum. These results stress the high sensitivity of FRIC to uncover intricate emission mechanisms. We have also shown that the FRIC is significantly affected by the combined Debye-Waller/Franck-Condon factor at this laser frequency.

  Our analysis has neglected dephasing effects, assuming that the emitters are at sufficiently low temperatures. Interestingly, the signatures of subradiance in the one-photon spectrum have been shown to be highly sensitive to dephasing in Ref. [261]. Therefore, the complex behavior that we predict for both the

color-blind intensity correlation and the FRIC under subradiant excitation could be modified even by low values of dephasing, making them a subject of potential further study. We emphasize that such a study would likely require more sophisticated models that rigorously incorporate the influence of emitter vibrations and interactions with the phonon environment of the host medium, as developed in Refs. [197, 198] for the single-emitter case.

Another potential direction for future research involves extending the use of intensity correlation measurements to estimate a set of emitters' configuration parameters, beyond just the distance between the two emitters with parallel transition dipole moments. A more detailed approach would aim to determine the full three-dimensional orientation of the dipole moments and the relative positions of the emitters. This may be achieved by measuring different components of the normalized second-order correlation tensor defined in Eq. (2.44), rather than relying exclusively on the scalar normalized second-order correlation function.

- In Chapter 4, we have developed a more sophisticated description of the two interacting solid-state quantum emitters by incorporating additional states that represent vibrational or phononic levels in the electronic ground state. This refinement has enabled the analysis of the correlation of Stokes-shifted photons, which arise from the radiative decay from the electronic excited state to these vibrational/phononic levels. This inelastic emission is particularly relevant in typical fluorescence experiments, where resonant excitation is used and optical filters eliminate both the laser photons and the ZPL emission due to their near-identical frequencies. As a result, only Stokes-shifted photons are detected in such setups.

  Using this model, we have demonstrated that quantum coherence can significantly impact the correlation of Stokes-shifted photons emitted from two strongly interacting emitters, contrary to what previous models in the literature had assumed. To confirm this, we have compared the theoretical predictions with experimental measurements performed by the Bordeaux Nanophotonics Group, led by Brahim Lounis, and shown that including quantum coherence leads to better agreement with the data.

  Furthermore, we have found that quantum coherence can influence the Stokes-shifted photon correlations even in the case of two distant, non-interacting emitters. Additionally, our analysis has shown that the discrepancy between theory and experiments in the value of the intensity correlation at zero time delay for light emitted from two uncorrelated emitters can be attributed to the insufficient time resolution of the detectors used in available experiments in the literature.

  Moreover, we have compared the correlations of Stokes-shifted photons and ZPL photons emitted from two interacting solid-state emitters and demonstrated that they can differ substantially. This highlights the need to develop theoretical models of light emission from solid-state emitters that go

beyond the typical two-level system framework, particularly to describe usual fluorescence experiments in which the electronic excited states are resonantly driven and only the Stokes-shifted photons are measured.

Importantly, the sophisticated description of light emission from solid-state emitters developed in this chapter opens up a range of promising directions for future research. For example, a systematic and detailed analysis of the Stokes-shifted intensity correlations as a function of laser parameters, as provided in Chapter 3 for ZPL emission, could be of large interest. Additionally, such a sophisticated description could also be used to explore other aspects of Stokes-shifted emission, such as the FRIC and the first-order correlation function. Further, a common future direction for the analysis of both the ZPL correlation and the Stokes-shifted correlation is the extension to a larger number of interacting quantum emitters.

- In Chapter 5, we have demonstrated that two interacting quantum emitters can serve as a source of polarization-entangled photon pairs. To this end, we have considered the Hamiltonian describing the interaction between the electromagnetic vacuum field and two quantum emitters, derived in Chapter 3, and used the Wigner-Weisskopf approximation. In this way, we have obtained the complete two-photon state resulting from the relaxation of two initially excited emitters, capturing the two-photon emission probabilities across all frequencies, polarizations, and directions.

  Moreover, we have derived the post-selected two-photon state by considering that (i) the transition dipole moments of the emitters are perpendicularly oriented, (ii) optical filters are applied, and (iii) light is detected along directions perpendicular to the dipole moments. The post-selected state exhibits a high degree of entanglement when narrow-band filters are used, at the cost of reducing the detection probability. Moreover, we have shown that this photon entanglement remains largely unaffected by the influence of the combined Debye-Waller/Franck-Condon factor, indicating that a broad range of solid-state emitters can be employed to generate entangled photons. This robustness has also been found for small misalignments in the relative orientation of the dipole moments. Additionally, we have verified that moderate deviations in the detection direction only slightly impact the post-selected state, suggesting that standard lenses can be used in experiments to enhance collection efficiency without significantly degrading the photon entanglement.

  Future analyses might require addressing the complete influence of lenses and characterizing the balance between the degree of two-photon entanglement and the collection efficiency. Another promising line of future research relies on extending the description in this chapter to the case in which the emitters additionally interact with an optical cavity, with the aim of improving the collection efficiency of the entangled photon pairs. Additionally, the extension of the analysis in this chapter to a larger number of emitters may also unveil

the possibility of generating multi-photon entangled states from interacting quantum emitters.

It has been the aim of this thesis that the results found herein contribute to achieving a deeper fundamental understanding of light emission from two interacting quantum emitters, as well as to improving the characterization of cutting-edge experiments involving this type of coupled system. Moreover, these results may help to advance the implementation of interacting quantum emitters as light sources, potentially contributing to the development of novel sources of quantum light.

Appendices

Appendix A

Density matrix formalism

The state of a closed quantum system S can be generally described by a state vector $|\psi\rangle$, which is called a *pure state*. However, in practice S usually interacts with an environment B (Section 1.4.1), whose degrees of freedom we cannot access. The lack of information about the whole system $(S + B)$ makes that the state of S cannot be described as a pure state. Instead, the quantum state of S is described in this case as a statistical mixture of pure states, which is represented by an operator $\hat{\rho}$ called *density matrix*. In this appendix, we introduce the density matrix formalism, which plays a crucial role in this thesis. We mainly follow Refs. [139, 262] to this regard.

A.1 Pure states

The state of a quantum system S is represented by a pure state $|\psi\rangle$ when all the degrees of freedom of the system are accessible. The norm of this state is normalized to one, such that

$$\langle\psi|\psi\rangle = 1. \tag{A.1}$$

We write next $|\psi\rangle$ in an orthonormal basis $\{|c_n\rangle\}$ of the Hilbert space $\mathcal{H}_S$ of S. Here, n labels the different states of the basis, ranging from 1 to the dimension of $\mathcal{H}_S$, denoted by $\dim(\mathcal{H}_S)$. As $\{|c_n\rangle\}$ is an orthonormal basis, it satisfies the *completeness relation*, given by

$$\sum_n |c_n\rangle \langle c_n| = \mathbb{1}, \tag{A.2}$$

with $\mathbb{1}$ the identity operator in $\mathcal{H}_S$. Any pure state $|\psi\rangle$ can be expressed in this basis as

$$|\psi\rangle = \sum_n c_n |c_n\rangle , \tag{A.3}$$

where c_n are complex coefficients referred to as *probability amplitudes*. By using

Eq. (A.1), we obtain that these coefficients satisfy the normalization condition

$$\sum_n |c_n|^2 = 1. \tag{A.4}$$

Importantly, if a measurement is performed in the basis $\{|c_n\rangle\}$, the pure state $|\psi\rangle$ collapses into one of the basis states. The probability of collapsing to $|c_n\rangle$ is $|c_n|^2$, which is bounded between 0 and 1. These probabilities do not arise from a lack of information about the system state, but from the intrinsic quantum nature of the system.

As an example of pure state, within the description of the interaction between one or two quantum emitters and the electromagnetic vacuum field in Sections 1.3 and 5.2.2, the entire system (including the electromagnetic degrees of freedom) is described by a pure state. However, when we reduce this description to the Hilbert space of the quantum emitters by tracing out the electromagnetic degrees of freedom (Sections 1.4.5 and 3.1.4), pure states are no longer suitable to describe the state of the emitters.

A.2 Mixed states

The state of a quantum system S is described more generally by a mixture of pure states $|\psi_m\rangle$, each one with probability P_m. These probabilities satisfy the normalization condition $\sum_m P_m = 1$ and they result from the lack of information about the state of the system, as it occurs if S interacts with an environment (also referred to as a bath). In this case, the state of the system is thus referred to as a *mixed* (instead of pure) one and represented by the operator

$$\hat{\rho} = \sum_m P_m \, |\psi_m\rangle \langle\psi_m| \,, \tag{A.5}$$

which is called *density matrix* or *density operator*. We emphasize that the density matrix can also be used to describe a pure state, for which a single probability equals 1. For example, if $P_1 = 1$, $\hat{\rho} = |\psi_1\rangle \langle\psi_1|$ describes a pure state.

We show next that the diagonal and off-diagonal elements of the density matrix, when expressed in an orthonormal basis, contain significant information. To this end, we consider that $|\psi_m\rangle$ is expressed in the orthonormal basis $\{|c_n\rangle\}$ as

$$|\psi_m\rangle = \sum_n c_n^{(m)} \, |c_n\rangle \,. \tag{A.6}$$

Here, the probability amplitudes $c_n^{(m)}$ are defined as

$$c_n^{(m)} \equiv \langle c_n | \psi_m \rangle \,, \tag{A.7}$$

and they satisfy the normalization condition $\sum_n |c_n^{(m)}|^2 = 1$ [Eq. (A.4)]. The

density matrix $\hat{\rho}$ can thus be rewritten in the basis $\{|c_n\rangle\}$ as

$$\hat{\rho} = \sum_{n,n'} \sum_{m} P_m c_n^{(m)} c_{n'}^{(m)*} |c_n\rangle \langle c_{n'}| = \sum_{n,n'} \rho_{nn'} |c_n\rangle \langle c_{n'}| , \tag{A.8}$$

where we have defined $\rho_{nn'} \equiv \langle c_n| \hat{\rho} |c_{n'}\rangle$.

The diagonal elements of $\hat{\rho}$ in the basis $\{|c_n\rangle\}$ are given by

$$p_n \equiv \rho_{nn} = \langle c_n| \hat{\rho} |c_n\rangle = \sum_{m} P_m |c_n^{(m)}|^2. \tag{A.9}$$

These elements thus correspond to non-negative real numbers, meaning that $\hat{\rho}$ is a positive semi-definite operator. p_n is referred to as *population* of the state $|c_n\rangle$ and it gives the probability that the density $\hat{\rho}$ collapses to $|c_n\rangle$ due to a measurement in the basis $\{|c_n\rangle\}$. The sum of all the populations equals one, as

$$\sum_{n} p_n = \sum_{m} P_m \sum_{n} |c_n^{(m)}|^2 = \sum_{m} P_m = 1. \tag{A.10}$$

Additionally, the trace Tr of an operator is defined as the sum of all its diagonal matrix elements in any chosen basis. Thus, Eq. (A.10) reveals that the trace of the density matrix is one:

$$\mathrm{Tr}\hat{\rho} = \sum_{n} p_n = 1. \tag{A.11}$$

We emphasize that the trace is independent of the choice of basis.

On the other hand, the off-diagonal elements of the density matrix $\hat{\rho}$ in the basis $\{|c_n\rangle\}$ are complex numbers given by

$$\rho_{nn'} \equiv \langle c_n| \hat{\rho} |c_{n'}\rangle = \sum_{m} P_m c_n^{(m)} c_{n'}^{(m)*}, \tag{A.12}$$

with $n \neq n'$. This equation indicates that $\rho_{nn'} = \rho_{n'n}^*$, meaning that the density matrix is a Hermitian operator:

$$\hat{\rho} = \hat{\rho}^\dagger. \tag{A.13}$$

Additionally, Eq. (A.12) also indicates that the off-diagonal element $\rho_{nn'}$ can be nonzero if at least one of the states $|\psi_m\rangle$ in Eq. (A.5) is given by a coherent superposition of $|c_n\rangle$ and $|c_{n'}\rangle$. As a consequence, $\rho_{nn'}$ can be interpreted as due to interference effects between $|c_n\rangle$ and $|c_{n'}\rangle$. The off-diagonal elements of the density matrix are thus usually referred to as *coherences*.

A.3 Expectation value

In this section, we describe how to calculate the expectation value $\langle \hat{O} \rangle$ of an arbitrary operator $\hat{O}$ at an initial time, before the system evolves. The expectation value at an arbitrary later time is discussed in Appendix B.

We first consider the case in which the system is in a pure state $|\psi\rangle$. In this case, the expectation value of $\hat{O}$ is simply given by

$$\langle \hat{O} \rangle = \langle \psi | \hat{O} | \psi \rangle . \tag{A.14}$$

More generally, if the system is in a mixed state described by the density matrix $\hat{\rho}$, the expectation value is calculated as

$$\langle \hat{O} \rangle = \mathrm{Tr}(\hat{O}\hat{\rho}) = \sum_{n,n'} \langle c_n | \hat{O} | c_{n'} \rangle \rho_{n'n}. \tag{A.15}$$

When the density matrix corresponds to a pure state, $\hat{\rho} = |\psi\rangle \langle\psi|$, the expectation value given by Eq. (A.15) reduces to that in Eq. (A.14). This can be shown by choosing a basis $|c_n\rangle$ that includes the state $|\psi\rangle$. For instance, if we take $|c_1\rangle = |\psi\rangle$, then $p_1 = \rho_{11} = 1$, and all the other matrix elements in this basis are zero. Therefore, $\langle \hat{O} \rangle = \mathrm{Tr}(\hat{O}\hat{\rho}) = \langle \psi | \hat{O} | \psi \rangle$ in this case.

Moreover, Eq. (A.15) can be used to demonstrate that Hermitian operators ($\hat{O} = \hat{O}^\dagger$), which are commonly referred to as *observables* due to their real eigenvalues, have also real expectation values. Specifically, since $\hat{O} = \hat{O}^\dagger$, we can write $\langle c_n | \hat{O} | c_{n'} \rangle = (\langle c_{n'} | \hat{O} | c_n \rangle)^*$. As the density matrix is also Hermitian [Eq. (A.13)], it follows that $\rho_{n'n} = \rho^*_{nn'}$. As a result, in the sum in Eq. (A.15), each term $\langle c_n | \hat{O} | c_{n'} \rangle \rho_{n'n}$ (with $n \neq n'$) has a complex conjugate counterpart:

$$\langle c_n | \hat{O} | c_{n'} \rangle \rho_{n'n} = \Big(\langle c_{n'} | \hat{O} | c_n \rangle \rho_{nn'} \Big)^* . \tag{A.16}$$

Further, the terms with $n = n'$ in the sum in Eq. (A.15) are real by themselves, since both $\langle c_n | \hat{O} | c_n \rangle$ and ρ_{nn} correspond to diagonal matrix elements of Hermitian operators. Consequently, the expectation value of a Hermitian operator is always real.

For completeness, we finally note that the variance of an arbitrary operator $\hat{O}$ (whether Hermitian or not) can be calculated from the expectation value of this operator and that of $\hat{O}^2$. Specifically, the variance is given by

$$\langle (\Delta \hat{O})^2 \rangle = \langle \hat{O}^2 \rangle - \langle \hat{O} \rangle^2 = \mathrm{Tr}(\hat{O}^2 \hat{\rho}) - [\mathrm{Tr}(\hat{O}\hat{\rho})]^2. \tag{A.17}$$

A.4 Purity

We next introduce a quantity $\mathcal{P}(\hat{\rho})$, known as *purity*, which is commonly used to quantify how pure or mixed a density matrix is. To this end, we recall that a density matrix $\hat{\rho}$ is a Hermitian [Eq. (A.13)] and semi-definite positive operator, with trace equals to one [Eq. (A.11)]. The eigenvalues of $\hat{\rho}$ are thus non-negative real numbers η_j, satisfying $\sum_j \eta_j = 1$. We denote by $|\eta_j\rangle$ the j^{th} eigenvector, which

has eigenvalue η_j. Thus, the diagonal form of $\hat{\rho}$ is

$$\hat{\rho} = \sum_j \eta_j \left|\eta_j\right\rangle \left\langle\eta_j\right| . \tag{A.18}$$

This expression allows us to express the square of the density matrix as

$$\hat{\rho}^2 = \sum_{j,j'} \eta_j \eta_{j'} \left|\eta_j\right\rangle \left\langle\eta_j|\eta_{j'}\right\rangle \left\langle\eta_{j'}\right| = \sum_j \eta_j^2 \left|\eta_j\right\rangle \left\langle\eta_j\right| . \tag{A.19}$$

The trace of $\hat{\rho}^2$ thus yields

$$\mathrm{Tr}(\hat{\rho}^2) = \sum_j \eta_j^2. \tag{A.20}$$

Taking into account that η_j are non-negative real numbers and sum one, we obtain

$$\mathrm{Tr}(\hat{\rho}^2) \leq 1. \tag{A.21}$$

The equality in Eq. (A.21) is obtained if, and only if, $\hat{\rho}$ represents a pure state $|\psi\rangle$, so that $\hat{\rho} = |\psi\rangle \langle\psi|$ (i.e., one of the eigenvalues η_j is equal to one and the others vanish). Additionally, the minimum value of $\mathrm{Tr}(\hat{\rho}^2)$ is:

$$\min\{\mathrm{Tr}(\hat{\rho}^2)\} = \frac{1}{\dim(\mathcal{H}_S)}. \tag{A.22}$$

This minimum value is obtained if, and only if, the density matrix is $\hat{\rho} = \mathbb{1}/\dim(\mathcal{H}_S)$. This density matrix $\hat{\rho} = \mathbb{1}/\dim(\mathcal{H}_S)$ corresponds to a *maximally mixed state*, which is given by a mixture of $\dim(\mathcal{H}_S)$ pure states that have equal probability $P_m = 1/\dim(\mathcal{H}_S)$. Therefore,

$$\mathcal{P}(\hat{\rho}) \equiv \mathrm{Tr}(\hat{\rho}^2) \tag{A.23}$$

is commonly used to quantify the degree of purity or mixedness of a density matrix $\hat{\rho}$. Notably, as the trace is independent of the choice of basis, so it is $\mathcal{P}(\hat{\rho})$.

A.5 Von Neumann entropy

Another quantity that can be used to quantify the degree of mixedness of a density matrix is the *von Neumann entropy* $S(\hat{\rho})$, defined as

$$\mathcal{S}(\hat{\rho}) = -\mathrm{Tr}(\hat{\rho} \log_2 \hat{\rho}) = -\sum_i \eta_i \log_2 \eta_i. \tag{A.24}$$

This quantity is always nonzero, as $0 \leq \eta_i \leq 1$. It vanishes for pure states and reaches its maximum value, $\log_2 \dim(\mathcal{H}_S)$, for maximally mixed states. The von Neumann entropy can be interpreted as a measure of the information one lacks about the system, thus extending the classical concept of Gibbs entropy to the

quantum domain [263]. In Eq. (A.24), the entropy is expressed in units of bits because the base-2 logarithm is used.

Interestingly, one can show that if S is composed of two subsystems A and B, such that the Hilbert space $S = A+B$ is given by the tensor product $\mathcal{H}_S = \mathcal{H}_A \otimes \mathcal{H}_B$, the von Neumann entropy satisfies the condition

$$\mathcal{S}(\hat{\rho}) \leq \mathcal{S}(\hat{\rho}_A) + \mathcal{S}(\hat{\rho}_B). \tag{A.25}$$

Here, $\hat{\rho}_A$ and $\hat{\rho}_B$ are the *reduced density matrices* of A and B, respectively, which are obtained as

$$\hat{\rho}_A = \mathrm{Tr}_B \hat{\rho} = \sum_{n=1}^{\dim(\mathcal{H}_B)} \langle b_n | \, \hat{\rho} \, | b_n \rangle \,, \tag{A.26a}$$

$$\hat{\rho}_B = \mathrm{Tr}_A \hat{\rho} = \sum_{n=1}^{\dim(\mathcal{H}_A)} \langle a_n | \, \hat{\rho} \, | a_n \rangle \,, \tag{A.26b}$$

where Tr_χ corresponds to the trace over only the subsystem χ, $\{|a_n\rangle\}$ is an orthonormal basis of $\mathcal{H}_A$, and $\{|b_n\rangle\}$ is an orthonormal basis of $\mathcal{H}_B$. Tr_χ is called *partial trace*.

Equality in Eq. (A.25) holds only for separable states [Eq. (5.15)]. Therefore, the following condition applies:

$$\mathcal{S}(\hat{\rho}) = \mathcal{S}(\hat{\rho}_A) + \mathcal{S}(\hat{\rho}_B) \Leftrightarrow \hat{\rho} = \hat{\rho}_A \otimes \hat{\rho}_B. \tag{A.27}$$

This means that the von Neumann entropy does not increase when tracing out one of the subsystems if the global state $\hat{\rho}$ is separable. However, if there is any non-zero degree of entanglement between subsystems A and B (see Section 5.1), so that $\hat{\rho}$ is not separable, then the von Neumann entropy of the reduced states increases upon tracing out a subsystem. This reflects the fact that our lack of information about the system increases when we reduce to the Hilbert space of only one subsystem (e.g., by applying the Markovian master equation described in Section 1.4). In other words, tracing out a subsystem yields a mixed state because the information on the quantum correlations between A and B is lost.

A.6 Fidelity

Last, we introduce a quantity that serves to quantify how similar two quantum states are, known as *fidelity* $\mathcal{F}$. In the simplest case, where one deals with two pure states $|\psi_1\rangle$ and $|\psi_2\rangle$, fidelity is given by

$$\mathcal{F}(|\psi_1\rangle, |\psi_2\rangle) = |\langle \psi_1 | \psi_2 \rangle|^2. \tag{A.28}$$

By considering that a system is in state $|\psi_2\rangle$, $\mathcal{F}(|\psi_1\rangle, |\psi_2\rangle)$ can be interpreted as quantifying the probability that $|\psi_2\rangle$ collapses to $|\psi_1\rangle$ as a result of a measurement

in a basis that contains $|\psi_1\rangle$. Fidelity is bounded between 0 and 1, reaching the lowest value (0) if $|\psi_1\rangle$ and $|\psi_2\rangle$ are orthogonal states and the largest value (1) if they are identical (up to a global phase).

Further, $\mathcal{F}$ can be easily extended to the case in which one of the states represents a mixed state. For example, if the first system is described by the pure state $|\psi_1\rangle$ and the second one is described by the density matrix $\hat{\rho}_2$, the fidelity can be computed as

$$\mathcal{F}(|\psi_1\rangle, \hat{\rho}_2) = \langle\psi_1| \hat{\rho}_2 |\psi_1\rangle . \tag{A.29}$$

Thus, the fidelity corresponds again to the probability that the state of the second system ($\hat{\rho}_2$) collapses to $|\psi_1\rangle$ as a result of performing a measurement in a basis that includes $|\psi_1\rangle$. Equivalently, the fidelity is given by the population of $|\psi_1\rangle$ carried by the density matrix $\hat{\rho}_2$ [see Eq. (A.9)].

The extension of the fidelity to the general case in which both states are mixed becomes more intricate, both in its derivation and in its physical interpretation. The fidelity in this case is given by [264, 265]

$$\mathcal{F}(\hat{\rho}_1, \hat{\rho}_2) = \left(\mathrm{Tr}\sqrt{\sqrt{\hat{\rho}_1}\hat{\rho}_2\sqrt{\hat{\rho}_1}} \right)^2 = \sum_{i=1}^{4} \lambda_i, \tag{A.30}$$

where $\{\lambda_i\}$ are the eigenvalues of $\sqrt{\hat{\rho}_1}\hat{\rho}_2\sqrt{\hat{\rho}_1}$. These eigenvalues $\{\lambda_i\}$ are as well the eigenvalues of $\sqrt{\hat{\rho}_1\hat{\rho}_2}$. We remark that fidelity is symmetric:

$$\mathcal{F}(\hat{\rho}_1, \hat{\rho}_2) = \mathcal{F}(\hat{\rho}_2, \hat{\rho}_1). \tag{A.31}$$

Additionally, $\mathcal{F}$ is invariant under unitary transformations, implying that it does not depend on the choice of basis.

Appendix B

Schrödinger, Heisenberg and interaction pictures

We review in this appendix the usual Schrödinger and Heisenberg dynamical pictures in quantum mechanics. We also introduce the interaction picture, which becomes of special interest in the context of open quantum systems. A more detailed discussion on this topic can be found in Ref. [139].

B.1 Schrödinger picture

We consider a general closed quantum system with Hamiltonian $\hat{H}(t)$, which can be time dependent in general (as it is the case of a quantum emitter under the driving of classical light, see Section 1.5). At some initial time t_0, the system is in a pure state $|\psi(t_0)\rangle$ independently of the particular dynamical picture. In the *Schrödinger picture*, the time evolution is encoded in the quantum state. More specifically, the time evolution of the state vector is governed by the well-known *Schrödinger equation*

$$i\hbar\frac{d}{dt}|\psi^{(S)}(t)\rangle = \hat{H}(t)\,|\psi^{(S)}(t)\rangle\,, \tag{B.1}$$

where the superscript (S) in $|\psi^{(S)}(t)\rangle$ stresses the use of the Schrödinger picture. Equation (B.1) provides a set of differential equations for the probability amplitudes of the state $|\psi^{(S)}(t)\rangle$ [Eq. (A.3)]. Alternatively, the Schrödinger equation can be solved in terms of the unitary propagator [124, 266, 267]

$$\hat{U}(t,t_0) = \prod_{t_n=t_0}^{t}\exp\Big[-\frac{i}{\hbar}dt_n\hat{H}(t_n)\Big], \tag{B.2}$$

which corresponds to a product of exponentials running over infinitesimal time intervals $dt_n = t_{n+1} - t_n$, with the time intervals ordered increasingly in time

(i.e., the exponential with the latest time argument appears to the right). If the Hamiltonians $\hat{H}(t_n)$ at different times commute, one can rewrite the unitary operator in terms of a time integral:

$$\hat{U}(t, t_0) = \exp\left[-\frac{i}{\hbar}\int_{t_0}^{t} dt' \hat{H}(t')\right]. \tag{B.3}$$

Furthermore, if the Hamiltonian is time-independent, the unitary propagator simply becomes

$$\hat{U}(t, t_0) = \exp\left[-\frac{i}{\hbar}(t - t_0)\hat{H}\right]. \tag{B.4}$$

The time evolution of the state in terms of the propagator $\hat{U}(t, t_0)$ can be obtained as

$$|\psi^{(S)}(t)\rangle = \hat{U}(t, t_0)\,|\psi(t_0)\rangle\,. \tag{B.5}$$

In the case of a mixed quantum state described by a density matrix $\hat{\rho}^{(S)}(t)$, the Schrödinger equation (B.1) is generalized to the *von Neumann equation*:

$$\frac{d}{dt}\hat{\rho}^{(S)}(t) = -\frac{i}{\hbar}[\hat{H}(t), \hat{\rho}^{(S)}(t)]. \tag{B.6}$$

The evolution of the density matrix from the state $\hat{\rho}(t_0)$ at initial time t_0 can be obtained using again the unitary propagator $\hat{U}(t, t_0)$. Specifically, the density matrix at time t is given by

$$\hat{\rho}^{(S)}(t) = \hat{U}(t, t_0)\hat{\rho}(t_0)\hat{U}^{\dagger}(t, t_0). \tag{B.7}$$

Moreover, the expectation value of an arbitrary operator $\hat{O}$ at initial time ($t = t_0$) was described in Section A.3. By using the Schrödinger picture, the expectation value of $\hat{O}$ at an arbitrary time t can be obtained as

$$\langle\hat{O}\rangle\,(t) = \mathrm{Tr}[\hat{O}\hat{\rho}^{(S)}(t)], \tag{B.8}$$

with the time evolution fully encoded in the time-dependent density matrix $\hat{\rho}^{(S)}(t)$.

B.2 Heisenberg picture

We next introduce the *Heisenberg picture*, which enables an alternative derivation of the expectation value $\langle\hat{O}\rangle\,(t)$. In this picture, the quantum state remains time-independent and the time evolution is encoded in the operator. The time evolution of $\hat{O}(t)$ is governed by the *Heisenberg equation*, which is given by

$$\frac{d}{dt}\hat{O}^{(H)}(t) = -\frac{i}{\hbar}[\hat{O}^{(H)}(t), \hat{H}(t)]. \tag{B.9}$$

The time evolution of $\hat{O}^{(H)}(t)$ from time t_0 can also be calculated using the unitary time propagator $\hat{U}(t,t_0)$ as

$$\hat{O}^{(H)}(t) = \hat{U}^\dagger(t,t_0)\hat{O}\hat{U}(t,t_0). \tag{B.10}$$

In the Heisenberg picture, the expectation value of $\hat{O}$ at time t can thus be obtained as

$$\langle\hat{O}\rangle(t) = \mathrm{Tr}[\hat{O}^{(H)}(t)\hat{\rho}(t_0)]. \tag{B.11}$$

This expression is mathematically equivalent to that of Eq. (B.8), as

$$\begin{aligned}\mathrm{Tr}[\hat{O}^{(H)}(t)\hat{\rho}(t_0)] &= \mathrm{Tr}[\hat{U}^\dagger(t,t_0)\hat{O}\hat{U}(t,t_0)\hat{\rho}(t_0)] \\ &= \mathrm{Tr}[\hat{U}^\dagger(t,t_0)\hat{O}\hat{U}(t,t_0)\hat{\rho}(t_0)\hat{U}^\dagger(t,t_0)\hat{U}(t,t_0)] \\ &= \mathrm{Tr}[\hat{U}^\dagger(t,t_0)\hat{O}\hat{\rho}^{(S)}(t)\hat{U}(t,t_0)] = \mathrm{Tr}[\hat{O}\hat{\rho}^{(S)}(t)],\end{aligned} \tag{B.12}$$

where we have used that $\hat{U}(t,t_0)$ is a unitary operator and that the trace is invariant under unitary transformations. As a consequence, the Heisenberg and Schrödinger pictures yield the same results.

B.3 Interaction picture

We next describe the *interaction picture*, which is particularly useful for describing interacting systems. To this end, we consider that the Hamiltonian can be decomposed as

$$\hat{H}(t) = \hat{H}_0 + \hat{H}_I(t). \tag{B.13}$$

Here, $\hat{H}_I(t)$ is the interaction Hamiltonian, and $\hat{H}_0$ represents the Hamiltonian of the systems in the absence of interaction. In the context of open quantum systems (Section 1.4.1), $\hat{H}_0$ typically includes the Hamiltonians of both the system of interest and the bath, while $\hat{H}_I(t)$ accounts for the interaction between them. For simplicity, we assume that $\hat{H}_0$ is time-independent, as otherwise the derivation becomes considerably more complex [139–141], and beyond the scope of this thesis.

In the interaction picture both the quantum state and the operators evolve in time. The time evolution of an arbitrary operator $\hat{O}$ in the interaction picture does not depend on the interaction Hamiltonian, but it only depends on the Hamiltonian $\hat{H}_0$. More specifically, the time evolution of $\hat{O}$ can be obtained as

$$\hat{O}^{(I)}(t) = \hat{U}_0^\dagger(t,t_0)\hat{O}\hat{U}_0(t,t_0), \tag{B.14}$$

where

$$\hat{U}_0(t,t_0) = \exp\left[-\frac{i}{\hbar}(t-t_0)\hat{H}_0\right]. \tag{B.15}$$

For example, the interaction Hamiltonian $\hat{H}_I$ in the interaction picture can thus be derived as

$$\hat{H}_I^{(I)}(t) = \hat{U}_0^\dagger(t,t_0)\hat{H}_I(t)\hat{U}_0(t,t_0), \tag{B.16}$$

while the density matrix in the interaction picture is related with the density matrix in the Schrödinger picture as

$$\hat{\rho}^{(I)}(t) = \hat{U}_0^\dagger(t,t_0)\hat{\rho}^{(S)}(t)\hat{U}_0(t,t_0) = \hat{U}_0^\dagger(t,t_0)\hat{U}(t,t_0)\hat{\rho}(t_0)(t)\hat{U}^\dagger(t,t_0)\hat{U}_0(t,t_0). \tag{B.17}$$

The interaction-picture density matrix $\hat{\rho}^{(I)}(t)$ and the interaction-picture interaction Hamiltonian $\hat{H}_I^{(I)}(t)$ satisfy the dynamics equation

$$\frac{d}{dt}\hat{\rho}^{(I)}(t) = -\frac{i}{\hbar}[H_I^{(I)}(t), \hat{\rho}^{(I)}(t)]. \tag{B.18}$$

This equation depends only on the interaction Hamiltonian $H_I^{(I)}(t)$ in the interaction picture, rather than on the total Hamiltonian, which usually facilitates analytical and numerical calculations in the context of interacting systems and open quantum systems (Section 1.4).

The time evolution of the expectation value of $\hat{O}$ in the interaction picture is given by

$$\langle \hat{O} \rangle (t) = \mathrm{Tr}[\hat{O}^{(I)}(t)\hat{\rho}^{(I)}(t)]. \tag{B.19}$$

This expectation value is equivalent to that obtained using the Schrödinger and Heisenberg pictures because

$$\begin{aligned} \mathrm{Tr}[\hat{O}^{(I)}(t)\hat{\rho}^{(I)}(t)] &= \mathrm{Tr}[\hat{U}_0^\dagger(t,t_0)\hat{O}\hat{U}_0(t,t_0)\hat{U}_0^\dagger(t,t_0)\hat{\rho}^{(S)}(t)\hat{U}_0(t,t_0)] \\ &= \mathrm{Tr}[\hat{U}_0^\dagger(t,t_0)\hat{O}\hat{\rho}^{(S)}(t)\hat{U}_0(t,t_0)] \\ &= \mathrm{Tr}[\hat{O}\hat{\rho}^{(S)}(t)] = \mathrm{Tr}[\hat{O}^{(H)}(t)\hat{\rho}(t_0)], \end{aligned} \tag{B.20}$$

where we have used Eq. (B.12), taken into account that $\hat{U}_0(t,t_0)$ is a unitary operator and that the trace is invariant under unitary transformations.

The equivalence between the three pictures is summarized in Table B.1.

Quantity	Schrödinger ($X = S$)	Heisenberg ($X = H$)	Interaction ($X = I$)
$\langle \hat{O} \rangle (t)$	$\mathrm{Tr}[\hat{O}\hat{\rho}^{(S)}(t)]$	$\mathrm{Tr}[\hat{O}^{(H)}(t)\hat{\rho}(t_0)]$	$\mathrm{Tr}[\hat{O}^{(I)}(t)\hat{\rho}^{(I)}(t)]$
$\hat{\rho}^{(X)}$	$\hat{U}(t,t_0)\hat{\rho}(t_0)\hat{U}^\dagger(t,t_0)$	$\hat{\rho}(t_0)$	$\hat{U}_0^\dagger(t,t_0)\hat{\rho}^{(S)}(t)\hat{U}_0(t,t_0)$
$\hat{O}^{(X)}$	$\hat{O}$	$\hat{U}^\dagger(t,t_0)\hat{O}\hat{U}(t,t_0)$	$\hat{U}_0^\dagger(t,t_0)\hat{O}\hat{U}_0(t,t_0)$

Table B.1: Equivalence between the Schrödinger (S), Heisenberg (H) and interaction (I) pictures. For an initial state $\hat{\rho}(t_0)$, the expectation value of an arbitrary operator $\hat{O}$ at time t can be calculated as $\langle \hat{O} \rangle (t) = \mathrm{Tr}[\hat{O}^{(X)}\hat{\rho}^{(X)}]$, with $X = S, H, I$ labeling the corresponding picture.

Appendix C

Unitary transformations

Unitary transformations are sometimes used to simplify the Hamiltonian that governs the dynamics of a quantum system, facilitating the calculation of the expectation values of observables. These unitary transformations can represent a change of reference frame, such as a change to a reference frame rotating at the frequency of a laser driving a quantum emitter (see Section 1.5.3). Additionally, the transformation from a dynamical picture to another (Appendix B) can be also understood as the consequence of a unitary transformation. Importantly, in addition to modifying the expression of the Hamiltonian, unitary transformations also affect the expression of the observables (operators) and that of the quantum state of the system. However, the expectation value of an arbitrary operator at any time remains unchanged under unitary transformations because the change in the Hamiltonian and in the quantum state balance each other. In this appendix, we derive the effect of unitary transformations in the Hamiltonian, in the quantum state and in an arbitrary operator.

First, we consider a closed quantum system with Hamiltonian $\hat{H}(t)$ and quantum state $|\psi(t)\rangle$ at time t in the Schrödinger picture, whose dynamics is governed by the Schrödinger equation

$$i\hbar\frac{d}{dt}|\psi(t)\rangle = \hat{H}(t)\,|\psi(t)\rangle\,. \tag{C.1}$$

The evolution of the quantum state from the initial time t_0 can be obtained through the unitary operator $\hat{U}(t,t_0)$ in Eq. (B.2). We consider now a general linear transformation $\hat{\tilde{T}}(t)$ and assume that it is unitary, meaning that

$$\hat{\tilde{T}}(t)\hat{\tilde{T}}^{\dagger}(t) = \hat{\tilde{T}}^{\dagger}(t)\hat{\tilde{T}}(t) = \mathbb{1}. \tag{C.2}$$

The quantum state $|\psi(t)\rangle$ at time t is transformed by $\hat{\tilde{T}}(t)$ as

$$|\tilde{\psi}(t)\rangle = \hat{\tilde{T}}(t)\,|\psi(t)\rangle\,. \tag{C.3}$$

To obtain the expression of the transformed Hamiltonian $\hat{\tilde{H}}(t)$, we impose next that $|\tilde{\psi}(t)\rangle$ and $\hat{\tilde{H}}(t)$ satisfy the (transformed) Schrödinger equation

$$i\hbar\frac{d}{dt}|\tilde{\psi}(t)\rangle = \hat{\tilde{H}}(t)\,|\tilde{\psi}(t)\rangle\,. \tag{C.4}$$

The left-hand side of this equation can be rewritten as

$$\begin{aligned} i\hbar\frac{d}{dt}|\tilde{\psi}(t)\rangle &= i\hbar\frac{d}{dt}[\hat{\tilde{T}}(t)\,|\psi(t)\rangle] = i\hbar\frac{d\hat{\tilde{T}}(t)}{dt}|\psi(t)\rangle + i\hbar\hat{\tilde{T}}(t)\frac{d}{dt}|\psi(t)\rangle \\ &= i\hbar\frac{d\hat{\tilde{T}}(t)}{dt}|\psi(t)\rangle + \hat{\tilde{T}}(t)\hat{H}(t)\,|\psi(t)\rangle\,, \end{aligned} \tag{C.5}$$

where we have used Eq. (C.1) to obtain the equality in the second line. Substituting Eq. (C.5) into the left-hand side of Eq. (C.4), we find

$$i\hbar\frac{d\hat{\tilde{T}}(t)}{dt}|\psi(t)\rangle + \hat{\tilde{T}}(t)\hat{H}(t)\,|\psi(t)\rangle = \hat{\tilde{H}}(t)\,|\tilde{\psi}(t)\rangle\,. \tag{C.6}$$

Additionally, substituting Eq. (C.3) into the right-hand side of the above equation one obtains

$$i\hbar\frac{d\hat{\tilde{T}}(t)}{dt}|\psi(t)\rangle + \hat{\tilde{T}}(t)\hat{H}(t)\,|\psi(t)\rangle = \hat{\tilde{H}}(t)\hat{\tilde{T}}(t)\,|\psi(t)\rangle\,. \tag{C.7}$$

Next, we drop $|\psi(t)\rangle$ on both sides of this equation and multiply by $\hat{\tilde{T}}^\dagger(t)$ to the right. In this way, we obtain

$$\hat{\tilde{H}} = i\hbar\frac{d\hat{\tilde{T}}(t)}{dt}\hat{\tilde{T}}^\dagger(t) + \hat{\tilde{T}}(t)\hat{H}(t)\hat{\tilde{T}}^\dagger(t) = -i\hbar\hat{\tilde{T}}(t)\frac{d\hat{\tilde{T}}^\dagger(t)}{dt} + \hat{\tilde{T}}(t)\hat{H}(t)\hat{\tilde{T}}^\dagger(t), \tag{C.8}$$

where in the last equality we have used that

$$\frac{d\hat{\tilde{T}}(t)}{dt}\hat{\tilde{T}}^\dagger(t) + \hat{\tilde{T}}(t)\frac{d\hat{\tilde{T}}^\dagger(t)}{dt} = 0, \tag{C.9}$$

which is satisfied by any unitary operator $\hat{\tilde{T}}(t)\hat{\tilde{T}}^\dagger(t) = \mathbb{1}$ [Eq. (C.2)]. The transformed Hamiltonian $\hat{\tilde{H}}$ in Eq. (C.8) is the key result of this appendix. For example, we use the expression for the transformed Hamiltonian in Chapters 1, 3, and 4 when transforming the master equation that governs the dynamics to the rotating frame at the frequency of the incident laser.

In the following, we consider a more general scenario in which the state of the system is described by a density matrix $\hat{\rho}(t)$ and discuss how it is affected by unitary transformations. In this case, the dynamics (in the Schrödinger picture) is

governed by the von Neumann equation [Eq. (B.6)]

$$\frac{d}{dt}\hat{\rho}(t) = -\frac{i}{\hbar}[\hat{H}, \hat{\rho}(t)]. \tag{C.10}$$

The time evolution of $\hat{\rho}(t)$ from the initial time t_0 can be obtained through the unitary propagator $\hat{U}(t, t_0)$ in Eq. (B.2) as $\hat{\rho}(t) = \hat{U}(t, t_0)\hat{\rho}(t_0)\hat{U}^\dagger(t, t_0)$ (see Appendix B). We impose that an equivalent von Neumann equation is satisfied by the transformed Hamiltonian $\hat{\tilde{H}}(t)$ in Eq. (C.8) and by the transformed density matrix $\hat{\tilde{\rho}}$, namely:

$$\frac{d}{dt}\hat{\tilde{\rho}} = -\frac{i}{\hbar}[\hat{\tilde{H}}(t), \hat{\tilde{\rho}}]. \tag{C.11}$$

The unitary propagator that provides the evolution of the transformed density matrix $\hat{\tilde{\rho}}(t)$ from the initial time t_0 is given by

$$\hat{U}_\rho(t, t_0) = \hat{\tilde{T}}(t)\hat{U}(t, t_0), \tag{C.12}$$

as shown below. In this way, the transformed density matrix can be calculated as

$$\hat{\tilde{\rho}}(t) = \hat{U}_\rho(t, t_0)\hat{\rho}(t_0)\hat{U}_\rho^\dagger(t, t_0) = \hat{\tilde{T}}(t)\hat{\rho}(t)\hat{\tilde{T}}^\dagger(t). \tag{C.13}$$

In the following, we justify the definition of $\hat{U}_\rho(t, t_0)$ in Eq. (C.12). On the one hand, this definition yields that the left-hand side of Eq. (C.11) can be rewritten as

$$\begin{aligned}
\frac{d}{dt}\hat{\tilde{\rho}}(t) &= \frac{d\hat{U}_\rho}{dt}\hat{\rho}(t_0)\hat{U}_\rho^\dagger + \hat{U}_\rho\hat{\rho}(t_0)\frac{d\hat{U}_\rho^\dagger}{dt} \\
&= \frac{d\hat{\tilde{T}}(t)}{dt}\hat{U}\hat{\rho}(t_0)\hat{U}^\dagger\hat{\tilde{T}}^\dagger(t) + \hat{\tilde{T}}(t)\frac{d\hat{U}}{dt}\hat{\rho}(t_0)\hat{U}^\dagger\hat{\tilde{T}}^\dagger(t) \\
&+ \hat{\tilde{T}}(t)\hat{U}\hat{\rho}(t_0)\frac{d\hat{U}^\dagger}{dt}\hat{\tilde{T}}^\dagger(t) + \hat{\tilde{T}}(t)\hat{U}\hat{\rho}(t_0)\hat{U}^\dagger\frac{d\hat{\tilde{T}}^\dagger(t)}{dt} \\
&= \frac{d\hat{\tilde{T}}(t)}{dt}\hat{\rho}(t)\hat{\tilde{T}}^\dagger(t) + \hat{\tilde{T}}(t)\hat{\rho}(t)\frac{d\hat{\tilde{T}}^\dagger(t)}{dt} - \frac{i}{\hbar}\hat{\tilde{T}}(t)[\hat{H}(t), \hat{\rho}(t)]\hat{\tilde{T}}^\dagger(t).
\end{aligned} \tag{C.14}$$

In order to obtain the expression in the last line of this equation we have used Eq. (B.2). On the other hand, the definition of $\hat{U}_\rho(t, t_0)$ in Eq. (C.12) implies that the

right-hand side of Eq. (C.11) is equal to

$$
\begin{aligned}
-\frac{i}{\hbar}[\hat{\tilde{H}}(t),\hat{\tilde{\rho}}(t)] &= -\frac{i}{\hbar}[i\hbar\frac{d\tilde{T}(t)}{dt}\hat{\tilde{T}}^\dagger(t)+\hat{\tilde{T}}(t)\hat{H}(t)\hat{\tilde{T}}^\dagger(t),\hat{\tilde{T}}(t)\hat{\rho}(t)\hat{\tilde{T}}^\dagger(t)] \\
&= -\frac{i}{\hbar}\Big(\hat{\tilde{T}}(t)\hat{H}(t)\hat{\tilde{T}}^\dagger(t)\hat{\tilde{T}}(t)\hat{\rho}(t)\hat{\tilde{T}}^\dagger(t)-\hat{\tilde{T}}(t)\hat{\rho}(t)\hat{\tilde{T}}^\dagger(t)\hat{\tilde{T}}(t)\hat{H}(t)\hat{\tilde{T}}^\dagger(t)\Big) \\
&+ \frac{d\hat{\tilde{T}}(t)}{dt}\hat{\tilde{T}}^\dagger(t)\hat{\tilde{T}}(t)\hat{\rho}(t)\hat{\tilde{T}}^\dagger(t)-\hat{\tilde{T}}(t)\hat{\rho}(t)\hat{\tilde{T}}^\dagger(t)\frac{d\hat{\tilde{T}}(t)}{dt}\hat{\tilde{T}}^\dagger(t) \\
&= \frac{d\hat{\tilde{T}}(t)}{dt}\hat{\rho}(t)\hat{\tilde{T}}^\dagger(t)+\hat{\tilde{T}}(t)\hat{\rho}(t)\frac{d\hat{\tilde{T}}^\dagger(t)}{dt}-\frac{i}{\hbar}\hat{\tilde{T}}(t)[\hat{H}(t),\hat{\rho}(t)]\hat{\tilde{T}}^\dagger(t)=\frac{d}{dt}\hat{\tilde{\rho}}(t),
\end{aligned}
\tag{C.15}
$$

where we have used Eqs. (C.8) and (C.13) to obtain the expression in the first line, and we have used Eqs. (C.2) and (C.9) to obtain the expression in the last line. Thus, $\hat{U}_\rho(t,t_0)$ in Eq. (C.12) guarantees that an equivalent Von Neumann equation [Eq. (C.11)] is satisfied in the transformed picture, as desired.

Last, we analyze how an arbitrary operator $\hat{O}$ (which is written in the Schrödinger picture) is transformed by $\hat{\tilde{T}}(t)$. The expression of the transformed operator $\hat{\tilde{O}}(t)$ must leave the expectation value unchanged at any time, so that $\mathrm{Tr}[\hat{O}\hat{\rho}(t)]=\mathrm{Tr}[\hat{\tilde{O}}(t)\hat{\tilde{\rho}}(t)]$. To this end, we develop the expression of the expectation value $\langle\hat{O}\rangle(t)$ from the original frame as

$$
\begin{aligned}
\langle\hat{O}\rangle(t) &= \mathrm{Tr}\Big[\hat{O}\hat{\rho}(t)\Big]=\mathrm{Tr}\Big[\hat{O}\hat{U}(t,t_0)\hat{\rho}(t_0)\hat{U}^\dagger(t,t_0)\Big] \\
&= \mathrm{Tr}\Big[\hat{\tilde{T}}(t)\hat{O}\hat{\tilde{T}}^\dagger(t)\hat{\tilde{T}}(t)\hat{U}(t,t_0)\hat{\rho}(t_0)\hat{U}^\dagger(t,t_0)\hat{\tilde{T}}^\dagger(t)\Big] \\
&= \mathrm{Tr}\Big[\hat{\tilde{T}}(t)\hat{O}\hat{\tilde{T}}^\dagger(t)\hat{U}_\rho(t,t_0)\hat{\rho}(t_0)\hat{U}_\rho^\dagger(t,t_0)\Big].
\end{aligned}
\tag{C.16}
$$

Therefore, by defining

$$
\hat{\tilde{O}}(t)=\hat{\tilde{T}}(t)\hat{O}\hat{\tilde{T}}^\dagger(t),
\tag{C.17}
$$

we obtain

$$
\langle\hat{O}\rangle(t)=\mathrm{Tr}\Big[\hat{O}\hat{\rho}(t)\Big]=\mathrm{Tr}\Big[\hat{\tilde{O}}(t)\hat{\tilde{\rho}}(t)\Big].
\tag{C.18}
$$

We finally note that if the system is considered as open and described by a Markovian master equation (Section 1.4), all the dissipators $\mathcal{D}[\hat{O}_1,\hat{O}_2]\hat{\rho}(t)$ [see Eq. (1.191)] need to be replaced by transformed dissipators $\mathcal{D}[\hat{\tilde{O}}_1,\hat{\tilde{O}}_2]\hat{\tilde{\rho}}(t)$.

List of abbreviations

TLS	Two-level system
QE	Quantum emitter
WWA	Wigner-Weisskopf approximation
RWA	Rotating-Wave approximation
MME	Markovian Master Equation
DBATT	dibenzanthanthrene
HBT	Hanbury-Brown Twiss
ss	steady state
FRIC	Frequency-resolved intensity correlation
ZPL	Zero-Phonon Line
FWHM	Full-width at half maximum
PDC	parametric-down conversion
QD	quantum dot
TE	transverse electric
TM	transverse magnetic

List of publications

The results presented in this thesis are based on the following publications:

- **Chapter 3:**
  A. Juan-Delgado, R. Esteban, Á. Nodar, J.-B. Trebbia, B. Lounis, and J. Aizpurua: "Tailoring the statistics of light emitted from two interacting quantum emitters", Physical Review Research **6**, 023207 (2024).
  https://doi.org/10.1103/PhysRevResearch.6.023207

- **Chapter 4:**
  A. Juan-Delgado, J.-B. Trebbia, R. Esteban, Q. Deplano, P. Tamarat, R. Avriller, B. Lounis, and J. Aizpurua: "Addressing the correlation of Stokes-shifted photons emitted from two quantum emitters", Under review. arXiv preprint arXiv:2501.19356 (2025).
  https://doi.org/10.48550/arXiv.2501.19356

- **Chapter 5:**
  A. Juan-Delgado, G. Giedke, J. Aizpurua, and R. Esteban: "Generation of polarization-entangled photon pairs from two interacting quantum emitters", Under review. arXiv preprint arXiv:2503.02739 (2025).
  https://doi.org/10.48550/arXiv.2503.02739

Other publications:

- L. A. Jakob*, **A. Juan-Delgado***, N. S. Mueller, S. Hu, R. Arul, R. A. Boto, R. Esteban, J. Aizpurua, and J. J. Baumberg: "Optomechanical Pumping of Collective Molecular Vibrations in Plasmonic Nanocavities", ACS Nano **19**, 10977-10988 (2025).
  https://doi.org/10.1021/acsnano.4c16535
  * These authors contributed equally to this work.

- **A. Juan-Delgado**, and A. Chenu: "First law of quantum thermodynamics in a driven open two-level system", Physical Review A **104**, 022219 (2021).
  https://doi.org/10.1103/PhysRevA.104.022219

- S. Ribeiro, **A. Juan-Delgado**, and S. A. Gardiner: "Determining the absolute number density of a thermal vapor via photon correlations", Physical Review A **110**, L031701 (2024).
https://doi.org/10.1103/PhysRevA.110.L031701

Bibliography

[1] J.-B. Trebbia, Q. Deplano, P. Tamarat, and B. Lounis, "Tailoring the superradiant and subradiant nature of two coherently coupled quantum emitters", Nature Communications **13**, 1–9 (2022).

[2] A. Einstein, "Über einen die Erzeugung und Verwandlung des Lichtes betreffenden heuristischen Gesichtspunkt", Annalen der Physik **17** (1905).

[3] N. Bohr, "I. On the constitution of atoms and molecules", The London, Edinburgh, and Dublin Philosophical Magazine and Journal of Science **26**, 1–25 (1913).

[4] N. Bohr, "XXXVII. on the constitution of atoms and molecules", The London, Edinburgh, and Dublin Philosophical Magazine and Journal of Science **26**, 476–502 (1913).

[5] N. Bohr, "LXXIII. on the constitution of atoms and molecules", The London, Edinburgh, and Dublin Philosophical Magazine and Journal of Science **26**, 857–875 (1913).

[6] M. Born and P. Jordan, "Zur quantenmechanik", Zeitschrift für Physik **34**, 858–888 (1925).

[7] E. Schrödinger, "An undulatory theory of the mechanics of atoms and molecules", Physical Review **28**, 1049 (1926).

[8] P. Dirac, "The quantum theory of the emission and absorption of radiation", Proceedings of the Royal Society of London. Series A, Containing Papers of a Mathematical and Physical Character **114**, 243–265 (1927).

[9] P. Dirac, "The quantum theory of dispersion", Proceedings of the Royal Society of London. Series A, Containing Papers of a Mathematical and Physical Character **114**, 710–728 (1927).

[10] P. Dirac, "The quantum theory of the electron", Proceedings of the Royal Society of London. Series A, Containing Papers of a Mathematical and Physical Character **117**, 610–624 (1928).

[11] P. Jordan and W. Pauli, “Zur quantenelektrodynamik ladungsfreier felder”, Zeitschrift für Physik **47**, 151–173 (1928).

[12] E. Fermi, “Sopra l’elettrodinamica quantistica”, Rendiconti Lincei **9**, 881–887 (1929).

[13] W. Heisenberg and W. Pauli, “Zur quantendynamik der wellenfelder”, Zeitschrift für Physik **56**, 1–61 (1929).

[14] W. Heisenberg and W. Pauli, “Zur quantentheorie der wellenfelder. II”, Zeitschrift für Physik **59**, 168–190 (1930).

[15] E. Fermi, “Sopra l’elettrodinamica quantistica. II”, Rendiconti Lincei **12**, 431–435 (1930).

[16] V. Weisskopf and E. Wigner, “Berechnung der natürlichen linienbreite auf grund der diracschen lichttheorie”, Zeitschrift für Physik **63** (1930).

[17] W. Heisenberg, “Bemerkungen zur Strahlungstheorie”, Annalen der Physik **401**, 338–346 (1931).

[18] E. Fermi, “Quantum theory of radiation”, Reviews of Modern Physics **4**, 87 (1932).

[19] A. Schawlow and C. Townes, “Infrared and optical masers”, Physical Review **112**, 1940 (1958).

[20] T. Maiman, “Stimulated optical radiation in ruby”, Nature **187**, 493–494 (1960).

[21] N. Holonyak and S. Bevacqua, “Coherent (visible) light emission from Ga(As1–xPx) junctions”, Applied Physics Letters **1**, 82–83 (1962).

[22] R. Logan, H. White, and W. Wiegmann, “Efficient green electroluminescence in nitrogen-doped GaP p-n junctions”, Applied Physics Letters **13**, 139–141 (1968).

[23] H. Amano, N. Sawaki, I. Akasaki, and Y. Toyoda, “Metalorganic vapor phase epitaxial growth of a high quality GaN film using an AlN buffer layer”, Applied Physics Letters **48**, 353–355 (1986).

[24] H. Amano, M. Kito, K. Hiramatsu, and I. Akasaki, “P-type conduction in Mg-doped GaN treated with low-energy electron beam irradiation (LEEBI)”, Japanese Journal of Applied Physics **28**, L2112–L2114 (1989).

[25] S. Nakamura, T. Mukai, and M. Senoh, “Candela-class high-brightness InGaN/AlGaN double-heterostructure blue-light-emitting diodes”, Applied Physics Letters **64**, 1687–1689 (1994).

[26] J. Dowling and G. Milburn, "Quantum technology: the second quantum revolution", Philosophical Transactions of the Royal Society of London. Series A: Mathematical, Physical and Engineering Sciences **361**, 1655–1674 (2003).

[27] M. Lukin, "Colloquium: Trapping and manipulating photon states in atomic ensembles", Reviews of Modern Physics **75**, 457 (2003).

[28] I. Walmsley, "Quantum optics: Science and technology in a new light", Science **348**, 525–530 (2015).

[29] S. Mukamel *et al.*, "Roadmap on quantum light spectroscopy", Journal of Physics B: Atomic, Molecular and Optical Physics **53**, 072002 (2020).

[30] U. Bhattacharya, T. Lamprou, A. Maxwell, A. Ordonez, E. Pisanty, J. Rivera-Dean, P. Stammer, M. Ciappina, M. Lewenstein, and P. Tzallas, "Strong–laser–field physics, non–classical light states and quantum information science", Reports on Progress in Physics **86**, 094401 (2023).

[31] B. Lounis and M. Orrit, "Single-photon sources", Reports on Progress in Physics **68**, 1129 (2005).

[32] C. H. Bennett and G. Brassard, "Proceedings of the IEEE International Conference on Computers, Systems and Signal Processing", (1984).

[33] C. H. Bennett and G. Brassard, *Advances in Cryptology* (Springer Berlin Heidelberg, 1985) pp. 475–480.

[34] C. H. Bennett, G. Brassard, C. Crépeau, R. Jozsa, A. Peres, and W. K. Wootters, "Teleporting an unknown quantum state via dual classical and Einstein-Podolsky-Rosen channels", Physical Review Letters **70**, 1895 (1993).

[35] D. Bouwmeester, J.-W. Pan, K. Mattle, M. Eibl, H. Weinfurter, and A. Zeilinger, "Experimental quantum teleportation", Nature **390**, 575–579 (1997).

[36] H. Kimble, "The quantum internet", Nature **453**, 1023–1030 (2008).

[37] C. Couteau, S. Barz, T. Durt, T. Gerrits, J. Huwer, R. Prevedel, J. Rarity, A. Shields, and G. Weihs, "Applications of single photons to quantum communication and computing", Nature Reviews Physics **5**, 326–338 (2023).

[38] G. Milburn, "Quantum optical Fredkin gate", Physical Review Letters **62**, 2124 (1989).

[39] E. Knill, R. Laflamme, and G. Milburn, "A scheme for efficient quantum computation with linear optics", Nature **409**, 46–52 (2001).

[40] P. Kok, W. Munro, K. Nemoto, T. Ralph, J. Dowling, and G. Milburn, "Linear optical quantum computing with photonic qubits", Reviews of Modern Physics **79**, 135–174 (2007).

[41] C. Toninelli, I. Gerhardt, A. S. Clark, A. Reserbat-Plantey, S. Götzinger, Z. Ristanović, M. Colautti, P. Lombardi, K. D. Major, I. Deperasińska, W. Pernice, F. Koppens, B. Kozankiewicz, A. Gourdon, V. Sandoghdar, and M. Orrit, "Single organic molecules for photonic quantum technologies", Nature Materials **20**, 1615–1628 (2021).

[42] W. Louisell, A. Yariv, and A. Siegman, "Quantum fluctuations and noise in parametric processes. I.", Physical Review **124**, 1646 (1961).

[43] D. Burnham and D. Weinberg, "Observation of simultaneity in parametric production of optical photon pairs", Physical Review Letters **25**, 84 (1970).

[44] C. Couteau, "Spontaneous parametric down-conversion", Contemporary Physics **59**, 291–304 (2018).

[45] J. Rarity, P. Tapster, and E. Jakeman, "Observation of sub-poissonian light in parametric downconversion", Optics Communications **62**, 201–206 (1987).

[46] E. Bocquillon, C. Couteau, M. Razavi, R. Laflamme, and G. Weihs, "Coherence measures for heralded single-photon sources", Physical Review A **79**, 035801 (2009).

[47] H. Kimble, M. Dagenais, and L. Mandel, "Photon antibunching in resonance fluorescence", Physical Review Letters **39**, 691 (1977).

[48] A. Kuhn, M. Hennrich, and G. Rempe, "Deterministic single-photon source for distributed quantum networking", Physical Review Letters **89**, 067901 (2002).

[49] T. Wilk, S. Webster, A. Kuhn, and G. Rempe, "Single-atom single-photon quantum interface", Science **317**, 488–490 (2007).

[50] F. Diedrich and H. Walther, "Nonclassical radiation of a single stored ion", Physical Review Letters **58**, 203 (1987).

[51] W. Itano, J. Bergquist, and D. Wineland, "Photon antibunching and sub-Poissonian statistics from quantum jumps in one and two atoms", Physical Review A **38**, 559 (1988).

[52] D. Leibfried, R. Blatt, C. Monroe, and D. Wineland, "Quantum dynamics of single trapped ions", Reviews of Modern Physics **75**, 281 (2003).

[53] W. Moerner and L. Kador, "Optical detection and spectroscopy of single molecules in a solid", Physical Review Letters **62**, 2535 (1989).

[54] M. Orrit and J. Bernard, "Single pentacene molecules detected by fluorescence excitation in a p-terphenyl crystal", Physical Review Letters **65**, 2716 (1990).

[55] B. Gurlek and D. Wang, "Small but large: Single organic molecules as hybrid platforms for quantum technologies", Physical Review Research **7**, 021001 (2025).

[56] A. Gruber, A. Drabenstedt, C. Tietz, L. Fleury, J. Wrachtrup, and C. von Borczyskowski, "Scanning confocal optical microscopy and magnetic resonance on single defect centers", Science **276**, 2012–2014 (1997).

[57] I. Aharonovich, S. Castelletto, D. Simpson, C.-H. Su, A. Greentree, and S. Prawer, "Diamond-based single-photon emitters", Reports on Progress in Physics **74**, 076501 (2011).

[58] P. Michler, A. Kiraz, C. Becher, W. Schoenfeld, P. Petroff, L. Zhang, E. Hu, and A. Imamoglu, "A quantum dot single-photon turnstile device", Science **290**, 2282–2285 (2000).

[59] S. Buckley, K. Rivoire, and J. Vučković, "Engineered quantum dot single-photon sources", Reports on Progress in Physics **75**, 126503 (2012).

[60] A. Shields, "Semiconductor quantum light sources", Nature Photonics **1**, 215–223 (2007).

[61] G. Grosso, H. Moon, B. Lienhard, S. Ali, D. Efetov, M. Furchi, P. Jarillo-Herrero, M. Ford, I. Aharonovich, and D. Englund, "Tunable and high-purity room temperature single-photon emission from atomic defects in hexagonal boron nitride", Nature Communications **8**, 1–8 (2017).

[62] M. Toth and I. Aharonovich, "Single photon sources in atomically thin materials", Annual Review of Physical Chemistry **70**, 123–142 (2019).

[63] V. Vedral, M. Plenio, M. Rippin, and P. Knight, "Quantifying entanglement", Physical Review Letters **78**, 2275 (1997).

[64] V. Vedral and M. Plenio, "Entanglement measures and purification procedures", Physical Review A **57**, 1619 (1998).

[65] M. Plenio and S. Virmani, "An Introduction to Entanglement Theory", in *Quantum Information and Coherence*, edited by E. Andersson and P. Öhberg (Springer International Publishing, Cham, 2014).

[66] A. Ekert, "Quantum cryptography based on Bell's theorem", Physical Review Letters **67**, 661 (1991).

[67] V. Scarani, H. Bechmann-Pasquinucci, N. Cerf, M. Dušek, N. Lütkenhaus, and M. Peev, "The security of practical quantum key distribution", Reviews of Modern Physics **81**, 1301–1350 (2009).

[68] S. Pironio *et al.*, "Random numbers certified by Bell's theorem", Nature **464**, 1021–1024 (2010).

[69] D. Nadlinger, P. Drmota, B. Nichol, G. Araneda, D. Main, R. Srinivas, D. Lucas, C. Ballance, K. Ivanov, E.-Z. Tan, P. Sekatski, R. Urbanke, R. Renner, N. Sangouard, and J.-D. Bancal, "Experimental quantum key distribution certified by Bell's theorem", Nature **607**, 682–686 (2022).

[70] W. Zhang, T. van Leent, K. Redeker, R. Garthoff, R. Schwonnek, F. Fertig, S. Eppelt, W. Rosenfeld, V. Scarani, C. Lim, and H. Weinfurter, "A device-independent quantum key distribution system for distant users", Nature **607**, 687–691 (2022).

[71] T. Ono, R. Okamoto, and S. Takeuchi, "An entanglement-enhanced microscope", Nature Communications **4**, 2426 (2013).

[72] A. Bennett, J. Lee, D. Ellis, T. Meany, E. Murray, F. Floether, J. Griffths, I. Farrer, D. Ritchie, and A. Shields, "Cavity-enhanced coherent light scattering from a quantum dot", Science Advances **2**, e1501256 (2016).

[73] M. Müller, H. Vural, C. Schneider, A. Rastelli, O. Schmidt, S. Höfling, and P. Michler, "Quantum-dot single-photon sources for entanglement enhanced interferometry", Physical Review Letters **118**, 257402 (2017).

[74] P.-A. Moreau, E. Toninelli, T. Gregory, and M. Padgett, "Imaging with quantum states of light", Nature Reviews Physics **1**, 367–380 (2019).

[75] E. Toninelli, P.-A. Moreau, T. Gregory, A. Mihalyi, M. Edgar, N. Radwell, and M. Padgett, "Resolution-enhanced quantum imaging by centroid estimation of biphotons", Optica **6**, 347–353 (2019).

[76] H. Defienne, M. Reichert, J. Fleischer, and D. Faccio, "Quantum image distillation", Science Advances **5** (2019).

[77] R. Camphausen, Á. Cuevas, L. Duempelmann, R. Terborg, E. Wajs, S. Tisa, A. Ruggeri, I. Cusini, F. Steinlechner, and V. Pruneri, "A quantum-enhanced wide-field phase imager", Science Advances **7** (2021).

[78] S. Lloyd, "A potentially realizable quantum computer", Science **261**, 1569–1571 (1993).

[79] D. Dzsotjan, A. Sørensen, and M. Fleischhauer, "Quantum emitters coupled to surface plasmons of a nanowire: A Green's function approach", Physical Review B **82**, 075427 (2010).

[80] V. Paulisch, H. Kimble, and A. González-Tudela, "Universal quantum computation in waveguide QED using decoherence free subspaces", New Journal of Physics **18**, 043041 (2016).

[81] V. Schäfer, C. Ballance, K. Thirumalai, L. Stephenson, T. Ballance, A. Steane, and D. Lucas, "Fast quantum logic gates with trapped-ion qubits", Nature **555**, 75–78 (2018).

[82] J. Reina, C. Susa, and R. Hildner, "Conditional quantum dynamics and nonlocal states in dimeric and trimeric arrays of organic molecules", Physical Review A **97**, 063422 (2018).

[83] M. Zanner, T. Orell, C. Schneider, R. Albert, S. Oleschko, M. Juan, M. Silveri, and G. Kirchmair, "Coherent control of a multi-qubit dark state in waveguide quantum electrodynamics", Nature Physics **18**, 538–543 (2022).

[84] V. Paulisch, M. Perarnau-Llobet, A. González-Tudela, and J. Cirac, "Quantum metrology with one-dimensional superradiant photonic states", Physical Review A **99**, 043807 (2019).

[85] A. Asenjo-Garcia, M. Moreno-Cardoner, A. Albrecht, H. J. Kimble, and D. E. Chang, "Exponential improvement in photon storage fidelities using subradiance and "selective radiance" in atomic arrays", Physical Review X **7**, 031024 (2017).

[86] P. O. Guimond, A. Grankin, D. V. Vasilyev, B. Vermersch, and P. Zoller, "Subradiant Bell states in distant atomic arrays", Physical Review Letters **122**, 093601 (2019).

[87] K. E. Ballantine and J. Ruostekoski, "Quantum single-photon control, storage, and entanglement generation with planar atomic arrays", PRX Quantum **2**, 040362 (2021).

[88] M. Kasha, H. Rawls, and M. Ashraf El-Bayoumi, "The exciton model in molecular spectroscopy", Pure and Applied Chemistry VIIIth **11**, 371–392 (1965).

[89] N. Hestand and F. Spano, "Molecular aggregate photophysics beyond the Kasha model: novel design principles for organic materials", Accounts of Chemical Research **50**, 341–350 (2017).

[90] S. Jang and B. Mennucci, "Delocalized excitons in natural light-harvesting complexes", Reviews of Modern Physics **90**, 035003 (2018).

[91] M. Moreno-Cardoner, R. Holzinger, and H. Ritsch, "Efficient nano-photonic antennas based on dark states in quantum emitter rings", Optics Express **30**, 10779–10791 (2022).

[92] C. Hettich, C. Schmitt, J. Zitzmann, S. Kuhn, I. Gerhardt, and V. Sandoghdar, "Nanometer resolution and coherent optical dipole coupling of two individual molecules", Science **298**, 385–389 (2002).

[93] S. Reitzenstein, A. Löffler, C. Hofmann, A. Kubanek, M. Kamp, J. Reithmaier, A. Forchel, V. Kulakovskii, L. Keldysh, I. Ponomarev, and T. Reinecke, "Coherent photonic coupling of semiconductor quantum dots", Optics Letters **31**, 1738–1740 (2006).

[94] A. Laucht, J. Villas-Bôas, S. Stobbe, N. Hauke, F. Hofbauer, G. Böhm, P. Lodahl, M.-C. Amann, M. Kaniber, and J. Finley, "Mutual coupling of two semiconductor quantum dots via an optical nanocavity", Physical Review B **82**, 075305 (2010).

[95] F. Albert, K. Sivalertporn, J. Kasprzak, M. Strauss, C. Schneider, S. Höfling, M. Kamp, A. Forchel, S. Reitzenstein, E. Muljarov, and W. Langbein, "Microcavity controlled coupling of excitonic qubits", Nature Communications **4**, 1747 (2013).

[96] M. Delbecq, L. Bruhat, J. Viennot, S. Datta, A. Cottet, and T. Kontos, "Photon-mediated interaction between distant quantum dot circuits", Nature Communications **4**, 1400 (2013).

[97] J. Wolters, N. Sadzak, A. Schell, T. Schröder, and O. Benson, "Measurement of the ultrafast spectral diffusion of the optical transition of nitrogen vacancy centers in nano-size diamond using correlation interferometry", Physical Review Letters **110**, 027401 (2013).

[98] P. Lodahl, S. Mahmoodian, and S. Stobbe, "Interfacing single photons and single quantum dots with photonic nanostructures", Reviews of Modern Physics **87**, 347–400 (2015).

[99] C. M. Lange, E. Daggett, V. Walther, L. Huang, and J. D. Hood, "Superradiant and subradiant states in lifetime-limited organic molecules through laser-induced tuning", Nature Physics **20**, 836–842 (2024).

[100] D. Rattenbacher, A. Shkarin, J. Renger, T. Utikal, S. Götzinger, and V. Sandoghdar, "On-chip interference of scattering from two individual molecules", Optica **10**, 1595–1601 (2023).

[101] J. Nobakht, A. Pscherer, J. Renger, S. Götzinger, and V. Sandoghdar, "Cavity-mediated hybridization of several molecules in the strong coupling regime", arXiv preprint arXiv:2501.00414 (2024).

[102] J.-H. Kim, S. Aghaeimeibodi, C. Richardson, R. Leavitt, and E. Waks, "Super-radiant emission from quantum dots in a nanophotonic waveguide", Nano Letters **18**, 4734–4740 (2018).

[103] J. Grim, A. Bracker, M. Zalalutdinov, S. Carter, A. Kozen, M. Kim, C. Kim, J. Mlack, M. Yakes, B. Lee, and D. Gammon, "Scalable in operando strain tuning in nanophotonic waveguides enabling three-quantum-dot superradiance", Nature Materials **18**, 963–969 (2019).

[104] A. Tiranov, V. Angelopoulou, C. J. van Diepen, B. Schrinski, O. A. D. Sandberg, Y. Wang, L. Midolo, S. Scholz, A. D. Wieck, A. Ludwig, A. Sørensen, and P. Lodahl, "Collective super-and subradiant dynamics between distant optical quantum emitters", Science **379**, 389–393 (2023).

[105] X. Chu, C. Papon, N. Bart, A. D. Wieck, A. Ludwig, L. Midolo, N. Rotenberg, and P. Lodahl, "Independent electrical control of two quantum dots coupled through a photonic-crystal waveguide", Physical Review Letters **131**, 033606 (2023).

[106] C. van Diepen, V. Angelopoulou, O. Sandberg, A. Tiranov, Y. Wang, S. Scholz, A. Ludwig, A. Sørensen, and P. Lodahl, "Resonant energy transfer and collectively driven emitters in waveguide QED", arXiv preprint arXiv:2502.17662 (2025).

[107] R. Evans, M. Bhaskar, D. Sukachev, C. Nguyen, A. Sipahigil, M. Burek, B. Machielse, G. Zhang, A. Zibrov, E. Bielejec, H. Park, M. Lončar, and M. Lukin, "Photon-mediated interactions between quantum emitters in a diamond nanocavity", Science **362**, 662–665 (2018).

[108] D. Levonian, R. Riedinger, B. Machielse, E. Knall, M. Bhaskar, C. Knaut, R. Bekenstein, H. Park, M. Lončar, and M. Lukin, "Optical entanglement of distinguishable quantum emitters", Physical Review Letters **128**, 213602 (2022).

[109] D. Lukin, M. Guidry, J. Yang, M. Ghezellou, S. Deb Mishra, H. Abe, T. Ohshima, J. Ul-Hassan, and J. Vučković, "Two-emitter multimode cavity quantum electrodynamics in thin-film silicon carbide photonics", Physical Review X **13**, 011005 (2023).

[110] Y. Zhang, Y. Luo, Y. Zhang, Y.-J. Yu, Y.-M. Kuang, L. Zhang, Q.-S. Meng, Y. Luo, J.-L. Yang, Z.-C. Dong, and J. Hou, "Visualizing coherent intermolecular dipole–dipole coupling in real space", Nature **531**, 623–627 (2016).

[111] R. Glauber, "The Quantum Theory of Optical Coherence", Physical Review **130**, 2529 (1963).

[112] R. Glauber, "Coherent and incoherent states of the radiation field", Physical Review **131**, 2766 (1963).

[113] R. Glauber, "Nobel Lecture: One hundred years of light quanta", Reviews of Modern Physics **78**, 1267–1278 (2006).

[114] R. Glauber, *Quantum theory of optical coherence: selected papers and lectures* (John Wiley & Sons, 2007).

[115] M. Planck, "Zur Theorie des Gesetzes der Energieverteilung im Normalspectrum", Verhandlungen der Deutschen Physikalischen Gesellschaft **2**, 237 (1900).

[116] L. Mandel and E. Wolf, *Optical Coherence and Quantum Optics* (Cambridge University Press, 1995).

[117] R. Loudon, *The Quantum Theory of Light* (Oxford University Press, 2000).

[118] C. Gerry and P. Knight, *Introductory Quantum Optics* (Cambridge University Press, 2005).

[119] P. Milonni, *The Quantum Vacuum: An Introduction to Quantum Electrodynamics* (Academic Press, 1993).

[120] C. Cohen-Tannoudji, J. Dupont-Roc, and G. Grynberg, *Photons and Atoms: Iintroduction to Quantum Electrodynamics* (John Wiley & Sons, Ltd, 1997).

[121] J. Jackson, *Classical Electrodynamics* (John Wiley and Sons, 1975).

[122] P. Dirac, "The quantum theory of the emission and absorption of radiation", Proceedings of the Royal Society of London. Series A, Containing Papers of a Mathematical and Physical Character **114**, 243–265 (1927).

[123] P. Dirac, *The principles of quantum mechanics*, 27 (Oxford University Press, 1958).

[124] D. Steck, *Quantum and atom optics* (2007).

[125] W. Meath and E. Power, "On the importance of permanent moments in multiphoton absorption using perturbation theory", Journal of Physics B: Atomic and Molecular Physics **17**, 763 (1984).

[126] W. Meath and E. Power, "On the effects of diagonal dipole matrix elements in multi-photon resonance profiles using two-level systems as models", Molecular Physics **51**, 585–600 (1984).

[127] V. Kovarskii, "Quantum processes in biological molecules. Enzyme catalysis", Physics-Uspekhi **42**, 797 (1999).

[128] D. Andrews and P. Allcock, *Optical Harmonics in Molecular Systems: Quantum Electrodynamical Theory*, Vol. 1 (Wiley Online Library, 2002).

[129] F. Oster, C. Keitel, and M. Macovei, "Generation of correlated photon pairs in different frequency ranges", Physical Review A **85**, 063814 (2012).

[130] E. Paspalakis, J. Boviatsis, and S. Baskoutas, "Effects of probe field intensity in nonlinear optical processes in asymmetric semiconductor quantum dots", Journal of Applied Physics **114** (2013).

[131] S. Barnett and P. Radmore, *Methods in Theoretical Quantum Optics*, Vol. 15 (Oxford University Press, 2002).

[132] L. Novotny and B. Hecht, *Principles of Nano-Optics* (Cambridge University Press, 2012).

[133] T. Von Foerster, "Quantum theory of a damped two-level atom", American Journal of Physics **40**, 854–862 (1972).

[134] L. Khalfin, "Contribution to the decay theory of a quasi-stationary state", Soviet Physics JETP **6**, 1053–1063 (1958).

[135] P. Knight and P. Milonni, "Long-time deviations from exponential decay in atomic spontaneous emission theory", Physics Letters A **56**, 275–278 (1976).

[136] Y. Sokhotski, "On definite integrals and functions employed in expansions into series", (1873).

[137] J. Plemelj, "Ein ergänzungssatz zur cauchyschen integraldarstellung analytischer funktionen, randwerte betreffend", Monatshefte für Mathematik und Physik **19**, 205–210 (1908).

[138] F. Gakhov, *Boundary value problems* (Pergamon Press, New York, 1966).

[139] H.-P. Breuer and F. Petruccione, *The Theory of Open Quantum Systems* (Oxford University Press, 2002).

[140] K. Szczygielski, "On the floquet analysis of commutative periodic Lindbladians in finite dimension", Linear Algebra and its Applications **609**, 176–202 (2021).

[141] A. Juan-Delgado and A. Chenu, "First law of quantum thermodynamics in a driven open two-level system", Physical Review A **104**, 022219 (2021).

[142] R. Alicki and K. Lendi, *Quantum dynamical semigroups and applications*, Vol. 717 (Springer Science & Business Media, 1987).

[143] D. Fernández de la Pradilla, E. Moreno, and J. Feist, "Recovering an accurate Lindblad equation from the Bloch-Redfield equation for general open quantum systems", Physical Review A **109**, 062225 (2024).

[144] J. Evers and C. Keitel, "Spontaneous-emission suppression on arbitrary atomic transitions", Physical Review Letters **89**, 163601 (2002).

[145] M. Macovei, J. Evers, and C. Keitel, "Spontaneous decay processes in a classical strong low-frequency laser field", Physical Review A **102**, 013718 (2020).

[146] J. Johansson, P. Nation, and F. Nori, "QuTiP: An open-source Python framework for the dynamics of open quantum systems", Computer Physics Communications **183**, 1760–1772 (2012).

[147] M. Born and E. Wolf, *Principles of Optics: Electromagnetic Theory of Propagation, Interference and Diffraction of Light* (Cambridge University Press, 1937).

[148] L. Mandel and E. Wolf, "Coherence properties of optical fields", Reviews of Modern Physics **37**, 231 (1965).

[149] T. Young, "I. The Bakerian Lecture. Experiments and calculations relative to physical optics", Philosophical Transactions of the Royal Society of London , 1–16 (1804).

[150] A. A. Michelson, "I. On the application of interference methods to astronomical measurements", The London, Edinburgh, and Dublin Philosophical Magazine and Journal of Science **30**, 1–21 (1890).

[151] E. Fermi, *Nuclear physics: a course given by Enrico Fermi at the University of Chicago* (University of Chicago Press, 1950).

[152] J. Sakurai and J. Napolitano, *Modern Quantum Mechanics* (Cambridge University Press, 2020).

[153] N. Wiener, "Generalized harmonic analysis", Acta Mathematica **55** (1930).

[154] M. Born and E. Wolf, *Principles of optics: electromagnetic theory of propagation, interference and diffraction of light* (Elsevier, 2013).

[155] P. Hariharan, *Basics of interferometry* (Academic Press, 1994).

[156] C. Page, "Instantaneous power spectra", Journal of Applied Physics **23**, 103–106 (1952).

[157] D. Lampard, "Generalization of the Wiener-Khintchine Theorem to Nonstationary Processes", Journal of Applied Physics **25**, 802–803 (1954).

[158] J. Eberly and K. Wodkiewicz, "The time-dependent physical spectrum of light", Journal of the Optical Society of America **67**, 1252–1261 (1977).

[159] J. Cresser, "Intensity correlations of frequency-filtered light fields", Journal of Physics B: Atomic and Molecular Physics **20**, 4915 (1987).

[160] B. Mollow, "Power spectrum of light scattered by two-level systems", Physical Review **188** (1969).

[161] C. Cohen-Tannoudji and S. Reynaud, "Dressed-atom description of resonance fluorescence and absorption spectra of a multi-level atom in an intense laser beam", Journal of Physics B: Atomic and Molecular Physics **10**, 345 (1977).

[162] P. Dirac, "The quantum theory of the emission and absorption of radiation", Proceedings of the Royal Society of London. Series A, Containing Papers of a Mathematical and Physical Character **114**, 243–265 (1927).

[163] R. Hanbury Brown and R. Twiss, "LXXIV. A new type of interferometer for use in radio astronomy", The London, Edinburgh, and Dublin Philosophical Magazine and Journal of Science **45**, 663–682 (1954).

[164] R. Hanbury Brown and R. Twiss, "Correlation between photons in two coherent beams of light", Nature **177**, 27–29 (1956).

[165] R. Hanbury Brown and R. Twiss, "2. A test of a new type of stellar interferometer on Sirius", Nature **178**, 1046–48 (1956).

[166] B. Saleh, *Photoelectron Statistics: With Applications to Spectroscopy and Optical Communication*, Vol. 6 (Springer, 2013).

[167] Á. Nodar, *Theoretical description of light emission in the presence of nanoscale resonators: from classical scattering to photon states entanglement and statistics* (2023).

[168] X. Zou and L. Mandel, "Photon-antibunching and sub-Poissonian photon statistics", Physical Review A **41**, 475 (1990).

[169] E. del Valle, A. Gonzalez-Tudela, F. Laussy, C. Tejedor, and M. Hartmann, "Theory of frequency-filtered and time-resolved n-photon correlations", Physical Review Letters **109**, 183601 (2012).

[170] L. Knoll and G. Weber, "Theory of n-fold time-resolved correlation spectroscopy and its application to resonance fluorescence radiation", Journal of Physics B: Atomic and Molecular Physics **19**, 2817 (1986).

[171] G. Nienhuis, "Spectral correlations in resonance fluorescence", Physical Review A **47**, 510 (1993).

[172] D. Holdaway, V. Notararigo, and A. Olaya-Castro, "Perturbation approach for computing frequency-and time-resolved photon correlation functions", Physical Review A **98**, 063828 (2018).

[173] A. Gonzalez-Tudela, F. P. Laussy, C. Tejedor, M. J. Hartmann, and E. Del Valle, "Two-photon spectra of quantum emitters", New Journal of Physics **15**, 033036 (2013).

[174] E. del Valle, "Distilling one, two and entangled pairs of photons from a quantum dot with cavity QED effects and spectral filtering", New Journal of Physics **15**, 025019 (2013).

[175] M. Peiris, B. Petrak, K. Konthasinghe, Y. Yu, Z. C. Niu, and A. Muller, "Two-color photon correlations of the light scattered by a quantum dot", Physical Review B **91**, 195125 (2015).

[176] C. Sánchez Muñoz, F. P. Laussy, C. Tejedor, and E. Del Valle, "Enhanced two-photon emission from a dressed biexciton", New Journal of Physics **17**, 123021 (2015).

[177] M. K. Schmidt, R. Esteban, G. Giedke, J. Aizpurua, and A. González-Tudela, "Frequency-resolved photon correlations in cavity optomechanics", Quantum Science and Technology **6**, 034005 (2021).

[178] E. Darsheshdar, M. Hugbart, R. Bachelard, and C. J. Villas-Boas, "Photon-photon correlations from a pair of strongly coupled two-level emitters", Physical Review A **103**, 053702 (2021).

[179] P. Milonni and P. Knight, "Retardation in the resonant interaction of two identical atoms", Physical Review A **10**, 1096 (1974).

[180] W. Moerner, "Physical Principles and Methods of Single-Molecule Spectroscopy in Solids", in *Single-Molecule Optical Detection, Imaging and Spectroscopy* (John Wiley & Sons, Ltd, 1996) Chap. 1.1, pp. 1–30.

[181] G. Nienhuis and C. Alkemade, "Atomic radiative transition probabilities in a continuous medium", Physica B+C **81**, 181–188 (1976).

[182] R. D. Griffin and S. M. Harris, "Two-atom resonance fluorescence including the dipole-dipole interaction", Physical Review A **25**, 1528 (1982).

[183] Z. Ficek, R. Tanas, and S. Kielich, "Effect of interatomic interactions on resonance fluorescence of two atoms coherently driven by a strong resonant laser field", Optica acta **30**, 713–731 (1983).

[184] Z. Ficek, R. Tanaś, and S. Kielich, "Photon antibunching and squeezing in resonance fluorescence of two interacting atoms", Physical Review A **29**, 2004 (1984).

[185] S. V. Lawande, B. N. Jagatap, and Q. V. Lawande, "Inhibition of fluorescence in a system of two interacting two-level atoms: A quantum jump like behaviour", Optics Communications **73**, 126–130 (1989).

[186] T. G. Rudolph, Z. Ficek, and B. J. Dalton, "Two-atom resonance fluorescence in running-and standing-wave laser fields", Physical Review A **52**, 636 (1995).

[187] A. Beige and G. C. Hegerfeldt, "Transition from antibunching to bunching for two dipole-interacting atoms", Physical Review A **58**, 4133 (1998).

[188] J. Gillet, G. S. Agarwal, and T. Bastin, "Tunable entanglement, antibunching, and saturation effects in dipole blockade", Physical Review A **81**, 013837 (2010).

[189] A. Vivas-Viaña and C. Sánchez Muñoz, "Two-photon resonance fluorescence of two interacting nonidentical quantum emitters", Physical Review Research **3**, 033136 (2021).

[190] C. Downing, E. del Valle, and A. Fernández-Domínguez, "Resonance fluorescence of two asymmetrically pumped and coupled two-level systems", Physical Review A **107**, 023717 (2023).

[191] S. Wolf, S. Richter, J. von Zanthier, and F. Schmidt-Kaler, "Light of two atoms in free space: Bunching or antibunching?" Physical Review Letters **124**, 063603 (2020).

[192] G. S. Agarwal, "Quantum statistical theories of spontaneous emission and their relation to other approaches", in *Quantum Optics*, edited by G. Höhler (Springer Berlin Heidelberg, Berlin, Heidelberg, 1974) pp. 1–128.

[193] M. Cordier, M. Schemmer, P. Schneeweiss, J. Volz, and A. Rauschenbeutel, "Tailoring photon statistics with an atom-based two-photon interferometer", Physical Review Letters **131**, 183601 (2023).

[194] S. Ribeiro, T. F. Cutler, C. S. Adams, and S. A. Gardiner, "Collective effects in the photon statistics of thermal atomic ensembles", Physical Review A **104**, 013719 (2021).

[195] T. J. Arruda, R. Bachelard, J. Weiner, S. Slama, and P. W. Courteille, "Controlling photon bunching and antibunching of two quantum emitters near a core-shell sphere", Physical Review A **101**, 023828 (2020).

[196] Z. Ficek and S. Swain, *Quantum Interference and Coherence: Theory and Experiments*, Vol. 100 (Springer Science & Business Media, 2005).

[197] C. Clear, R. C. Schofield, K. D. Major, J. Iles-Smith, A. S. Clark, and D. P. S. McCutcheon, "Phonon-induced optical dephasing in single organic molecules", Physical Review Letters **124**, 153602 (2020).

[198] M. Reitz, C. Sommer, B. Gurlek, V. Sandoghdar, D. Martin-Cano, and C. Genes, "Molecule-photon interactions in phononic environments", Physical Review Research **2**, 033270 (2020).

[199] C. Hettich, *Coherent Optical Dipole Coupling of Two Individual Molecules at Nanometre Separation*, Ph.D. thesis, Universität Konstanz, Konstanz (2002).

[200] A. Juan-Delgado, J.-B. Trebbia, R. Esteban, Q. Deplano, P. Tamarat, R. Avriller, B. Lounis, and J. Aizpurua, "Addressing the correlation of Stokes-shifted photons emitted from two quantum emitters", arXiv preprint arXiv:2501.19356 (2025).

[201] F. Zhelezko, I. Gulis, B. Lounis, and M. Orrit, "Spectroscopic characteristics of single dibenzanthanthrene molecules isolated in a low-temperature naphthalene matrix", Journal of Applied Spectroscopy **66**, 344–352 (1999).

[202] P. Tamarat, A. Maali, B. Lounis, and M. Orrit, "Ten years of single-molecule spectroscopy", The Journal of Physical Chemistry A **104**, 1–16 (1999).

[203] W. Moerner, "A dozen years of single-molecule spectroscopy in physics, chemistry, and biophysics", The Journal of Physical Chemistry B **106**, 910–927 (2002).

[204] W. Ambrose and W. Moerner, "Fluorescence spectroscopy and spectral diffusion of single impurity molecules in a crystal", Nature **349**, 225–227 (1991).

[205] G. Hegerfeldt, "How to reset an atom after a photon detection: Applications to photon-counting processes", Physical Review A **47**, 449 (1993).

[206] U. Fano, "Quantum theory of interference effects in the mixing of light from phase-independent sources", American Journal of Physics **29**, 539–545 (1961).

[207] A. Aspect, "Hanbury Brown and Twiss, Hong Ou and Mandel effects and other landmarks in Quantum Optics: from photons to atoms", in *Current Trends in Atomic Physics* (Oxford University Press, 2019).

[208] F. Jelezko, B. Lounis, and M. Orrit, "Pump–probe spectroscopy and photophysical properties of single di-benzanthanthrene molecules in a naphthalene crystal", The Journal of Chemical Physics **107**, 1692–1702 (1997).

[209] J. Zirkelbach, M. Mirzaei, I. Deperasińska, B. Kozankiewicz, B. Gurlek, A. Shkarin, T. Utikal, S. Götzinger, and V. Sandoghdar, "High-resolution vibronic spectroscopy of a single molecule embedded in a crystal", The Journal of Chemical Physics **156** (2022).

[210] A. Auffèves, D. Gerace, S. Portolan, A. Drezet, and M. F. Santos, "Few emitters in a cavity: from cooperative emission to individualization", New Journal of Physics **13**, 093020 (2011).

[211] D. Meiser and M. J. Holland, "Intensity fluctuations in steady-state superradiance", Physical Review A **81**, 063827 (2010).

[212] R. Jones, R. Saint, and B. Olmos, "Far-field resonance fluorescence from a dipole-interacting laser-driven cold atomic gas", Journal of Physics B: Atomic, Molecular and Optical Physics **50**, 014004 (2016).

[213] V. Gomer, F. Strauch, B. Ueberholz, S. Knappe, and D. Meschede, "Single-atom dynamics revealed by photon correlations", Physical Review A **58**, R1657 (1998).

[214] S. Pezzagna, B. Naydenov, F. Jelezko, J. Wrachtrup, and J. Meijer, "Creation efficiency of nitrogen-vacancy centres in diamond", New Journal of Physics **12**, 065017 (2010).

[215] C. Bennett, H. Bernstein, S. Popescu, and B. Schumacher, "Concentrating partial entanglement by local operations", Physical Review A **53**, 2046 (1996).

[216] W. Wootters, "Entanglement of formation and concurrence", Quantum Information and Computation **1**, 27–44 (2001).

[217] C. Bennett, D. P. DiVincenzo, J. Smolin, and W. Wootters, "Mixed-state entanglement and quantum error correction", Physical Review A **54**, 3824 (1996).

[218] S. Hill and W. Wootters, "Entanglement of a pair of quantum bits", Physical Review Letters **78**, 5022 (1997).

[219] W. Wootters, "Entanglement of formation of an arbitrary state of two qubits", Physical Review Letters **80**, 2245 (1998).

[220] C. Kocher and E. Commins, "Polarization correlation of photons emitted in an atomic cascade", Physical Review Letters **18**, 575 (1967).

[221] S. Freedman and J. Clauser, "Experimental test of local hidden-variable theories", Physical Review Letters **28**, 938 (1972).

[222] J. Clauser, "Experimental investigation of a polarization correlation anomaly", Physical Review Letters **36**, 1223 (1976).

[223] E. Fry and R. Thompson, "Experimental test of local hidden-variable theories", Physical Review Letters **37**, 465 (1976).

[224] A. Aspect, P. Grangier, and G. Roger, "Experimental tests of realistic local theories via Bell's theorem", Physical Review Letters **47**, 460 (1981).

[225] A. Aspect, P. Grangier, and G. Roger, "Experimental realization of Einstein-Podolsky-Rosen-Bohm Gedankenexperiment: a new violation of Bell's inequalities", Physical Review Letters **49**, 91 (1982).

[226] E. Santos, "Does quantum mechanics violate the Bell inequalities?" Physical Review Letters **66**, 1388 (1991).

[227] J.-W. Pan, Z.-B. Chen, C.-Y. Lu, H. Weinfurter, A. Zeilinger, and M. Żukowski, "Multiphoton entanglement and interferometry", Reviews of Modern Physics **84**, 777–838 (2012).

[228] K. Edamatsu, "Entangled photons: generation, observation, and characterization", Japanese Journal of Applied Physics **46**, 7175 (2007).

[229] A. Orieux, M. Versteegh, K. Jöns, and S. Ducci, "Semiconductor devices for entangled photon pair generation: a review", Reports on Progress in Physics **80**, 076001 (2017).

[230] Y. Shih and C. Alley, "New type of Einstein-Podolsky-Rosen-Bohm experiment using pairs of light quanta produced by optical parametric down conversion", Physical Review Letters **61**, 2921 (1988).

[231] Z. Ou and L. Mandel, "Violation of Bell's inequality and classical probability in a two-photon correlation experiment", Physical Review Letters **61**, 50 (1988).

[232] T. Kiess, Y. Shih, A. Sergienko, and C. Alley, "Einstein-Podolsky-Rosen-Bohm experiment using pairs of light quanta produced by type-II parametric down-conversion", Physical Review Letters **71**, 3893 (1993).

[233] P. Kwiat, K. Mattle, H. Weinfurter, A. Zeilinger, A. Sergienko, and Y. Shih, "New high-intensity source of polarization-entangled photon pairs", Physical Review Letters **75**, 4337 (1995).

[234] P. Kwiat, E. Waks, A. White, I. Appelbaum, and P. Eberhard, "Ultrabright source of polarization-entangled photons", Physical Review A **60**, R773 (1999).

[235] O. Benson, C. Santori, M. Pelton, and Y. Yamamoto, "Regulated and entangled photons from a single quantum dot", Physical Review Letters **84**, 2513 (2000).

[236] K. Edamatsu, G. Oohata, R. Shimizu, and T. Itoh, "Generation of ultraviolet entangled photons in a semiconductor", Nature **431**, 167–170 (2004).

[237] R. Stevenson, R. Young, P. Atkinson, K. Cooper, D. Ritchie, and A. Shields, "A semiconductor source of triggered entangled photon pairs", Nature **439**, 179–182 (2006).

[238] N. Akopian, N. Lindner, E. Poem, Y. Berlatzky, J. Avron, D. Gershoni, B. Gerardot, and P. Petroff, "Entangled photon pairs from semiconductor quantum dots", Physical Review Letters **96**, 130501 (2006).

[239] J. Claudon, J. Bleuse, N. Malik, M. Bazin, P. Jaffrennou, N. Gregersen, C. Sauvan, P. Lalanne, and J.-M. Gérard, "A highly efficient single-photon source based on a quantum dot in a photonic nanowire", Nature Photonics **4**, 174–177 (2010).

[240] O. Gazzano, S. Michaelis de Vasconcellos, C. Arnold, A. Nowak, E. Galopin, I. Sagnes, L. Lanco, A. Lemaître, and P. Senellart, "Bright solid-state sources of indistinguishable single photons", Nature Communications **4**, 1425 (2013).

[241] Y. Chen, M. Zopf, R. Keil, F. Ding, and O. Schmidt, "Highly-efficient extraction of entangled photons from quantum dots using a broadband optical antenna", Nature Communications **9**, 2994 (2018).

[242] J. Liu, R. Su, Y. Wei, B. Yao, S. Silva, Y. Yu, J. Iles-Smith, K. Srinivasan, A. Rastelli, J. Li, and X. Wang, "A solid-state source of strongly entangled photon pairs with high brightness and indistinguishability", Nature Nanotechnology **14**, 586–593 (2019).

[243] D. Gammon, E. Snow, B. Shanabrook, D. Katzer, and D. Park, "Fine structure splitting in the optical spectra of single GaAs quantum dots", Physical Review Letters **76**, 3005 (1996).

[244] D. Huber, M. Reindl, S. F. Covre da Silva, C. Schimpf, J. Martín-Sánchez, H. Huang, G. Piredda, J. Edlinger, A. Rastelli, and R. Trotta, "Strain-tunable GaAs quantum dot: a nearly dephasing-free source of entangled photon pairs on demand", Physical Review Letters **121**, 033902 (2018).

[245] I. Inlek, C. Crocker, M. Lichtman, K. Sosnova, and C. Monroe, "Multispecies trapped-ion node for quantum networking", Physical Review Letters **118**, 250502 (2017).

[246] P. Drmota, D. Main, D. Nadlinger, B. Nichol, M. Weber, E. Ainley, A. Agrawal, R. Srinivas, G. Araneda, C. Ballance, and D. Lucas, "Robust quantum memory in a trapped-ion quantum network node", Physical Review Letters **130**, 090803 (2023).

[247] M. Taylor and W. Bowen, "Quantum metrology and its application in biology", Physics Reports **615**, 1–59 (2016).

[248] R. Camphausen, A. Sansa Perna, Á. Cuevas, A. Demuth, J. Arrés Chillón, M. Gräfe, F. Steinlechner, and V. Pruneri, "Fast quantum-enhanced imaging with visible-wavelength entangled photons", Optics Express **31**, 6039–6050 (2023).

[249] J.-B. Trebbia, P. Tamarat, and B. Lounis, "Indistinguishable near-infrared single photons from an individual organic molecule", Physical Review A **82**, 063803 (2010).

[250] M. Rezai, J. Wrachtrup, and I. Gerhardt, "Polarization-entangled photon pairs from a single molecule", Optica **6**, 34–40 (2019).

[251] D. Wang, T. Neuman, and P. Narang, "Dipole-coupled emitters as deterministic entangled photon-pair sources", Physical Review Research **2**, 043328 (2020).

[252] F. Sciarrino, G. Vallone, G. Milani, A. Avella, J. Galinis, R. Machulka, A. Perego, K. Spasibko, A. Allevi, M. Bondani, and P. Mataloni, "High degree of entanglement and nonlocality of a two-photon state generated at 532 nm", The European Physical Journal Special Topics **199**, 111–125 (2011).

[253] A. Sansa Perna, E. Ortega, M. Gräfe, and F. Steinlechner, "Visible-wavelength polarization-entangled photon source for quantum communication and imaging", Applied Physics Letters **120** (2022).

[254] M. Müller, S. Bounouar, K. Jöns, M. Glässl, and P. Michler, "On-demand generation of indistinguishable polarization-entangled photon pairs", Nature Photonics **8**, 224–228 (2014).

[255] V. Ernst and P. Stehle, "Emission of radiation from a system of many excited atoms", Physical Review **176**, 1456 (1968).

[256] C. Raymond Ooi, Y. Rostovtsev, and M. Scully, "Two-photon correlation of radiation emitted by two excited atoms: Detailed analysis of a Dicke problem", Laser Physics **17**, 956–964 (2007).

[257] J. Altepeter, E. Jeffrey, and P. Kwiat, "Photonic state tomography", Advances in Atomic, Molecular, and Optical Physics **52**, 105–159 (2005).

[258] Á. Nodar, R. Esteban, C. Maciel-Escudero, J. Lasa-Alonso, J. Aizpurua, and G. Molina-Terriza, "Preservation and destruction of the purity of two-photon states in the interaction with a nanoscatterer", arXiv preprint arXiv:2211.14244 (2022).

[259] R. Johne, N. Gippius, G. Pavlovic, D. Solnyshkov, I. Shelykh, and G. Malpuech, "Entangled photon pairs produced by a quantum dot strongly coupled to a microcavity", Physical Review Letters **100**, 240404 (2008).

[260] A. Dousse, J. Suffczyński, A. Beveratos, O. Krebs, A. Lemaître, I. Sagnes, J. Bloch, P. Voisin, and P. Senellart, "Ultrabright source of entangled photon pairs", Nature **466**, 217–220 (2010).

[261] X. L. Chu, V. Angelopoulou, P. Lodahl, and N. Rotenberg, "Subradiant states for two imperfect quantum emitters coupled by a nanophotonic waveguide", Physical Review A **106**, 053702 (2022).

[262] C. Cohen-Tannoudji, B. Diu, and F. Laloe, "Quantum Mechanics, Volume 1", Quantum Mechanics **1**, 898 (1986).

[263] E. Jaynes, "Information theory and statistical mechanics", Physical Review **106**, 620 (1957).

[264] A. Uhlmann, "The "transition probability" in the state space of a$*$-algebra", Reports on Mathematical Physics **9**, 273–279 (1976).

[265] R. Jozsa, "Fidelity for mixed quantum states", Journal of Modern Optics **41**, 2315–2323 (1994).

[266] V. Berestetskii, E. Lifshitz, and V. Pitaevskii, *Relativistic Quantum Theory. Part 1* (Pergamon Press).

[267] G. Hegerfeldt, "The quantum jump approach and some of its applications", in *Time in Quantum Mechanics-Vol. 2* (Springer, 2009) pp. 127–174.

Glossary